# MIDUS Transportation Package Safety Analysis Report

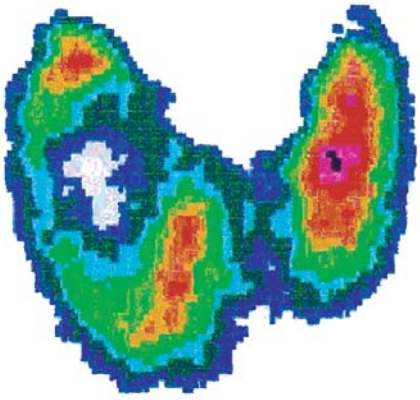

*TYC01-1600*
*Docket No. 71-9320*

ENERGYSOLUTIONS

# MIDUS Transportation Package
## Safety Analysis Report

**Revision 7**
**March 2022**

**Document No. TYC01-1600**
**Docket No. 71-9320**

Prepared by:
Energy*Solutions*

This page intentionally blank.

## Table of Contents

| Section | Title | Page |
|---|---|---|
| 1 | General Information | 1-1 |
| 1.1 | Introduction | 1-1 |
| 1.2 | Package Description | 1-1 |
| 1.2.1 | Packaging | 1-1 |
| 1.2.2 | Contents | 1-5 |
| 1.2.3 | Special Requirements for Plutonium | 1-8 |
| 1.2.4 | Operational Features | 1-8 |
| 1.3 | Appendix | 1-9 |
| 1.3.1 | References | 1-9 |
| 1.3.2 | Drawings | 1-9 |
| 2 | Structural Evaluation | 2-1 |
| 2.1 | Description of Structural Design | 2-2 |
| 2.1.1 | Discussion | 2-2 |
| 2.1.2 | Design Criteria | 2-4 |
| 2.1.3 | Weights and Centers of Gravity | 2-12 |
| 2.1.4 | Identification of Codes and Standards for Package Design | 2-13 |
| 2.2 | Materials | 2-31 |
| 2.2.1 | Material Properties and Specifications | 2-31 |
| 2.2.2 | Chemical, Galvanic, or Other Reactions | 2-35 |
| 2.2.3 | Effects of Radiation on Materials | 2-35 |
| 2.3 | Fabrication and Examination | 2-49 |

## Table of Contents (continued)

| Section | Title | Page |
|---|---|---|
| 2.3.1 | Fabrication | 2-49 |
| 2.3.2 | Examination | 2-52 |
| 2.4 | General Requirements for All Packages | 2-55 |
| 2.4.1 | Minimum Package Size | 2-55 |
| 2.4.2 | Tamper-Indicating Feature | 2-55 |
| 2.4.3 | Positive Closure | 2-55 |
| 2.5 | Lifting and Tie-down Standards for All Packages | 2-56 |
| 2.5.1 | Lifting Devices | 2-56 |
| 2.5.2 | Tie-Down Devices | 2-60 |
| 2.6 | Normal Conditions of Transport | 2-69 |
| 2.6.1 | Heat | 2-69 |
| 2.6.2 | Cold | 2-77 |
| 2.6.3 | Reduced External Pressure | 2-78 |
| 2.6.4 | Increased External Pressure | 2-81 |
| 2.6.5 | Vibration | 2-84 |
| 2.6.6 | Water Spray | 2-87 |
| 2.6.7 | Free Drop | 2-87 |
| 2.6.8 | Corner Drop | 2-104 |
| 2.6.9 | Compression | 2-104 |
| 2.6.10 | Penetration | 2-107 |
| 2.7 | Hypothetical Accident Conditions | 2-108 |
| 2.7.1 | Free Drop | 2-108 |

## Table of Contents (continued)

| Section | Title | Page |
|---|---|---|
| 2.7.2 | Crush | 2-150 |
| 2.7.3 | Puncture | 2-150 |
| 2.7.4 | Thermal | 2-163 |
| 2.7.5 | Immersion — Fissile Material | 2-164 |
| 2.7.6 | Immersion — All Packages | 2-164 |
| 2.7.7 | Deep Water Immersion Test (for Type B Packages Containing More than $10^5$ $A_2$) | 2-168 |
| 2.7.8 | Summary of Damage | 2-168 |
| 2.8 | Accident Conditions for Air Transport of Plutonium | 2-170 |
| 2.9 | Accident Conditions for Fissile Material Packages for Air Transport | 2-170 |
| 2.10 | Special Form | 2-170 |
| 2.11 | Fuel Rods | 2-170 |
| 2.12 | Appendix | 2-171 |
| 2.12.1 | References | 2-171 |
| 2.12.2 | Computer Code Descriptions | 2-173 |
| 2.12.3 | Dynamic Load Factors | 2-174 |
| 2.12.4 | Confirmatory Tests | 2-177 |
| 3 | Thermal Evaluation | 3-1 |
| 3.1 | Description of Thermal Design | 3-2 |
| 3.1.1 | Design Features | 3-2 |
| 3.1.2 | Content's Decay Heat | 3-3 |
| 3.1.3 | Summary Tables of Temperatures | 3-3 |

## Table of Contents (continued)

| Section | Title | Page |
|---|---|---|
| 3.1.4 | Summary Tables of Maximum Pressures | 3-4 |
| 3.2 | Material Properties and Component Specifications | 3-8 |
| 3.2.1 | Material Properties | 3-8 |
| 3.2.2 | Component Specifications | 3-8 |
| 3.3 | Thermal Evaluation under Normal Conditions of Transport | 3-14 |
| 3.3.1 | Heat and Cold | 3-16 |
| 3.3.2 | Maximum Normal Operating Pressure | 3-17 |
| 3.4 | Thermal Evaluation under Hypothetical Accident Conditions | 3-25 |
| 3.4.1 | Initial Conditions | 3-25 |
| 3.4.2 | Fire Test Conditions | 3-25 |
| 3.4.3 | Maximum Temperatures and Pressure | 3-29 |
| 3.4.4 | Maximum Thermal Stresses | 3-30 |
| 3.4.5 | Accident Conditions for Fissile Material Packages for Air Transport | 3-30 |
| 3.5 | Appendix | 3-37 |
| 3.5.1 | References | 3-37 |
| 3.5.2 | Computer Analysis Results | 3-39 |
| 3.5.3 | Heat Transfer Correlations | 3-39 |
| 3.5.4 | Foam Response to Fire | 3-43 |
| 3.5.5 | Radiolytic Gas Generation in Mallinckrodt Produced $^{99}$Mo Solutions | 3-48 |
| 3.5.6 | Hydrogen Generation in Mallinckrodt Produced $^{99}$Mo Solutions | 3-49 |
| 4 | Containment | 4-1 |
| 4.1 | Description of the Containment System | 4-1 |

## Table of Contents (continued)

| Section | Title | Page |
|---|---|---|
| 4.2 | Containment under Normal Conditions of Transport | 4-5 |
| 4.2.1 | NCT Pressurization of the Containment Vessel | 4-5 |
| 4.2.2 | NCT Containment Criterion | 4-5 |
| 4.2.3 | Compliance with NCT Containment Criterion | 4-5 |
| 4.3 | Containment under Hypothetical Accident Conditions | 4-5 |
| 4.3.1 | HAC Pressurization of the Containment Vessel | 4-5 |
| 4.3.2 | HAC Containment Criterion | 4-5 |
| 4.3.3 | Compliance with HAC Containment Criterion | 4-5 |
| 4.4 | Leak Rate Tests for Type B Packages | 4-6 |
| 4.4.1 | Fabrication Leak Rate Test | 4-6 |
| 4.4.2 | Maintenance Leak Rate Test | 4-6 |
| 4.4.3 | Periodic Leak Rate Test | 4-6 |
| 4.4.4 | Pre-shipment Leak Rate Test | 4-6 |
| 4.5 | Appendix | 4-7 |
| 5 | Shielding Evaluation | 5-1 |
| 5.1 | Description of Shielding Design | 5-1 |
| 5.1.1 | Design Features | 5-1 |
| 5.1.2 | Summary of Maximum Radiation Levels | 5-3 |
| 5.2 | Source Specification | 5-7 |
| 5.2.1 | Gamma Source | 5-7 |
| 5.2.2 | Neutron Source | 5-7 |
| 5.3 | Shielding Model | 5-9 |

## Table of Contents (continued)

| Section | Title | Page |
|---|---|---|
| 5.3.1 | Configuration of Source and Shielding | 5-9 |
| 5.3.2 | Material Properties | 5-12 |
| 5.4 | Shielding Evaluation | 5-22 |
| 5.4.1 | Methods | 5-22 |
| 5.4.2 | Input and Output Data | 5-22 |
| 5.4.3 | Flux-to-Dose-Rate Conversion | 5-23 |
| 5.4.4 | External Radiation Levels | 5-23 |
| 5.5 | Appendix | 5-38 |
| 5.5.1 | References | 5-38 |
| 6 | Criticality Evaluation | 6-1 |
| 7 | Package Operations | 7-1 |
| 7.1 | Package Loading | 7-1 |
| 7.1.1 | Preparation for Loading | 7-1 |
| 7.1.2 | Loading of Contents | 7-3 |
| 7.1.3 | Preparation for Transport | 7-4 |
| 7.2 | Package Unloading | 7-6 |
| 7.2.1 | Receipt of Package from Carrier | 7-6 |
| 7.2.2 | Removal of Contents | 7-7 |
| 7.3 | Preparation of Empty Package for Transport | 7-7 |
| 7.4 | Other Operations | 7-9 |
| 7.4.1 | Pre-Shipment Leak Rate Test | 7-9 |

## Table of Contents (continued)

| Section | Title | Page |
|---|---|---|
| 7.5 | Appendix | 7-10 |
| 7.5.1 | References | 7-10 |
| 8 | Acceptance tests and maintenance program | 8-1 |
| 8.1 | Acceptance Tests | 8-1 |
| 8.1.1 | Visual Inspections and Measurements | 8-1 |
| 8.1.2 | Weld Examinations | 8-1 |
| 8.1.3 | Structural and Pressure Tests | 8-1 |
| 8.1.4 | Leakage Tests | 8-1 |
| 8.1.5 | Component and Material Tests | 8-2 |
| 8.1.6 | Shielding Tests | 8-3 |
| 8.1.7 | Thermal Tests | 8-3 |
| 8.1.8 | Miscellaneous Tests | 8-3 |
| 8.2 | Maintenance Program | 8-4 |
| 8.2.1 | Structural and Pressure Tests | 8-4 |
| 8.2.2 | Periodic and Maintenance Leak Test | 8-4 |
| 8.2.3 | Component and Material Tests | 8-5 |
| 8.2.4 | Thermal Tests | 8-7 |
| 8.2.5 | Miscellaneous Tests | 8-7 |
| 8.3 | Appendix | 8-10 |
| 8.3.1 | References | 8-10 |
| 9 | Evaluation of Content #02 | 9-1 |

## Table of Contents (continued)

| Section | Title | Page |
|---|---|---|
| 9.1 | Content #02 – General Information | 9-1 |
| 9.2 | Content #02 – Structural Evaluation | 9-3 |
| 9.3 | Content #02 – Thermal Evaluation | 9-3 |
| 9.4 | Content #02 –Containment Evaluation | 9-4 |
| 9.5 | Content #02 – Shielding Evaluation | 9-4 |
| 9.5.1 | Source Specification | 9-4 |
| 9.6 | Content #02 – Criticality Evaluation | 9-5 |
| 9.7 | Content #02 – Operating Procedures | 9-5 |
| 9.8 | Content #02 – Acceptance Tests and Maintenance Program | 9-5 |

## List of Tables

| Section | Title | Page |
|---|---|---|
| Table 2-1 | Load Combinations for Normal Conditions of Transport | 2-14 |
| Table 2-2 | Load Combinations for Hypothetical Accident Conditions | 2-15 |
| Table 2-3 | Containment System Allowable Stress Design Criteria | 2-16 |
| Table 2-4 | Non-Containment Component Allowable Stress Design Criteria | 2-17 |
| Table 2-5 | Cask Shell Buckling Geometric Parameters | 2-18 |
| Table 2-6 | Buckling Reduction Factors and Theoretical Buckling Stresses | 2-19 |
| Table 2-7 | Cask Shell Allowable Buckling Stresses | 2-20 |
| Table 2-8 | Package Mass Properties Summary | 2-21 |
| Table 2-9 | MIDUS Package ASME BPVC Section III, Division 1, Requirements Compliance Summary (4 Pages) | 2-22 |
| Table 2-10 | MIDUS Package ASME BPVC Section III, Division 3, Requirements Compliance Summary (3 Pages) | 2-25 |
| Table 2-11 | Packaging Material Specifications (2 Pages) | 2-37 |
| Table 2-12 | Mechanical Properties of Type 304 Stainless Steel | 2-39 |
| Table 2-13 | Mechanical Properties of Type 316 Stainless Steel | 2-39 |
| Table 2-14 | Mechanical Properties of A240, Type XM-19 Stainless Steel | 2-40 |
| Table 2-15 | Mechanical Properties of SA-320/A320, Grade L43 Bolting Steel | 2-40 |
| Table 2-16 | Mechanical Properties of A193, Grade B8 Bolting Steel | 2-41 |
| Table 2-17 | Stainless Steel True Stress-Strain Design Data | 2-42 |
| Table 2-18 | SA-320/A320, Grade L43 Alloy Bolting Steel Plastic-Kinematic Properties | 2-42 |
| Table 2-19 | Mechanical Properties of DU Alloy | 2-43 |
| Table 2-20 | Overpack Foam Static Stress-Strain Data at Room Temperature | 2-43 |
| Table 2-21 | Foam Dynamic Stress-Strain Properties | 2-44 |

## List of Figures (continued)

| Section | Title | Page |
|---|---|---|
| Table 2-22 – | Overpack Foam Upper- and Lower-Bound Dynamic Stress-Strain Data | 2-45 |
| Table 2-23 – | SB-152 Copper Sheet Plastic-Kinematic Properties | 2-45 |
| Table 2-24 – | Summary of MIDUS Material Interactions | 2-46 |
| Table 2-25 – | Tie-Down Reaction Loads | 2-63 |
| Table 2-26 – | Overpack Lid Lug Weld Stresses | 2-63 |
| Table 2-27 – | Cask Body Differential Thermal Expansion Summary | 2-73 |
| Table 2-28 – | Reduced External Pressure Stress Summary | 2-80 |
| Table 2-29 – | Increased External Pressure Stress Summary | 2-83 |
| Table 2-30 – | Cask Stress Summary, NCT Vibration | 2-86 |
| Table 2-31 – | NCT Free Drop Loads Summary | 2-96 |
| Table 2-32 – | Overpack Closure Bolt NCT Free Drop Stress Summary | 2-97 |
| Table 2-33 – | NCT Free Drop Equivalent-Static Acceleration Design Loads | 2-97 |
| Table 2-34 – | NCT Free Drop Stress Summary | 2-98 |
| Table 2-35 – | Cask Closure Bolt NCT Free Drop Stress Summary | 2-99 |
| Table 2-36 – | NCT Free Drop Buckling Evaluation Summary | 2-99 |
| Table 2-37 – | Summary of HAC Free Drop Cases Evaluated | 2-111 |
| Table 2-38 – | HAC End Drop Loads Summary | 2-118 |
| Table 2-39 – | Overpack Closure Bolt HAC End Drop Stress Summary | 2-118 |
| Table 2-40 – | HAC Bottom End Drop Maximum Stress Summary | 2-119 |
| Table 2-41 – | HAC Top End Drop Maximum Stress Summary | 2-119 |
| Table 2-42 – | HAC End Drop Buckling Evaluation Summary | 2-120 |
| Table 2-43 – | HAC Side Drop Loads Summary | 2-124 |

## List of Figures (continued)

**Section** **Title** **Page**

Table 2-44 – Overpack Closure Bolt HAC Side Drop Stress Summary ..... 2-124

Table 2-45 – HAC Side Drop Maximum Stress Summary..... 2-125

Table 2-46 – HAC Side Drop Buckling Evaluation Summary..... 2-125

Table 2-47 – HAC Corner Drop Loads Summary..... 2-129

Table 2-48 – Overpack Closure-Bolt HAC Corner Drop Stress Summary..... 2-129

Table 2-49 – HAC Bottom Oblique Drop Loads Summary ..... 2-135

Table 2-50 – HAC Top Oblique Drop Loads Summary..... 2-136

Table 2-51 – Overpack Closure-Bolt HAC Oblique Drop Stress Summary ..... 2-137

Table 2-52 – HAC Bottom Oblique Drop Maximum Stress Summary..... 2-138

Table 2-53 – HAC Top Oblique Drop Maximum Stress Summary ..... 2-139

Table 2-54 – HAC Oblique Drop Buckling Evaluation Summary..... 2-140

Table 2-55 – Summary of HAC Puncture Drop Cases Evaluated..... 2-154

Table 2-56 – HAC Puncture Drop Summary..... 2-154

Table 2-57 – Overpack Closure-Bolt HAC Puncture Drop Stress Summary..... 2-155

Table 2-58 – “HAC Immersion - All Packages” Maximum Stress Summary..... 2-166

Table 2-59 – Cask-Shell Buckling Stresses, Immersion - All Packages ..... 2-166

Table 3-1 – Summary of Package Temperatures for NCT ..... 3-5

Table 3-2 – Summary of Package Temperatures for HAC Thermal Test ..... 3-6

Table 3-3 – Summary Table of Maximum Pressures in the Containment System..... 3-6

Table 3-4 – Thermal Properties of Packaging Materials (2 Pages) ..... 3-10

Table 3-5 – Thermal Properties of Air..... 3-12

Table 3-6 – Package Surface Emissivity and Absorptivity Properties ..... 3-13

## List of Figures (continued)

**Section** **Title** **Page**

Table 3-7 – Calculated MNOP as a Function of Activity and Dispensed Volume ..... 3-19

Table 5-1 – Key Cask Body Shielding Parameters[1,2] ..... 5-4

Table 5-2 – Key Shield Lid Shielding Parameters..... 5-4

Table 5-3 – Summary Table of External NCT Radiation Levels ..... 5-5

Table 5-4 – Summary Table of External HAC Radiation Levels..... 5-5

Table 5-5 – Photon Source..... 5-8

Table 5-6 – Summary of Key Component Dimensions..... 5-13

Table 5-7 – Summary of Post-HAC Source Region Volumes ..... 5-14

Table 5-8 – Post-HAC Reductions in Foam Thickness ..... 5-14

Table 5-9 – Shielding Material Properties ..... 5-15

Table 5-10 – Photon Dose Rate Response Functions ..... 5-28

Table 8-1 – Package Maintenance Program Summary..... 8-9

## List of Figures

| Section | Title | Page |
|---|---|---|
| Figure 1-1 – | Content #01 Payload Internals | 1-7 |
| Figure 2-1 – | Cask Containment Component Stress Evaluation Locations | 2-28 |
| Figure 2-2 – | Cask Non-Containment Component Stress Section Locations | 2-29 |
| Figure 2-3 – | MIDUS Package Mass Properties Schematic | 2-30 |
| Figure 2-4 – | Stainless Steel True Stress-Strain Design Curves | 2-47 |
| Figure 2-5 – | Overpack Foam Dynamic Stress-Strain Curves | 2-48 |
| Figure 2-6 – | Package Lifting Free Body Diagram | 2-64 |
| Figure 2-7 – | Overpack Lifting Lug Weld Lifting Loads | 2-65 |
| Figure 2-8 – | Cask Closure Lid Quarter-Symmetry Finite Element Model | 2-65 |
| Figure 2-9 – | Acceptable Package Tie-Down Configuration | 2-66 |
| Figure 2-10 – | Tie-Down Cases Evaluated | 2-67 |
| Figure 2-11 – | MIDUS Package Tie-Down Finite Element Model | 2-68 |
| Figure 2-12 – | Overpack Lid Lug Weld Tie-Down Loading Diagram | 2-68 |
| Figure 2-13 – | MIDUS Cask Assembly Axisymmetric FE Model | 2-74 |
| Figure 2-14 – | Axisymmetric FE Model Contact Surfaces | 2-75 |
| Figure 2-15 – | Bounding NCT Heat Temperature Distribution | 2-76 |
| Figure 2-16 – | NCT Free Drop Impact Orientations | 2-100 |
| Figure 2-17 – | MIDUS Overpack 3-D Half-Symmetry Finite Element Model | 2-101 |
| Figure 2-18 – | Overpack Permanent Deformation, NCT Top Corner Drop (Case N4) | 2-102 |
| Figure 2-19 – | MIDUS Cask Assembly Half-Symmetry FE Model | 2-103 |
| Figure 2-20 – | MIDUS Overpack Outer Shell Finite Element Model | 2-106 |
| Figure 2-21 – | HAC Free Drop Impact Orientations | 2-112 |

## List of Figures (continued)

**Section** **Title** **Page**

Figure 2-22 – Overpack Permanent Deformation, HAC Hot Bottom-End Drop (Case H2) . 2-143

Figure 2-23 – Overpack Permanent Deformation, HAC Hot Top-End Drop (Case H4) ..... 2-144

Figure 2-24 – Overpack Permanent Deformation, HAC Hot Side Drop (Case H10)..... 2-145

Figure 2-25 – Overpack Permanent Deformation, HAC Hot Bottom-Corner Drop (Case H6) .. 2-146

Figure 2-26 – Overpack Permanent Deformation, HAC Hot Top-Corner Drop (Case H8) .. 2-147

Figure 2-27 – Overpack Permanent Deformation, HAC Hot 5° Bottom-End Oblique Drop (Case H12) ..... 2-148

Figure 2-28 – Overpack Permanent Deformation, HAC Hot 5° Top-End Oblique Drop (Case H20) ..... 2-149

Figure 2-29 – HAC Puncture Drop Impact Orientations ..... 2-156

Figure 2-30 – Overpack Deformation, HAC Hot Bottom-Center Puncture (Case P1) ..... 2-157

Figure 2-31 – Overpack Deformation, HAC Hot Bottom-Oblique Puncture (Case P2) ..... 2-158

Figure 2-32 – Overpack Deformation, HAC Hot Top-Center Puncture (Case P3A) ..... 2-159

Figure 2-33 – Overpack Deformation, HAC Hot Top-Oblique Puncture (Case P4)..... 2-160

Figure 2-34 – Overpack Deformation, HAC Hot Side-Center Puncture (Case P5) ..... 2-161

Figure 2-35 – Overpack Deformation, HAC Hot Side-Oblique Puncture (Case P6) ..... 2-162

Figure 2-36 – Immersion - All Packages, Applied Pressure and Temperature Loads..... 2-167

Figure 2-37 – MIDUS Cask Modal Analysis FE Model ..... 2-176

Figure 2-38 – Cask Body Containment Shell Cantilever Bending Mode Shape ..... 2-176

Figure 3-1 – Package Thermal Design Features ..... 3-7

Figure 3-2 – MIDUS Package Thermal Model for NCT ..... 3-20

Figure 3-3 – NCT Heat Temperature Transient Results ..... 3-21

## List of Figures (continued)

**Section** **Title** **Page**

Figure 3-4 – NCT Cold Temperature Transient Results ..... 3-22

Figure 3-5 – Package NCT Heat Temperature Distribution at Time of Peak Overpack Shell Temperature (28.5 Hours After Loading) ..... 3-23

Figure 3-6 – Package NCT Heat Temperature Distribution at Time of Peak Payload/Cavity Gas Temperature (34.25 Hours After Loading) ..... 3-24

Figure 3-7 – MIDUS Package HAC Thermal Model, Bottom End Drop Damage Configuration ..... 3-31

Figure 3-8 – MIDUS Package HAC Thermal Model, Top End Drop Damage Configuration 3-32

Figure 3-9 – MIDUS Package HAC Thermal Model, Side Drop Damage Configuration ..... 3-33

Figure 3-10 – Package Temperatures for HAC Thermal Test with Bottom End Damage ..... 3-34

Figure 3-11 – Package Temperatures for HAC Thermal Test with Top End Damage ..... 3-35

Figure 3-12 – Package Temperatures for HAC Thermal Test with Side Damage ..... 3-36

Figure 3-13 – TGA Analysis of Foam Decomposition in Nitrogen ..... 3-46

Figure 3-14 – Foam Recession vs. Density for 30-Minute Fire ..... 3-46

Figure 3-15 – Foam HAC Performance, Corrected for 1,475°F Flame Temperature ..... 3-47

Figure 4-1 – Containment System Overview ..... 4-3

Figure 4-2 – Package Containment Boundary ..... 4-4

Figure 5-1 – MIDUS Cask Shielding Features ..... 5-6

Figure 5-2 – MIDUS Package Shielding Model Overview (NCT Baseline Case) ..... 5-16

Figure 5-3 – Cask Body Top End Gaps (mm) All Models - NCT & HAC ..... 5-17

Figure 5-4 – Cleanliness Seal Area Gaps (mm) - NCT & HAC ..... 5-18

Figure 5-5 – Cask Body Bottom End Gaps (mm) NCT & HAC ..... 5-18

Figure 5-6 – Inverted NCT Model Geometries (Different Snap Ring Assumptions) ..... 5-19

## List of Figures (continued)

| Section | Title | Page |
|---|---|---|
| Figure 5-7 – Horizontal NCT Model Geometry | | 5-20 |
| Figure 5-8 – Spherical Source Cases NCT Model Geometry | | 5-21 |
| Figure 5-9 – Summary Profile for 1-Meter NCT Dose Rates | | 5-29 |
| Figure 5-10 – Top-End 1-Meter Dose Rate Profile | | 5-30 |
| Figure 5-11 – Side 1-Meter Dose Rate Profile | | 5-31 |
| Figure 5-12 – Bottom-End 1-Meter Dose Rate Profile | | 5-32 |
| Figure 5-13 – Summary Profile for Package Surface NCT Dose Rates | | 5-33 |
| Figure 5-14 – Top-End-Surface Dose Rate Profile | | 5-34 |
| Figure 5-15 – Side-Surface Dose Rate Profile | | 5-35 |
| Figure 5-16 – Bottom-Surface Dose Rate Profile | | 5-36 |
| Figure 5-17 – 1-Meter HAC Results | | 5-37 |
| Figure 7-1 - Shield Plug Fit-Up | | 7-4 |
| Figure 9-1 – Content #02 Payload Internals | | 9-2 |
| Figure 9-2 – Solid Source MCNP Model | | 9-4 |

## Nomenclature

| | |
|---|---|
| ALARA | At least as low as reasonably achievable |
| ASME | American Society of Mechanical Engineers |
| B&PV | Boiler and Pressure Vessel Code, the ASME B&PV Code |
| CMS | Computational modeling software |
| DU | Depleted uranium, the DU alloy used to construct MIDUS |
| HAC | Hypothetical accident conditions: the tests specified in 10 CFR 71.73, or the condition of the packaging after such tests |
| LMC | Least material condition |
| MIDUS | Medical Isotope Depleted Uranium Shielded |
| MNOP | Maximum normal operating pressure |
| NCT | Normal conditions of transport: the tests specified in 10 CFR 71.71, or the condition of the packaging after such tests |
| Package | The packaging with its radioactive contents, or payload, as presented for transport. For MIDUS, the package includes the packaging plus the payload internals (the radioactive product, product container(s), and optional dunnage) |
| Packaging | The MIDUS cask assembly (cask body, shield plug, cask closure lid, cask shield lid, and fasteners) and overpack assembly (overpack base, overpack lid, and fasteners) |
| Product | Radioactive payload |
| SAR | Safety Analysis Report |
| Shield Lid | A shielded lid that installs onto the cask closure lid to provide additional gamma shielding in the post-HAC configuration |
| Shield Plug | The cylindrical plug that provides gamma shielding for normal operating conditions |
| T.I. | Transport index, as defined in 10 CFR 71.4 |

This page intentionally blank.

# 1 GENERAL INFORMATION

## 1.1 Introduction

This Safety Analysis Report (SAR) describes a reusable Type B(U) package design named MIDUS, which stands for Medical Isotope Depleted Uranium Shielded Transport Package. MIDUS will be used to transport $^{99}$Mo, which decays to $^{99m}$Tc, an important source for medical imaging. The package will deliver enough $^{99}$Mo for millions of annual patient doses. The package is also suitable for other radioisotope sources as defined in Section 1.2.2.

The package is designed for non-exclusive use conveyance. The contents are normal or special form, non-fissile, and are Category II as defined by Regulatory Guide 7.11 [1.1].

The package is designed and manufactured in accordance with the Energy*Solutions*' 10 CFR 71, Subpart H quality assurance program, NRC approval number 0935.

This SAR demonstrates that the package meets the applicable requirements of 10 CFR 71. The basis for qualification is the safety analysis contained herein, supplemented by the results of full-scale confirmatory testing. The testing validates the analytical tools used in the safety analyses, and it physically demonstrates the robustness of the design. The complete test report is included in this SAR in Section 2.12.4.

## 1.2 Package Description

### 1.2.1 Packaging

Due to the short half-life of $^{99}$Mo, the package is designed to be as small and light as possible to allow conveyance by land or air. The overall dimensions are 520 mm diameter by 551 mm high, and the maximum weight is 330 kg.

Drawing TYC01-1601 in Section 1.3.2 shows the package general arrangement, including the payload specification, major cask features, and packaging markings. The remainder of the drawings include general arrangements of the overpack and cask assemblies, containment system, closure devices, gamma shielding, heat transfer features, energy absorbing features, and lifting and tie-down features.

#### 1.2.1.1 Overpack

Drawing TYC01-1602 in Section 1.3.2 shows the general arrangement of the overpack, including overall dimensions, material specifications, and weld callouts for the shells.

The overpack is a two-piece stainless steel shell filled with polyurethane foam. The foam is discussed in Section 1.2.1.7. The lid unit has four welded stainless steel lugs used for lifting and tie-down purposes. The base unit has a bottom flange with four integral lugs that may be used for additional tie-downs as needed. The outer shell is relatively thick for resistance to the normal

wear and tear of frequent use. The inner shell is relatively thinner to obtain the desired response to the hypothetical accident condition (HAC) specified in 10 CFR 71.51. This package crushes from the inside-out during the drop.

The inside radius at the top end of the overpack base unit is chamfered to provide lead-in for insertion of the cask during loading operations. The overpack flange is dog-leg shaped to provide a barrier for moisture and dirt. The flange mates snugly at the bolting ring to provide shear resistance in the drop.

Eight recessed alloy steel bolts fasten the overpack lid to the base unit. The design of the overpack closure is described below in Section 1.2.1.4.

Each of the lid and base units have four holes leading into the foam cavity. The holes are plugged with nylon screws intended to melt during the HAC fire test, providing pressure relief from the hot gas generated by the foam. This feature helps prevent the overpack shell from bursting during the fire, thus keeping the foam from direct contact with the flames. The thermal relief plugs have elastomeric O-rings to protect the foam from weather.

The overpack base unit has a copper thermal shunt, the thermal spider, which is brazed to the inner and outer shell. The thermal spider is described in Section 1.2.1.6 below.

Polymeric dunnage may be placed in the annular space between the cask assembly and overpack as needed to minimize scuffing or other wear.

A tamper-indicating security seal provides assurance that the package cannot be opened inadvertently and provides evidence of unauthorized opening if it occurs.

### 1.2.1.2 Cask Assembly

Drawing TYC01-1602 in Section 1.3.2 shows the cask assembly general arrangement, including overall dimensions, material specifications, and weld callouts for the shells.

The cask assembly includes a cask body, closure lid, shield plug, contents, and a separate shield lid that is installed on top of the closure lid.

The cask body is constructed from stainless steel and depleted uranium (DU). It has three main structural pieces and two DU parts. The containment shell is a monolithic, machined component that includes the cask inner shell, cask flange, and bolting circle. This part is described in detail in Section 1.2.1.3 below. The cask outer shell is welded to the containment shell and bottom shell, capturing the radial and bottom DU gamma shields. These shields are described below in Section 1.2.1.5.

The cask flange has two O-ring seals: an inner containment seal, and an outer test seal. The flange has a recessed step on the edge that forms a shear lip for the closure lid and prevents the closure bolts from shearing under transverse impact loads.

The shield plug is a DU core clad in stainless steel. It has a tapered bottom to assist remote insertion and reduce gamma streaming. The tapered surface has a "cleanliness" O-ring that serves two purposes. First, it provides a housekeeping seal which is useful as a redundant barrier for the $^{99}$Mo production facility. Second, it provides enough compliance so that the shield plug protrudes slightly above the plane of the cask flange. When the cask lid is bolted shut, the cleanliness seal compresses, assuring that the shield plug is in close contact with the closure lid. This feature reduces the potential volume of fluid that can collect between the shield plug and closure lid in the worst-case HAC scenario, thus reducing the accident dose rates to as low as reasonably achievable.

The cask closure lid is secured by eight recessed alloy steel bolts, which are described in Section 1.2.1.4. The lid has a test port that communicates with the space between the test and containment O-rings. The test port has an elastomeric seal to protect the cask O-ring interspace from dust and moisture. The closure lid has two tapped holes with threaded inserts used for lifting the cask to and from the overpack. Two more threaded holes with thread inserts are located near the outer perimeter of the lid for attaching the shield lid. The closure lid's top surface has a warning marking to remind operators that the shield lid must be installed before closing the overpack.

The shield lid is a stainless steel-clad DU plate designed to maintain dose rates within allowable limits under the worst-case HAC scenario. If the product were to breach the product container(s) and the shield plug cleanliness seal, then the product could migrate up and around the shield plug, thereby bypassing most of the package's top end gamma shielding. The shield lid provides the extra required top end axial shielding *outside* the containment boundary. The shield lid is fastened to the cask closure lid using two captive bolts. The captive bolts are an operational aid, serving as a lift point and helping to minimize damage and loss of the bolts. By preventing separation of the shield lid in an end drop event, the shield lid fasteners also prevent radiation streaming between the shield lid and cask assembly.

### 1.2.1.3 Containment System

Drawing TYC01-1604 in Section 1.3.2 shows the specifications for the package containment system, including the location of the containment boundary, and the specifications for materials of construction, surface finishes, and key dimensions and tolerances.

The containment boundary has no welds, valves, pressure relief devices, or penetrations of any kind. Chapter 4 discusses the containment design in further detail.

### 1.2.1.4 Closure Devices

Drawing TYC01-1605 in Section 1.3.2 shows the specifications for the package closure devices.

The cask body closure is designed to protect the eight closure bolts from damage due to puncture and shear. The closure bolts are recessed in the lid to minimize damage by direct impact. The closure lid has a shear lip feature to prevent the bolts from being loaded in shear by transverse impact loads. The bolt holes are fitted with threaded inserts for improved maintenance.

The overpack closure is designed to protect its eight closure bolts in a similar fashion. The bolts are recessed, and the overpack lid has a shear lip, similar to the cask body. The closure is designed with shear pockets to further prevent shear loading of the bolts in oblique drops. The overpack closure bolt holes are also fitted with threaded inserts for improved maintenance.

#### 1.2.1.5 Gamma Shielding

Drawing TYC01-1606 in Section 1.3.2 shows the specifications for the package gamma shielding.

Two DU parts provide the primary gamma shielding in the cask body: one radial piece, and an interlocking bottom piece. The joint is a stepped design to reduce radiation streaming. The shield plug has a third DU block. The removable shield lid has the fourth DU block in the form of a disk.

#### 1.2.1.6 Heat Transfer Features

Drawing TYC01-1607 in Section 1.3.2 shows the specifications for the package heat transfer features.

The package generates a small amount of heat, which must be dissipated. Section 3.1.2 discusses the package heat generation. Heat flows from package top end through the steel in the overpack flange. The thermal spider provides the corresponding heat flow path through the bottom end of the packaging.

The thermal spider is constructed from copper and brazed to the bottom of the overpack inner shell. The legs are brazed to the overpack outer shell, near the base flange. The base flange provides a relatively large thermal mass of stainless steel that helps distribute the heat evenly.

The overpack foam serves as both an energy absorbing material and as thermal protection in the HAC fire event. The foam is discussed in Section 1.2.1.7 below.

During the fire, the thermal relief plugs discussed in Section 1.2.1.1 above are designed to melt and blow out of the overpack shell, reducing the overpack cavity pressure and allowing heat to escape via mass transfer.

#### 1.2.1.7 Energy Absorbing Features

Drawing TYC01-1608 in Section 1.3.2 shows the specifications for the package's energy absorbing features. The polyurethane foam in the overpack is the primary energy absorbing feature for the free HAC drop.

The only penetrations through the overpack shells are the thermal relief plug ports, which have O-ring seals for weather and dust protection. The shells protect the foam from deterioration due to sunlight, atmospheric pollutants, or biological matter.

### 1.2.1.8 Lifting and Tie-Down Devices

Drawing TYC01-1609 in Section 1.3.2 shows the specifications for the package lifting and tie-down features.

There are four lifting/tie-down lugs on the overpack lid and four tie-down lugs on the overpack base. The lugs are sized for a standard-sized anchor shackle. Sections 2.5.1 and 2.5.2 describe the design and analysis of the lifting and tie-downs.

## 1.2.2 Contents

The contents of the MIDUS package are discussed in the following subsections. The MIDUS package was first designed for a natrium molybdate solution containing up to 4,400 Ci of $^{99}$Mo, as described in Section 1.2.2.1 below. This payload is now referred to as Content #01 and all subsequent MIDUS payloads shall be identified with a unique sequential number. The safety analyses presented in Chapters 2 through 8 are for Content #01, but may also be applicable for other contents, as described in Chapters 9 and above. For clarity, the chapter material is not revised for additional contents. Instead, evaluations to demonstrate that the additional contents comply with the applicable performance requirements of 10 CFR 71 are provided in the SAR addenda beginning with Chapter 9.

### 1.2.2.1 Content #01 - $^{99}$Mo as Natrium Molybdate Solution

Content #01 is a liquid payload, or product, consisting of $^{99}$Mo with its daughter products as natrium molybdate ($NaNO_3$ 1M / NaOH 0.2M). This payload is non-fissile and does not generate neutrons. The specification for Content #01 is provided on Drawing No. TYC01-1601 in Section 1.3.2 and discussed below.

The maximum product activity is 4,400 Ci of $^{99}$Mo at the time of shipment. Section 5.2.1 discusses the photon source term calculations, including all significant equilibrium daughter products. Section 3.1.2 discusses the payload's maximum calculated thermal source term. The maximum product *specific* activity is 60 Ci/ml $^{99}$Mo at the time of shipment. The specific activity affects the concentration of the potential radiological source terms for HAC. Section 5.3.1.2 describes the shielding assumptions made for HAC.

The product generates gas by radiolytic decomposition. This gas production affects package internal pressures and the composition of the internal gas mixture. The safety evaluations are based on experimental data for $^{99}$Mo product solution produced by Mallinckrodt Medical, B.V., therefore the activity specifications above are only valid for Mallinckrodt-produced product solution.

The product volume may vary from 0 to 150 ml. The product volume affects potential gas pressures in the product bottle and cask containment. The package's maximum normal operating pressure (MNOP) is discussed further in Section 3.3.2.

The package materials of construction have been evaluated and are compatible with the chemical form of the product. Section 2.2.2 discusses the materials evaluation in further detail.

The payload internals for Content #01 include a user-supplied product bottle, secondary container, and snap ring, illustrated in Figure 1-1. These items are important for the $^{99}$Mo manufacturing process and will always be present during shipping. Optional dunnage may be included in the form of a spacer to reduce vibration of the secondary container during shipment.

The product bottle is a stainless steel flask with a stainless steel cap sealed by a compression fitting metal-to-metal seal. It has a one-piece body with a welded base ring for stability. The design pressure for the product bottle is much higher than the package MNOP and the metal-to-metal seal offers containment-grade closure, although no credit is taken for this as containment.

The secondary container serves a housekeeping function in the $^{99}$Mo manufacturing process. It is constructed from stainless steel and it provides a second barrier to the payload solution when its lid is installed. The lid is also constructed from stainless steel, and the seal is an elastomeric O-ring.

The snap ring has a threaded stud that screws into the bottom of the package's shield plug. It allows the other payload internals to be handled remotely in the $^{99}$Mo production facility hot cell by use of spring-loaded detent-balls that engage the groove on top of the secondary container lid. The snap ring is constructed from stainless steel.

The maximum volume of the product bottle, secondary container, secondary container O-ring, snap ring, and dunnage is 125 ml. This is the volume of the materials of construction, not counting enclosed spaces. It is necessary to specify this volume because it impacts the pressure buildup during shipment.

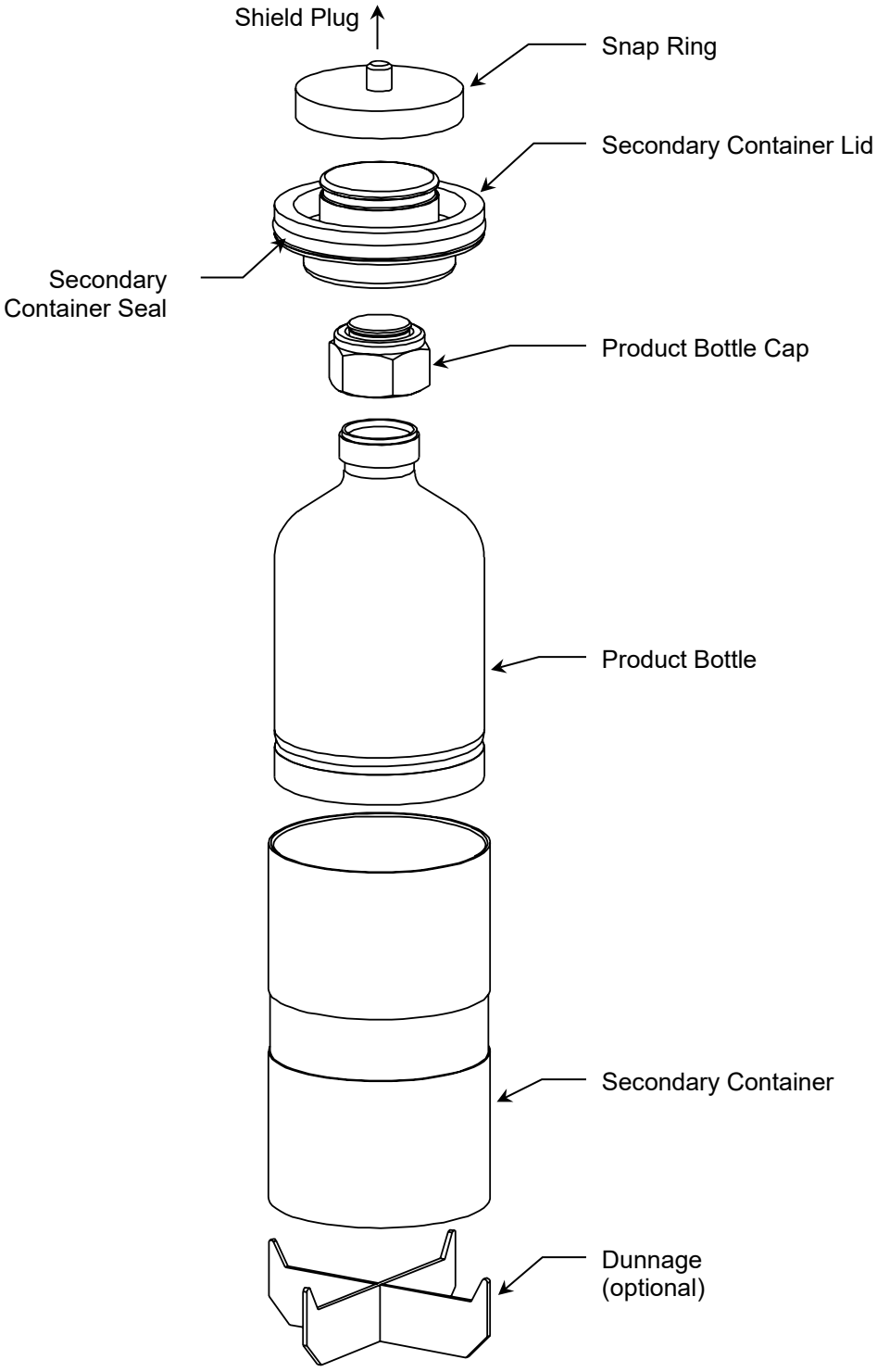


**Figure 1-1 – Content #01 Payload Internals**

#### 1.2.2.2 Content #02 - $^{99}$Mo as Metallic Molybdenum

Content #02 is specified on Drawing No. TYC01-1601 in Section 1.3.2, and described further in Section 9.1. Chapter 9 contains the safety evaluations for Content #02.

### 1.2.3 Special Requirements for Plutonium

Not applicable.

### 1.2.4 Operational Features

The package has no special or complex operational features. All operational features are described in the general arrangement drawings in Section 1.3.2. Chapter 7 describes the operational steps, including use of the package's operational features.

# 1.3 Appendix

## 1.3.1 References

[1.1] Regulatory Guide 7.11, *Fracture Toughness Criteria of Base Material for Ferritic Steel Shipping Cask Containment Vessels with a Maximum Wall Thickness of 4 Inches (0.1 m)*, U.S. Nuclear Regulatory Commission, June 1991.

[1.2] NUREG/CR-5502, *Engineering Drawings for 10 CFR Part 71 Package Approvals*, U.S. Nuclear Regulatory Commission, May 1998.

## 1.3.2 Drawings

Drawings 1601 through 1609 show the package's general arrangement and design features in accordance with NUREG/CR-5502 [1.2]. The drawings refer to material specifications, welding requirements, inspection and test requirements, and dimensions as necessary to support the safety analyses.

| Drawing No. | Title | Rev. |
|---|---|---|
| TYC01-1601 | General Arrangement of Packaging and Contents | 2 |
| TYC01-1602 | General Arrangement of Cask Assembly | 2 |
| TYC01-1603 | General Arrangement of Overpack Assembly | 1 |
| TYC01-1604 | Containment System | 3 |
| TYC01-1605 | Closure Devices | 2 |
| TYC01-1606 | Gamma Shielding | 2 |
| TYC01-1607 | Heat Transfer Features | 0 |
| TYC01-1608 | Energy Absorbing Features | 0 |
| TYC01-1609 | Lifting and Tie-Down Devices | 0 |

Drawings withheld on the basis that they are Security-Related Information

This page intentionally blank.

# 2 STRUCTURAL EVALUATION

The structural evaluation of the MIDUS package demonstrates compliance with the applicable performance requirements of 10 CFR 71. The structural evaluation presented in the body of this chapter is for the liquid payload (i.e., Content #01) described in Section 1.2.2.1. For clarity, the body of this chapter is not revised extensively for additional contents. Instead, the structural evaluation of each additional payload is presented in SAR addenda, starting in Chapter 9. Compliance with the applicable general standards (§71.43) and lifting and tie-down standards (§71.45) is demonstrated in Sections 2.4 and 2.5, respectively. The structural evaluation for NCT tests (§71.71) and HAC tests (§71.73) presented in Sections 2.6 and 2.7, respectively, demonstrates that the structural components of the package satisfy the applicable structural design criteria of Subsections WB [2.1] and NF [2.2] of the ASME Boiler and Pressure Vessel Code. Furthermore, under NCT tests (§71.71), the package will experience no loss or dispersal of radioactive contents, no significant increase in external surface radiation levels, and no substantial reduction in the effectiveness of the packaging. Therefore, the package satisfies the requirements of §71.43(f) and §71.51(a)(1). The structural evaluation also shows that the cumulative package damage resulting from the HAC test sequence (§71.73) does not result in escape of other radioactive material exceeding a total amount of $A_2$ in one week, nor does it result in an external radiation dose rate that exceeds 10 mSv/h at 1 m from the external surface of the package. Thus, the package satisfies the requirements of §71.51(a)(2).

The structural evaluation of the package is performed by analysis using computational modeling software (CMS) and classical closed-form solutions (hand calculations). The analytic techniques used for the structural evaluation comply with guidance provided in Regulatory Guide 7.9 [2.3], as supplemented by Interim Staff Guidance – 21 (ISG-21) [2.4]. The ANSYS Mechanical and ANSYS LS-DYNA PC computer programs are used for the structural evaluation of the package. These computer programs are well-benchmarked and widely used for structural analyses of transportation packages for radioactive materials. Descriptions of these computer programs, including discussion of validation of the computer codes, are provided in Section 2.12.2. The computer models used for the structural evaluation are identified and described in the following sections.

The adequacy of the analytic techniques used to evaluate the package dynamic response to NCT and HAC free drop and puncture drop impacts is demonstrated by comparison to results of full-scale confirmatory drop tests. The confirmatory tests performed, along with comparisons to pretest predictions determined using the same analytic techniques used for the structural analysis of the package, are discussed in Section 2.12.4. The results confirm that the computer model developed to evaluate the dynamic response of the package for NCT and HAC drop tests provides accurate predictions of the cask rigid-body response, the structural response of the overpack assembly, and the extent of damage sustained by the overpack.

## 2.1 Description of Structural Design

### 2.1.1 Discussion

The principal structural members that are important to the safe operation of the package are the cask assembly, shield lid assembly, and overpack assembly. The cask is the central component of the package that provides containment of the radioactive contents, radiation shielding, and structural support. The shield lid provides supplemental shielding on the top end of the cask. The overpack limits the impact loads imparted to the cask under NCT and HAC free drop tests and insulates the cask from the effects of the HAC thermal test. The structural design of these assemblies is described in the following sections.

#### 2.1.1.1 Cask Assembly

The cask assembly includes a cask body assembly, a shield plug assembly, a closure lid assembly, and eight cask closure bolts. The shield plug is placed in the top end of the cask body and captured by the closure lid and closure bolts. The internal cylindrical cavity volume, which is formed by the cask body and shield plug, houses the payload.

The cask body consists of a stainless steel shell assembly that encases the cask body gamma shield components. The cask body shell assembly is constructed entirely from austenitic stainless steel material and is formed from three pieces: a containment shell, an outer shell, and an outer bottom. The containment shell and outer bottom are both machined from solid pieces of steel. The containment shell forms the inner shell for the cask cavity and shield plug regions, as well as the bolting flange for the cask closure. The top plate of the containment shell includes grooves that accommodate the containment and leak-test O-rings. A 3:1 taper transition is included between the containment shell wall that surrounds the shield plug cavity and the top flange to minimize stress concentration at the structural discontinuity. The containment shell bolting flange includes eight closure bolt holes, fitted with threaded inserts. The cask body outer shell is rolled from plate and formed with a full-penetration longitudinal seam weld. The outer shell is connected to the containment shell and outer bottom with full-penetration circumferential groove welds.

The cask body gamma shield, which is sealed inside the cask body shell, consists of two pieces: a bottom shield and radial shield. Both the cask body bottom shield and radial shield are fabricated from depleted uranium (DU) that is alloyed with 2% molybdenum by weight (U-2% Mo). A stepped interface is provided between the DU bottom shield and radial shield to minimize radiation streaming through the interface. The cask body assembly is designed with nominal radial clearances of 0.65 mm between the containment shell and radial shield and 0.35 mm between the outer shell and radial shield. The larger clearance on the inside of the radial shield assures that the containment shell will not support the weight of the radial shield when subjected to transverse loads, such as a side drop. A longitudinal clearance of 0.7 mm is provided between the bottom end of the cask containment shell and the top surface of the bottom shield to assure that the cask containment shell does not support the weight of the bottom shield when subjected to loads such as a top-end drop or top-corner drop.

The shield plug consists of U-2% Mo shielding material that is fully encased in stainless steel. The shield plug top plate has an integral lifting boss located on the centerline. The bottom end of the shield plug includes a pocket that accommodates the top end fitting of the payload hardware. The bottom corner of the shield plug casing is chamfered and includes a groove that houses an elastomeric "cleanliness" O-ring seal, whose function is to prevent radioactive material from contaminating the cavity spaces that surround the shield plug. The cleanliness O-ring seal is compressed when the closure lid is bolted to the cask body.

The closure lid is a circular plate that is equipped with a test port, holes for the closure bolts, and threaded holes for lifting the cask and attaching the shield lid. The eight equally spaced holes that accommodate the cask closure bolts include a recess for heads of the closure bolts. The two holes used for lifting the cask are fitted with threaded inserts. Two additional holes located near the perimeter of the closure lid are used to attach the shield lid to the cask. The closure lid includes an integral shear lip on the outer bottom edge that interfaces with the top end of the cask body. The closure lid shear lip is designed to resist all shear forces resulting from NCT and HAC impact loads, thereby protecting the closure bolts from shear failure. A shear pocket is machined into the outer top edge of the closure lid to accommodate the shield lid shear lip.

The cask containment system, which is designed for a maximum normal operating pressure (MNOP) of 700 kPa, is formed by the cask body containment shell, closure lid, containment O-ring seal, and eight closure bolts. There are no welds in the cask containment system since the cask containment shell is machined from a single, solid piece of steel. Furthermore, the containment boundary does not include any ports, valves, or pressure relief devices. The leak-test port in the cask closure lid is used to perform helium leak tests on the containment system during fabrication and pre-shipment pressure rise or drop leakage tests following cask assembly. A sealed plug is installed in the leak-test port prior to shipment to prevent debris or water from entering the leak-test port cavity.

#### 2.1.1.2 Shield Lid Assembly

The shield lid assembly, which provides additional shielding on the top end of the package, is bolted to the top end of the cask prior to installing the overpack lid. The shield lid consists of DU shield plate that is fully encased in a stainless steel shell assembly. The shield lid has an integral shear lip on the outer bottom edge that interfaces with the top end of the closure lid. The shield lid is attached to the top end of the closure lid by two captured socket head cap screws that are fabricated from austenitic stainless steel. The shield lid is lifted and handled using the two capture attachment bolts. The shield lid must be installed on the cask after its placement in the overpack base cavity. When the shield lid is installed, the cask lifting attachments and leak-test port on the closure lid are not accessible.

#### 2.1.1.3 Overpack Assembly

The overpack assembly consists of a base assembly and a lid assembly that are bolted together. The overpack has a flat bottom-end that provides a stable base for transport. Four high-strength steel lugs are attached to the overpack lid for lifting and tie-down of the package. The base of the

overpack also includes four integral lugs that may be used for additional tie-down attachments, but only in combination with the lid lugs, as described in Section 2.5.2.

The overpack base and lid assemblies are constructed in a similar manner. Both consist of a water-tight stainless steel shell assembly, inside which polyurethane foam is placed. The overpack base and lid shell are fabricated entirely from mild austenitic stainless steels, with the exception of the overpack lid lugs, which are fabricated from higher strength stainless steel material. The overpack base and lid shell are filled with LAST-A-FOAM® FR-3714 polyurethane foam with a nominal density of 13.5 $lb/ft^3$. The foam is placed in-situ with the direction of foam rise parallel to the longitudinal axis of the package. Following foam placement, stainless steel covers are welded over the foam pour holes to protect the foam from water intrusion and contamination.

The overpack base and lid both have 6 mm thick outer shells and 3.0 mm thick inner shells. The thicker outer shells provides a rugged exterior that is resistant to damage from normal handling and that prevents penetration and perforation under NCT and HAC loading. The thin inner shell of the overpack protects the foam from damage due to normal handling, but is designed to deform under NCT and HAC free drops, allowing the polyurethane foam to absorb energy and limit the impact loads imparted to the cask.

The overpack bolted closure, which includes the overpack base and lid bolting flanges and eight closure bolts made from high strength alloy steel bolting material, is designed to withstand all NCT and HAC tests without significant permanent deformation or bolt failure. The overpack base and lid bolting flanges are relatively large in comparison to the package size to accommodate a shear relief pocket on the overpack base flange for each closure bolt. The use of longer closure bolts and shear relief pockets allows the overpack closure bolts to flex without breaking under severe impact loads. Furthermore, the bolting flange also includes an integral shear lip that is designed to withstand shear loads resulting from impacts and to protect the overpack closure bolts from shear failure.

Thermal relief plugs are provided in the both the overpack base and lid to prevent over-pressurization of the shell assemblies during the HAC thermal test. The thermal relief plugs are nylon thumb screws with elastomeric O-ring seals that prevent water from intruding into the foam cavities under normal conditions, but are designed to melt under the extreme temperatures of a fire and to allow gasses generated by the foam to escape. Four thermal relief plugs are equally spaced around both the overpack lid bolting flange and overpack base tie-down flange. The number and locations of the thermal relief ports are designed to preclude blockage that could prevent pressure relief.

### 2.1.2 Design Criteria

The design criteria used for the structural design of the package is selected in accordance with the codes and standards identified in Section 2.1.4. Structural analyses of the package are performed for the applicable NCT tests [§71.71] and HAC tests [§71.73]. The combination of initial conditions used for the structural evaluation of each NCT and HAC test are discussed in Section 2.1.2.1. The stresses in the package structural components are calculated for the NCT

and HAC load combinations and compared to the allowable stress design criteria described in Section 2.1.2.2. Other structural failure modes, such as brittle buckling, fatigue, and brittle fracture, are evaluated using the design criteria discussed in Sections 2.1.2.3 through 2.1.2.5.

### 2.1.2.1 Load Combinations

The load combinations used for the structural evaluation of the package are developed in accordance with Regulatory Guide 7.8 [2.5]. The load combinations are based on Table 1 of Regulatory Guide 7.8, with additional load combinations for intermediate initial conditions that could possibly create a more limiting case for the package design. The NCT and HAC load combinations are summarized in Table 2-1 and Table 2-2.

### 2.1.2.2 Allowable Stresses

The pressure-retaining components of the cask containment system, which consist of the cask containment shell, closure lid, and closure bolts, are designed in accordance with the requirements of Subsection WB of the ASME Code [2.1]. In addition, the non-pressure-retaining circumferential weld that attaches the cask outer shell to the cask containment shell, is designed in accordance with the applicable requirements of Subsection WB of the ASME Code. The containment component stress intensity limits for NCT and HAC, which are developed in accordance with Figures WB-3221-1 and WB-3224-1, respectively, are summarized in Table 2-3.

With the exception of the overpack assembly, all package structural components that are not relied upon for containment are designed in accordance with the allowable stress design criteria for Class 2 plate- and shell-type supports from Subsection NF of the ASME Code [2.2]. The NCT and HAC allowable stress design criteria for the package non-containment components are summarized in Table 2-4.

Subsections NF and WB of the ASME Code impose stress limitations on primary membrane, local membrane, membrane (primary or local) plus bending, and primary plus secondary stress intensities. To demonstrate conformance to the ASME Code limits, it is necessary to determine the required code stress intensities at the critical cross-sections of the cask. Since the critical cross-section locations are load-condition-dependent, several “stress evaluation sections” are established to ensure that all critical locations have been evaluated for every load condition. The stress evaluation sections selected for the cask containment system and non-containment components are illustrated in Figure 2-1 and Figure 2-2, respectively. Multiple sections are selected in the high stress regions near the ends of the shells. For evaluation of conditions producing a stress distribution in the cask that is not axisymmetric, section stress evaluations are performed at multiple circumferential locations to assure that the maximum stresses are captured. For the cask shell buckling evaluation, membrane stress components at the mid-length of the cask inner and outer shell (sections C5 and N5) are used.

The section stresses at each stress evaluation location are obtained using the ANSYS “stress linearization” post-processing feature. The stress linearization provides membrane, bending, membrane plus bending, peak, and total stress intensities at each section. These stresses are

classified in accordance with the ASME Code for comparison to the applicable allowable stress design criteria as follows:

*Membrane Stress Intensity*

The membrane stress intensities are classified as primary membrane ($P_m$) or local membrane ($P_l$) based upon the location in the structure and the nature of the stress. Membrane stresses occurring at a structural discontinuity (e.g., at the transition inner shell thickness transitions and at the shell-to-flange transitions) are classified as local membrane, provided that the distance over which the membrane stress intensity exceeds the $P_m$ limit does not exceed $1.0(Rt)^{1/2}$, where R is the minimum mid-surface radius of curvature and t is the minimum thickness in the region considered. Membrane stresses at all other sections are classified as primary.

*Membrane Plus Bending Stress Intensity*

The membrane plus bending stress intensities at each section are classified as either primary ($P_m+P_b$) or secondary ($P_m+P_b+Q$) based upon the location in the structure. Bending stresses at gross structural discontinuities, such as flange-to-shell junctions and junctions between shells of different diameters or thickness, are classified as secondary. Membrane plus bending stress intensities at all other stress sections are classified as primary.

*Total Stress Intensity*

Total stress intensities include primary plus secondary plus peak stresses. In accordance with the ASME Code, these stresses are objectionable only as a possible source of a fatigue crack or a brittle fracture. As shown in Section 2.1.2.4, evaluation of cyclic loading is not required for the cask components other than bolts.

Using the critical sections from each load case, minimum design margins are calculated and reported for all bounding load combinations. The design margin (D.M.) is defined as follows:

$$\text{D.M.} = \left( \frac{\text{Allowable Value}}{\text{Calculated Value}} \right) - 1 ;$$

where the allowable and calculated values are in consistent units.

The overpack shell is designed to deform plastically and absorb the kinetic energy when subjected to the NCT free drop, HAC free drop, and HAC puncture drop load conditions. Therefore, a strain-based design criteria is used for the overpack. The maximum crush depth of the polyurethane foam in the overpack is generally limited to 70% of the nominal foam section thickness. In cases of highly localized foam crush, e.g., that due to the HAC hot top-corner drop impact, the maximum foam crush depth may not exceed 80% of the nominal foam section thickness. The maximum strain in the overpack stainless steel shell components is limited to the lower-bound maximum elongation from the ASME material specifications for all material options.

The overpack closure bolts are designed to satisfy the Service Level A allowable stress design criteria for Class 2 supports from Subsection NF of the ASME Code for NCT. The bolt allowable stress design criteria for NCT is summarized in Table 2-3. However, a strain-based design criteria is used for the overpack closure bolts for HAC free drop and HAC puncture drop load conditions. The maximum strain in the overpack closure bolts is limited to the bolt material maximum elongation from the ASME material specification. In addition, the average shear stress in the overpack closure bolts for HAC is limited to the lesser of $0.6S_y$ and $0.42S_u$ in accordance with Appendix F [2.6] of the ASME Code.

#### 2.1.2.3 Buckling

The cask inner and outer shells are evaluated for buckling in accordance with the requirements of ASME Code Case N-284-1 [2.7]. The geometric parameters of the cask inner and outer shells used for the buckling evaluation are summarized in Table 2-5. Capacity reduction factors are calculated in accordance with Section -1511 of ASME Code Case N-284-1 to account for possible reductions in the capacity of the shells due to imperfections and nonlinearity in geometry and boundary conditions. Plasticity reduction factors, which account for nonlinear material properties when the product of the classical buckling stresses and capacity reduction factors exceed the proportional limit, are calculated in accordance with Section -1610 of ASME Code Case N-284-1. The theoretical buckling stresses of the cask inner and outer shells under uniform stress fields are calculated in accordance with Section -1712.1.1 of ASME Code Case N-284-1. Cask shell lower-bound material properties at an upper bound temperature of 93°C are conservatively used to determine the buckling factors and theoretical buckling stresses. The capacity reduction factors, plasticity reduction factors, and theoretical buckling stresses for the cask inner and outer shells are summarized in Table 2-6.

The allowable elastic and inelastic buckling stresses for NCT and HAC are calculated in accordance with the formulas given in Section -1713.1.1 and Section -1713.2.1 of ASME Code Case N-284-1. The allowable buckling stresses include factors of safety of 2.0 for NCT and 1.34 for HAC in accordance with Section -1400 of ASME Code Case N-284-1. Table 2-7 provides a summary of the cask inner and outer shell elastic and inelastic buckling stresses for NCT and HAC. Buckling interaction ratios are calculated for the cask inner and outer shells for all NCT and HAC tests that load the shells in compression. The interaction ratios for elastic buckling and inelastic buckling are calculated using the highest values of compressive stress and shear stress from the finite element analysis solutions in accordance with the formulas given in Section -1713.1.1 and Section -1713.2.1 of ASME Code Case N-284-1.

#### 2.1.2.4 Fatigue

##### 2.1.2.4.1 Structural Components, Other Than Bolts

Analysis of the package structural components for cyclic service is not required because the conditions stipulated in WB-3221.9(d)(1) through (6) are met. The analysis is conservatively based on the assumption that the package will be used for 20 years of service and be used for one shipment per week, for a total of 1,040 shipments. This analysis is summarized as follows:

1. The number of atmospheric-to-operating pressure cycles, which is equal to the number of shipments (1,040 cycles), is less than 13,688 cycles, corresponding to an $S_a$ value of $3S_m$ = 414 MPa for Type 304 and Type 316 stainless steel over the temperature range of interest. Thus, condition (1) of WB-3221.9(d) is met.

2. Normal operating pressure fluctuation cycles in the package result from diurnal fluctuations in ambient conditions (temperature and insolation). Thus, it is assumed that the cask will experience one normal operating pressure fluctuation per day, or 7,300 cycles over its 20-year service life. The thermal analysis of the package shows that the maximum temperature fluctuation of the cavity gas due to diurnal cycles is approximately 10°C, which results in a pressure change of approximately 20 kPa based on the ideal gas law. The 20 kPa pressure change is much less than the significant pressure fluctuation (SPF) of 330 kPa, which is based on a bounding design pressure of 700 kPa gauge, an $S_a$ value of 195 MPa at $10^6$ cycles per Table I-9.1 of Appendix I [2.8] of the ASME Code, and $S_m$ of 138 MPa for Type 304 and Type 316 stainless steel over the temperature range of interest. Thus, condition (2) of WB-3221.9(d) is met.

3. The temperature difference between any two adjacent points on the cask shell during startup and shutdown is limited to 127°C. This is based on an $S_a$ value of 758 MPa for 1,040 startup-shutdown cycles and the elastic modulus and mean coefficient of thermal expansion for the cask shell Type 304 and Type 316 stainless steel material at room temperature. The thermal evaluation of the package shows that the temperature difference between any two adjacent points on the cask does not exceed 127°C under any NCT thermal condition. Thus, condition (3) of WB-3221.9(d) is met.

4. Normal operating temperature fluctuation cycles in the package result from diurnal fluctuations in ambient conditions (temperature and insolation). Thus, it is assumed that the cask will experience one normal operating temperature fluctuation per day, or 7,300 cycles over its 20-year service life. The package's significant temperature fluctuation (STF) is 33°C based on an $S_a$ value of 195 MPa at $10^6$ cycles and the elastic modulus and mean coefficient of thermal expansion for the cask shell Type 304 and Type 316 stainless steel material at room temperature. The thermal evaluation of the package shows that the temperature difference in the cask does not vary significantly under NCT and is less than 33°C. Thus, condition (4) of WB-3221.9(d) is met.

5. With the exception of the closure bolts, the only dissimilar materials used in the construction of the cask are austenitic stainless steel and DU. DU has a lower coefficient of thermal expansion that the austenitic stainless steel materials of the components that encase the DU. Under elevated temperatures, differential thermal expansion between these materials results in growth of the clearance between the DU and cask shells. However, differential thermal expansion at reduced temperatures produces interference-related stresses in the cask. The STF for temperature difference in dissimilar material of the cask is 102°C based on a total of 7,300 temperature cycles and the cask material properties at a lower-bound temperature of -40°C. The thermal evaluation of the

package shows that the temperature difference in the cask does not vary significantly under NCT and is less than 102°C. Thus, condition (5) of WB-3221.9(d) is met.

6. The only significant cyclic mechanical loads, excluding pressure, that the package is subjected to during normal operation are those resulting from handling and NCT vibration. The only handling operation that creates any significant stress in the cask is the cask lift. The number of cask lift operations performed for each shipment is small, but conservatively assumed to be 10 or less per shipment for a maximum of 10,400 lifting cycles of the 20-year service life. As discussed in Section 2.6.5, a bounding 10*g* vertical vibration load is conservatively assumed for the package evaluation. It is conservatively assumed that the package will experience a total of $10^6$ cycles of vibration loading per shipment with a magnitude of 10*g*, or 1.04E10 cycles over the 20-year service life. The value of $S_a$ for 1E10 cycles and higher, for austenitic stainless steels is 94 MPa per Figure I-9.2.2 (curve C) of Appendix I [2.8] of the ASME Code. As discussed in Section 2.5.1.2 and Section 2.6.5, the maximum stress intensity in the cask due to the cask lift and NCT vibration loads are 9 MPa and 11 MPa, respectively. These stresses are less than one-eighth of the $S_a$ value for the total number mechanical load cycles. Thus, condition (6) of WB-3221.9(d) is met.

#### 2.1.2.4.2 Cask Closure Bolts

The cask closure bolts are subjected to cyclic loading due to startup-shutdown cycles of bolt preload, temperature, and pressure loading, normal fluctuation cycles of pressure and temperature, and cyclic loading due to vibration normally incident to transport. The cask closure bolts are evaluated for fatigue failure due to cyclic loading using the methods of WB-3221.9(e) in accordance with the requirements of WB-3232(d)(2). In accordance with the requirements of WB-3232(d)(2)(d), a fatigue strength reduction factor of 4.0 is used for the cask closure bolt fatigue evaluation.

*Startup-Shutdown Cycles*

The package is conservatively assumed to undergo 1,040 startup-shutdown cycles over its 20-year design life. The maximum stress in the cask closure bolt due to the maximum bolt preload, MNOP, and NCT heat loading is 209 MPa. The minimum stress in the closure bolt for startup-shutdown cycles is zero. Thus, the alternating stress in the closure bolts for startup-shutdown cycles, including a fatigue reduction factor of 4, is 418 MPa. The allowable number of startup-shutdown cycles for an alternating stress of 418 MPa is 1,678 per Figure I-9.4 of Appendix I [2.8] of the ASME Code. Therefore, the cask closure bolt usage factor for startup-shutdown cycles is 0.62 (1,040/1,678).

*Thermal and Pressure Fluctuations – Normal Operating Cycles*

Normal operating temperature and pressure fluctuations in the cask result from diurnal ambient temperature fluctuations. The package is conservatively assumed to undergo one normal operating cycle for every day of its 20-year design life, or 7,300 cycles. The maximum temperature fluctuations of the cask in the region of the closure bolts (e.g., the cask seals) and the

bulk average temperature of the cask cavity gas in the cask cavity both fluctuate by approximately 10°C during each diurnal cycle. This temperature fluctuation produces an alternating stress in the closure bolts.

The maximum stress in the cask closure bolt due to the maximum bolt preload, MNOP, and NCT heat loading (based on a bounding bolt temperature of 68.3°C) is 209 MPa. At room temperature (21°C) the bolt stress due to the maximum preload of 7,219 N is 92 MPa. Thus, a temperature change of 47.3°C combined with an internal pressure load of 700 kPa gauge increases the bolt stress by 117 MPa (209 MPa – 92 MPa). The stress range due to a 10°C temperature fluctuation is 25 MPa (=117 x 10/47.3). Thus, the alternating stress in the closure bolts for normal operating thermal and pressure cycles, including a fatigue reduction factor of 4, is 50 MPa. The allowable number of normal operating cycles for an alternating stress of 50 MPa is 184,062 per Figure I-9.4 of Appendix I [2.8] of the ASME Code. Therefore, the cask closure bolt usage factor for normal operating thermal and pressure cycles is 0.04 (7,300/184,062).

*Vibration Cycles*

The results of the cask closure bolt evaluation show that NCT vibration loading results in only a 1 MPa increase in the closure bolt stress. Thus, the alternating stress in the closure bolts for NCT vibration cycles, including a fatigue reduction factor of 4, is $S_{alt3}$ = 2.0 MPa. The value of $S_a$ at 1E6 cycles is 37 MPa per Figure I-9.4 of Appendix I [2.8] of the ASME Code. Since $S_{alt3}$ is much lower that $S_a$ at the endurance limit of 1E6 cycles, the usage factor for NCT vibration is insignificant (i.e., $U_3$ = 0.00).

*Cumulative Usage Factor*

The cumulative usage factor for cyclic loading of the cask closure bolts is:

$$U = U_1 + U_2 + U_3$$
$$= 0.62 + 0.04 + 0.00 = 0.66$$

Since the cumulative usage factor is less than 1.0, the cask closure bolt will not fail due to fatigue during their 20-year design life.

### 2.1.2.5 Brittle Fracture

The cask is designed in accordance with the fracture toughness requirements of Regulatory Guide 7.11 [2.9] and NUREG/CR-1815 [2.10] for Category II containers, since it is designed to transport normal form content with a maximum activity between 3,000 $A_2$ and 30 $A_2$ and not greater than 1.11 PBq (30,000 Ci). The criteria for Category II containers assures that the fracture toughness is sufficient to prevent fracture initiation of preexisting cracks under dynamic loading.

With the exception of the cask closure bolts and overpack closure bolts, all structural components of the package are fabricated of austenitic stainless steels. These materials do not undergo a ductile-to-brittle transition in the temperature range of interest for load conditions that

involve impact loads, i.e., down to -20°F (-29°C), and, thus, do not need to be evaluated for brittle fracture. As stated in Regulatory Guide 7.11 [2.9], "Since austenitic stainless steels are not susceptible to brittle failure at temperatures encountered in transport, their use in containment vessels is acceptable to the staff and no tests are needed to demonstrate resistance to brittle fracture."

The cask closure bolts and overpack closure bolts are fabricated from SA-320 and A320, Grade L43 bolting material, respectively. In accordance with Section 5 of NUREG/CR-1815 [2.10], bolts are generally not considered as fracture-critical components because multiple load paths exist and bolting systems are generally redundant, as is the case with the cask and overpack closure bolts. However, for purposes of comparison, the nil-ductility transition (NDT) temperature of the closure bolts is calculated and compared with the requirements of NUREG/CR-1815.

The closure bolt material is required to have a minimum impact energy absorption of 27 N-m (20 ft-lbf) at a temperature of -101°C (-150°F). The Charpy impact measurement may be transformed into a fracture toughness value by using the empirical relationship from Section 4.2 of NUREG/CR-1815:

$$K_{ID} = \sqrt{5C_v E} = 59 \text{ MPa}\sqrt{\text{m}} \ (54 \text{ ksi}\sqrt{\text{in}})$$

where E is 199 MPa (28.8 X $10^6$ psi) at -101°C (-150°F) from Table TM-1, Material Group B of Section II, Part D, of the ASME Code [2.11].

The dynamic fracture toughness is conservatively translated to an equivalent NDT temperature by using the Design Reference $K_{ID}$ curve provided in Figure 2 of NUREG/CR-1815. By interpolation, the temperature relative to NDT (i.e., T - NDT) is approximately 18°C (32°F). Accordingly, the NDT temperature is:

$$\text{NDT} = -101°\text{C} - (18°\text{C}) = -119°\text{C} \ (-182°\text{F})$$

For Category II fracture critical components with a minimum section thickness of 15.9 mm (0.625 inches) and a yield strength of 690 MPa (100 ksi), Figure 7 of NUREG/CR-1815 gives the minimum offset "A" as approximately 0°C (0°F). Thus, for Lowest Service Temperature (LST) of -29°C (-20°F), the maximum NDT temperature value is:

$$T_{NDT} = \text{LST} - \text{A} = -29°\text{C} - 0°\text{C} = -29°\text{C} \ (-20°\text{F})$$

The closure bolts experience a ductile-to-brittle transition temperature at -119°C, whereas the criterion of NUREG/CR-1815 prescribes a maximum NDT temperature of -29°C. The 90°C margin provides conservative assurance that brittle fracture will not occur in the closure bolts.

The shielding components of the package are fabricated from DU alloyed with 2% molybdenum by weight (U-2% Mo). This material was selected for the MIDUS package design because the addition of 2% molybdenum results in the formation of a second phase that increases the yield strength of DU and provides good ductility over the temperature range of interest [2.12]. Since the ductile-to-brittle transition temperature of U-2% Mo falls within the package operating

temperature range, four additional measures are taken to assure that the DU will not be susceptible to brittle fracture.

All the DU components receive inspections for fracture toughness, chemical composition, and density. The specified fracture toughness is a minimum Charpy V-notch impact energy of 6 ft-lb at 70 °F. The chemical composition is tested to assure that alloy meets specifications because unalloyed DU is more susceptible to brittle fracture then the 2% Mo alloy. Density measurements are performed on each DU component to assure that the material is free of significant voids that might affect shielding or promote brittle fracture. Lastly, visual inspections are performed on each part after final machining to assure that the surfaces are free of voids, cracks, or porosity. The visual inspection gives assurance that no significant material flaws exist which might promote brittle fracture. The DU casting process does not favor the creation of cracking, and any cracks which might form during cooling are preferentially located on the surface of the part. The critical flaw size required for fracture is very large, about ¼ or more of the part thickness, and so visual inspection is a reliable testing method.

Since the maximum stress in the DU shield for all NCT and HAC tests is very low (i.e., less than 40% of the yield strength of U-2% Mo at -29°C), the lower-bound critical flaw size that must exist for fracture is calculated to be 17 mm using the following equation from SAND80-1836 [2.12]:

$$K \approx 2\sigma\sqrt{a}$$

Where;

K = $K_{IC(min)}$ or 42.3 MPa·$m^{1/2}$, lower-bound value of the critical stress intensity factor for plane strain failure at -40°C [2.12]

$\sigma$ = 162 MPa, maximum stress intensity in the DU shield for all NCT and HAC tests (resulting from the HAC top oblique drop)

a = crack depth (m)

### 2.1.3 Weights and Centers of Gravity

The nominal mass properties of the package, including each of the major individual packaging subassemblies and contents, are summarized in Table 2-8. The mass, center of gravity, and moment of inertia of each major individual subassembly and the package are provided. The reference point for all centers of gravity is the bottom centerline of the overpack base, as shown in Figure 2-3. Moments of inertia are taken about the local center of gravity of each major individual subassembly and the package. The package has a total nominal mass of 320.6 kg and a center of gravity located at 267 mm above the bottom end of the overpack base. The mass moment of inertia of the package is 8.91E+06 kg-$mm^2$.

### 2.1.4 Identification of Codes and Standards for Package Design

The package, which is designed to transport normal form content with a maximum activity between 3,000 $A_2$ and 30 $A_2$ and not greater than 30,000 Ci, is designed, fabricated, tested, and maintained in accordance with codes and standards that are appropriate for transportation packages with Category II container contents. The codes and standards are selected based on guidance provided in Regulatory Guide 7.6 [2.13] and NUREG/CR-3854 [2.14].

The package containment system is designed in accordance with the applicable requirements of the ASME Code, Section III, Division 3, Subsection WB [2.1]. The non-containment structural components of the package are designed in accordance with the applicable requirements for plate- and shell-type Class 2 supports from the ASME Code, Section III, Division 1, Subsection NF [2.2]. The design criteria for the package is discussed in Section 2.1.2. The load combinations used in the package structural evaluation are developed in accordance with Regulatory Guide 7.8 [2.5], as discussed in Section 2.1.2.1. The buckling evaluation of the cask cylindrical shells is performed in accordance with ASME Code Case N-284-1 [2.7], as discussed in Section 2.1.2.3. Fracture toughness of the package components is evaluated in accordance with the requirements of Regulatory Guide 7.11 [2.9] and NUREG/CR-1815 [2.10] for Category II containers.

The package containment system is fabricated in accordance with the applicable requirements of Subsections WA and WB of Section III, Division 3, of the ASME Code [2.1]. The non-containment structural components of the package are fabricated in accordance with the applicable requirements of Subsection NF [2.2] of the ASME Code for plate- and shell-type Class 2 supports. The exceptions taken to the ASME Code design and fabrication requirements, along with the alternate compliance basis, are summarized in Table 2-9 and Table 2-10. The weld that connects the cask outer shell to the cask containment shell is fabricated and inspected in accordance with the applicable requirements of Subsections WA and WB of Section III, Division 3, of the ASME Code [2.1]. All other package welds are fabricated and inspected in accordance with the applicable requirements of Subsection NF [2.2] of the ASME Code.

The package DU alloy gamma shield components are fabricated, installed, and tested in accordance with standard industry practices. Testing of the DU alloy gamma shield material is performed to assure that it satisfies the requirements for chemical composition and fracture toughness. In addition, the soundness of the DU alloy material used for the gamma shielding components is demonstrated through measurement of the component densities (i.e., weight and volume) and visual inspection of the component surfaces for unacceptable flaws (e.g., voids, cracks, or porosity.)

The polyurethane foam material that fills the overpack base and lid shells is fabricated, installed, and tested in accordance with the foam vendors' standard practices. The foam is installed in the overpack shells in-situ, with the foam rise parallel to the longitudinal axis of the package. Foam specimens from each foam batch are tested to assure that the foam has the specified physical characteristics, including density, crush strength, flame retardency, intumescences, and leachable chlorides.

**Table 2-1 – Load Combinations for Normal Conditions of Transport**

| Normal or Accident Condition | Initial Conditions[1] | | | | | | | | |
|---|---|---|---|---|---|---|---|---|---|
| | Ambient Temperature | | Insolation[2] | | Decay Heat | | Internal Pressure[3] | | Fabric-ation Stress[4] |
| | 38°C | -29°C | Max. | Zero | Max. | Zero | Max. | Min. | |
| Hot Environment (38°C ambient temp.) | | | X | | X | | X | | X |
| Cold Environment (-40°C ambient temp.) | | | | X | | X | | X | X |
| Reduced External Pressure | X | | X | | X | | X | | X |
| Increased External Pressure | | X | | X | | X | | X | X |
| Vibration | X | | X | | X | | X | | X |
| | | X | | X | | X | | X | X |
| Free Drop | X | | X | | X | | X | | X |
| | | X | | X | | X | | X | X |

Notes:
1. Initial cask temperature distributions are considered to be at steady-state.
2. Maximum insolation in accordance with §71.71(c)(1).
3. Internal pressure is consistent with the other initial conditions being considered. Minimum internal pressure is taken as atmospheric pressure.
4. Stresses due to assembly of the major components of the packaging, including stresses due to closure bolt preload.

**Table 2-2 – Load Combinations for Hypothetical Accident Conditions**

| Normal or Accident Condition | Initial Conditions[1] | | | | | | | | |
|---|---|---|---|---|---|---|---|---|---|
| | Ambient Temperature | | Insolation[2] | | Decay Heat | | Internal Pressure[3] | | Fabric-ation Stress[4] |
| | 38°C | -29°C | Max. | Zero | Max. | Zero | Max. | Min. | |
| Free Drop | X | | X | | X | | X | | X |
| | | X | | X | | X | | X | X |
| Puncture | X | | X | | X | | X | | X |
| | | X | | X | | X | | X | X |
| Thermal | X | | X | | X | | X[5] | | X |

Notes:
1. Initial cask temperature distributions are considered to be at steady-state.
2. Maximum insolation in accordance with §71.71(c)(1).
3. Internal pressure is consistent with the other initial conditions being considered. Minimum internal pressure is taken as atmospheric pressure.
4. Stresses due to assembly of the major components of the packaging, including stresses due to closure bolt preload.
5. Maximum internal pressure for the HAC thermal condition includes increased pressure due to increased fill gas temperatures during the fire transient.

**Table 2-3 – Containment System Allowable Stress Design Criteria**

| Stress Type | Allowable Stress Limits(1) | |
|---|---|---|
| | NCT | HAC |
| **Other Than Bolts** | | |
| Primary Membrane Stress Intensity ($P_m$) | $S_m$ | Lesser of $2.4S_m$ and $0.7S_u$ |
| Primary + Bending Stress Intensity ($P_L$ or $P_L + P_b$) | $1.5S_m$ | Lesser of $3.6S_m$ and $S_u$ |
| Primary + Secondary Stress Intensity ($P_L + P_b + Q$) | $3.0S_m$ | N/A(2) |
| Average Bearing Stress | $S_y$ | Not required |
| Pure Shear Stress | $0.6S_m$ | $0.42S_u$ |
| **Bolts** | | |
| Average Shear Stress | $0.4S_y$ | Lesser of $0.42S_u$ and $0.6S_y$ |
| Average Stress(3) | $2S_m$(4) | Lesser of $3S_m$ and $0.7S_u$ |
| Maximum Stress(5) | $3S_m$ | (6) |

Notes:
1. Stress limits applicable for components and systems evaluated using elastic system analysis.
2. Evaluation of secondary stress is not required for HAC.
3. The axial stress component averaged across the bolt cross-section and neglecting stress concentrations.
4. The stress due to internal pressure and gasket seating loads (e.g., bolt torque) shall not exceed one times $S_m$.
5. The maximum value of stress intensity at the periphery of the bolt cross-section resulting from direct tension plus bending, neglecting stress concentrations.
6. Evaluation of maximum bolt stress not required for HAC.

**Table 2-4 – Non-Containment Component Allowable Stress Design Criteria**

| Stress Type | Allowable Stress Limits[1] | |
|---|---|---|
| | NCT | HAC |
| **Other Than Bolts** | | |
| Primary Membrane Stress Intensity ($P_m$) | $S_m$ | Greater of $1.2S_y$ and $1.5S_m$, but $\leq 0.7S_u$ |
| Primary Membrane + Bending Stress Intensity ($P_L$ or $P_m + P_b$) | $1.5S_m$ | 150% of $P_m$ allowable |
| Average Bearing Stress | $S_y$ | [2] |
| Pure Shear Stress | $0.6S_m$ | $0.42S_u$ |
| **Bolts** | | |
| Tensile Stress ($f_t$) | $F_{tb} = S_u/2$ (ferritic steels) or $F_{tb} = S_u/3.33$ (austenitic steels) | Lesser of $0.7S_u$ and $S_y$[3][4] |
| Shear Stress ($f_v$) | $F_{vb} = 0.62S_u/3$ (ferritic steels) or $F_{vb} = 0.62S_u/5$ (austenitic steels) | Lesser of $0.42S_u$ and $0.6S_y$ |
| Combined Tensile & Shear Stress | $\frac{f_t^2}{F_{tb}^2} + \frac{f_v^2}{F_{vb}^2} \leq 1$ | $\frac{f_t^2}{F_{tb}^2} + \frac{f_v^2}{F_{vb}^2} \leq 1$ [4] |

Notes:
1. Stress limits applicable for components and systems evaluated using elastic system analysis.
2. Evaluation of secondary stress is not required for HAC.
3. Limit applies to average tensile stress across the entire bolt cross-section. For high-strength bolts ($S_u > 100$ ksi), the maximum value of tensile stress at the periphery of the bolt cross-section resulting from direct tension plus bending and excluding stress concentrations shall not exceed $S_u$.
4. Stress limit is not applicable to the overpack closure bolts, since they are evaluated for HAC tests using plastic-system analysis.

**Table 2-5 – Cask Shell Buckling Geometric Parameters**

| Geometric Parameter | Inner Shell | Outer Shell |
|---|---|---|
| Outside Diameter (mm) | 90.0 | 225.0 |
| Inside Diameter (mm) | 85.0 | 217.0 |
| Length, L (mm) | 134.0 | 221.0 |
| Mean Radius, R (mm) | 43.8 | 110.5 |
| Shell Thickness, t (mm) | 2.5 | 4 |
| R/t | 17.5 | 27.6 |
| Unsupported Axial Length, $l_\phi$ (mm) | 134.0 | 220.5 |
| Unsupported Circumferential Length, $l_\theta$ (mm) | 274.9 | 694.3 |
| $M_\phi = l_\phi/\sqrt{Rt}$ | 12.81 | 10.49 |
| $M_\theta = l_\theta/\sqrt{Rt}$ | 26.28 | 33.02 |
| M = smaller of $M_\phi$ and $M_\theta$ | 12.81 | 10.49 |

**Table 2-6 – Buckling Reduction Factors and Theoretical Buckling Stresses**

| Calculation | Parameter | Inner Shell | Outer Shell |
|---|---|---|---|
| Capacity Reduction Factors (-1511) | $\alpha_{\phi L}$ | 0.269 | 0.269 |
| | $\alpha_{\theta L}$ | 0.800 | 0.800 |
| | $\alpha_{\phi\theta L}$ | 0.800 | 0.800 |
| Plasticity Reduction Factors (-1610) | $\Delta=\alpha_{\phi L}*\sigma_{\phi eL}/\sigma_y$ | 10.257 | 6.498 |
| | $\Delta=\alpha_{\theta L}*\sigma_{\theta eL}/\sigma_y$ | 3.988 | 3.157 |
| | $\Delta=\alpha_{\phi\theta L}*\sigma_{\phi\theta eL}/\sigma_y$ | 10.610 | 7.488 |
| | $\eta_\phi$ | 0.097 | 0.154 |
| | $\eta_\theta$ | 0.250 | 0.307 |
| | $\eta_{\phi\theta}$ | 0.057 | 0.080 |
| Theoretical Buckling Values (-1712.1.1) | $C_\phi$ | 0.605 | 0.605 |
| | $\sigma_{\phi eL}$ | 6,579 MPa | 4,168 MPa |
| | $C_{\theta r}$ | 0.0790 | 0.0987 |
| | $\sigma_{\theta eL} = \sigma_{reL}$ | 859 MPa | 680 MPa |
| | $C_{\theta h}$ | 0.0756 | 0.0934 |
| | $\sigma_{\theta eL} = \sigma_{heL}$ | 822 MPa | 643 MPa |
| | $C_{\phi\theta}$ | 0.2102 | 0.2342 |
| | $\sigma_{\phi\theta eL}$ | 2,286 MPa | 1,614 MPa |

**Table 2-7 – Cask Shell Allowable Buckling Stresses**

| Buckling Regime | Stress Type | Allowable Buckling Stress (MPa) | | | |
|---|---|---|---|---|---|
| | | Inner Shell | | Outer Shell | |
| | | NCT | HAC | NCT | HAC |
| Elastic Buckling | Axial Compression, $\sigma_{xa}$ | 884 | 1,319 | 560 | 836 |
| | Hydrostatic Pressure, $\sigma_{ha}$ | 329 | 491 | 257 | 384 |
| | Hoop Compression, $\sigma_{ra}$ | 344 | 513 | 272 | 406 |
| | In-Plane Shear, $\sigma_{\tau a}$ | 914 | 1,365 | 645 | 963 |
| Inelastic Buckling | Axial Compression, $\sigma_{xc}$ | 86 | 129 | 86 | 129 |
| | Radial External Pressure, $\sigma_{rc}$ | 86 | 128 | 84 | 125 |
| | In-Plane Shear, $\sigma_{\tau c}$ | 52 | 77 | 52 | 77 |

**Table 2-8 – Package Mass Properties Summary**

| Package Component or Assembly | Mass (kg) | Center of Gravity[1] (mm) | Moment of Inertia[2] (kg-mm$^2$) |
|---|---|---|---|
| Cask Body Assembly | 167.5 | 235 | 1.70E+06 |
| Cask Shield Plug Assembly | 13.8 | 354 | 1.81E+04 |
| Closure Lid Assembly | 5.8 | 409 | 1.83E+04 |
| Cask Payload | 1.1 | 247 | 1.72E+03 |
| Misc. Cask Hardware | 0.3 | 402 | 5.00E+01 |
| **Cask Assy. Subtotals** | **188.5** | **250** | **2.08E+06** |
| Shield Lid Assembly | 13.6 | 430 | 4.22E+04 |
| **Cask & Shield Lid Subtotals** | **202.1** | **262** | **2.53E+06** |
| Overpack Base Assy. | 83.1 | 197 | 3.77E+06 |
| Overpack Lid Assy. | 35.1 | 464 | 8.12E+05 |
| Misc. Overpack Hardware | 0.4 | 410 | 1.03E+02 |
| **Package Totals** | **320.6** | **267** | **8.91E+06** |

Notes:
1. Longitudinal distance from the bottom end of the overpack base to the center of gravity of the individual packaging subassembly or assembly, as shown in Figure 2-3.
2. Moment of inertia about the center of gravity of the associated component or assembly.

**Table 2-9 – MIDUS Package ASME BPVC Section III, Division 1, Requirements Compliance Summary (4 Pages)**

| Item | ASME Code Requirement or Issue | Alternative Compliance Basis | ASME BPVC Sections |
|---|---|---|---|
| 1 | ASME BPVC Section III, Division 1, uses the following terminology that is not consistent with the terminology used for the MIDUS package: | The equivalent terminology or compliance basis used for the MIDUS package are as follows: | |
| | (a) "Owner's Certificate" | (a) Energy*Solutions* will notify the USNRC of the intent to design and fabricate the package, but will not seek an Owner's Certificate from the ASME. | NCA-1210 & NCA-3230 |
| | (b) "Design Specification" | (b) The information typically contained in the ASME BPVC Design Specification shall be included in the MIDUS Transportation Package Safety Analysis Report (SAR). | NCA-1210 & NCA-3250 |
| | (c) "Review of Design Report" and "Design Report" | (c) The information typically contained in an ASME BPVC Design Report shall be included in the MIDUS Transportation Package SAR and submitted for review and approval by the USNRC. | NCA-1210, NCA-3260 & NCA-3350 |
| | (d) "Certificate Holder" or "Owner" | (d) Energy*Solutions* bears the responsibilities associated with a "Certificate Holder" or "Owner" relative to the package, with the exceptions as noted. | Throughout |
| | (d) "Certificate of Authorization" | (d) Replaced by USNRC-issued Certificate of Compliance (CofC). | Throughout |
| | (e) "Data Report" and "Stamping" | (e) Replaced by a Final Records Package and Energy*Solutions'* CofC for each fabricated package. | NCA-1210 & NCA-8000 |
| 2 | Metallic materials shall be manufactured to an SA, SB, or SFA Specification, or any other material specification permitted by this Section. Such material shall be manufactured, identified, and certified in accordance with the requirements of this Section. | As permitted by USNRC NUREG/CR-3854 via NUREG-1609, ASTM materials may be used for the fabrication/construction of the non-containment structural components of the package otherwise governed by the applicable requirements of ASME BPVC Section III, Division 1, Subsection NF. | NCA-1221 |

**Table 2-9 – MIDUS Package ASME BPVC Section III, Division 1, Requirements Compliance Summary (4 Pages)**

| Item | ASME Code Requirement or Issue | Alternative Compliance Basis | ASME BPVC Sections |
|---|---|---|---|
| 3 | Metallic materials produced under an ASTM designation may be accepted as complying with the corresponding ASME Specification, provided that the ASME Specification is designated as being identical with the ASTM Specification for the grade, class, or type produced and provided that the material is confirmed as complying with the ASTM Specification by a certified Material Test Report or Certificate of Compliance from the Material Organization. | See Items 2 & 8. | NCA-1221.1 |
| 4 | The package overpack assembly (i.e., impact limiter) is constructed to the requirements of Subsection NF, but not designed to the requirements of Article NF-3000 or Appendix NF-III. | The package overpack assembly is designed by analysis and confirmed by scaled test to provide sufficient crush strength and structural integrity. | NF-3000, Appendix NF-III |
| 5 | The maximum temperature of the metal shall not exceed the maximum temperatures listed in the applicable tables of Section II, Part D, Subpart 1. However, the package is designed for a HAC fire that is not within the scope of the loading conditions typically considered for components designed in accordance with ASME BPVC Subsection NF. | The short-term allowable temperature limits for the package materials that are used for the HAC evaluation shall be defined in the system's calculation packages and SAR. | NF-3112.1 |
| 6 | The ASME BPVC requires that the Design Specification be certified by one or more Registered Professional Engineers. | The Design Specification for the package (i.e., its SAR per Item 1(b)) shall be prepared and verified by personnel qualified in accordance with the USNRC-approved Energy*Solutions* QA Program. | NCA-3255 |
| 7 | The ASME BPVC requires that the Owner or his designee review the Design Report for compliance with the Design Specification. | The Design Report for the package (i.e., its SAR per Item 1(c)) shall be prepared and verified by personnel qualified in accordance with the USNRC-approved Energy*Solutions* QA Program. | NCA-3260 |

**Table 2-9 – MIDUS Package ASME BPVC Section III, Division 1, Requirements Compliance Summary (4 Pages)**

| Item | ASME Code Requirement or Issue | Alternative Compliance Basis | ASME BPVC Sections |
|---|---|---|---|
| 8 | Subsection NF requires the Certificate Holder to certify, by application of the appropriate Code symbol and completion of the appropriate Data Report in accordance with NCA-8000, that the materials used comply with all the requirements of NF-2000 and that the fabrication and installation complies with the requirements of NF-4000. | The package will be purchased, identified, controlled, and manufactured in accordance with the USNRC-approved Energy*Solutions* QA Program based on NQA-1 and USNRC Regulatory Guide 7.10 and NUREG/CR-6407 criteria. Therefore, Code symbol stamping will not be applied to the fabrication and installation of the package. | NCA-1281, NCA-3800, NCA-8000 & NF-4121 |
| 9 | The ASME BPVC requires the use of an Authorized Inspection Agency (AIA) to provide inspection and audit services during the construction and installation of the supports. | The activities associated with the AIA, including the Authorized Nuclear Inspector (ANI), will be replaced by the auditing and inspection activities of the QA/QC organization performing the fabrication with oversight by the Design Owner (Energy*Solutions*). | NCA-5000, NCA-8000 & NF-4121 |
| 10 | Material for supports shall conform to the requirements of the specifications for materials listed in the tables of Section II, Part D applicable to the Class of construction. | See Item 2. | NF-2121 |
| 11 | Only those welding processes which are capable of producing welds in accordance with the welding procedure qualification requirements of ASME BPVC Section IX and this Subsection shall be used for welding support material or attachments thereto. | As permitted by USNRC NUREG/CR-3019 via NUREG-1609, welding criteria of ASME BPVC Section VIII, Division 1, may also be used for non-containment structural component welding. | NF-4311 |

**Table 2-10 – MIDUS Package ASME BPVC Section III, Division 3, Requirements Compliance Summary (3 Pages)**

| Item | ASME Code Requirement or Issue | Alternative Compliance Basis | ASME BPVC Sections |
|---|---|---|---|
| 1 | ASME BPVC Section III, Division 3, uses the following terminology that is not consistent with the terminology used for the MIDUS package:<br><br>(a) "N3 Certificate Holder"<br><br>(b) "Packaging Owner"<br><br>(c) "Design Specification"<br><br>(d) "Design Report"<br><br>(e) "Fabrication Specification"<br><br>(f) "Certificate of Authorization" | The equivalent terminology and compliance basis used for the MIDUS package are as follows:<br><br>(a) Energy*Solutions* has the responsibility of the N3 Certificate Holder, with the exceptions as noted.<br><br>(b) Energy*Solutions* has the responsibility of the Packaging Owner, with the exceptions as noted.<br><br>(c) The information typically contained in an ASME BPVC Design Specification will be included in the MIDUS Transportation Package Safety Analysis Report (SAR) to be submitted to the USNRC for review and approval.<br><br>(d) The information typically contained in an ASME BPVC Design Report will be included in the MIDUS Transportation Package SAR.<br><br>(e) Replaced by Energy*Solutions'* fabrication specification, quality category assessment, and procurement drawing documentation.<br><br>(f) Replaced by USNRC-issued C of C. | Throughout Subsections WA and WB |
| 2 | The ASME BPVC Edition and Addenda dates shall be established in the Design Specification. | The ASME BPVC Edition and Addenda to be used for the design and fabrication of the package shall be the 2001 Edition with Addenda through 2003. | WA-1140(a) |

**Table 2-10 – MIDUS Package ASME BPVC Section III, Division 3, Requirements Compliance Summary (3 Pages)**

| Item | ASME Code Requirement or Issue | Alternative Compliance Basis | ASME BPVC Sections |
|---|---|---|---|
| 3 | ASME BPVC Section III, Division 3, requires that the N3 Certificate Holder use a NPT Certificate Holder to construct the containment system. The following Code requirements apply to the NPT Certificate Holder: | A NPT Certificate Holder is not required to construct the containment system (i.e., cask assembly) of the package. | WA-3420. |
| | (a) The NPT Certificate Holder shall construct the containment system under the provisions of a Quality Assurance (QA) Program that has been accepted by the Society. The QA Program shall meet the requirements of the latest Division 3 Edition and Addenda issued at the time that the containment system is constructed. | (a) The package will be purchased, identified, controlled, and manufactured in accordance with the USNRC-approved Energy*Solutions* QA Program based on NQA-1, USNRC Regulatory Guide 7.10, and NUREG/CR-6407 criteria. | WA-1140(b), WA-3111, WA-3113 & WA-3420(e) |
| | (b) The NPT Certificate Holder shall obtain an N-type Certification of Authorization and apply a Code Symbol Stamp to the completed containment system of the transportation packaging. | (b) See Item 3(a). | WA-3111, WA-3113, WA-3130 & WA-3470 |
| 4 | The ASME BPVC requires that the Design Specification, Design Report, and Fabrication Specification be certified by one or more Registered Professional Engineers, competent in the applicable field of construction and related transport packaging requirements of ANSI/ASME N626.3. | The design and fabrication documents for the package shall be prepared and verified by personnel qualified in accordance with the USNRC-approved Energy*Solutions* QA Program. | WA-3351.4,WA-3356 & WA-3361.3 |

**Table 2-10 – MIDUS Package ASME BPVC Section III, Division 3, Requirements Compliance Summary (3 Pages)**

| Item | ASME Code Requirement or Issue | Alternative Compliance Basis | ASME BPVC Sections |
|---|---|---|---|
| 5 | The ASME BPVC requires the use of an Authorized Inspection Agency (AIA) to provide inspection and audit services during the construction and installation of the containment system. Other requirements related to the use of an AIA are as follows: | The activities associated with the AIA, including the Authorized Nuclear Inspector (ANI), will be replaced with auditing and inspection activities of the QA/QC organization performing the fabrication with oversight by the Design Owner (Energy*Solutions*). | WA-5000 & WB-6113 |
| | (a) The N3 and NPT Certificate Holder shall obtain written agreement with an AIA to provide inspection and audit services prior to application. | (a) The agreement with an AIA is replaced with auditing and inspection activities of the QA/QC organization performing the fabrication with oversight by the Design Owner (Energy*Solutions*). | WA-3320(o), WA-3420(h) & WA-8130 |
| | (b) The N3 and NPT Certificate Holder shall file copies of the QA Manual with the AIA. | (b) Instead of an AIA, the QA Manual of the Design Owner (Energy*Solutions*) is filed with and has been reviewed and approved by the USNRC. | WA-3373 & WA-3461 |
| 6 | The containment system shall be designed to account for buckling due to compressive stresses. However, the rules for evaluating buckling are under development. | The inner and outer shells of the cask are designed to withstand compressive loads without buckling in accordance with the design criteria of ASME BPVC Code Case N-284-1. | WB-3211(c) & WB-3133 |
| 7 | Stress Limits for Bolts | The closure bolts are evaluated in accordance with the guidance and design criteria provided in NUREG/CR-6007. | WB-3230 |

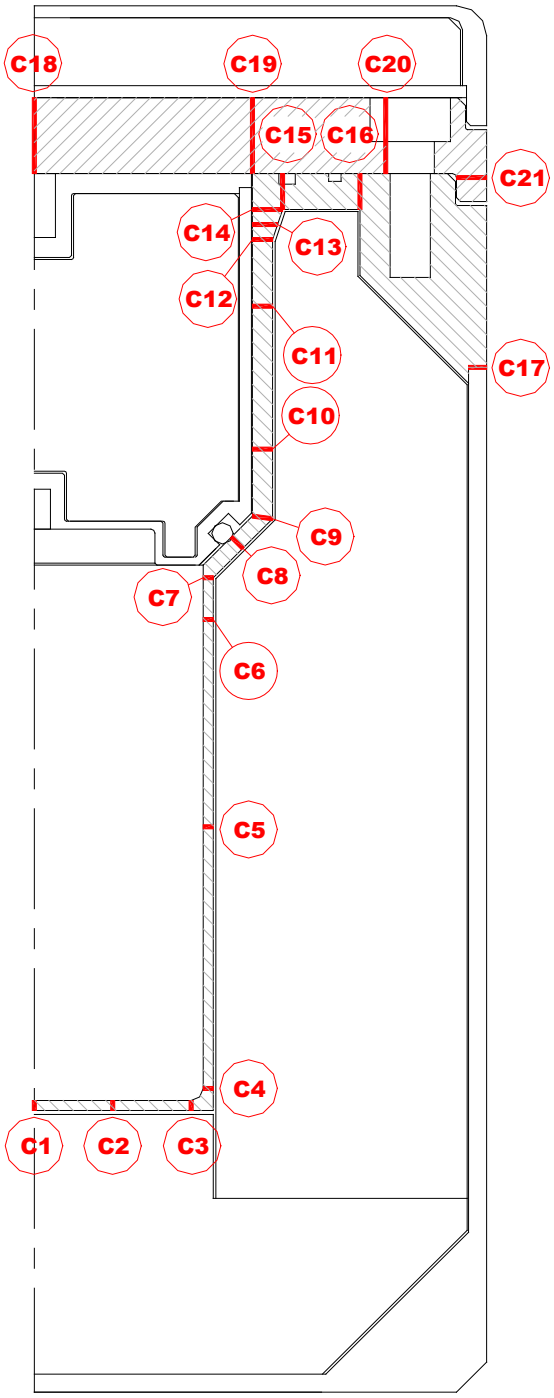


**Figure 2-1 – Cask Containment Component Stress Evaluation Locations**

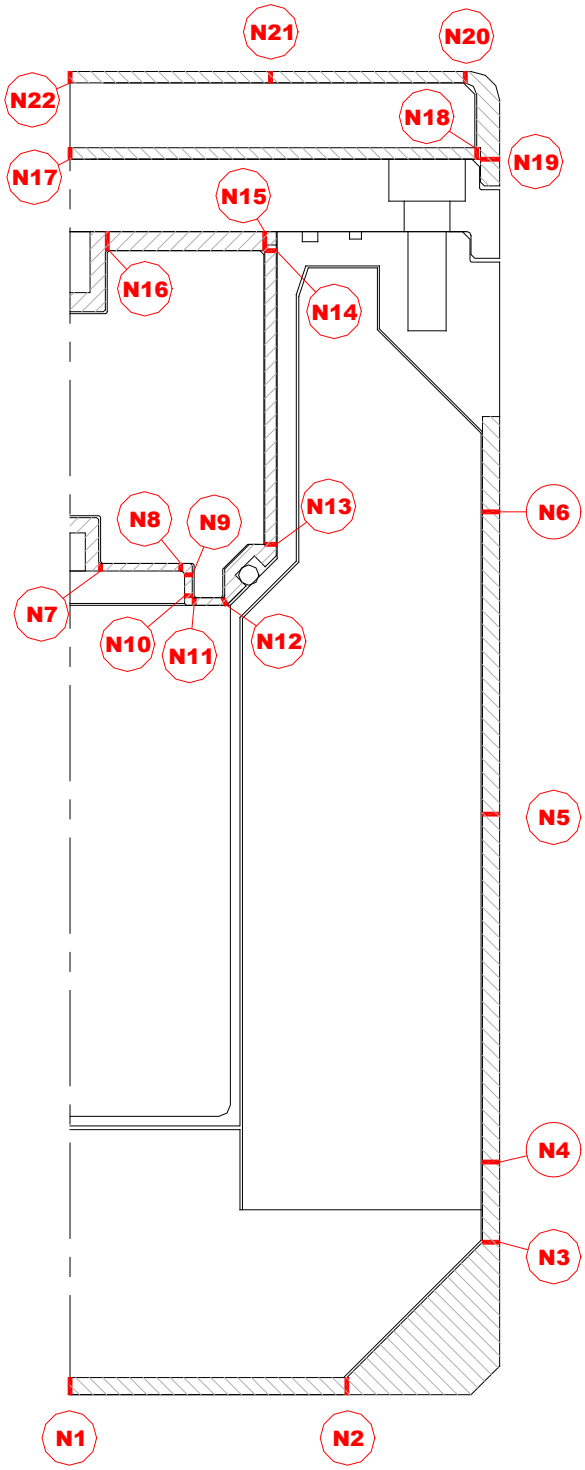


**Figure 2-2 – Cask Non-Containment Component Stress Section Locations**

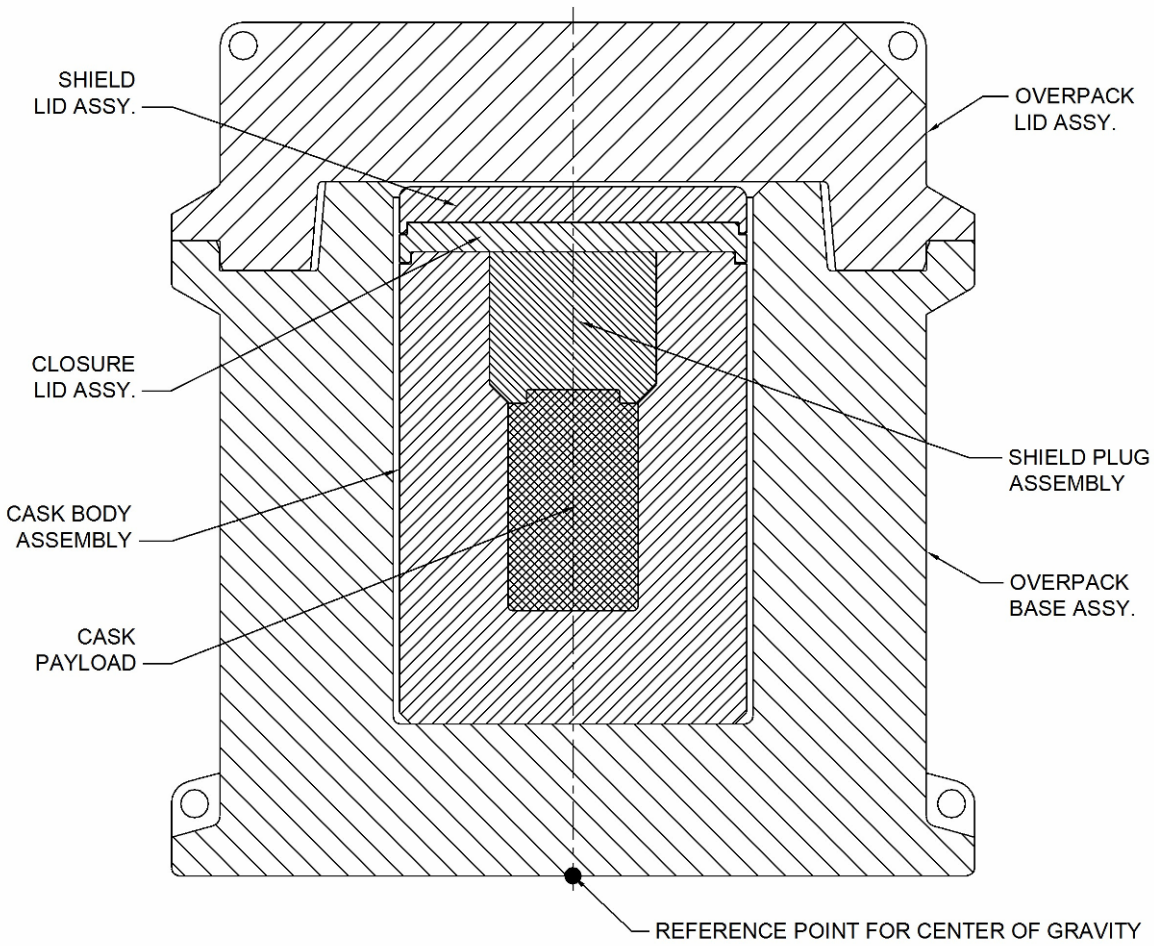


**Figure 2-3 – MIDUS Package Mass Properties Schematic**

# 2.2 Materials

## 2.2.1 Material Properties and Specifications

The specifications for the package materials of construction are summarized in Table 2-11. The mechanical properties of the package materials that are used in the structural evaluation are described in this section. The material properties for all steel components of the packaging are described in Section 2.2.1.1. The material properties of DU shielding material are described in Section 2.2.1.2. The crush strength properties of the overpack foam material are described in Section 2.2.1.3. The material properties of other materials considered in the structural evaluation are described in Section 2.2.1.4.

### 2.2.1.1 Structural Materials

The structural components of the package are fabricated from stainless steel material and alloy steel bolting material. Type 304 and/or Type 316 austenitic stainless steel, in either bar (SA-479/A479) or plate (SA-240/A240) form, is used to fabricate the structural components of the cask body, shield plug, closure lid, shield lid, and overpack. The shield lid attachment bolts are fabricated from A193, Grade B8 stainless steel material. The cask closure bolts and overpack closure bolts are fabricated from high-strength SA-320/A320, Grade L43 alloy bolting steel material.

The structural evaluation of the package is performed using mechanical properties of materials that are appropriate for the anticipated service conditions. The temperature range of interest for NCT is -40°C to 93°C. A mass density of 8,030 kg/m$^3$ and a Poisson's ratio of 0.3 are used for all stainless steel materials. A mass density of 7,865 kg/m$^3$ and a Poisson's ratio of 0.3 are used for the cask and overpack closure bolts. Temperature-dependent mechanical properties for the structural material of the package, including design stress intensity ($S_m$), yield strength ($S_y$), tensile strength ($S_u$), modulus of elasticity (E), and mean coefficient of thermal expansion ($\alpha$), are obtained from the ASME Code, Section II, Part D [2.11] and summarized in Table 2-12 through Table 2-18.

The mechanical properties of Type 304 and Type 316 stainless steel material are summarized in Table 2-12 and Table 2-13, respectively. Since many of the package's structural components may be fabricated using either Type 304 or Type 316 stainless steel material, the structural evaluation of the package is performed using the most conservative mechanical properties of these materials for the condition being analyzed. As shown in Table 2-12 and Table 2-13, the only differences between the mechanical properties of Type 304 and Type 316 stainless steel over the temperature range of interest are the yield and ultimate strengths at 93°C. Thus, the allowable stresses that depend on the yield and/or ultimate strength of Type 304 and Type 316 stainless steel at 93°C are calculated based on the lower strength values. The mechanical properties of A240, Type XM-19 stainless steel, which is used only for the overpack lid lugs, are summarized in Table 2-14. The mechanical properties of SA-320/A320, Grade L43 alloy bolting steel material, which is used for the cask closure bolts and overpack closure bolts, and A193,

Grade B8 stainless steel bolting material, which is used for the shield lid attachment bolts, are summarized in Table 2-15 and Table 2-16, respectively.

Elastic-plastic true stress-strain properties are used for overpack shell stainless steel material in the structural evaluation of the overpack for NCT free drop, HAC free drop, and HAC puncture tests. The stainless steel materials that form the overpack shells are modeled using a piecewise linear plasticity model. The data points on the true stress-strain curves are developed using the Ramberg-Osgood relationship [2.15] as follows:

$$\frac{\varepsilon}{\varepsilon_o} = \frac{\sigma}{\sigma_o} + \alpha\left(\frac{\sigma}{\sigma_o}\right)^n$$

where;

$\varepsilon$ = true strain

$\sigma$ = true stress

$\varepsilon_o$ = $S_y/E$, true yield strain

$\sigma_o$ = $S_y$, true yield stress

$S_y$ = Yield strength

E = Elastic modulus

$$\alpha = \left[\frac{\ln(1+e_u)}{\ln\left(1+S_y/E\right)} - \frac{S_u(1+e_u)}{S_y\left(1+S_y/E\right)}\right]\left[\frac{S_u(1+e_u)}{S_y\left(1+S_y/E\right)}\right]^{-n}$$

$S_u$ = Ultimate tensile strength

$e_u$ = Ultimate strain

n = $1/[\ln(1+e_u)]$

Using this relationship, and the material properties from Table 2-12 and Table 2-13, the upper-bound and lower-bound true stress-strain curves are developed for all of the overpack shell stainless steel materials (except for the lid lug Type XM-19 material) over the temperature range of interest (-20°F to 200°F). The resulting stress-strain curves are shown in Figure 2-4 along with enveloping upper-bound and lower-bound stress-strain curves used for the overpack NCT and HAC free drop structural analyses. The enveloping upper-bound and lower-bound true stress-strain design data used for the overpack stainless steel shells in the drop loads analysis are summarized in Table 2-17. The lower-bound curve is developed based on the minimum yield

and ultimate strength values from Table 2-12 and Table 2-13 at an upper-bound temperature of 93°C and the lowest maximum elongation for all product forms and material types permitted for the fabrication of the overpack shell assembly components (i.e., 30% for A479, Type 304 and Type 316 stainless steels). However, the upper-bound design curve is based on a yield strength of 310 MPa and a tensile strength of 655 MPa since the values given in Table 2-12 and Table 2-13 represent the minimum expected values at temperature. In addition, the upper-bound design curve is conservatively extended beyond the failure strain of the overpack shell materials to a maximum strain of approximately 60%. This is done to avoid material failure that may lead to non-conservative predictions of the upper-bound drop loads.

The structural evaluation of the overpack for the HAC free drop and HAC puncture tests is performed using a plastic kinematic material model for the overpack closure bolts. The material model is defined by an elastic modulus, yield stress, tangent slope, and failure strain. The tangent modulus ($E_t$) is calculated based upon the yield stress ($S_y$), yield strain ($\varepsilon_y$), ultimate tensile stress ($S_u$), and failure strain ($\varepsilon_u$) as follows:

$$E_t = \frac{S_u - S_y}{\varepsilon_u - \varepsilon_y}$$

Where;

$\varepsilon_y$ = $(S_y/E) + 0.002$

$S_y$ = Yield stress (0.2% offset)

E = Elastic modulus

The upper-bound and lower-bound plastic-kinematic material properties for the overpack closure bolt material used for the structural evaluation of the package for the HAC free drop and HAC puncture tests are summarized in Table 2-18.

### 2.2.1.2 Shielding Material

The shielding components of the package are fabricated from DU that is alloyed with 2% molybdenum by weight (U-2% Mo). The addition of molybdenum results in the formation of a second phase that increases the yield strength of DU and improves the ductility of the material. The mechanical properties of DU over the temperature range of interest are summarized in Table 2-19.

### 2.2.1.3 Overpack Foam

The overpack base and lid assemblies are filled with rigid, closed-cell LAST-A-FOAM® FR-3714 polyurethane foam having a nominal density of 13.5 pcf (216 kg/m$^3$). The polyurethane foam is installed in-situ in the overpack shells, with foam rise parallel to the longitudinal axis of the package. The nominal static crush strength data of the polyurethane foam at room

temperature, both parallel and perpendicular to the direction of foam rise, are summarized in Table 2-20.

The dynamic stress versus strain curves for the polyurethane foam material, which are used for the NCT and HAC free drop test evaluations, are developed based on data provided by the foam manufacturer [2.16]. Upper-bound and lower-bound dynamic stress versus strain curves are developed considering the effects of crush direction, i.e., parallel or perpendicular to the direction of foam rise; temperature; strain rate; and tolerance on foam crush strength. The minimum and maximum foam temperatures considered are -29°C and 82°C, respectively. These temperatures bound the range of temperatures that the foam will experience under all initial conditions for the NCT and HAC free drop tests. The dynamic crush strength ($\sigma_{Dynamic}$) of foam is proportional to the static crush strength ($\sigma_{Static}$) and is predicted by the following equations:

$$\sigma_{Dynamic} = (Y_{Int})(\sigma_{Static})^{S}$$

Where $Y_{Int}$ and S are the dynamic crush strength regression coefficients provided by the foam manufacturer ([2.16], Table 8). The static crush strength of foam at the lower- and upper-bound temperatures of -29°C and 82°C are calculated based on temperature correlation factors ($C_T$) provided by the foam manufacturer ([2.16], Tables 6 and 7).

The average static compressive strength of the polyurethane foam at room temperature is required to be within ±10% of the nominal value for crushing parallel and perpendicular to the direction of foam rise. Therefore, the maximum and minimum static crush strengths at each strain value are taken as 110% and 90% of the nominal crush strength value.

The dynamic crush strength versus strain data for foam temperatures of -29°C and 82°C are summarized in Table 2-21. The data shows that the dynamic crush strength of polyurethane foam parallel to the direction of foam rise is slightly higher than the perpendicular to rise dynamic crush strength in all cases. For design purposes, upper-bound and lower-bound dynamic stress versus strain curves are developed and used for all drop analyses, regardless of crush orientation. The bounding design dynamic crush strength data is summarized in Table 2-22 and shown in Figure 2-5 along with the maximum and minimum dynamic crush strength values at temperature.

#### 2.2.1.4 Other Materials

The overpack base thermal spider is a non-structural component that is fabricated from SB-152 copper sheet material. The function of the thermal spider is to conduct heat through the overpack base sidewall. Although the thermal spider is not relied upon for structural support, it is included in the structural evaluation of the overpack because its stiffness has a minor effect on the drop loads that are imparted to the cask. A plastic kinematic material model is used for the thermal spider. The material model is defined by an elastic modulus, yield stress, tangent slope, and failure strain. The elastic modulus, yield strength, and failure strain of SB-152 copper sheet material over the temperature range of interest are obtained from the ASME Code, Section II, Part B [2.17] and Part D [2.11]. The tangent modulus is calculated as described in Section 2.2.1.1. The upper-bound and lower-bound plastic-kinematic material properties for the

thermal spider material used for the structural evaluation of the package for the NCT free drop, HAC free drop, and HAC puncture tests are summarized in Table 2-23.

### 2.2.2 Chemical, Galvanic, or Other Reactions

The package's materials of construction are evaluated for possible chemical, galvanic, or other reactions considering the contact of dissimilar materials and the operating environments as shown in Table 2-24.

DU/steel interactions are considered, including galvanic corrosion, stress corrosion cracking, and eutectic formation. Eutectic formation does not affect package performance because the service temperatures are lower than the eutectic formation temperature. No significant DU interactions are found to occur that would affect package performance.

Hydrogen generation production by chemical and galvanic reactions is evaluated and found not to affect package effectiveness. The payload generates hydrogen through radiolysis, as discussed in Section 3.3.2.

The package has no significant chemical, galvanic, or other reactions that affect package performance.

### 2.2.3 Effects of Radiation on Materials

The package is designed using materials that will withstand damaging effects from radiation. Durable materials of construction such as austenitic stainless steel, ferritic bolting steel, and DU are unaffected by the radiation levels in this package.

The polyurethane foam material used for the overpack cores is unaffected by gamma radiation exposure up to $2 \times 10^8$ rads, equivalent to 1,000 rads/hour for a period of 20 years. At radiation exposure up to $2 \times 10^8$ rads, testing shows no effect on density or crush strength ([2.16], Table 4). Furthermore, the resistance of the polyurethane foam material to water absorption is unaffected by radiation exposure up to $1 \times 10^7$ rads ([2.16], Table 5).

The ethylene propylene O-ring material has good radiation-resistance properties [2.18]. Most elastomers exhibit unacceptable compression set after $10^8$ rads. Ethylene propylene O-rings tested to $10^7$ rads exhibit moderate compression set, and exposures to $10^6$ rads produce little effect on all elastomer O-ring materials. The package containment and test O-rings only receive direct radiation from the payload momentarily as the package is loaded. Many hundreds of loading cycles would be required to reach $10^6$ rads, therefore normal wear is the main factor affecting their replacement frequency. The cleanliness seal is more directly irradiated by the payload since it is inside the shielded region of the cask assembly. The cleanliness seal is therefore replaced every shipment to assure that it is not adversely affected by radiation.

The O-rings are coated with a thin film of silicone-based lubricant to help protect the O-ring from damage by abrasion, pinching, or cutting. The lubricant also helps to seat the O-ring properly and protect the polymer from environmental damage. Because the O-ring lubricant is

frequently cleaned and replaced, and because most of the lubricant's benefit occurs during installation, radiation damage is not a concern.

A nickel-based thread lubricant is specified for threaded fasteners. This material is commonly used for nuclear applications and is suitable for use in radiation environments. None of the package fasteners are located in high exposure areas, and the lubricant is frequently cleaned and replaced, so the lubricant is not subject to radiation damage.

**Table 2-11 – Packaging Material Specifications (2 Pages)**

| Packaging Assembly | Packaging Component | Material Specification | Reference Section |
|---|---|---|---|
| Cask Body Assembly | Containment Shell | SA-479, Type 304 or Type 316 | 2.2.1.1 |
| | Outer Shell and Bottom | A240, Type 304 or Type 316 | 2.2.1.1 |
| | Radial and Bottom Shields | DU Alloy | 2.2.1.2 |
| | Threaded Insert, Closure Bolt Holes | Type 304 Stainless Steel | 2.2.1.1 |
| Closure Lid Assembly | Closure Lid | SA-240 or SA-479, Type 304 or Type 316 | 2.2.1.1 |
| Cask Closure Bolts | --- | SA-320, Grade L43 | 2.2.1.1 |
| Shield Plug Assembly | Casing and Top Plate | A240 or A479, Type 304 or Type 316 | 2.2.1.1 |
| | Shield Plug Core | DU Alloy | 2.2.1.2 |
| | Threaded Insert, Lifting Hole | Type 304 Stainless Steel | 2.2.1.1 |
| Shield Lid Assembly | Top Plate | A240 or A479, Type 304 or Type 316 | 2.2.1.1 |
| | Casing Plate | A240, Type 304 or Type 316 | 2.2.1.1 |
| | Shield lid | DU Alloy | 2.2.1.2 |
| | Attachment Bolts | A193, Grade B8 | 2.2.1.1 |
| Overpack Base Assembly | Inner Bottom, Outer Bottom, Flange, and Pour Hole Covers | A240 or A479, Type 304 or Type 316 | 2.2.1.1 |
| | Inner and Outer Shells | A240, Type 304 or Type 316 | 2.2.1.1 |
| | Threaded Inserts, Overpack Bolting Flange | Type 304 Stainless Steel | 2.2.1.1 |
| | Thermal Spider | Copper, B152 | 2.2.1.4 |
| | Inner Foam Core | LAST-A-FOAM® FR-3714 Polyurethane Foam | 2.2.1.3 |

**Table 2-11 – Packaging Material Specifications (2 Pages)**

| Packaging Assembly | Packaging Component | Material Specification | Reference Section |
|---|---|---|---|
| Overpack Lid Assembly | Outer Top, Flange, and Pour Hole Covers | A240 or A479, Type 304 or Type 316 | 2.2.1.1 |
| | Lugs | A240, Type XM-19 | 2.2.1.1 |
| | Inner Foam Core | LAST-A-FOAM® FR-3714 Polyurethane Foam | 2.2.1.3 |
| Overpack Closure Bolts | --- | A320, Grade L43 | 2.2.1.1 |

**Table 2-12 – Mechanical Properties of Type 304 Stainless Steel**

| Temp. (°C) | Design Stress Intensity, $S_m$[2] (MPa) | Yield Strength, $S_y$[3] (MPa) | Tensile Strength, $S_u$[4] (MPa) | Modulus of Elasticity, E[5] (MPa X $10^3$) | Mean Coef. Of Thermal Expansion, α[6] (m/m/°C x $10^{-6}$) |
|---|---|---|---|---|---|
| -40 | 138 | 207 | 517 | *199* | *14.7* |
| -29 | 138 | 207 | 517 | *198* | *14.8* |
| 21 | 138 | 207 | 517 | 195 | 15.3 |
| 38 | 138 | 207 | 517 | *194* | 15.5 |
| 93 | 138 | 172 | 490 | 190 | 16.0 |

Notes:
1. Values for SA-240/A240 and SA-479/A479 product specifications.
2. ASME Code, Section II, Part D [2.11], Table 2A.
3. ASME Code, Section II, Part D [2.11], Table Y-1.
4. ASME Code, Section II, Part D [2.11], Table U.
5. ASME Code, Section II, Part D [2.11], Table TM-1, Material Group G.
6. ASME Code, Section II, Part D [2.11], Table TE-1, Group 3, Coefficient B (mean from 70°F).
7. Values shown in *italics* are calculated using linear interpolation or linear extrapolation.

**Table 2-13 – Mechanical Properties of Type 316 Stainless Steel**

| Temp. (°C) | Design Stress Intensity, $S_m$[2] (MPa) | Yield Strength, $S_y$[3] (MPa) | Tensile Strength, $S_u$[4] (MPa) | Modulus of Elasticity, E[5] (MPa X $10^3$) | Mean Coef. Of Thermal Expansion, α[6] (m/m/°C x $10^{-6}$) |
|---|---|---|---|---|---|
| -40 | 138 | 207 | 517 | *199* | *14.7* |
| -29 | 138 | 207 | 517 | *198* | *14.8* |
| 21 | 138 | 207 | 517 | 195 | 15.3 |
| 38 | 138 | 207 | 517 | *194* | 15.5 |
| 93 | 138 | 179 | 517 | 190 | 16.0 |

Notes:
1. Values for SA-240/A240 and SA-479/A479 product specifications.
2. ASME Code, Section II, Part D [2.11], Table 2A.
3. ASME Code, Section II, Part D [2.11], Table Y-1.
4. ASME Code, Section II, Part D [2.11], Table U.
5. ASME Code, Section II, Part D [2.11], Table TM-1, Material Group G.
6. ASME Code, Section II, Part D [2.11], Table TE-1, Group 3, Coefficient B (mean from 70°F).
7. Values shown in *italics* are calculated using linear interpolation or linear extrapolation.

**Table 2-14 – Mechanical Properties of A240, Type XM-19 Stainless Steel**

| Temp. (°C) | Design Stress Intensity, $S_m$[2] (MPa) | Yield Strength, $S_y$[3] (MPa) | Tensile Strength, $S_u$[4] (MPa) | Modulus of Elasticity, E[5] (MPa X $10^3$) | Mean Coef. Of Thermal Expansion, α[6] (m/m/°C x $10^{-6}$) |
|---|---|---|---|---|---|
| -40 | *230* | *379* | *690* | *199* | *14.3* |
| -29 | 230 | 379 | 690 | *198* | *14.4* |
| 21 | 230 | 379 | 690 | 195 | 14.8 |
| 38 | 230 | 379 | 690 | *194* | 14.8 |
| 66 | 229 | 343 | *688* | *192* | 15.1 |
| 93 | 228 | 325 | 685 | 190 | 15.3 |

Notes:
1. ASME Code, Section II, Part D [2.11], Table 2A.
2. ASME Code, Section II, Part D [2.11], Table Y-1.
3. ASME Code, Section II, Part D [2.11], Table U.
4. ASME Code, Section II, Part D [2.11], Table TM-1, Material Group G.
5. ASME Code, Section II, Part D [2.11], Table TE-1, Group 4, Coefficient B (mean from 70°F).
6. Values shown in *italics* are calculated using linear interpolation or linear extrapolation.

**Table 2-15 – Mechanical Properties of SA-320/A320, Grade L43 Bolting Steel**

| Temp. (°C) | Design Stress Intensity, $S_m$[1] (MPa) | Yield Strength, $S_y$[2] (MPa) | Tensile Strength, $S_u$[3] (MPa) | Modulus of Elasticity, E[4] (MPa X $10^3$) | Mean Coef. Of Thermal Expansion, α[5] (m/m/°C x $10^{-6}$) |
|---|---|---|---|---|---|
| -40 | 241 | 724 | 862 | *195* | *11.1* |
| -29 | 241 | 724 | 862 | *194* | *11.1* |
| 21 | 241 | 724 | 862 | 192 | 11.5 |
| 38 | 241 | 724 | 862 | *191* | 11.7 |
| 93 | 228 | 683 | 862 | 187 | 12.1 |

Notes:
1. ASME Code, Section II, Part D [2.11], Table 4.
2. In accordance with ASME Code, Section II, Part D [2.11], Table 4, General Note (a), the yield strength is equal to 3 times the allowable stress value, $S_m$.
3. Minimum tensile strength from ASME Code, Section II, Part D [2.11], Table 4. The tensile strength is assumed to remain constant up to 93°C.
4. ASME Code, Section II, Part D [2.11], Table TM-1, Material Group B.
5. ASME Code, Section II, Part D [2.11], Table TE-1, Group 1, Coefficient B (mean from 70°F).
6. Values shown in *italics* are calculated using linear interpolation or linear extrapolation.

**Table 2-16 – Mechanical Properties of A193, Grade B8 Bolting Steel**

| Temp. (°C) | Design Stress Intensity, $S_m$[1] (MPa) | Yield Strength, $S_y$[2] (MPa) | Tensile Strength, $S_u$[3] (MPa) | Modulus of Elasticity, E[4] (MPa X $10^3$) | Mean Coef. Of Thermal Expansion, α[5] (m/m/°C x $10^{-6}$) |
|---|---|---|---|---|---|
| -40 | 69 | 207 | 517 | *199* | *14.7* |
| -29 | 69 | 207 | 517 | *198* | *14.8* |
| 21 | 69 | 207 | 517 | 195 | 15.3 |
| 38 | 69 | 207 | 517 | *194* | 15.5 |
| 93 | 57 | 172 | 490 | 190 | 16.0 |

Notes:
1. ASME Code, Section II, Part D [2.11], Table 4.
2. ASME Code, Section II, Part D [2.11], Table Y-1.
3. ASME Code, Section II, Part D [2.11], Table U.
4. ASME Code, Section II, Part D [2.11], Table TM-1, Material Group G.
5. ASME Code, Section II, Part D [2.11], Table TE-1, Group 3, Coefficient B (mean from 70°F).
6. Values shown in *italics* are calculated using linear interpolation or linear extrapolation.

**Table 2-17 – Stainless Steel True Stress-Strain Design Data**

| Lower-Bound Curve | | Upper-Bound Curve | |
|---|---|---|---|
| **True Strain** | **True Stress (Pa)** | **True Strain** | **True Stress (Pa)** |
| 0.00055 | 5.99E+07 | 0.00049 | 8.81E+07 |
| 0.00250 | 1.20E+08 | 0.00153 | 1.76E+08 |
| 0.00718 | 1.80E+08 | 0.00434 | 2.64E+08 |
| 0.01593 | 2.39E+08 | 0.01077 | 3.52E+08 |
| 0.03004 | 2.99E+08 | 0.02328 | 4.40E+08 |
| 0.05083 | 3.59E+08 | 0.04485 | 5.28E+08 |
| 0.07959 | 4.19E+08 | 0.07901 | 6.17E+08 |
| 0.11761 | 4.79E+08 | 0.12982 | 7.05E+08 |
| 0.16616 | 5.39E+08 | 0.20181 | 7.93E+08 |
| 0.22653 | 5.99E+08 | 0.30000 | 8.81E+08 |
| 0.30000 | 6.59E+08 | 0.42991 | 9.69E+08 |
| --- | --- | 0.59749 | 1.06E+09 |

Notes:
1. Lower-bound data calculated based on the lowest yield and ultimate strength of all overpack shell stainless steel materials at an upper-bound temperature of 93°C and an ultimate strain of 40%. The stress-strain data is terminated at a strain of 30%, equal to the lowest maximum elongation for all product forms and material types permitted for the fabrication of the overpack shell assembly components.
2. Upper-bound data based on an upper-bound yield strength 310 MPa, an upper-bound ultimate strength of 655 MPa, and an ultimate strain of 30%. The upper-bound stress-strain data is extended to a strain of approximately 60% to avoid material failure that may lead to non-conservative predictions of the upper-bound drop loads.

**Table 2-18 – SA-320/A320, Grade L43 Alloy Bolting Steel Plastic-Kinematic Properties**

| Parameter | Upper Bound, -29°C | Lower Bound, 93°C |
|---|---|---|
| Elastic Modulus, $E^{(1)}$ (MPa) | 1.94E5 | 1.87E5 |
| Yield Strength, $S_y^{(1)}$ (MPa) | 724 | 683 |
| Tensile Strength, $S_u^{(1)}$ (MPa) | 862 | 862 |
| Tangent Modulus, $E_t$ (MPa) | 894 | 1,158 |
| Failure Strain, $\varepsilon_u^{(2)}$ | 0.16 | 0.16 |

Notes:
1. Values from Table 2-15 at temperature.
2. Maximum elongation of SA-320, Grade L43 alloy bolting steel from ASME BPVC, Section II, Part A [2.19], Specification SA-320. Table 1.

**Table 2-19 – Mechanical Properties of DU Alloy**

| Temperature (°C) | Yield Strength, $S_y$(1) (MPa) | Tensile Strength, $S_u$(1) (MPa) | Modulus of Elasticity, E(2) (MPa X $10^3$) | Mean Coef. Of Thermal Expansion, α(3) (m/m/°C x $10^{-6}$) |
|---|---|---|---|---|
| -40 | 420 | 850 | --- | 11.5 |
| -29 | 420 | 850 | --- | 11.7 |
| 21 | 405 | 810 | 172 | 12.7 |
| 38 | 400 | 780 | --- | 13.0 |
| 93 | 380 | 690 | --- | 14.1 |

Notes:
1. Yield and ultimate strength of U-2% Mo from Figure 5 of [2.12].
2. Average tension modulus of DU from [2.20].
3. Properties from Figure I-2 of [2.21]. Values shown in *italics* are calculated by linear extrapolation.

**Table 2-20 – Overpack Foam Static Stress-Strain Data at Room Temperature**

| Strain | Static Crush Strength (psi) | |
|---|---|---|
| | Parallel-to-Rise | Perpendicular-to-Rise |
| 10% | 464 | 472 |
| 20% | 469 | 490 |
| 30% | 500 | 524 |
| 40% | 560 | 591 |
| 50% | 695 | 734 |
| 60% | 1,003 | 1,059 |
| 65% | 1,306 | 1,377 |
| 70% | 1,821 | 1,910 |

Notes:
1. Properties from [2.16].

**Table 2-21 – Foam Dynamic Stress-Strain Properties**

| Strain | Dynamic Crush Strength (psi) | | | |
|---|---|---|---|---|
| | Cold (-29°C/-20°F) | | Hot (82°C/180°F) | |
| | Nominal | Upper-Bound | Nominal | Lower-Bound |
| **Parallel-to-Rise** | | | | |
| 0.10 | 1,005 | 1,109 | 450 | 403 |
| 0.20 | 939 | 1,033 | 442 | 398 |
| 0.30 | 964 | 1,060 | 477 | 429 |
| 0.40 | 1,038 | 1,142 | 514 | 462 |
| 0.50 | 1,236 | 1,359 | 617 | 556 |
| 0.60 | 1,649 | 1,811 | 834 | 752 |
| 0.65 | 2,169 | 2,384 | 1,091 | 983 |
| 0.70 | 2,406 | 2,636 | 1,334 | 1,206 |
| **Perpendicular-to-Rise** | | | | |
| 0.10 | 1,015 | 1,120 | 458 | 411 |
| 0.20 | 981 | 1,080 | 462 | 416 |
| 0.30 | 1,010 | 1,111 | 492 | 443 |
| 0.40 | 1,112 | 1,224 | 542 | 488 |
| 0.50 | 1,295 | 1,424 | 652 | 587 |
| 0.60 | 1,713 | 1,881 | 880 | 793 |
| 0.65 | 2,215 | 2,434 | 1,168 | 1,052 |
| 0.70 | 2,346 | 2,570 | 1,376 | 1,244 |

**Table 2-22 – Overpack Foam Upper- and Lower-Bound Dynamic Stress-Strain Data**

| Strain | Dynamic Crush Strength (psi) | |
|---|---|---|
| | Upper Bound | Lower Bound |
| 0.05[1] | 1,120 (7.72 MPa) | 398 (2.74 MPa) |
| 0.10 | 1,120 (7.72 MPa) | 398 (2.74 MPa) |
| 0.20 | 1,120 (7.72 MPa) | 398 (2.74 MPa) |
| 0.30 | 1,120 (7.72 MPa) | 429 (2.96 MPa) |
| 0.40 | 1,225 (8.45 MPa) | 462 (3.19 MPa) |
| 0.50 | 1,430 (9.86 MPa) | 556 (3.83 MPa) |
| 0.60 | 1,890 (13.03 MPa) | 752 (5.19 MPa) |
| 0.65 | 2,440 (16.82 MPa) | 980 (6.76 MPa) |
| 0.70 | 2,640 (18.20 MPa) | 1,220 (8.41 MPa) |

Notes:
1. The foam manufacturer's crush strength data [2.16] is provided at 10% strain increments. However, the foam manufacturer's literature indicates that the foam crush strength typically reaches the yield strength at strains of approximately 5%. Therefore, the foam crush strength is assumed to increases linearly from zero at 0% strain to the 10% strain crush strength value at 5% strain.

**Table 2-23 – SB-152 Copper Sheet Plastic-Kinematic Properties**

| Parameter | Upper Bound, -29°C | Lower Bound, 93°C |
|---|---|---|
| Elastic Modulus, $E^{(1)}$ (MPa) | 1.19E5 | 1.14E5 |
| Yield Strength, $S_y^{(2)}$ (MPa) | 69 | 56 |
| Tensile Strength, $S_u^{(3)}$ (MPa) | 207 | 188 |
| Tangent Modulus, $E_t$ (MPa) | 345 | 330 |
| Failure Strain, $\varepsilon_u^{(4)}$ | 0.40 | 0.40 |

Notes:
1. ASME BPVC, Section II, Part D [2.11], Table TM-4, Material C12200.
2. ASME BPVC, Section II, Part D [2.11], Table Y-1.
3. ASME BPVC, Section II, Part D [2.11], Table U.
4. Maximum elongation of ASME BPVC, Section II, Part B [2.17], Specification SB-152, Section 8.1.

**Table 2-24 – Summary of MIDUS Material Interactions**

| | Decon Fluid | DU | E-P O-rings | Nylon (screw) | O-ring lubricant | Foam | Product | Stainless Steel | Ni-Cr-Mo Fasteners | Thread Lubricant | Copper | Brazing Metal |
|---|---|---|---|---|---|---|---|---|---|---|---|---|
| **Decon Fluid** | | -- | S | S | S | -- | S | S | S | S | -- | -- |
| **DU** | | | -- | -- | -- | -- | -- | NHS | -- | -- | -- | -- |
| **EP O-rings** | | | | NHS | NHS | NHS | H | NHS | -- | -- | -- | -- |
| **Nylon Screw** | | | | | NHS | NHS | -- | NHS | -- | -- | -- | -- |
| **O-ring lubricant** | | | | | | -- | H | NHS | -- | -- | -- | -- |
| **Foam** | | | | | | | -- | NHS | -- | -- | NHS | NHS |
| **Product** | | | | | | | | NHS | -- | -- | -- | -- |
| **Stainless Steel** | | | | | | | | | NHS | NHS | NHS | NHS |
| **Ni-Cr-Mo Fastener** | | | | | | | | | | NHS | -- | -- |
| **Thread Lubricant** | | | | | | | | | | | -- | -- |
| **Copper** | | | | | | | | | | | | NHS |

**Notes:**

N = normal conditions of transportation; H = hypothetical accident conditions; S = service conditions at medical isotope facilities.

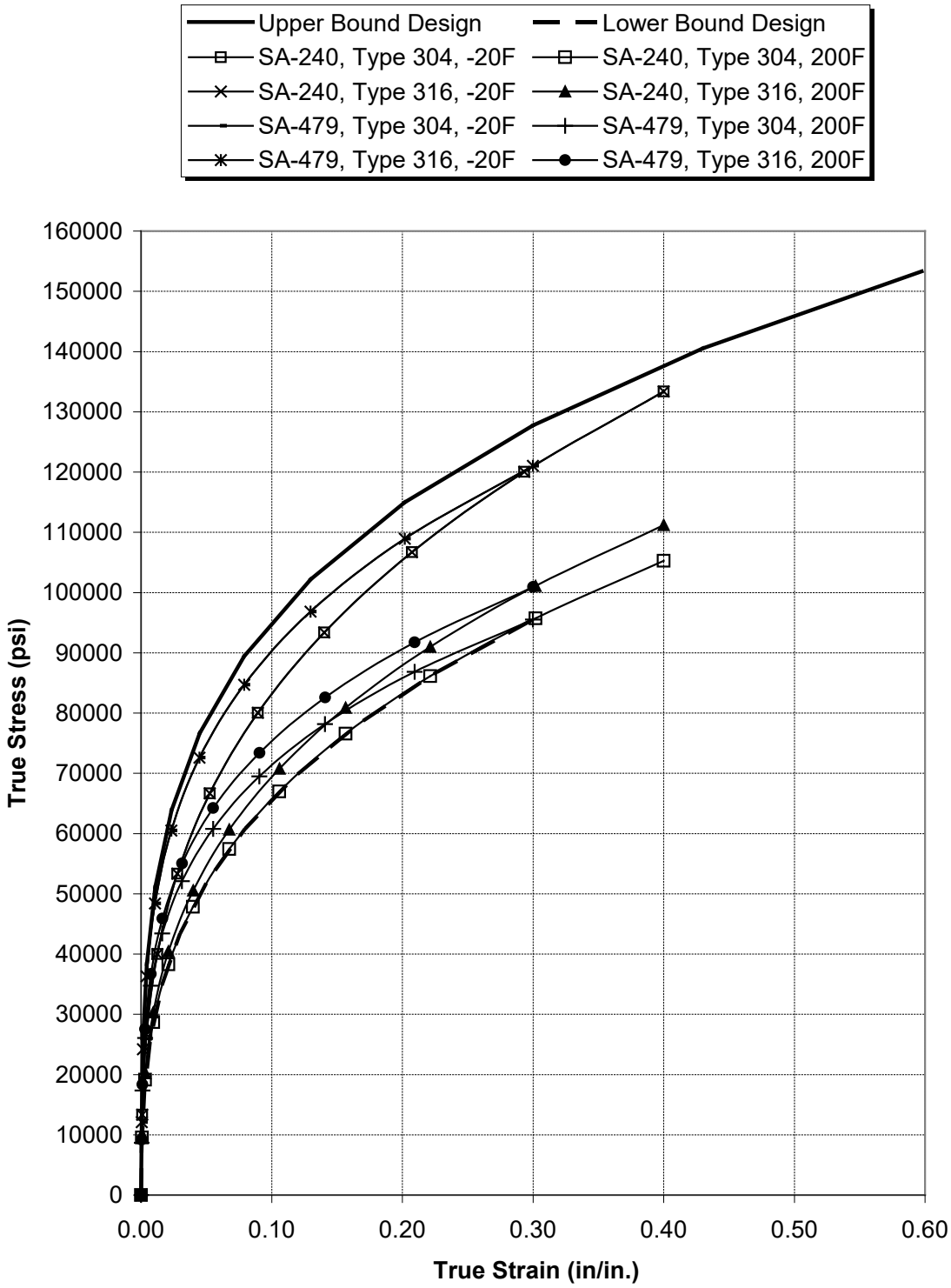


**Figure 2-4 – Stainless Steel True Stress-Strain Design Curves**

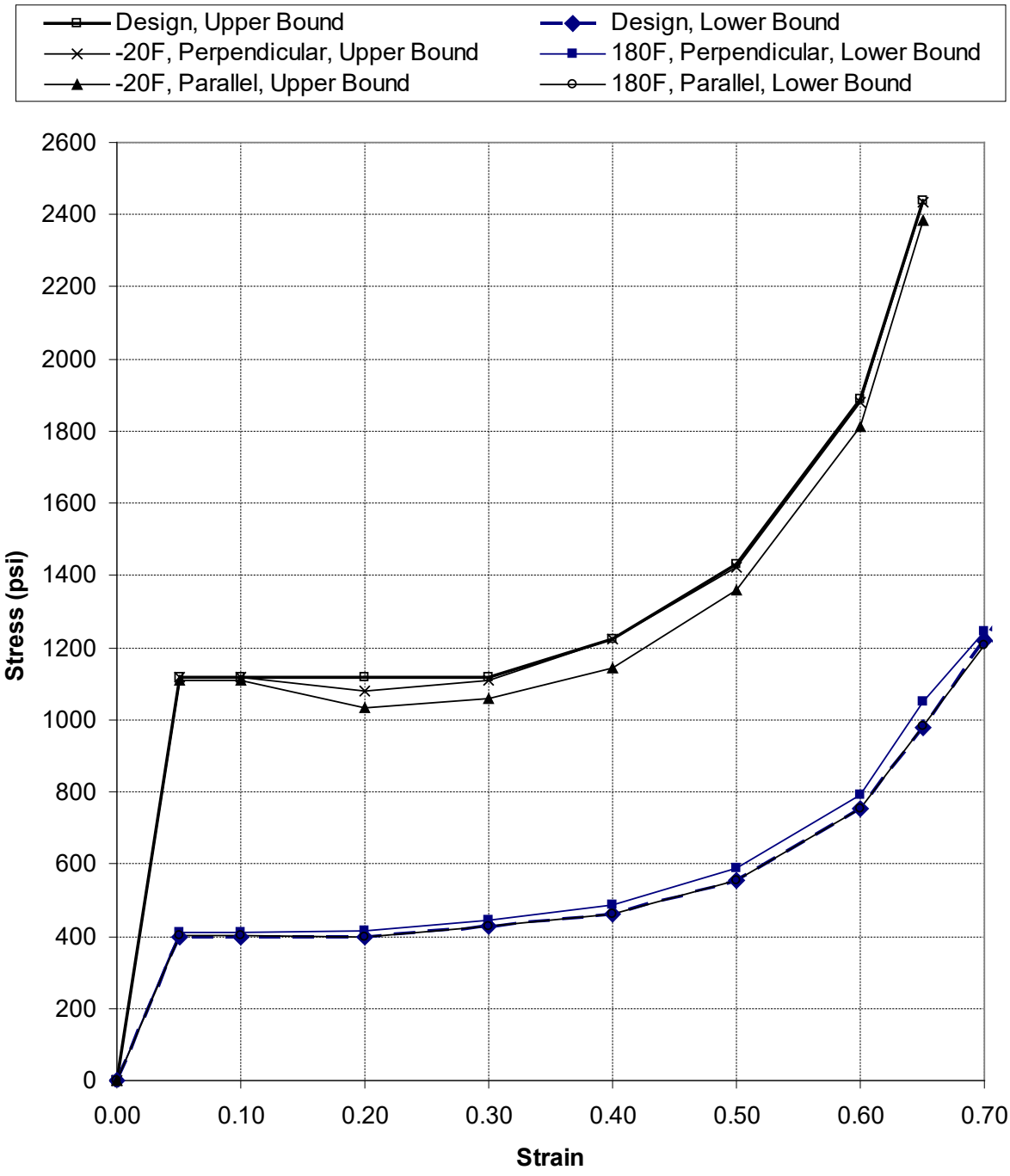


**Figure 2-5 – Overpack Foam Dynamic Stress-Strain Curves**

## 2.3 Fabrication and Examination

### 2.3.1 Fabrication

All work performed to fabricate the package is performed under Energy*Solutions*' 10 CFR 71, Subpart H quality assurance program, NRC approval number 0935. The package containment system is fabricated in accordance with the applicable requirements of Subsections WA and WB of Section III, Division 3 of the ASME Code [2.1]. Use of an NPT Certificate Holder and an Authorized Inspection Agency is not required for the construction of the package containment system. The non-containment structural components of the package are fabricated in accordance with the applicable requirements of Subsection NF [2.2] of the ASME Code for plate- and shell-type Class 2 supports. Standard industry practices are used for the fabrication of the DU alloy gamma shield components, the overpack base thermal spider and its brazed connections to the overpack base shells, and the overpack base and lid assembly polyurethane foam cores.

All components that form the package containment system are fabricated from materials permitted by Subsection WB [2.1] of the ASME Code and included in Section II, Part D, of the ASME Code [2.11]. All other non-containment structural components of the package are fabricated from ASTM materials that are equivalent to ASME materials, as permitted by NUREG/CR-3854 [2.14]. All package welds, with the exception of the overpack lid lug attachment welds, are made with SFA-5.9 ER308L, ER308LSi, or ER316L weld filler metal. The overpack lid lug attachment welds are made with SFA-5.9 ER309L or ER309LSi weld filler metal. All weld filler metal is required to have a minimum delta ferrite content of 5 FN. The quality category of the weld material is required be equal to or greater than the higher quality category of the components being joined. A certified material test report (CMTR) is provided for all steel materials, including weld filler metals, used to fabricate the package.

Consumables, such as threaded inserts and elastomeric O-rings, are procured from commercial suppliers and commercially dedicated in accordance with the requirements of the Energy*Solutions* QA program, commensurate with their safety functions.

All materials, components, and assemblies used for the fabrication of the package, including the weld filler metal, are labeled to maintain control and traceability of materials throughout the fabrication process. Marking of materials, components, and assemblies is done using permanent methods that do not result in harmful contamination or sharp discontinuities, or infringe upon the minimum required material thickness.

All operations associated with the fabrication and assembly of the package are included in written shop instructions, e.g., fabrication travelers and/or procedures. All welding and brazing is performed in accordance with a written welding procedure specification (WPS) or brazing procedure specification (BPS) that is qualified in accordance with the applicable requirements of the ASME Code. All personnel performing welding or brazing are qualified to use the welding or brazing procedure, and their qualifications are documented in accordance with the applicable requirements of Section IX of the ASME Code [2.22]. Only GTAW and GMAW welding processes are permitted for the fabrication of the package.

The general processes used to fabricate each finished assembly of the package are described as follows:

*Cask Body Assembly*

The cask body assembly is constructed from a containment shell, outer bottom, outer shell, bottom shield, radial shield, and threaded inserts. The DU alloy material is cast into molds that are slightly larger than the finished dimensions of the cask body gamma shield components. The DU alloy castings are heat-treated in a vacuum induction furnace to obtain the desired mechanical properties. The heat-treated DU alloy castings are then precision-machined to the dimensions shown on the general arrangement drawings in Section 1.3.2.

The cask body containment shell and outer bottom are both fabricated by machining solid pieces of bar or plate material. This minimizes the amount of welding and/or forming operations required to fabricate the package, which results in less weld distortion and residual stress. The cask body outer shell is fabricated from rolled steel plate with a full-penetration longitudinal seam weld to form a cylinder. The use of a backing bar made from similar material is permitted for the longitudinal seam weld, provided that it is removed for the finished assembly. The cask body outer shell may be rolled to the required finished dimensions or formed from thicker plate that is machined to achieve the required dimensions. The outer shell is aligned with the containment shell and outer bottom and attached using full-penetration circumferential seam welds, sealing the DU-alloy gamma shield components inside the cask body shell.

Some of the critical features of the cask body, such as the top face of the cask bolting flange, the leak-test and containment O-ring grooves, and closure bolt holes may be machined to the final dimensions shown on the general arrangement drawings in Section 1.3.2 after completing the cask body welds. Following completion of machining operations, threaded inserts are installed in the closure bolt holes in accordance with the manufacturer's recommendations for bottoming taps.

*Shield Plug Assembly*

The cask shield plug assembly is constructed from a casing shell, top plate, DU core, and a threaded insert. The processes used to fabricate the DU core of the shield plug are the same as those described above for the cask body DU shield components. The shield plug casing shell and top plate are both fabricated by machining solid pieces of bar or plate material to minimize the amount of welding and/or forming operations required to fabricate the finished shield plug. The DU core is placed inside the casing shell, and the top plate is attached using a full-penetration circumferential seam weld. After completing the weld, the shield plug assembly is machined to the final dimensions shown on the general arrangement drawings in Section 1.3.2. Following completion of machining operations, the threaded insert is installed in the shield plug lifting hole in accordance with the manufacturer's recommendations for bottoming taps.

*Closure Lid Assembly*

The closure lid assembly is constructed from a closure lid, test port plug, and threaded inserts. The closure lid is fabricated by machining a solid piece of bar or plate material to the dimensions shown on the general arrangement drawings in Section 1.3.2. Following completion of machining operations, the threaded inserts are installed in the cask lifting attachment holes and shield lid attachment holes in accordance with the manufacturer's recommendations for bottoming taps. The test port plug is installed in the leak-test port of the closure lid after coating the test port plug O-ring seal and the associated sealing surface in the leak-test port of the closure lid with O-ring lubricant in accordance with the O-ring manufacturer's recommendations.

*Shield Lid Assembly*

The shield lid assembly is constructed from a top plate, casing plate, DU shield plate, and two shield lid attachment bolts. The processes used to fabricate the DU alloy core of the shield lid are the same as those described above for the cask body DU shield components. The shield lid top plate is fabricated by machining a solid piece of bar or plate material, whereas the shield lid top plate is fabricated from a single piece of plate. The shield lid core is placed inside the shield lid top plate and the casing plate is attached using a full-thickness, all-around, partial-penetration groove weld to seal the DU alloy gamma shield inside the cask body shell. The shield lid attachment bolts are fabricated from M10 X 1.5 socket heat cap screws that are machined as shown on the general arrangement drawings in Section 1.3.2. The shield lid attachment bolts are threaded through the tapped holes in the shield lid top plate, making them captured hardware.

*Overpack Base Assembly*

The overpack base assembly is constructed from a shell assembly that is filled with polyurethane foam. The shell assembly is constructed from an outer bottom, outer shell, flange, inner shell, inner bottom, thermal spider, and thermal relief plugs. The outer bottom, flange, and inner bottom are all fabricated from a solid piece of bar or plate material that is machined to the dimensions shown on the general arrangement drawings in Section 1.3.2. The inner and outer shells are both fabricated from rolled steel plate with a full-penetration longitudinal seam weld to form a cylinder. The use of backing bars made from similar material is permitted for the shell longitudinal seam welds. The shells may be rolled to the required finished dimensions or formed from thicker plate and machined to achieve the required dimensions. The thermal spider is fabricated from copper sheet or plate material that is cut to size and mechanically formed to the dimensions shown on the general arrangement drawings in Section 1.3.2. The outer shell, flange, inner shell, and inner bottom are aligned and attached with all-around, full-penetration, circumferential seam welds, as shown on the general arrangement drawings in Section 1.3.2. Prior to welding the outer bottom in place, the thermal spider is brazed to the inner bottom and outer shell. The outer bottom is then aligned with the outer shell and attached with a full-penetration, circumferential seam weld.

Some features of the overpack base that are not required for foam installation, such as the finished dimensions of the bolting flange, the overpack bolt holes, and the holes for the tamper-indicating device, may be machined before or after completing the foam installation

process. However, the four nylon thermal relief plugs must be installed in the corresponding threaded holes of the overpack base shell prior to installing the polyurethane foam core. The polyurethane foam core of the overpack base is installed in-situ at the foam manufacturer's facility. The overpack base shell is positioned upside-down and filled with the liquid foam mixture through two pour holes located on the bottom plate of the shell . The foam is allowed to cure completely before welding the steel cover plates over the pour holes. Final machining operations of the overpack base features not completed prior to foam installation are then performed. Following completion of machining operations, threaded inserts are installed in each of the overpack base closure bolt holes in accordance with the manufacturer's recommendations and two locating pins are installed in the flange to facilitate overpack lid assembly installation operations.

*Overpack Lid Assembly*

The processes used to fabricate the overpack lid assembly are similar to those used to fabricate the overpack base. The overpack lid is constructed from a shell assembly that is filled with polyurethane foam. The shell assembly consists of a lid flange, outer top, four lid lugs, and four thermal relief plugs. The overpack lid flange and outer top are both fabricated from single, solid pieces of bar or plate material that are machined to the dimensions shown on the general arrangement drawings in Section 1.3.2. The lid flange and outer top are positioned and joined using an all-around, full-penetration, circumferential weld. The lid lugs, which are machined from plate material, are positioned and welded to the overpack lid outer top. The outer surfaces of the overpack lid may be machined to the finished dimensions following attachment of the lid lugs. Some features of the overpack lid that are not required for foam installation, such as the finished dimensions of the bolting flange, overpack bolt holes, and the holes for the tamper-indicating device, may be machined before or after completing the foam installation process. However, the four nylon thermal relief plugs must be installed in the corresponding threaded holes of the overpack base shell prior to installing the polyurethane foam core. The polyurethane foam core of the overpack lid is installed in-situ at the foam manufacturer's facility. The overpack lid shell is positioned upside-down and filled through two pour holes located on the overpack lid bottom plate with the liquid foam mixture. The foam is allowed to cure completely before welding the steel cover plates over the pour holes. Final machining operations of the overpack lid features not completed prior to foam installation are then performed.

### 2.3.2 Examination

Examination and testing of the package is performed under Energy*Solutions*' NRC-approved QA program. The components and assemblies of the package are inspected to assure that the package satisfies the dimensional requirements shown on the general arrangement drawings in Section 1.3.2 and are examined using non-destructive techniques to assure quality of workmanship. In addition, materials, components, and assemblies are tested to assure that they have the required critical characteristics and that they satisfy the acceptance criteria for all required functional tests. All operations associated with the examination and testing of the package are included in written shop instructions, e.g., fabrication travelers and/or procedures,

and performed by personnel that are trained and qualified in accordance with the requirements of the Energy*Solutions* QA program and the requirements of the applicable codes and standards using calibrated measuring and test equipment (M&TE). Witness and hold points are included in the written shop instructions for activities that require QA inspection or oversight. Copies of all written shop instructions, personnel training and qualification records, and M&TE calibration records are maintained with the final records package.

The processes used for the examination and testing of the package are described as follows:

*Material Tests*

The steel materials used to fabricate the components and assemblies of the package are furnished with CMTRs that assure that the materials possess the critical characteristics that are required to perform their safety functions. No additional examination or testing of these steel materials is required prior to fabrication.

The DU alloy material used to fabricate the gamma shield components of the package is tested to assure that it has the 2.0% ± 0.2% molybdenum by weight, a maximum carbon content of 0.2% by weight, and a minimum Charpy V-notch impact energy of 6 ft-lb at 70°F (21°C). The density of the finished DU alloy components, as determined from the measured weight and volume, is tested to assure that it is not less than 18.0 g/cc.

The polyurethane foam used to fill the overpack base and lid is tested to assure that it has the required density, static crush strength, flame retardancy, and intumescence. Assurance of the physical properties of each batch of foam used to fill the overpack base and lid is provided through specimen testing performed by the foam manufacturer in accordance with standard procedures. The average density of the test specimens from each batch of foam must be within ±10% of the nominal foam density (13.5 pcf). The average static compressive strength of each batch of foam, tested both parallel-to-rise and perpendicular-to-rise, is required to be within ±10% of the nominal crush strength values at 10%, 30%, and 50% strain levels. Following application of a 816°C flame for at least 60 seconds, the foam must not sustain a flame for more than 15 seconds. The intumescence of the foam specimens shall not be less than 100%. Furthermore, the foam specimens are tested to assure they have no more than 1 ppm of leachable chlorides. Conformance with these testing requirements is certified by the foam manufacturer.

*Fabrication Tests and Examinations*

The dimensions of the components and assemblies of the package are measured with calibrated M&TE to assure compliance with the dimensional requirements shown on the general arrangement drawings in Section 1.3.2. In addition, the weight of the finished cask and packaging are measured to assure that they meet the weight requirements.

All welded joints receive a workmanship visual examination and liquid penetrant (PT) non-destructive examination (NDE) to assure that they do not include visible defects, such as lack of fusion, lack of penetration, linear or crack-like indications, or porosity. All accessible surfaces of brazed joints are visually examined to assure adequate flow of brazing metal through

the joint. Examinations of welded and brazed joints are performed in accordance with the applicable requirements of the ASME Code. Areas of surface defect removal and completed weld repairs require thickness checks, using either a mechanical or ultrasonic testing (UT) device, by qualified personnel to verify compliance with the minimum thickness requirements. Written reports of each weld examination are prepared and maintained with the final records package.

Prior to assembly of the cask body, the containment shell is leak-tested in accordance with ANSI N14.5 to demonstrate a leak rate of the base metal that is less than or equal to $1.0 \times 10^{-7}$ ref-$cm^3$/s. The components of the finished cask that form the containment system, i.e., the cask body, closure lid, cask closure bolts, and containment O-ring seal are leak-tested in accordance with ANSI N14.5 to demonstrate a leak rate less than or equal to $1.0 \times 10^{-7}$ ref-$cm^3$/s. The cask is also tested for an internal pressure not less than 1,050 kPa in accordance with the requirements of WB-6220 to verify the structural integrity of the cask containment system at 150% MNOP.

*Functional Tests*

Functional tests are performed to assure proper fit-up of the packaging components. The shield plug assembly, with the cleanliness O-ring installed, must fit within the cask body and its entire top surface must protrude above the top surface of the cask body. This test is performed to assure that the cleanliness O-ring will be compressed when the closure lid is installed, thereby minimizing the air space between the shield plug and closure lid where radioactive product could potentially collect following the HAC free drop or puncture drop tests.

## 2.4 General Requirements for All Packages

### 2.4.1 Minimum Package Size

In accordance with the requirement of §71.43(a), the smallest overall dimension of a package may not be less than 10 cm. The package has an overall height of 55.1 cm and an outside diameter of 52 cm. Therefore, the package meets the minimum package size requirement of §71.43(a).

### 2.4.2 Tamper-Indicating Feature

In accordance with the requirement of §71.43(b), the outside of a package must incorporate a feature, such as a seal, that is not readily breakable and that, while intact, would be evidence that the package has not been opened by unauthorized persons. The outside of the package includes a one-piece wire cable tamper-indicating seal that is looped through holes in the bolting flange of the assembled package and secured in place. The location of the seal and its materials of construction minimize the potential for accidental damage during transport. The tamper-indicating seal must be removed to open the package and cannot be removed by unauthorized persons without damaging the seal or the package. Thus, the package satisfies the tamper-indicating feature requirements of §71.43(b). The tamper-indicating seal is not required to be installed for empty shipments.

### 2.4.3 Positive Closure

In accordance with the requirement of §71.43(c), the package must include a containment system securely closed by a positive fastening device that cannot be opened unintentionally or by a pressure than may arise within the package. The cask is completely enclosed inside the overpack, which includes a tamper-indicating seal, as discussed in Section 2.4.2. The tamper-indicating seal will prevent the overpack from being unintentionally opened. Furthermore, the containment system includes a closure lid that is secured to the cask body by eight closure bolts. Since tools are required to remove these bolts, the cask containment system cannot be unintentionally opened. The containment system does not include any covers, valves, or other access that could be inadvertently opened.

The cask containment system is evaluated for internal pressure loads that arise during NCT and HAC in Section 2.6.3 and Section 2.7.4.3, respectively. The evaluations demonstrate that the cask closure bolts satisfy the applicable allowable stress design criteria and that the containment seal remains intact under NCT and HAC. Hence, the package containment system satisfies the positive closure requirements of §71.43(c).

# 2.5 Lifting and Tie-down Standards for All Packages

## 2.5.1 Lifting Devices

In accordance with the requirements of §71.45(a), the lifting attachments that are structural parts of the package are designed with a minimum factor of safety of three against yield when used to lift the package in the intended manner. The lifting attachments are also designed so that failure of any lifting device under excessive load would not impair the ability of the package to meet the other requirements of 10 CFR 71 Subpart E.

### 2.5.1.1 Package Lift

The package is intended to be lifted vertically using the four lifting lugs that are integral to the overpack lid. The nominal mass of the package is 320.6 kg. It is conservatively assumed that the package is lifted using only two diametrically opposed lifting lugs, as shown in Figure 2-6. Each lifting lug must support one half of the package weight, or a vertical force (Fv) of 1,619 N, conservatively based on an upper-bound package mass of 330 kg. The resultant lug force (Fr) is a function of the lift angle (α). Conservatively assuming a minimum lift angle of 30°, the maximum resultant lug force is 3,238 N. The average bearing stress and shear tear-out stress in the overpack lid lug and the maximum stress intensity in the lug attachment weld due to the maximum resultant lug force are determined using hand calculations and shown to satisfy the requirements of §71.45(a).

*Average Bearing Stress*

The maximum resultant lug force produces an average bearing stress in the lifting lug of 10 MPa, based on the projected area of a 16 mm diameter shackle pin inside the hole of the 20 mm thick overpack lid lug. The yield strength of the overpack lid lug Type XM-19 material at a bounding design temperature of 93°C is 324 MPa. The average bearing stress in the lifting lug due to the maximum resultant lug force is less than one-third of the lug material yield strength (108 MPa). The minimum design margin for average bearing stress in the lid lifting lug is +9.80. Therefore, the stress limit requirement of §71.45(a) is satisfied.

*Shear Tear-Out Stress*

The shear tear-out stress in the lifting lug due to the lifting load is conservatively calculated using the resultant lug load and the smallest shear tear-out area, as follows.

$$f_v = \frac{Fr}{A_v} = 13 \text{ MPa}$$

Where:

$A_v$ = $2b(R_o - R_h)$, shear tear-out area of lifting lug hole
= 240 $mm^2$

b = 20.0 mm, lifting lug thickness

$R_o$ = 15.0 mm, corner radius lifting lug

$R_h$ = 9.0 mm, lifting lug hole radius

The allowable shear stress for lifting devices is taken as 60% of the allowable stress for the base material, or 65 MPa for Type XM-19 material at a bounding design temperature of 93°C. The maximum shear tear-out stress in the overpack lid lug is less than 65 MPa. The minimum design margin for shear tear-out stress in the lid lifting lug is +4.00. Therefore, the stress limit requirement of §71.45(a) is satisfied.

*Lug Attachment Weld Stress*

Each overpack lifting lug is attached to the top outer shell of the overpack lid by a two-sided full thickness groove weld with 4 mm cover fillet welds. Under the lifting loads, the lifting lug attachment weld is subjected to tensile, shear, and bending loads, as shown in Figure 2-7. The weld loads are calculated as follows.

$$Vw = Fr \cdot \cos(15^\circ) = 3{,}128 \text{ N}$$

$$Nw = Fr \cdot \sin(15^\circ) = 838 \text{ N}$$

$$Mw = Vw \cdot e = 51{,}612 \text{ N-mm}$$

$$e = \frac{53.3}{\sqrt{2}} - 15.0 \cdot \sqrt{2} = 16.5 \text{ mm}$$

The stresses in the overpack lifting lug attachment weld due to the lifting loads are calculated as follows.

$$f_a = \frac{Nw}{A_w} = 0.6 \text{ MPa}$$

$$f_v = \frac{Vw}{A_w} = 2.1 \text{ MPa}$$

$$f_b = \frac{Mw}{S_w} = 2.7 \text{ MPa}$$

Where:

$A_w$ = bd, Weld area
= 1,508 $mm^2$

$S_w$ = $bd^2/6$, Weld area
= 18,951 $mm^3$

b = 20 mm, weld thickness (assumed equal to lifting lug thickness)

d = 75.4 mm, weld length

The resulting maximum stress intensity in the lifting lug attachment weld is:

$$P_m + P_b = \frac{f_a + f_b}{2} + \sqrt{\left(\frac{f_a + f_b}{2}\right)^2 + f_v^{\,2}} = 4.3 \text{ MPa}$$

The allowable weld stress is equal to one third of the yield strength of the weaker base material. The lower-bound yield strength of the overpack lid top plate Type 304 and Type 316 stainless steel at 93°C is 172.4 MPa. Therefore, the allowable stress for the lifting lug attachment weld is 57.5 MPa and the minimum design margin is +12.7. The results demonstrate that the overpack lifting lug attachment weld satisfies the lifting standards of §71.45(a).

The results of the package lifting evaluation show that the lowest design margin is +4.00 for shear tear-out stress. Therefore, under excessive load, the overpack lid lug is expected to fail by shear tear-out. Shear tear-out failure of the overpack lid lug would not significantly affect the structural or thermal performance of package under NCT and HAC loadings, nor would it impair the ability of the package to meet the other requirements of 10 CFR 71 Subpart E.

### 2.5.1.2 Cask Assembly Lift

The cask, without the shield lid attached, is intended to be lifted in a vertical orientation by two threaded holes located on the top of the closure lid for insertion or removal from the overpack. The nominal mass of the cask assembly is 188.5 kg. An upper-bound cask mass of 195 kg is conservatively assumed for the cask lifting analysis. Each lifting attachment must support half of the cask weight, or 956 N. The cask assembly lift structural evaluation demonstrates that the stresses in the cask lifting attachment threads, the cask closure lid, and the cask closure bolts satisfy the requirements of §71.45(a).

*Lifting Attachment Thread Shear Stress*

The cask assembly is lifted by two M10 x 1.5 x 10 mm deep threaded inserts located on a 94.0 mm bolt circle on the centerline of the closure lid. Each lifting attachment must support half of the cask weight, or a force of 956 N. The thread shear stress in the cask lid lifting attachment resulting from a 956 N lifting load is 6.4 MPa, based on an internal thread shear area of 150 $mm^2$ for the M10 x 1.5 threaded insert with a minimum engagement length of 7.0 mm.

The allowable shear stress for lifting devices is taken as 60% of the allowable stress for the base material, conservatively neglecting the higher strength of the threaded insert material. The lowest yield strength of closure-lid stainless steel material at 93°C is 172.4 MPa. Therefore the

allowable shear stress for the closure lid at a bounding design temperature of 93°C is 34.5 MPa. The corresponding minimum design margin for the thread shear stress is +4.39. Therefore, the cask lifting attachment satisfies the lifting standards of §71.45(a).

*Closure Lid Stresses*

The stresses in the cask closure lid resulting from the cask lift load are determined using the 3-D quarter-symmetry finite element model of the closure lid shown in Figure 2-8. The finite element model includes the closure lid, closure bolts, and the top face of the cask bolting flange. The closure lid, closure bolt heads, and cask bolting flange are modeled using 3-D structural solid elements. The closure bolt shanks are modeled using 3-D beam elements. Surface-to-surface contact elements are used to model the nonlinear interfaces between the bolt heads and closure lid and between the cask flange and closure lid and capture prying effects on the closure bolts. The closure lid is modeled using the linear-elastic material properties for Type 304 or 316 stainless steel at a bounding design temperature of 93°C. The closure bolts are modeled using the material properties of SA-320, Grade L43 bolting steel at 93°C.

Symmetry boundary displacement constraints are applied to the nodes lying on the quarter-symmetry planes. The nodes located on the underside of the cask bolting flange face are restrained from vertical translation. In addition, the nodes at the base of each bolt beam element are restrained in all degrees of freedom. A total upward force of 478 N, which is equivalent to ¼ of the cask upper bound mass (195 kg), is applied to the closure plate at the centerline of the lifting attachment hole. A linear-elastic static analysis is performed using the ANSYS Mechanical finite element program.

The finite element analysis results show that the maximum stress intensities due to the vertical lift loads occur in the top plate near the lifting post. The results show that the maximum stress intensity in the closure lid due to the vertical lift is 9 MPa. The allowable stress is equal to one third of the material yield strength. The lower-bound yield strength of Type 304 and Type 316 stainless steel at an upper-bound design temperature of 93°C is 172 MPa. Therefore the allowable stress for the closure lid is 57 MPa and the minimum design margin is +5.33. Therefore, the closure lid satisfies the lifting standards of §71.45(a).

*Closure Bolt Stress*

The maximum closure-bolt reaction force due to the cask lifting load is shown to be 449 N from the results of the closure-lid finite element analysis. For the M10 x 1.5 closure bolt, with a stress area of 54.7 $mm^2$ based on a minor diameter of 8.344 mm, the bolt tensile stress is 8 MPa.

The allowable closure-bolt tensile stress is equal to one third of the material yield strength. The SA-320, Grade L43 closure bolt material has a yield strength of 683 MPa at 93°C. Therefore, the allowable tensile stress for the closure bolt is 228 MPa. The corresponding minimum design margin in the closure bolt is +27.5.

The thread shear stress in the cask closure bolt due to the 449 N lifting load is 2 MPa based on the external thread shear area of 296 $mm^2$ for the M10 x 1.5 closure bolt with an engagement length of 19.0 mm.

The allowable shear stress for lifting devices is taken as 60% of the allowable stress for the base material, conservatively neglecting the higher strength of the threaded insert material. The yield strength of SA-320, Grade L43 bolting steel at 93°C is 683 MPa. Therefore, the allowable closure-bolt thread shear stress is 137 MPa and the minimum design margin for the closure bolt thread shear stress is +67.5. Therefore, the closure bolt satisfies the applicable allowable stress design criteria for normal lifting loads.

The shear stress in the cask flange base metal due to the maximum bolt tensile force for the cask lift is evaluated for the maximum bolt tensile load of 449 N resulting from the cask lift. The maximum thread shear stress in the cask flange closure bolt attachment is 1.7 MPa based on an internal thread shear area of 269 $mm^2$ for the M10 x 1.5 thread of the cask flange base metal and a thread engagement length of 17.0 mm.

The allowable shear stress for lifting devices is taken as 60% of the allowable stress for the cask flange base material. The lower-bound yield strength of the cask bolting flange stainless steel material at an upper-bound design temperature of 93°C is 172.4 MPa. Therefore, the allowable shear stress for the closure lid is 34.5 MPa, and the minimum design margin for the thread shear stress is +19.3. These results demonstrate that the cask flange closure bolt attachment satisfies the lifting standards of §71.45(a).

The results of the cask lifting evaluation show that the lowest design margin is +4.39 for thread shear stress in the closure lid lifting attachments. Therefore, under excessive load, the closure lid lifting attachments threads are expected to fail in shear, which does not result in a loss of containment nor significantly affect the structural or thermal performance of the package under NCT and HAC loadings. Thus, it does not impair the ability of the package to meet the other requirements of 10 CFR 71 Subpart E.

### 2.5.2 Tie-Down Devices

The package tie-down system is comprised of the lugs that are integral to the bottom ring of the overpack base plus the four lugs that are integral to the overpack lid. The acceptable package tie-down configuration is shown in Figure 2-9. The package must be tied down using four tension-only members, e.g., cables or slings, attached to overpack lid lugs. The base of the package may be tied down by the four bottom lugs, blocked, or left unrestrained. The tie-down analysis conservatively assumes that the base of the package is left unrestrained. As shown in Figure 2-9, the angle of the four tie-down attachments is allowed to vary by ±22.5° from radial and between 35° and 65° from vertical to provide operational flexibility.

The tie-down loads are calculated based on a bounding package mass of 330 kg. The horizontal load is conservatively taken as the resultant of the 10*g* horizontal and 5*g* transverse loads for a maximum horizontal load of 11.18*g* or 36,193 N. In addition, a 2*g* upward vertical load, or 6,475 N, is applied to the package center of gravity. A lower-bound value of 0.09 for the

coefficient of sliding friction between the bottom of the package and the supporting surface is conservatively assumed for the tie-down evaluation. The tie-down evaluation is performed for a range of acceptable tie-down configurations, both with and without tie-down pretension loads, to assure that the applicable design requirements are satisfied. Six different tie-down configurations expected to cause the highest stresses in the package tie-down attachments are evaluated, as shown in Figure 2-10.

The reaction loads at each of the package tie-down attachment points for each tie-down configuration considered are determined using the finite element model shown in Figure 2-11. The model includes the package, the tie-down contact surface, and the tie-downs. The package is modeled using rigid, massless 3-D beam elements and a rigid, massless solid bottom end for a contact surface. The ends of the beam elements on the top of the package are located at the center of the lid lug holes. A single 3-D mass element is included in the model at the location of the package center of gravity. The nonlinear contact between the bottom surface of the package and the supporting tie-down surface is modeled using surface-to-surface contact elements. The tie-downs are modeled using 3-D tension-only spar elements. These elements are oriented in accordance with the angles specified in Figure 2-10 for each case analyzed.

For each evaluation, the lower ends of the tie-downs are fixed and an initial strain is applied to the tie-down elements to account for tie-down pretension loads. For each tie-down configuration, analyses are performed for essentially no tie-down pretension and for a maximum tie-down pretension load of 22.3 kN. The tie-down reaction loads for cases 1 through 6 are summarized in Table 2-25. The maximum bearing stress and shear tear-out stress in the overpack lid lug and the maximum stress intensity in the overpack lid lug attachment weld are calculated by hand for the maximum tie-down reaction loads from each tie-down case.

The maximum bearing stress, resulting from case 1, is 195 MPa. The allowable bearing stress, which is equal to the yield strength of Type XM-19 stainless steel at the overpack lid lug upper-bound design temperature of 66°C, is 343 MPa. Thus, the minimum design margin for bearing stress in the package tie-down attachment is +0.76.

The maximum shear tear-out stress in the tie-down lug subjected to the maximum tie-down load is calculated by hand using the maximum tie-down reaction loads in each case. The maximum shear tear-out stress, resulting from case 3, is 189 MPa. The allowable shear tear-out stress is taken as 60% of the allowable stress for the base material, or 206 MPa. The corresponding minimum design margin for shear stress in the lug is +0.09.

Each overpack lid lug is attached to the overpack lid outer shell by a full thickness weld with 4 mm cover fillet welds on both sides. The weld stresses are calculated at two sections, as shown in Figure 2-12. Section 1 is the smaller section that passes through the higher strength lug base material. Section 2 is the larger section located at the base of the lug weld adjacent to the weaker outer shell base material. The maximum tie-down reaction is used to calculate the normal stress, shear stress, and bending stress on each section as follows:

$$f_{a,i} = \frac{F_y}{A_i} = \frac{F_{max}\sin(a-45^\circ)\cos(b)}{c_i d_i}$$

$$f_{v,i} = \frac{F_v}{A_i} = \frac{\sqrt{F_x^{\,2} + F_z^{\,2}}}{c_i d_i} = \frac{\sqrt{\left(F_{max}\sin(b)\cos(a-45^\circ)\right)^2 + \left(F_{max}\cos(b)\cos(a-45^\circ)\right)^2}}{c_i d_i}$$

$$f_{b,i} = \frac{M_{x.i}}{S_{x,i}} + \frac{M_{z,i}}{S_{z,i}} = \frac{6(F_z e_i)}{c_i d_i^{\,2}} + \frac{6(F_x e_i)}{c_i^{\,2} d_i}$$

Where;

$F_{max}$ = Maximum tie-down reaction from Table 2-25.

a = Vertical tie-down angle from Figure 2-10.

b = Radial tie-down angle from Figure 2-10.

$c_i$ = Section width (see Figure 2-12).
= 20.0 mm at Section 1
= 28.0 mm at Section 2

$d_i$ = Section length (see Figure 2-12).
= 67.4 mm at Section 1
= 75.4 mm at Section 2

$e_i$ = Moment arm to section (see Figure 2-12).
= 12.5 mm at Section 1
= 16.5 mm at Section 2

The resulting stresses on each weld section from tie-down cases 1 and 2 are calculated as described above and summarized in Table 2-26. The results show that the maximum stress intensities at both sections result from case 1. The maximum stress intensities at sections 1 and 2 are 87 MPa and 60 MPa, respectively. The allowable stress is equal to the material yield strength. At section 1, the yield strength of the Type XM-19 base material at an upper bound temperature of 93°C is 325 MPa. Therefore, the minimum design margin at section 1 is +2.74. At section 2, the yield strength of the weaker Type 304 or 316 stainless steel base material at an upper-bound temperature of 93°C is 172 MPa. Therefore, the minimum design margin at section 2 is +1.87.

The results of the tie-down stress analysis show that the minimum design margin for shear tear-out stress in the lug is less than the minimum design margin for stresses in the lug attachment weld. Therefore, under excessive loading, the lug will fail due to shear tear-out instead of failure at the lug welded connection. Shear tear-out failure of the lug will not impair the ability of the package to meet other requirements of 10 CFR 71.

**Table 2-25 – Tie-Down Reaction Loads**

| Tie-Down Case | Tie-Down Pretension | Tie-Down Reaction Forces (kN) | | | |
|---|---|---|---|---|---|
| | | $F_A$ | $F_B$ | $F_C$ | $F_D$ |
| 1 | Minimum | 0.0 | 5.4 | 67.5 | 43.4 |
| | Maximum | 0.0 | 8.9 | 62.9 | 46.1 |
| 2 | Minimum | 0.0 | 20.7 | 52.5 | 21.2 |
| | Maximum | 4.2 | 23.2 | 50.9 | 25.5 |
| 3 | Minimum | 12.1 | 20.3 | 60.5 | 51.2 |
| | Maximum | 11.1 | 18.9 | 55.7 | 47.2 |
| 4 | Minimum | 13.7 | 31.2 | 50.0 | 29.0 |
| | Maximum | 13.3 | 30.6 | 47.0 | 28.8 |
| 5 | Minimum | 0.0 | 21.6 | 51.9 | 21.6 |
| | Maximum | 2.1 | 26.5 | 50.9 | 26.5 |
| 6 | Minimum | 13.5 | 30.9 | 48.2 | 30.9 |
| | Maximum | 13.7 | 29.8 | 46.0 | 29.8 |

**Table 2-26 – Overpack Lid Lug Weld Stresses**

| Stress Type | Weld Section | Tie-Down Case | | | | | |
|---|---|---|---|---|---|---|---|
| | | 1 | 2 | 3 | 4 | 5 | 6 |
| Normal Stress, $f_a$ (MPa) | 1 | 8.0 | 6.3 | 14.2 | 11.7 | 6.7 | 12.2 |
| | 2 | 5.1 | 4.0 | 9.1 | 7.5 | 4.3 | 7.8 |
| Shear Stress, $f_v$ (MPa) | 1 | 49.3 | 38.4 | 42.2 | 34.9 | 37.9 | 33.6 |
| | 2 | 31.5 | 24.5 | 26.9 | 22.3 | 24.2 | 21.5 |
| Bending Stress, $f_b$ (MPa) | 1 | 50.7 | 39.4 | 43.4 | 35.8 | 42.1 | 37.3 |
| | 2 | 38.2 | 29.7 | 32.7 | 27.0 | 31.8 | 28.1 |
| Maximum Stress Intensity, $P_m+P_b$ (MPa) | 1 | 87 | 67 | 80 | 66 | 70 | 67 |
| | 2 | 60 | 47 | 55 | 45 | 48 | 46 |

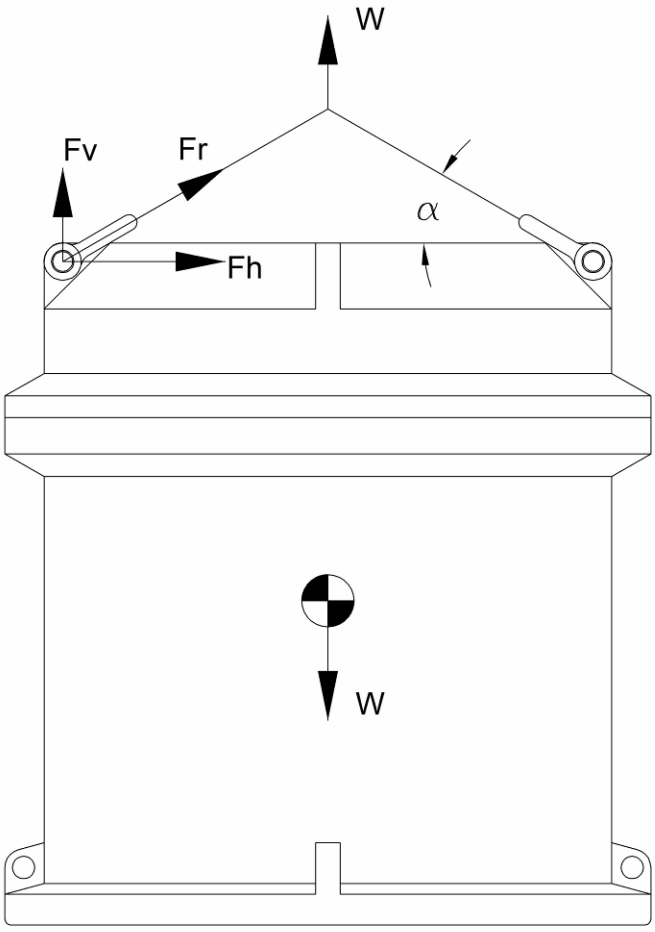


**Figure 2-6 – Package Lifting Free Body Diagram**

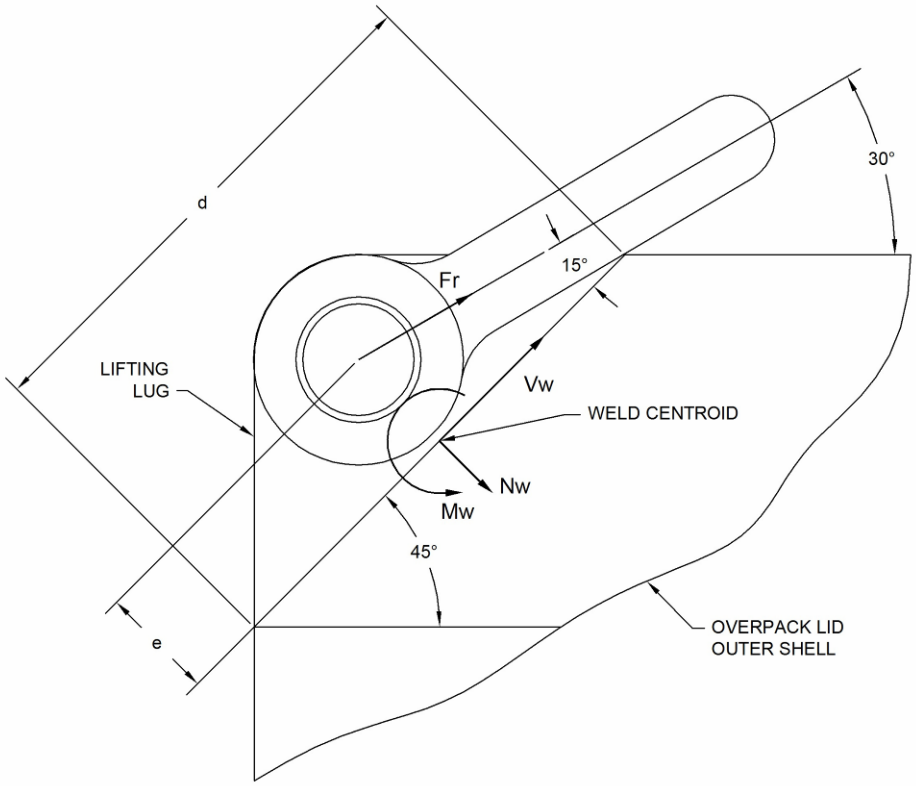


**Figure 2-7 – Overpack Lifting Lug Weld Lifting Loads**

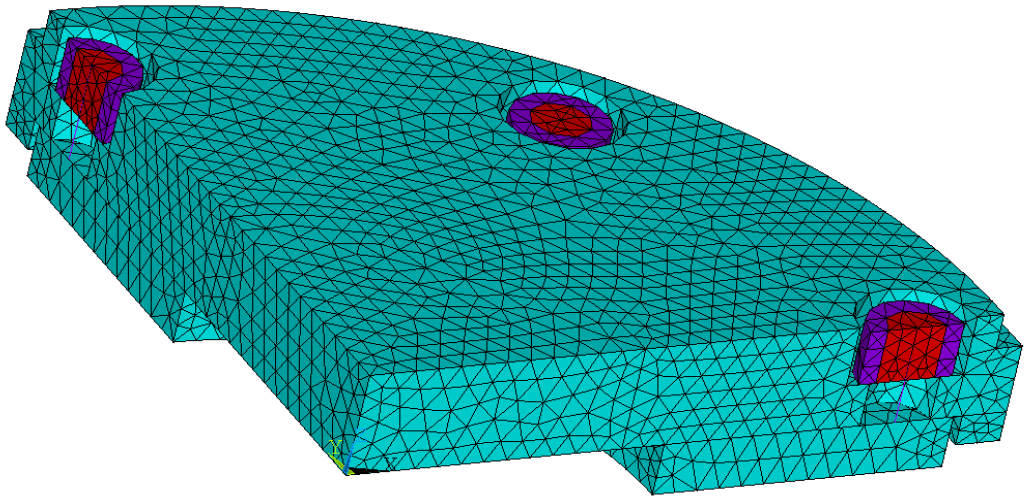

**Figure 2-8 – Cask Closure Lid Quarter-Symmetry Finite Element Model**

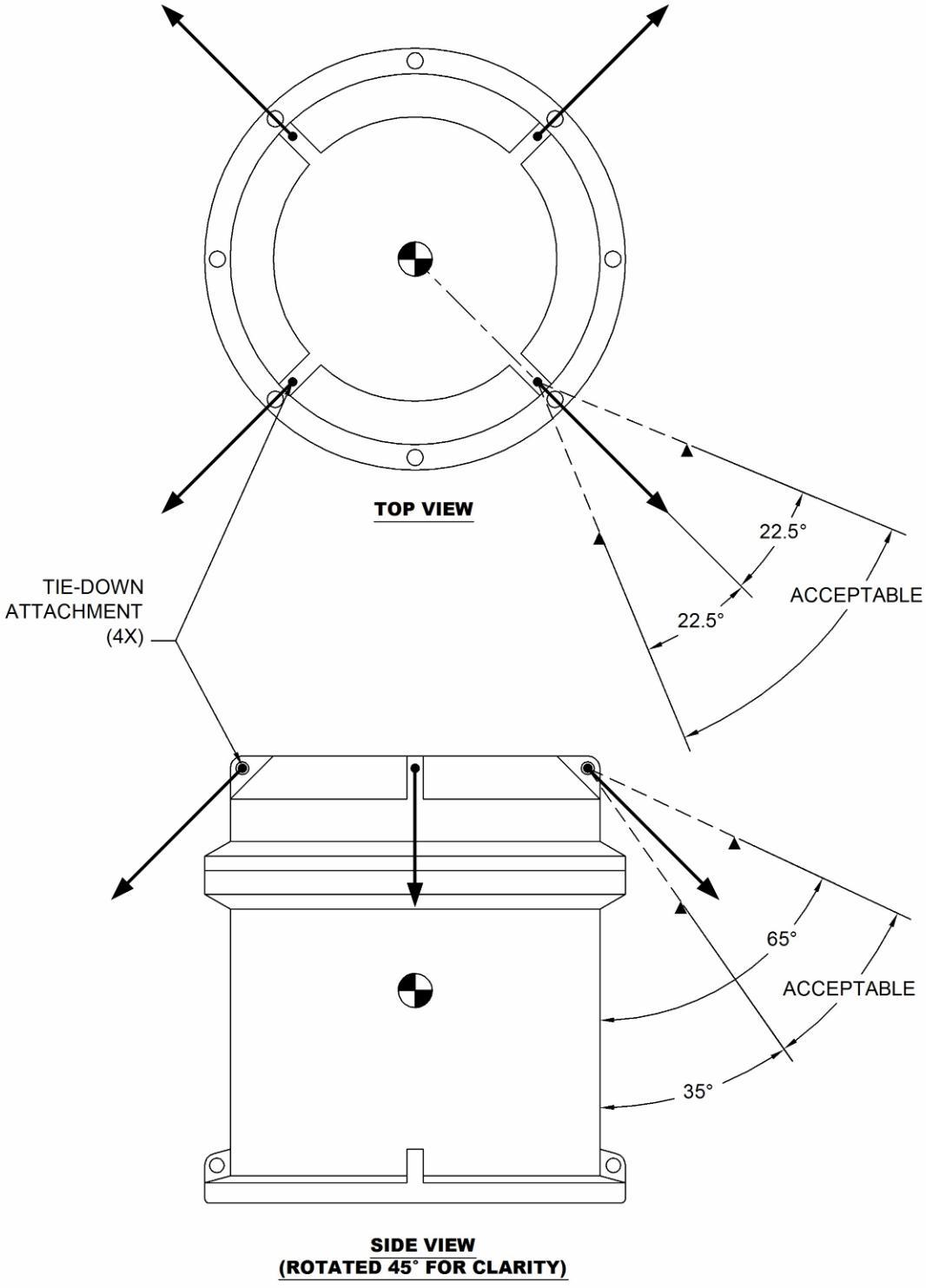


**Figure 2-9 – Acceptable Package Tie-Down Configuration**

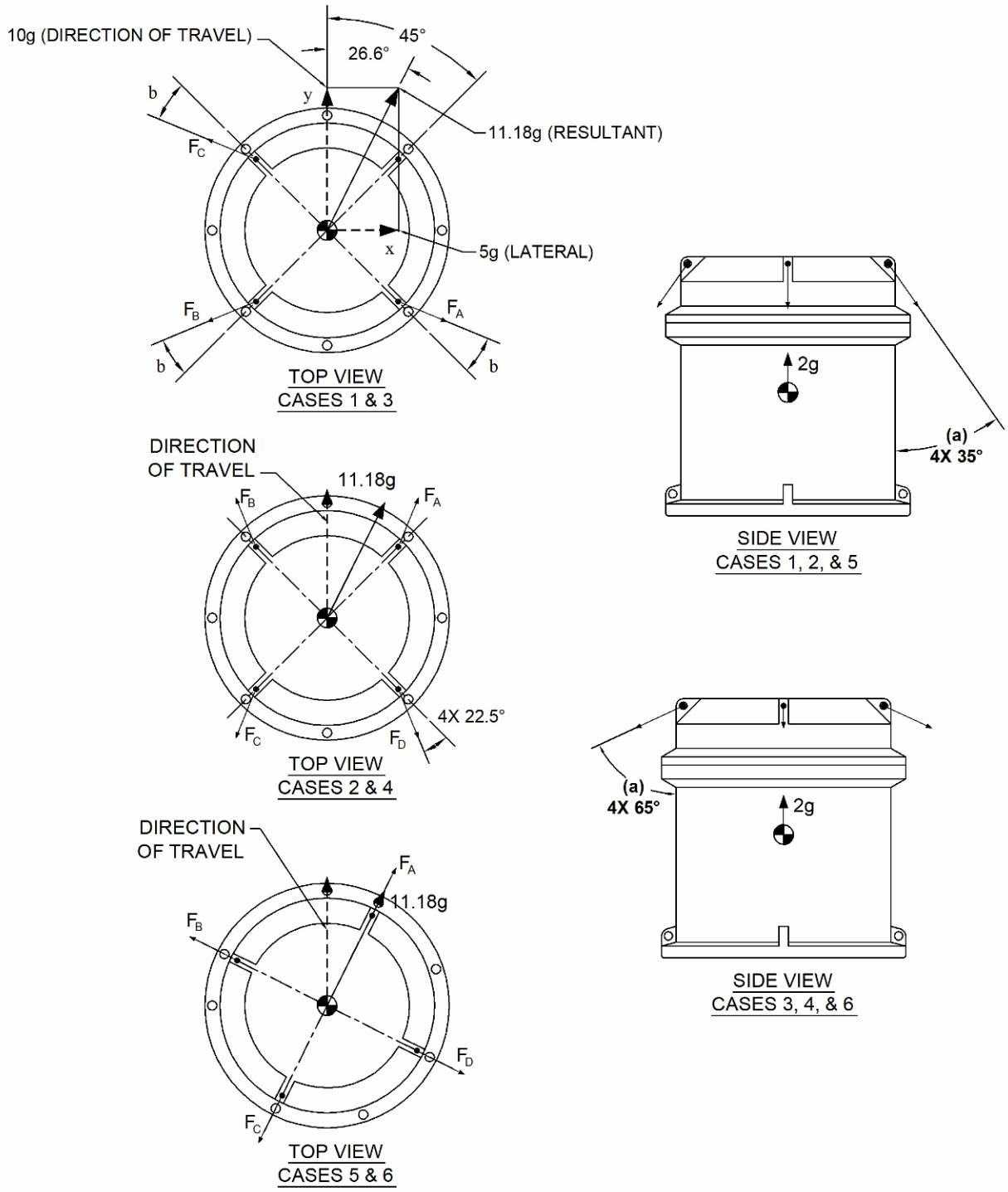


**Figure 2-10 – Tie-Down Cases Evaluated**

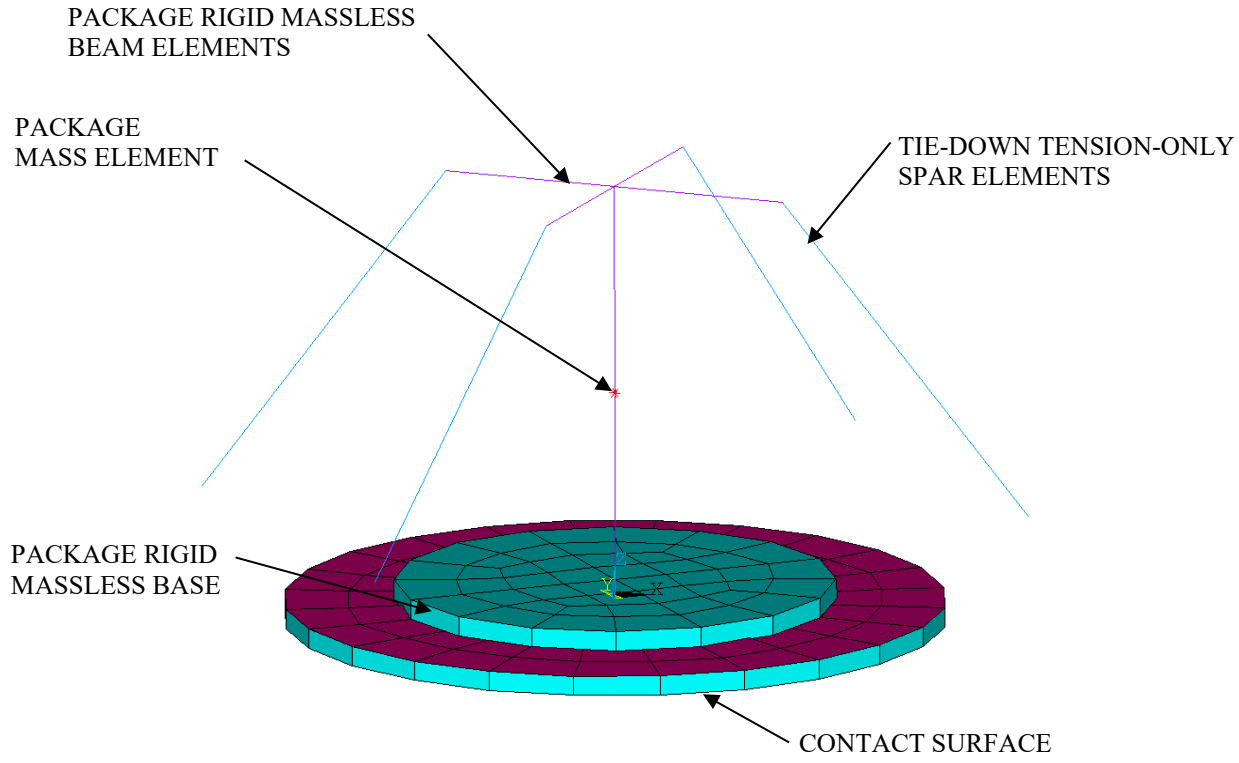


**Figure 2-11 – MIDUS Package Tie-Down Finite Element Model**

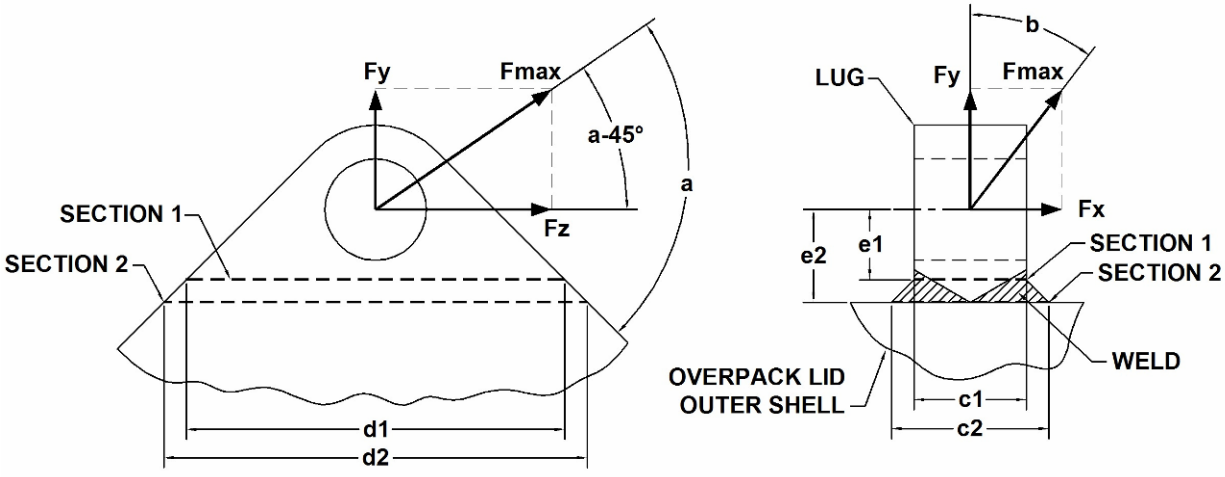


(Note: Lug rotated 45° for clarity)

**Figure 2-12 – Overpack Lid Lug Weld Tie-Down Loading Diagram**

## 2.6 Normal Conditions of Transport

This section presents the structural evaluation of the package that demonstrates compliance with the requirements of §71.43(f) and §71.51(a)(1) when subjected to the NCT tests specified in §71.71. The package is evaluated for each NCT test individually based on the most unfavorable initial conditions, including an ambient temperature between -29°C and +38°C and an internal pressure between zero and the MNOP. The structural evaluation shows that there would be no loss or dispersal of radioactive contents, no significant increase in external surface radiation levels, and no substantial reduction in the effectiveness of the packaging.

### 2.6.1 Heat

In accordance with §71.71(c)(1), the package is subjected to an ambient temperature of 38°C in still air and insolation. The cask maximum internal pressure and temperatures resulting from NCT heat conditions are summarized in Section 2.6.1.1. Differential thermal expansion between the various components of the package under NCT heat loading is evaluated in Section 2.6.1.2. The cask stresses due to NCT heat loading are evaluated in Section 2.6.1.3. The results of the NCT heat structural evaluation demonstrate that the cask satisfies the applicable structural design criteria.

#### 2.6.1.1 Summary of Pressures and Temperatures

The maximum temperatures of the cask for NCT thermal conditions from Chapter 3 are summarized in Table 3-1. The maximum package temperatures result from the NCT hot thermal condition. The maximum temperature of the cask, not including the cask cavity gas or overpack, is 72°C. The allowable stress intensities used for the evaluation of the cask are conservatively based on an upper bound temperature of 74°C.

As discussed in Section 3.3.2, the maximum gauge pressure that would develop in the cask containment system in a period of one year under the heat conditions (MNOP) is less than 700 kPa. A bounding internal pressure of 700 kPa is used to perform the cask structural analysis for NCT.

#### 2.6.1.2 Differential Thermal Expansion

Differential thermal expansion of the packaging components is evaluated considering possible interference resulting from a reduction in gap sizes. The differential thermal expansion evaluation includes radial and longitudinal differential thermal expansion between the cask assembly and the overpack cavity. In addition, radial and longitudinal differential thermal expansion between the cask body DU shield and shells is evaluated. The results of the evaluation of differential thermal expansion show that the cask expands freely within the overpack cavity under NCT thermal loading.

The package is designed with sufficient clearances between the overpack cavity and the outside surfaces of the cask and shield lid to permit free thermal expansion of the cask under NCT and

HAC. Nominal axial and radial clearances of 5 mm and 2.5 mm are provided between the overpack cavity and the outside surfaces of the cask and shield lid. The results of the NCT heat finite element analysis show that the maximum thermal expansion of the cask and shield lid is 0.20 mm in the longitudinal direction and 0.08 mm in the radial direction. Since the thermal expansion of the cask and shield lid is less than the nominal clearances provided, no interference will result from differential thermal expansion between the overpack and the cask and shield lid.

The cask body is designed with a nominal axial clearance of 0.7 mm between the DU bottom shield and the bottom end of the containment shell (i.e., below the cavity). The cask body design also provides nominal radial clearances of 0.65 mm and 0.35 mm on the inside radius and outside radius of the DU radial shield. Under NCT heat loading, differential thermal expansion caused by thermal gradients (i.e., the cask inner shell becomes hotter than the outer shell) and dissimilar materials (i.e., the coefficient of thermal expansion of DU is less than that of the stainless steel shells) causes a reduction in the clearances provided between the cask body DU and shells.

Differential thermal expansion between the cask body components is evaluated using the results of the finite element analysis described in Section 2.6.1.3. The clearances between the cask body DU and stainless steel shells under NCT heat loading are determined based on the minimum gap sizes of contact elements modeled between the adjacent surfaces. The results, which are summarized in Table 2-27, show that no interference will result from differential thermal expansion between the cask DU shield stainless steel shells under NCT heat loading. The amount of differential thermal expansion between the cask body DU shield and the adjacent cask shell components is small in comparison to the nominal design clearances.

### 2.6.1.3 Stress Calculations

The cask is designed to withstand the effects of heat loading in accordance with §71.71(c)(1). Per Table 2-1, heat loading is evaluated in combination with maximum decay heat, insolation, maximum internal pressure, and fabrication stresses.

The stresses in the cask body, closure lid, and shield lid due to the NCT heat loading are calculated using the axisymmetric finite element model shown in Figure 2-13. The model is comprised of a total of 2,012 nodes and 2,135 elements, representing all of the major structural and shielding components of the cask and shield lid. The model geometry is based on the nominal component dimensions. Design features such as fillets, chamfers, and bolt holes are not included in the model to simplify the finite element mesh.

All components of the packaging, with the exception of the closure bolts and O-rings, are modeled using 2-D structural solid axisymmetric elements. The closure bolts are modeled using 2-D spar elements. The closure-bolt element real constants are used to define the closure-bolt cross-section area and initial strain due to preload. The closure-bolt area is calculated based on the nominal bolt diameter of 10 mm. The containment O-ring, leak test O-ring, and cleanliness O-ring are all modeled using 3-D combination spring elements. The elastomeric O-ring linear spring stiffness constants are determined based on manufacturer's data for compressive loads versus percent compression and O-ring durometer over the range of compression permitted by

the O-ring groove design (i.e., up to approximately 25%). The nonlinear contact interface between the various components of the cask and shield lid are modeled using surface-to-surface contact elements. Figure 2-14 shows the surfaces on which contact elements are modeled.

All steel components of the cask and shield lid are modeled with a density of 8030 kg/m$^3$, Poisson's ratio of 0.3, and the temperature-dependent modulus of elasticity for Type 304/316 stainless steel from Table 2-12 and Table 2-13. The closure bolts are modeled with a density of 8030 kg/m$^3$, Poisson's ratio of 0.3, and the temperature-dependent modulus of elasticity for SA-320, Grade L43 bolting steel from Table 2-15. The DU shielding material in the cask body, shield plug, and shield lid is modeled with an elastic modulus of 172 MPa, an assumed Poisson's ratio of 0.3, and a mass density of 18,800 kg/m$^3$.

The cask body is restrained from longitudinal translation at a single node located on the bolting flange face at the bolt circle radius. In addition, coupled node sets are used to prevent rigid-body displacement of the cask body DU shields, shield plug DU shield, and the shield lid components. This is necessary for numerical stability since these components become unconstrained as differential thermal expansion between the cask stainless steel shells and DU shields creates gaps at the longitudinal contact surfaces.

The bounding NCT heat temperature gradient shown in Figure 2-15 is applied to the finite element model in combination with the internal pressure and maximum initial bolt preload. A bounding internal pressure load of 700 kPa gauge is applied to the inner surfaces of the cask containment boundary. The maximum bolt preload is 7.2 kN per bolt. The bolt preload is applied on a 360° basis as an initial strain in the cask closure bolt elements that produces a total preload (for eight closure bolts) of 57.8 kN on the closure lid.

The results of the NCT heat stress analysis show that the maximum total ($P_m+P_b+Q$) stress intensity in the cask due to NCT heat loading is 97 MPa, occurring at the center of the containment shell bottom plate (section C1 in Figure 2-1). This stress is due almost entirely to the internal pressure loading and not to the NCT heat temperature gradient. The maximum $P_m+P_b+Q$ stress intensity in the cask containment system for NCT is limited to $3.0S_m$. The minimum value of $S_m$ for the cask shell materials at a bounding design temperature of 74°C is 138 MPa. Therefore, the allowable $P_m+P_b+Q$ stress intensity for the containment system is 414 MPa and the minimum design margin in the cask containment system due to NCT heat loading is +3.27.

The stresses in the cask closure bolts due to NCT heat loading are determined using the 3-D quarter-symmetry finite element model described in Section 2.5.1.2. The NCT hot temperature loading for the cask closure bolt analysis is applied as a uniform elevated temperature load of 68.3°C. This conservatively bounds the maximum temperature of the cask closure bolt for the NCT heat of 67°C. Elevated temperature produces differential thermal expansion between the closure bolts and closure lid, due to the differences in their material model coefficient of thermal expansion values, thereby causing thermal stress. Thermal stresses in the closure bolts due to closure plate through-thickness temperature gradients are not considered since these temperature gradients are very small and they create bolt-prying loads that oppose those due to internal pressure. Therefore, they are conservatively neglected. In combination with the NCT heat

loading, a maximum bolt preload of 7221 N is applied to each closure bolt and an internal pressure is applied as a uniform pressure load of 700 kPa on the inner surface of the closure plate over the entire area inside the containment O-ring.

The maximum average stress (i.e., axial stress) and maximum stress (i.e., axial plus bending stress) in the closure bolts due to NCT heat loading are 201 MPa and 209 MPa, respectively. The average axial stress due to internal pressure and gasket seating loads (i.e., bolt torque) must not exceed one times the tabulated values of $S_m$ at the corresponding design temperature for NCT. The allowable maximum stress for NCT is limited to $3S_m$. The value of $S_m$ for SA-320, Grade L43 bolting steel at a bounding closure bolt design temperature of 68.3°C is 234 MPa. Therefore, the allowable average stress and maximum stress are 234 MPa and 701 MPa, respectively. The maximum closure bolt stress ratios for NCT heat loading are 0.86 for average stress and 0.30 for maximum stress.

The results of the NCT heat structural evaluation demonstrate that the cask containment system satisfies the applicable NCT allowable stress design criteria. NCT heat loading does not cause any permanent deformation of the package, nor does it substantially reduce the effectiveness of the packaging. Furthermore, since the evaluation shows that the containment seal is maintained under NCT heat loading, there would be no loss or dispersal of radioactive contents. Finally, the configuration of the package under NCT heat loading is the same as that considered in the shielding evaluation. Therefore, NCT heat loading does not cause any significant increase in external surface radiation levels. The package thus complies with the requirements of §71.43(f) and §71.51(a)(1) when subjected to the NCT heat test specified in §71.71(c)(1).

### 2.6.1.4 Comparison with Allowable Stresses

The results of the NCT heat structural evaluation demonstrate that the cask containment system satisfies the applicable NCT allowable stress design criteria. The minimum design margins due to NCT heat loading are +0.16 for average tensile stress in the closure bolts and +3.27 primary plus secondary stress intensity in all other cask components. NCT heat loading does not cause any permanent deformation of the package, nor does it substantially reduce the effectiveness of the packaging. Furthermore, since the evaluation shows that the containment seal is maintained under NCT heat loading, there would be no loss or dispersal of radioactive contents. Finally, the configuration of the package under NCT heat loading is the same as that considered in the shielding evaluation. Therefore, NCT heat loading does not cause any significant increase in external surface radiation levels. Therefore, the package complies with the requirements of §71.43(f) and §71.51(a)(1) when subjected to the NCT heat test specified in §71.71(c)(1).

The structural evaluation of the package for reduced external pressure, increased external pressure, vibration normally incident to transport, and NCT free drop tests is discussed in the following sections. Each NCT test is evaluated in combination with the initial conditions expected to cause maximum package damage. The structural evaluation demonstrates that the package satisfies the applicable performance requirements specified in the regulations under all NCT tests. The evaluation of the cask for cyclic service under NCT, which is presented in Section 2.1.2.4, demonstrates that the package satisfies the applicable fatigue design criteria of the ASME Code.

**Table 2-27 – Cask Body Differential Thermal Expansion Summary**

| Cask Body DU Shield Clearances | Nominal Design Clearance (mm) | Clearance Under NCT Heat Loading (mm) | Differential Thermal Expansion (mm) |
|---|---|---|---|
| Axial (Under Cavity) | 0.70 | 0.54 | -0.16 |
| Outer Radius | 0.35 | 0.36 | +0.01 |
| Inner Radius | 0.65 | 0.63 | -0.02 |

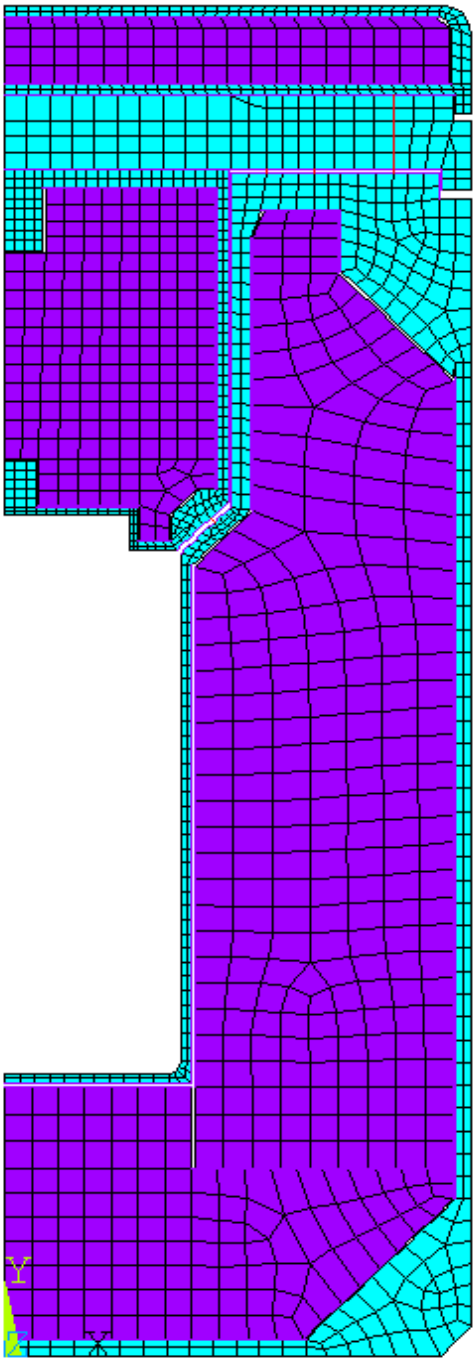


**Figure 2-13 – MIDUS Cask Assembly Axisymmetric FE Model**

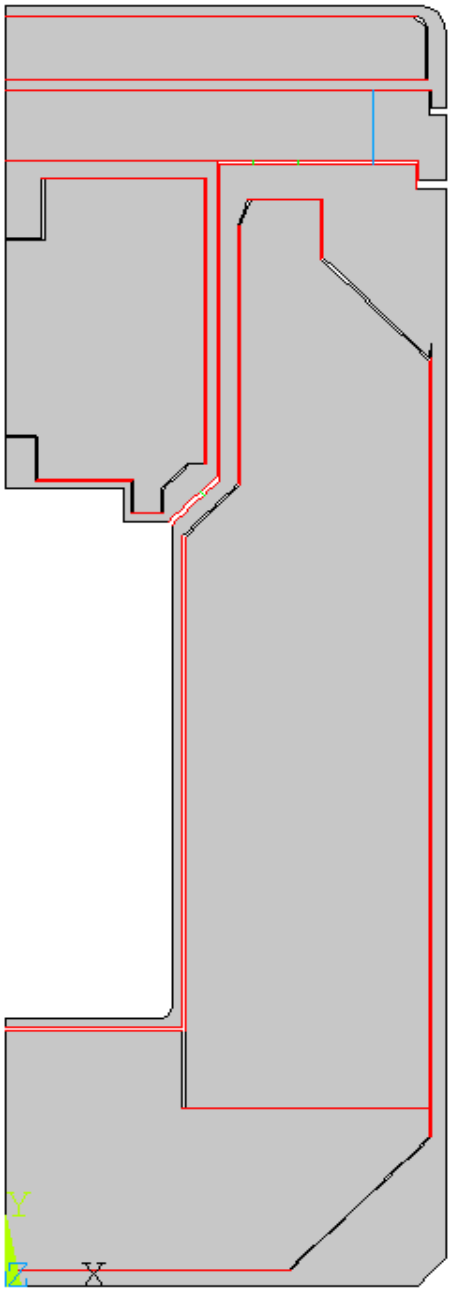


(Note: Contact surfaces shown in red)

**Figure 2-14 – Axisymmetric FE Model Contact Surfaces**

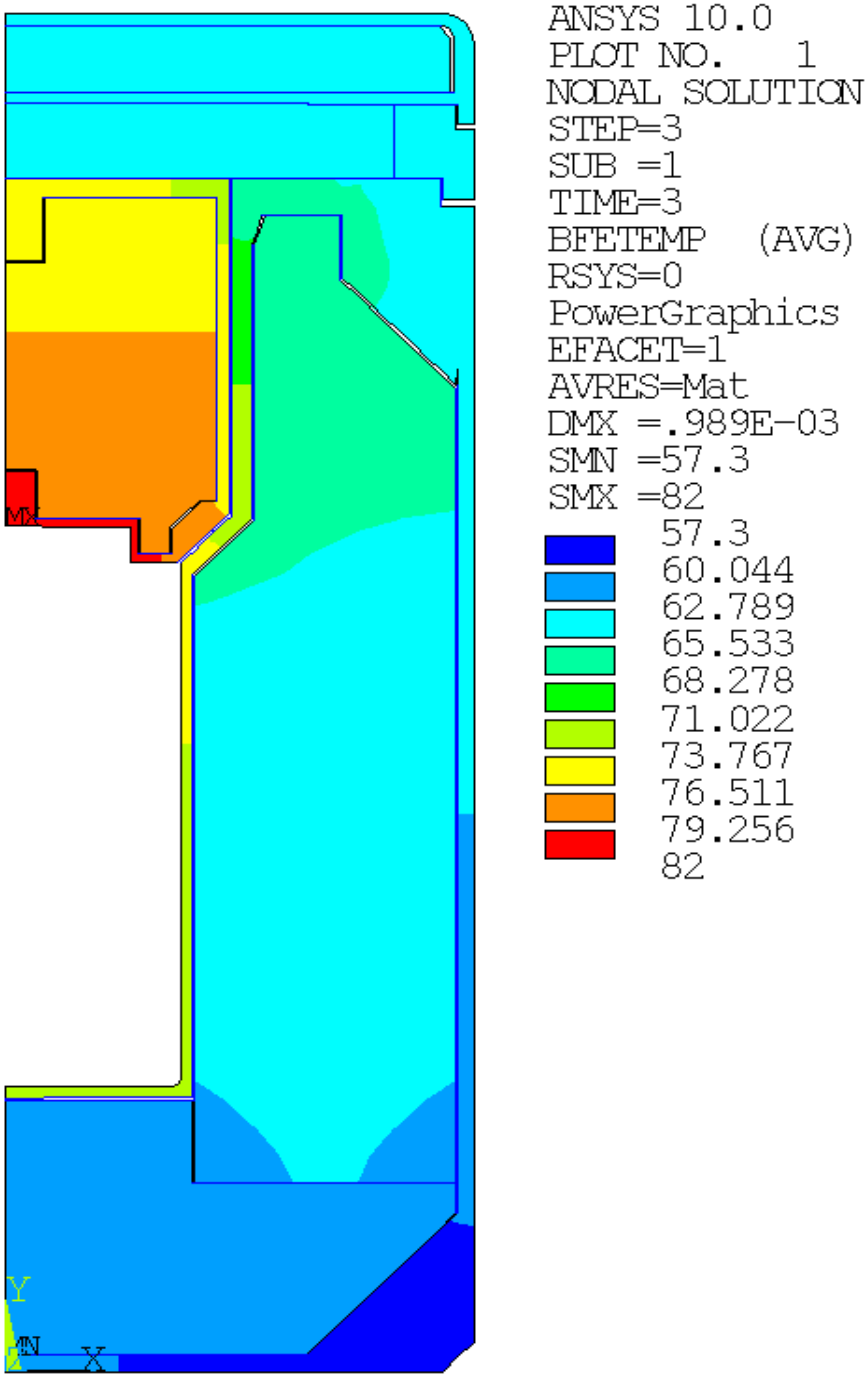


**Figure 2-15 – Bounding NCT Heat Temperature Distribution**

### 2.6.2 Cold

The cask is designed to withstand the effects of a steady-state ambient temperature of -40°C in still air and shade in accordance with §71.71(c)(2). Per Table 2-1, the NCT cold environment is evaluated in combination with zero insolation, zero decay heat, and zero internal pressure. The NCT cold environment with zero insolation and zero decay heat results in a uniform temperature of –40°C throughout the package. The cask body, shield plug, and shield lid all include DU shield cores that are encased in austenitic stainless steel. Because the coefficient of thermal expansion of austenitic stainless steel is higher than that of DU, reduced temperatures cause the stainless steel casing to contract more than the DU cores. The resulting differential thermal expansion produces thermal stress in the cask and shield lid.

The stresses in the cask body, closure lid, and shield lid due to the NCT cold loading are calculated using the axisymmetric finite element model described in Section 2.6.1.3. A uniform temperature of –40°C is applied to the finite element model in combination with the maximum initial bolt preload. The results of the NCT cold linear-elastic static analysis show that the highest stress intensities in the cask containment system and non-containment components are 26 MPa (at section C17 in Figure 2-1) and 60 MPa (at section N3 in Figure 2-2), respectively.

Per WB-3213.13, general thermal stress, neglecting stress concentrations, is classified as secondary stress (Q). The NCT allowable $P_m+P_b+Q$ stress intensities for the cask containment system components at -40°C is 414 MPa and the minimum design margin in the cask containment system due to NCT cold loading is +14.9 (=414/26 - 1). Therefore, the cask satisfies the applicable NCT allowable stress design criteria under NCT cold conditions.

Evaluation of secondary stresses is not required for the cask non-containment components, which are designed in accordance with Subsection NF of the ASME Code. However, the maximum stress intensity in the cask non-containment components due to NCT cold loading is much less than the shell material minimum yield strength at -40°C of 207 MPa. Therefore, NCT cold loading will not cause any yielding of the cask non-containment components.

The stresses in the cask closure bolts due to NCT cold loading are determined using the 3-D quarter-symmetry finite element model described in Section 2.5.1.2. NCT cold loading is applied in combination with maximum internal pressure and minimum bolt preload to assure that the minimum bolt preload is sufficient to maintain the minimum required gasket load under the worst-case combination of loads. The combination of minimum bolt preload and NCT cold temperature loading produces the lowest possible value of non-prying tensile bolt force because temperature change associated with the NCT cold thermal condition produces differential thermal expansion between the closure bolts and closure lid that relaxes the initial bolt preload. (The maximum internal pressure loading produces the highest outward-acting non-prying tensile force on the closure bolts.) The NCT cold temperature loading is applied to the finite element model as a uniform temperature load of -40°C. The minimum bolt preload of 5,366 N is applied to each bolt, and a uniform pressure load of 700 kPa is applied on the inner surface of the closure plate over the area inside the containment O-ring.

The maximum average stress (i.e., axial stress) and maximum stress (i.e., axial plus bending stress) in the closure bolts due to NCT cold loading are 14 MPa and 39 MPa, respectively. The average axial stress due to internal pressure and gasket seating loads, i.e., bolt torque, is limited to one times the tabulated values of $S_m$ at the corresponding design temperature for NCT. The allowable maximum stress for NCT is limited to $3S_m$. The value of $S_m$ for SA-320, Grade L43 bolting steel at 68.3°C is 234 MPa based on linear interpolation of the $S_m$ values shown in Table 2-15. Therefore, the allowable average stress and maximum stress are 234 MPa and 701 MPa, respectively. The corresponding minimum design margins in the closure bolt for NCT cold loading are +15.7 for average stress and +17.0 for maximum stress.

The maximum gap separation at the inside edge of the bolting flange due to the NCT cold loading is approximately 0.013 mm, or 1.5% of the O-ring compression. For the cask closure to maintain containment under these conditions, the elastomeric O-ring must have sufficient elasticity to expand to fill the gap, considering potential material degradation due to environmental effects such as radiation and temperature. This is satisfied provided that the maximum compression set does not exceed 98% (i.e., (0.88-0.013)/0.88). As shown in Section 3.9.14 of the Parker O-Ring Handbook [2.18], the compression set in ethylene propylene O-rings after exposure to $10^7$ rads of gamma radiation at room temperature ranges from 28.6% to 46.6%, based on the compound. The data also shows that these materials will take on a compression set of less than 18% when exposed to a maximum temperature of 100°C for 70 hours ([2.18], Figure 2-13). This data suggests that the maximum O-ring compression set due to the combined effects of temperature and radiation will be sufficient to maintain a tight seal for the NCT cold loading.

The results of the NCT cold structural evaluation demonstrate that the cask containment system satisfies the applicable NCT allowable stress design criteria. NCT cold loading does not cause any permanent deformation of the package, nor does it substantially reduce the effectiveness of the packaging. Furthermore, since the evaluation shows that the containment seal is maintained under NCT cold loading, there would be no loss or dispersal of radioactive contents. Finally, the configuration of the package under NCT cold loading is the same as that considered in the shielding evaluation. Therefore, NCT cold loading does not cause any significant increase in external surface radiation levels. The package thus complies with the requirements of §71.43(f) and §71.51(a)(1) when subjected to the NCT cold test specified in §71.71(c)(2).

### 2.6.3 Reduced External Pressure

In accordance with §71.71(c)(3), the package is designed to withstand the effects of a reduced external pressure of 25 kPa absolute. Per Table 2-1, reduced external pressure loading is considered in combination with maximum internal pressure, and NCT hot thermal loading (i.e., 38°C ambient temperature, maximum decay heat, and maximum insolation). Under these conditions, the maximum internal pressure is less than 700 kPa. Therefore, the greatest pressure difference between the inside and outside of the containment system is 775 kPa.

The stresses in the cask due to reduced external pressure loading are determined using the axisymmetric finite element model described in Section 2.6.1.3. A bounding internal pressure

load of 795 kPa is applied in combination with maximum bolt preload and NCT heat temperature loading. The stresses in the cask are calculated assuming linear-elastic static behavior.

The maximum stress intensities in the cask containment system and non-containment components are summarized in Table 2-28, along with the corresponding allowable stress intensities and minimum design margins. The results show that the maximum stress intensities in the cask due to reduced external pressure loading are lower than the corresponding allowable stress intensities. The minimum design margin for reduced external pressure loading is +0.88 for primary membrane plus bending stress intensity ($P_m+P_b$) at the center of the cask containment shell bottom plate (section C1 in Figure 2-1).

The results of the NCT reduced external pressure structural evaluation demonstrate that the cask containment system satisfies the applicable NCT allowable stress design criteria. Reduced external pressure loading does not cause any permanent deformation of the package, substantially reduce the effectiveness of the packaging, result in any loss or dispersal of radioactive contents, or cause any significant increase in external surface radiation levels. Therefore, the package complies with the requirements of §71.43(f) and §71.51(a)(1) when subjected to the NCT reduced external pressure test specified in §71.71(c)(3).

**Table 2-28 – Reduced External Pressure Stress Summary**

| Cask System | Stress Type | Maximum Stress Intensity (MPa) | Stress Location[1] | Allowable Stress Intensity[2] (MPa) | Minimum Design Margin[3] |
|---|---|---|---|---|---|
| Containment System | $P_m$ | 25 | C4 | 138 | +4.52 |
| | $P_m+P_b$ | 110 | C1 | 207 | +0.88 |
| | $P_m+P_b+Q$ | 110 | C1 | 414 | +2.76 |
| Non-Containment Components | $P_m$ | 31 | N11 | 138 | +3.45 |
| | $P_m+P_b$ | 85 | N7 | 207 | +1.44 |
| | $P_m+P_b+Q$ | 91 | N7 | N/A[4] | N/A[4] |

Notes:
1. Containment system and non-containment component stress locations are shown in Figure 2-1 and Figure 2-2, respectively.
2. Allowable stresses are based on the lower-bound strength properties of all cask shell material alternatives at an upper-bound design temperature of 74°C.
3. Design margin is calculated as (Allowable S.I./Maximum S.I) – 1.
4. Evaluation of secondary stress is not required for non-containment components.

### 2.6.4 Increased External Pressure

In accordance with §71.71(c)(4), the package is designed to withstand the effects of an increased external pressure of 140 kPa absolute. Per Table 2-1, increased external pressure loading is considered in combination with an ambient temperature of -29°C, zero decay heat, and zero insolation, minimum internal pressure, and fabrication stresses. The minimum internal pressure for the cask is zero. Therefore, under these conditions the greatest pressure difference between the inside and outside of the containment system is 140 kPa gauge.

The stresses in the cask due to increased external pressure loading are determined using the axisymmetric finite element model described in Section 2.6.1.3. An external pressure load of 140 kPa is applied to the outside of the cask containment system, conservatively taking no credit for any pressure-retaining ability of the cask outer shell. In addition, the maximum bolt preload and NCT cold temperature loading (i.e., a uniform temperature of -29°C) are applied to the model. The stresses in the cask for increased external pressure loading are calculated assuming linear-elastic static behavior.

The maximum stress intensities in the cask assembly containment system and non-containment components for increased external pressure loading are summarized in Table 2-29, along with the corresponding allowable stress intensities and minimum design margins. The results show that the maximum stress intensities in the cask due to increased external pressure loading are lower than the corresponding allowable stress intensities. The minimum design margin for increased external pressure loading is +3.31 for primary membrane plus bending stress intensity ($P_m+P_b$) in the cask outer shell (section N3). Furthermore, since all of the stresses in the cask are below the material yield strength, no plastic deformation occurs under increased external pressure loading.

Buckling of the containment shell for the increased external pressure loading is evaluated in accordance with ASME Code Case N-284-1 [2.7]. A factor of safety of 2.0 against buckling is used for NCT in accordance with the requirements of ASME Code Case N-284-1. The results of the increased external pressure stress analysis for the cask show that only the cask containment shell is loaded in compression. The outer shell is loaded in tension due to thermal stresses arising from differential thermal expansion between the cask body DU and the stainless steel outer shell at reduced temperatures. The axial and hoop compressive stresses in the cask containment shell due to increased external pressure loading are 1,296 kPa and 2,524 kPa, respectively. The corresponding maximum buckling interaction ratio is 0.03. The cask containment shell satisfies the buckling design criteria of Code Case N-284-1 for increased external pressure loading because the maximum buckling interaction ratio does not exceed 1.0.

The results of the NCT increased external pressure structural evaluation demonstrate that the cask containment system satisfies the applicable NCT allowable stress design criteria. NCT increased external pressure loading does not cause any permanent deformation of the package, nor does it substantially reduce the effectiveness of the packaging. Increased external pressure loading will not result in any loss or dispersal of radioactive contents. Finally, the configuration of the package under NCT increased external pressure loading is the same as that considered in

the shielding evaluation. Therefore, NCT increased external pressure loading does not cause any significant increase in external surface radiation levels. The package thus complies with the requirements of §71.43(f) and §71.51(a)(1) when subjected to the NCT increased external pressure test specified in §71.71(c)(4).

**Table 2-29 – Increased External Pressure Stress Summary**

| Cask System | Stress Type | Maximum Stress Intensity (MPa) | Stress Location[1] | Allowable Stress Intensity[2] (MPa) | Minimum Design Margin[3] |
|---|---|---|---|---|---|
| Containment System | $P_m$ | 14 | C17 | 138 | +8.86 |
| | $P_m+P_b$ | 20 | C17 | 207 | +9.35 |
| | $P_m+P_b+Q$ | 20 | C17 | 414 | +19.7 |
| Non-Containment Components | $P_m$ | 29 | N3 | 138 | +3.76 |
| | $P_m+P_b$ | 48 | N3 | 207 | +3.31 |
| | $P_m+P_b+Q$ | 48 | N3 | N/A[4] | N/A[4] |

Notes:
1. Containment system and non-containment component stress locations are shown in Figure 2-1 and Figure 2-2, respectively.
2. Allowable stresses are based on the lower-bound strength properties of all cask shell material alternatives at an upper-bound design temperature of 74°C.
3. Design margin is calculated as (Allowable S.I./Maximum S.I) – 1.
4. Evaluation of secondary stress is not required for non-containment components.

### 2.6.5 Vibration

In accordance with §71.71(c)(5), the package is subjected to vibration normally incident to transport. The package is transported by truck and air in a vertical orientation. The package is supported by the bottom end of the overpack base and tied down by the four lugs on the overpack lid. Table 2 of ANSI N14.23 [2.23] shows peak vibration accelerations of a trailer bed as a function of the package and tie-down system natural frequency. The maximum peak accelerations (99% level) for light packages (< 15 tons) are 2.0*g* in the vertical direction, 1.3*g* in the longitudinal direction, and 0.5*g* lateral. To provide a conservative, yet simple analysis, the longitudinal and transverse vibration loads are neglected and a bounding ±10*g* vertical acceleration load is used for the cask vibration stress evaluation. This load is expected to bound the vibration loads resulting from both truck and air transport.

The stresses in the cask and shield lid resulting from a 10*g* NCT vibration load are determined using the axisymmetric finite element model described in Section 2.6.1.3. The applied loading for the NCT vibration consist of a 10*g* equivalent-static acceleration load to account for the inertial load of the modeled components, a pressure load to account for the payload, and a reaction pressure load for static equilibrium. The load on the cask cavity due to the payload is conservatively modeled as a uniformly distributed pressure over the cavity bottom end. The magnitude of the payload pressure load is modeled as 22.0 kPa based on an upper-bound payload mass of 1.1 kg and a cavity bottom-end surface area of 4,902 $mm^2$. The NCT vibration reaction load is modeled as a uniformly distributed pressure load on the bottom end of the cask assembly. The magnitude of the reaction pressure load is modeled as 574.5 kPa based on the modeled combined mass of the cask and shield lid of 202.6 kg and a cask bottom-end surface area of 34,636 $mm^2$.

The maximum bolt preload of 7.2 kN per bolt is applied to the model on a 360° basis, producing a total preload (for eight closure bolts) of 57.8 kN on the closure lid. A uniform temperature of 75°C, which bounds the maximum cask temperature under the NCT heat thermal condition, is also applied to the model.

A linear-elastic static analysis is performed for NCT vibration loading. The membrane, membrane plus bending, and total stress intensity at each of the stress evaluation locations shown in Figure 2-1 and Figure 2-2 are evaluated for NCT vibration loading. The maximum stress intensities in the cask containment system and non-containment components due to NCT vibration loading are summarized in Table 2-30, along with the corresponding allowable stress intensities and minimum design margins. The results show that the maximum stress intensities in the cask due to NCT vibration loading are lower than the corresponding allowable stress intensities. The minimum design margin for NCT vibration loading is +19.7 for primary membrane plus bending stress intensity ($P_m+P_b$). Therefore, the cask and shield lid satisfy the applicable NCT allowable stress design criteria for the NCT vibration.

A detailed stress analysis of the cask closure bolts for NCT vibration loading is performed using the 3-D quarter-symmetry finite element model described in Section 2.5.1.2. A 10*g* acceleration load is applied to the model to account for the inertia load from the closure lid. In addition, a

uniform pressure load is applied to the underside of the closure lid to account for the loading from the combined mass of the shield plug and payload. For modeling simplicity, a uniform pressure load is applied over the entire area inside the containment O-ring diameter. Although the O-ring diameter upon which the pressure load is calculated is approximately 18% larger than the outside diameter of the shield plug, it does not significantly affect the solution results. In fact, the assumption of a uniform pressure distribution is conservative; the load from the shield plug will concentrate at its outer edge because the shield plug is relatively stiff compared to the closure plate. Thus, the prying moment resulting from the assumed uniform pressure load distribution is conservative.

NCT vibration loading is applied in combination with NCT heat temperature loading, maximum internal pressure, and maximum bolt preload. The NCT heat temperature loading is applied to the finite element model as a uniform temperature load of 68.3°C. The maximum bolt preload of 7.2 kN is applied to each bolt and a uniform pressure load of 700 kPa is applied on the inner surface of the closure plate over the area inside the containment O-ring.

The maximum average stress (i.e., axial stress) and maximum stress (i.e., axial plus bending stress) in the closure bolts due to NCT vibration loading are 201 MPa and 210 MPa, respectively. The average axial stress and maximum stress are limited to $2S_m$ and $3S_m$, respectively. The value of $S_m$ for SA-320, Grade L43 bolting steel at 68.3°C is 234 MPa based on linear interpolation of the $S_m$ values shown in Table 2-15. Therefore, the allowable average stress and maximum stress are 468 MPa and 701 MPa, respectively. The corresponding minimum design margins in the closure bolt for NCT vibration loading are +1.33 for average stress and +2.34 for maximum stress.

The results of the NCT vibration structural evaluation demonstrate that the cask satisfies the applicable NCT allowable stress design criteria. NCT vibration loading does not cause any permanent deformation of the package, nor does it substantially reduce the effectiveness of the packaging. Furthermore, the evaluation shows that NCT vibration loading does not result in any significant lid separation. Thus, under NCT vibration loading, the containment seal is maintained, and no loss or dispersal of radioactive contents occurs. Finally, the configuration of the package under NCT vibration loading is the same as that considered in the shielding evaluation. Therefore, NCT vibration loading does not cause any significant increase in external surface radiation levels. The package thus complies with the requirements of §71.43(f) and §71.51(a)(1) when subjected to the NCT vibration test specified in §71.71(c)(5).

**Table 2-30 – Cask Stress Summary, NCT Vibration**

| Cask System | Stress Type | Maximum Stress Intensity (MPa) | Stress Location[1] | Allowable Stress Intensity[2] (MPa) | Minimum Design Margin[3] |
|---|---|---|---|---|---|
| Containment System | $P_m$ | 5 | C16 | 138 | +26.6 |
| | $P_m+P_b$ | 10 | C13 | 207 | +19.7 |
| | $P_m+P_b+Q$ | 11 | C20 | 414 | +36.6 |
| Non-Containment Components | $P_m$ | 4 | N13 | 138 | +33.5 |
| | $P_m+P_b$ | 4 | N13 | 207 | +50.8 |
| | $P_m+P_b+Q$ | 5 | N13 | N/A[4] | N/A[4] |

Notes:
1. Containment system and non-containment component stress locations are shown in Figure 2-1 and Figure 2-2, respectively.
2. Allowable stresses are based on the lower-bound strength properties of all cask shell material alternatives at an upper-bound design temperature of 74°C.
3. Design margin is calculated as (Allowable S.I./Maximum S.I) – 1.
4. Evaluation of secondary stress is not required for non-containment components.

### 2.6.6 Water Spray

In accordance with the requirements of §71.71(c)(6), the package must be subjected to a water spray that simulates exposure to rainfall of approximately 5 cm/h for at least 1 hour. Quenching effects due to the water spray test will not significantly affect the package. The cask assembly is isolated from the quenching effects of the water spray by the overpack assembly, which insulates the cask from sudden environmental changes. Furthermore, the thermal mass of the cask is large enough to significantly slow the thermal response to sudden external temperature changes. Therefore, this condition is not significant in the structural design of the cask and is not analyzed.

### 2.6.7 Free Drop

In accordance with §71.71(c)(7), the package, which weighs less than 5,000 kg, is subjected to a free drop through a distance of 1.2 m "*onto a flat, essentially unyielding, horizontal surface, striking in a position for which maximum damage is expected.*" The package is evaluated for seven different NCT free drop orientations, as shown in Figure 2-16. They include a bottom end drop, top end drop, bottom corner drop, top corner drop, horizontal side drop, bottom end oblique drop, and top end oblique drop. For the oblique drop impacts, a primary impact angle of 5° from horizontal is assumed (i.e., 85° for the bottom oblique impact and 95° for the top oblique impact) because it is expected to result in the worst-case NCT free drop secondary (slapdown) impact loads.

The dynamic response of the package to the NCT free drop test conditions is determined using explicit dynamic finite element analysis methods. The ANSYS LS-DYNA PC computer code, which is described in Section 2.12.2.2, is used for this analysis. The explicit dynamic finite element analysis of the package is used to predict the rigid-body response of the cask to each NCT free drop test. In addition, this analysis demonstrates the structural adequacy of the overpack assembly for the NCT free drop tests. The maximum stresses in the overpack closure bolts are shown to satisfy the applicable allowable stress design criteria of Subsection NF of the ASME Code. Furthermore, the maximum crush depth of the overpack polyurethane foam due to each NCT free drop is much less than the allowable crush depth. The drop loads analysis of the package is discussed further in Section 2.6.7.1.

A detailed stress analysis of the cask and shield lid is performed using linear-elastic static finite element analysis methods. The ANSYS Mechanical computer program, which is described in Section 2.12.2.1, is used for this analysis. Bounding equivalent-static acceleration design loads are applied to the cask finite element model for each NCT free drop orientation. The bounding equivalent-static acceleration design loads are determined by multiplying the cask peak rigid-body accelerations determined in Section 2.6.7.1 by dynamic load factors (DLFs) to account for possible dynamic amplification within the cask. The maximum stresses in the cask and shield lid due to each NCT free drop are calculated and shown to satisfy the applicable allowable stress design criteria of Subsections NF [2.2] and WB [2.1] of the ASME Code. In addition, the compressive stresses in the cask cylindrical shells due to each NCT free drop are evaluated in accordance with ASME Code Case N-284-1 [2.7] and shown to satisfy the

applicable buckling design criteria. The cask NCT free drop stress analysis and buckling analysis are discussed further in Sections 2.6.7.2 and 2.6.7.3, respectively.

The worst-case initial conditions are considered in accordance with §71.71(b) and Regulatory Guide 7.8 [2.5]. For the overpack analysis, which determines the cask rigid-body acceleration time-history response and evaluates the structural adequacy of the overpack components, the "cold" thermal condition (i.e., an ambient temperature of -29°C with zero decay heat and no insolation) is the worst case since it results in the lowest package temperatures, the highest crush strength of the overpack foam, and the highest cask acceleration loads. The "hot" thermal condition (i.e., an ambient temperature of 38°C with maximum decay heat and insolation), for which the package temperatures are highest and the foam crush strength is lowest, are not considered in the NCT free drop impact analysis since the cask accelerations will be bounded by those under "cold" thermal conditions and because there is no potential for the cask to "bottom-out" due to NCT free drop impacts.

For the cask NCT free drop stress evaluation, initial conditions include both "hot" and "cold" thermal conditions. However, the maximum cask accelerations calculated for the "cold" thermal conditions are conservatively used for all cask NCT free drop stress analyses. Furthermore, lower-bound allowable stresses are used for the cask NCT free drop stress evaluation, which are conservatively based on a design temperature that bounds the peak cask temperature under the "hot" thermal conditions. Further discussion of the load combinations considered in the stress evaluation is provided in Section 2.6.7.2.

The results of the NCT free drop structural evaluation demonstrate that the cask satisfies the applicable NCT allowable stress design criteria. NCT free drop loading does not cause any significant permanent deformation of the package, nor does it substantially reduce the effectiveness of the packaging. Furthermore, since the evaluation shows that the containment seal is maintained under NCT free drop loading, there would be no loss or dispersal of radioactive contents. Finally, the configuration of the package under NCT free drop loading is the same as that considered in the shielding evaluation. Therefore, NCT free drop loading does not cause any significant increase in external surface radiation levels. The package thus complies with the requirements of §71.43(f) and §71.51(a)(1) when subjected to the NCT free drop test specified in §71.71(c)(7).

### 2.6.7.1 Overpack Evaluation

The structural evaluation of the overpack for the NCT free drop test is performed using the ANSYS LS-DYNA PC finite element code and the 3-D half-symmetry finite element model shown in Figure 2-17. The finite element model, which consists of 27,973 elements and 36,382 nodes (not including the impact target), includes detailed representations of the overpack base, overpack lid, and the overpack closure bolts. All components are modeled based on the nominal design dimensions. Minor design features that do not affect the structural response of the package, such as small fillet radii on the overpack shells, thermal relief plug holes, drain holes, tamper-indicating feature holes, and foam pour hole covers, are not included in the model.

The exterior components of the overpack base and lid are all modeled using explicit 3-D structural solid elements, whereas the inner shells are modeled using explicit 4-node shell elements. Shell-to-solid constraints are used to "tie" the edge of the inner shell element nodes to the outer shell solid element nodes at the interfaces. The overpack inner and outer shells are modeled using a piecewise-linear plasticity material model, as discussed in Section 2.2.1.1. For the NCT free drop, the upper-bound stress-strain design curve shown in Figure 2-4 is conservatively used.

The overpack base and lid foam cores are modeled using explicit 3-D structural solid elements with a crushable foam material model. The foam stress-strain curves are developed as described in Section 2.2.1.3, considering foam crush strength tolerance, temperature effects, and dynamic (strain-rate) effects. The overpack analyses for all NCT free drop tests are conservatively performed using the upper-bound foam stress-strain curve shown in Figure 2-5.

The thermal spider, which connects the overpack base outer shell to the overpack base inner bottom plate, is also included in the model. Each leg of the thermal spider is modeled using explicit 3-D beam elements. The inside end of each leg is connected to the bottom corner of the overpack base inner shell and the outer end of the leg is connected to the inside of the overpack base outer shell. The thermal spider beam elements are modeled using the upper-bound bilinear kinematic material model for copper described in Section 2.2.1.4.

The overpack closure bolts are modeled using explicit 3-D beam elements, which support axial, shear, and bending loads. The bolt element cross-section properties are based on the overpack closure bolt nominal diameter. The cross-section properties of the bolts located on the half-symmetry plane are equivalent to that of the bolt half-circle. The bolts are modeled using the bilinear kinematic material model for A320, Grade L43 bolting steel, as described in Section 2.2.1.1. Each bolt is modeled using two elements: one spanning the length of thread engagement in the overpack base flange, and the other spanning from the top of the threads to the node located at the base of the bolt head.

The cask and shield lid are modeled using explicit 4-node shell elements. For the purpose of the drop loads analysis, these assemblies are treated as a single rigid-body having an outside diameter of 225.0 mm and a total height of 347.0 mm. The rigid-body is also modeled with a 7.5 mm by 45° chamfer on the bottom corner and a 7.5 mm radius on the top corner. The mass properties of the cask/shield lid rigid-body are defined by its mass, center of gravity, and a mass moment of inertia. The center of gravity of the cask/shield lid rigid-body is located on its centerline at a distance of 262 mm from the bottom end of the overpack assembly. The mass moment of inertia of the cask/shield lid rigid-body is defined relative to its local center of gravity. For the NCT free drop evaluation, the cask/shield lid rigid-body is modeled using lower-bound mass and mass moment of inertia, which results in upper-bound cask accelerations. The lower-bound mass properties of the cask and shield lid rigid-body are 2.5% lower than the nominal mass properties shown in Table 2-8.

The nonlinear contact between the various components of the package finite element model are modeled using the surface-to-surface contact type. All of the package contact surfaces are modeled without friction for the NCT free drop analyses. The results of a sensitivity study shows

that the frictionless surface contact assumption produces bounding results for the package response, including higher peak cask rigid-body accelerations, higher overpack sidewall foam crush, and higher overpack bolt stresses. Therefore, the frictionless surface contact assumed for the free drop analyses is conservative and bounding.

Each NCT free drop time-history analyses is started at the moment of initial contact between the package outer surface and the impact surface. An initial vertical velocity of 4.85 m/s, corresponding to a free-fall velocity from a height of 1.2 m, is applied to the package in all cases. In addition, a constant gravitational acceleration of 9.81 $m/s^2$ is applied to the model. For stable drop orientations (i.e., end, side, and corner drops), the duration of the time-history analysis is sufficient to capture the primary impact. The durations of the time-history analysis for the oblique drop impacts are sufficient to capture both the primary and secondary (slapdown) impacts.

The maximum rigid-body accelerations resulting from each NCT free drop test are summarized in Table 2-31. The results show that the highest longitudinal cask acceleration (262*g*) results from the NCT bottom end drop and the highest transverse cask acceleration (-573*g*) results from the NCT bottom oblique drop. Table 2-31 also summarizes the maximum foam crush, as a percentage of the total foam thickness, that results from each NCT free drop test. The maximum overpack foam crush for NCT free drop of 15% is much lower than the general limit of 70%.

The maximum axial stress, shear stress, and combined stress (i.e., interaction ratio) in the overpack closure bolts for each NCT free drop test are evaluated in accordance with the Service Level A allowable stress design criteria for Class 2 supports from Subsection NF [2.2] of the ASME Code. The overpack closure bolt maximum axial stress, shear stress, stress interaction ratio, and minimum design margins resulting from each NCT free drop test are summarized in Table 2-32. The minimum design margin in the overpack closure bolts is +0.35 due to the maximum axial bolt stress resulting from the NCT bottom oblique drop. Thus, the overpack closure bolts satisfy the applicable allowable stress design criteria for the NCT free drop.

The overpack damage resulting from the NCT free drop is minimal and will not affect the ability of the package to withstand the HAC tests required by §71.73. The most noticeable overpack damage for all NCT free drop cases evaluated results from the NCT top-corner drop. As shown in Figure 2-18, the extent of damage to the overpack resulting from the NCT top-corner drop is limited to the impacted overpack lid lug and the outer shell adjacent to the lug. In this case, the overpack lid outer shell at the base of the lug is permanently deformed inward by less than 15 mm. Although slightly more overpack damage results from the “hot” thermal condition with lower-bound material strength properties, this damage does not affect the ability of the package to withstand the HAC tests required by §71.73.

### 2.6.7.2 Cask Stress Evaluation

The stresses in the cask and shield lid due to NCT free drop loading are determined using finite element analysis methods. Equivalent-static linear-elastic analyses are performed for those NCT free drop orientations expected to cause maximum damage to the package. The equivalent-static acceleration loads for each NCT free drop orientation are equal to the peak rigid-body

accelerations of the cask multiplied by a DLF that accounts for possible dynamic amplification within the cask. As discussed in Section 2.12.3, upper-bound DLFs are conservatively applied to all NCT free drop longitudinal and transverse rigid-body accelerations, respectively. Table 2-33 provides a summary of the equivalent-static acceleration loads used for the structural evaluation of each NCT free drop orientation.

In accordance with Regulatory Guide 7.8 [2.5], NCT free drop loads are evaluated in combination with internal pressure, thermal, and fabrication stresses. As discussed in Section 2.6.1.1, a bounding internal design pressure of 700 kPa gauge is conservatively used for the structural evaluation of the cask. NCT cold and NCT hot thermal loadings are considered in combination with NCT free drop loading. The only significant fabrication stresses in the cask are those resulting from closure bolt preload. Therefore, the following load combinations are considered for each NCT free drop load orientation evaluated:

(A) NCT Free Drop + Bolt Preload

(B) NCT Free Drop + Bolt Preload + Maximum Internal Pressure

(C) NCT Free Drop + Bolt Preload + Max. Internal Pressure + NCT Heat[1]

(D) NCT Free Drop + Bolt Preload + NCT Cold1

Thermally induced stress intensities are classified as secondary in accordance with the ASME Code since they are self-limiting. Therefore, the stress intensities obtained from load combinations C and D are compared to the stress limits for primary plus secondary ($P_m+P_b+Q$) stress intensity.

The stress analyses for the NCT end drops are performed using the axisymmetric finite element model described in Section 2.6.1.3. For all other NCT free drop analysis, the stresses are calculated using the 3-D half-symmetry finite element model shown in Figure 2-19. The 3-D half-symmetry finite element model, which has the same basic cross-section geometry as the axisymmetric finite element model described in Section 2.6.1.3, is comprised of a total of 35,248 nodes and 35,504 elements, representing all of the major structural and shielding components of the cask and shield lid. With the exception of the closure bolts and O-rings, the model is constructed entirely of 3-D structural solid elements. The closure bolts are modeled using 3-D elastic beam elements with no credit taken for the bolt bending stiffness. The closure bolt element real constants are used to define the closure bolt cross-section properties and initial strain due to preload. The closure bolt area is calculated based on the nominal bolt diameter of 10 mm.

[1] Load combinations including NCT heat and NCT cold temperature loading are not evaluated for the NCT side, corner, and oblique drops. The results of the NCT end drop analyses show that these temperature loads do not cause any significant increase in the cask's maximum stress intensities.

The containment O-ring, leak test O-ring, and cleanliness O-ring are all modeled using a series of 3-D node-to-node gap elements in the 3-D half-symmetry finite element model. These O-ring gap elements transfer only compressive loads across the O-ring interface. Each O-ring gap element's contact stiffness is calculated based its tributary width (circumference) and the O-ring spring stiffness constants that are determined based on the manufacturer's data for O-ring compressive loads versus percent compression. The O-ring gap elements located on the symmetry plane have half the contact stiffness of those not located on the symmetry plane. Since the shield plug and closure lid are modeled at the initial positions of contact with the O-rings, the O-ring gap elements are all modeled as initially closed.

In the 3-D half-symmetry finite element model, the nonlinear contact interface between the various components of the cask components are modeled using 3-D surface-to-surface contact elements. Contacts are modeled on the same surfaces shown in Figure 2-14 and revolved around the circumference. Additional contact surfaces are modeled on the shield lid shear lip and between the outer diameter of the shield lid DU and the inner diameter of the shield lid casing side plate.

The material properties modeled in the 3-D half-symmetry finite element model are the same as those used for the cask axisymmetric finite element model, as described in Section 2.6.1.3.

The applied loading for each NCT free drop analysis consists of the equivalent-static acceleration design loads from Table 2-33, which account for the inertial load of the modeled components, pressure-loading to account for the payload mass, and reaction pressure-loads for static equilibrium. As shown in Table 2-33, the magnitude of the transverse acceleration varies along the length of the cask for the NCT side and oblique drop impacts. The axially-varying transverse acceleration loads are modeled by applying a uniform transverse acceleration load, equal to the average of the accelerations at the top and bottom ends of the cask, and a rotational acceleration around the mid-length of the cask.

The longitudinal loading on the cask cavity from the payload mass is applied as a uniformly distributed pressure on the end of the cask cavity nearest the impacted end of the package for the NCT end, corner, and oblique drops. The magnitude of the longitudinal payload pressure load is calculated based on the longitudinal equivalent-static acceleration design load from Table 2-33, a maximum payload mass of 1.1 kg, and the area of the surface over which the load is applied. The longitudinal reaction loads for the NCT end, corner, and oblique drops are modeled as uniformly distributed pressure loads on the impacted end of the cask. The magnitude of the longitudinal reaction pressure loads are calculated based on the longitudinal equivalent-static acceleration design loads from Table 2-33, a total cask and shield lid mass of 202.3 kg, and an end-surface area of 34,636 $mm^2$.

The transverse loading from the cask payload for the NCT side, corner, and oblique drops is applied as an axially-uniform pressure load on the impacted side of the cask cavity. The applied transverse pressure loads are calculated assuming a cosine distribution around the circumference as follows:

$$p = p_o \cos(90\theta/\theta_o),$$

where $p_o$ is the maximum pressure amplitude based on the included mass and the transverse equivalent-static acceleration load at the payload center of gravity, $\theta$ is the angle from the point of maximum pressure, and $\theta_o$ is the half-angle over which the pressure load is applied (assumed to be 45°).

The transverse reaction loads on the cask closure lid and shield lid are applied as pressure loads on the impacted side of the cask. The reaction pressure loads are assumed to be uniformly distributed over the length and have a cosine distribution over a 45° half-angle of the circumference. The reaction pressures are calculated in the same manner as the payload inertia pressure loads, as discussed above.

The transverse reaction loads on the cask body are also applied as pressure loads on the impacted side of the cask. The pressure load is applied with a cosine distribution over a 45° half-angle of the circumference. For the NCT corner drops, the magnitude of the cask body reaction pressure is uniform along the length of the cask body. For the NCT side and oblique drops, the reaction pressure loading on the cask body is applied as a series of stepped uniform pressure loads over six axial zones. The axial distribution of the pressure loading is determined such that it balances the applied inertia loads due to the applied transverse and angular acceleration loads. The net transverse load on each axial zone is determined based on the principle of static equilibrium.

For all NCT free drop analyses, the maximum bolt preload of 7.2 kN per bolt is applied to the model. For the NCT end drop analyses, the bolt preload is applied on a 360° basis resulting in a total preload (for eight closure bolts) of 57.8 kN on the closure lid. For all other NCT free drop analyses, a bolt preload of 7.2 kN is applied to each individual bolt element (3.6 N for the bolts on the half-symmetry plane).

For those load combinations that include internal pressure, a pressure load of 700 kPa gauge is applied to the inside surfaces of the cask containment boundary. The internal pressure load is added to the payload pressure load acting on the impacted end of the cask cavity.

For the NCT free drop load combinations that do not include temperature loading, a uniform temperature of 75°C is applied to the model. For those NCT free drop load combinations that do include temperature loading, the bounding NCT heat temperature distribution shown in Figure 2-15 is applied to the model.

For the axisymmetric finite element model, a single node on the outer edge at the impacted end of the cask is restrained from vertical translation. For the 3-D half-symmetry finite element model, symmetry boundary displacement constraints are applied on all nodes located on the cask half-symmetry plane. The 3-D half-symmetry finite element model is also pinned at a single node at the top and bottom ends of the cask body to prevent rigid-body translation and rotation. The pinned boundary conditions applied to the models are required only for numerical stability since the applied inertial loads are balanced by equal and opposite applied reaction loads.

A linear-elastic equivalent-static analysis is performed for each of the NCT free drop impact orientations. The membrane, membrane plus bending, and total stress intensity at each of the stress evaluation locations shown in Figure 2-1 and Figure 2-2 are evaluated for each NCT free drop load combination. The maximum stress intensities resulting from each NCT free drop test, along with the location of the maximum stress intensity, the corresponding allowable stress intensity, and the resulting minimum design margin, are summarized in Table 2-34. The minimum design margin for primary stress intensities ($P_m$ and $P_m+P_b$) due to NCT free drop loading is +0.06 for primary membrane plus bending ($P_m+P_b$) stress intensity due to the NCT bottom end drop. The lowest design margin for local membrane and primary plus secondary stress intensities for all NCT free drops is +0.02 for local membrane ($P_l$) stress intensity due to the NCT bottom oblique drop.

A detailed stress analysis of the cask closure bolts for NCT free drop loading is performed using the 3-D quarter-symmetry finite element model described in Section 2.5.1.2. Analyses are performed for the NCT top end drop and NCT top corner drop because these impact orientations result in the highest outward-acting forces on the closure lid and closure bolts. Transverse loads due to NCT free drops are not included in the closure bolt evaluation since the cask includes a shear lip to protect the closure bolts from shear loading.

The applied NCT top end drop and NCT top corner drop loads are based on the maximum calculated equivalent-static longitudinal accelerations from Table 2-33 of 253*g* and 98*g*, respectively. The inertia load from the closure lid self-weight due to the NCT free drop longitudinal acceleration is accounted for by applying the equivalent-static acceleration load to the model. In addition, a uniform pressure load is applied to the underside of the closure lid to account for the loading from the combined mass of the shield plug and payload. For modeling simplicity, a uniform pressure load is applied over the entire area inside the containment O-ring diameter. Although the O-ring diameter upon which the pressure load is calculated is approximately 18% larger than the outside diameter of the shield plug, it does not significantly affect the solution results. In fact, the assumption of a uniform pressure distribution is conservative; the load from the shield plug will concentrate at its outer edge because it is relatively stiff compared to the closure plate. Thus, the prying moment resulting from the assumed uniform pressure load distribution is conservative.

NCT free drop loading is applied in combination with NCT heat temperature loading, maximum internal pressure, and maximum bolt preload. The NCT heat temperature loading is applied to the finite element model as a uniform temperature load of 68.3°C. The maximum bolt preload of 7.2 kN is applied to each bolt and a uniform pressure load of 700 kPa is applied on the inner surface of the closure plate over the area inside the containment O-ring.

The maximum average stress (i.e., axial stress) and maximum stress (i.e., axial plus bending stress) in the closure bolts and the maximum gap lid separation at the inside edge of the bolting flange due to NCT top end drop and NCT top corner drop loading are summarized in Table 2-35. The maximum average stress and maximum stress in the cask closure bolts, which result from the NCT top end drop condition, are 242 MPa and 311 MPa, respectively. The average axial stress and maximum stress are limited to $2S_m$ and $3S_m$, respectively. The value of $S_m$ for SA-320,

Grade L43 bolting steel at 68.3°C is 234 MPa based on linear interpolation of the $S_m$ values shown in Table 2-15. Therefore, the allowable average stress and maximum stress are 468 MPa and 701 MPa, respectively. The corresponding minimum design margins in the closure bolt for NCT free drop loading are +0.93 for average stress and +1.25 for maximum stress.

The maximum lid separation at the inside edge of the bolting flange, resulting from the NCT top end drop loading, is approximately 0.047 mm, or 5.3% of the O-ring compression. For the cask closure to maintain containment under these conditions, the elastomeric O-ring must have sufficient elasticity to expand to fill the gap, with consideration of potential material degradation due to environmental effects such as radiation and temperature. This is satisfied provided that the maximum compression set does not exceed 94.7% (i.e., (0.88-0.047)/0.88). As shown in Section 3.9.14 of the Parker O-Ring Handbook [2.18], the compression set in ethylene propylene O-rings after exposure to $10^7$ rads of gamma radiation at room temperature ranges from 28.6% to 46.6%, based on the compound. The data also shows that these materials will take on a compression set of less than 18% when exposed to a maximum temperature of 100°C for 70 hours ([2.18], Figure 2-13). This data shows that the maximum O-ring compression set due to the combined effects of temperature and radiation will be sufficient to maintain a tight seal for the NCT free drop loading.

### 2.6.7.3 Cask Shell Buckling Evaluation

Buckling evaluations of the cask containment shell and outer shell are performed for each NCT free drop test in accordance with the requirements of ASME Code Case N-284-1 [2.7]. The maximum compressive stresses and shear stresses near the mid-lengths of the cask inner shell and outer shell (i.e., Sections C5 and N5 in Figure 2-1 and Figure 2-2) are used for the buckling evaluation. As discussed in Section 2.1.2.3, elastic and inelastic buckling interaction ratios are calculated based on the NCT allowable buckling stresses shown in Table 2-7, which include a factor of safety of 2.0. The maximum interaction ratios must not exceed 1.0.

The maximum calculated cask shell stresses and the resulting maximum buckling interaction ratios are summarized in Table 2-36. The maximum buckling interaction ratio in the cask inner shell is 0.18, resulting from the NCT side drop. The maximum buckling interaction ratio in the cask outer shell is 0.41, resulting from the NCT bottom end drop. Therefore, the cask satisfies the buckling design criteria of ASME Code Case N-284-1 for the NCT free drop.

**Table 2-31 – NCT Free Drop Loads Summary**

| NCT Drop Case I.D. | Case Description[1] | Maximum Overpack Foam Crush[2] | Cask Peak Rigid-Body Accelerations[3] | | |
|---|---|---|---|---|---|
| | | | Transverse | | |
| | | | Top End | Bottom End | Longitudinal |
| N1 | Bottom End Drop | 9% | [4] | [4] | +262g |
| N2 | Top End Drop | 9% | [4] | [4] | -230g |
| N3 | Bottom Corner Drop | 5% | -128g | -128g[5] | +144g |
| N4 | Top Corner Drop | 15% | -116g | -116g[5] | -89g |
| N5 | Side Drop | 8% | -394g | -265g[6] | [4] |
| N6 | Bottom Oblique Drop<br>- Primary Impact<br>- Secondary Impact | 7% | <br>+75g[6]<br>-573g | <br>-279g<br>+139g[6] | <br>+14g[6]<br>+77g[6] |
| N7 | Top Oblique Drop<br>- Primary Impact<br>- Secondary Impact | 7% | <br>-517g<br>+108g | <br>-47g[6]<br>-280g | <br>-12g[6]<br>-32g |

Notes:
1. Impact orientations shown in Figure 2-16.
2. Value equal to the maximum deformation divided by the nominal foam thickness in the corresponding direction.
3. The highest peak accelerations on either the top or bottom centerline of the cask/shield lid rigid-body in the transverse (X) and longitudinal (Y) directions are reported, unless otherwise noted.
4. Peak accelerations are insignificant.
5. Conservatively assumed equal to higher peak acceleration at the other end of the cask.
6. Acceleration occurring at the same time as the highest peak transverse acceleration.

**Table 2-32 – Overpack Closure Bolt NCT Free Drop Stress Summary**

| NCT Drop Case I.D. | Case Description[1] | Maximum Axial Stress (MPa) | Maximum Shear Stress (MPa) | Maximum Stress Interaction Ratio[2] | Minimum Bolt Design Margin[3] |
|---|---|---|---|---|---|
| N1 | Bottom End Drop | 241 | 45 | 0.31 | +0.79 |
| N2 | Top End Drop | 151 | 9 | 0.13 | +1.85 |
| N3 | Bottom Corner Drop | 78 | 67 | 0.14 | +1.66 |
| N4 | Top Corner Drop | 156 | 74 | 0.17 | +1.41 |
| N5 | Side Drop | 311 | 84 | 0.54 | +0.39 |
| N6 | Bottom Oblique Drop | 320 | 92 | 0.56 | +0.35 |
| N7 | Top Oblique Drop | 298 | 93 | 0.55 | +0.45 |

Notes:
1. Impact orientations shown in Figure 2-16.
2. Calculated per Table 2-4.
3. The minimum design margin is calculated as (Allowable Value/Maximum Value) – 1, where the allowable axial and shear stresses for A320, Grade L43 bolting steel at an upper-bound temperature of 93°C are 431 MPa and 178 MPa, respectively. The allowable value for the stress interaction ratio is 1.0.

**Table 2-33 – NCT Free Drop Equivalent-Static Acceleration Design Loads**

| NCT Free Drop Orientation[1] | Equivalent-Static Accelerations (g) | | | | | |
|---|---|---|---|---|---|---|
| | Calculated Loads | | | Applied Loads | | |
| | Transverse | | | Transverse[2] (g) | | |
| | Top End | Bottom End | Longitudinal | Top End | Bottom End | Longitudinal |
| Bottom End (N1) | --- | --- | 288 | --- | --- | 290 |
| Top End (N2) | --- | --- | 253 | --- | --- | 290 |
| Bottom Corner (N3) | -141 | --- | 158 | 180 | --- | 160 |
| Top Corner (N4) | -128 | --- | 98 | 130 | --- | 100 |
| Side (N5) | -445 | -299 | --- | -460 | -300 | --- |
| Bottom Oblique (N6) | -647 | +162 | +87 | -650 | +50 | +90 |
| Top Oblique (N7) | -584 | -53 | -14 | -585 | -55 | -85 |

Notes:
1. Impact orientations shown in Figure 2-16.
2. The transverse loads are applied as an average transverse linear acceleration and a rotation acceleration about the cask mid-length.

**Table 2-34 – NCT Free Drop Stress Summary**

| NCT Free Drop Orientation (Case I.D.) | Stress Type | Maximum Stress Intensity (MPa) | Stress Location[1] | Allowable Stress Intensity[2] (MPa) | Minimum Design Margin[3] |
|---|---|---|---|---|---|
| Bottom End (N1) | $P_m$ | 95 | N13 | 138 | +0.45 |
| | $P_l$ | 120 | C6 | 207 | +0.73 |
| | $P_m+P_b$ | 195 | C1 | 207 | +0.06 |
| | $P_m+P_b+Q$ | 197 | C7 | 414 | +1.10 |
| Top End (N2) | $P_m$ | 72 | N9 | 138 | +0.92 |
| | $P_l$ | 72 | N9 | 207 | +1.88 |
| | $P_m+P_b$ | 147 | N9 | 207 | +0.41 |
| | $P_m+P_b+Q$ | 88 | C1 | 414 | +3.70 |
| Bottom Corner (N3) | $P_m$ | 123 | C6, 60° | 138 | +0.12 |
| | $P_l$ | 171 | C7, 67.5° | 207 | +0.21 |
| | $P_m+P_b$ | 153 | C6, 90° | 207 | +0.35 |
| | $P_m+P_b+Q$ | 230 | C7, 67.5° | 414 | +0.80 |
| Top Corner (N4) | $P_m$ | 40 | N4, 0° | 138 | +2.45 |
| | $P_l$ | 89 | N3, 0° | 207 | +1.33 |
| | $P_m+P_b$ | 89 | C1, 0° | 207 | +1.33 |
| | $P_m+P_b+Q$ | 101 | C14, 0° | 414 | +3.10 |
| Side Drop (N5) | $P_m$ | 121 | C11, 37.5° | 138 | +0.14 |
| | $P_l$ | 170 | C13, 0° | 207 | +0.22 |
| | $P_m+P_b$ | 191 | C11, 37.5° | 207 | +0.08 |
| | $P_m+P_b+Q$ | 379 | C13, 0° | 414 | +0.09 |
| Bottom Oblique Drop (N6) | $P_m$ | 118 | C11, 37.5° | 138 | +0.17 |
| | $P_l$ | 203 | C14, 0° | 207 | +0.02 |
| | $P_m+P_b$ | 190 | C11, 37.5° | 207 | +0.09 |
| | $P_m+P_b+Q$ | 320 | C13, 0° | 414 | +0.29 |
| Top Oblique Drop (N7) | $P_m$ | 112 | C11, 37.5° | 138 | +0.23 |
| | $P_l$ | 174 | C14, 0° | 207 | +0.19 |
| | $P_m+P_b$ | 173 | C11, 37.5° | 207 | +0.20 |
| | $P_m+P_b+Q$ | 260 | C13, 0° | 414 | +0.59 |

Notes:
1. Containment system and non-containment component stress locations are shown in Figure 2-1 and Figure 2-2, respectively. For cases N3 through N6, the circumferential location of the maximum stress intensity is shown, where 0° is at the side of impact.
2. Allowable stress intensities are based on an upper-bound design temperature of 74°C.
3. Design margin is calculated as (Allowable S.I./Maximum S.I) – 1.

**Table 2-35 – Cask Closure Bolt NCT Free Drop Stress Summary**

| NCT Free Drop | Max. Average Stress | | | Maximum Stress | | | Maximum Lid Separation (mm) |
|---|---|---|---|---|---|---|---|
| | Max. (MPa) | Limit (MPa) | D.M. | Max. (MPa) | Limit (MPa) | D.M. | |
| Top End Drop | 242 | 468 | +0.93 | 311 | 701 | +1.25 | 0.047 |
| Top Corner Drop | 207 | 468 | +1.26 | 226 | 701 | +2.10 | 0.017 |

**Table 2-36 – NCT Free Drop Buckling Evaluation Summary**

| NCT Free Drop Orientation (Case I.D.) | Inner Shell[1] | | | | Outer Shell[2] | | | |
|---|---|---|---|---|---|---|---|---|
| | Maximum S.I.[3] (kPa) | | | Maximum Buckling IR | Maximum S.I.[3] (kPa) | | | Maximum Buckling IR |
| | Axial | Hoop | Shear | | Axial | Hoop | Shear | |
| Bottom End (N1) | 0[4] | 0[4] | 0 | 0.00 | 35,670 | 59 | 0 | 0.41 |
| Top End (N2) | 2,431 | 8 | 0 | 0.03 | 7,782 | 35 | 0 | 0.09 |
| Bottom Corner (N3) | 4,846 | 985 | 7,596 | 0.08 | 25,229 | 13,309 | 7,293 | 0.31 |
| Top Corner (N4) | 4,803 | 543 | 4,037 | 0.06 | 9,230 | 12,616 | 4,306 | 0.16 |
| Side (N5) | 10,246 | 2,107 | 12,901 | 0.18 | 8,939 | 22,701 | 8,594 | 0.30 |
| Bottom Oblique (N6) | 11,063 | 1,187 | 7,846 | 0.15 | 25,384 | 34,418 | 14,436 | 0.49 |
| Top Oblique (N7) | 8,077 | 1,433 | 8,634 | 0.12 | 19,511 | 18,529 | 9,957 | 0.26 |

Notes:
1. Maximum stress intensities at section C5 in Figure 2-1 at all locations around the inner shell circumference.
2. Maximum stress intensities at section N5 in Figure 2-2 at all locations around the outer shell circumference.
3. The maximum compressive axial and hoop stress intensities and maximum in-plane shear stress intensities are reported.
4. Zero stress is assumed for the buckling evaluation since all stresses are tensile.

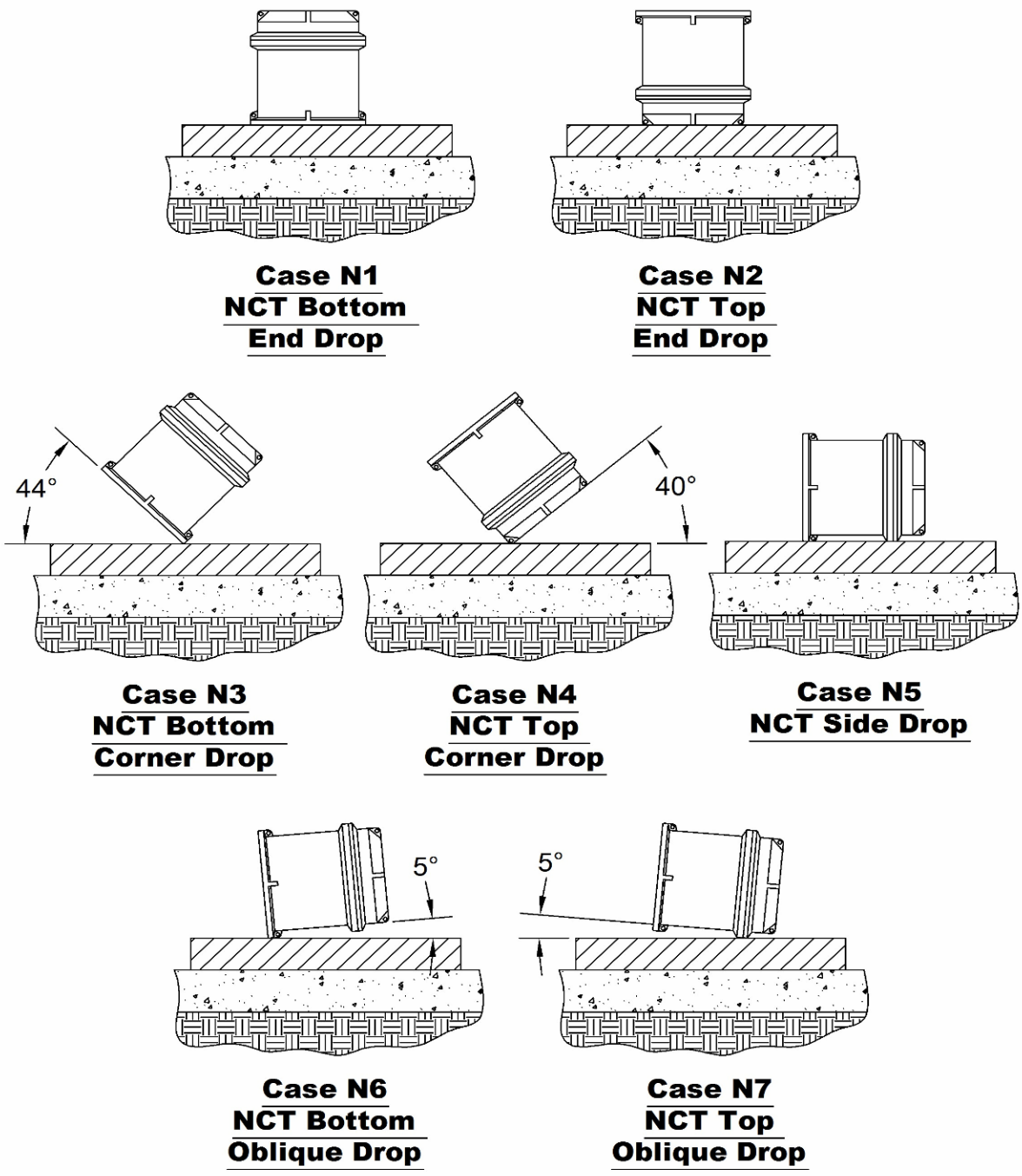


**Figure 2-16 – NCT Free Drop Impact Orientations**

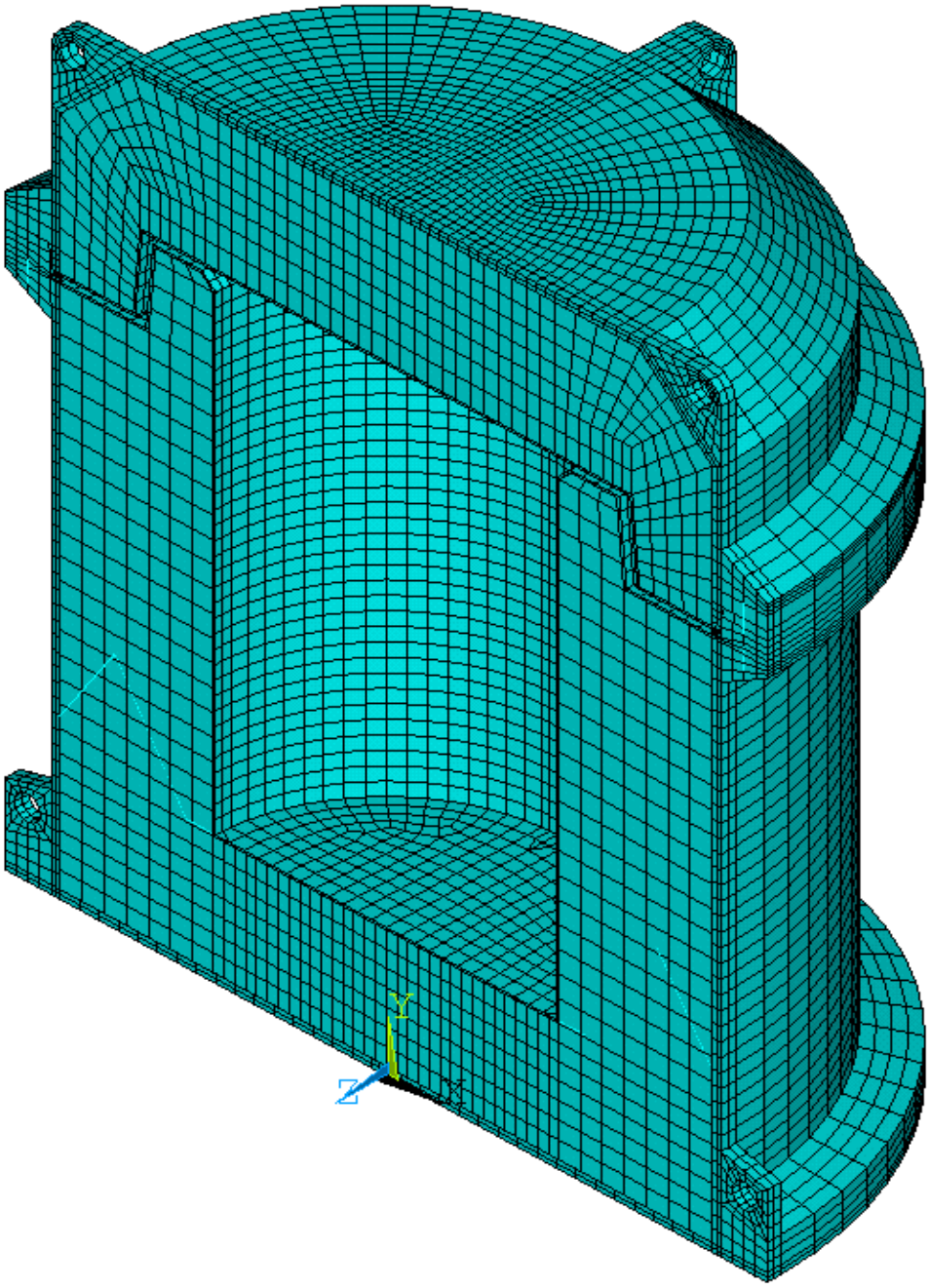


(Note: Cask/shield-lid rigid-body not shown)

**Figure 2-17 – MIDUS Overpack 3-D Half-Symmetry Finite Element Model**

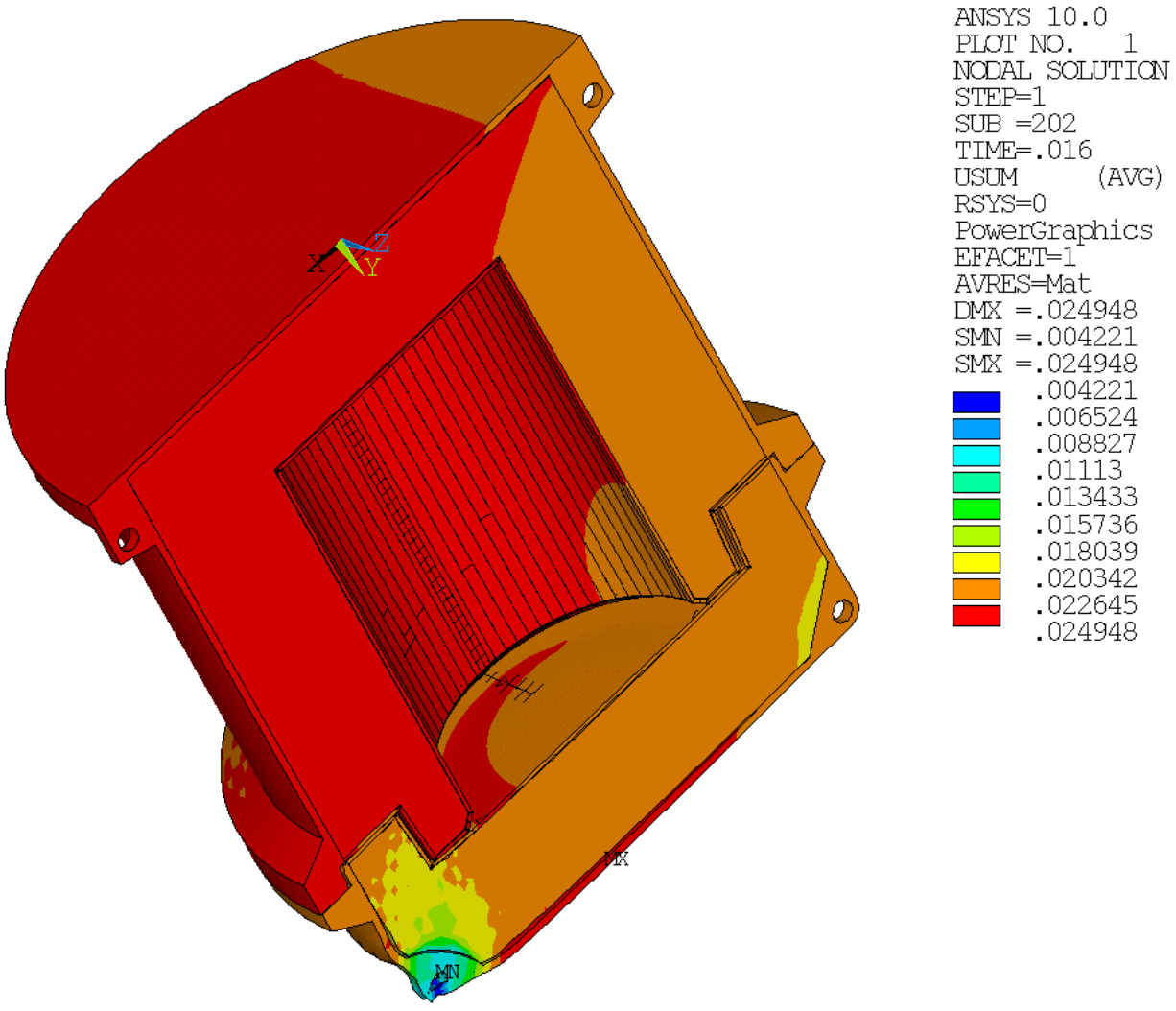


(Notes: Displacement units are meters. Deformed shape shown at 1:1 scale.)

**Figure 2-18 – Overpack Permanent Deformation, NCT Top Corner Drop (Case N4)**

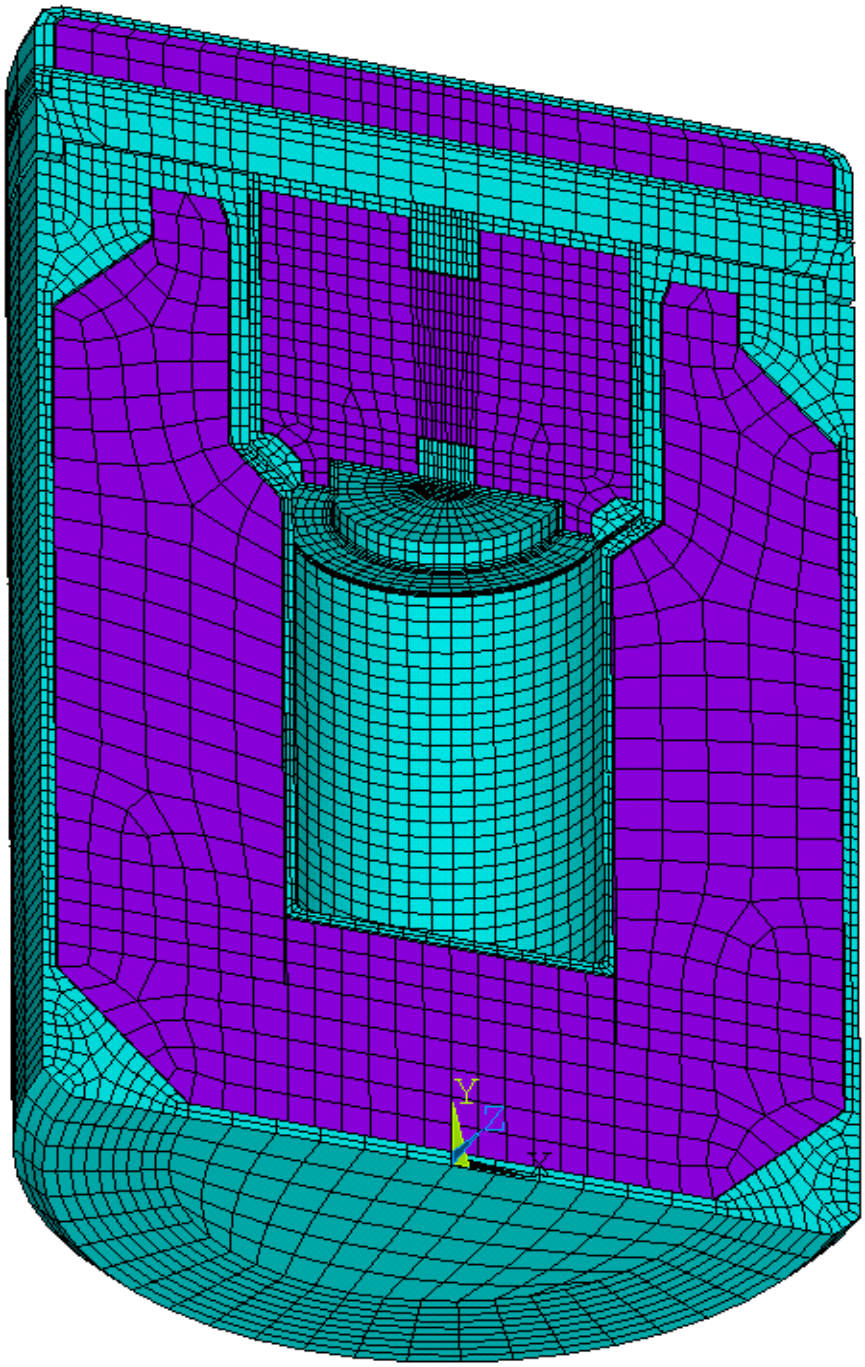


**Figure 2-19 – MIDUS Cask Assembly Half-Symmetry FE Model**

### 2.6.8 Corner Drop

In accordance with §71.71(c)(8), fiberboard, wood, or fissile material rectangular packages not exceeding 50 kg (110 lbs) and fiberboard, wood, or fissile material cylindrical packages not exceeding 100 kg (220 lbs) must be subjected to a free drop onto each corner of the package in succession, or in the case of a cylindrical package onto each quarter of each rim, from a height of 0.3 m (1 ft) onto a flat, essentially unyielding, horizontal surface. The package is not a fiberboard, wood, or fissile material package and it weighs more than 100 kg (220 lbs). Therefore, the corner drop test of §71.71(c)(8) is not applicable to the package.

### 2.6.9 Compression

In accordance with §71.71(c)(9), the package is subjected to a compressive load, applied uniformly to the top and bottom of the package in a position in which the package would normally be transported, for a period of 24 hours. The compressive load is equal to the greater of the equivalent of: (1) 5 times the weight of the package, and (2) 13 kPa multiplied by the vertically projected area of the package.

The package is evaluated for the NCT compression load using the ANSYS Mechanical quarter-symmetry finite element model of the overpack outer shell shown in Figure 2-20. The model includes only the external components of the overpack base and lid, conservatively neglecting structural support provided by the overpack foam cores and inner shells. The finite element model includes 8,763 nodes and 5,890 elements. The overpack shell components are modeled using 3-D structural solid elements. The overpack closure bolts are modeled using uniaxial tension-compression 3-D spar elements. The nonlinear contact interface between the overpack base and lid at the bolting flange is modeled using 3-D surface-to-surface contact.

The overpack base and lid shell components are modeled with a density of 8,030 kg/m$^3$, Poisson's ratio of 0.3, and a modulus of elasticity of 198E9 Pa for the overpack shell stainless steel materials at -29°C. The overpack closure bolts are modeled using the material properties of SA-320, Grade L43 bolting steel at -29°C.

Symmetry boundary conditions are applied to the symmetry planes of the model (i.e., UX=0 at X=0 and UZ=0 at Z=0). In addition, a single node located on the bottom centerline of the overpack base is restrained in the vertical direction (i.e., UY=0) for numerical stability.

The applied loading for the NCT compression analysis consists of a uniform pressure load on the top surface of the overpack lid and the bottom surface of the overpack base equivalent to five times the weight of the package.

The results of the NCT compression linear-elastic static analysis show that the maximum primary membrane plus bending stress intensity ($P_m+P_b$) and the maximum primary plus secondary ($P_m+P_b+Q$) stress intensity in the overpack outer shell are 85 MPa and 111 MPa, respectively. The allowable $P_m+P_b$ and $P_m+P_b+Q$ stress intensities for the overpack shell at a bounding design temperature of 74°C are 207 MPa and 414 MPa, respectively. Therefore, the

minimum design margin in the overpack shells due to the NCT compression loading (due to primary membrane plus bending stress intensity) is +1.44.

The results of the NCT compression analysis show that the package satisfies the applicable NCT allowable stress design criteria. Furthermore, the maximum stress intensity in the overpack shells due to the NCT compression loading is lower than the material yield strength. Therefore, NCT compression loading will not cause any permanent deformation to the package.

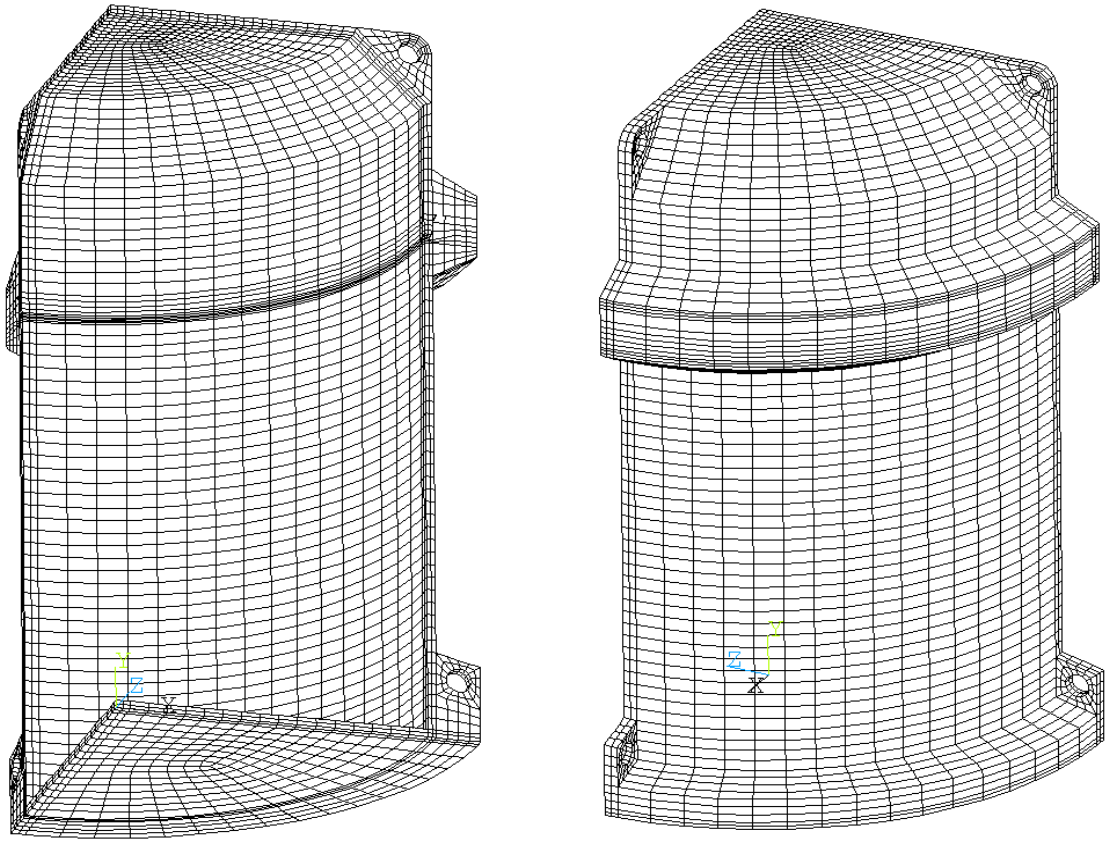

**Figure 2-20 – MIDUS Overpack Outer Shell Finite Element Model**

### 2.6.10 Penetration

In accordance with §71.71(c)(10), the package must be subjected to an impact of the hemispherical end of a vertical steel cylinder of 3.2 cm diameter and 6 kg mass. Per Regulatory Guide 7.8 [2.5], the penetration condition of §71.71(c)(10) is not structurally limiting for large packages without unprotected valves. Furthermore, the impact of the hemispherical end of a vertical steel cylinder of 3.2 cm diameter and 6 kg, dropped from a height of 1 meter will not penetrate 10 gage (3.4 mm thick) material. The outer shell of the overpack is 6.0 mm thick and has no valves. In addition, the package mass is over 50 times that of the steel penetration cylinder. Thus, the package need not be evaluated for NCT penetration.

## 2.7 Hypothetical Accident Conditions

The package meets the standards specified in §71.51 when subjected to the HAC tests specified in §71.73. In accordance with Regulatory Guide 7.6 [2.13], "design-by-analysis" is used for the structural evaluation of the package. The structural evaluation for HAC is based on sequential application of the HAC tests specified in §71.73 to determine the cumulative effect on the package, in accordance with §71.73(a). As discussed in Section 2.6, no significant package damage results from the NCT tests of §71.71. Thus, the evaluation of the package for the HAC test sequence is performed starting with an undamaged specimen. The package is evaluated for the most unfavorable initial conditions specified in §71.73(b). The HAC load combinations considered in the structural evaluation are developed in accordance with Regulatory Guide 7.8 [2.5] and summarized in Section 2.1.2.1.

The results of the structural evaluation show that the package satisfies the applicable allowable stress design criteria of the ASME Code when subjected to the HAC tests of §71.73. A summary of the cumulative package damage resulting from the HAC tests is provided in Section 2.7.8. The predicted package damage is considered in the package thermal, containment, and shielding HAC evaluations. The containment and shielding evaluations of the package show that the cumulative package damage resulting from the HAC test sequence results in no escape of other radioactive material exceeding a total amount of $A_2$ in one week and no external radiation dose rate exceeding 10 mSv/h at 1 m from the external surface of the package, in accordance with §71.51(a)(2).

### 2.7.1 Free Drop

In accordance with §71.73(c)(1), the package is subjected to a free drop through a distance of 9 m "*onto a flat, essentially unyielding, horizontal surface, striking in a position for which maximum damage is expected.*" The package is evaluated for a total of 26 different HAC free drop conditions, including thirteen different HAC free drop orientations. These HAC free drop conditions are summarized in Table 2-37 and shown in Figure 2-21. They include upper-bound and lower-bound analyses for a bottom end drop, a top end drop, a bottom corner drop, a top corner drop, a horizontal side drop, four different bottom-end oblique drop angles, and four different top-end oblique drop angles.

The dynamic response of the package to the HAC free drop test conditions is determined using explicit dynamic finite element analysis methods. The ANSYS LS-DYNA PC computer code, which is described in Section 2.12.2.2, is used for this analysis. In accordance with the requirements of Regulatory Guide 7.8 [2.5], the worst-case initial conditions are considered. For each HAC free drop impact orientation considered, upper-bound and lower-bound analyses are performed. The upper-bound analyses are performed using the overpack material upper-bound strength properties for the "cold" thermal condition temperature of -29°C with a lower-bound cask mass of 197 kg. The upper-bound analyses produces the maximum peak rigid-body cask accelerations that are used for the cask stress analysis. The lower-bound analyses are performed using the overpack material lower-bound strength properties for the "hot" thermal condition ambient temperature of 38°C, maximum decay heat, and insolation, combined with an

upper-bound cask mass of 207 kg. The lower-bound analyses, which produce the maximum overpack deformation and the lowest peak rigid-body cask acceleration, are evaluated to assure that the overpack will not "bottom-out," causing large impact loads to be imparted to the cask.

The explicit dynamic finite element analysis of the package is used to predict the rigid-body response of the cask to each HAC free drop test. In addition, this analysis demonstrates the structural adequacy of the overpack assembly for the HAC free drop tests. The maximum stresses in the overpack closure bolts are shown to satisfy the applicable allowable stress design criteria described in Section 2.1.2.2. Furthermore, the maximum crush depth of the overpack polyurethane foam due to each HAC free drop is shown to be less than the allowable crush depth. The drop loads analysis of the package for each HAC free drop impact orientation are discussed in the following sections.

Detailed stress analyses of the cask and shield lid for HAC free drop loading are performed using linear-elastic equivalent-static finite element analysis methods. The ANSYS Mechanical computer program, which is described in Section 2.12.2.1, is used for this analysis. Bounding equivalent-static acceleration design loads are applied to the cask finite element model for each HAC free drop orientation. The bounding equivalent-static acceleration design loads are determined by multiplying the cask peak rigid-body accelerations for each HAC free drop condition by a DLF to account for possible dynamic amplification within the cask.

In accordance with Regulatory Guide 7.8 [2.5], HAC free drop loads are evaluated in combination with internal pressure, thermal, and fabrication stresses. A bounding internal design pressure of 700 kPa gauge is conservatively used for the structural evaluation of the cask. NCT cold and NCT hot thermal loading are considered in combination with HAC free drop loading. Thermally induced stress intensities are classified as secondary in accordance with the ASME Code, since they are self-limiting, and do not require evaluation for HAC. Furthermore, the only significant stresses in the cask body due to NCT thermal loading result from differential thermal expansion of the closure bolts and closure lid. The stresses elsewhere in the cask are not significantly affected by NCT thermal loading, as shown by the results of the NCT end drop evaluation discussed in Section 2.6.7.2. Therefore, NCT thermal loading is not included in the HAC free drop load combinations. However, the effects of elevated temperature are considered for differential thermal expansion between the closure bolts and closure lid and for material properties and allowable stresses used for the HAC free drop evaluation. Furthermore, the only significant fabrication and assembly stresses in the cask are those resulting from closure bolt preload. Therefore, the following load combinations are considered for each HAC free drop load orientation evaluated:

(A) HAC Free Drop + Bolt Preload

(B) HAC Free Drop + Bolt Preload + Maximum Internal Pressure

The maximum stresses in the cask and shield lid due to each HAC free drop are calculated and shown to satisfy the applicable allowable stress design criteria of Subsection NF and Subsection WB of the ASME Code. In addition, the compressive stresses in the cask cylindrical shells due to each HAC free drop are evaluated in accordance with ASME Code Case N-284-1

and shown to satisfy the applicable buckling design criteria. The cask stress analysis and buckling analysis for each HAC impact orientation are discussed further in the following sections.

The results of the HAC free drop structural evaluation demonstrate that the cask satisfies the applicable HAC allowable stress design criteria. HAC free drop loading does not cause any significant permanent deformation of the cask, nor does it substantially reduce the effectiveness of the packaging. The evaluation shows that, under HAC free loading, the containment seal is maintained, and there is no loss or dispersal of radioactive contents. The damage to the overpack resulting from HAC free drop loading is considered in the HAC shielding evaluation, which demonstrates that the external dose rate limit requirement of §71.51(a)(1) is satisfied. Therefore, the package complies with the requirements of §71.51(a)(1) when subjected to the HAC free drop test of §71.73(c)(2).

**Table 2-37 – Summary of HAC Free Drop Cases Evaluated**

| Case I.D. | Case Description | Mass Properties[1] | Thermal Condition[2] | Material Properties[3] | Impact Angle[4] |
|---|---|---|---|---|---|
| H1 | Cold Bottom End Drop | Lower Bound | Cold | Upper Bound | 0° |
| H2 | Hot Bottom End Drop | Upper Bound | Hot | Lower Bound | 0° |
| H3 | Cold Top End Drop | Lower Bound | Cold | Upper Bound | 180° |
| H4 | Hot Top End Drop | Upper Bound | Hot | Lower Bound | 180° |
| H5 | Cold Bottom Corner Drop | Lower Bound | Cold | Upper Bound | 44° |
| H6 | Hot Bottom Corner Drop | Upper Bound | Hot | Lower Bound | 44° |
| H7 | Cold Top Corner Drop | Lower Bound | Cold | Upper Bound | 140° |
| H8 | Hot Top Corner Drop | Upper Bound | Hot | Lower Bound | 140° |
| H9 | Cold Side Drop | Lower Bound | Cold | Upper Bound | 90° |
| H10 | Hot Side Drop | Upper Bound | Hot | Lower Bound | 90° |
| H11 | Cold 5° Bottom Oblique Drop | Lower Bound | Cold | Upper Bound | 85° |
| H12 | Hot 5° Bottom Oblique Drop | Upper Bound | Hot | Lower Bound | 85° |
| H13 | Cold 10° Bottom Oblique Drop | Lower Bound | Cold | Upper Bound | 80° |
| H14 | Hot 10° Bottom Oblique Drop | Upper Bound | Hot | Lower Bound | 80° |
| H15 | Cold 15° Bottom Oblique Drop | Lower Bound | Cold | Upper Bound | 75° |
| H16 | Hot 15° Bottom Oblique Drop | Upper Bound | Hot | Lower Bound | 75° |
| H17 | Cold 20° Bottom Oblique Drop | Lower Bound | Cold | Upper Bound | 70° |
| H18 | Hot 20° Bottom Oblique Drop | Upper Bound | Hot | Lower Bound | 70° |
| H19 | Cold 5° Top Oblique Drop | Lower Bound | Cold | Upper Bound | 95° |
| H20 | Hot 5° Top Oblique Drop | Upper Bound | Hot | Lower Bound | 95° |
| H21 | Cold 10° Top Oblique Drop | Lower Bound | Cold | Upper Bound | 100° |
| H22 | Hot 10° Top Oblique Drop | Upper Bound | Hot | Lower Bound | 100° |
| H23 | Cold 15° Top Oblique Drop | Lower Bound | Cold | Upper Bound | 105° |
| H24 | Hot 15° Top Oblique Drop | Upper Bound | Hot | Lower Bound | 105° |
| H25 | Cold 20° Top Oblique Drop | Lower Bound | Cold | Upper Bound | 110° |
| H26 | Hot 20° Top Oblique Drop | Upper Bound | Hot | Lower Bound | 110° |

Notes:
1. Upper- and lower-bound mass properties are 2.5% higher and lower than the nominal values shown in Table 2-8.
2. A lower-bound uniform package temperature -29°C is assumed for the “cold” thermal condition. Upper-bound temperatures of 93°C for the overpack steel and 82°C for the overpack foam core are assumed for the “hot” thermal condition.
3. Upper- and lower-bound strength properties of the overpack materials are described in Section 2.2.1.
4. Impact angle is measured relative to the vertical upright package position (refer to Figure 2-21).

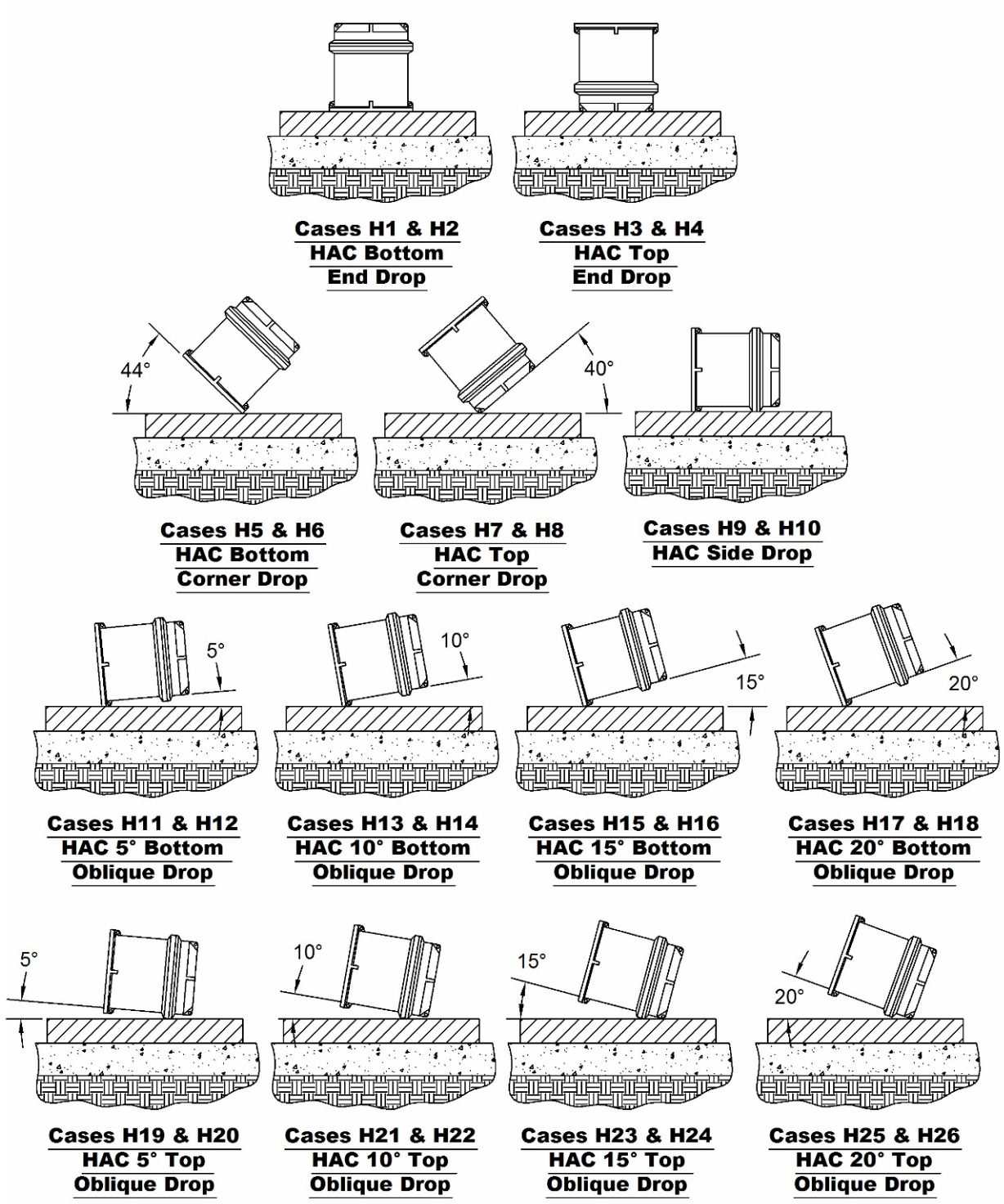


**Figure 2-21 – HAC Free Drop Impact Orientations**

#### 2.7.1.1 End Drop

The package is evaluated for a 9 m HAC end drop, occurring on either the top or bottom end of the package, considering the worst-case initial conditions in accordance with Regulatory Guide 7.8 [2.5]. The structural evaluation of the package for the HAC bottom end and top end drop tests is described in the following sections.

##### 2.7.1.1.1 Overpack Evaluation

The structural evaluation of the overpack for the HAC end drop orientations is performed using the ANSYS LS-DYNA PC finite element code and the 3-D half-symmetry finite element model described in Section 2.6.7.1. As discussed in Section 2.7.1, HAC drop analyses are performed for the bottom end impact and top end impact orientations for "cold" thermal conditions using the upper-bound strength properties of the overpack materials and the lower-bound mass of the cask to determine the maximum cask rigid-body accelerations for use in the cask stress analysis. In addition, analyses are performed for "hot" thermal conditions using the lower-bound strength properties of the overpack material and the upper-bound mass of the cask to determine the maximum possible crush of the overpack foam.

Each HAC end drop time-history analysis is started at the moment of initial contact between the package outer surface and the impact surface. An initial vertical velocity of 13.29 m/s, corresponding to a free-fall velocity from a height of 9 m, and a constant gravitational acceleration of 9.81 $m/s^2$ are applied to the package. Each HAC end drop time-history analysis is performed for a duration that is sufficient to capture the primary impact.

The maximum crush depth of the overpack foam, as a percentage of the total foam thickness, and the maximum peak rigid-body accelerations resulting from each HAC end drop test are summarized in Table 2-38. The highest peak rigid-body acceleration of the cask assembly due to the HAC bottom and top end drops are 424*g* and 419*g*, respectively. The results also show that the maximum foam crush due to all HAC end drop conditions is less than or equal to 70% of the foam thickness. This is within the acceptable crush range for the overpack foam material. Therefore, the overpack will not experience excessive deformation that would allow the cask to "bottom-out" under the most severe HAC end drop conditions. The overpack damage resulting from the HAC end drop test is described in Section 2.7.1.5.

The maximum shear stress and maximum axial strain in the overpack closure bolts resulting from each HAC end drop test are summarized in Table 2-39. The maximum shear stresses in the overpack closure bolts for each HAC end drop test are evaluated in accordance with the Service Level D allowable stress design criteria for Class 2 supports from Subsection NF of the ASME Code. As discussed in Section 2.1.2.2, the maximum axial strain in the overpack closure bolts under HAC loading is limited to 16% (i.e., the maximum specified elongation of the overpack closure bolt A320, Grade L43 bolting material) to assure that the overpack bolts do not experience any gross failure. The minimum design margin in the overpack closure bolts for the HAC end drop is +2.58 due to the maximum shear stress resulting from the cold bottom end

drop. Thus, the overpack closure bolts satisfy the applicable allowable stress design criteria for the HAC end drop.

#### 2.7.1.1.2 Cask Stress Evaluation

The stresses in the cask and shield lid resulting from the HAC bottom end drop and top end drop loads are determined using equivalent-static linear-elastic finite element analysis methods. The equivalent-static acceleration load for each HAC end drop orientation is equal to the peak rigid-body acceleration of the cask multiplied by a DLF that accounts for possible dynamic amplification within the cask. As shown in Table 2-38, the cask peak rigid-body acceleration loads due to the HAC cold end drop conditions are much higher than those due to the HAC hot end drop conditions. Thus, bounding equivalent-static acceleration loads are calculated based on the peak rigid-body accelerations resulting from the HAC cold bottom and top end drops, which are 424*g* and 419*g*, respectively. As discussed in Section 2.12.3, a bounding DLF of 1.1 is conservatively used for all HAC end drop evaluations. Thus, the equivalent-static acceleration loads for the HAC cold bottom end drop and HAC cold top end drop are 466*g* and 461*g*, respectively. A bounding equivalent-static acceleration load of 470*g* is conservatively used for the HAC bottom end drop and HAC top end drop stress evaluations.

The stresses in the cask and shield lid due to a 470*g* HAC bottom end drop and a 470*g* HAC top end drop load are determined using the axisymmetric finite element model described in Section 2.6.1.3. The finite element model boundary conditions used for the HAC end drop stress analyses are the same as those used for the NCT end drop stress analyses, as described in Section 2.6.7.2. Also, the 470*g* HAC end drop loading is applied to the finite element model in the same manner as the loads for the NCT end drop stress analysis, as described in Section 2.6.7.2. As discussed in Section 2.7.1, bolt preload and internal pressure loads are evaluated in combination with the HAC end drop loading per the following load combinations:

H1-A: HAC Bottom End Drop + Bolt Preload

H1-B: HAC Bottom End Drop + Bolt Preload + Maximum Internal Pressure

H3-A: HAC Top End Drop + Bolt Preload

H3-B: HAC Top End Drop + Bolt Preload + Maximum Internal Pressure

For all load combinations, the maximum bolt preload of 7.2 kN per bolt is applied to the closure bolt elements on a 360° basis, producing a total preload (for eight closure bolts) of 57.8 kN on the closure lid. For load combinations H1-B and H3-B, the maximum internal pressure load of 700 kPa gauge is applied to the inner surfaces of the cask containment boundary. On the impacted end of the cask cavity, this pressure load is added to the applied pressure that accounts for the payload inertial load due to the HAC end drop acceleration. In addition, a uniform temperature of 75°C is applied to the model for all HAC end drop analyses to account for the cask material properties at elevated temperature

The maximum stress intensities in the cask's containment system and non-containment components due to the HAC bottom end drop and HAC top end drop, along with the corresponding allowable stress intensities and minimum design margins, are summarized in Table 2-40 and Table 2-41, respectively. The minimum design margin for the HAC bottom end drop is +0.44 for primary membrane stress intensity ($P_m$) occurring at the outer diameter of the cask outer bottom plate (section N2 in Figure 2-2). The minimum design margin for the HAC top end drop is +0.57 for primary membrane plus bending stress intensity ($P_m+P_b$) in the shield plug bottom casing plate (section N7 in Figure 2-2). The results of the HAC end drop stress evaluation show that the stresses in the cask and shield lid satisfy the applicable HAC allowable stress design criteria of the ASME Code.

To prevent inelastic deformation of the cask's containment system closure, the maximum stresses in the cask flange and closure lid in the region of the containment O-ring seal are limited to the yield strength of the cask material. The maximum stress intensity in the cask's closure seal region due to the HAC top end drop loading is 116 MPa. This is less than the 184 MPa yield strength of the cask body stainless steel material at the upper-bound design temperature of 74°C. Therefore, the HAC top end drop will not cause any plastic deformation in the region of the containment O-ring seal.

As discussed in Section 2.1.2.5, the DU alloy material used for the cask gamma shield components is not expected to experience brittle fracture failure if it does not undergo substantial plastic deformation. Therefore, the maximum stresses in the cask gamma shield are limited to the yield strength of the DU alloy material. The maximum stress intensity in the cask body DU shields due to the HAC top end drop, which occurs at the top end of the radial DU shield, is 152 MPa. This stress is much less than the 380 MPa yield strength of DU at an upper-bound temperature of 93°C. Therefore, the HAC top end drop is not expected to cause any plastic deformation or brittle fracture failure of the cask body DU shields.

In addition to the stress analysis of the cask and shield lid described above, a detailed stress analysis of the cask closure bolts for HAC top end drop loading is performed using the 3-D quarter-symmetry finite element model described in Section 2.5.1.2. The applied HAC top end drop loads are based on the maximum calculated equivalent-static longitudinal acceleration of 461*g*. The inertia load from the closure lid self-weight due to the HAC top end drop acceleration is accounted for by applying the 461*g* equivalent-static acceleration load to the model. In addition, a uniform pressure load is applied to the underside of the closure lid to account for the loading from the combined mass of the shield plug and payload.

For modeling simplicity, a uniform pressure load is applied over the entire area inside the containment O-ring diameter. Although the O-ring diameter upon which the pressure load is calculated is approximately 18% larger than the outside diameter of the shield plug, this does not significantly affect the solution results. In fact, the assumption of a uniform pressure distribution is conservative; the load from the shield plug will concentrate at its outer edge because it is relatively stiff compared to the closure plate. Thus, the prying moment resulting from the assumed uniform pressure load distribution is conservative.

The HAC top end drop loading is applied in combination with NCT heat temperature loading, maximum internal pressure, and maximum bolt preload. The NCT heat temperature loading is applied to the finite element model as a uniform temperature load of 68.3°C. The maximum bolt preload of 7.2 kN is applied to each bolt and a uniform pressure load of 700 kPa is applied on the inner surface of the closure plate over the area inside the containment O-ring.

The maximum average stress (i.e., axial stress) in the closure bolts due to HAC top end drop loading is 322 MPa. The average axial stress for HAC is limited to the less of $3S_m$ or $0.7S_u$. The values of $S_m$ and $S_u$ for SA-320, Grade L43 bolting steel at 68.3°C are 234 MPa and 862 MPa, respectively, based on linear interpolation of the values shown in Table 2-15. Therefore, the allowable average stress for HAC is 603 MPa. The corresponding minimum design margin in the closure bolt for the HAC top end drop loading is +0.87.

The maximum lid separation at the inside edge of the bolting flange resulting from the HAC top end drop loading is approximately 0.093 mm, or 10.5% of the O-ring compression. However, separation of the closure lid is not expected to occur during the HAC top end drop because the reaction pressure on the top end of the cask, which is conservatively neglected in the closure bolt evaluation, would compress the seal. Nevertheless, the maximum calculated lid separation is considered in the evaluation of the cask containment seal.

For the cask closure to maintain containment under these conditions, the elastomeric O-ring must have sufficient elasticity to expand to fill the gap, considering potential material degradation due to environmental effects such as radiation and temperature. This is satisfied provided that the maximum compression set does not exceed 89.4% (i.e., (0.88-0.093)/0.88). As shown in Section 3.9.14 of the Parker O-Ring Handbook [2.18], the compression set in ethylene propylene O-rings after exposure to $10^7$ rads of gamma radiation at room temperature ranges from 28.6% to 46.6%, based on the compound. The data also shows that these materials will take on a compression set of less than 18% when exposed to a maximum temperature of 100°C for 70 hours ([2.18], Figure 2-13). This data shows that the maximum O-ring compression set due to the combined effects of temperature and radiation will be sufficient to maintain a tight seal for the HAC end drop loading.

#### 2.7.1.1.3 Cask Shell Buckling Evaluation

Buckling evaluations of the cask's containment shell and outer shell are performed for the HAC bottom end drop and HAC top end drop tests in accordance with the requirements of ASME Code Case N-284-1 [2.7]. The maximum compressive stresses and shear stresses near the mid-lengths of the cask's inner shell and outer shell (i.e., Sections C5 and N5 in Figure 2-1 and Figure 2-2) are used for the cask shell buckling evaluation. As discussed in Section 2.1.2.3, elastic and inelastic buckling interaction ratios are calculated based on the HAC allowable buckling stresses shown in Table 2-7, which include a factor of safety of 1.34. The maximum interaction ratios must not exceed 1.0.

The maximum calculated cask shell stresses and the resulting maximum buckling interaction ratios for the HAC bottom end drop and HAC top end drop are summarized in Table 2-42. The maximum buckling interaction ratio in the cask's inner shell is 0.03, resulting from the HAC top

end drop. The maximum buckling interaction ratio in the cask's outer shell is 0.43, resulting from the HAC bottom end drop. Therefore, the cask satisfies the buckling design criteria of ASME Code Case N-284-1 for the HAC end drop test.

**Table 2-38 – HAC End Drop Loads Summary**

| HAC Drop Case I.D. | Case Description[1] | Maximum Overpack Foam Crush[2] | Cask Peak Rigid-Body Accelerations[3] | |
|---|---|---|---|---|
| | | | Transverse | Longitudinal |
| H1 | Cold Bottom End Drop | 36% | [4] | 424g |
| H2 | Hot Bottom End Drop | 70% | [4] | 281g |
| H3 | Cold Top End Drop | 36% | [4] | 419g |
| H4 | Hot Top End Drop | 65% | [4] | 286g |

Notes:
1. Impact orientations are shown in Figure 2-16.
2. Value equal to the maximum deformation divided by the nominal foam thickness in the corresponding direction.
3. The highest peak accelerations on either the top or bottom centerline of the cask/shield lid rigid-body in the transverse (X) and longitudinal (Y) directions are reported.
4. The transverse acceleration of the cask due to HAC end drop impacts is insignificant.

**Table 2-39 – Overpack Closure Bolt HAC End Drop Stress Summary**

| HAC Drop Case I.D. | Case Description[1] | Maximum Shear Stress (MPa) | Maximum Axial Strain | Minimum Bolt Design Margin[2] |
|---|---|---|---|---|
| H1 | Cold Bottom End Drop | 101 | 0.5% | +2.58 |
| H2 | Hot Bottom End Drop | 94 | 0.5% | +2.85 |
| H3 | Cold Top End Drop | 24 | 0.3% | +14.1 |
| H4 | Hot Top End Drop | 11 | 0.2% | +31.9 |

Notes:
1. Impact orientations are shown in Figure 2-16.
2. The minimum design margin is calculated as (Allowable Value/Maximum Value) – 1, where the allowable shear stresses for A320, Grade L43 bolting steel at an upper-bound temperature of 93°C is 362 MPa, and the allowable axial strain is equal to the maximum elongation of A320, Grade L43 bolting steel (i.e., 16%).

**Table 2-40 – HAC Bottom End Drop Maximum Stress Summary**

| Cask Components | Stress Type | Maximum Stress Intensity (MPa) | Controlling Load Combination & Location[1] | Allowable Stress Intensity[2] (MPa) | Minimum Design Margin[3] |
|---|---|---|---|---|---|
| Containment System | $P_m$ | 191 | H1-B, C7 | 331 | +0.73 |
| | $P_m+P_b$ | 313 | H1-B, C7 | 492 | +0.57 |
| | $P_m+P_b+Q$ | 313 | H1-B, C7 | N/A[4] | N/A[4] |
| Non-Containment Components | $P_m$ | 153 | H1-B, N2 | 221 | +0.44 |
| | $P_m+P_b$ | 187 | H1-B, N13 | 332 | +0.78 |
| | $P_m+P_b+Q$ | 192 | H1-A, N13 | N/A[4] | N/A[4] |

Notes:
1. Load combinations H1-A and H1-B are defined in Section 2.7.1.1. Containment system and non-containment component stress locations are shown in Figure 2-1 and Figure 2-2, respectively.
2. Allowable stress intensities are based on an upper-bound design temperature of 74°C.
3. Design margin is calculated as (Allowable S.I./Maximum S.I) – 1.
4. Evaluation of secondary stress is not required for HAC.

**Table 2-41 – HAC Top End Drop Maximum Stress Summary**

| Cask Components | Stress Type | Maximum Stress Intensity (MPa) | Controlling Load Combination & Location[1] | Allowable Stress Intensity[2] (MPa) | Minimum Design Margin[3] |
|---|---|---|---|---|---|
| Containment System | $P_m$ | 55 | H3-B, C15 | 331 | +5.02 |
| | $P_m+P_b$ | 91 | H3-B, C15 | 492 | +4.41 |
| | $P_m+P_b+Q$ | 91 | H3-B, C15 | N/A[4] | N/A[4] |
| Non-Containment Components | $P_m$ | 88 | H3-B, N9 | 221 | +1.51 |
| | $P_m+P_b$ | 212 | H3-B, N7 | 332 | +0.57 |
| | $P_m+P_b+Q$ | 233 | H3-B, N8 | N/A[4] | N/A[4] |

Notes:
1. Load combinations H3-A and H3-B are defined in Section 2.7.1.1. Containment system and non-containment component stress locations are shown in Figure 2-1 and Figure 2-2, respectively.
2. Allowable stress intensities are based on an upper-bound design temperature of 74°C.
3. Design margin is calculated as (Allowable S.I./Maximum S.I) – 1.
4. Evaluation of secondary stress is not required for HAC.

**Table 2-42 – HAC End Drop Buckling Evaluation Summary**

| HAC End Drop Orientation | Inner Shell[1] | | | | Outer Shell[2] | | | |
|---|---|---|---|---|---|---|---|---|
| | Maximum S.I.[3] (kPa) | | | Maximum Buckling IR | Maximum S.I.[3] (kPa) | | | Maximum Buckling IR |
| | Axial | Hoop | Shear | | Axial | Hoop | Shear | |
| Bottom End (H1) | 0[4] | 0[4] | 0 | 0.00 | 54,680 | 5 | 0 | 0.43 |
| Top End (H3) | 3,940 | 15 | 0 | 0.03 | 12,610 | 3 | 0 | 0.10 |

Notes:
1. Maximum stress intensities at section C5 in Figure 2-1.
2. Maximum stress intensities at section N5 in Figure 2-2.
3. The maximum compressive axial and hoop stress intensities and maximum in-plane shear stress intensities from load combinations "-A" and "-B" are reported.
4. Zero stress is assumed for the buckling evaluation since all stresses are tensile.

### 2.7.1.2 Side Drop

The package is evaluated for a 9 m HAC side drop considering the worst-case initial conditions in accordance with Regulatory Guide 7.8 [2.5]. The structural evaluation of the package for the HAC side drop test is described in the following sections.

#### 2.7.1.2.1 Overpack Evaluation

The structural evaluation of the overpack for the HAC side drop orientation is performed using the ANSYS LS-DYNA PC finite element code and the 3-D half-symmetry finite element model described in Section 2.6.7.1. As discussed in Section 2.7.1, HAC side drop analyses are performed for "cold" thermal conditions using the upper-bound strength properties of the overpack materials and the lower-bound mass of the cask to determine the maximum cask rigid-body accelerations for use in the cask stress analysis. In addition, analyses are performed for "hot" thermal conditions using the lower-bound strength properties of the overpack material and the upper-bound mass of the cask to determine the maximum possible crush of the overpack foam.

Each HAC side drop time-history analysis is started at the moment of initial contact between the package's outer surface and the impact surface. An initial vertical velocity of 13.29 m/s, corresponding to a free-fall velocity from a height of 9 m, and a constant gravitational acceleration of 9.81 $m/s^2$ are applied to the package. Each HAC side drop time-history analysis is performed for a duration that is sufficient to capture the primary impact.

The maximum crush depth of the overpack foam (as a percentage of the total foam thickness) and the maximum peak rigid-body accelerations resulting from each HAC side drop test are summarized in Table 2-43. The highest peak rigid-body acceleration of the cask assembly due to the HAC side drop is 739*g*. The results also show that the maximum foam crush due to all HAC side drop conditions is 66%, which is less than the maximum acceptable crush of 70% for the overpack foam material. Therefore, the overpack will not experience excessive deformation that would allow the cask to "bottom-out" under the most severe HAC side drop condition. The extent of overpack damage resulting from the HAC side drop is discussed further in Section 2.7.1.5.

The maximum shear stress and maximum axial strain in the overpack closure bolts resulting from each HAC side drop test are summarized in Table 2-44. The maximum shear stresses in the overpack closure bolts for each HAC side drop test are evaluated in accordance with the Service Level D allowable stress design criteria for Class 2 supports from Subsection NF of the ASME Code. As discussed in Section 2.1.2.2, the maximum axial strain in the overpack closure bolts under HAC loading is limited 16% (i.e., the maximum specified elongation of the overpack closure bolt A320, Grade L43 bolting material) to assure that the overpack bolts do not experience any gross failure. The minimum design margin in the overpack closure bolts for the HAC side drop is +2.93 due to the maximum shear stress resulting from the HAC hot side drop (Case H10). Thus, the overpack closure bolts satisfy the applicable allowable-stress design criteria for the HAC side drop.

#### 2.7.1.2.2 Cask Stress Evaluation

The stresses in the cask and shield lid resulting from the HAC side drop loads are determined using equivalent-static linear-elastic finite element analysis methods. The equivalent-static acceleration load for the HAC side drop is equal to the peak rigid-body acceleration of the cask multiplied by a DLF that accounts for possible dynamic amplification within the cask. As shown in Table 2-43, the cask peak rigid-body acceleration loads due to the HAC cold side drop conditions are much higher than those due to the HAC hot side drop conditions. The peak transverse rigid-body acceleration due to the HAC cold side drop varies from 739*g* at the top end of the shield lid to 292*g* at the bottom end of the cask. As discussed in Section 2.12.3, a bounding DLF of 1.13 is conservatively used for the HAC side drop evaluation. The resulting equivalent-static transverse acceleration load for the HAC cold side drop is 835*g* at the top end of the shield lid and 330*g* at the bottom end of the cask. The HAC side drop analysis is performed using bounding equivalent-static acceleration loads of 850*g* at the top end of the shield lid and 350*g* at the bottom end of the cask. These loads are applied as an average transverse linear acceleration of 5,886 m/s$^2$ (600*g*) and a rotational acceleration load of 14,135 rads/s$^2$ about the mid-length of the cask (i.e., 173.5 mm from the bottom end of the cask).

The stresses in the cask and shield lid due to the HAC side drop loading are determined using the 3-D half-symmetry finite element model described in Section 2.6.7.2. The finite element model boundary conditions used for the HAC side drop stress analyses are the same as those used for the NCT side drop stress analyses, as described in Section 2.6.7.2. Also, the HAC side drop loading is applied to the finite element model in the same manner as the loads for the NCT side drop stress analysis, as described in Section 2.6.7.2. As discussed in Section 2.7.1, bolt preload and internal pressure loads are evaluated in combination with the HAC side drop loading per the following load combinations:

H9-A: HAC Side Drop + Bolt Preload

H9-B: HAC Side Drop + Bolt Preload + Maximum Internal Pressure

The maximum bolt preload of 7.2 kN is applied to each closure bolt element (3.6 N for the bolts on the half-symmetry plane). For load combinations H9-B, the maximum internal pressure load of 700 kPa gauge is applied to the inner surfaces of the cask's containment boundary. On the impacted side of the cask cavity, this pressure load is added to the applied pressure that accounts for the payload inertial load due to the HAC side drop acceleration. In addition, a uniform temperature of 75°C is applied to the model for both HAC side drop analyses to account for the cask's material properties at elevated temperature

The maximum stress intensities in the cask's containment system and non-containment components due to the HAC side drop, along with the corresponding allowable stress intensities and minimum design margins, are summarized in Table 2-45. The minimum design margin for the HAC side drop is +0.40 for primary membrane stress intensity ($P_m$) occurring in the shield plug bottom plate (section N11 in Figure 2-2). The results of the HAC side drop stress evaluation show that the stresses in the cask and shield lid satisfy the applicable HAC allowable-stress design criteria of the ASME Code.

#### 2.7.1.2.3 Cask Shell Buckling Evaluation

A buckling evaluation of the cask's containment shell and outer shell is performed for the HAC side drop test in accordance with the requirements of ASME Code Case N-284-1 [2.7]. The maximum compressive stresses and shear stresses near the mid-lengths of the cask's inner shell and outer shell (i.e., Sections C5 and N5 in Figure 2-1 and Figure 2-2) are used for the cask-shell buckling evaluation. As discussed in Section 2.1.2.3, elastic and inelastic buckling interaction ratios are calculated based on the HAC allowable buckling stresses shown in Table 2-7, which include a factor of safety of 1.34. The maximum interaction ratios must not exceed 1.0.

The maximum calculated cask-shell stresses and the resulting maximum buckling interaction ratios for the HAC side drop are summarized in Table 2-46. The maximum buckling interaction ratios in the cask's inner and outer shells, calculated using the bounding shell stresses from load combinations H9-A and H9-B, are 0.19 and 0.27, respectively. Therefore, the cask satisfies the buckling design criteria of ASME Code Case N-284-1 for the HAC side drop test.

**Table 2-43 – HAC Side Drop Loads Summary**

| HAC Drop Case I.D. | Case Description[1] | Maximum Overpack Foam Crush[2] | Cask Peak Rigid-Body Accelerations[3] | | |
|---|---|---|---|---|---|
| | | | Transverse | | |
| | | | Top End | Bottom End | Longitudinal |
| H9 | Cold Side Drop | 32% | -739*g* | -292*g*[4] | [5] |
| H10 | Hot Side Drop | 66% | -534*g* | -342*g* | [5] |

Notes:
1. Impact orientations are shown in Figure 2-16.
2. Value is equal to the maximum deformation divided by the nominal foam thickness in the corresponding direction.
3. The highest peak accelerations on either the top or bottom centerline of the cask/shield lid rigid-body in the transverse (X) and longitudinal (Y) directions are reported, unless otherwise noted.
4. Transverse acceleration on the cask bottom end at the time of the peak transverse acceleration at the cask top end.
5. The longitudinal acceleration of the cask due to HAC side drop impacts is insignificant.

**Table 2-44 – Overpack Closure Bolt HAC Side Drop Stress Summary**

| HAC Drop Case I.D. | Case Description[1] | Maximum Shear Stress (MPa) | Maximum Axial Strain | Minimum Bolt Design Margin[2] |
|---|---|---|---|---|
| H9 | Cold Side Drop | 84 | 1.4% | +3.31 |
| H10 | Hot Side Drop | 92 | 3.2% | +2.93 |

Notes:
1. Impact orientations are shown in Figure 2-16.
2. The minimum design margin is calculated as (Allowable Value/Maximum Value) – 1, where the allowable shear stresses for A320, Grade L43 bolting steel at an upper-bound temperature of 93°C is 362 MPa, and the allowable axial strain is equal to the maximum elongation of A320, Grade L43 bolting steel (i.e., 16%).

**Table 2-45 – HAC Side Drop Maximum Stress Summary**

| Cask Components | Stress Type | Maximum Stress Intensity (MPa) | Controlling Load Combination & Location[1] | Allowable Stress Intensity[2] (MPa) | Minimum Design Margin[3] |
|---|---|---|---|---|---|
| Containment System | $P_m$ | 189 | H9-A, C11, 37.5° | 331 | +0.75 |
| | $P_l$ | 261 | H9-B, C14, 0° | 492 | +0.89 |
| | $P_m+P_b$ | 287 | H9-A, C11, 37.5° | 492 | +0.71 |
| | $P_m+P_b+Q$ | 568 | H9-B, C13, 0° | N/A[4] | N/A[4] |
| Non-Containment Components | $P_m$ | 158 | H9-B, N11, 0° | 221 | +0.40 |
| | $P_l$ | 173 | H9-B, N3, 0° | 332 | +0.92 |
| | $P_m+P_b$ | 214 | H9-B, N18, 180° | 332 | +0.55 |
| | $P_m+P_b+Q$ | 228 | H9-A, N3, 0° | N/A[4] | N/A[4] |

Notes:
1. The load combination and the location of the maximum stress intensity (section number and circumferential location) is identified. Load combinations H9-A and H9-B are defined in Section 2.7.1.1. Containment system and non-containment component stress locations are shown in Figure 2-1 and Figure 2-2, respectively. The circumferential location is identified with 0° at the side of impact and 180° opposite the side of impact.
2. Allowable stress intensities are based on an upper-bound design temperature of 74°C.
3. Design margin is calculated as (Allowable S.I./Maximum S.I) – 1.
4. Evaluation of secondary stress is not required for HAC.

**Table 2-46 – HAC Side Drop Buckling Evaluation Summary**

| | Inner Shell[1] | | | | Outer Shell[2] | | | |
|---|---|---|---|---|---|---|---|---|
| | Maximum S.I.[3] (kPa) | | | Maximum Buckling IR | Maximum S.I.[3] (kPa) | | | Maximum Buckling IR |
| Load Case I.D. | Hoop | Axial | Shear | | Hoop | Axial | Shear | |
| H9-A | 3,039 | 17,349 | 18,624 | --- | 31,837 | 10,191 | 8,714 | --- |
| H9-B | [4] | 11,664 | 18,641 | --- | 31,771 | 9,053 | 9,165 | --- |
| Bounding Values | 3,039 | 17,349 | 18,641 | 0.19 | 31,837 | 10,191 | 9,165 | 0.27 |

Notes:
1. Maximum stress intensities at section C5 in Figure 2-1.
2. Maximum stress intensities at section N5 in Figure 2-2.
3. The maximum compressive axial and hoop stress intensities and maximum in-plane shear stress intensities from load combinations "-A" and "-B" are reported.
4. Zero stress is assumed for the buckling evaluation since all stresses are tensile.

### 2.7.1.3 Corner Drop

The package is evaluated for a 9 m HAC drop with the package center of gravity loaded directly over either the top or bottom corner of the package, considering the worst-case initial conditions in accordance with Regulatory Guide 7.8 [2.5]. The package orientations for the bottom corner drop and top corner drop, given as the angle of the package relative to the vertical upright orientation in which it is transported, are 44° and 140°, respectively. The structural evaluation of the package for the HAC bottom-corner drop and top-corner drop tests is described in the following sections.

#### 2.7.1.3.1 Overpack Evaluation

The structural evaluation of the overpack for the HAC bottom corner drop and top corner drop tests is performed using the ANSYS LS-DYNA PC finite element code and the 3-D half-symmetry finite element model described in Section 2.6.7.1. As discussed in Section 2.7.1, HAC drop analyses are performed for "cold" thermal conditions using the upper-bound strength properties of the overpack materials and the lower-bound mass of the cask to determine the maximum cask rigid-body accelerations for use in the cask stress analysis, and for "hot" thermal conditions using the lower-bound strength properties of the overpack material and the upper-bound mass of the cask to determine the maximum possible crush of the overpack foam.

Each HAC corner drop time-history analysis is started at the moment of initial contact between the package's outer surface and the impact surface. An initial vertical velocity of 13.29 m/s, corresponding to a free-fall velocity from a height of 9 m, and a constant gravitational acceleration of 9.81 $m/s^2$ are applied to the package. Each HAC corner drop time-history analysis is performed for a duration that is sufficient to capture the primary impact.

The maximum crush depth of the overpack foam (as a percentage of the total foam thickness) and the maximum peak rigid-body accelerations resulting from the HAC bottom-corner drop and top-corner drop tests are summarized in Table 2-47. The highest transverse and longitudinal peak rigid-body acceleration of the cask resulting from the HAC cold bottom-corner drop are 171*g* and 211*g*, respectively. The highest transverse and longitudinal peak rigid-body accelerations of the cask resulting from the HAC cold top-corner drop are 272*g* and 298*g*, respectively. The maximum foam crush due to the HAC hot bottom-corner drop and HAC hot top-corner drop, given as a percentage of the overall foam thickness, are 77% and 71%, respectively. In both cases, the maximum foam crush results from localized deformation of the overpack outer shell at the location of an overpack lug. Due to the localized nature of the deformation, the volume of foam that is crushed beyond 70% is small and does not account for a significant portion of the overall energy absorption. As discussed in Section 2.1.2.2, the maximum localized foam crush is limited to 80% of the foam thickness. Therefore, the overpack foam meets the maximum crush acceptance criteria and will not experience excessive deformation that would allow the cask to "bottom-out" under the HAC hot bottom-corner drop and HAC hot top-corner drop tests. The extent of overpack damage resulting from the HAC corner drop is discussed further in Section 2.7.1.5.

The maximum shear stress and maximum axial strain in the overpack closure bolts resulting from each HAC bottom-corner and top-corner drop tests are summarized in Table 2-48. The maximum shear stresses in the overpack closure bolts for each HAC corner drop test are evaluated in accordance with the Service Level D allowable-stress design criteria for Class 2 supports from Subsection NF of the ASME Code. As discussed in Section 2.1.2.2, the maximum axial strain in the overpack closure bolts under HAC loading is limited to 16% (i.e., the maximum specified elongation of the overpack closure bolt A320, Grade L43 bolting material) to assure that the overpack bolts do not experience any gross failure. The minimum design margin in the overpack closure bolts for the HAC corner drop is +1.81 due to the maximum axial strain resulting from the HAC hot top-corner drop (Case H8). Thus, the overpack closure bolts satisfy the applicable allowable-stress design criteria for the HAC bottom-corner and top-corner drop tests.

#### 2.7.1.3.2 Cask Stress Evaluation

As discussed in Section 2.7.1.4.2, the stress analysis of the cask and shield lid for the HAC oblique drops is performed using transverse and longitudinal equivalent-static-acceleration loads that bound the maximum equivalent-static accelerations for all HAC corner drop and HAC oblique drop tests. The results of that bounding evaluation show that the cask and shield lid satisfy the applicable HAC allowable-stress design criteria for all HAC corner drop and oblique drop tests.

A detailed stress analysis of the cask's closure bolts for HAC top-corner drop loading is performed using the 3-D quarter-symmetry finite element model described in Section 2.5.1.2. The applied HAC top-corner drop loads are based on the maximum calculated equivalent-static longitudinal acceleration of 328*g*. The inertia load from the closure lid self-weight due to the HAC top-corner drop acceleration is accounted for by applying the 328*g* equivalent-static acceleration load to the model. In addition, a uniform pressure load is applied to the underside of the closure lid to account for the loading from the combined mass of the shield plug and payload. For modeling simplicity, a uniform pressure load is applied over the entire area inside the containment O-ring diameter. Although the O-ring diameter upon which the pressure load is calculated is approximately 18% larger than the outside diameter of the shield plug, this does not significantly affect the solution results. The assumption of a uniform pressure distribution is conservative; the load from the shield plug will concentrate at its outer edge because it is relatively stiff compared to the closure plate. Thus, the prying moment resulting from the assumed uniform pressure load distribution is conservative.

The HAC top-corner loading is applied in combination with NCT heat-temperature loading, maximum internal pressure, and maximum bolt preload. The NCT heat-temperature loading is applied to the finite element model as a uniform temperature load of 68.3°C. The maximum bolt preload of 7.2 kN is applied to each bolt and a uniform pressure load of 700 kPa is applied on the inner surface of the closure plate over the area inside the containment O-ring.

The maximum average stress (i.e., axial stress) in the closure bolts due to the HAC top-corner drop loading is 270 MPa. The average axial stress for HAC is limited to the less of $3S_m$ or $0.7S_u$. The values of $S_m$ and $S_u$ for SA-320, Grade L43 bolting steel at 68.3°C are 234 MPa and

862 MPa, respectively, based on linear interpolation of the values shown in Table 2-15. Therefore, the allowable average stress for HAC is 603 MPa. The corresponding minimum design margin in the closure bolt for the HAC top-corner drop loading is +1.23.

The maximum lid separation at the inside edge of the bolting flange resulting from the HAC top-corner drop loading is approximately 0.004 mm, or 0.4% of the O-ring compression. This lid separation is much less than the maximum weld separation from the HAC end drop. As discussed in Section 2.7.1.1.2, the maximum compression set in the cask's containment O-ring seal due to the combined effects of radiation and temperature is sufficient to maintain a tight seal under the bounding HAC end drop test. Therefore, a tight containment seal will also be maintained under the most severe HAC top-corner drop test conditions.

**Table 2-47 – HAC Corner Drop Loads Summary**

| HAC Drop Case I.D. | Case Description(1) | Maximum Overpack Foam Crush(2) | Cask Peak Rigid-Body Accelerations(3) | |
|---|---|---|---|---|
| | | | Transverse | Longitudinal |
| H5 | Cold Bottom Corner Drop | 47% | 171g | 211g |
| H6 | Hot Bottom Corner Drop | 77% | 123g | 149g |
| H7 | Cold Top Corner Drop | 50% | 272g | 298g |
| H8 | Hot Top Corner Drop | 71% | 191g | 214g |

Notes:
1. Impact orientations are shown in Figure 2-16.
2. Value is equal to the maximum deformation divided by the nominal foam thickness in the corresponding direction.
3. The highest peak accelerations on either the top or bottom centerline of the cask/shield lid rigid-body in the transverse (X) and longitudinal (Y) directions are reported.

**Table 2-48 – Overpack Closure-Bolt HAC Corner Drop Stress Summary**

| HAC Drop Case I.D. | Case Description(1) | Maximum Shear Stress (MPa) | Maximum Axial Strain | Minimum Bolt Design Margin(2) |
|---|---|---|---|---|
| H5 | Cold Bottom Corner Drop | 78 | 0.4% | +3.64 |
| H6 | Hot Bottom Corner Drop | 56 | 0.3% | +5.46 |
| H7 | Cold Top Corner Drop | 105 | 3.9% | +2.45 |
| H8 | Hot Top Corner Drop | 108 | 5.7% | +1.81 |

Notes:
1. Impact orientations are shown in Figure 2-16.
2. The minimum design margin is calculated as (Allowable Value/Maximum Value) – 1, where the allowable shear stresses for A320, Grade L43 bolting steel at an upper-bound temperature of 93°C is 362 MPa, and the allowable axial strain is equal to the maximum elongation of A320, Grade L43 bolting steel (i.e., 16%).

### 2.7.1.4 Oblique Drops

The package is evaluated for HAC oblique drop loading resulting from bottom-end and top-end primary impact angles of 5°, 10°, 15°, and 20° from horizontal. The structural evaluation of the package for the HAC oblique drop considers the effects of both primary and secondary (slapdown) impact loadings. The structural evaluation of the package for the HAC oblique drop tests is presented in the following sections.

#### 2.7.1.4.1 Overpack Evaluation

The structural evaluation of the overpack for the HAC bottom-oblique drop and top-oblique drop tests is performed using the ANSYS LS-DYNA PC finite element code and the 3-D half-symmetry finite element model described in Section 2.6.7.1. As discussed in Section 2.7.1, HAC drop analyses are performed for "cold" thermal conditions using the upper-bound strength properties of the overpack materials and the lower-bound mass of the cask assembly to determine the maximum cask rigid-body accelerations for use in the cask stress analysis, and for "hot" thermal conditions using the lower-bound strength properties of the overpack material and the upper-bound mass of the cask to determine the maximum possible crush of the overpack foam.

Each HAC oblique drop time-history analysis is started at the moment of initial contact between the package's outer surface and the impact surface. An initial vertical velocity of 13.29 m/s, corresponding to a free-fall velocity from a height of 9 m, and a constant gravitational acceleration of 9.81 $m/s^2$ are applied to the package. Each HAC oblique drop time-history analysis is performed for a duration that is sufficient to capture both the primary and secondary impact.

The maximum crush depth of the overpack foam (as a percentage of the total foam thickness) and the maximum peak rigid-body accelerations resulting from each of the HAC bottom-end oblique drop and top-end oblique drop tests are summarized in Table 2-49 and Table 2-50, respectively. The maximum foam crush resulting from the full range of HAC bottom-end oblique drop tests analyzed is 61% from the HAC hot 5° bottom-end oblique drop (Case H12). The maximum foam crush resulting from the full range of HAC top-end oblique drop tests analyzed is 57% from the HAC hot 5° top-end oblique drop (Case H20). The maximum foam crush due to all HAC bottom- and top-end oblique drop tests is within the acceptable crush range for the overpack foam material. Therefore, the overpack will not experience excessive deformation that would allow the cask to "bottom-out" under the most severe HAC oblique drop conditions. The extent of permanent damage to the overpack assembly resulting from the HAC oblique drop tests is discussed in Section 2.7.1.5.

As shown in Table 2-49, the HAC bottom-end oblique drop primary impacts produce the highest transverse accelerations at the cask bottom end, while the secondary impacts produce the highest transverse accelerations at the cask top end. The magnitude of the peak transverse acceleration resulting from the secondary impact is higher than that due to the primary impact in all cases. The highest transverse peak rigid-body acceleration of the cask for all HAC bottom-end oblique drop tests is 985*g* for the HAC cold 15° bottom-end oblique drop (Case H15). The highest

longitudinal peak rigid-body acceleration of the cask for all HAC bottom-end oblique drop tests is +433*g* for the HAC cold 20° bottom-end oblique drop (Case H17). This maximum peak longitudinal acceleration also occurs during the slapdown impact.

As shown in Table 2-50, HAC top-end oblique drop primary impacts produce the highest transverse accelerations at the cask top end, while the secondary impacts produce the highest transverse accelerations at the cask bottom end. The magnitude of the peak transverse acceleration resulting from the primary impact is higher than that due to the secondary impact in all cases. The highest transverse peak rigid-body acceleration of the cask assembly for all HAC top-end oblique drop tests is -898*g* for the HAC cold 15° top-end oblique drop (Case H23). The highest longitudinal peak rigid-body acceleration of the cask for all HAC top-end oblique drop tests is -258*g* for the HAC cold 20° top-end oblique drop (Case H25) secondary impact.

The maximum shear stress and maximum axial strain in the overpack closure bolts resulting from each HAC bottom-corner and top-corner drop tests are summarized in Table 2-51. The maximum shear stresses in the overpack closure bolts for each HAC oblique drop test are evaluated in accordance with the Service Level D allowable-stress design criteria for Class 2 supports from Subsection NF of the ASME Code. As discussed in Section 2.1.2.2, the maximum axial strain in the overpack closure bolts under HAC loading is limited to 16% (i.e., the maximum specified elongation of the overpack closure bolt A320, Grade L43 bolting material) to assure that the overpack bolts do not experience any gross failure. The minimum design margin in the overpack closure bolts for the HAC oblique drop is +0.45 due to the maximum axial strain resulting from the HAC cold 20° top-oblique drop (Case H25). Thus, the overpack closure bolts satisfy the applicable structural design criteria for the HAC oblique drop tests.

#### 2.7.1.4.2 Cask Stress Evaluation

The stresses in the cask and shield lid resulting from the HAC bottom-oblique drop and HAC top-oblique drop loads are determined using equivalent-static linear-elastic finite element analysis methods. The equivalent-static acceleration load for each HAC oblique drop test is equal to the peak rigid-body acceleration of the cask multiplied by a DLF that accounts for possible dynamic amplification within the cask. As discussed in Section 2.12.3, a bounding DLF of 1.13 is conservatively used for all HAC oblique drop evaluations.

As shown in Table 2-49 and Table 2-50, the cask peak rigid-body acceleration loads due to the HAC cold oblique drop conditions are much higher than those due to the HAC hot oblique drop conditions. Thus, bounding equivalent-static-acceleration loads are calculated based on the peak rigid-body accelerations resulting from the HAC cold oblique drops.

As shown in Table 2-49, the HAC bottom oblique drop primary impacts produce the highest transverse rigid-body acceleration load at the bottom end of the cask, with a maximum value of -553*g* for the 20° drop orientation (case H17). The HAC bottom oblique drop secondary impacts produce the highest transverse rigid-body acceleration load at the top end of the cask, with a maximum value of -985*g* for the 15° drop orientation (case H15). Based upon the relative magnitudes of the primary and secondary impact acceleration loads, the cask stresses due to the HAC bottom oblique drop secondary impact are expected to bound those due to the primary

impact. A bounding HAC bottom oblique drop stress analysis is performed using transverse and longitudinal accelerations that envelope the secondary impact loads for all HAC bottom oblique drop orientations. These include a transverse acceleration load that varies linearly from -985*g* at the top end of the cask to -437*g* at the cask mid-length, and a longitudinal acceleration of +444*g*. Multiplying these values by the bounding DLF of 1.13 results in a transverse equivalent-static acceleration load that varies from -1,113*g* at the cask top end to -494*g* at the cask mid-length, and a longitudinal equivalent static acceleration load of +489*g*. The HAC bottom oblique drop stress analysis of the cask is performed using a bounding transverse acceleration load that varies linearly from -1,120*g* at the cask top end to -560*g* at the cask mid-length, and a longitudinal equivalent static acceleration load of +490*g*.

As shown in Table 2-50, the HAC top oblique drop primary impacts produce the highest transverse rigid-body acceleration load at the top end of the cask, with a maximum value of -898*g* for the 15° drop orientation (case H23). The HAC top oblique drop secondary impacts produce the highest transverse rigid-body acceleration load at the bottom end of the cask, with a maximum value of -592*g* for the 15° drop orientation (case H23). Based upon the relative magnitudes of the primary and secondary impact acceleration loads, the cask stresses due to the HAC top oblique drop primary impact are expected to bound those due to the secondary impact. A bounding HAC top oblique drop stress analysis is performed using transverse and longitudinal accelerations that envelope the secondary impact loads for all HAC top oblique drop orientations. These include a transverse acceleration load that varies linearly from -898*g* at the top end of the cask to -519*g* at the cask mid-length, and a longitudinal acceleration of -258*g*. Multiplying these values by the bounding DLF of 1.13 results in a transverse equivalent-static acceleration load that varies from -1,015*g* at the cask top end to -586*g* at the cask mid-length, and a longitudinal equivalent static acceleration load of -292*g*. The HAC top oblique drop stress analysis of the cask is performed using a bounding transverse acceleration load that varies linearly from -1,015*g* at the cask top end to -590*g* at the cask mid-length, and a longitudinal equivalent static acceleration load of -340*g*.

The stresses in the cask and shield lid due to the bounding HAC bottom oblique drop and top oblique drop loads are determined using the 3-D half-symmetry finite element model described in Section 2.6.7.2. The finite element model boundary conditions used for the HAC top and bottom oblique drop stress analyses are the same as those used for the NCT top and bottom corner drop stress analyses, as described in Section 2.6.7.2. Also, the loading due to the HAC top and bottom oblique drops is applied to the finite element model in the same manner as the loads for the NCT top and bottom oblique drop stress analysis, as described in Section 2.6.7.2. As discussed in Section 2.7.1, bolt preload and internal pressure loads are evaluated in combination with the HAC oblique drop loading per the following load combinations:

H11-18-A: HAC Bottom Oblique Drop + Bolt Preload

H11-18-B: HAC Bottom Oblique Drop + Bolt Preload + Maximum Internal Pressure

H19-26-A: HAC Top Oblique Drop + Bolt Preload

H19-26-B: HAC Top Oblique Drop + Bolt Preload + Maximum Internal Pressure

For all load combinations, the maximum bolt preload of 7.2 kN per bolt is applied to the closure bolt elements on a 360° basis, producing a total preload (for eight closure bolts) of 57.8 kN on the closure lid. For load combinations H11-18-B and H19-26-B, the maximum internal pressure load of 700 kPa gauge is applied to the inner surfaces of the cask's containment boundary. On the impacted end and side of the cask cavity, this pressure load is added to the applied pressures that account for the payload inertial loads due to the transverse and longitudinal accelerations. In addition, a uniform temperature of 75°C is applied to the model for all HAC oblique drop analyses to account for the cask's material properties at elevated temperature.

The maximum stress intensities in the cask's containment system and non-containment components from the bounding HAC bottom oblique drop and bounding HAC top oblique drop finite element analyses, along with the corresponding allowable stress intensities and minimum design margins, are summarized in Table 2-52 and Table 2-53, respectively. The minimum design margin for the bounding HAC bottom oblique drop is +0.20 for local membrane stress intensity ($P_l$) occurring in the cask containment shell (section C7 in Figure 2-1). The minimum design margin for the bounding HAC top oblique drop is +0.69 for primary membrane stress intensity ($P_m$) in the shield lid shear lip (section N19 in Figure 2-2). The results of the bounding HAC oblique drop stress evaluations show that the stresses in the cask and shield lid satisfy the applicable HAC allowable-stress design criteria of the ASME Code.

To prevent inelastic deformation of the cask's containment system closure, the maximum stresses in the cask flange and closure lid in the region of the containment O-ring seal are limited to the yield strength of the cask material. The maximum stress intensity in the cask's closure seal region due to the bounding HAC top oblique drop loading is 179 MPa. This is less than the 184 MPa yield strength of the cask-body stainless steel material at the upper-bound design temperature of 74°C. Therefore, the bounding HAC top oblique drop will not cause any plastic deformation in the region of the containment O-ring seal.

As discussed in Section 2.1.2.5, the DU alloy material used for the cask gamma shield components is not expected to experience brittle fracture failure if it does not undergo substantial plastic deformation. Therefore, the maximum stresses in the cask gamma shield are limited to the yield strength of the DU alloy material. The maximum stress intensity in the cask-body DU shields due to the bounding HAC top oblique drop, which is highly localized and occurs on the impacted side of the cask-body bottom DU shield, is 162 MPa. This stress is much less than the 380 MPa yield strength of DU at an upper-bound temperature of 93°C. Therefore, the bounding HAC top oblique drop is not expected to cause any plastic deformation or brittle fracture failure of the cask-body DU shields.

#### 2.7.1.4.3 Cask Shell Buckling Evaluation

A buckling evaluation of the cask's containment shell and outer shell is performed for the HAC oblique drop tests in accordance with the requirements of ASME Code Case N-284-1 [2.7]. The maximum compressive stresses and shear stresses near the mid-lengths of the cask's inner shell and outer shell (i.e., Sections C5 and N5 in Figure 2-1 and Figure 2-2) are used for the cask-shell buckling evaluation. As discussed in Section 2.1.2.3, elastic and inelastic buckling interaction

ratios are calculated based on the HAC allowable buckling stresses shown in Table 2-7, which include a factor of safety of 1.34. The maximum interaction ratios must not exceed 1.0.

The maximum calculated cask-shell stresses and the resulting maximum buckling interaction ratios for the HAC bottom oblique drop and HAC top oblique drop tests are summarized in Table 2-46. The maximum buckling interaction ratios in the cask's inner and outer shells, calculated using the bounding shell stresses for the HAC bottom oblique drop (cases H11-16-A and –B) and HAC top oblique drop (cases H17-22-A and -B), are 0.21 and 0.70, respectively. Therefore, the cask satisfies the buckling design criteria of ASME Code Case N-284-1 for the HAC oblique drop test.

**Table 2-49 – HAC Bottom Oblique Drop Loads Summary**

| HAC Drop Case I.D. | Case Description[1] | Maximum Overpack Foam Crush[2] | Cask Peak Rigid-Body Accelerations[3] | | |
|---|---|---|---|---|---|
| | | | Transverse | | |
| | | | Top | Bottom | Longitudinal |
| H11 | Cold 5° Bottom Oblique Drop<br>- Primary Impact<br>- Secondary Impact | 27% | +87g<br>-853g | -503g<br>-20g | +30g<br>+75g |
| H12 | Hot 5° Bottom Oblique Drop<br>- Primary Impact<br>- Secondary Impact<br>- Tertiary Impact | 61% | -39g<br>-438g<br>+51g | -215g<br>-101g<br>-260g | +8g<br>+18g<br>+19g |
| H13 | Cold 10° Bottom Oblique Drop<br>- Primary Impact<br>- Secondary Impact | 28% | +100g<br>-920g | -513g<br>+109g | +54g<br>+208g |
| H14 | Hot 10° Bottom Oblique Drop<br>- Primary Impact<br>- Secondary Impact | 44% | +31g<br>-595g | -272g<br>+26g | +38g<br>+104g |
| H15 | Cold 15° Bottom Oblique Drop<br>- Primary Impact<br>- Secondary Impact | 26% | +118g<br>-985g | -543g<br>+262g | +87g<br>+361g |
| H16 | Hot 15° Bottom Oblique Drop<br>- Primary Impact<br>- Secondary Impact | 43% | +98g<br>-599g | -277g<br>+73g | +56g<br>+178g |
| H17 | Cold 20° Bottom Oblique Drop<br>- Primary Impact<br>- Secondary Impact | 33% | +106g<br>-898g | -553g<br>+89g | +118g<br>+433g |
| H18 | Hot 20° Bottom Oblique Drop<br>- Primary Impact<br>- Secondary Impact | 36% | +48g<br>-515g | -184g<br>+27g | +32g<br>+169g |

Notes:
1. Impact orientations are shown in Figure 2-16.
2. Value is equal to the maximum deformation divided by the nominal foam thickness in the corresponding direction.
3. Accelerations reported at the time that the peak transverse rigid-body acceleration is reached.

**Table 2-50 – HAC Top Oblique Drop Loads Summary**

| HAC Drop Case I.D. | Case Description[1] | Maximum Overpack Foam Crush[2] | Cask Peak Rigid-Body Accelerations[3] | | |
|---|---|---|---|---|---|
| | | | Transverse | | |
| | | | Top | Bottom | Longitudinal |
| H19 | Cold 5° Top Oblique Drop<br>- Primary Impact<br>- Secondary Impact | 26% | -801g<br>+174g | -106g<br>-536g | -45g<br>-107g |
| H20 | Hot 5° Top Oblique Drop<br>- Primary Impact<br>- Secondary Impact | 57% | -495g<br>+45g | -22g<br>-311g | -40g<br>-49g |
| H21 | Cold 10° Top Oblique Drop<br>- Primary Impact<br>- Secondary Impact | 24% | -853g<br>90g | -113g<br>-463g | -103g<br>-86g |
| H22 | Hot 10° Top Oblique Drop<br>- Primary Impact<br>- Secondary Impact | 45% | -513g<br>+50g | -17g<br>-261g | -45g<br>-68g |
| H23 | Cold 15° Top Oblique Drop<br>- Primary Impact<br>- Secondary Impact | 21% | -898g<br>+209g | -114g<br>-592g | -126g<br>+124g |
| H24 | Hot 15° Top Oblique Drop<br>- Primary Impact<br>- Secondary Impact | 38% | -500g<br>+49g | -27g<br>-221g | -79g<br>-73g |
| H25 | Cold 20° Top Oblique Drop<br>- Primary Impact<br>- Secondary Impact | 23% | -889g<br>+126g | -148g<br>-493g | -157g<br>-258g |
| H26 | Hot 20° Top Oblique Drop<br>- Primary Impact<br>- Secondary Impact | 37% | -477g<br>+62g | -27g<br>-247g | -85g<br>+74g |

Notes:
1. Impact orientations are shown in Figure 2-16.
2. Value is equal to the maximum deformation divided by the nominal foam thickness in the corresponding direction.
3. Accelerations reported at the time that the peak transverse rigid-body acceleration is reached.

**Table 2-51 – Overpack Closure-Bolt HAC Oblique Drop Stress Summary**

| HAC Drop Case I.D. | Case Description[1] | Maximum Shear Stress (MPa) | Maximum Axial Strain | Minimum Bolt Design Margin[2] |
|---|---|---|---|---|
| H11 | Cold 5° Bottom Oblique Drop | 107 | 1.5% | +2.38 |
| H12 | Hot 5° Bottom Oblique Drop | 97 | 0.6% | +2.73 |
| H13 | Cold 10° Bottom Oblique Drop | 113 | 1.2% | +2.20 |
| H14 | Hot 10° Bottom Oblique Drop | 101 | 3.0% | +2.58 |
| H15 | Cold 15° Bottom Oblique Drop | 116 | 6.2% | +1.58 |
| H16 | Hot 15° Bottom Oblique Drop | 104 | 2.4% | +2.48 |
| H17 | Cold 20° Bottom Oblique Drop | 169 | 4.9% | +1.14 |
| H18 | Hot 20° Bottom Oblique Drop | 95 | 1.9% | +2.81 |
| H19 | Cold 5° Top Oblique Drop | 87 | 1.0% | +3.16 |
| H20 | Hot 5° Top Oblique Drop | 74 | 0.7% | +3.89 |
| H21 | Cold 10° Top Oblique Drop | 107 | 2.8% | +2.38 |
| H22 | Hot 10° Top Oblique Drop | 97 | 0.8% | +2.73 |
| H23 | Cold 15° Top Oblique Drop | 120 | 7.4% | +1.16 |
| H24 | Hot 15° Top Oblique Drop | 93 | 1.8% | +2.89 |
| H25 | Cold 20° Top Oblique Drop | 132 | 11.0% | +0.45 |
| H26 | Hot 20° Top Oblique Drop | 107 | 4.0% | +2.38 |

Notes:
1. Impact orientations are shown in Figure 2-16.
2. The minimum design margin is calculated as (Allowable Value/Maximum Value) – 1, where the allowable shear stresses for A320, Grade L43 bolting steel at an upper-bound temperature of 93°C is 362 MPa, and the allowable axial strain is equal to the maximum elongation of A320, Grade L43 bolting steel (i.e., 16%).

**Table 2-52 – HAC Bottom Oblique Drop Maximum Stress Summary**

| Cask Components | Stress Type | Maximum Stress Intensity (MPa) | Controlling Load Combination & Location[1] | Allowable Stress Intensity[2] (MPa) | Minimum Design Margin[3] |
|---|---|---|---|---|---|
| Containment System | $P_m$ | 227 | H11-16-B, C8, 30° | 331 | +0.46 |
| | $P_l$ | 409 | H11-16-B, C7, 67.5° | 492 | +0.20 |
| | $P_m+P_b$ | 320 | H11-16-A, C11, 37.5° | 492 | +0.54 |
| | $P_m+P_b+Q$ | 624 | H11-16-B, C7, 67.5° | N/A[4] | N/A[4] |
| Non-Containment Components | $P_m$ | 159 | H11-16-A, N13, 60° | 221 | +0.39 |
| | $P_l$ | 247 | H11-16-A, N2, 37.5° | 332 | +0.34 |
| | $P_m+P_b$ | 209 | H11-16-A, N19, 22.5° | 332 | +0.59 |
| | $P_m+P_b+Q$ | 334 | H11-16-B, N12, 37.5° | N/A[4] | N/A[4] |

Notes:
1. The load combination and the location of the maximum stress intensity (section number and circumferential location) is identified. Load combinations H11-16-A and H11-16-B are defined in Section 2.7.1.4.2. Containment system and non-containment component stress locations are shown in Figure 2-1 and Figure 2-2, respectively. The circumferential location is identified with 0° at the side of impact and 180° opposite the side of impact.
2. Allowable stress intensities are based on an upper-bound design temperature of 74°C.
3. Design margin is calculated as (Allowable S.I./Maximum S.I) – 1.
4. Evaluation of secondary stress is not required for HAC.

**Table 2-53 – HAC Top Oblique Drop Maximum Stress Summary**

| Cask Components | Stress Type | Maximum Stress Intensity (MPa) | Controlling Load Combination & Location[1] | Allowable Stress Intensity[2] (MPa) | Minimum Design Margin[3] |
|---|---|---|---|---|---|
| Containment System | $P_m$ | 145 | H19-26-A, C11, 30° | 331 | +1.28 |
| | $P_l$ | 287 | H19-26-A, C14, 0° | 492 | +0.71 |
| | $P_m+P_b$ | 213 | H19-26-A, C11, 37.5° | 492 | +1.31 |
| | $P_m+P_b+Q$ | 402 | H19-26-B, C17, 0° | N/A[4] | N/A[4] |
| Non-Containment Components | $P_m$ | 131 | H19-26-A, N19, 22.5° | 221 | +0.69 |
| | $P_l$ | 151 | H19-26-A, N3, 0° | 332 | +1.20 |
| | $P_m+P_b$ | 192 | H19-26-A, N19, 22.5° | 332 | +0.73 |
| | $P_m+P_b+Q$ | 221 | H19-26-A, N3, 0° | N/A[4] | N/A[4] |

Notes:
1. The load combination and the location of the maximum stress intensity (section number and circumferential location) is identified. Load combinations H17-22-A and H17-22-B are defined in Section 2.7.1.4.2. Containment system and non-containment component stress locations are shown in Figure 2-1 and Figure 2-2, respectively. The circumferential location is identified with 0° at the side of impact and 180° opposite the side of impact.
2. Allowable stress intensities are based on an upper-bound design temperature of 74°C.
3. Design margin is calculated as (Allowable S.I./Maximum S.I) – 1.
4. Evaluation of secondary stress is not required for HAC.

**Table 2-54 – HAC Oblique Drop Buckling Evaluation Summary**

| Load Case I.D. | Inner Shell[1] | | | | Outer Shell[2] | | | |
|---|---|---|---|---|---|---|---|---|
| | Maximum S.I.[3] (kPa) | | | Maximum Buckling IR | Maximum S.I.[3] (kPa) | | | Maximum Buckling IR |
| | Hoop | Axial | Shear | | Hoop | Axial | Shear | |
| H11-18-A | 2,503 | 19,465 | 15,170 | --- | 34,744 | 80,332 | 20,216 | --- |
| H11-18-B | [4] | 21,578 | 15,214 | --- | 36,237 | 76,112 | 20,965 | --- |
| Bounding Values | 2,503 | 21,578 | 15,214 | 0.21 | 36,237 | 80,332 | 20,965 | 0.70 |
| H19-26-A | 1,924 | 16,108 | 14,447 | --- | 27,778 | 31,634 | 17,378 | --- |
| H19-26-B | [4] | 10,729 | 5,861 | --- | 28,131 | 34,082 | 17,370 | --- |
| Bounding Values | 1,924 | 16,108 | 14,447 | 0.16 | 28,131 | 34,082 | 17,378 | 0.32 |

Notes:
1. Maximum stress intensities at section C5 in Figure 2-1.
2. Maximum stress intensities at section N5 in Figure 2-2.
3. The maximum compressive axial and hoop stress intensities and maximum in-plane shear stress intensities from load combinations "-A" and "-B" are reported.
4. Zero stress is assumed for the buckling evaluation since all stresses are tensile.

### 2.7.1.5 Summary of Results

The structural evaluation of the package for the HAC free drop test of §71.73(c)(1) shows that the applicable structural design criteria is satisfied for all cases analyzed. The HAC free drop does not cause any significant permanent deformation in the cask and shield lid. Furthermore, no inelastic deformation of the cask's closure bolts and containment sealing surfaces results from the HAC free drop tests analyzed. The only significant package damage resulting from the HAC free drop occurs in the overpack. The overpack damage resulting from each HAC free drop position is described as follows:

*HAC End Drop*

The permanently deformed shape of the overpack following the HAC hot bottom-end drop (Case H2) and HAC hot top-end drop (Case H4) is shown in Figure 2-22 and Figure 2-23, respectively. The HAC hot bottom-end drop results in a permanent deformation of the overpack base inner shell and foam toward the bottom end of approximately 45 mm, but no significant permanent deformation in the overpack lid. As shown in Figure 2-22, this results in the formation of a conical-shaped gap at the top of the overpack base leading into the overpack cavity. As shown in Figure 2-23, the HAC hot top-end drop results in a permanent deformation of the overpack lid inner shell and foam of approximately 56 mm over the entire cask diameter, but only minor permanent deformation in the overpack-base inner shell. This deformation creates additional air space at the interface between the overpack base and lid. The overpack deformation resulting from the HAC bottom-end drop and HAC top-end drop is considered in the package HAC thermal evaluation.

*HAC Side Drop*

The HAC hot side drop (case H10) results in the maximum damage to the overpack. The permanently deformed shape of the overpack following the HAC hot side drop is shown in Figure 2-24. It shows that the overpack-base side-wall foam crush on the impacted side ranges from approximately 35 mm at the top end of the overpack cavity to approximately 58 mm at the bottom end of the overpack cavity. Because the overpack crush is primarily inside-out, a gap forms between the overpack-base foam core and overpack-base inner shell the at the bottom end of the overpack cavity on the side opposite impact. The only significant damage to the overpack exterior surfaces occurs near the impacted portions of the overpack tie-down flange and bolting flange. As shown in Figure 2-24, a slight indentation of the flanges occurs on the side of impact. The overpack deformation resulting from the HAC side drop is considered in the package HAC thermal evaluation.

*HAC Corner Drop*

The permanently deformed shape of the overpack following the HAC hot bottom-corner drop (Case H6) is shown in Figure 2-25. The overpack base tie-down flange is permanently bent upward and the tie-down flange lug is permanently pushed into the overpack-base outer shell. The foam sidewall thickness in the region directly behind the overpack base lug is reduced from

104.5 mm to approximately 30 mm. The HAC hot bottom-corner drop also results in a permanent longitudinal shift of the overpack-base inner shell of approximately 15 mm toward the bottom end of the package. In addition, a gap of approximately the same size is formed around the entire circumference of the overpack-cavity top end due to this longitudinal shift. As shown in Figure 2-25, small gaps are also developed between the overpack foam core and the inner and outer shells at the bottom end of the package due to elastic spring-back effects in the overpack shells.

The permanently deformed shape of the overpack following the HAC hot top-corner drop (Case H8) is shown in Figure 2-26. The most significant damage to the package resulting from the HAC hot top-corner drop occurs in the local vicinity of the impacted overpack lid lug, which is permanently crushed into the overpack lid foam core. As discussed above, the region of maximum crush in the overpack lid foam core due to the HAC hot top-corner drop impact is very localized. The HAC hot top-corner drop impact also results in a permanent depression of the overpack lid inner shell of approximately 45 mm toward the top end of the package. In addition, the outermost portion of the lid lug (i.e., the material outside the lug hole) is shown to reach the ultimate strain, causing local failure.

*HAC Oblique Drop*

As discussed in Section 2.7.1.4.1, the maximum foam crush depths for the HAC oblique drop result from the HAC hot 5° bottom-end oblique drop (Case H12) and the HAC hot 5° top-end oblique drop (Case H20). These two cases also cause the greatest extent of permanent damage to the overpack for all HAC oblique drops evaluated.

The permanently deformed shape of the overpack resulting from the HAC hot 5° bottom-end oblique drop (Case H12) is shown in Figure 2-27. The HAC hot 5° bottom-end oblique drop causes damage to both the internal and external surfaces of the overpack on the impacted side of the package, with the maximum damage occurring at the bottom end of the overpack cavity. The most significant damage to the overpack due the HAC hot 5° bottom-end oblique drop results from inside-out crush. This is most evident at the bottom end of the overpack cavity where the sidewall foam crush is highest. The permanent crush of the overpack sidewall foam is approximately 40 mm at the top end of the overpack cavity and 60 mm at the bottom end of the overpack cavity. As shown in Figure 2-27, a large air gap is also developed between the overpack foam core and inner shell on the side opposite impact at the bottom end of the overpack cavity.

The permanently deformed shape of the overpack resulting from the HAC hot 5° top-end oblique drop (Case H20) is shown in Figure 2-28. The HAC hot 5° top-end oblique drop causes damage to both the internal and external surfaces of the overpack on the impacted side of the package, with the maximum damage occurring at the top end of the overpack cavity. The most significant damage to the overpack due the HAC hot 5° top-end oblique drop results from inside-out crush at the top end of the overpack cavity on the side of impact. The permanent crush of the overpack sidewall foam resulting from the HAC hot 5° top-end oblique drop (Case H20) is less than 44 mm over the entire length of the overpack cavity.

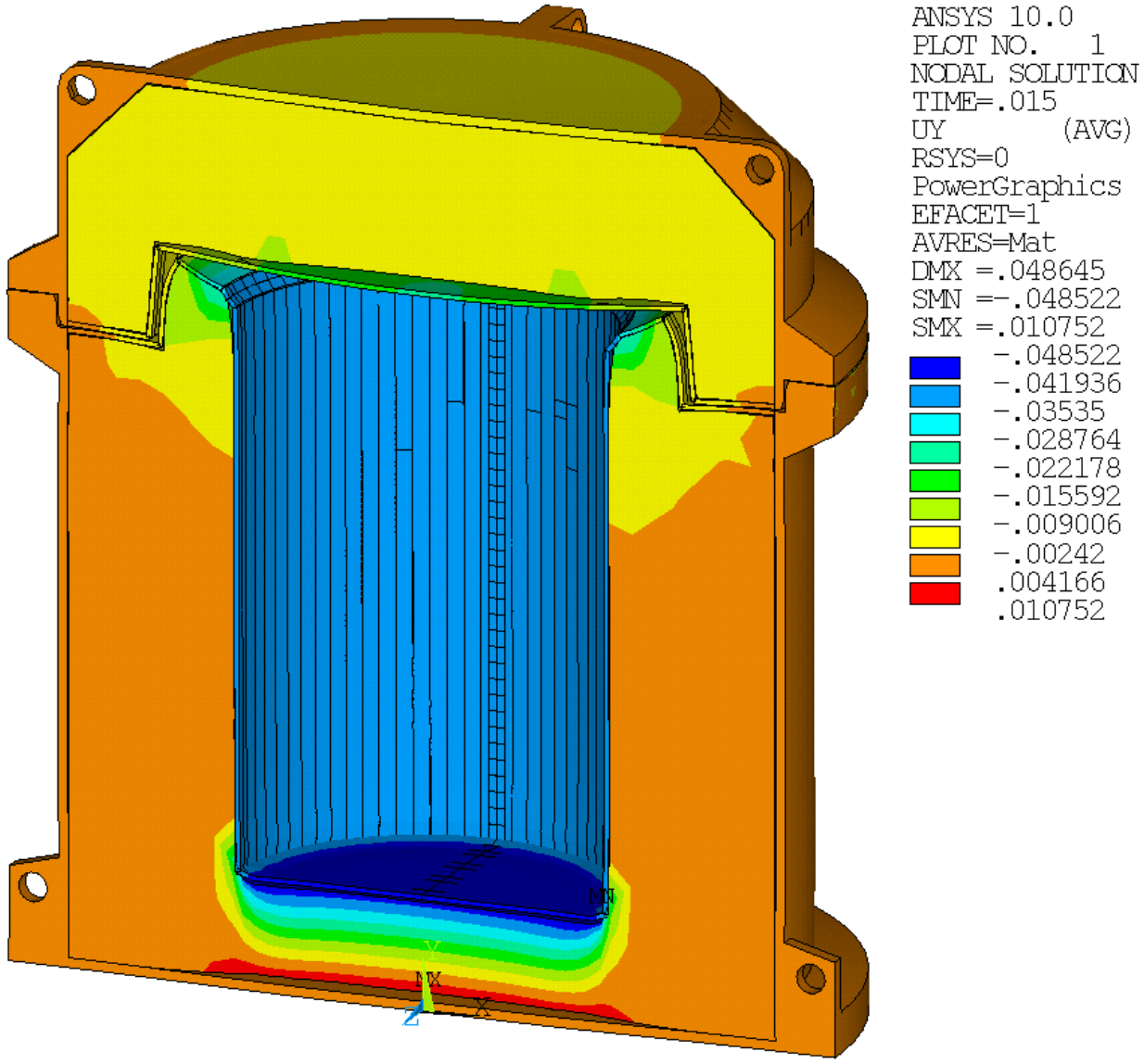


(Notes: Displacement units are meters. Deformed shape shown at 1:1 scale)

**Figure 2-22 – Overpack Permanent Deformation, HAC Hot Bottom-End Drop (Case H2)**

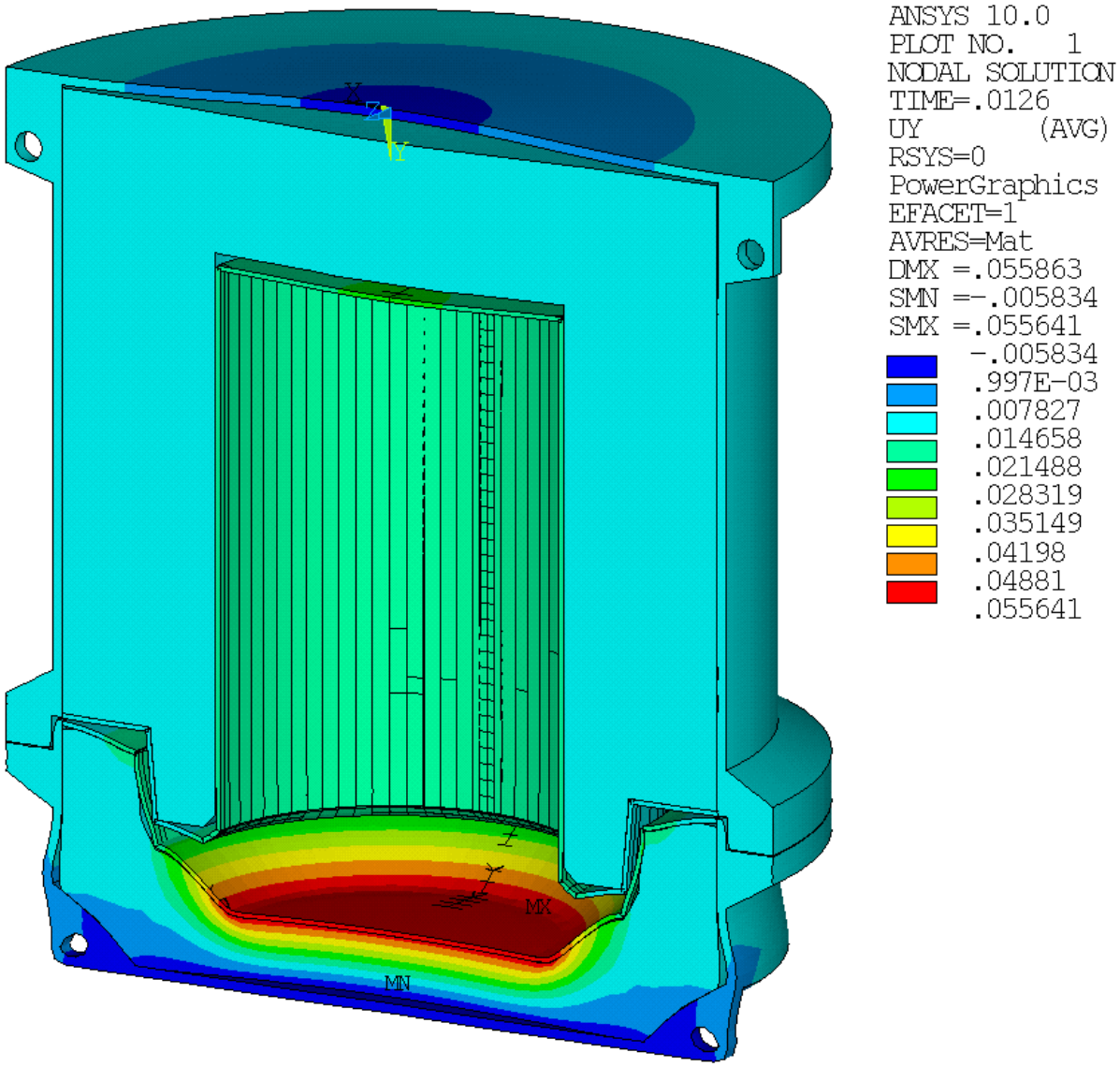


(Notes: Displacement units are meters. Deformed shape shown at 1:1 scale)

**Figure 2-23 – Overpack Permanent Deformation, HAC Hot Top-End Drop (Case H4)**

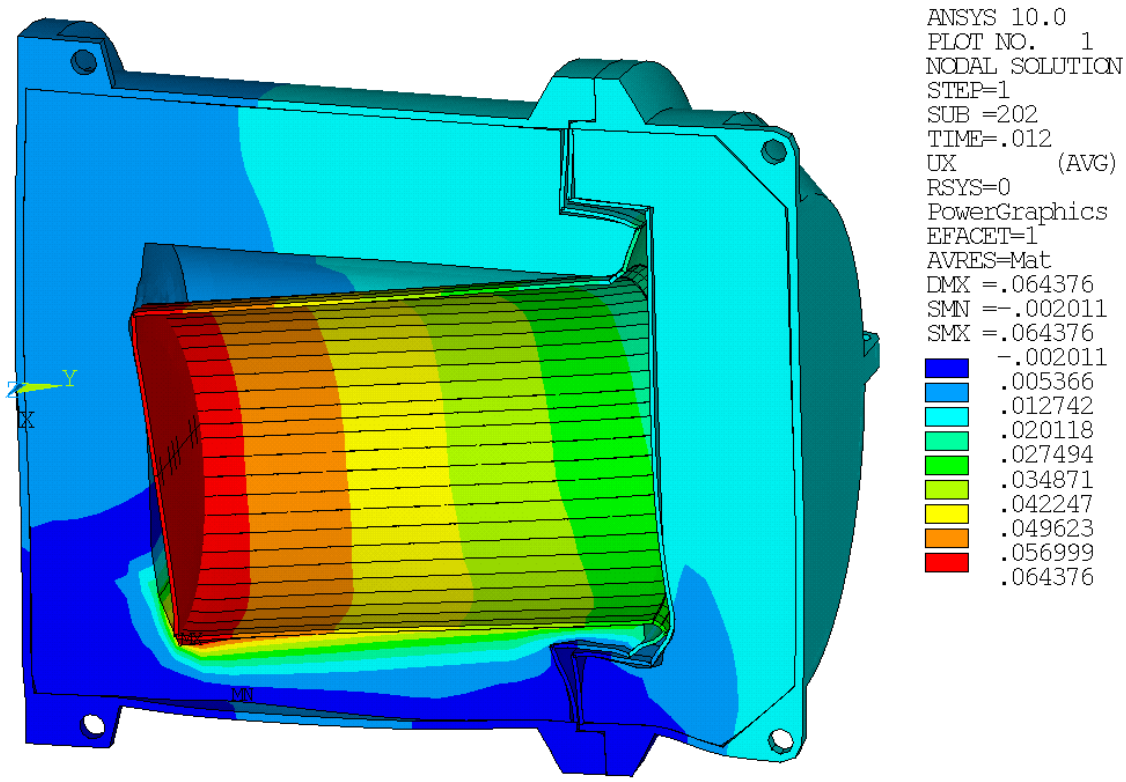


(Notes: Displacement units are meters. Deformed shape shown at 1:1 scale)

**Figure 2-24 – Overpack Permanent Deformation, HAC Hot Side Drop (Case H10)**

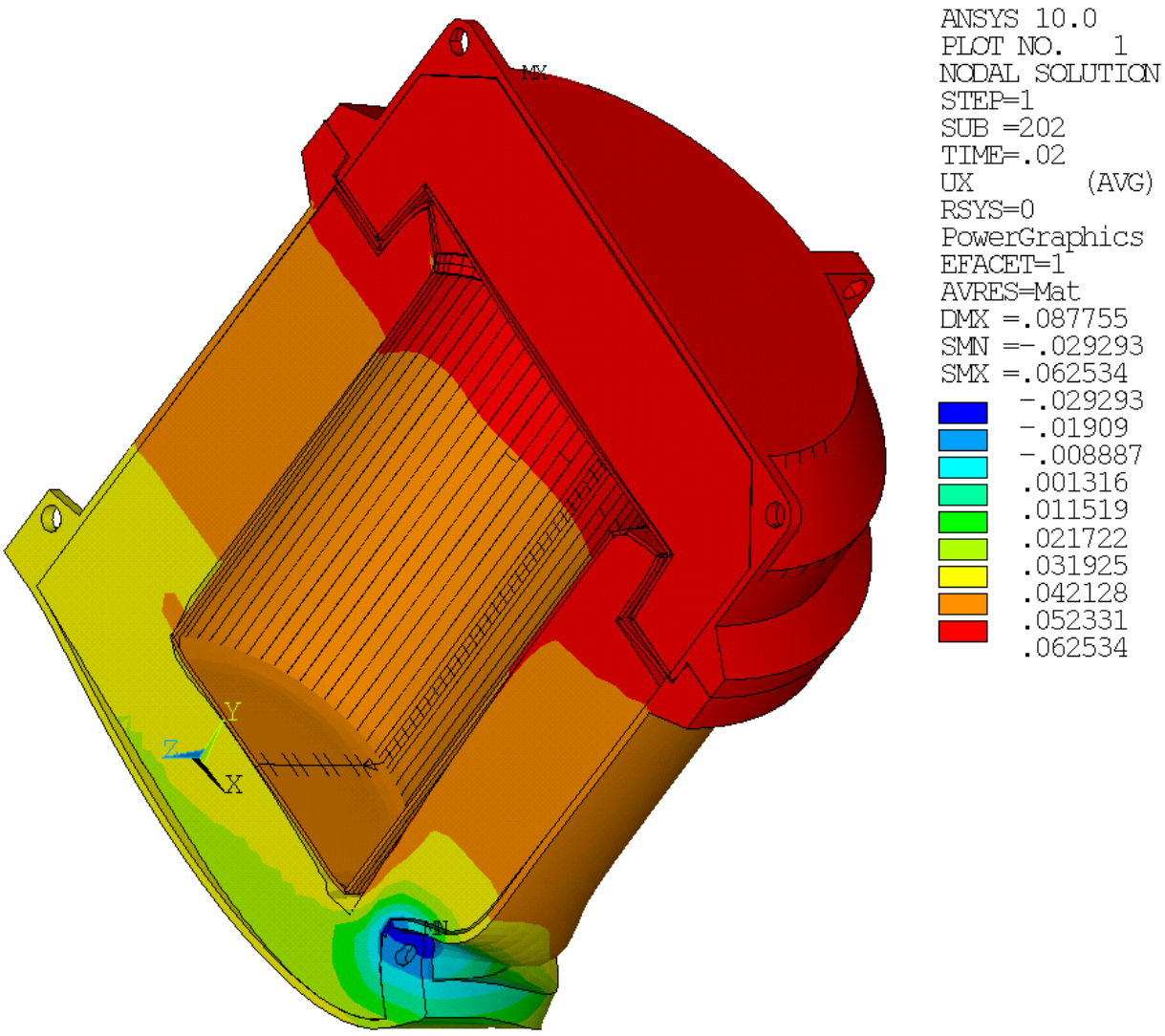


(Notes: Displacement units are meters. Deformed shape shown at 1:1 scale)

**Figure 2-25 – Overpack Permanent Deformation, HAC Hot Bottom-Corner Drop (Case H6)**

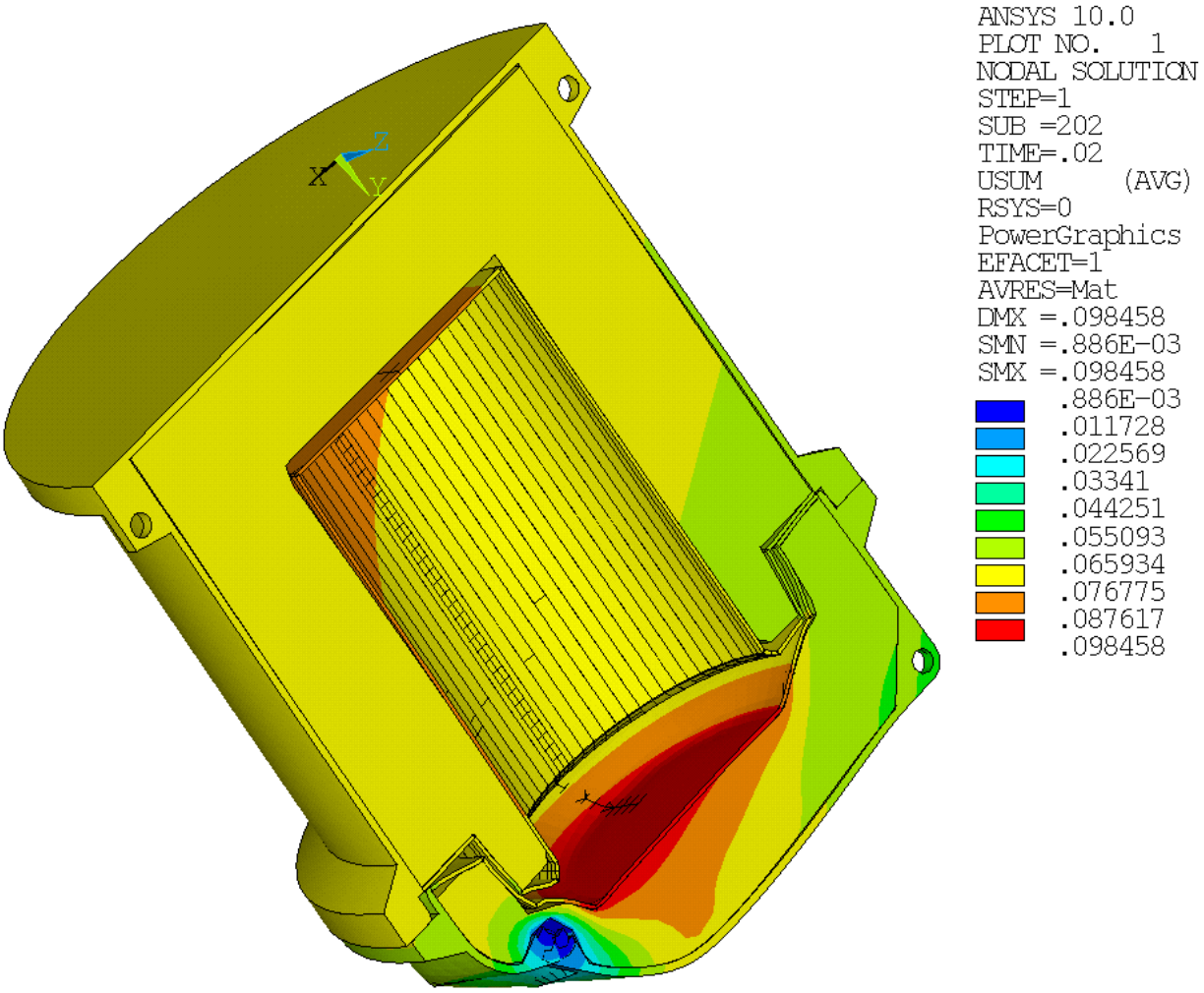


(Notes: Displacement units are meters. Deformed shape shown at 1:1 scale)

**Figure 2-26 – Overpack Permanent Deformation, HAC Hot Top-Corner Drop (Case H8)**

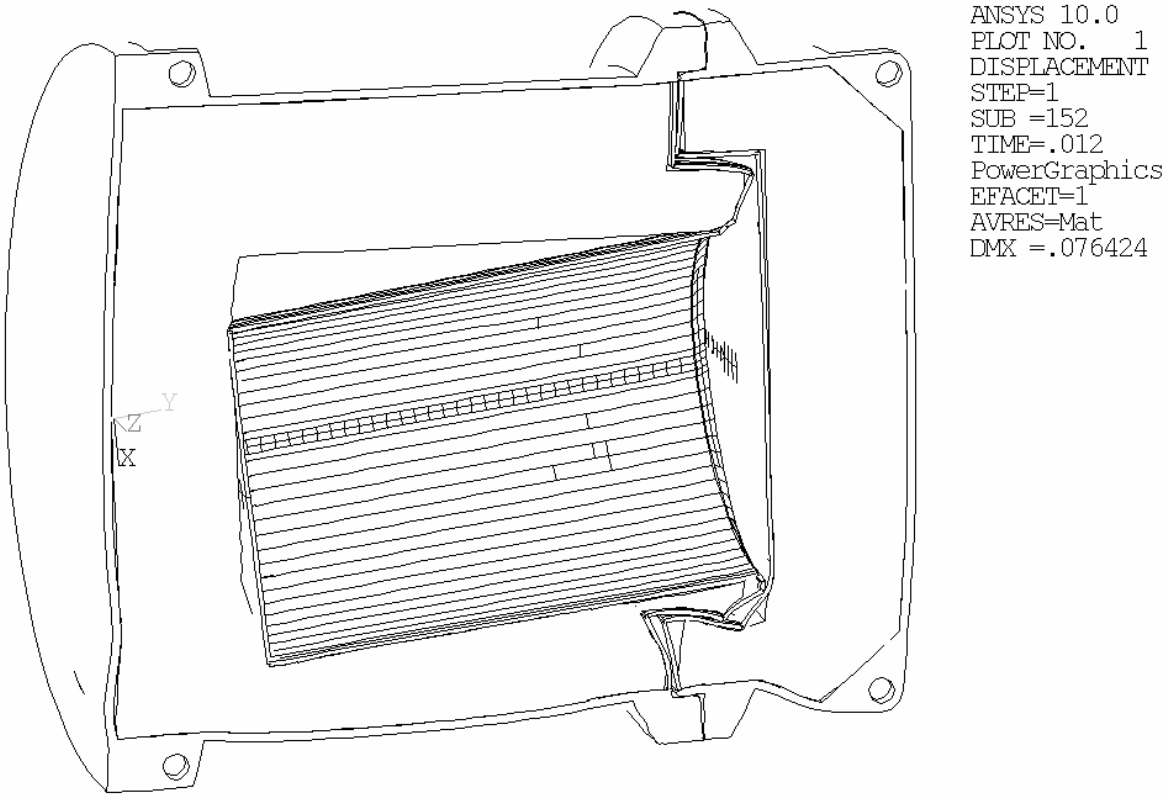


(Note: Deformed shape shown at 1:1 scale)

**Figure 2-27 – Overpack Permanent Deformation, HAC Hot 5° Bottom-End Oblique Drop (Case H12)**

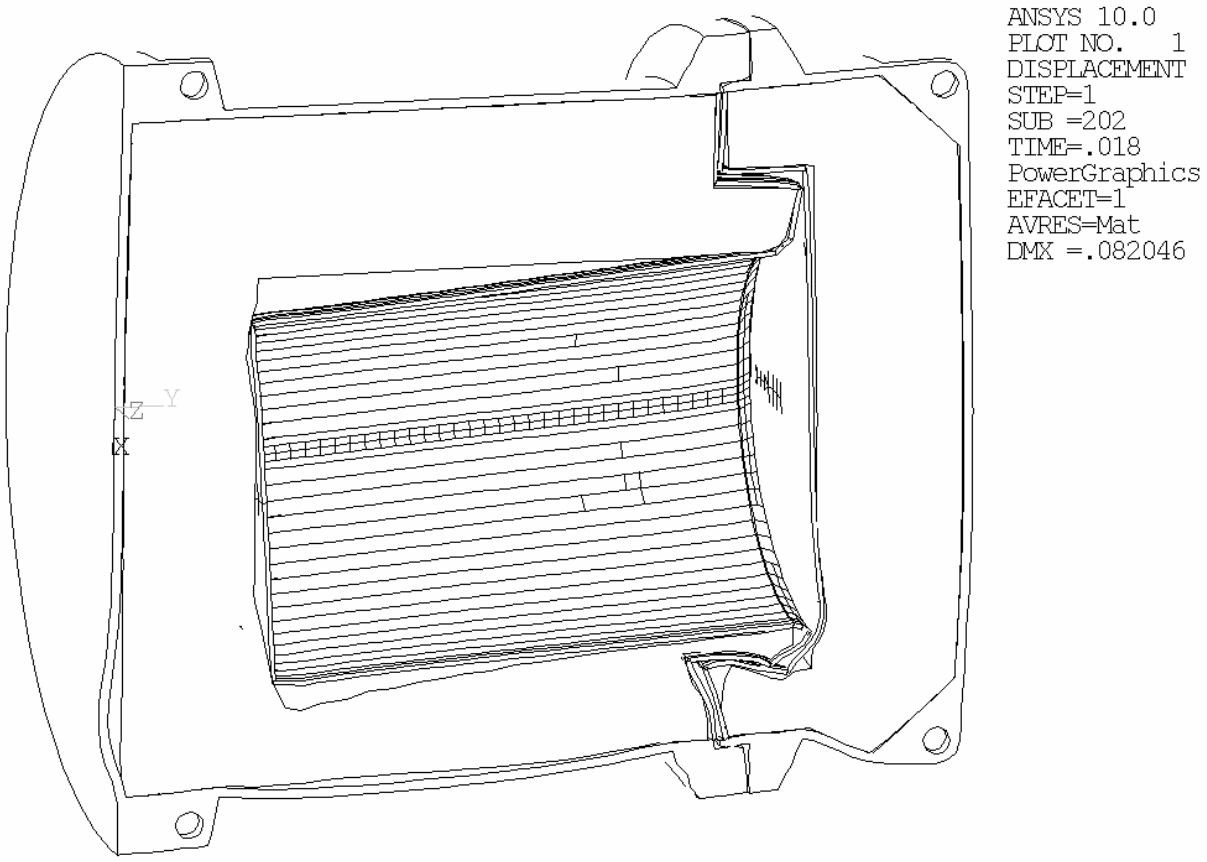


(Note: Deformed shape shown at 1:1 scale)

**Figure 2-28 – Overpack Permanent Deformation, HAC Hot 5° Top-End Oblique Drop (Case H20)**

### 2.7.2 Crush

The crush test of §71.73(c)(2) is required only when the specimen has a mass not greater than 500 kg (1,100 lb), an overall density not greater than 1,000 kg/m$^3$ (62.4 lb/ft$^3$) based on external dimensions, and radioactive contents greater than 1,000 $A_2$ not as a special form radioactive material. The $A_2$ value for $^{99}$Mo is 16 Ci per Table A-1 of 10 CFR 71. Therefore, the crush test is required only if the maximum activity of the radioactive contents is greater than 16,000 Ci. Since the maximum activity of the product is limited to a maximum of 4,400 Ci, the crush test is not applicable.

### 2.7.3 Puncture

In accordance with §71.73(c)(3), the package is evaluated for "*a free drop through a distance of 1 m (40 in) in a position for which maximum damage is expected, onto the upper end of a solid, vertical, cylindrical, mild steel bar, mounted on an essentially unyielding horizontal surface. The bar must be 15 cm (6 in) in diameter, with the top horizontal and its edge rounded to a radius of not more than 6 mm (0.25 in), and a length as to cause maximum damage to the package, but not less than 20 cm (8 in) long.*" The puncture drop test is performed in sequence following the HAC free drop test in accordance with §71.73(a). Therefore, the package damage resulting from the HAC free drop is considered in the HAC puncture drop evaluation. The maximum extent of damage sustained by the overpack for each HAC free drop orientation is discussed in Section 2.7.1.5.

When subjected to the HAC puncture drop test, the outer shell of the overpack is designed to prevent penetration or perforation by the puncture bar. The maximum damage to the overpack and the greatest potential for penetration or perforation of the overpack outer shell exists under initial conditions for which the outer shell material and foam core material is weakest. Therefore, the HAC puncture drop analysis is performed using the overpack material lower-bound strength properties for the "hot" initial conditions (i.e., an ambient temperature of 38°C, maximum decay heat, and insolation) and an upper-bound cask mass of 207 kg. Since damage to the overpack foam core material (i.e., crushing) resulting from the HAC free drop generally results in local densification that effectively increases the foam crush strength, a subsequent HAC puncture drop impact on a damaged portion of the overpack would have less potential for maximum damage than the same HAC puncture drop with an undamaged package. Therefore, the HAC puncture drop analyses are performed with an undamaged overpack since it is expected to cause maximum damage.

Six HAC puncture drop orientations for which maximum damage is expected are considered in the evaluation of the package, as summarized in Table 2-55 and illustrated in Figure 2-29. These include three "center" impact orientations and three "oblique" impact orientations that are expected to cause maximum damage to the package. Each center impact orientation has the package center of gravity located directly over the centerline of the puncture bar and results in the outer surface of the overpack striking the top flat surface of the puncture pin. Each oblique impact orientation has the package center of gravity located directly over the struck corner of the puncture bar to impart maximum impact energy to the package.

The HAC puncture drop impact analysis are performed using the LS-DYNA finite element model described in Section 2.6.7.1. As discussed above, the HAC puncture drop analysis is performed using the overpack material lower-bound strength properties for the "hot" thermal condition and an upper-bound cask mass of 207 kg. In addition, a single puncture drop impact analysis is performed for the "cold" thermal condition with upper-bound material strength properties and lower-bound cask weight (Case P3B). This case is evaluated primarily to determine the highest peak rigid-body acceleration of the cask resulting from the top-end puncture drop impact for use in the cask closure bolt evaluation.

Each HAC puncture drop time-history analyses is started at or near the moment of initial contact between the package's outer surface and the top surface of the puncture bar. An initial vertical velocity of 4.43 m/s, corresponding to a free-fall velocity from a height of 1 m, is applied to the package in all cases. The time-history analysis durations used for the puncture drop impacts are sufficient to capture the entire duration of the primary impact between the package and puncture bar.

The maximum overpack foam crush, maximum total strain in the overpack shell, and peak rigid-body cask acceleration loads resulting from the HAC puncture drop orientations analyzed are summarized in Table 2-56. The overpack satisfies the applicable design criteria for the HAC puncture drop orientations expected to cause maximum damage. The maximum foam crush of 38%, resulting from the HAC hot top-oblique puncture drop (Case P4), is within the acceptable crush range for the foam material. The highest strain in the overpack outer shell for all HAC puncture drop impact orientations considered is 23% (Case P6), which is lower than the lowest maximum elongation (30%) of the overpack shell material. Therefore, the HAC puncture drop will not cause perforation or penetration of the overpack outer shell. The highest peak rigid-body longitudinal acceleration of 139*g* results from the HAC cold top-center puncture drop (Case P3B). As expected, the highest peak rigid-body cask accelerations due to the HAC puncture drop conditions are much lower than those resulting from the HAC free drop conditions.

Table 2-57 summarizes the maximum shear stress, maximum total strain intensity, and minimum design margins for the most heavily loaded overpack closure bolt in each HAC puncture drop analysis. The results show that the maximum total strain intensity in the most heavily loaded bolt never exceeds the yield strain (0.37%) of the overpack closure bolt A320, Grade L43 material at an upper-bound design temperature of 93°C. Therefore, the overpack closure bolts will not experience any plastic deformation due to the HAC puncture drop. The maximum shear stress in the most heavily loaded closure bolt is 32 MPa for cases P4, P5, and P6. The allowable bolt shear stress for HAC is $0.42S_u$, or 362 MPa for the overpack closure bolt A320, Grade L43 material at an upper-bound design temperature of 93°C. The corresponding minimum design margin in the overpack closure bolts for all HAC puncture drop impact orientations is +10.3. Therefore, the overpack closure bolts satisfy the applicable HAC structural design criteria for the HAC puncture drop impact.

The permanent deformation of the overpack following each HAC hot puncture drop tests (i.e., case P3B not included) are shown in Figure 2-30 through Figure 2-35. The results show that the

permanent deformation of the overpack resulting from the HAC puncture drop is small and localized in comparison to the permanent deformation resulting from the HAC free drop tests. As shown in Figure 2-30 and Figure 2-32, the damage to the overpack resulting from the HAC hot bottom and top center puncture drops (cases P1 and P3A) is similar. In these cases the package damage is limited to a circular-shaped dent centered on the bottom or top outer end plate of the overpack assembly that is approximately 150 mm in diameter (i.e., the puncture bar diameter) and 20 mm deep. For the HAC hot bottom and top oblique puncture drops (cases P2 and P4), the package damage is limited to a crescent-shaped dent in the impacted outer end plate of the overpack assembly with a maximum depth of approximately 30 mm, as shown in Figure 2-31 and Figure 2-33. The package damage resulting from the HAC hot side-center puncture drop (case P5), shown in Figure 2-34, is limited to a dent in the overpack base outer shell that is approximately 150 mm long (i.e., the puncture bar diameter) and 20 mm deep. The package damage resulting from the HAC hot side-oblique puncture drop (case P6), shown in Figure 2-35, is limited to a crescent-shaped dent in the overpack-base outer shell with a maximum depth of approximately 27 mm.

The structural evaluation of the overpack for the HAC puncture test demonstrates that the overpack outer shell will not be penetrated or perforated by the puncture bar, thereby preventing the puncture bar from impinging directly upon the exterior surface of the cask assembly. Furthermore, the cask peak rigid-body acceleration loads due to the HAC puncture tests are much lower than those resulting from the HAC free drop test. Therefore, a detailed structural evaluation of the cask and shield lid is not required for the HAC puncture test since the stresses in the cask and shield lid due to the HAC puncture test are expected to be much lower than those calculated for the HAC free drop test.

A detailed stress analysis of the cask closure bolts for HAC puncture test is performed using the 3-D quarter-symmetry finite element model described in Section 2.5.1.2. The evaluation is performed for the HAC cold top center puncture impact, which results in the maximum cask longitudinal peak rigid-body acceleration load of 139*g*. A 153*g* equivalent-static longitudinal acceleration load, which includes a DLF of 1.1 to account for possible dynamic amplification within the cask assembly, is used for the analysis. The inertia load from the closure lid self-weight due to the HAC puncture drop is accounted for by applying the 153*g* equivalent-static acceleration load to the model. A uniform pressure load of 22,832 kPa is applied over the center region of the closure plate to model the inward-acting reaction from the puncture bar. This pressure load is distributed over a circular area with a diameter of 126.95 mm, which is less than the 150 mm diameter of the puncture bar, resulting in a total load of 289 kN. A uniform pressure load is applied to the underside of the closure lid to account for the loading from the combined mass of the shield plug and payload. For modeling simplicity, a uniform pressure load is applied over the entire area inside the containment O-ring diameter. Although the O-ring diameter upon which the pressure load is calculated is approximately 18% larger than the outside diameter of the shield plug, it does not significantly affect the solution results. In fact, the assumption of a uniform pressure distribution is conservative since the load from the shield plug will concentrate at its outer edge because it is relatively stiff compared to the closure plate. Thus, the prying moment resulting from the assumed uniform pressure load distribution is conservative.

The HAC puncture loading is applied in combination with NCT heat temperature loading, maximum internal pressure, and maximum bolt preload. The NCT heat temperature loading is applied to the finite element model as a uniform temperature load of 68.3°C. The maximum bolt preload of 7.2 kN is applied to each bolt and a uniform pressure load of 700 kPa is applied on the inner surface of the closure plate over the area inside the containment O-ring.

The maximum average stress (i.e., axial stress) in the closure bolts due to HAC puncture loading is 212 MPa. The average axial stress for HAC is limited to the less of $3S_m$ or $0.7S_u$. The values of $S_m$ and $S_u$ for SA-320, Grade L43 bolting steel at 68.3°C are 234 MPa and 862 MPa, respectively, based on linear interpolation of the values shown in Table 2-15. Therefore, the allowable average stress for HAC is 603 MPa. The corresponding minimum design margin in the closure bolt for the HAC puncture loading is +1.84.

The maximum lid separation at the inside edge of the bolting flange resulting from the HAC top end drop loading is approximately 0.004 mm, or 0.4% of the O-ring compression. The maximum lid separation resulting from the HAC puncture test is not significant and no radioactive material is expected to escape from the cask containment system under HAC puncture loading.

**Table 2-55 – Summary of HAC Puncture Drop Cases Evaluated**

| Case I.D. | Case Description | Mass Properties[1] | Thermal Condition[2] | Material Properties[3] | Impact Angle[4] |
|---|---|---|---|---|---|
| P1 | Hot Bottom Center Puncture | Upper Bound | Hot | Lower Bound | 0° |
| P2 | Hot Bottom Oblique Puncture | Upper Bound | Hot | Lower Bound | 25° |
| P3A | Hot Top Center Puncture | Upper Bound | Hot | Lower Bound | 180° |
| P3B | Cold Top Center Puncture | Lower Bound | Cold | Upper Bound | 180° |
| P4 | Hot Top Oblique Puncture | Upper Bound | Hot | Lower Bound | 155° |
| P5 | Hot Side Center Puncture | Upper Bound | Hot | Lower Bound | 90° |
| P6 | Hot Side Oblique Puncture | Upper Bound | Hot | Lower Bound | 105° |

Notes:
1. Upper- and lower-bound mass properties are 2.5% higher and lower than the nominal values shown in Table 2-8.
2. A lower-bound uniform package temperature -29°C is assumed for the "cold" thermal condition. Upper-bound temperatures of 93°C for the overpack steel and 82°C for the overpack foam core are assumed for the "hot" thermal condition.
3. Upper- and lower-bound strength properties of the overpack materials are described in Section 2.2.1.
4. Impact angle is measured relative to the vertical upright package position (refer to Figure 2-29).

**Table 2-56 – HAC Puncture Drop Summary**

| Case I.D. | Case Description[1] | Overpack Foam Maximum Crush[2] | Overpack Shell Maximum Total Strain | Cask Peak Rigid-Body Accelerations[3] | |
|---|---|---|---|---|---|
| | | | | Transverse | Longitudinal |
| P1 | Hot Bottom Center Puncture | 24% | 6% | --- | 83g |
| P2 | Hot Bottom Oblique Puncture | 37% | 19% | 37g | 65g |
| P3A | Hot Top Center Puncture | 22% | 9% | --- | 72g |
| P3B | Cold Top Center Puncture | 11% | 8% | --- | 139g |
| P4 | Hot Top Oblique Puncture | 38% | 21% | 43g | 50g |
| P5 | Hot Side Center Puncture | 22% | 21% | 96g | --- |
| P6 | Hot Side Oblique Puncture | 30% | 23% | 66g | 16g |

Notes:
1. Puncture drop impact orientations shown in Figure 2-29.
2. Value is equal to the maximum deformation divided by the nominal foam thickness in the corresponding direction.
3. The highest peak accelerations on either the top or bottom centerline of the cask/shield lid rigid-body in the transverse (X) and longitudinal (Y) directions are reported.

**Table 2-57 – Overpack Closure-Bolt HAC Puncture Drop Stress Summary**

| Case I.D. | Case Description[1] | Maximum Shear Stress (MPa) | Maximum Total Strain Intensity | Minimum Bolt Design Margin[2] |
|---|---|---|---|---|
| P1 | Hot Bottom Center Puncture | <2 | 0.02% | Large[3] |
| P2 | Hot Bottom Oblique Puncture | 22 | 0.11% | +15.5 |
| P3A | Hot Top Center Puncture | <4 | 0.05% | Large[3] |
| P3B | Cold Top Center Puncture | <4 | 0.05% | Large[3] |
| P4 | Hot Top Oblique Puncture | 32 | <0.20% | +10.3 |
| P5 | Hot Side Center Puncture | 32 | <0.15% | +10.3 |
| P6 | Hot Side Oblique Puncture | 32 | <0.15% | +10.3 |

Notes:
1. Puncture drop impact orientations are shown in Figure 2-29.
2. The minimum design margin is calculated as (Allowable Value/Maximum Value) – 1, where the allowable shear stresses for A320, Grade L43 bolting steel at an upper-bound temperature of 93°C is 362 MPa, and the allowable axial strain is equal to the maximum elongation of A320, Grade L43 bolting steel (i.e., 16%).
3. The minimum bolt design margin for this case is greater than +50.0 and does not control the design.

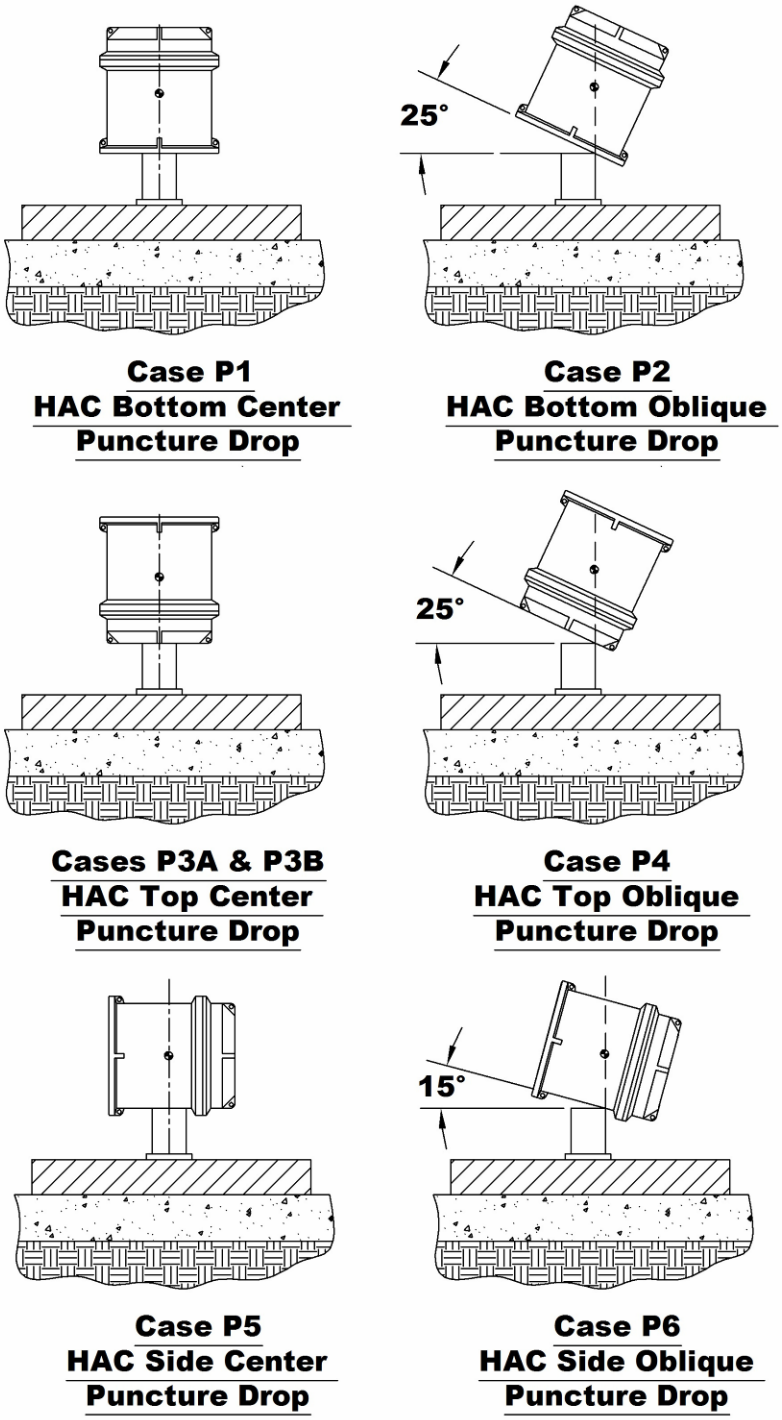


**Figure 2-29 – HAC Puncture Drop Impact Orientations**

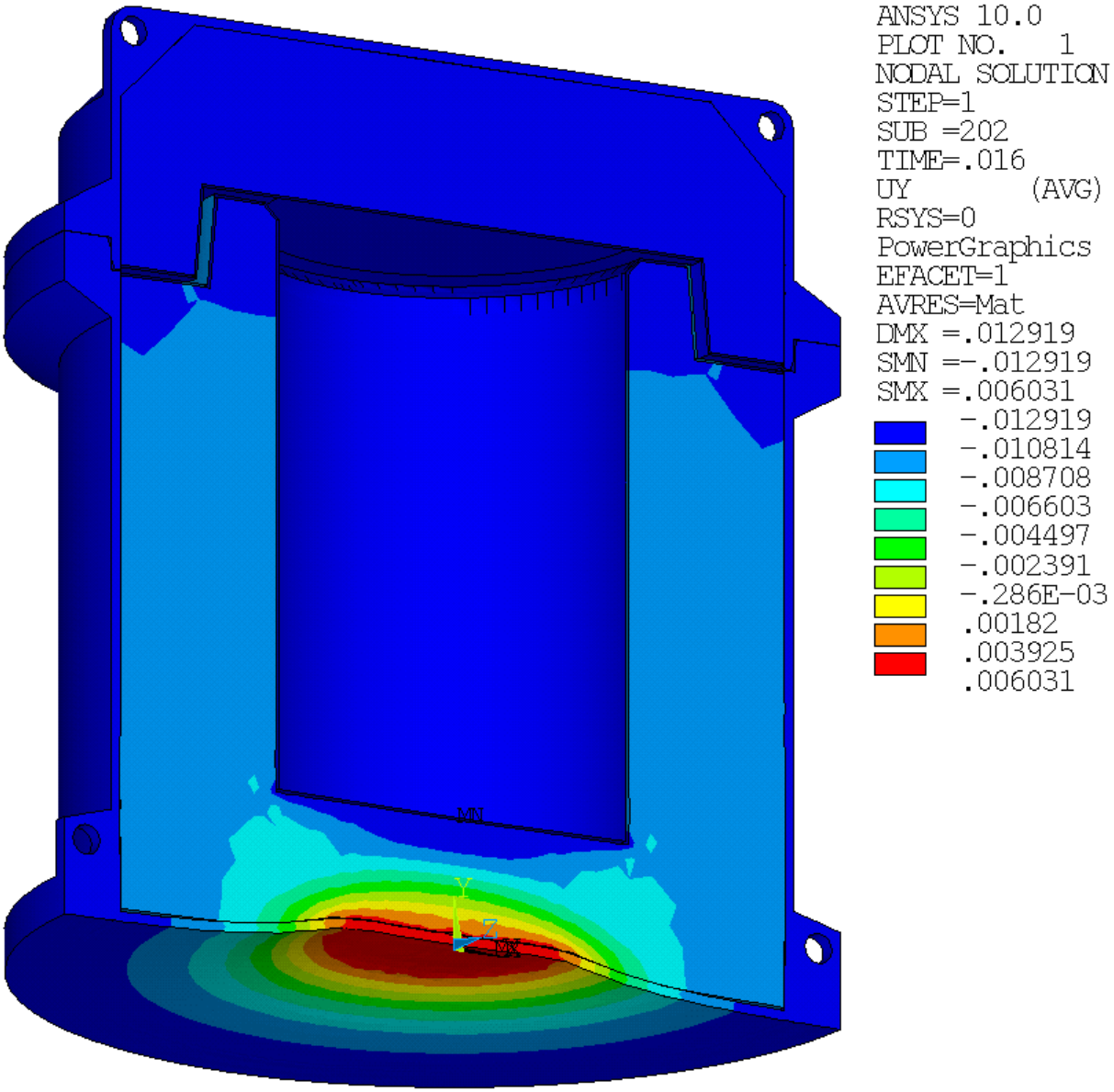


(Note: Displacement units are meters)

**Figure 2-30 – Overpack Deformation, HAC Hot Bottom-Center Puncture (Case P1)**

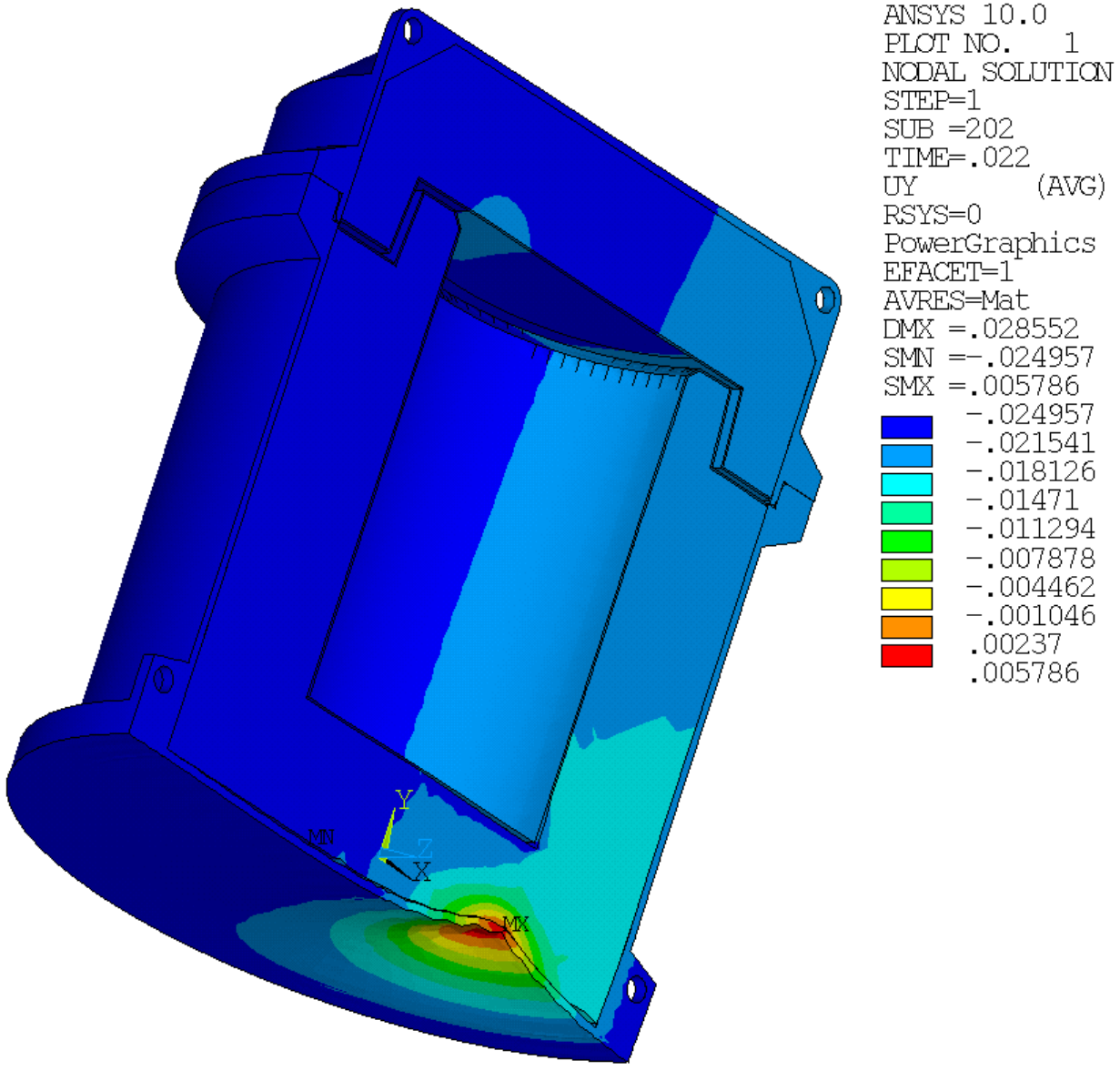


(Note: Displacement units are meters)

**Figure 2-31 – Overpack Deformation, HAC Hot Bottom-Oblique Puncture (Case P2)**

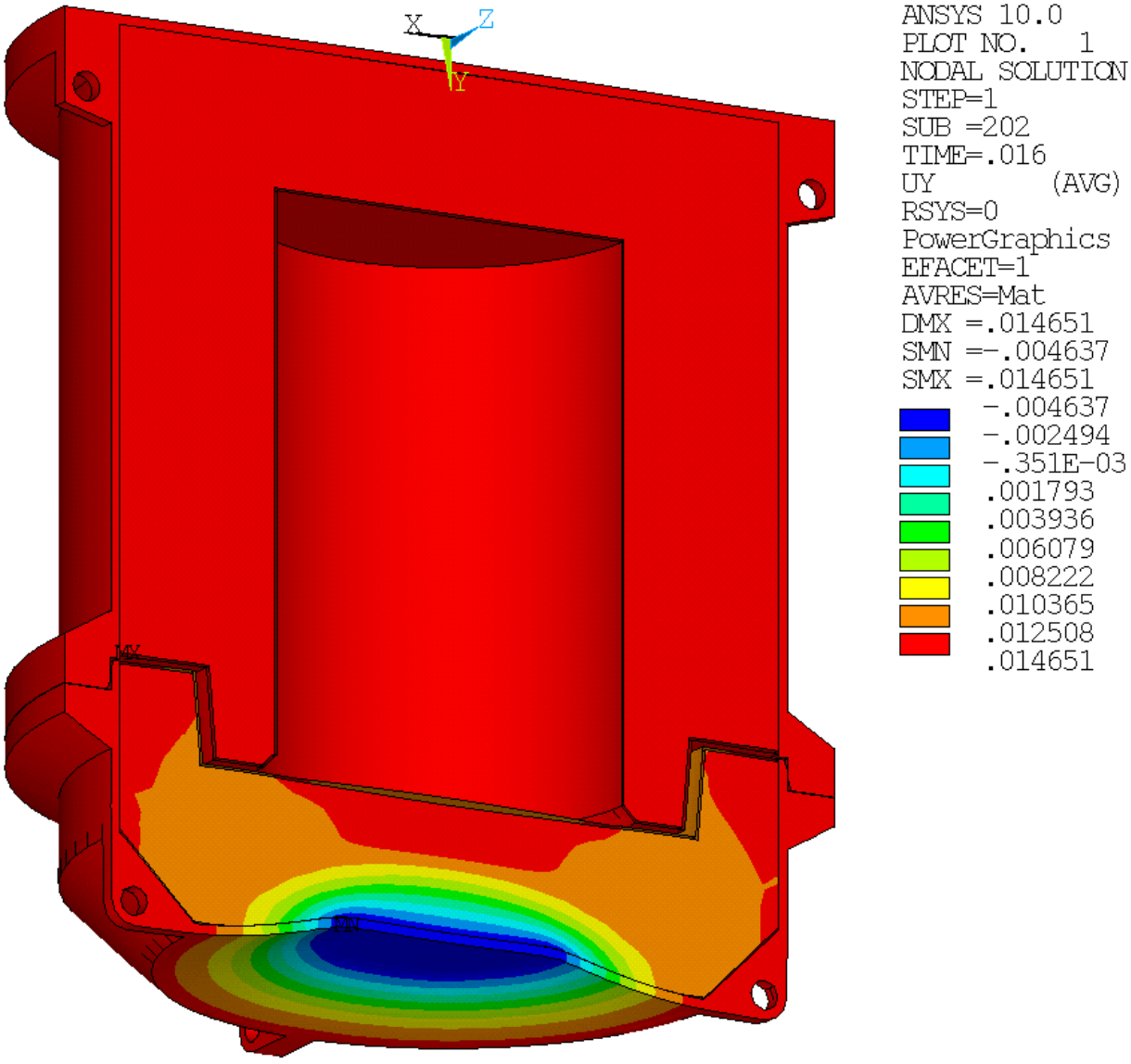


(Note: Displacement units are meters)

**Figure 2-32 – Overpack Deformation, HAC Hot Top-Center Puncture (Case P3A)**

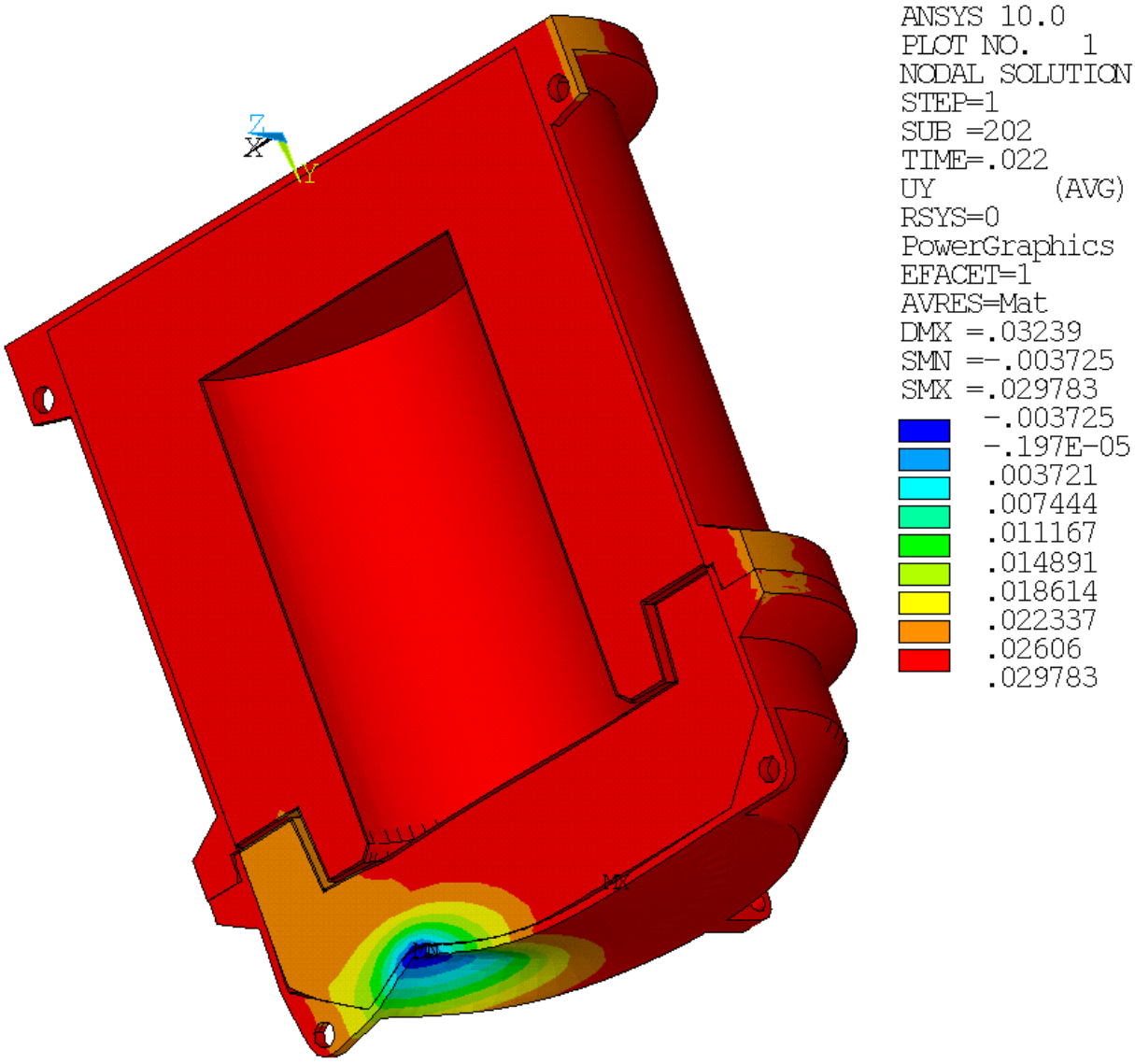


(Note: Displacement units are meters)

**Figure 2-33 – Overpack Deformation, HAC Hot Top-Oblique Puncture (Case P4)**

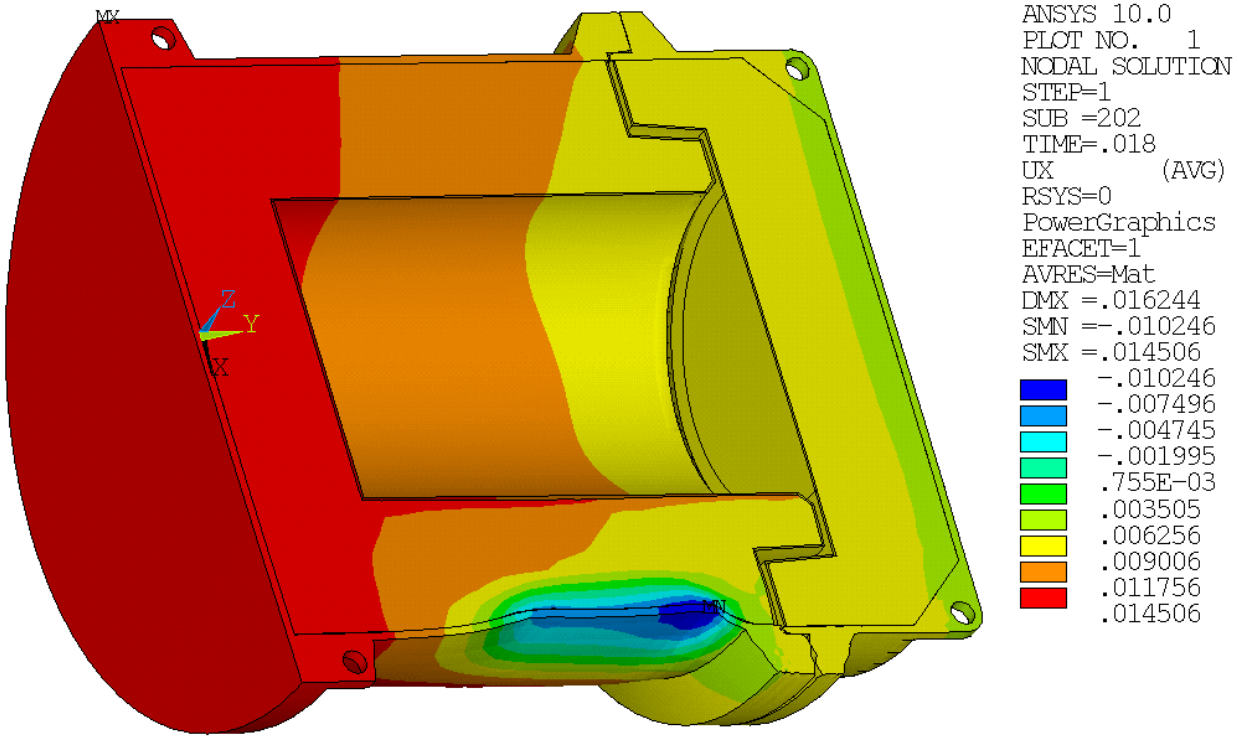


(Note: Displacement units are meters)

**Figure 2-34 – Overpack Deformation, HAC Hot Side-Center Puncture (Case P5)**

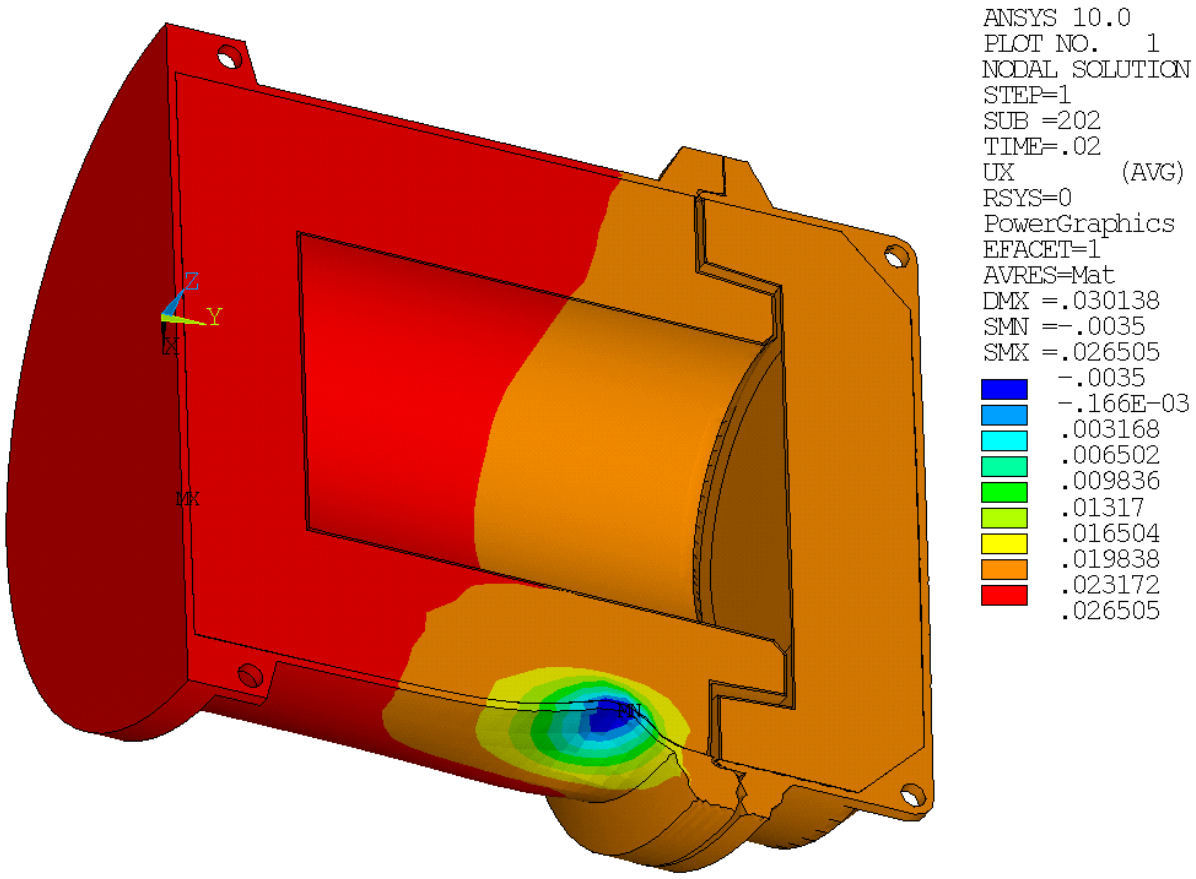


(Note: Displacement units are meters)

**Figure 2-35 – Overpack Deformation, HAC Hot Side-Oblique Puncture (Case P6)**

## 2.7.4 Thermal

In accordance with §71.73(c)(4), the package is designed to withstand the 30-minute fire with the flame temperature of 800°C. This section presents the structural evaluation of the cask for the HAC thermal loading. The package temperatures and pressure resulting from the HAC thermal test are discussed in Section 2.7.4.1. Differential thermal expansion between the components of the package due to the HAC thermal loading is discussed in Section 2.7.4.2. The stresses in the cask due to the HAC thermal loading are evaluated in Section 2.7.4.3. Compliance with the applicable structural design criteria and the applicable regulatory performance requirements is discussed in Section 2.7.4.4.

### 2.7.4.1 Summary of Pressures and Temperatures

The cask is insulated from the full effects of the HAC fire by the overpack. The thermal evaluation of the package for the HAC fire shows that, while the outer shell of the overpack reaches a peak temperature of approximately 782°C during the HAC fire transient, the peak temperature of the cask only reaches 221°C. The cask maximum internal pressure during the HAC fire is 12.6 bar or 1,260 kPa gauge.

### 2.7.4.2 Differential Thermal Expansion

Differential thermal expansion in the cask due to the HAC thermal loading causes the clearances between the cask components to increase. The HAC thermal evaluation shows that the pre-fire temperature gradient between the cask's inner and outer shells is essentially reduced to zero during the fire and remains lower over the post-fire transient. Therefore, the differential thermal expansion between the cask shells and DU during the HAC fire is expected to be bounded by the results for NCT heat from Section 2.6.1.2.

### 2.7.4.3 Stress Calculations

With the exception of closure-bolt stresses, the stresses in the package resulting from temperature loading are classified as secondary and need not be evaluated for HAC in accordance with the ASME Code. The HAC thermal evaluation of the package shows that the thermal gradients within the cask during the HAC fire are much greater than those due to NCT conditions. For instance, the temperature gradient between the cask's inner and outer shells is approximately +3.7°C for the NCT hot thermal condition and approximately -83.8°C for the HAC fire (bottom end drop damage case). However, due to the construction of the cask, these thermal gradients are not expected to cause significant thermal stresses in the cask. The through-wall gradient results in free thermal longitudinal thermal expansion of the cask's inner and outer shells. The only significant thermal stresses in the cask body are expected to occur in the closure bolts (due to differential thermal expansion of the closure bolts and closure lid) and at the cask outer shell-to-flange junctions. However, HAC fire is not expected to cause any permanent deformation or gross structural failure in the cask.

The stresses in the cask closure bolts due to HAC thermal loading are determined using the 3-D quarter-symmetry finite element model described in Section 2.5.1.2. The HAC thermal temperature loading for the cask closure-bolt analysis is applied as a uniform elevated temperature load of 204°C, which bounds the peak temperature of the cask closure bolt for the HAC thermal of 147.4°C. Elevated temperature produces differential thermal expansion between the closure bolts and closure lid, due to the differences in their material model coefficient of thermal expansion values, causing thermal stress. Thermal stresses in the closure bolts due to closure plate through-thickness temperature gradients are not considered since these temperature gradients are small. In combination with the HAC thermal temperature loading, a maximum bolt preload of 7.2 kN is applied to each closure bolt and a bounding accident internal pressure load of 1,800 kPa is applied on the inner surface of the closure plate over the entire area inside the containment O-ring.

The maximum average stress (i.e., axial stress) in the closure bolts due to HAC thermal loading is 486 MPa. The average bolt axial stress for HAC is limited to the lesser of $3S_m$ or $0.7S_u$. The values of $S_m$ and $S_u$ for SA-320, Grade L43 bolting steel at a bounding closure-bolt design temperature of 204°C are 234 MPa and 862 MPa, respectively. Therefore, the allowable average stress for HAC is 603 MPa, and the corresponding maximum closure bolt stress ratio is 0.81.

#### 2.7.4.4 Comparison with Allowable Stresses

The results of the structural evaluation for the HAC thermal test demonstrate that the cask satisfies the applicable HAC allowable-stress design criteria. The HAC thermal loading does not cause any significant permanent deformation of the cask or shield lid, nor does it substantially reduce the effectiveness of the packaging. The evaluation shows that no inelastic deformation of the closure bolts results from the HAC thermal loading. Thus, the containment seal will be maintained under HAC thermal loading, and there will be no loss or dispersal of radioactive contents. The damage to the overpack resulting from HAC free drop loading is considered in the HAC shielding evaluation, which demonstrates that the external dose-rate limit requirement of §71.51(a)(1) is satisfied. Therefore, the package complies with the requirements of §71.51(a)(1) when subjected to the HAC thermal test of §71.73(c)(4).

### 2.7.5 Immersion — Fissile Material

Not applicable.

### 2.7.6 Immersion — All Packages

In accordance with §71.73(c)(6), an undamaged package is subjected to a water pressure equivalent to immersion under a head of water of at least 15 m, or an equivalent external pressure load of 150 kPa gauge. In addition to the external pressure loading, the quenching effects of immersion in water are considered.

The stresses in the cask and shield lid resulting from “HAC immersion - all packages” loading are determined using the axisymmetric finite element model described in Section 2.6.1.3. The applied loads and boundary conditions for the “HAC immersion - all packages” analysis are

shown in Figure 2-36. An external pressure load of 150 kPa gauge is applied to the outer surfaces of the cask's containment system, conservatively taking no credit for any pressure-retaining ability of the package non-containment components. Zero internal pressure is assumed in combination with the immersion external pressure load to maximize the net pressure load acting on the containment system. The temperature gradient applied to the model for the "HAC immersion - all packages" analysis is the same as the bounding NCT heat temperature gradient discussed in Section 2.6.1.3, except that the temperatures of the outer shells of the cask and shield lid are conservatively set to 21°C to account for the quenching effect of water. This is conservative since it neglects the relatively large thermal mass of the cask and assumes an instantaneous temperature change on the outside of the cask and no temperature change in the rest of the cask.

The maximum stresses in the cask's containment system and non-containment components due to the "HAC immersion - all packages" loading, along with the corresponding allowable stress intensities and minimum design margins, are summarized in Table 2-58. The minimum design margin is +1.63 for primary membrane plus bending stress intensity ($P_m+P_b$) at the bottom end of the cask-body outer shell (section N3 in Figure 2-2). Thus, the cask satisfies the applicable HAC allowable-stress design criteria for the "HAC immersion - all packages" test.

A buckling evaluation of the cask's containment shell and outer shell is performed for the "HAC immersion - all packages" loading in accordance with the requirements of ASME Code Case N-284-1 [2.7]. The maximum compressive stresses and shear stresses near the mid-lengths of the cask's inner shell and outer shell (i.e., Sections C5 and N5 in Figure 2-1 and Figure 2-2) are used for the cask-shell buckling evaluation. As discussed in Section 2.1.2.3, elastic and inelastic buckling interaction ratios are calculated based on the HAC allowable buckling stresses shown in Table 2-7, which include a factor of safety of 1.34. The maximum interaction ratios must not exceed 1.0.

The maximum calculated cask-shell stresses and the resulting maximum buckling interaction ratios for the "HAC immersion - all packages" loading are summarized in Table 2-59. The maximum buckling interaction ratios in the cask's inner and outer shells are 0.03 and 0.00, respectively. Therefore, the cask satisfies the buckling design criteria of ASME Code Case N-284-1 for the "HAC immersion—all packages" test.

**Table 2-58 – "HAC Immersion - All Packages" Maximum Stress Summary**

| Cask Components | Stress Type | Maximum Stress Intensity (MPa) | Controlling Location[1] | Allowable Stress Intensity[2] (MPa) | Minimum Design Margin[3] |
|---|---|---|---|---|---|
| Containment System | $P_m$ | 99 | C21 | 331 | +2.34 |
| | $P_m+P_b$ | 106 | C21 | 492 | +3.64 |
| | $P_m+P_b+Q$ | 109 | C21 | N/A[4] | N/A[4] |
| Non-Containment Components | $P_m$ | 84 | N3 | 221 | +1.63 |
| | $P_m+P_b$ | 140 | N3 | 332 | +1.37 |
| | $P_m+P_b+Q$ | 141 | N3 | N/A[4] | N/A[4] |

Notes:
1. Containment system and non-containment component stress locations are shown in Figure 2-1 and Figure 2-2, respectively.
2. Allowable stress intensities are based on an upper-bound design temperature of 74°C.
3. Design margin is calculated as (Allowable S.I./Maximum S.I) – 1.
4. Evaluation of secondary stress is not required for HAC.

**Table 2-59 – Cask-Shell Buckling Stresses, Immersion - All Packages**

| Stress Type | Calculated Stresses[1], kPa | |
|---|---|---|
| | Inner Shell[2] | Outer Shell[3] |
| Axial Stress, SY ($\sigma_\phi$) | 1,389 | 0[4] |
| Hoop Stress, SZ ($\sigma_\theta$) | 2,706 | -103 |
| Shear Stress, SXZ ($\sigma_{\phi\theta}$) | 0 | 0 |

Notes:
1. The maximum compressive axial and hoop stress intensities and maximum in-plane shear stress intensities are reported.
2. Maximum stress intensities at section C5 in Figure 2-1.
3. Maximum stress intensities at section N5 in Figure 2-2.
4. Zero stress is assumed for the buckling evaluation since the stress is tensile.

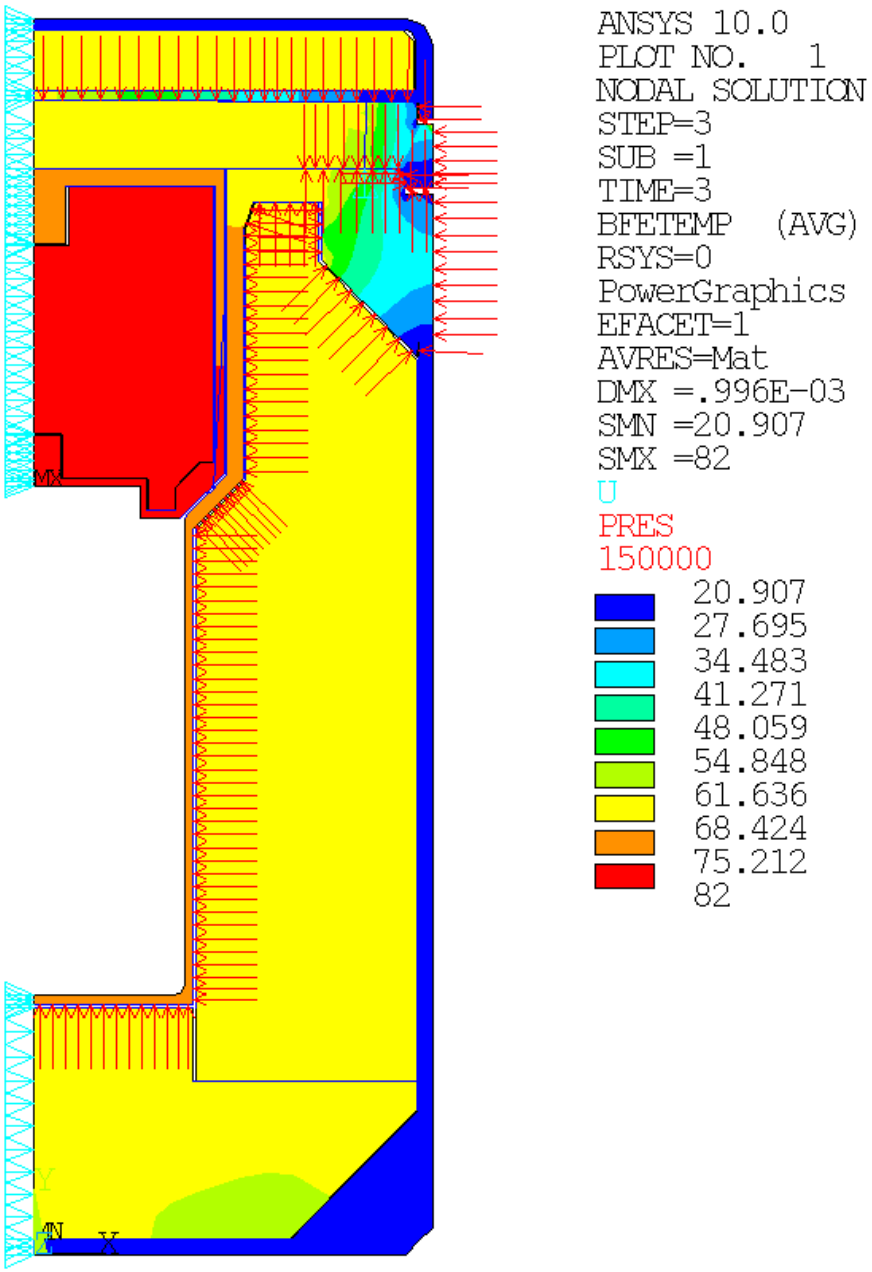


(Note: Temperatures in °C and pressure in units of Pa)

**Figure 2-36 – Immersion - All Packages, Applied Pressure and Temperature Loads**

### 2.7.7 Deep Water Immersion Test (for Type B Packages Containing More than $10^5$ $A_2$)

Not applicable.

### 2.7.8 Summary of Damage

The preceding structural evaluation demonstrates that the package satisfies the applicable structural design criteria and the performance requirements of 10 CFR 71 for the HAC test sequence of §71.73. The condition of the package after each test of the HAC sequence, based on the sequential application of the free drop, puncture, and thermal tests, is summarized as follows.

*HAC Free Drop*

The HAC free drop does not cause any significant permanent deformation in the cask assembly and shield lid assembly. No inelastic deformation of the cask closure bolts and containment sealing surfaces results from the HAC free drop test. The only significant package damage resulting from the HAC free drop occurs in the overpack assembly. The overpack damage resulting from each of the HAC free drop orientations is discussed in Section 2.7.1.5. The HAC end drops and side drop are shown to cause the greatest extent of damage to the overpack. The HAC hot bottom end drop results in 45 mm of permanent crush in the bottom end of the overpack base, or 47% of the overpack bottom end thickness. The HAC hot top end drop results in 56 mm of permanent crush in the top end of the overpack lid, or 54% of the overpack top end thickness. The overpack side wall thickness is permanently reduced by about 40 mm, or 35% of the overpack side wall thickness, as a result of the HAC hot side drop.

*HAC Puncture*

The package is subjected to the HAC puncture test of §71.73(c)(1), considering the damage sustained from the HAC free drop of §71.73(c)(3). The damage to the package resulting from the HAC free drop does not affect the package's ability to withstand the HAC puncture. As discussed in Section 2.7.3, the extent of package damage resulting from the HAC puncture test is limited to local deformation (i.e., denting) of the overpack outer shell. The puncture bar will not pierce the overpack outer shell or cause any significant damage to the bolted closure of the overpack assembly.

The cumulative damage of the overpack resulting from the HAC free drop and HAC puncture tests is considered in the HAC thermal evaluation presented in Section 3.4. The HAC thermal evaluation is performed for three separate bounding damage scenarios: bottom end impact damage, top end impact damage, and side impact damage. The extent of overpack damage assumed in the HAC thermal analysis bounds the effects of the cumulative damage that result from the HAC free drop and HAC puncture tests. The results of the HAC thermal evaluation demonstrate that the cumulative damage does not affect the overpack's ability to satisfy the performance requirements of 10 CFR 71.

*HAC Fire*

The package is subjected to the HAC thermal test of §71.73(c)(4), considering the damage sustained from the HAC free drop of §71.73(c)(1) and HAC puncture of §71.73(c)(3). The extent of package damage resulting from the HAC free drop and HAC puncture tests does not affect the package's ability to withstand the HAC thermal test. This is demonstrated by the HAC thermal evaluation, which considers the cumulative package damage resulting from the HAC free drop and HAC puncture tests. The overpack thermal relief plugs are designed to fail during the HAC thermal test to allow gases generated by the foam material to escape. The HAC thermal test will cause some charring to the outer portion of the overpack foam. However, the foam will provide sufficient thermal protection to prevent the cask temperatures from exceeding any of the cask component temperature limits. The structural evaluation of the package for the temperature and pressure loads resulting from the HAC thermal test shows that no additional damage of the cask and shield lid will result from the HAC thermal test. As discussed in Section 2.7.4.3, the cask closure bolts satisfy the applicable HAC allowable stress design criteria and will maintain leak-tight containment under the worst-case HAC thermal loading.

## 2.8 Accident Conditions for Air Transport of Plutonium

Not applicable.

## 2.9 Accident Conditions for Fissile Material Packages for Air Transport

Not applicable.

## 2.10 Special Form

Not applicable.

## 2.11 Fuel Rods

Not applicable.

# 2.12 Appendix

## 2.12.1 References

[2.1] American Society of Mechanical Engineers (ASME) Boiler and Pressure Vessel Code, Section III, Division 3, *Containment Systems for Storage and Transport Packagings of Spent Nuclear Fuel and High Level Radioactive Material and Waste*, 2001 Edition with Addenda through July 1, 2003.

[2.2] American Society of Mechanical Engineers (ASME) Boiler and Pressure Vessel Code, Section III, Division 1, Subsection NF, *Supports*, 2001 Edition with Addenda through July 1, 2003.

[2.3] Regulatory Guide 7.9, *Standard Format and Content of Part 71 Applications for Approval of Packages for Radioactive Material*, Revision 2, March 2005.

[2.4] Interim Staff Guidance – 21 (ISG-21), *Use of Computational Modeling Software*, U.S. Nuclear Regulatory Commission, Spent Fuel Project Office, April 2006.

[2.5] Regulatory Guide 7.8, *Load Combinations for the Structural Analysis of Shipping Casks for Radioactive Material*, Revision 1, U.S. Nuclear Regulatory Commission, Office of Standards Development, March 1989.

[2.6] American Society of Mechanical Engineers (ASME) Boiler and Pressure Vessel Code, Section III, Division 1, Appendix F, *Rules for Evaluation of Service Loadings with Level D Service Limits*, 2001 Edition with Addenda through July 1, 2003.

[2.7] American Society of Mechanical Engineers (ASME) Boiler and Pressure Vessel Code, Section III, Division 1, Code Cases: Nuclear Components, Case N-284-1, *Metal Containment Shell Buckling Design Methods, Class MC*, 2001 Edition with Addenda through July 1, 2003.

[2.8] American Society of Mechanical Engineers (ASME) Boiler and Pressure Vessel Code, Division 1, Appendix I, *Design Stress Intensity Values, Allowable Stresses, Material Properties, and Design Fatigue Curves*, 2001 Edition with Addenda through July 1, 2003.

[2.9] Regulatory Guide 7.11, *Fracture Toughness Criteria of Base Material for Ferritic Steel Shipping Cask Containment Vessels with a Maximum Wall Thickness of 4 Inch (0.1 m)*, U.S. Nuclear Regulatory Commission, Office of Standards Development, June 1991.

[2.10] Holman, W. R., and Langland, R. T., *Recommendations for Protecting Against Failure by Brittle Fracture in Ferritic Steel Shipping Containers Up to Four Inches Thick*, NUREG/CR-1815, UCRL-53013, U.S. Nuclear Regulatory Commission, August 1981.

[2.11] American Society of Mechanical Engineers (ASME) Boiler and Pressure Vessel Code, Section II, Part D, *Materials*, 2001 Edition with Addenda through July 1, 2003.

[2.12] Eckelmeyer, K. H., *An Investigation of the Mechanical Behavior of Cast U-2 wt. % Mo for Breeder Reactor Spent Fuel Shipping Cask–Radiation Shielding*, SANDIA Report SAND80-1836, February 1982.

[2.13] Regulatory Guide 7.6, *Design Criteria for the Structural Analysis of Shipping Cask Containment Vessels*, Revision 1, March 1978.

[2.14] Fischer, L. E., and Lai, W., *Fabrication Criteria for Shipping Containers*, NUREG/CR-3854, UCRL-53544, U.S. Nuclear Regulatory Commission, March 1985.

[2.15] Gerber, T. L., et. al., *Evaluation of High-Energy Pipe Rupture Experiments*, EPRI Report No. NP-5531, January 1988.

[2.16] General Plastics Manufacturing Co., Design Guide for Use of LAST-A-FOAM® FR-3700 for *Crash and Fire Protection of Radioactive Material Shipping Containers*, Revision iss001.

[2.17] American Society of Mechanical Engineers Boiler and Pressure Vessel Code, Section II, *Materials*, Part B, *Nonferrous Material Specifications*, 2001 Edition with Addenda through July 1, 2003.

[2.18] Parker Hannifin Corporation, *Parker O-Ring Handbook*, ORD 5700/USA, 2001.

[2.19] American Society of Mechanical Engineers Boiler and Pressure Vessel Code, Section II, *Materials*, Part A, *Ferrous Material Specifications*, 2001 Edition with Addenda through July 1, 2003.

[2.20] Penton Publications, *Materials Engineering, Materials Selector 1990*, December 1989.

[2.21] Weakley, E. A., *Fuels Engineering Technical Handbook*, UNI-M-61, April 1979.

[2.22] American Society of Mechanical Engineers (ASME) Boiler and Pressure Vessel Code, Section IX, *Welding and Brazing Qualifications.* Latest Edition.

[2.23] ANSI N14.23, *Design Basis for Resistance to Shock and Vibration of Radioactive Material Packages Greater Than One Ton in Truck Transport*, American National Standards Institute, Inc., New York, 1980.

[2.24] Blevins, R. D., *Formulas for Natural Frequency and Mode Shape*, Van Nostrand Reinhold Company, 1979.

[2.25] NUREG/CR-3966, *Methods for Impact Analysis of Shipping Containers*, UCID-20639, U. S. Nuclear Regulatory Commission, November 1987.

### 2.12.2 Computer Code Descriptions

The structural evaluation of the package includes analyses performed using the ANSYS/Mechanical and ANSYS LS-DYNA PC modules of the ANSYS Release 10.0 computer program. These programs are both run on a PC platform under the Windows XP operating system. Descriptions of the models used to perform the structural analyses are provided in the respective sections of this chapter. Descriptions of these computer codes are provided in this section and the sections that follow.

The ANSYS computer code is acquired from and supported by ANSYS Incorporated as a fully-compiled executable program. The ANSYS/Mechanical and ANSYS LS-DYNA PC modules of the ANSYS computer code are tested, installed, operated, and maintained in accordance with the requirements of the Energy*Solutions* QA program. Prior to use for quality-affecting work, several validation test problems are solved using the ANSYS ANSYS/Mechanical and LS-DYNA PC computer codes. The validation tests include a large number of test problems included in the ANSYS Verification Manual and other independent test problems with solutions that are known either by classical means or by comparison to computer solutions that have been reviews and accepted by Energy*Solutions*. The validation tests demonstrate that the computer codes correctly solve the general classes of problems for which they will be used.

Errors in the ANSYS computer codes are identified and controlled in accordance with the requirements of the Energy*Solutions* QA program. All errors that are discovered either internally or externally are reviewed for impact on past and present work, and potential impact on future work. Errors that are identified to have potential impact on work are evaluated using the Corrective Action Process of the Energy*Solutions* QA program.

#### 2.12.2.1 ANSYS Mechanical

The ANSYS/Mechanical computer code is an implicit finite element program that is used to solve a wide range of structural, heat transfer, and electromagnetic problems. The use of the ANSYS/Mechanical computer code for the structural analysis of the package is limited to mode-frequency analysis, and static structural analysis using linear-elastic material properties and non-linear contact behavior.

#### 2.12.2.2 ANSYS LS-DYNA PC

The ANSYS LS-DYNA PC computer code combines the LS-DYNA explicit finite element program with the pre- and post-processing modules of the ANSYS program. The ANSYS LS-DYNA PC computer code is well-suited to simulate short-duration, large deformation dynamic impacts and complex contact problems. The code has been well benchmarked and is widely used for the structural analysis of transportation package drop tests.

### 2.12.3 Dynamic Load Factors

The stresses in the cask and shield lid due to NCT and HAC free drop loading are calculated using equivalent-static linear-elastic finite element analyses. The equivalent-static acceleration loads for each NCT and HAC free drop test are equal to the peak rigid-body accelerations of the cask multiplied by a DLF that accounts for possible dynamic amplification within the cask. The DLF is a function of the general shape of the rigid-body acceleration time-history pulse and the ratio of the duration of the rigid-body acceleration time-history to the cask period (t/T).

The longitudinal vibration modes of the cask that are of interest for the NCT and HAC free drop analyses include the axial compression/extension mode of the cask's outer shell and the plate bending mode of the closure lid.

The natural frequency of the cask's outer shell in compression is determined using classical hand calculations. The cask's outer shell is idealized as a linear spring with the bottom end fixed and a mass attached to the top end. The mass supported by the outer shell is equal to the total mass of cask assembly, less the mass of the cask-body DU shields and the cask's bottom plate, or 48.4 kg. The natural frequency of the cask's outer shell in compression is calculated using case 1 in Table 6-2 of Blevins [2.24] to be 1,121 Hz based on the nominal design dimensions and the elastic modulus of the cask's outer shell material at a bounding temperature of 93°C. This corresponds to a closure-lid natural period (T) of 0.000892 seconds.

The natural frequency of the closure lid in bending is determined using classical hand calculations. The closure plate is idealized as a 19 mm thick circular plate having a clamped edge at the bolt circle radius and a 15.3 kg point mass (i.e., the mass of shield plug and payload) at its center. The lowest natural frequency of the closure plate is calculated using case 12 in Table 11-1 of Blevins [2.24] to be 1,066 Hz based on the elastic modulus of the cask closure lid material at a bounding temperature of 93°C. This corresponds to a closure-lid natural period (T) of 0.000938 seconds.

The transverse vibration mode of the cask that is of interest for the NCT and HAC free drop analyses is the cantilever beam bending mode of the cask's inner containment shell. A finite element modal analysis of the cask is performed to determine the natural frequency of the cask for the inner-shell cantilever bending mode. The 3-D half-symmetry finite element model used for this analysis is shown in Figure 2-37. This model is essentially the same as the 3-D half-symmetry finite element model that is used for the detailed stress analysis of the cask assembly for those conditions that include transverse loading. The main difference between the two models are that the model used for the modal analysis does not include the shield lid assembly and that the nonlinear contact elements, which are not permitted for modal analyses, are deleted from the model. Instead, coupled nodes and displacement constraints are applied to the model to account for the expected boundary conditions under transverse impact loading conditions. The results of the analysis show that the natural frequency of the cask for the inner shell cantilever bending mode shown in Figure 2-38 is 897 Hz (i.e., T = 0.001115 s).

The general shape of the rigid-body acceleration time-history curve for all NCT and HAC free drop tests are characterized as a half-sine wave. The DLF for a half-sine wave pulse is shown in Figure 2.15 of NUREG/CR-3966 [2.25]. It shows that the DLF curve for a half-sine wave peaks at a maximum value of approximately 1.75 at t/T equal to 0.8 and reduces to 1.13 for t/T ratios of 2.5 and higher. Thus, the highest DLF results from the shortest acceleration time-history pulse duration and the longest natural period (i.e., the lowest natural frequency) of the cask. The NCT and HAC oblique drop acceleration time-histories have the shortest durations for all free drops at approximately 0.0035 seconds. Using the lowest natural frequency of the cask of 897 Hz (T = 0.001115 s) yields the lowest t/T ratio of 3.1 for all NCT and HAC free drop tests. Thus, a bounding DLF of 1.13 is conservatively used for all NCT and HAC free drop evaluations. The only exception to this is for the HAC end drop orientations, for which the shortest acceleration time-history pulse duration is approximately 0.004 seconds and the lowest longitudinal response frequency is 1,066 Hz, yielding a lower bound t/T ratio of 4.3. Based on the Figure 2.15 of NUREG/CR-3966 [2.25], the DLF for a t/T ratio of 4.3 is less than 1.1.

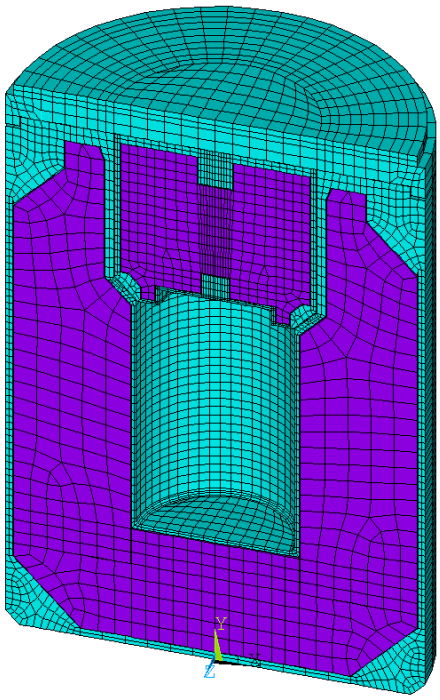


**Figure 2-37 – MIDUS Cask Modal Analysis FE Model**

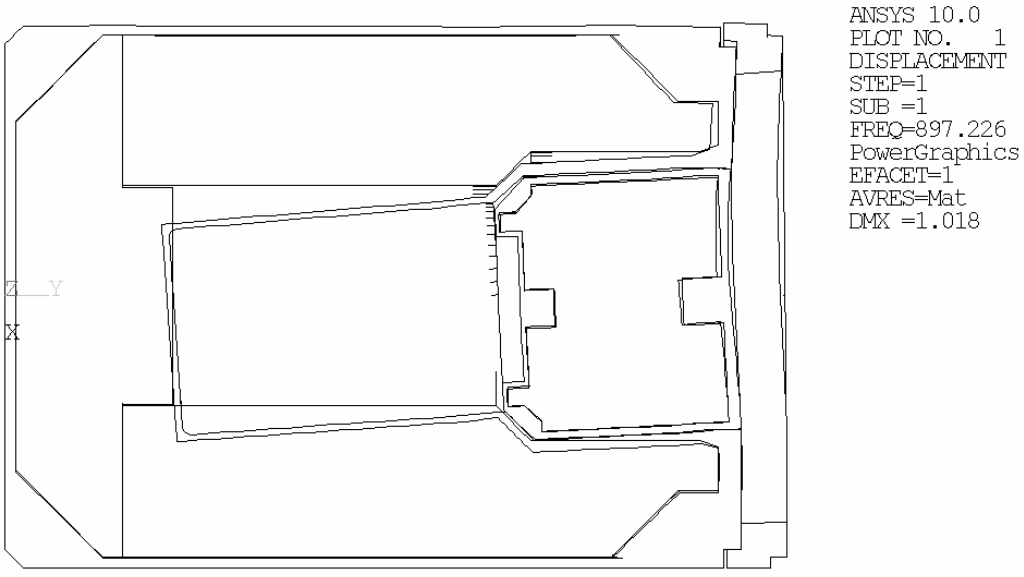


**Figure 2-38 – Cask Body Containment Shell Cantilever Bending Mode Shape**

## 2.12.4 Confirmatory Tests

### 2.12.4.1 Confirmatory Test Report

This section includes the confirmatory test report that provides a summary of the confirmatory testing performed to demonstrate the adequacy of the analytical methodologies used to predict the structural and thermal response of the package for the NCT free drop, HAC free drop, HAC puncture, and HAC thermal tests. The results of the confirmatory tests are summarized and compared to pre-test predictions determined using the same analytical methodology as the safety analyses. In general, the results of the confirmatory tests show good agreement with the pre-test predictions. In those instances where the test conditions deviated from the test plan or significant differences existed between the test results and the pre-test predictions, a reconciliation analysis was performed. The confirmatory drop test reconciliation analysis is included in Section 2.12.4.2.

(Attachment: Report No. TYC01.1071, Revision 0, *MIDUS Transportation Package Confirmatory Test Report*)

BNG Fuel Solutions

TYC01.1071
Revision 0
October 20, 2006

# MIDUS Transportation Package
# Confirmatory Test Report

Prepared by:

BNG Fuel Solutions Corporation
Campbell, CA

Prepared for:

Mallinckrodt Medical, B.V
P.O. # IWOR-5001

Prepared by: Digitally signed by Carl H. Froehlich
Reason: I am the author of this document
Date: 2006.10.20 16:16:19 -07'00'

Checked by: Digitally signed by William H. Borter
Reason: I am the checker of this document
Date: 2006.10.20 16:22:34 -07'00'

Approved by: Digitally signed by Ram Srinivasan
Reason: approving for RDQ
Date: 2006.10.20 16:31:45 -07'00'

Manager of Operations

© 2006 BNG Fuel Solutions Corporation
All Rights Reserved

## Revision Record

| Revision | Change Description |
|---|---|
| 0 | Initial issue. |

BNG Fuel Solutions

Table of Contents

Page

1 Introduction ..... 1

2 Design vs. Test Article Configuration ..... 4

2.1 Production Unit vs. Test Article Configuration ..... 4

2.2 Production Unit vs. As-built Test Article Configuration ..... 4

3 Test Sequences ..... 11

3.1 Test 1A – NCT Bottom End Drop ..... 14

3.2 Test 1B – HAC Top End Drop ..... 14

3.3 Test 1C – HAC CG-Over-Top Corner Drop ..... 14

3.4 Test 1D – HAC Bottom End Oblique Puncture Drop ..... 15

3.5 Test 2A – HAC Side Drop ..... 19

3.6 Test 2B – HAC Side Puncture Drop ..... 19

3.7 Test 2C – HAC Thermal ..... 19

4 Proposed vs. Actual Test Characterization ..... 24

4.1 Drop Test Components/Facility ..... 24

4.2 Environmental Test Conditions ..... 24

4.3 Furnace Characterization ..... 24

5 Test Predictions ..... 30

5.1 Tests 1A through 2B ..... 30

5.2 Test 2C ..... 30

6 Test Results ..... 40

6.1 Tests 1A through 2B ..... 40

6.2 Test 2C ..... 40

7 Summary and Conclusions ..... 64

7.1 Summary of Results ..... 64

7.2 Summary of Significant Deviations and Conclusions ..... 66

8 References ..... 69

Appendix A – Supplemental Test 3X ..... A.0

BNG Fuel Solutions

List of Tables

Page

Table 1 – Overpack and Cask Assembly Weights (Mass) ..... 6

Table 2 - Overpack Base and Lid Assembly Shell Thicknesses ..... 7

Table 3 - Foam Properties ..... 8

Table 4 – Design vs. Test Article Manufacturing Discrepancies ..... 10

Table 5 – Test Sequences ..... 11

Table 6 – Required Instrumentation ..... 12

Table 7 - Puncture Pin Requirements for Tests 1D and 2B ..... 25

Table 8 - Drop Test Pad Requirements for Tests 1A through 2B ..... 26

Table 9 – Environmental Test Conditions ..... 27

Table 10 – Furnace Characterization Requirements ..... 28

Table 11 – Maximum Predicted Deformation Magnitudes ..... 31

Table 12 – Maximum Predicted Acceleration Magnitudes ..... 31

Table 13 – Maximum Predicted Peak Thermocouple Readings ..... 37

Table 14 – Maximum Predicted Peak Temperature-Indicating Strip Readings ..... 37

Table 15 – Actual Post-Test Deformation Measurements (mm) ..... 41

BNG Fuel Solutions

List of Figures

Page

Figure 1 – Overpack Assembly Component Configurations and Designations ..... 2
Figure 2 – Cask Assembly Component Configurations and Designations ..... 3
Figure 3 – Instrumentation Locations ..... 13
Figure 4 – Confirmatory Drop Test Sequence 1 Configurations ..... 15
Figure 5 – NCT Bottom End Drop Measurements ..... 17
Figure 6 – HAC Top End Drop Measurements ..... 17
Figure 7 - HAC CG Over Top Corner Drop Measurements ..... 18
Figure 8 – Confirmatory Drop Test Sequence 2 Configurations ..... 20
Figure 9 – HAC Side Drop Measurements ..... 21
Figure 10 – Test 2C Thermocouple Readings ..... 29
Figure 11 – Test 1A Predicted Overpack Permanent Deformation ..... 32
Figure 12 – Test 1B Predicted Overpack Permanent Deformation ..... 32
Figure 13 – Test 1C Predicted Overpack Permanent Deformation ..... 33
Figure 14 – Test 1D Predicted Overpack Permanent Deformation ..... 33
Figure 15 – Test 2A Predicted Overpack Permanent Deformation ..... 34
Figure 16 – Test 2B Predicted Overpack Permanent Deformation ..... 34
Figure 17 – Test 1A Predicted Acceleration Time-History ..... 35
Figure 18 – Test 1B Predicted Acceleration Time-History ..... 35
Figure 19 – Test 1C Predicted Acceleration Time-History ..... 36
Figure 20 – Test 2A Predicted Acceleration Time-History ..... 36
Figure 21 – Test 2C Predicted Temperature Distribution at End of Furnace Heating ..... 38
Figure 22– Test 2C Predicted Time-Dependent Thermocouple Temperature Trace ..... 39
Figure 23 – Test 1A Actual Acceleration Time History ..... 42

List of Figures

Page

Figure 24 – Test 1B Actual Acceleration Time History ..... 42

Figure 25 – Test 1C Actual Acceleration Time History (Longitudinal - Y) ..... 43

Figure 26 – Test 1C Actual Acceleration Time History (Transverse - X)..... 43

Figure 27 – Test 2A Actual Acceleration Time History (Longitudinal - Y) ..... 44

Figure 28 – Test 2A Actual Acceleration Time History (Transverse - X) ..... 44

Figure 29 – Test 2C TCs #1 & #3 Time-Temperature Traces..... 45

Figure 30 – Test 2C TCs #2 & #4 Time-Temperature Traces..... 45

Figure 31 – Test 2C TCs #5 & #6 Time-Temperature Traces..... 46

Figure 32 – Test 2C TCs #7 & #8 Time-Temperature Traces..... 46

BNG Fuel Solutions

List of Photographs

Page

Photograph 1 – Test 1A NCT Bottom End Drop Set-up ..... 16

Photograph 2 – Test 1B HAC Top End Drop Set-up ..... 16

Photograph 3 – Test 1C HAC CG-Over-Top Corner Drop Set-up..... 16

Photograph 4 – Test 1D HAC Bottom End Oblique Puncture Drop Set-up..... 16

Photograph 5 – Test 2A HAC Side Drop Set-up ..... 22

Photograph 6 – Test 2B HAC Side Puncture Drop Set-up ..... 22

Photograph 7 – Test 2C HAC Thermal Set-up Outside Furnace..... 23

Photograph 8 – Test 2C HAC Thermal Set-up Inside Furnace ..... 23

Photograph 9 – Test 2C HAC Thermal Heating..... 23

Photograph 10 – Test 2C Cooldown..... 23

Photograph 11 – Test 1A Post-Drop Condition (View 1)..... 47

Photograph 12 – Test 1A Post-Drop Condition (View 2)..... 47

Photograph 13 – Test 1B Post-Drop Condition (View 1)..... 48

Photograph 14 – Test 1B Post-Drop Condition (View 2)..... 48

Photograph 15 – Test 1C Post-Drop Condition (View 1)..... 49

Photograph 16 – Test 1C Post-Drop Condition (View 2)..... 49

Photograph 17 – Test 1D Overpack Post-Drop Condition (View 1)..... 50

Photograph 18 – Test 1D Puncture Pin Post-Drop Condition (View 2)..... 50

Photograph 19 – Test 2A Post-Drop Condition (View 1)..... 51

Photograph 20 – Test 2A Post-Drop Condition (View 2)..... 51

Photograph 21 – Test 2B Post-Drop Condition (View 1)..... 52

Photograph 22 – Test 2B Post-Drop Condition (View 2)..... 52

Photograph 23 – Test 2C Post-Test Condition (View 1)..... 53

BNG Fuel Solutions

List of Photographs

Page

Photograph 24 – Test 2C Post-Test Condition (View 2) ..... 53
Photograph 25 – Test 2C Post-Test Condition (View 3) ..... 54
Photograph 26 – Test 2C Post-Test Condition (View 4) ..... 54
Photograph 27 – Test 2C Post-Test Condition (View 5) ..... 55
Photograph 28 – Test 2C Post-Test Condition (View 6) ..... 55
Photograph 29 – Test 2C Post-Test Condition (View 7) ..... 56
Photograph 30 – Test 2C Post-Test Condition (View 8) ..... 56
Photograph 31 – Test 2C Post-Test Condition (View 9) ..... 57
Photograph 32 – Test 2C Post-Test Condition (View 10) ..... 57
Photograph 33 – Test 2C Post-Test Condition (View11) ..... 58
Photograph 34 – Test 2C Post-Test Condition (View 12) ..... 58
Photograph 35 – Test 2C Post-Test Condition (View 13) ..... 59
Photograph 36 – Test 2C Post-Test Condition (View 14) ..... 59
Photograph 37 – Test 2C Post-Test Condition (View 15) ..... 60
Photograph 38 – Test 2C Post-Test Condition (View 16) ..... 60
Photograph 39 – Test 2C Post-Test Overpack Base Foam Condition (View 1) ..... 61
Photograph 40 – Test 2C Post-Test Overpack Base Foam Condition (View 2) ..... 61
Photograph 41 – Test 2C Post-Test Overpack Base Foam Condition (View 3) ..... 62
Photograph 42 – Test 2C Post-Test Overpack Base Foam Condition (View 4) ..... 62
Photograph 43 – Test 2C Post-Test Overpack Lid Foam Condition (View 1) ..... 63
Photograph 44 – Test 2C Post-Test Overpack Lid Foam Condition (View 2) ..... 63
Photograph 45 – Test 2C Post-Test Overpack Lid Foam Condition (View 3) ..... 63
Photograph 46 – TC #4 vs. Foam Vent Hole Location ..... 68

BNG Fuel Solutions

List of Photographs

Page

Photograph 47 – TC #2 vs. Foam Vent Hole Location..... 68

Photograph 48 – Test 1C Post-Drop Inspection (View 1)..... A.3

Photograph 49 – Test 1C Post-Drop Inspection (View 2)..... A.3

Photograph 50 – Test 1C Post-Drop Inspection (View 3)..... A.4

Photograph 51 – Test 1C Post-Drop Inspection (View 4)`..... A.4

Photograph 52 – Test 1C Post-Drop Inspection (View 5)..... A.5

Photograph 53 – Test 1C Post-Drop Inspection (View 6)..... A.5

Photograph 54 – Supplemental Drop Test Implementation (View 1)..... A.6

Photograph 55 – Supplemental Drop Test Implementation (View 2)..... A.6

Photograph 56 – Supplemental Post-Drop Test Inspection (View 1)..... A.7

Photograph 57 – Supplemental Post-Drop Test Inspection (View 2)..... A.7

Photograph 58 – Supplemental Post-Drop Test Inspection (View 3)..... A.8

Photograph 59 – Supplemental Post-Drop Test Inspection (View 4)..... A.9

Photograph 60 – Supplemental Post-Drop Test Inspection (View 5)..... A.9

Photograph 61 – Supplemental Post-Drop Test Inspection (View 6)..... A.10

Photograph 62 – Supplemental Post-Drop Test Inspection (View 7)..... A.10

# 1 Introduction

BNG Fuel Solutions Corporation (BFS) is designing and licensing a new transportation package, called the Medical Isotope Depleted Uranium Shielded (MIDUS) transportation package, in accordance with the requirements of 10CFR71 (Reference 1). Evaluation-by-Analysis has been used to demonstrate the performance of the package for the Normal Conditions of Transport (NCT) and Hypothetical Accident Condition (HAC) tests of 10CFR71. In order to provide confirmation of the adequacy and accuracy of the analytical methodology used for the package evaluation, confirmatory tests have been performed for selected NCT and HAC test conditions using a full-scale MIDUS confirmatory test package, consisting of a MIDUS cask, shield lid, overpack base, overpack lid, dummy payload, and all associated package hardware. Confirmatory tests of a full-scale MIDUS transportation test package have not been performed for those NCT and HAC test conditions that are not expected to challenge the design (e.g., water spray, compression, penetration, crush, and immersion.) This report compares the results of the confirmatory tests with pre-test predictions determined using the same methodology employed in the safety evaluation to achieve this objective.

The general configuration of the MIDUS Transportation Package Overpack and Cask Assemblies are provided in Figure 1 and Figure 2. The confirmatory test article design and preparation of the confirmatory test specification and plan were the responsibility of BFS. The confirmatory testing was performed by the overpack and cask assembly fabricator, Manufacturing Sciences Corporation (MSC) of Oak Ridge, Tennessee, utilizing subcontracted facilities, qualified personnel, and certified equipment at the Southwest Research Institute (SwRI) in San Antonio, Texas, through Century Industries of Bristol, Virginia.

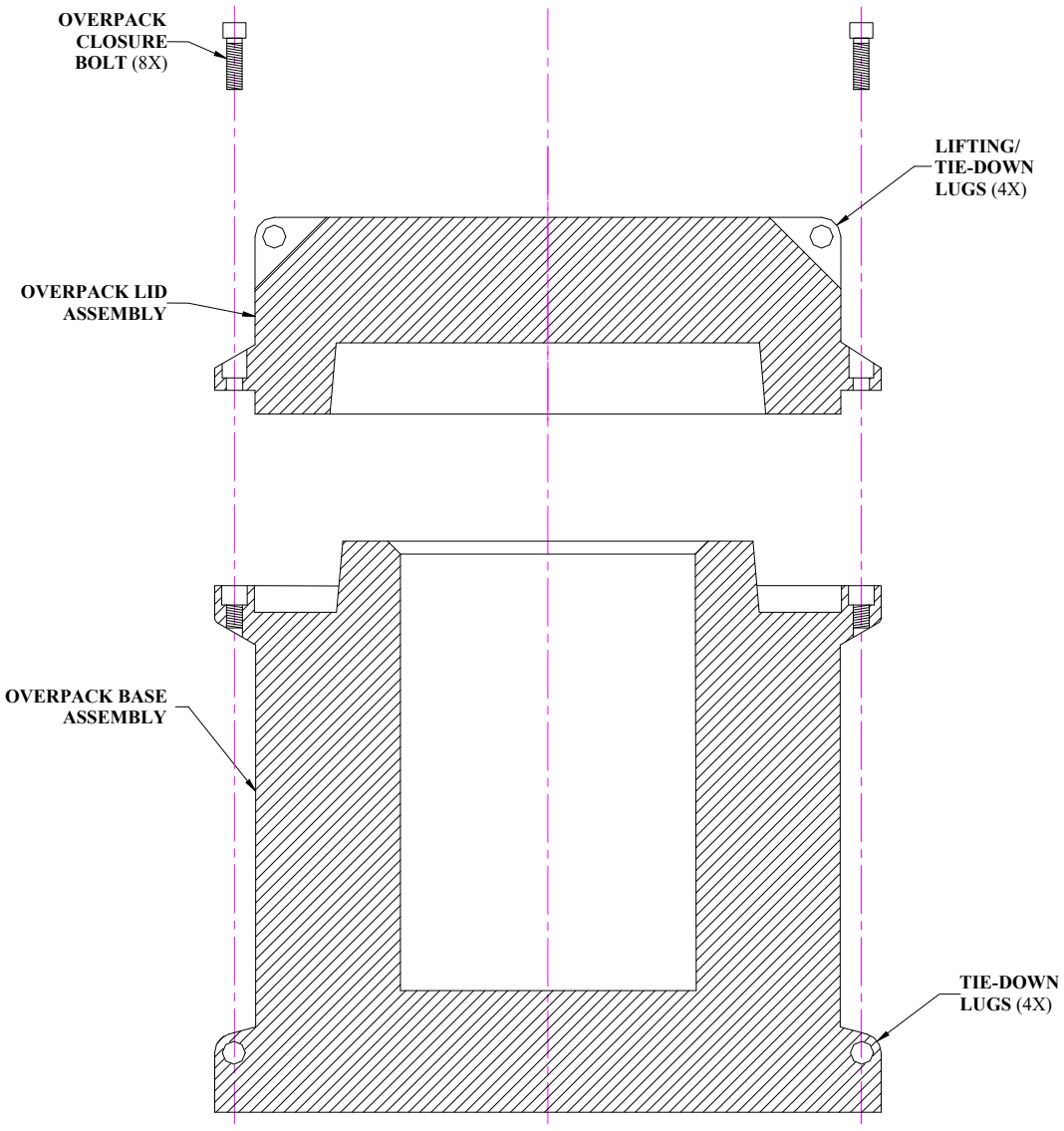


Figure 1 – **Overpack Assembly Component Configurations and Designations**

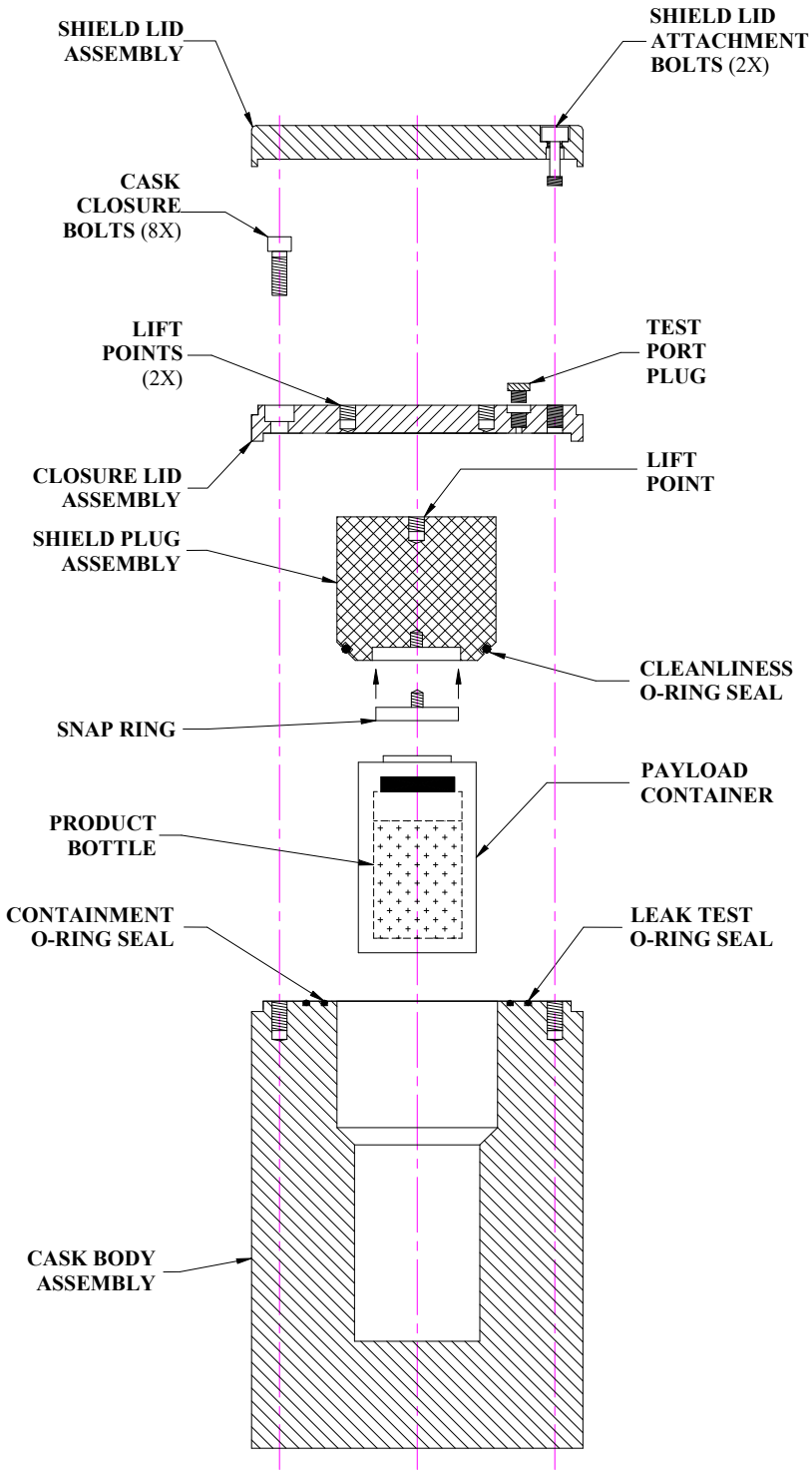


Figure 2 – **Cask Assembly Component Configurations and Designations**

# 2 Design vs. Test Article Configuration

## 2.1 Production Unit vs. Test Article Configuration

The test articles used in the confirmatory tests were full-scale versions of the MIDUS transportation package and only differ from the transportation package in the following ways to facilitate performance of the confirmatory test.

### 2.1.1 Cask Assembly

To accommodate the placement of accelerometer cables within the volume envelope of the cask body assembly, cable routing grooves and accelerometer cavities were machined into the outside surface of the cask assembly body as shown in the Reference 15 confirmatory test cask assembly drawing. The accelerometers were held in place using dental cement and their associated cables were held in place using duct tape. The cask assembly closure lid and bolts, shield plug, containment, leak test, and cleanliness O-rings, and dummy payload (i.e., the payload container and product bottle) were not modified for the confirmatory tests.

### 2.1.2 Overpack Assembly

To accommodate the placement of accelerometer and thermocouple cables on the cask body assembly, the overpack base assembly was modified to accommodate two instrumentation cable bulkheads as shown in the Reference 14 confirmatory test package assembly drawing and its associated component drawings. The cable access tubes running from the upper flange inner cavity bulkhead to the outer shell disc bulkhead were attached to the bulkheads with sealant to prevent the leakage of foam through these junctions during overpack assembly foam pouring operations. The overpack assembly lid and closure bolts and the cask shield lid assembly were not modified for the confirmatory tests.

## 2.2 Production Unit vs. As-built Test Article Configuration

Of the various characteristics of the MIDUS Transportation Package design versus test article configuration/material properties that could affect the confirmatory test results, the weight of the overpack and cask assemblies, the thickness of the overpack base and lid assembly inner and outer shells, and the properties of the polyurethane foam used to fill the overpack base and lid assemblies are considered the most important and are addressed in this section. This section also identifies and addresses manufacturing discrepancies encountered during the fabrication of the test articles relative to the proposed design.

### 2.2.1 Overpack and Cask Assembly Weights

Table 1 presents the design versus actual weights of the overpack and cask assembly components. The three (3) overpack base (OB) and overpack lid (OL) assemblies (OB1/OL1, OB2/OL2, and OB3/OL3) are 5 to 7 percent heavier than their design weight. The two (2) cask assemblies (M01 and M02) are less than 3% heavier than their design weight. These design versus actual weight differences were considered acceptable for the purposes of the confirmatory test.

### 2.2.2 Overpack Base and Lid Assembly Shell Thicknesses

Table 2 presents the design versus actual thicknesses of the overpack base and lid assembly inner and outer shells. All of these thicknesses are within their established fabrication tolerances and, therefore, were considered acceptable for the purposes of the confirmatory test.

### 2.2.3 Overpack Base and Lid Foam Properties

Table 3 presents the design versus actual density, static crush strength, and flame retardancy/intumescence properties of the polyurethane foam used to fill the overpack base and lid assemblies. All of the actual properties comply with the design requirements for this polyurethane foam and, therefore, were considered acceptable for the purposes of the confirmatory test.

### 2.2.4 Test Article Manufacturing Nonconformances

Table 4 presents design versus actual discrepancies in the manufacturing of the test articles. These discrepancies consisted of out-of-tolerance dimensions and material deviations which do not affect the form, fit, or function of the test articles. All of these discrepancies were considered acceptable for the purposes of the confirmatory test.

Table 1 – **Overpack and Cask Assembly Weights (Mass)**

| Component | | Weight (kg) | | |
|---|---|---|---|---|
| | | Design | Allowable Range[1] | Actual[2] |
| Overpack Lid (OL) 1 | | 34.7[3] | 33.8 - 35.6 | 36.9 |
| Overpack Base (OB) 1 | | 80.5[4] | 78.5 – 82.5 | 86.4 |
| Overpack 1 Total | | 115.2 | 112.3 -118.1 | 123.3 |
| OL2 | | 34.7[3] | 33.8 - 35.6 | 36.0 |
| OB2 | | 80.5[4] | 78.5 – 82.5 | 85.3 |
| Overpack 2 Total | | 115.2 | 112.3 -118.1 | 121.3 |
| OL3 | | 34.7[3] | 33.8 - 35.6 | 36.5 |
| OB3 | | 80.5[4] | 78.5 – 82.5 | 85.4 |
| Overpack 3 Total | | 115.2 | 112.3 -118.1 | 121.9 |
| M01: | Cask Body | 167.2[5] | 163.0 – 171.4 | 173.6 |
| | Shield Plug | 13.8[6] | 13.5 – 14.1 | 13.5 |
| | Closure Lid | 5.8[7] | 5.7 – 5.9 | 5.7 |
| | Shield Lid | 13.6[8] | 13.3 – 13.9 | 13.3 |
| | Total | 200.4 | 195.5 – 205.3 | 206.1 |
| M02: | Cask Body | 167.2[5] | 163.0 – 171.4 | 171.2 |
| | Shield Plug | 13.8[6] | 13.5 – 14.1 | 13.6 |
| | Closure Lid | 5.8[7] | 5.6 – 5.9 | 5.7 |
| | Shield Lid | 13.6[8] | 13.3 – 13.9 | 13.2 |
| | Total | 200.4 | 195.5 – 205.3 | 203.7 |

**Notes:**

(1) From Reference 3, Table 3 (i.e., ± 2.5%).
(2) From Reference 21 (MSC Quality Test Plan (Functional Tests) No. 1302006.03.02-FT (T1), dated 9/2/06).
(3) From Reference 19.
(4) From Reference 17.
(5) From Reference 16.
(6) From Reference 7.
(7) From Reference 8.
(8) From Reference 9.

Table 2 - **Overpack Base and Lid Assembly Shell Thicknesses**

| Component | Thickness (mm) | | | |
|---|---|---|---|---|
| | Inner Shell | | Outer Shell | |
| | Design | Actual | Design | Actual |
| Overpack Lid (OL) 1 | 2.7 – 3.3[(1)] | 2.9[(2)] | 5.5 – 6.5[(3)] | 5.9[(4)] |
| Overpack Base (OB) 1 | 2.7 – 3.3 [(5)] | 3.0[(6)] | 5.5 – 6.5 [(7)] | 6.3 [(8)] |
| OL2 | 2.7 – 3.3 [(1)] | 2.9[(2)] | 5.5 – 6.5 [(3)] | 6.5[(4)] |
| OB2 | 2.7 – 3.3 [(5)] | 3.0[(6)] | 5.5 – 6.5 [(7)] | 6.3 [(8)] |
| OL3 | 2.7 – 3.3 [(1)] | 2.9[(2)] | 5.5 – 6.5 [(3)] | 6.5[(4)] |
| OB3 | 2.7 – 3.3 [(5)] | 2.9[(6)] | 5.5 – 6.5 [(7)] | 6.3 [(8)] |

**Notes:**

(1) From Reference 12.
(2) From Reference 21 (MSC Quality Inspection Plan (QIP) No. 1302006.03.02-63, Completion Date: 7/31/06).
(3) From Reference 11.
(4) From Reference 21 (MSC QIP No. 1302006.03.02-62, Completion Date: 7/27/06).
(5) From Reference 10.
(6) From Reference 21 (MSC QIP No. 1302006.03.02-55, Completion Date: 7/22/06).
(7) From Reference 18.
(8) From Reference 21 (MSC QIP No. 1302006.03.02-53, Completion Date: 7/27/06).

Table 3 - **Foam Properties**

| **Average Foam Density** (pcf) | | |
|---|---|---|
| **Specimen** | **Design**[1] | **Actual** |
| Parallel | 12.3 to 14.9 | 13.28[2] |
| Perpendicular | | 13.27[3] |

| **Individual Specimen Foam Density** (pcf) | | |
|---|---|---|
| **Specimen** | **Design**[1] | **Actual** |
| Parallel | 11.7 to 15.5 | 13.21[2] |
| | | 13.23[2] |
| | | 13.46[2] |
| | | 13.29[2] |
| | | 13.22[2] |
| Perpendicular | | 13.29[3] |
| | | 13.09[3] |
| | | 13.23[3] |
| | | 13.41[3] |
| | | 13.34[3] |

| | **Average Static Crush Strength** (psi) | | | |
|---|---|---|---|---|
| | **Parallel-to-Rise** | | **Perpendicular-to-Rise** | |
| **Strain** | **Design**[1] | **Actual**[2] | **Design**[1] | **Actual**[3] |
| 10% | 422 - 510 | 494 | 429 - 519 | 494.9 |
| 30% | 455 - 550 | 541.3 | 476 - 576 | 552.1 |
| 50% | 632 - 765 | 744.1 | 667 - 807 | 768.8 |

Table 3 - **Foam Properties**
(concluded)

| Strain | Individual Specimen Static Crush Strength (psi) | | | |
|---|---|---|---|---|
| | Parallel-to-Rise | | Perpendicular-to-Rise | |
| | Design[1] | Actual[2] | Design[1] | Actual[3] |
| 10% | 403 - 534 | 488.8 | 410 - 543 | 496.1 |
| | | 488.9 | | 478.7 |
| | | 506.5 | | 498.4 |
| | | 496.3 | | 504.1 |
| | | 489.5 | | 497.0 |
| 30% | 436 – 575 | 535.5 | 456 - 603 | 556.7 |
| | | 536.3 | | 537.6 |
| | | 556.5 | | 553.0 |
| | | 542.6 | | 560.0 |
| | | 535.5 | | 553.3 |
| 50% | 604 - 799 | 735.1 | 638 - 844 | 779.2 |
| | | 741.0 | | 751.3 |
| | | 765.3 | | 764.5 |
| | | 743.6 | | 780.5 |
| | | 735.5 | | 768.4 |

| Property | Other Foam Properties | |
|---|---|---|
| | Requirement [1] | Actual[4] |
| Flame Retardancy | Foam shall not sustain a flame for a period > 15 seconds following the removal of a 1,500°F (min.) flame applied to the foam for ≥ 60 sec | 0.72 sec. |
| Intumescence | ≥ 100% | 252.76 |

**Notes:**

(1) From Reference 13.

(2) From Reference 21 (General Plastics Manufacturing Company Data Sheet; Sample ID: FR-3714, MIDUS, Batch Approval, parn (8-25-06) mss; Method: Load Deflection to 65% @ 10%, 30%, 50% msm; Test Date: 8/25/06).

(3) From Reference 21 (General Plastics Manufacturing Company Data Sheet; Sample ID: FR-3714, MIDUS, Batch Approval, perp (8-25-06) mss; Method: Load Deflection to 65% @ 10%, 30%, 50% msm; Test Date: 8/25/06).

(4) From Reference 21 (General Plastics Manufacturing Company Flammability Test Report (Nuclear) #060824-08R, Test Date: 8/24/06).

Table 4 – **Design vs. Test Article Manufacturing Discrepancies**

| CAQR* No. | Discrepancy Description | Disposition |
|---|---|---|
| 2006-10 | ER308L rather than ER309L weld wire used for root pass of all overpack lid weld joints. | Accepted As-Is |
| 2006-16 | Some dimensions of the overpack inner bulkhead (not part of overpack production units) are out-of-tolerance. | Accepted As-Is |
| 2006-22 | The density of depleted uranium for some components was measured as 18.61, 18.53, and 18.51 g/cc. Minimum required density is 18.65 g/cc. | Accepted As-Is |
| 2006-23 | Some thermal spider dimensions are slightly out-of-tolerance. | Accepted As-Is |
| 2006-25 | Some overpack lid lifting lugs are slightly out-of-tolerance relative to tear-out ligament thickness. | Accepted As-Is |
| 2006-26 | Two mislocated, but weld-repaired foam vent holes in Overpack Lid (OL) 5. | OL5 Not Used |
| 2006-28 | a) Flatness and perpendicularity of some overpack base outer bottom components are slightly out-of-tolerance.<br>b) Height of a overpack base flange slightly out-of-tolerance. | Accepted As-Is<br>Accepted As-Is |
| 2006-33 | Some dimensions of the overpack inner bulkhead opening (not part of production units) are slightly out-of-tolerance. | Accepted As-Is |
| 2006-34 | Some dimensions of a cask shield plug assembly are slightly out-of-tolerance. | Accepted As-Is |
| 2006-35 | Some dimensions of a cask upper flange are slightly out-of-tolerance. | Accepted As-Is |

* CAQR = MSC Condition Adverse to Quality Report (from Reference 21).

# 3 Test Sequences

As shown in Table 5, two separate test sequences were performed for the confirmatory test as described below:

Test Sequence #1: Included four separate independent confirmatory drop tests. These included an NCT free drop, two HAC free drops, and an HAC puncture drop. During this test sequence, the cask interior surfaces were inspected and measured and, as needed, damaged overpack lid and base assemblies were replaced between drops.

Test Sequence #2: Included sequential application of the HAC free drop, HAC puncture drop, and HAC thermal tests to the same test specimen, in accordance with the requirements of 10CFR71.73(c). The package was not disassembled during this test sequence for inspection and measurement of the package interior surfaces since cumulative damage is of primary interest and removing the overpack lid mid-sequence would have disturbed the package and possibly invalidated subsequent tests in the sequence.

Table 5 – **Test Sequences**

| Sequence Number | Test Number | Test Description | Test Articles (Cask/Base/Lid) | Test Objectives |
|---|---|---|---|---|
| 1 | 1A | NCT Bottom End Drop | M01/OB1/OL1 | Confirm cask peak accelerations, overpack deformations, and structural adequacy of the overpack shells and attachment bolts. |
| | 1B | HAC Top End Drop | M01/OB1/OL1 | |
| | 1C | HAC Top Corner Drop | M02/OB2/OL2 | |
| | 1D | HAC Bottom Puncture Drop | M02/OB2/OL2 | |
| 2 | 2A | HAC Side Drop | M01/OB3/OL3 | Confirm cask peak accelerations, overpack deformations, and structural adequacy of the overpack shells and attachment bolts. |
| | 2B | HAC Side Puncture Drop | M01/OB3/OL3 | |
| | 2C | HAC Thermal | M01/OB3/OL3 | Confirm package peak temperatures, foam performance, and containment seal leak rate. |

Table 6 and Figure 3 present the type and location of instrumentation utilized during the confirmatory test.

Table 6 – **Required Instrumentation**
(from Reference 4)

| Detector I.D.[1] | Instrumentation Required for Confirmatory Tests[2] | | | | | | |
|---|---|---|---|---|---|---|---|
| | 1A | 1B | 1C | 1D | 2A | 2B | 2C |
| **Accelerometers** | | | | | | | |
| AX[3] | O | O | R | | R | | |
| AZ[3] | R | R | R | | R | | |
| BX[3] | O | O | R | | R | | |
| BZ[3] | R | R | R | | R | | |
| CX[3] | O | O | R | | R | | |
| CZ[3] | R | R | R | | R | | |
| DX[3] | O | O | R | | R | | |
| DZ[3] | R | R | R | | R | | |
| **Thermocouples** | | | | | | | |
| T1 | | | | | | | R |
| T2 | | | | | | | R |
| T3 | | | | | | | R |
| T4 | | | | | | | R |
| T5 | | | | | R [4] | R [4] | R |
| T6 | | | | | R [4] | R [4] | R |
| T7 | | | | | | | R |
| T8 | | | | | | | R |
| **Temperature-Indicating Strips** | | | | | | | |
| S1 | | | | | R [4] | R [4] | R |
| S2 | | | | | R [4] | R [4] | R |
| S3 | | | | | R [4] | R [4] | R |
| S4 | | | | | R [4] | R [4] | R |

**Notes:**

1. See Figure 3 for approximate locations of instrumentation.
2. Legend: R = Required, O = Optional.
3. The "X" suffix indicates acceleration measurement in the package radial direction in a vertical plane. The "Z" suffix indicates acceleration measurement along the longitudinal axis of the package.
4. Thermocouples and temperature-indicating strips were installed prior to Test 2A, but were not connected to the data acquisition system until Test 2C.

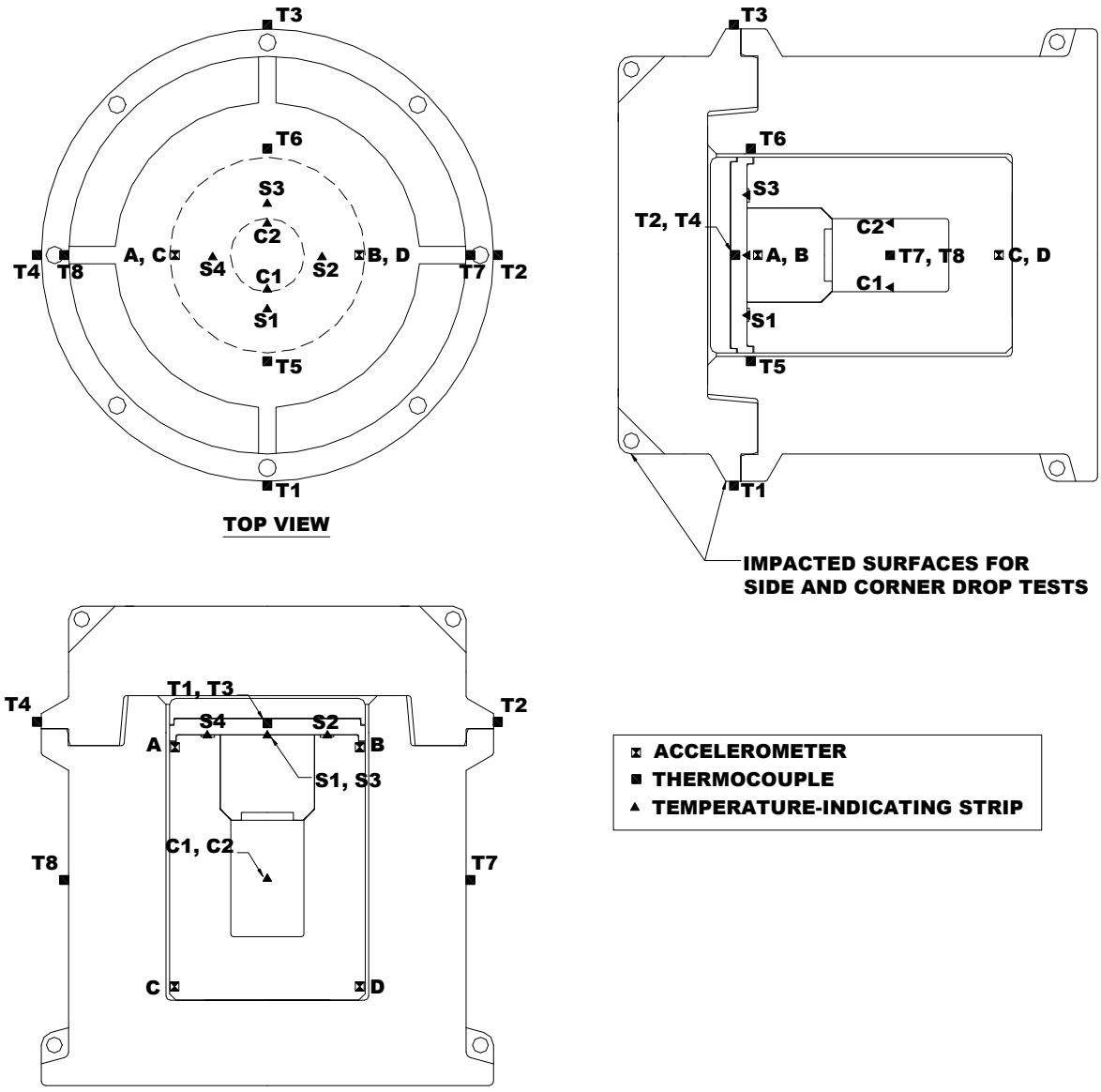


(Note: Approximate instrumentation locations are shown.)

Figure 3 – **Instrumentation Locations**
(from Reference 4)

## 3.1 Test 1A – NCT Bottom End Drop

As shown in Figure 4, Test 1A was a free drop onto the bottom end of an undamaged test package from a height of 1.2 meter (4 feet). As shown in Photograph 1, the instrumented test package, suspended from a crane by slings and a release mechanism, was lifted above the test pad in a vertical orientation such that the lowest point of the package was 1.2 meter (4 feet) above the top surface of the drop test pad. The bottom surface of the test package overpack was level and parallel to the surface of the test pad. The test package was released to free fall to the test pad. The test package used for Test 1A consisted of test cask and shield lid assembly M01 and undamaged test overpack base and lid assemblies OB1 and OL1. Figure 5 establishes the pre- versus post-test geometric information that was measured and recorded by MSC/SwRI.

## 3.2 Test 1B – HAC Top End Drop

As shown in Figure 4, Test 1B was a free drop onto the top end of the test package from a height of 9 meter (30 feet). As shown in Photograph 2, the instrumented test package, suspended from a crane by slings and a release mechanism, was lifted above the test pad in a vertical orientation such that the lowest point of the package was 9 meter (30 feet) above the top surface of the drop test pad. The top surface of the test package overpack was level and parallel to the surface of the test pad. The test package was released to free fall to the test pad.

Test 1B was performed using the same test package as used for Test 1A because the NCT bottom end drop (Test 1A) only resulted in minor permanent deformation of the OB1 overpack base and this deformation was not expected to affect the response or structural integrity of the package for Test 1B. Figure 6 establishes the pre- versus post-test geometric information that was measured and recorded by MSC/SwRI.

## 3.3 Test 1C – HAC CG-Over-Top Corner Drop

Test 1C was a center of gravity (CG)-over-top corner free drop from a height of 9 meter (30 feet), as shown in Figure 4. The test package used for Test 1C consisted of test cask and shield lid assembly M02 and test overpack base and lid assemblies OB2 and OL2 used in Test 1D prior to the performance of Test 1C. The damage associated with the Test 1D bottom end oblique puncture drop did not cause significant damage to the test overpack assembly and was not expected to affect the response or structural integrity of the package for Test 1C.

As shown in Photograph 3, the instrumented test package, suspended from a crane by slings and a release mechanism, was lifted above the test pad such that the lowest point of the package was 9 meter (30 feet) above the top surface of the drop test pad. The top surface of the test package overpack lid was oriented at an angle of 35° from horizontal, with the top end of the package facing toward the ground. The test package was released to free fall to the test pad. Figure 7 establishes the pre- versus post-test geometric information that was measured and recorded by MSC/SwRI.

## 3.4 **Test 1D – HAC Bottom End Oblique Puncture Drop**

Test 1D is a bottom end drop of the test package from a height of 1 meter (40 inches) onto the top end of a 6-inch diameter steel puncture pin, as shown in Figure 4. Test cask and shield lid assembly M02 was used for Test 1D with new test overpack base and lid assemblies OB2 and OL2. As shown in Photograph 4, the test package, suspended from a crane by slings and a release mechanism, was oriented with the bottom face of the overpack base at an angle of 25° from horizontal, as shown in Figure 4, and lifted above the puncture pin such that the lowest point of the package that would contact the puncture pin was 1 meter (40 inches) above the top end of the puncture pin. The puncture impact was expected to (and did) occur in the area of the overpack base pour hole cover plate. The puncture pin was mounted on the test pad to prevent it from sliding or overturning during the test. The test package was released to free fall to the puncture pin and the resulting bottom end gouge was measured for its overall width, length, and depth.

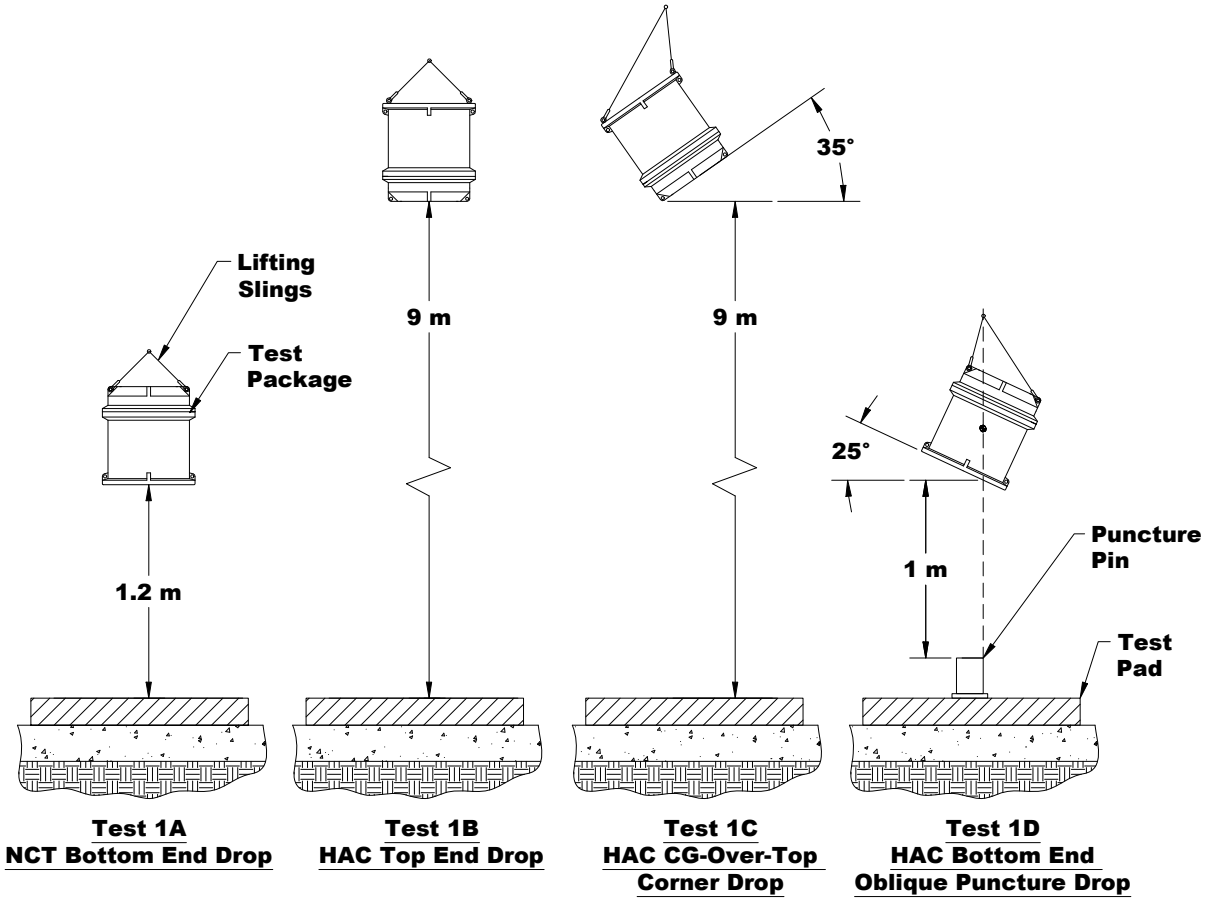


Figure 4 – **Confirmatory Drop Test Sequence 1 Configurations**
(from Reference 4)

Photograph 1 – **Test 1A NCT Bottom End Drop Set-up**

Photograph 2 – **Test 1B HAC Top End Drop Set-up**

Photograph 3 – **Test 1C HAC CG-Over-Top Corner Drop Set-up**

Photograph 4 – **Test 1D HAC Bottom End Oblique Puncture Drop Set-up**

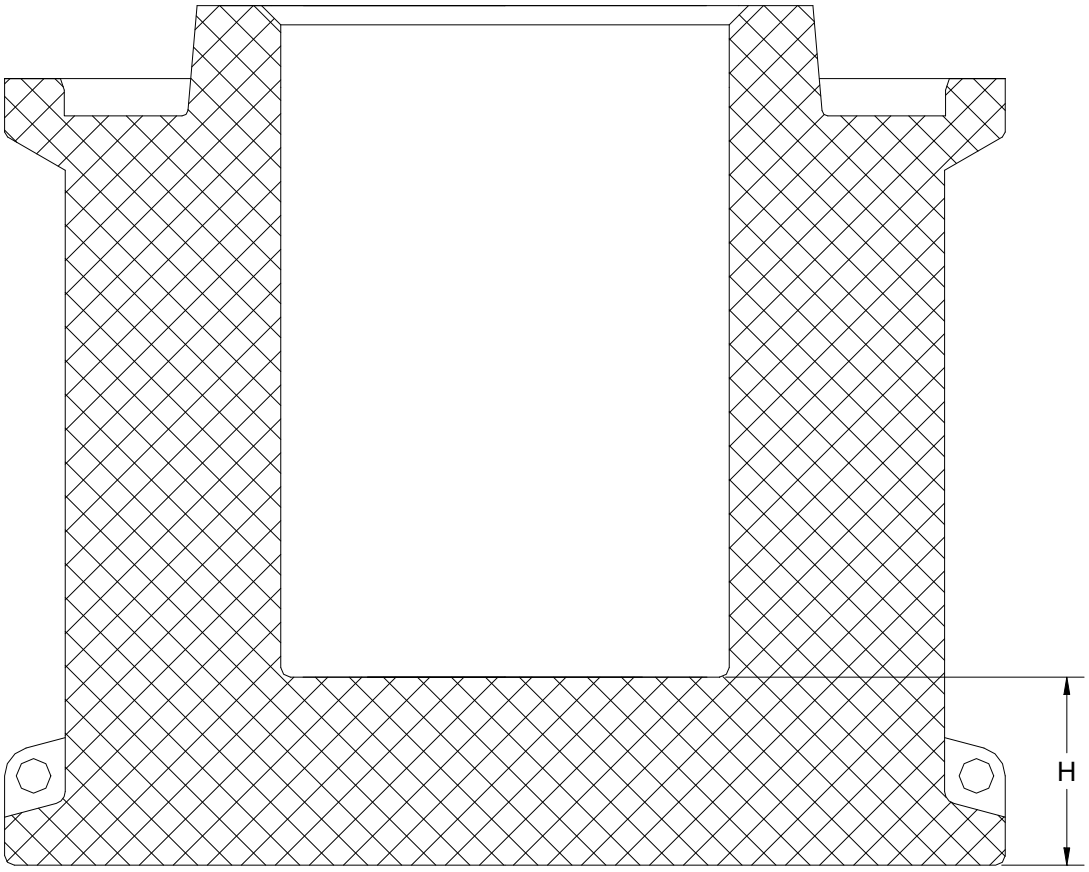


Figure 5 – **NCT Bottom End Drop Measurements**
(from Reference 4)

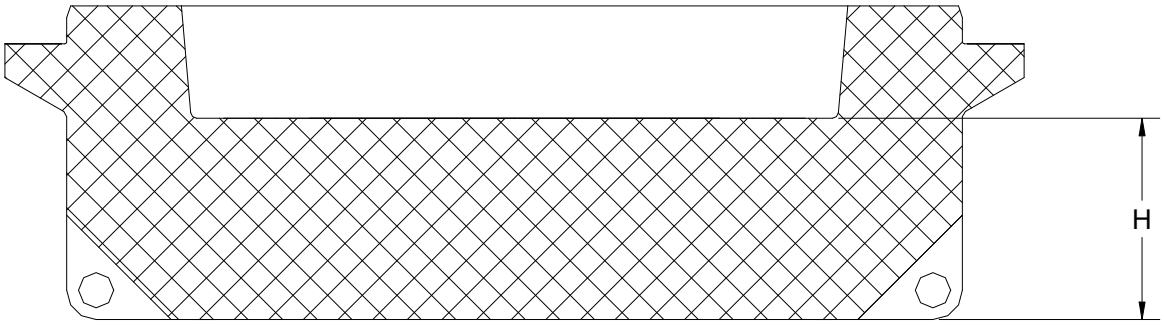


Figure 6 – **HAC Top End Drop Measurements**
(from Reference 4)

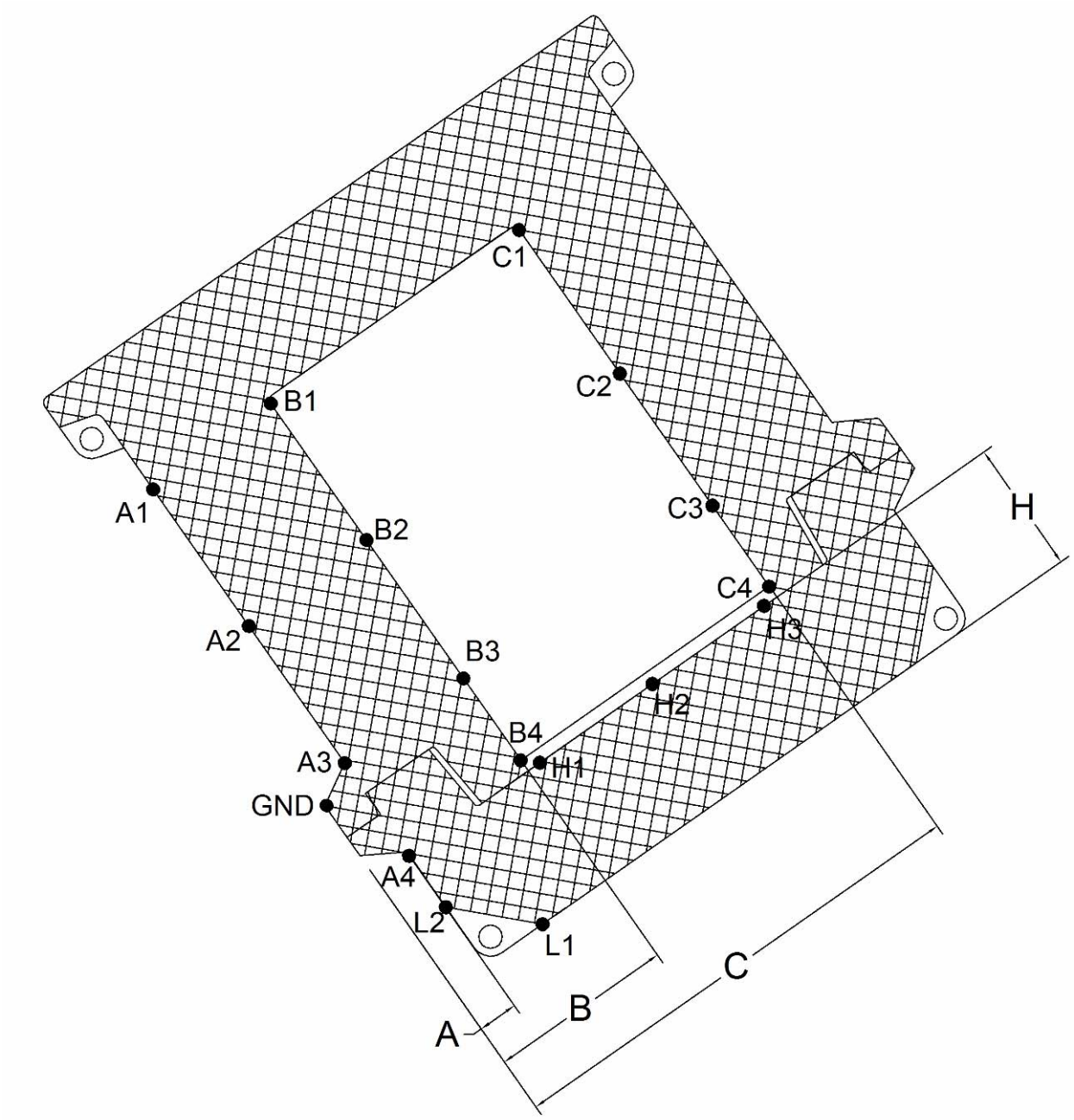


Figure 7 - **HAC CG Over Top Corner Drop Measurements**
(from Reference 6)

## 3.5 Test 2A – HAC Side Drop

Test 2A was a free drop onto the side of the test package from a height of 9 meters (30 feet), as shown in Figure 8. The test package used for Test 2A consisted of test cask and shield lid assembly M01 and new test overpack base and lid assemblies OB3 and OL3. As shown in Photograph 5, the test package was oriented with the 0° azimuth facing downward. The instrumented test package, suspended from a crane by slings and a release mechanism, was oriented horizontally and lifted above the test pad such that the lowest point of the package was 9 meter (30 feet) above the top surface of the drop test pad. The test package was released to free fall to the test pad. Figure 9 establishes the pre- versus post-test geometric information that was measured and recorded by MSC/SwRI.

## 3.6 Test 2B – HAC Side Puncture Drop

As shown in Figure 8, Test 2B was a puncture drop onto the side of the test package from a height of 1 meter (40 in) onto the top end of a 6-inch diameter steel puncture pin. Test 2B was performed using the same test package that was subjected to the HAC side drop test (2A). The test package was oriented with the 0° azimuth facing downward. As shown in Photograph 6, the instrumented test package, suspended from a crane by slings and a release mechanism, was oriented with the outer cylindrical surface of the overpack base at an angle of 10° from horizontal with the top end down and lifted above the puncture pin such that the lowest point of the package that would contact the puncture pin was 1 meter (40 in) above the top end of the puncture pin. The test package center of gravity was positioned directly above the strike edge of the puncture pin. The test package was positioned to strike the top end of the puncture pin on the overpack base outer shell between the overpack bolting flange and tiedown ring. The puncture pin was mounted on the test pad to prevent it from sliding or overturning during the test. The test package was released to free fall to the puncture pin and the resulting outer shell gouge was measured for its overall width, length, and depth.

## 3.7 Test 2C – HAC Thermal

Test 1C was a 30-minute furnace test of the same package subjected to the HAC side drop test (2A) and HAC side puncture test (2B) to simulate the effects of the HAC thermal test required by 10CFR71.73(c)(4). As shown in Photograph 7 through Photograph 9, the instrumented test package was moved into a furnace that was pre-heated to a temperature of 800°C (1,475°F). The package remained in the furnace for a period of 30 minutes after the furnace thermocouples recovered to a temperature of 800°C (1,475°F). After completion of the 30-minute soak time, the package was removed from the furnace and placed in an area where it was not exposed to artificial cooling and combustion of packaging materials was allowed to extinguish naturally (see Photograph 10). The test continued until the temperature reading of the inner-most thermocouples continuously decreased for a period of at least 2-hours.

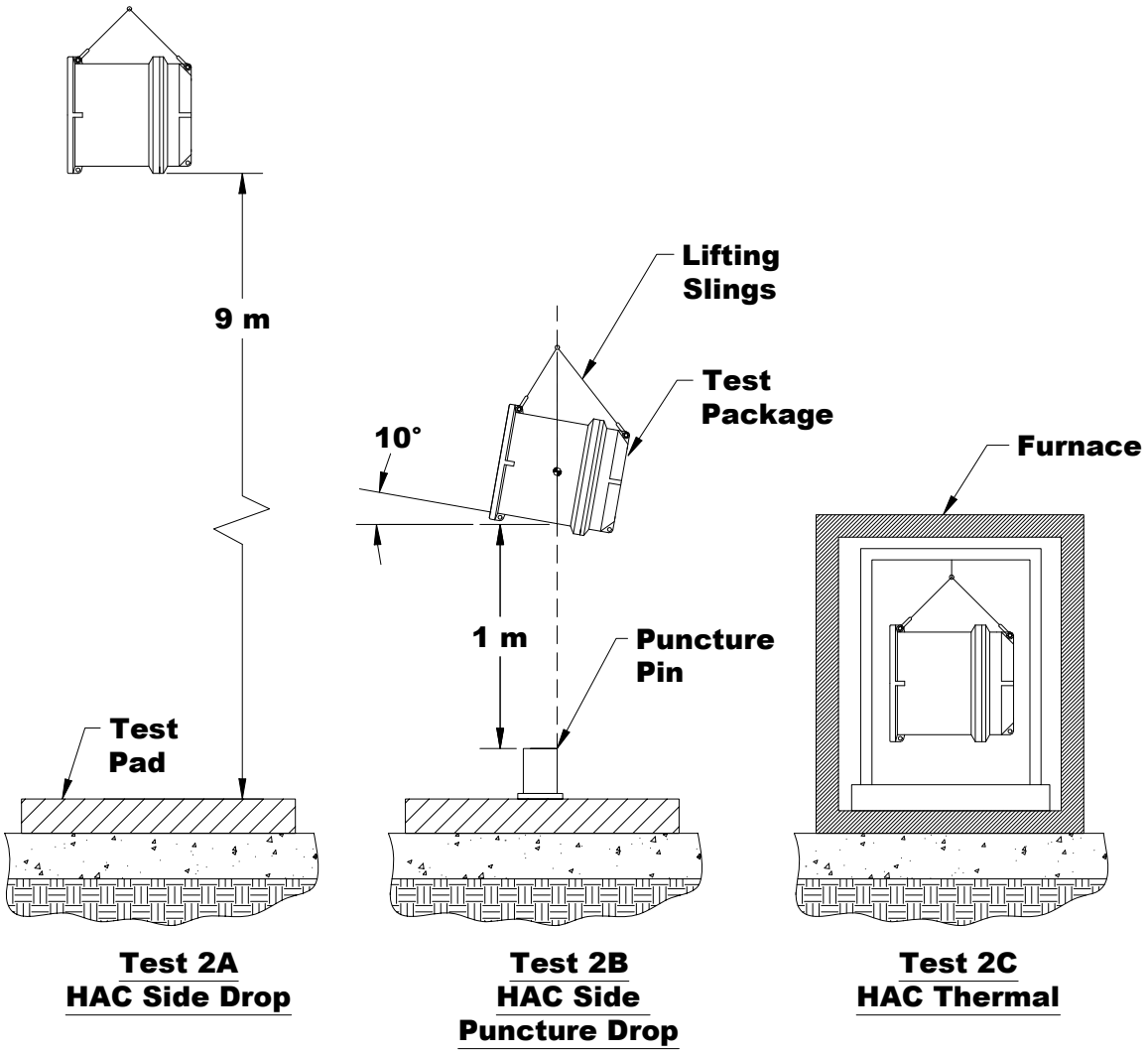


Figure 8 – **Confirmatory Drop Test Sequence 2 Configurations**
(from Reference 4)

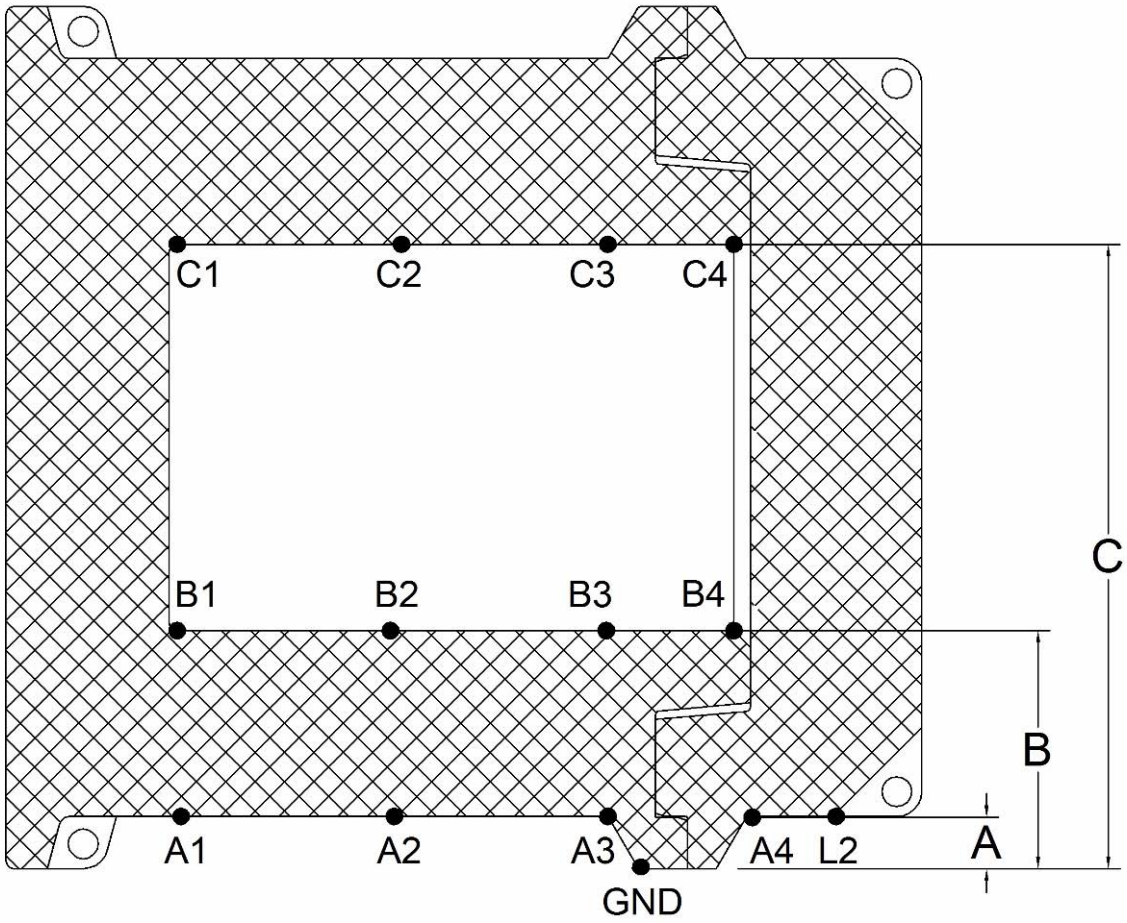


Figure 9 – **HAC Side Drop Measurements**
(from Reference 6)

Photograph 5 – **Test 2A HAC**
**Side Drop Set-up**

Photograph 6 – **Test 2B HAC**
**Side Puncture Drop Set-up**

Photograph 7 – **Test 2C HAC**
**Thermal Set-up Outside Furnace**

Photograph 8 – **Test 2C HAC**
**Thermal Set-up Inside Furnace**

Photograph 9 – **Test 2C HAC**
**Thermal Heating**

Photograph 10 – **Test 2C Cooldown**

# 4 Proposed vs. Actual Test Characterization

## 4.1 Drop Test Components/Facility

Table 7 and Table 8 present the original requirements for the puncture pin and drop test pad used for the MIDUS Transportation Package confirmatory test. As noted in these tables, with the minor exception of the drop test pad minimum steel plate thickness (i.e., 4 cm (1.6 in) required versus 1.5" provided), the puncture pin and drop test pad provided by SwRI at its drop test facility met all of the requirements of the confirmatory test. In addition, as illustrated in Chapter 3, SwRI also provided lifting equipment capable of lifting at least 1,000 lbs and able to suspend the test packages to the required orientations. This lifting equipment included a drop release mechanism also capable of lifting at least 1,000 lbs and able to release the test packages without itself causing the packages to rotate during free fall to the drop test pad/puncture pin. Therefore, the drop test components and facilities were acceptable for the confirmatory test.

## 4.2 Environmental Test Conditions

Table 9 presents the original requirements for the confirmatory test environmental conditions. As noted in this table, there was no precipitation and wind speed conditions were almost completely acceptable during the confirmatory drop tests. However, ambient air temperatures at SwRI's outdoor drop test facility caused the test package/article temperatures to be noticeably higher than originally permitted for the confirmatory test during the two days of drop testing. Only Test 1C conducted during the morning of September 16 under almost complete cloud cover met the originally required test package temperatures. In any case, these temperature conditions are not considered to significantly affect the acceptability of the confirmatory drop test results.

## 4.3 Furnace Characterization

Table 10 presents the original requirements for the characterization of the thermal test furnace. As noted in this table, the furnace provided by SwRI met all of the furnace characterization requirements with the exception of the 24 hour furnace soak period and the need to characterize the furnace after the 24 hour soak following the insertion of a simulated test package. These exceptions to the original furnace characterization criteria were considered unnecessary relative to the thermal capacity of SwRI's forced gas furnace as compared to the originally proposed use of a much smaller and less powerful electric furnace at MSC's facility. As demonstrated in Figure 10, these original 24 hour soak and insertion recovery furnace characterization requirements were eventually not needed for SwRI's furnace because:

a. The furnace was able to attain its 800°C soak temperature in less than 5 minutes, and
b. The furnace was able to recovery to this temperature after package insertion in less than 5 minutes.

In Figure 10, the package insertion point is clearly indicated by a very steep rise in the temperature for Ch. 10 (i.e., TC #10 mounted just below the Test Article) from ambient to 800°C.

Table 7 - **Puncture Pin Requirements for Tests 1D and 2B**

| | Requirement[1] | Test Compliance[2] |
|---|---|---|
| (1) | The puncture pin must be a solid cylindrical mild-steel bar that is mounted vertically on a test pad. | ✓ |
| (2) | The puncture pin must be 15 cm (6 in) in diameter and stand at least 20 cm (8 in) tall with the top horizontal and its edge rounded to not more than 6 mm (0.25 in). | ✓ |
| (3) | The base of the puncture pin should include provisions to allow it to be mounted on a test pad surface with its longitudinal axis in a vertical orientation. | ✓ |
| (4) | The puncture pin attachments must prevent it from sliding or overturning during the 1-meter puncture drop test. | ✓ |

**Notes:**

(1) From Reference 3.
(2) From Reference 22 (completed MSC Test Form 8).

Table 8 - **Drop Test Pad Requirements for Tests 1A through 2B**

| | Requirement[1] | Test Compliance[2] |
|---|---|---|
| (1) | Confirmatory tests must use a drop test pad that satisfies the IAEA (Reference 2) recommendations for an unyielding target for use in the confirmatory drop tests. | ✓ |
| (2) | The drop test pad must consist of either a: | |
| | a. Rigid steel plate mounted on a concrete pad<br>or | |
| | b. Rigid concrete block with a steel cover plate on the upper surface. | ✓ |
| (3) | The drop test pad must meet the following design requirements or a BFS-approved alternative: | |
| | a. Minimum mass of pad: 3,200 kg (7,056 lb.) | ✓[3] |
| | b. Minimum pad top surface: 5’ x 5’ | ✓ |
| | c. Pad top surface level: ± 1/8” | ✓ |
| | d. Minimum steel plate thickness: 4 cm (1.6 in.) | ✓[4] |
| | e. Steel/concrete interface: Tight contact between steel pad and concrete (e.g., floated on groat) and mechanically anchored to concrete base (e.g. anchor bolts). | ✓ |
| | f. Minimum concrete size: 5’ long x 5’ wide x 3.5’ deep | ✓[5] |
| | g. Concrete design compressive strength: 3,000 psi | ✓ |
| (4) | The drop test pad steel plate should be clean, uncoated, and free of significant surface imperfections (e.g., large gouges) that could effect the response of the package. | ✓ |
| (5) | The drop test pad must also include provisions for attaching the puncture pin fixture used for the 1-meter puncture drop. | ✓ |

**Notes:**

(1) From Reference 3.
(2) From Reference 22 (completed MSC Test Form 8).
(3) (10’ x 10’ x 6’)x 150 pcf (typical concrete) = 90,000 lbs > 7,056 lbs, therefore, acceptable.
(4) Actual plate thickness = 1.5”, but was considered acceptable for confirmatory test.
(5) (10’ x 10’ x 6’) > (5’ x 5’ x 3.5’), therefore, acceptable.

Table 9 – **Environmental Test Conditions**

| **Requirement**[1] | **Test Compliance**[2] (✓ = Yes; X = No) | | | | | | |
|---|---|---|---|---|---|---|---|
| | **1A** | **1B** | **1C** | **1D** | **2A** | **2B** | **2C** |
| Ambient Air Temperature (°F)[3] | 104 | 111.7 | 82 | 96.6 | 92.8 | 94.6 | N/A |
| Package Temp. (°F): 75°F ± 10°F. | ✓[4] (104) | ✓[4] (93.2) | ✓ (79.2) | ✓[4] (96.8) | ✓[4] (88.3) | ✓[4] (104.2) | N/A |
| No precipitation. | ✓ | ✓ | ✓ | ✓ | ✓ | ✓ | N/A |
| Wind Speed (mph): < 5 mph at min. 3-ft. above test pad. | ✓ (2.8) | [4] (8.2) | ✓ (5.0) | ✓ (4.6) | ✓ (4.4) | ✓ (2.7) | N/A |

**Notes:**

(1) From Reference 4.
(2) From Reference 22 (completed MSC Test Forms 1 through 7).
(3) For information only.
(4) Noncompliance not considered to significantly affect confirmatory test (see Section 7.2).

Table 10 – **Furnace Characterization Requirements**

| Requirement[1] | | Test Compliance[2] |
|---|---|---|
| (1) | The furnace must have an inner chamber and access opening large enough to accommodate the test package mounted on the support/transfer frame. | ✓ |
| (2) | The furnace must be capable of providing a radiation environment that produces a minimum temperature of 800°C (1,475°F) within the furnace and on the outer surface of the package. | ✓ |
| (3) | The required furnace temperatures shall be attained within the first 5 minutes after insertion of the test package into the furnace and maintained for a 30-minute test duration. | ✓ |
| (4) | The furnace environment shall include a sufficient amount of oxygen to allow possible combustion of flammable package materials to occur. | ✓ |
| (5) | The furnace must accommodate instrumentation cables that are routed from the data acquisition system to the confirmatory test package to pass through an access opening during the thermal test. | ✓ |
| (6) | The furnace must also include provisions to allow video recording of the test package in the furnace during the thermal test. | ✓ |
| (7) | Prior to performing the thermal test, the furnace must be characterized for the following: | |
| | (a) Temperature: | |
| | • Raise the temperature of the furnace until the average temperature reaches the minimum test temperature stated above and allow the furnace to soak for a period of 24 hours. | N/A |
| | • Measure and record the temperature within the furnace using calibrated thermocouples to characterize temperature variations within the furnace from front-to-back, side-to-side, and top-to-bottom. | ✓ |
| | (b) Heat Recovery Times: After soaking the furnace at the minimum temperature for a period of 24 hours, measure the furnace temperature using calibrated thermocouples during a simulation of the thermal test package insertion. | N/A |
| | (c) Emissivity: The surface emissivity of the interior of the furnace shall be characterized and recorded. | ✓[3] |
| | (d) Radiant View Factor: Calculated ≥ 95%. | ✓[3] |

**Notes:**

(1) From Reference 4.
(2) From Reference 22 (completed MSC Test Form 8).
(3) From Reference 23 (SwRI calculation by Barry Badders).

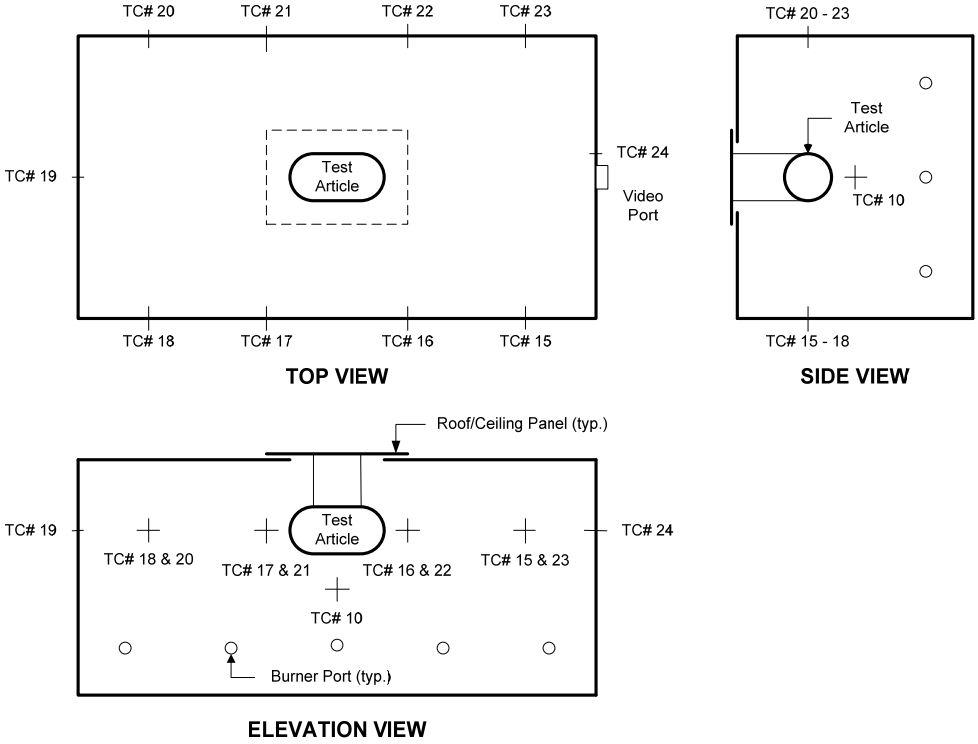


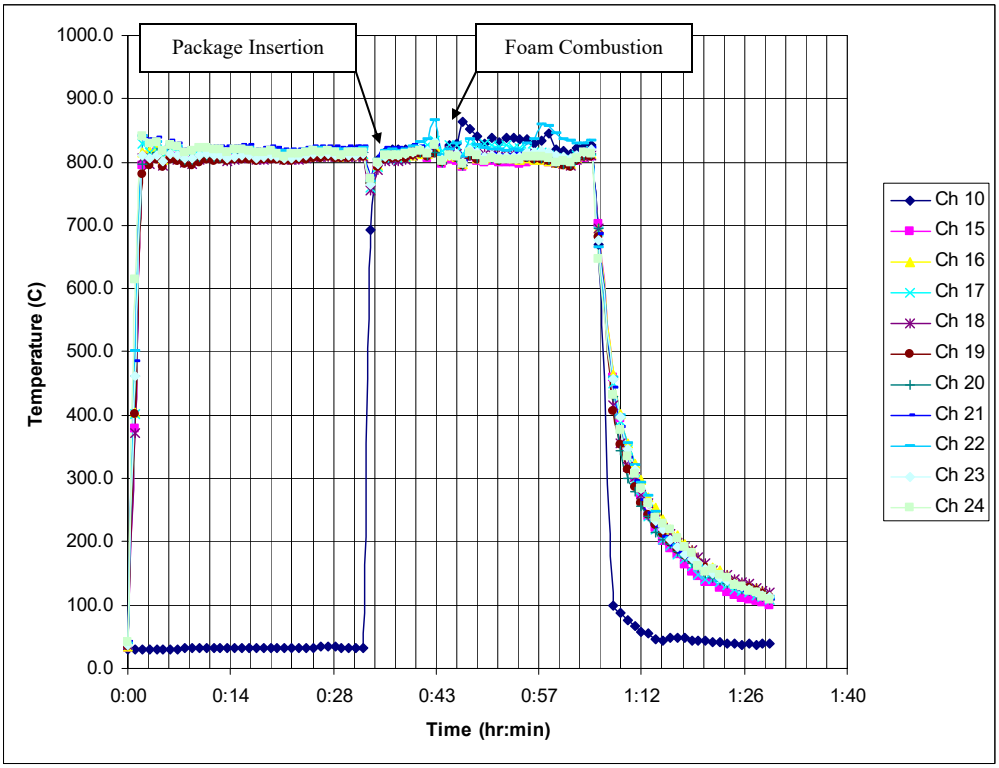


Figure 10 – **Test 2C Thermocouple Readings**
(from Reference 23, File "Raw Test Data.xls", dated 9/25/06)

# 5 Test Predictions

As applicable, the maximum predicted permanent deformation magnitudes and deformed shapes, maximum predicted acceleration magnitudes, and predicted acceleration time-histories for Tests 1A through 2B come from the Reference 6 calculation package. The maximum predicted peak thermocouple and temperature-indicating strip magnitudes and time-dependent temperature traces for Test 2C come from the Reference 5 calculation package.

## 5.1 Tests 1A through 2B

Table 11 presents the predicted test article deformation magnitudes for the Test 1A through 2B cases. Figure 11 through Figure 16 present the predicted test article deformed shapes for Tests 1A through Test 2B.

Table 12 presents the maximum predicted test article acceleration magnitudes for Tests 1A, 1B, 1C, and 2A. Figure 17 through Figure 20 present the associated predicted test article acceleration time-histories for these same test cases.

## 5.2 Test 2C

Table 13 and Table 14 present the maximum predicted test article thermocouple and temperature-indicating strip readings for Test 2C. Figure 21 and Figure 22 present the maximum predicted test article temperature distribution at the end of the Test 2C furnace heating cycle and the predicted thermocouple time-dependent temperature readings for this same test case.

Table 11 – **Maximum Predicted Deformation Magnitudes**

| Drop Test No. | Deformation Magnitude | Corresponding Figures | |
|---|---|---|---|
| | | Location | Deformation |
| 1A | 4 mm (0.2 in) | Figure 5 | Figure 11 |
| 1B | 40 mm (1.6 in) | Figure 6 | Figure 12 |
| 1C | 16 mm (0.6 in)(1)<br>33 mm (1.3 in)(2) | Figure 7 | Figure 13 |
| 1D | 22 mm (0.9 in) | N/A | Figure 14 |
| 2A | 31 mm (1.2 in)(3) | Figure 9 | Figure 15 |
| 2B | 22 mm (0.9 in) | N/A | Figure 16 |

**Notes:**

(1) Deformation parallel to longitudinal axis of package at location L2.
(2) Radial deformation at location H3.
(3) Radial deformation at locations A1 and B1.

Table 12 – **Maximum Predicted Acceleration Magnitudes**

| Drop Test No. | Acceleration Magnitude | Direction/ Orientation |
|---|---|---|
| 1A | 195g | Y (longitudinal) |
| 1B | 350g | Y (longitudinal) |
| 1C | 183g<br>298g | X (radial)<br>Y (longitudinal) |
| 2A | 496g<br>394g | X (top)<br>X (bottom) |

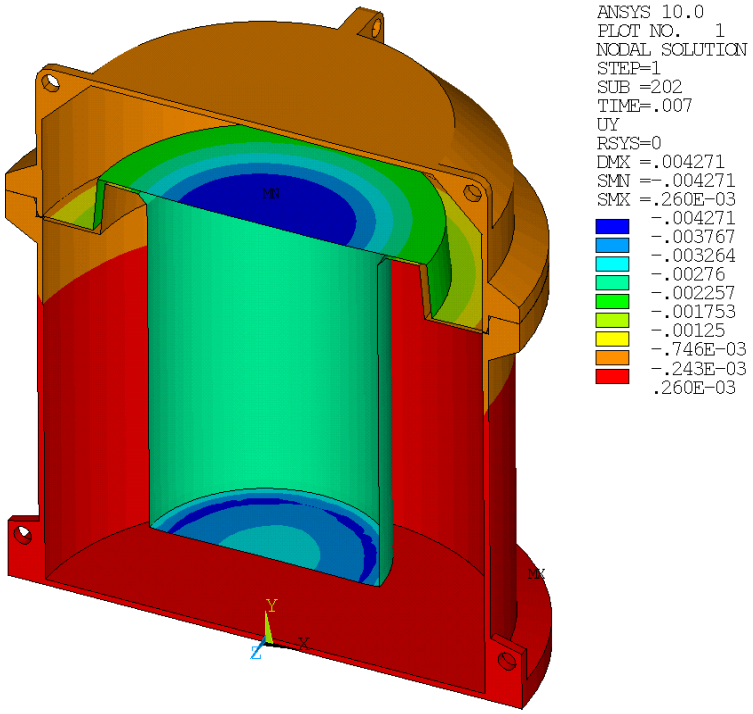


Figure 11 – **Test 1A Predicted Overpack Permanent Deformation**

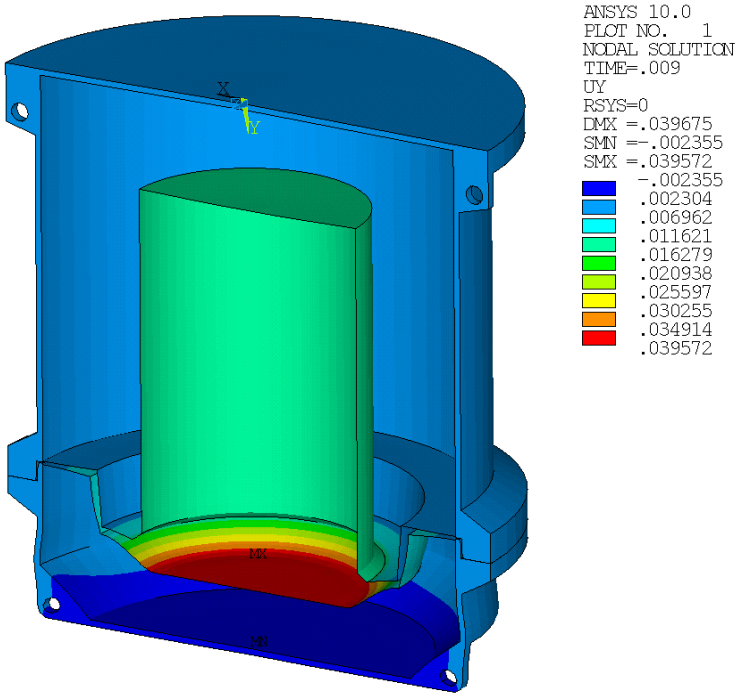


Figure 12 – **Test 1B Predicted Overpack Permanent Deformation**

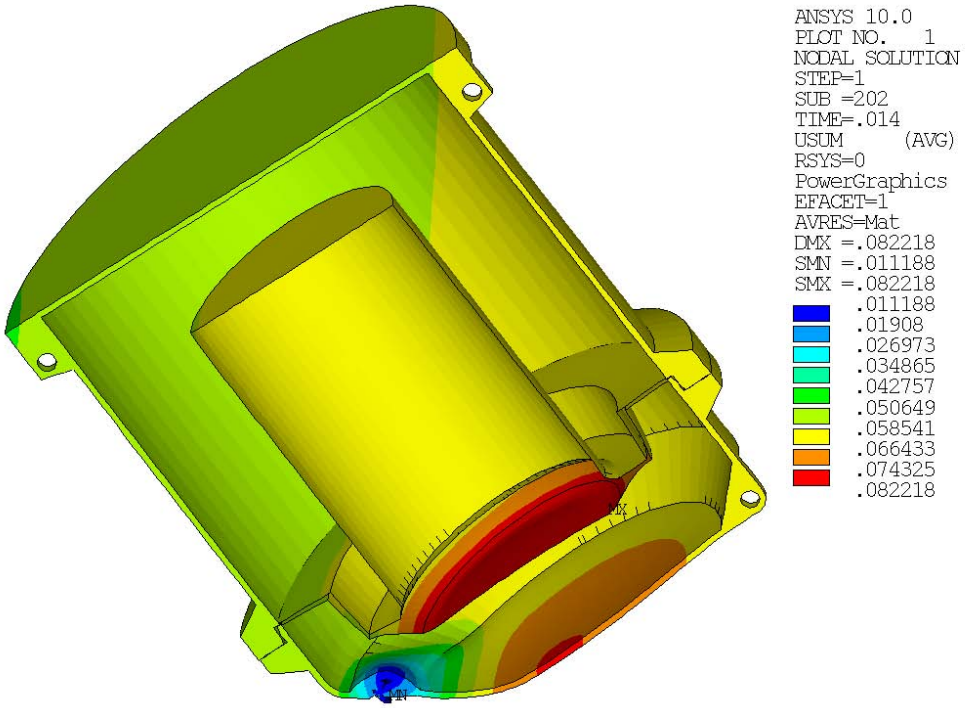


Figure 13 – **Test 1C Predicted Overpack Permanent Deformation**

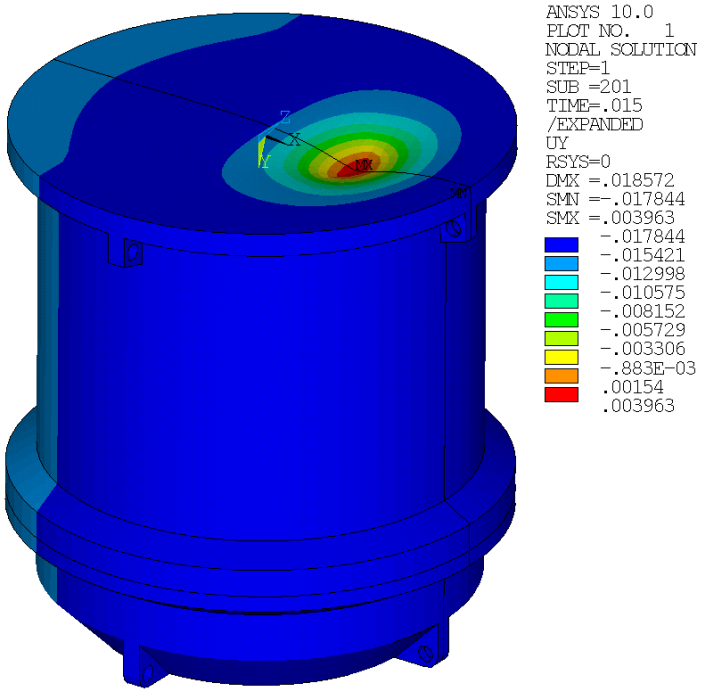


Figure 14 – **Test 1D Predicted Overpack Permanent Deformation**

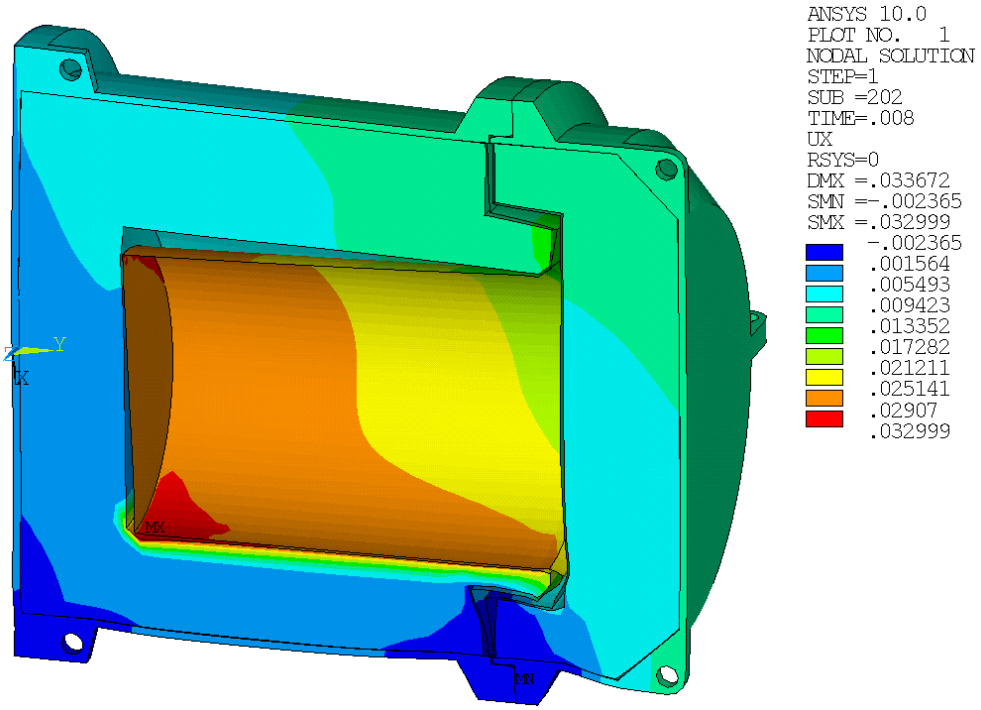


Figure 15 – **Test 2A Predicted Overpack Permanent Deformation**
(Shells and Foam Cores)

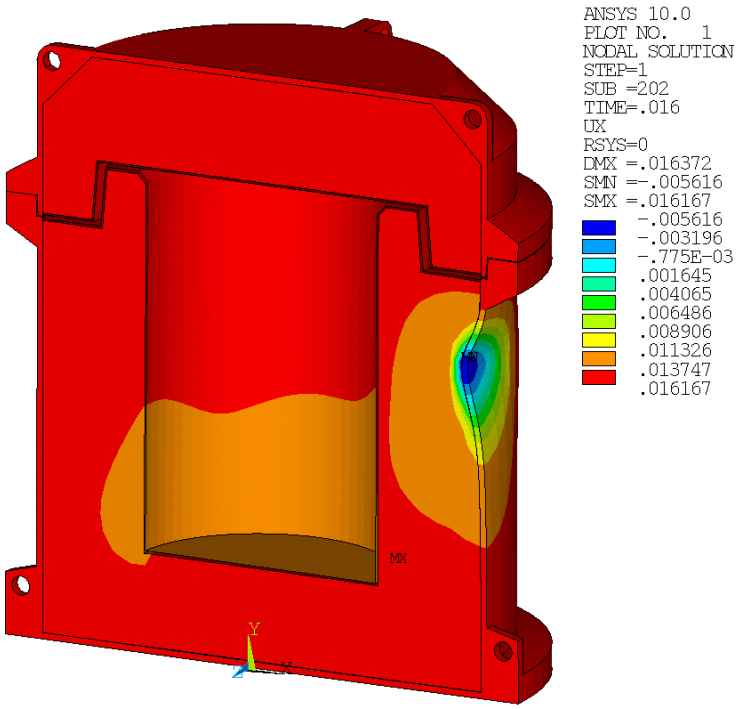


Figure 16 – **Test 2B Predicted Overpack Permanent Deformation**

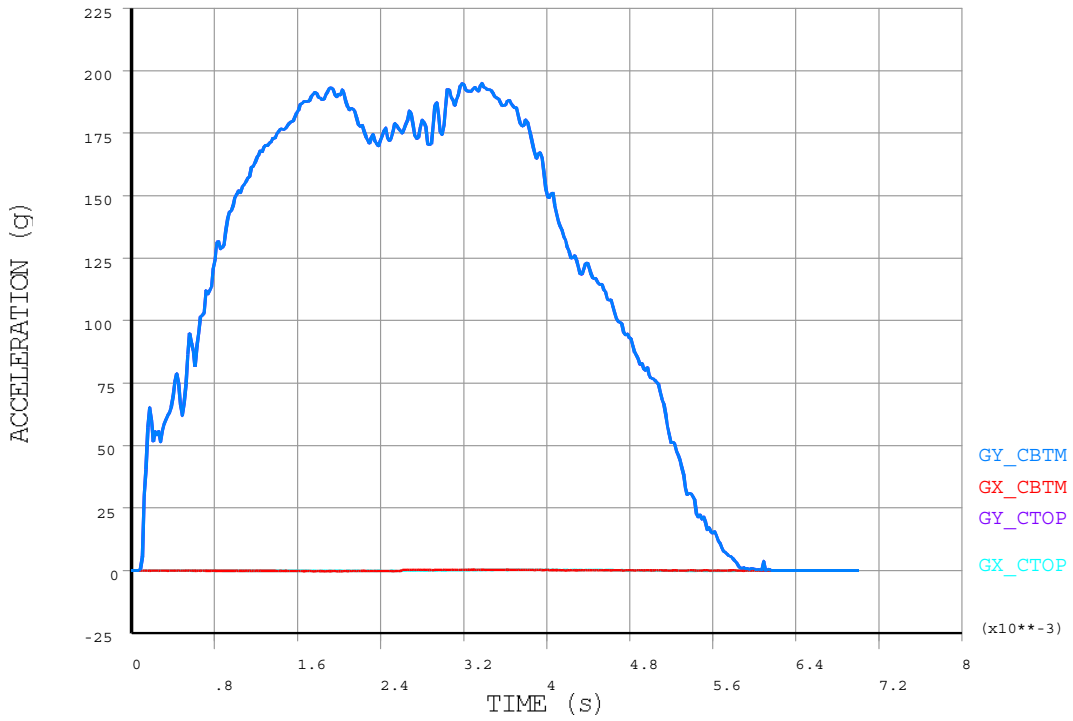


Figure 17 – **Test 1A Predicted Acceleration Time-History**

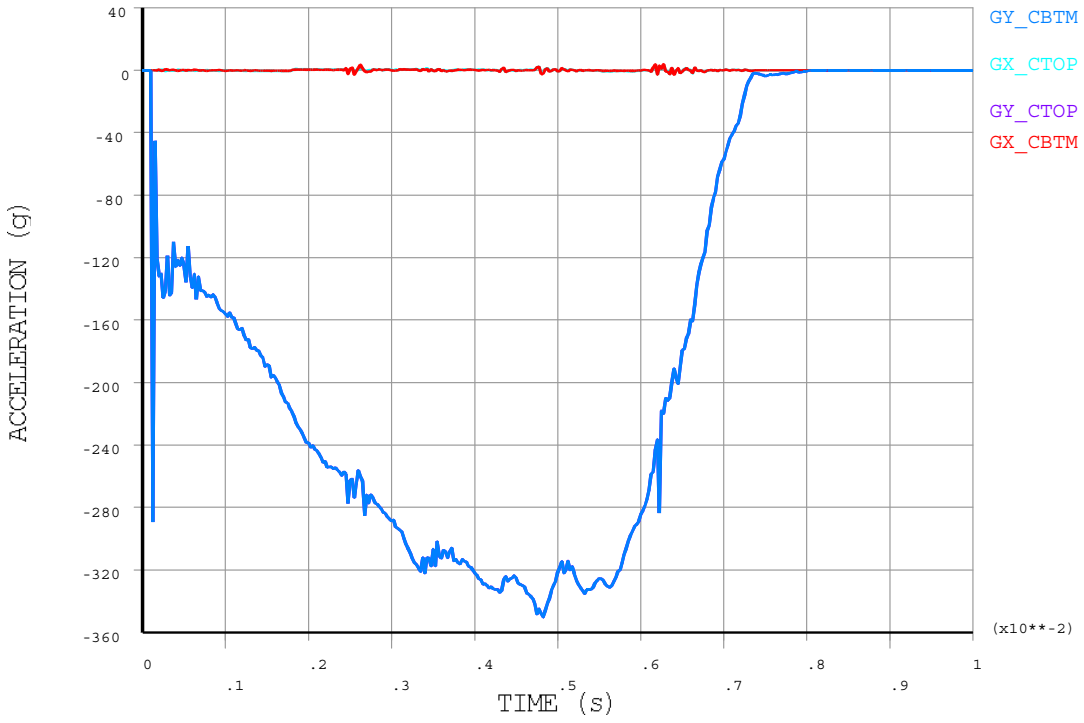


Figure 18 – **Test 1B Predicted Acceleration Time-History**

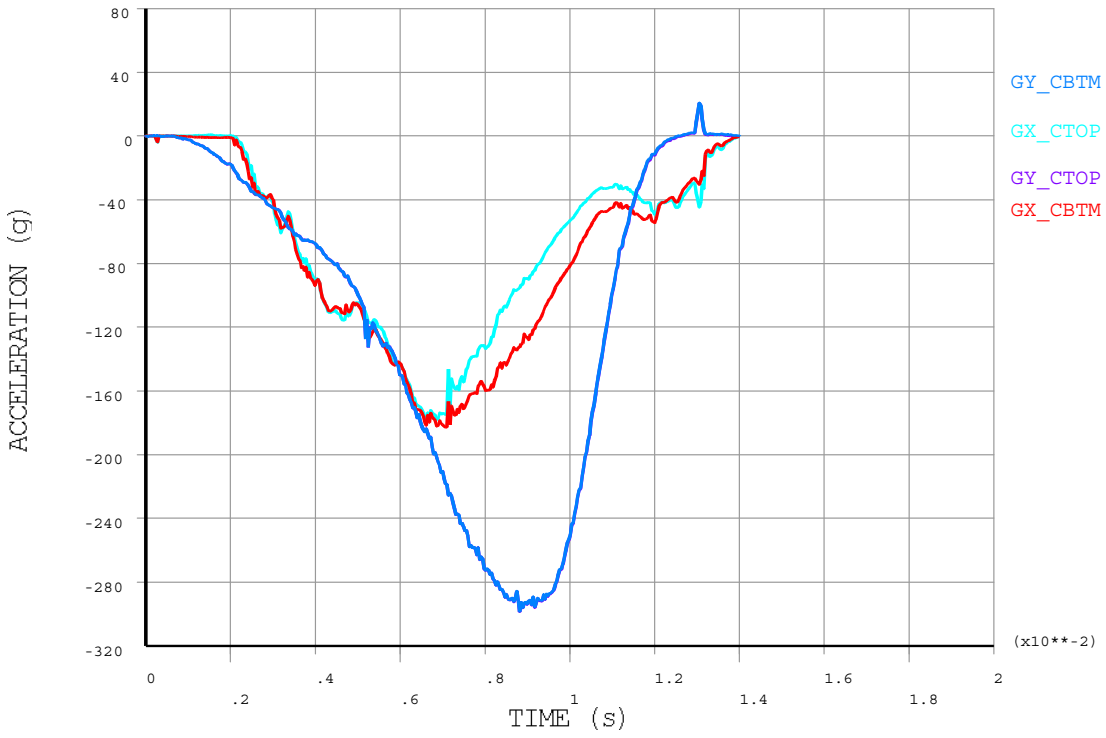


Figure 19 – **Test 1C Predicted Acceleration Time-History**

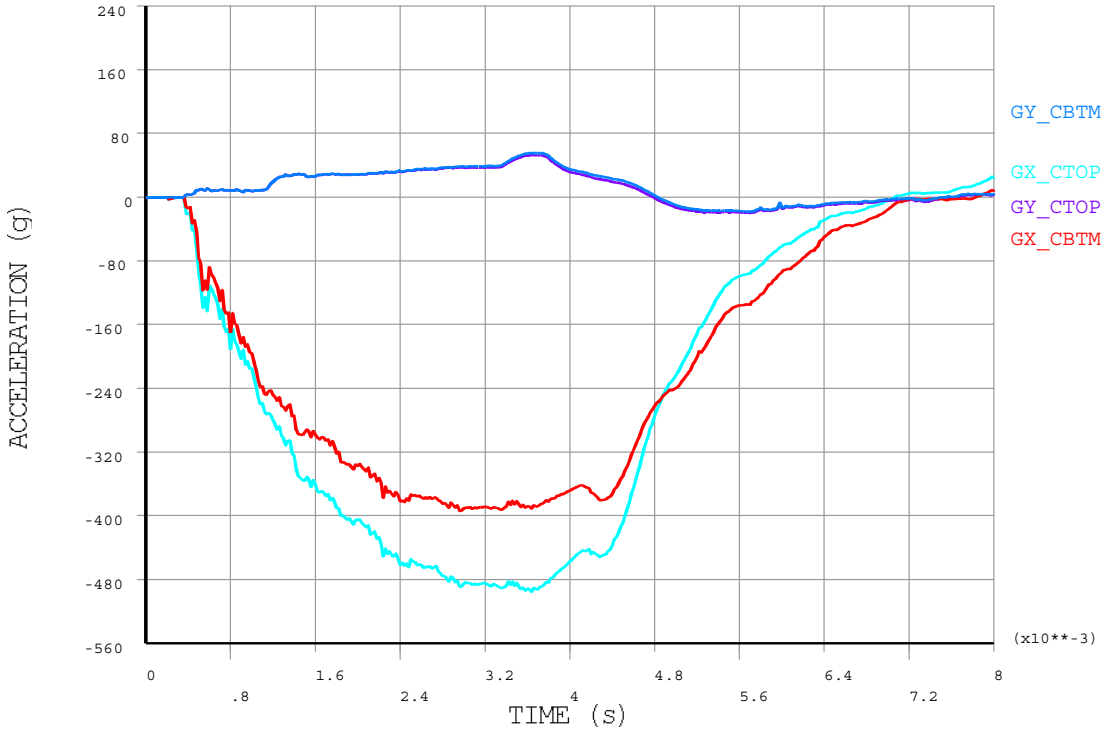


Figure 20 – **Test 2A Predicted Acceleration Time-History**

Table 13 – **Maximum Predicted Peak Thermocouple Readings**

| Location* | °F | °C |
|---|---|---|
| TC #1 | 1350 | 732 |
| TC #2 & TC #4 | 1350 | 732 |
| TC #3 | 1350 | 732 |
| TC #5 | 277 | 136 |
| TC #6 | 399 | 204 |
| TC #7 & TC #8 | 1415 | 768 |

* See Figure 3 for the thermocouple locations.

Table 14 – **Maximum Predicted Peak Temperature-Indicating Strip Readings**

| Location | °F | °C |
|---|---|---|
| S1 | 259 | 126 |
| S2 | 258 | 126 |
| S3 | 258 | 126 |
| S4 | 258 | 126 |
| C1 | 247 | 119 |
| C2 | 247 | 119 |

* See Figure 3 for the temperature-indicating strip locations.

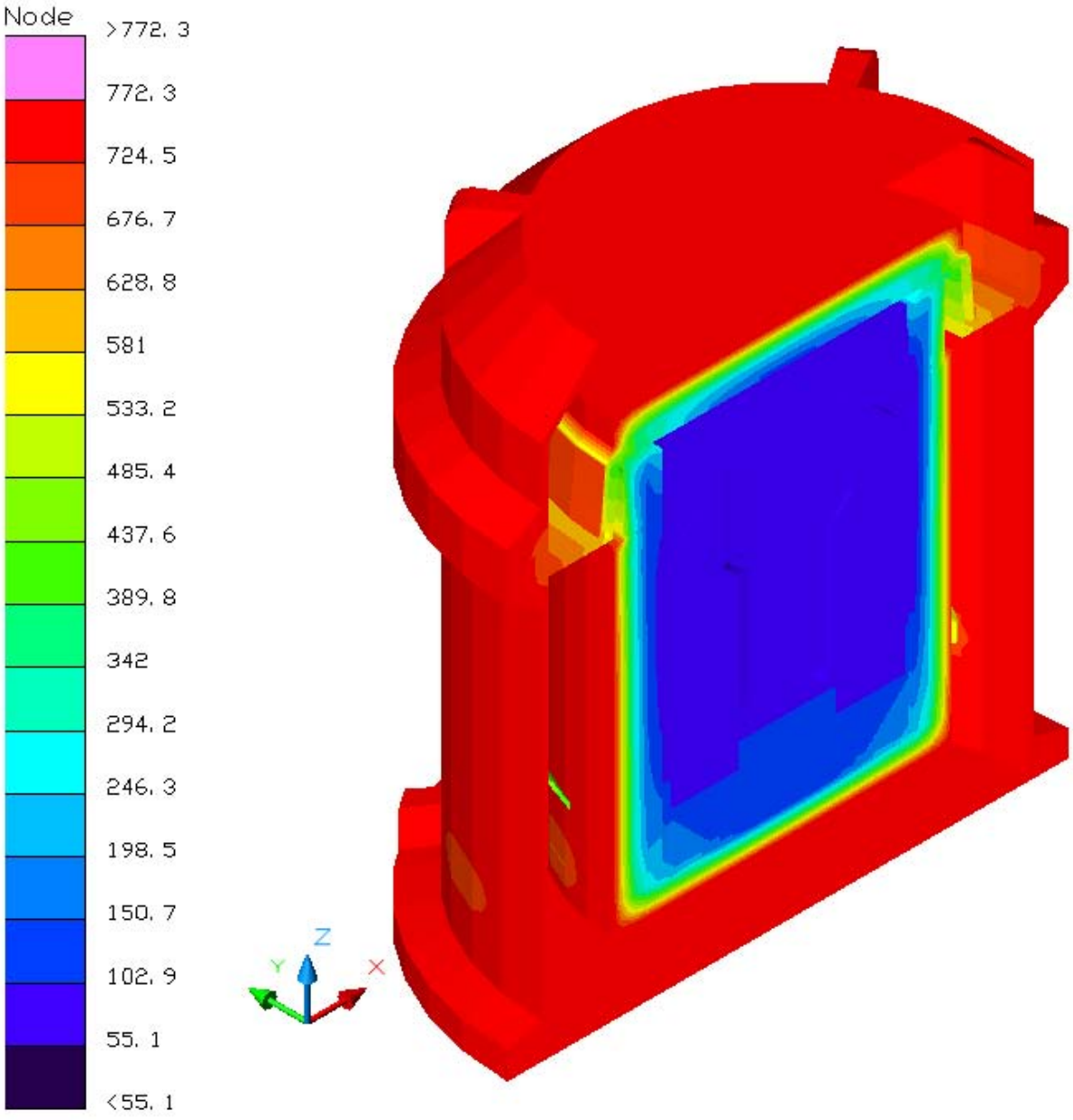


Figure 21 – **Test 2C Predicted Temperature Distribution at End of Furnace Heating**

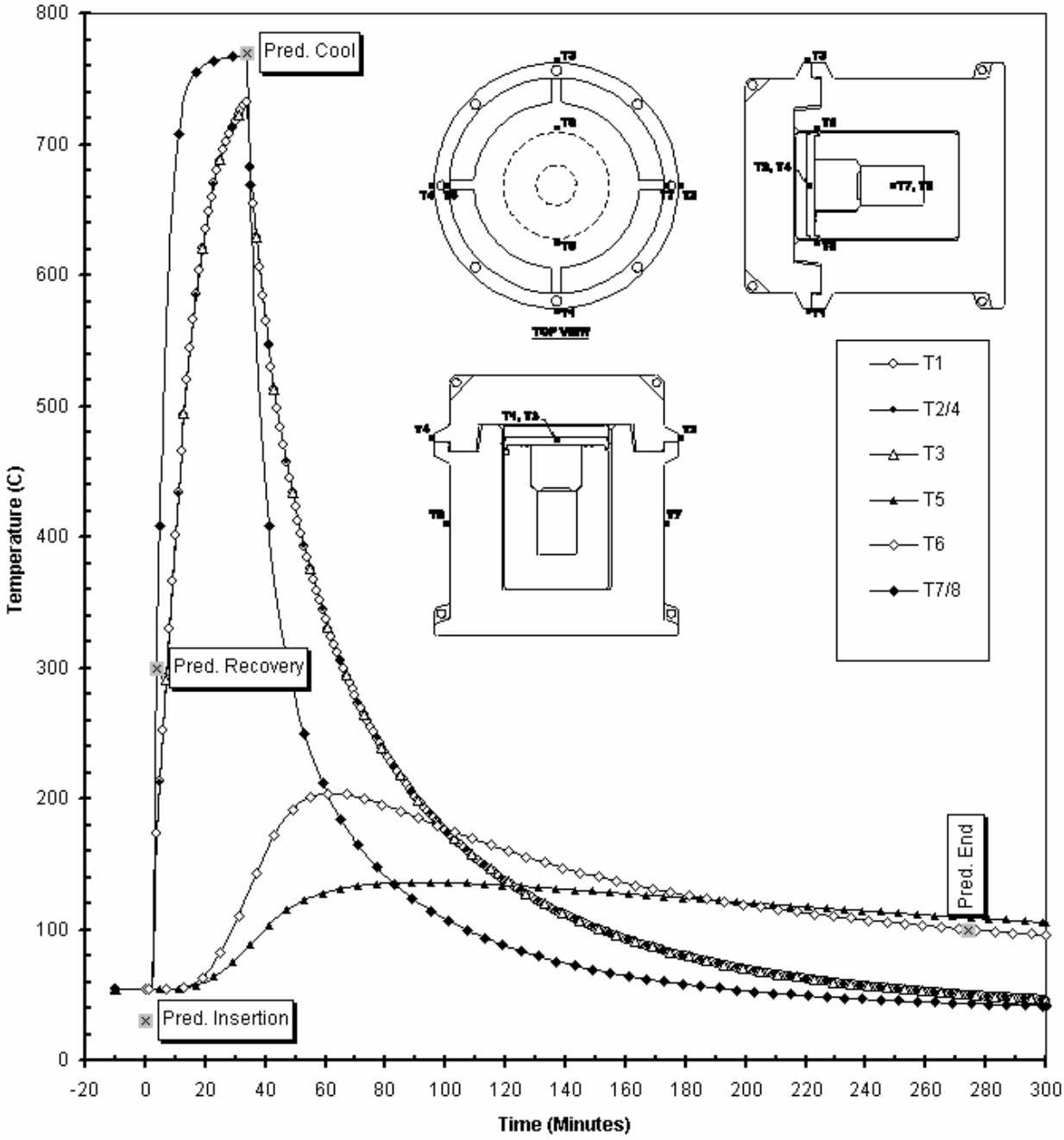


Figure 22– **Test 2C Predicted Time-Dependent Thermocouple Temperature Trace**

# 6 Test Results

The test articles for each of tests 1A through 1D and test sequence 2A through 2C were successfully subjected to pre- and post-drop pressure rise leak rate tests of the containment O-ring seal to a $10^{-3}$ ref cc/sec acceptance criteria as documented in completed MSC Test Forms (from Reference 22).

## 6.1 Tests 1A through 2B

Table 15 presents the actual post-drop test article deformation measurements for Tests 1A, 1B, 1C, and 2A. Photograph 11 through Photograph 22 present the post-drop condition of the MIDUS Transportation Package overpack base and lid assemblies for Tests 1A through 2B. For the Test 1D HAC bottom end puncture drop, completed MSC Test Form 4 (Reference 22) describes the gouge shown on the bottom of the package shown in Photograph 17 as "approximately 121 mm in length, 65 mm in width, and 15.55 mm in depth (Overpack not punctured)." For the Test 2B HAC side puncture drop, completed MSC Test Form 6 (from Reference 22) describes the gouge on the side of the package shown in Photograph 22 as "approximately 3" wide, 4" long, 1" deep."

Figure 23 through Figure 28 (from Reference 23, File ID "MIDUS Drop Test Acceleration Data.xls", dated 9/19/06) present the actual test article acceleration time histories for Tests 1A, 1B, 1C, and 2A.

## 6.2 Test 2C

Figure 29 through Figure 32 (from Reference 23, File ID "Raw Test Data.xls", dated 9/25/06) present the actual temperature-time traces for thermocouples (TCs) mounted on/in the Test 2C test article during its thermal test. These figures also include the predicted temperature-time traces for these same TCs provided in Figure 22. For the temperature-indicating strips, completed MSC Test Form 7 (from Reference 22) records the maximum temperature for these strips as less than their minimum sensitivity (i.e., S1 through S4 < 182°C; C1 and C2 < 132°C (both per Reference 20)).

As the test article began Test Sequence #2, it had a gross weight of 323.5 kg per completed MSC Test Form 5(from Reference 22). Following the Test 2C thermal test, the test article had a gross weight of 312.4 kg per completed MSC Test Form 7 (from Reference 22). Therefore, the test article experienced an 11.1 kg (24.4 lb) reduction in foam weight from its foam cavities. Photograph 23 through Photograph 38 present the post-test condition of the normally accessible internal and external surfaces of the test article following the thermal test. Photograph 39 through Photograph 45 present the post-test condition of the test article foam cavities following post-thermal test disassembly.

Table 15 – **Actual Post-Test Deformation Measurements** (mm)

| Test No. | Dimension | | | | | | | | | | | |
|---|---|---|---|---|---|---|---|---|---|---|---|---|
| | A | | | B | | | C | | | H | | |
| | Pre-Test | Post-Test | Diff. | Pre-Test | Post-Test | Diff. | Pre-Test | Post-Test | Diff. | Pre-Test | Post-Test | Diff. |
| **1A**[1] | | | | | | | | | | 96 | 94.7 | -1.3 |
| **1B**[2] | | | | | | | | | | 105 | 82 | -23 |
| **1C**[3] | | | | | | | | | | | | |
| Datum 1 | 31.54 | 34.24 | +2.70 | 145.55 | 147.4 | +1.85 | 375 | 372 | -3 | 105.65 | 101.18 | -4.47 |
| Datum 2 | 31.63 | 33.24 | +1.61 | | | | 375 | 372 | -3 | 105.35 | 122.13 | +16.78 |
| Datum 3 | 31.66 | 33.79 | +2.13 | | | | N/A[5] | N/A[5] | N/A | 105.57 | 139.98 | +34.41 |
| Datum 4 | 31.64 | 44.49 | +12.85 | | | | N/A[5] | N/A[5] | N/A | 105.39 | 115.0 | +9.61 |
| L1 | 53.90 | 105.33 | +51.43 | | | | | | | 53.89 | 65.0 | +11.11 |
| L2 | 30.88 | 33.56 | +2.68 | | | | | | | 0 | 38.0 | +38.0 |
| **1D** | See Section 6.1 | | | | | | | | | | | |
| **2A**[4] | | | | | | | | | | | | |
| Datum 1 | 32.21 | 32.53 | +0.32 | 146.34 | 142.75 | -3.59 | 377 | 370.36 | -6.64 | | | |
| Datum 2 | 32.27 | 31.11 | -1.16 | | 139.05 | -7.29 | 377 | 369.83 | -7.17 | | | |
| Datum 3 | 32.35 | 36.38 | +4.03 | | 136.24 | -10.1 | N/A[5] | N/A[5] | N/A | | | |
| Datum 4 | 33.46 | 33.23 | -0.23 | | 133.97 | -12.37 | N/A[5] | N/A[5] | N/A | | | |
| L2 | 35.91 | 28.39 | -7.52 | | | | | | | | | |
| **2B** | See Section 6.1 | | | | | | | | | | | |

**Notes:**

(1) From Reference 22 (completed MSC Test Form 1).
(2) From Reference 22 (completed MSC Test Form 2).
(3) From Reference 22 (completed MSC Test Form 3).
(4) From Reference 22 (completed MSC Test Form 5 and subsequent E. Chow-to-B. Thomas E-mail, Subject: Lid Dissection, dated 9/26/06).
(5) Upper bulkhead cavity precludes the recording of these dimensions..

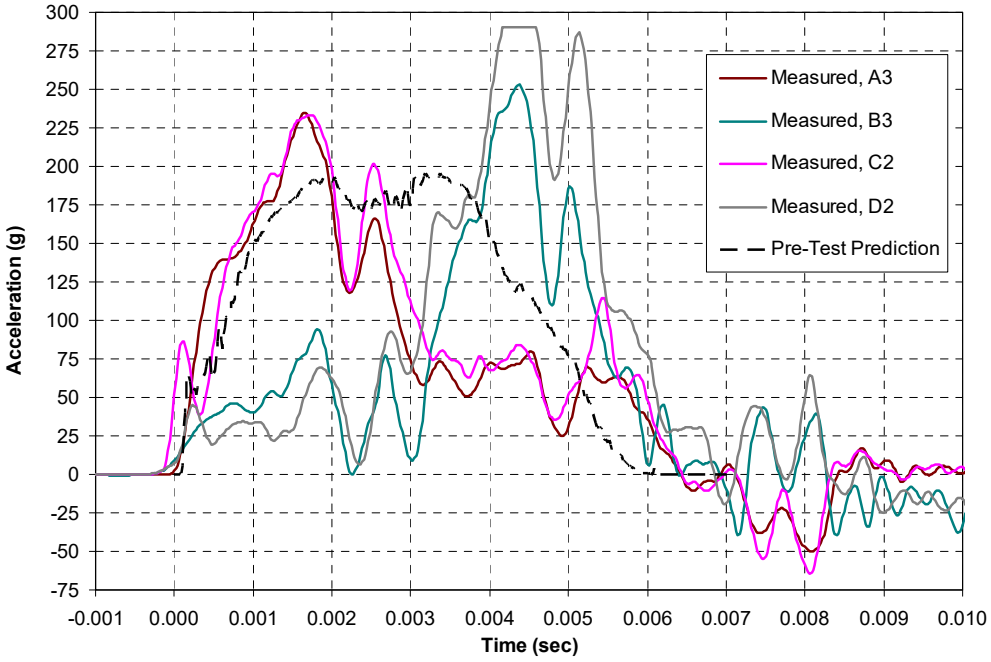


Figure 23 – **Test 1A Actual Acceleration Time History**

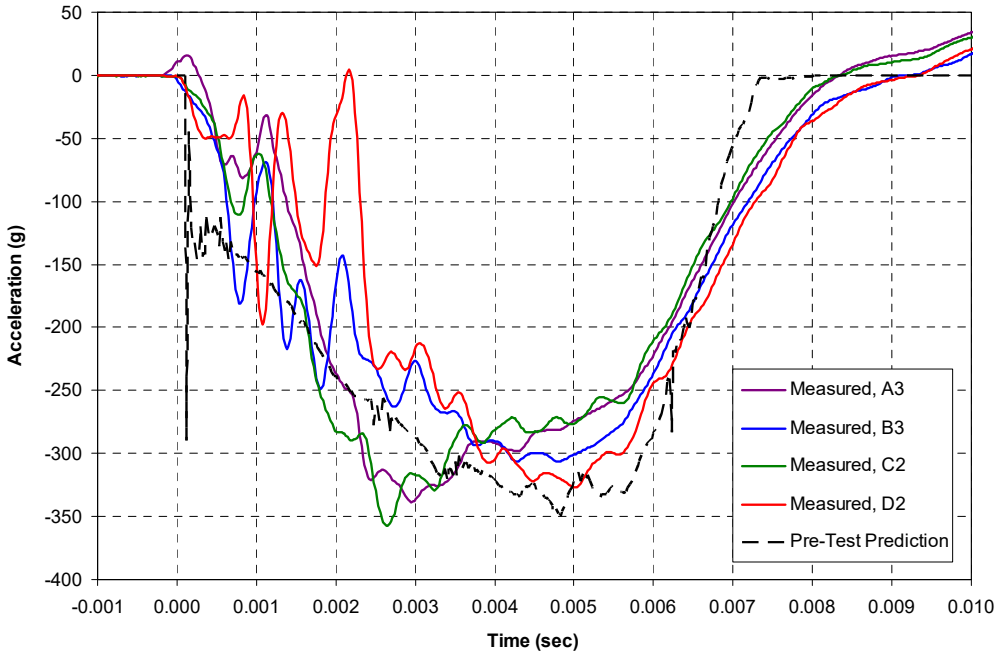


Figure 24 – **Test 1B Actual Acceleration Time History**

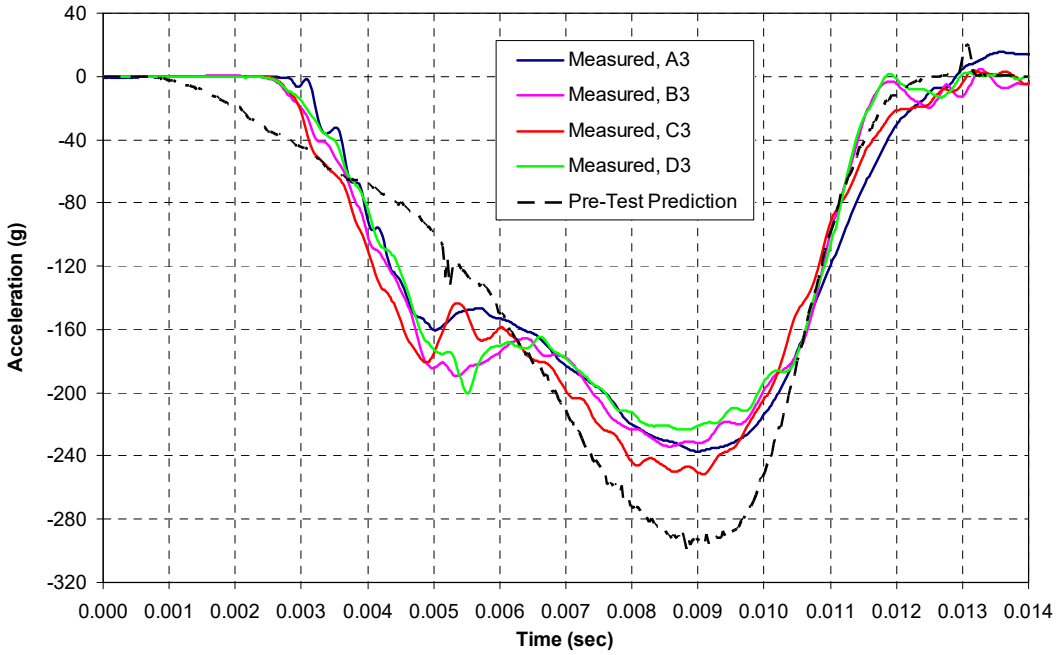


Figure 25 – **Test 1C Actual Acceleration Time History** (Longitudinal - Y)

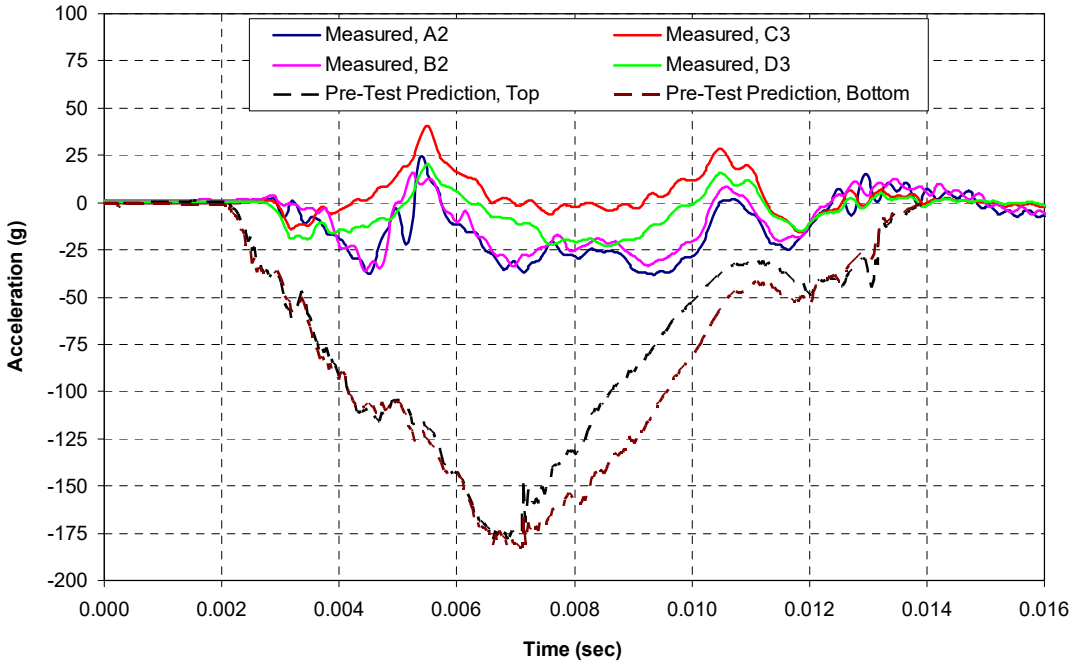


Figure 26 – **Test 1C Actual Acceleration Time History** (Transverse - X)

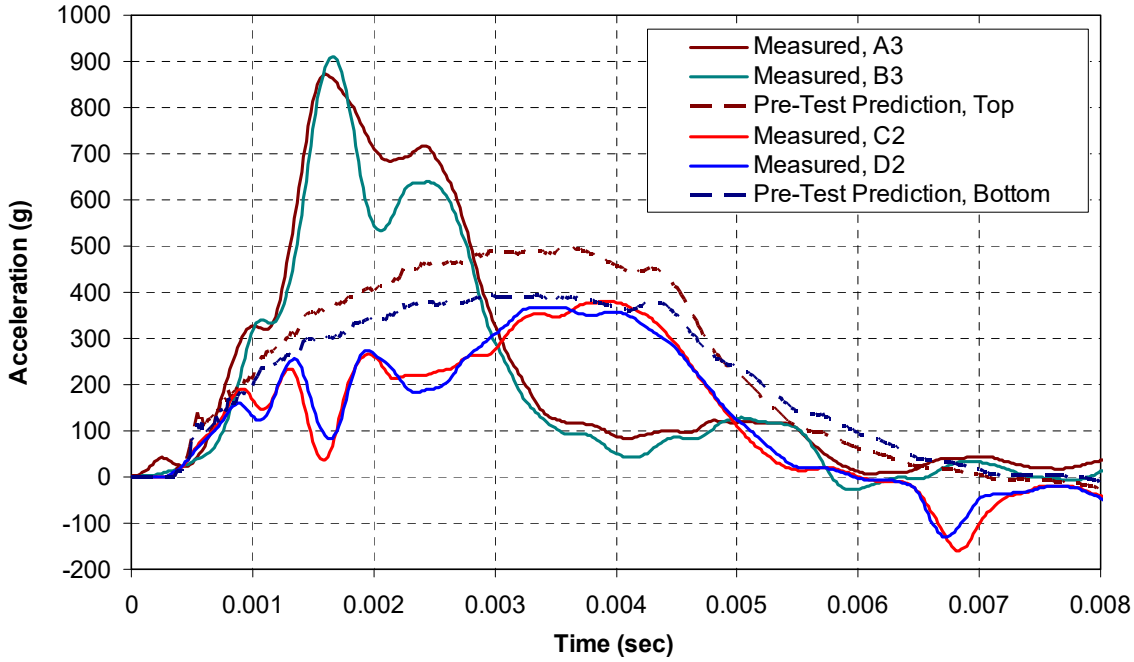


Figure 27 – **Test 2A Actual Acceleration Time History** (Longitudinal - Y)

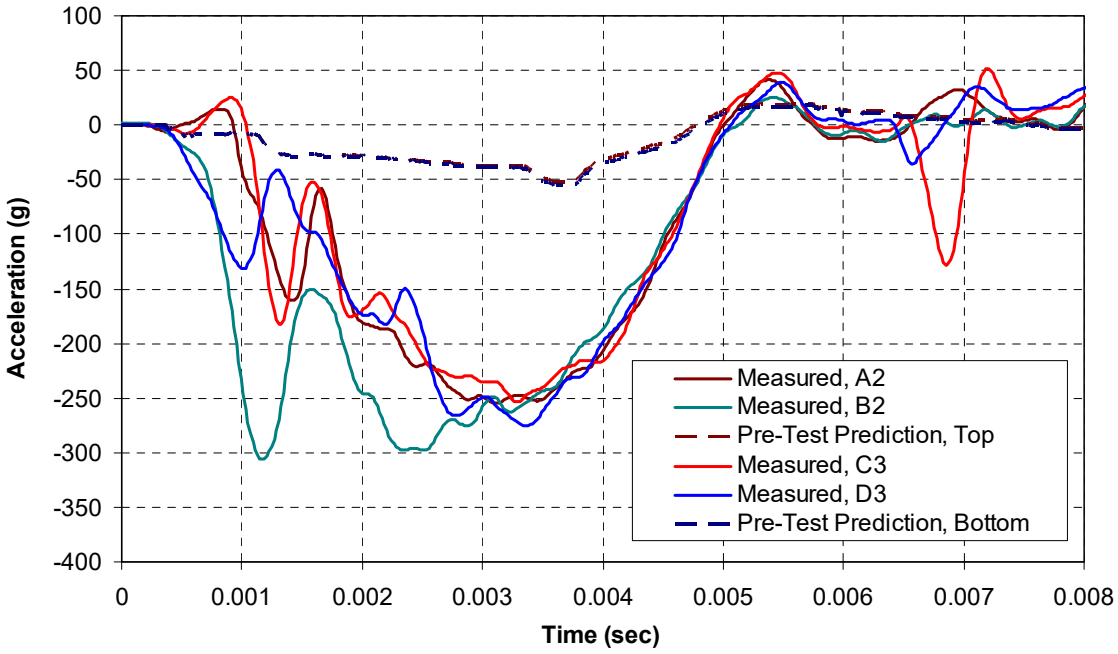


Figure 28 – **Test 2A Actual Acceleration Time History** (Transverse - X)

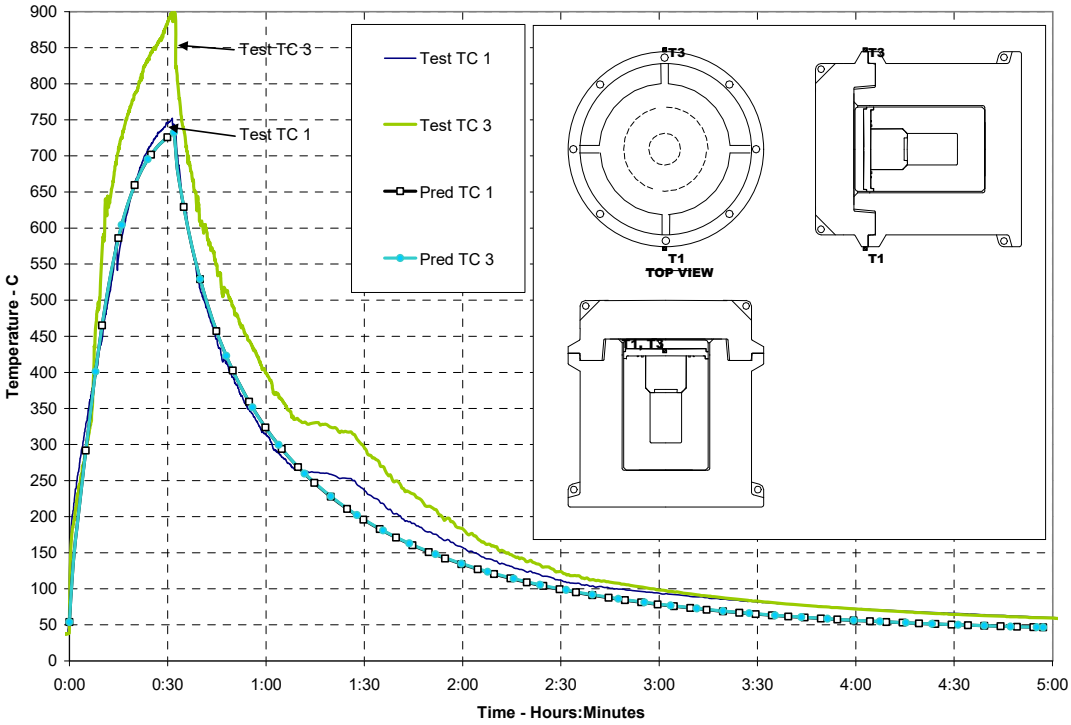


Figure 29 – **Test 2C TCs #1 & #3 Time-Temperature Traces**

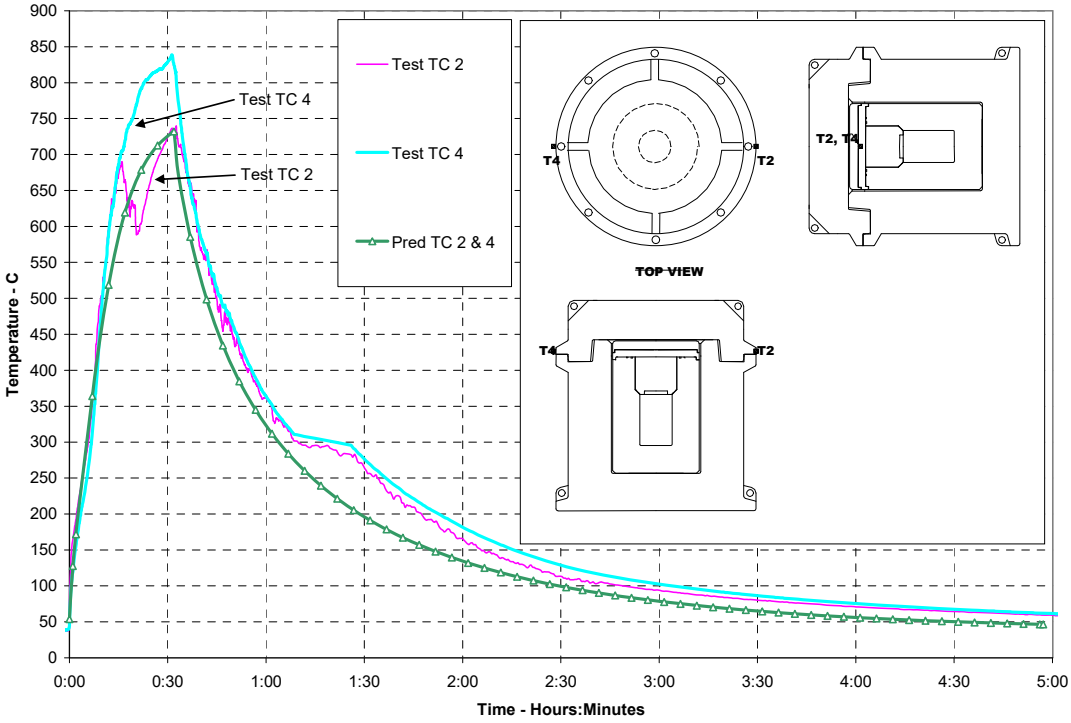


Figure 30 – **Test 2C TCs #2 & #4 Time-Temperature Traces**

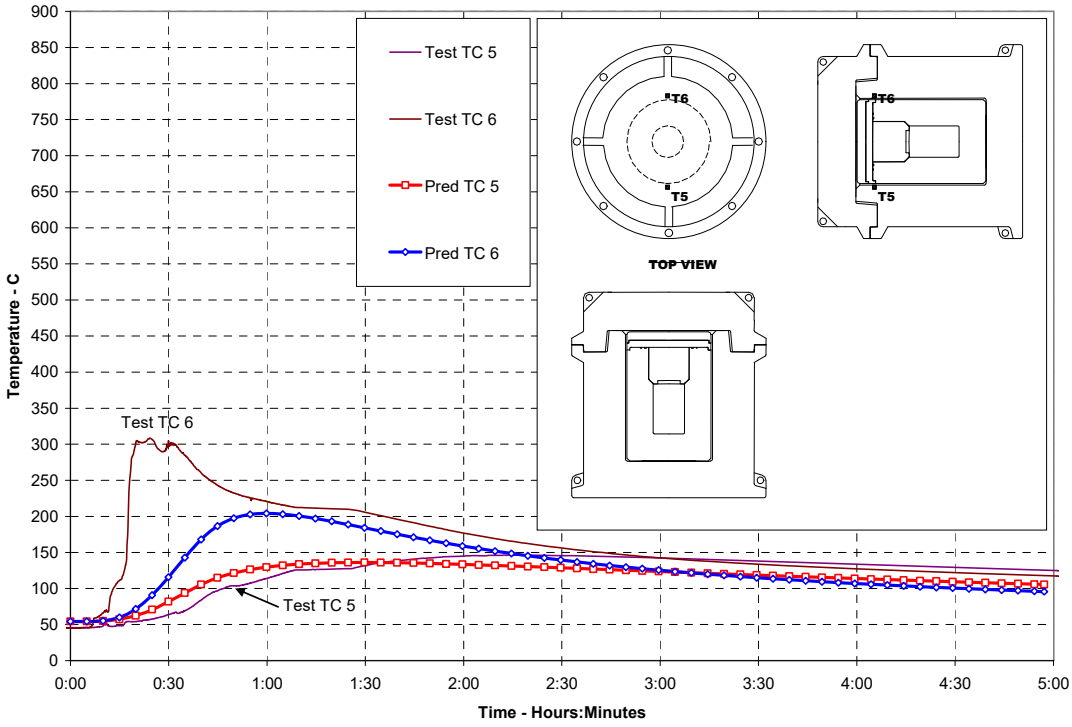


Figure 31 – **Test 2C TCs #5 & #6 Time-Temperature Traces**

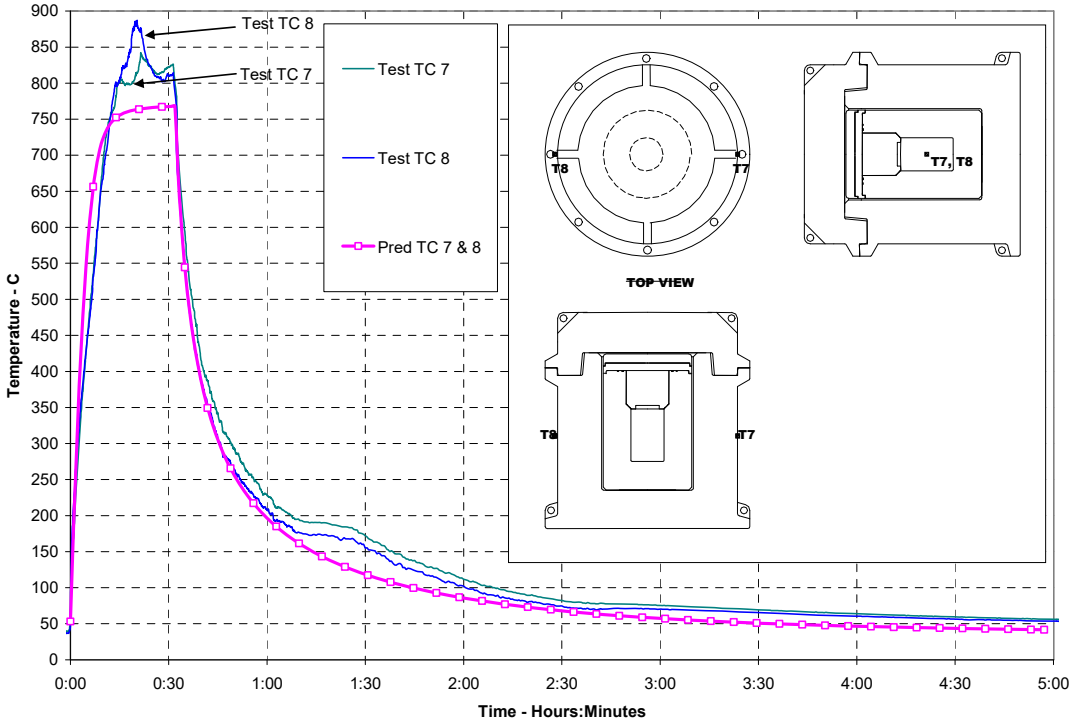


Figure 32 – **Test 2C TCs #7 & #8 Time-Temperature Traces**

Photograph 11 – **Test 1A Post-Drop Condition** (View 1)

Photograph 12 – **Test 1A Post-Drop Condition** (View 2)

Photograph 13 – **Test 1B Post-Drop Condition** (View 1)

Photograph 14 – **Test 1B Post-Drop Condition** (View 2)

Photograph 15 – **Test 1C Post-Drop Condition** (View 1)

Photograph 16 – **Test 1C Post-Drop Condition** (View 2)

Photograph 17 – **Test 1D Overpack Post-Drop Condition** (View 1)

Photograph 18 – **Test 1D Puncture Pin Post-Drop Condition** (View 2)

Photograph 19 – **Test 2A Post-Drop Condition** (View 1)

Photograph 20 – **Test 2A Post-Drop Condition** (View 2)

Photograph 21 – **Test 2B Post-Drop Condition** (View 1)

Photograph 22 – **Test 2B Post-Drop Condition** (View 2)

Photograph 23 – **Test 2C Post-Test Condition** (View 1)

Photograph 24 – **Test 2C Post-Test Condition** (View 2)

Photograph 25 – **Test 2C Post-Test Condition (View 3)**

Photograph 26 – **Test 2C Post-Test Condition** (View 4)

Photograph 27 – **Test 2C Post-Test Condition** (View 5)

Photograph 28 – **Test 2C Post-Test Condition** (View 6)

Photograph 29 – **Test 2C Post-Test Condition** (View 7)

Photograph 30 – **Test 2C Post-Test Condition** (View 8)

Photograph 31 – **Test 2C Post-Test Condition** (View 9)

Photograph 32 – **Test 2C Post-Test Condition** (View 10)

Photograph 33 – **Test 2C Post-Test Condition** (View11)

Photograph 34 – **Test 2C Post-Test Condition** (View 12)

Photograph 35 – **Test 2C Post-Test Condition** (View 13)

Photograph 36 – **Test 2C Post-Test Condition** (View 14)

Photograph 37 – **Test 2C Post-Test Condition** (View 15)

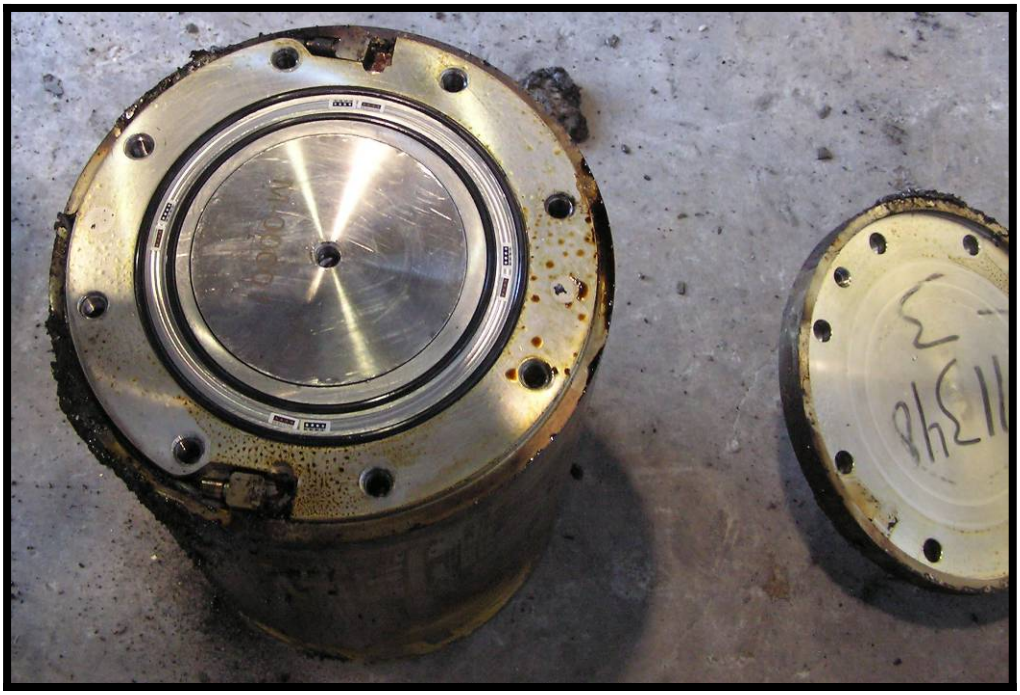

Photograph 38 – **Test 2C Post-Test Condition** (View 16)

Photograph 39 – **Test 2C Post-Test Overpack Base Foam Condition** (View 1)

Photograph 40 – **Test 2C Post-Test Overpack Base Foam Condition** (View 2)

Photograph 41 – **Test 2C Post-Test Overpack Base Foam Condition** (View 3)

Photograph 42 – **Test 2C Post-Test Overpack Base Foam Condition** (View 4)

Photograph 43 – **Test 2C Post-Test Overpack Lid Foam Condition** (View 1)

Photograph 44 – **Test 2C Post-Test Overpack Lid Foam Condition** (View 2)

Photograph 45 – **Test 2C Post-Test Overpack Lid Foam Condition** (View 3)

# 7 Summary and Conclusions

## 7.1 Summary of Results

### 7.1.1 Test 1A

As shown in Table 11, the maximum predicted deformation for the NCT bottom end drop was 4 mm. As shown in Table 15, no discernible post-drop permanent deformation was measured. Therefore, this result is considered acceptable.

As shown in Table 12, the maximum predicted acceleration magnitude for the NCT bottom end drop was 195g. As shown in Figure 23, the rough average of the measured peak accelerations is approximately 253g. The acceptability of this result is discussed Section 7.2.

### 7.1.2 Test 1B

As shown in Table 11, the maximum predicted deformation for the HAC top end drop was 40 mm. As shown in Table 15, the actual measured post-drop permanent deformation was 23 mm Therefore, this result is considered acceptable.

As shown in Table 12, the maximum predicted acceleration magnitude for the HAC top end drop was 350g. As shown in Figure 24, the rough average of the measured peak accelerations is approximately 325g. Therefore, this result is considered acceptable.

### 7.1.3 Test 1C

As shown in Table 11, the maximum predicted deformation for the HAC CG-over-top corner drop was 16 mm parallel to the longitudinal axis of the package at location L2 and 33 mm in the transvers direction at location H3. As shown in Table 15, the actual measured post-drop permanent deformation parallel to the longitudinal axis of the package was just under 10 mm and in the transverse direction was just over 27 mm for the average of locations L1 and L2. Therefore, this result is considered acceptable.

As shown in Table 12, the maximum predicted acceleration magnitude for the HAC CG-over-top corner drop was 298g. As shown in Figure 25 and Figure 26, the rough average of the measured peak acceleration is approximately 235g. Therefore, this result is considered acceptable.

### 7.1.4 Test 1D

As shown in Table 11, the maximum predicted deformation for the HAC bottom end oblique puncture drop was 22 mm. As presented in Section 6.1, the measured post-drop permanent deformation (gouge) depth was just under 16 mm. Therefore, this result is considered acceptable.

### 7.1.5 Test 2A

As shown in Table 11, the maximum predicted deformation for the HAC side drop was 31 mm. As shown in Table 15, the actual measured post-drop permanent deformation was under 1 mm along Datum A, just over 8 mm along Datum B, and just under 7 mm along Datum C. Therefore, this result is considered acceptable.

As shown in Table 12, the maximum predicted acceleration magnitude for the HAC side drop was 496g. As shown in Figure 27 and Figure 28, the rough average of the measured peak accelerations is approximately 650g with maximum measured peak accelerations of approximately 900g. The acceptability of this result is discussed Section 7.2.

### 7.1.6 Test 2B

As shown in Table 11, the maximum predicted deformation for the HAC side puncture drop was 22 mm. As presented in Section 6.1, the measured post-drop permanent deformation (gouge) depth was just over 25 mm (i.e., 1”). Therefore, this result is considered acceptable.

### 7.1.7 Test 2C

Figure 29 through Figure 32 present the maximum predicted vs. actual measured test article thermocouple traces for the HAC thermal test. As shown by these figures:

a. The predicted versus actual measured temperature-time traces for TC #1, TC #2, and TC #5 matched very well.

b. TC #3 saw a maximum measured temperature approximately 150°C higher than its predicted maximum temperature and TC # 6 actually saw a maximum measured temperature approximately 100°C higher than its predicted maximum temperature. For both of these top-dead-center thermocouple locations, it would appear that heat associated with the combustion of the large mound of foam material that extruded out of the overpack base assembly through both of its top-dead-center instrumentation cable bulkheads (see Photograph 23 and Photograph 24) is the most likely cause for these higher than predicted thermocouple readings. Proof of this proposed cause is demonstrated by the fact that the general furnace temperature is less than the recorded temperatures at these thermocouple locations.

c. It also appears that the heat associated with the large mound of foam also best explains the less pronounced differences in the predicted versus measured temperature-time traces for TC #7 and TC #8.

d. It also appears that the placement of the overpack lid foam vent holes may best explain the differences in the peak temperatures at TC #4 versus TC #2. As shown in Photograph 46 and Photograph 47, the foam vent plugs are located asymmetrically relative to TC #2 and TC #4 causing burning foam and flame jets erupting from these vent holes to affect these thermocouples differently.

Table 14 presents the maximum predicted peak temperatures at the temperature-indicating strip locations inside/on the cask assembly (i.e., S1 through S4 = 126°C; C1 and C2 = 119°C). As discussed in Section 6.2, the actual temperatures seen by the temperature-indicating strips were below their minimum sensitivity levels (i.e., S1 through S4 < 182°C; C1 and C2 < 132°C).

Photograph 39 appears to support the differences in temperatures between TC #1 versus TC #3 and TC # 5 versus TC #6. TC # 1 and TC #5 are on the side of the overpack base assembly away from the top-dead-center instrumentation cable bulkheads (to the left in Photograph 39). The foam in this bottom-dead-center area of the overpack base assembly foam cavity is noticeably less consumed (especially near TC #5) than the foam in the top-dead-center area.

Therefore, based above the above discussion, the thermocouple and temperature-indicating strip results are considered acceptable.

## 7.2 Summary of Significant Deviations and Conclusions

To the maximum extent practicable, the full-scale MIDUS confirmatory tests were performed by MSC utilizing subcontracted facilities, qualified personnel, and certified equipment at SwRI in accordance with the BFS confirmatory test specification (Reference 3) and test plan (Reference 4). The following deviations from the test specification and test plan requirements occurred:

a. As presented in Table 9, the package temperature was generally higher than the 65°F to 85°F temperature range specified in the Reference 3 test specification actually reaching as high as 104.2°F. It is not believed that these temperature differences significantly affected the results of the confirmatory test.

b. Based upon a careful study of the video recordings provided by SwRI:

    1. The bottom of the Test 1A test article impacted the drop test pad at an angle of approximately 1° as opposed to perfectly flat as shown in Figure 4. This difference in impact angle seems insignificant, but, as evidenced by Figure 23, the Test 1A results require further investigation.

    2. The top of the Test 1C test article impacted the drop test pad at an angle of approximately 20° as opposed to 35° from horizontal as shown in Figure 4. As evidenced by Figure 25 and Figure 26, it is not believed that this impact angle difference significantly affected the results of the confirmatory test.

    3. The side of the Test 2A test article impacted the drop test pad at an angle of approximately 17° as opposed to perfectly flat as shown in Figure 8. As evidenced by Figure 27 and Figure 28, this impact angle difference may have significantly affected the results of the confirmatory test and requires further investigation.

In addition, two anomalies were encountered during the post-drop inspections for Test 1C. The first anomaly involved the presence of a few drops of water inside the overpack as its lid was removed. The second anomaly involved the pressure rise leak rate test for Test 1C. Following

the removal of the cask closure lid assembly test port plug, an O-ring seal was found extruded up into the associated test port opening. A $10^{-3}$ ref cc/sec pressure rise leak rate test was successfully performed with the extruded O-ring in place, but it could not be determined that the post-drop containment O-ring seal integrity had actually been established especially in light of the drops of water discovered inside the overpack. Eventually, following the removal of the cask closure lid assembly from the cask body assembly, the leak test O-ring seal was found hanging from the test port plug opening on the bottom of the closure lid.

Appendix A presents an additional drop test (i.e., Supplemental Test 3X) designed to assure the integrity of the containment O-ring seal following a Test 1C HAC CG-over-top corner drop. This additional test confirmed that the containment O-ring seal maintains its integrity during this drop test. As a lesson-learned, a visual examination step has been added to the operational procedure to check for proper seating of the containment and leak test O-rings prior to installation of the closure lid. Consequently, the drops of water found inside the overpack during the post-drop inspections for Test 1C are believed to have been formed from condensation that occurred as the test article was moved from an air-conditioned (i.e., < 75°F) laboratory where it had been stored overnight to the very humid outside air environment at the drop pad. It is believed that this condensation formed over the cool inside surfaces of the test article, coalesced during the Test 1C drop, and was later found as water drops during the post-drop inspection activities.

Based upon the discussion above, it is believed that no further action is required relative to these test anomalies.

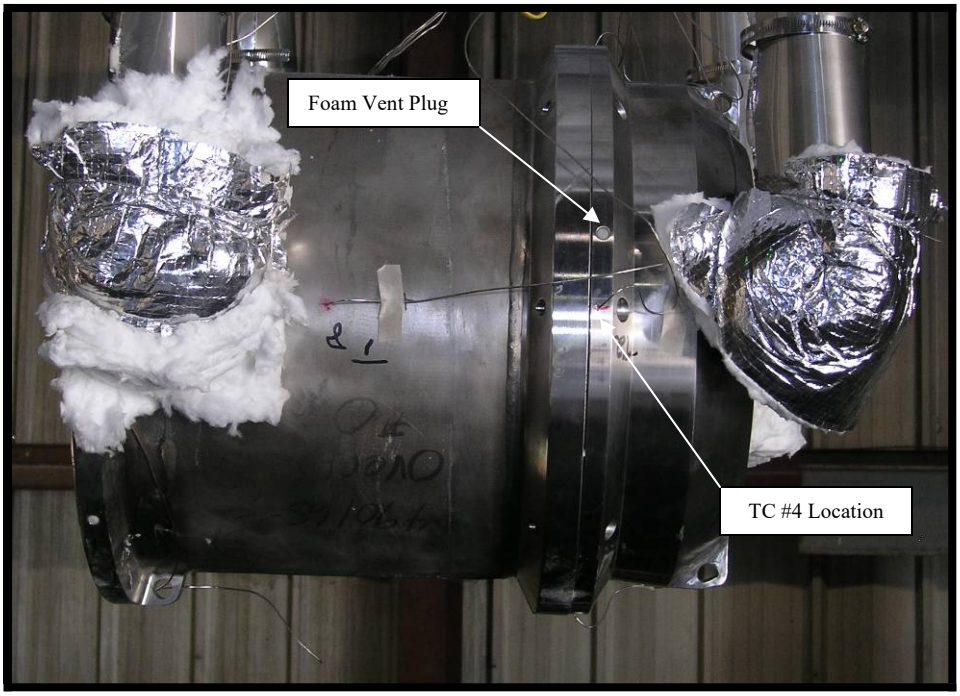


Photograph 46 – **TC #4 vs. Foam Vent Hole Location**

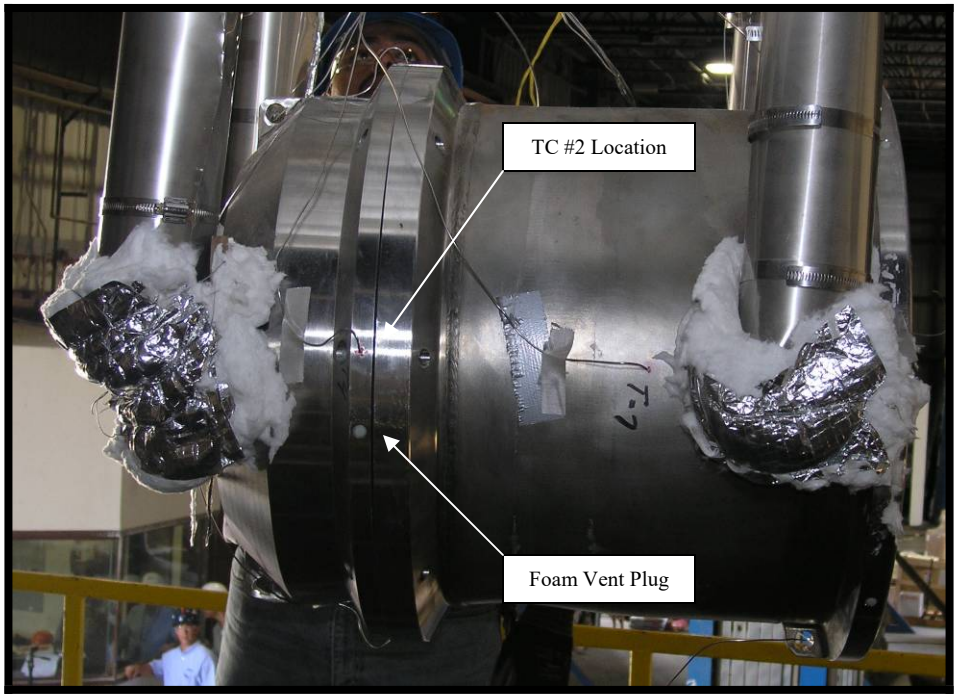


Photograph 47 – **TC #2 vs. Foam Vent Hole Location**

# 8 References


1. Title 10, Code of Federal Regulations, Part 71 (10CFR71), “Packaging and Transportation of Radioactive Material”, January 1, 2005.
2. International Atomic Energy (IAEA) Safety Series No. 37, “Advisory Material for the IAEA Regulations for the Safe Transport of Radioactive Material”, Third Edition.
3. BFS Document No. TYC01.1040, “MIDUS Transportation Package Confirmatory Test Specification”, Revision 2.
4. BFS Document No. TYC01-1041, “MIDUS Transportation Package Confirmatory Test Plan”, Revision 3.
5. BFS Calculation Package TYC01.1112, “MIDUS Confirmatory Thermal Predictions”, Revision 0.
6. BFS Calculation Package No. TYC01.1113, “MIDUS Confirmatory Drop Test Predictions”, Revision 0.
7. BFS Drawing No. TYC01-1230,” MIDUS Transportation Cask Shield Plug Assembly”, Revision 1.
8. BFS Drawing No. TYC01-1240, “MIDUS Transportation Cask Closure Lid Assembly”, Revision 1.
9. BFS Drawing No. TYC01-1246,” Shield Lid Assembly”, Revision 0.
10. BFS Drawing No. TYC01-1255, “Overpack Base Inner Shell”, Revision 1.
11. BFS Drawing No. TYC01-1262, “Overpack Lid Outer Top”, Revision 1.
12. BFS Drawing No. TYC01-1363, “Confirmatory Test Overpack Lid Flange”, Revision 2.
13. BFS Drawing No. TYC01-1272, “Polyurethane Foam”, Revision 1.
14. BFS Drawing No. TYC01-1300, “MIDUS Confirmatory Test Package Assembly”, Revision 0.
15. BFS Drawing No. TYC01-1310, “Confirmatory Test Cask Assembly”, Revision 1.
16. BFS Drawing No. TYC01-1320, “Confirmatory Test Cask Body Assembly”, Revision 1.
17. BFS Drawing No. TYC01-1350, “MIDUS Confirmatory Test Overpack Base Assembly”, Revision 1.
18. BFS Drawing No. TYC01-1353, “Confirmatory Test Overpack Base Outer Shell”, Revision 2.
19. BFS Drawing No. TYC01-1360, “Confirmatory Test Overpack Lid Assembly”, Revision 1.
20. BFS Drawing No. TYC01-1381, “Temperature-Indicating Strips”, Revision 1.
21. BFS File No. TYC01.1071.01, “MSC Test Article Fabrication Documentation”.
22. BFS File No. TYC01.1071.02, “MSC Confirmatory Test Documentation”.
23. BFS File No. TYC01.1071.03, “Century Industries/SwRI Confirmatory Test Documentation”.

Appendix A

**SUPPLEMENTAL TEST 3X**

## A.1 **Background**

As discussed in Section 7.2, two anomalies were encountered during the post-drop inspection for the Test 1C HAC CG-over-top corner drop. The first anomaly involved the presence of drops of water inside the overpack as its lid was removed (see Photograph 48 through Photograph 51). The second anomaly involved the pressure rise leak rate test for Test 1C. Following the removal of the cask closure lid test port plug, an O-ring seal was found extruded up into the associated test port opening as shown in Photograph 52. A $10^{-3}$ ref cc/sec pressure rise leak rate test was successfully performed with the extruded O-ring in place, but there was little confidence that the post-drop containment O-ring seal integrity had actually been established especially in light of the drops of water discovered inside the overpack. Eventually, as shown in Photograph 53, the extruded O-ring turned out to be the leak test O-ring seal.

This appendix presents the details for a supplemental drop test designed to assure the integrity of the containment O-ring seal following a Test 1C HAC CG-over-top corner drop.

## A.2 **Test Details**

The supplemental drop test utilized cask assembly M02 used in Tests 1A through 1D, overpack base OB2 used in Tests 1C and 1D, and deformed overpack lid OL1 used in the Test 1B HAC top end drop to repeat the Test 1C drop. The use of overpack lid OL1 was considered conservative because it had already experienced 23 mm of permanent deformation/foam compression during the Test 1B HAC top end drop and it was believed that this deformation would result in larger impact forces acting upon the containment O-ring seal and its clamping base and lid flanges than the original Test 1C drop test.

The supplemental drop test utilized the same testing procedure/sequence as original used for Test 1C, including a successful pre-drop pressure rise leak rate test to a $10^{-3}$ ref cc/sec acceptance criteria, but did not record any accelerometer readings because original Test 1C had already successfully recorded/provided this acceleration time history information. Instead, to establish that the containment O-ring seal had not "burped" during the original Test 1C drop test, the supplemental drop test utilizing colored (red) water as the dummy payload contents and assured that this colored water would reach the inside radius of the containment O-ring seal during the Test 1C drop by placing this water both inside and under the payload container.

## A.3 **Test Implementation**

As shown in Photograph 54, the instrumented test package, suspended from a crane by slings and a release mechanism, was again lifted above the test pad such that the lowest point of the package was 9 meter (30 feet) above the top surface of the drop test pad. The top surface of the test package overpack lid was oriented at an angle of 35° from horizontal, with the top end of the package facing toward the ground. The test package was released to free fall to the test pad and resulted in the permanent deformation shown in Photograph 55.

## A.4 **Test Results**

As shown in Photograph 56 and Photograph 57, the post-drop test inspection for the supplemental drop test found no water inside the overpack assembly and, as shown in Photograph 58, found no O-ring seal extruded up into the cask lid assembly test port. In addition, the containment O-ring seal successfully passed a $10^{-3}$ ref cc/sec pressure rise leak rate test. Following the removal of the cask lid assembly, it was found that the colored water had found its way to all parts of the cask assembly cavity inside the containment O-ring seal as shown in Photograph 59 through Photograph 62, but had not found its way through the containment O-ring seal during this second HAC CG-over-top corner drop.

The supplemental drop test confirmed that the containment O-ring seal maintains its integrity during a HAC CG-over-top corner drop. Consequently, the drops of water found inside the overpack during the post-drop inspections for Test 1C are now believed to be from condensation on the cool interior surfaces of the overpack assembly that occurred as the test article was moved from an air-conditioned (i.e., < 75°F) laboratory where it had been stored overnight to the very humid outside air environment at the drop pad. It is believed that this condensation coalesced during the Test 1C drop to be later found as water drops during the post-drop inspection activities. Therefore, in light of the success of the supplemental drop test, no further action is required relative to these latter test anomalies.

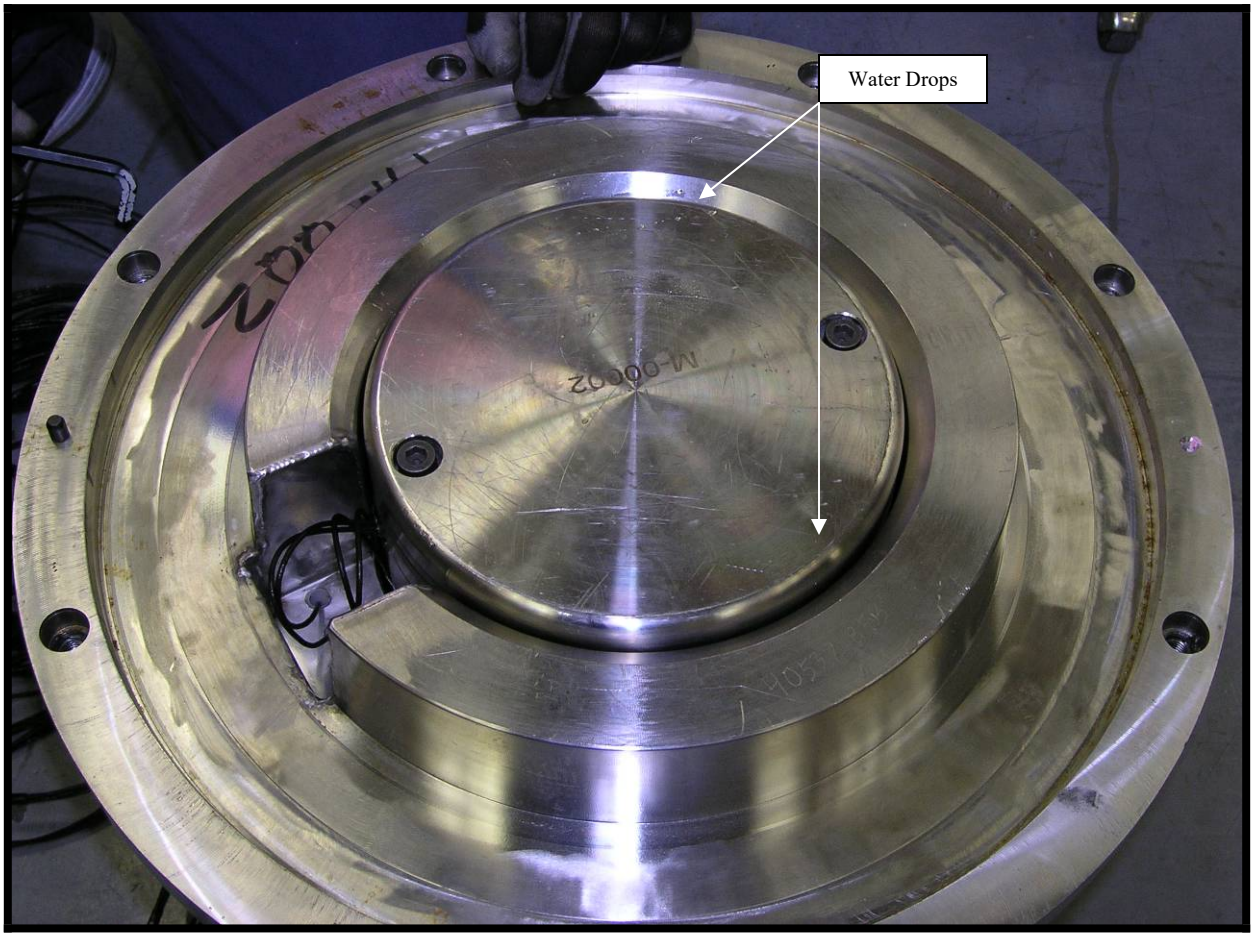


Photograph 48 – **Test 1C Post-Drop Inspection (**View 1)

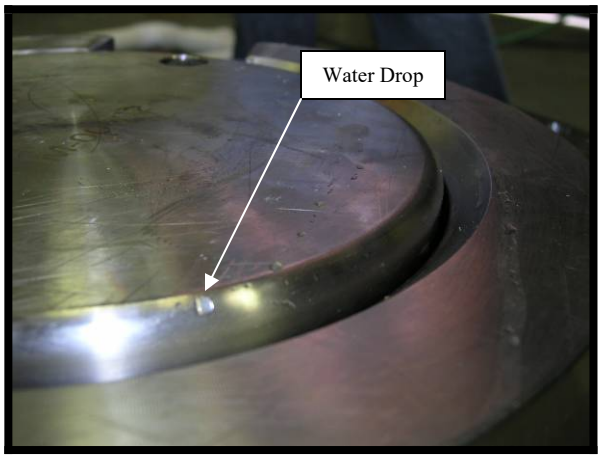


Photograph 49 – **Test 1C Post-Drop Inspection** (View 2)

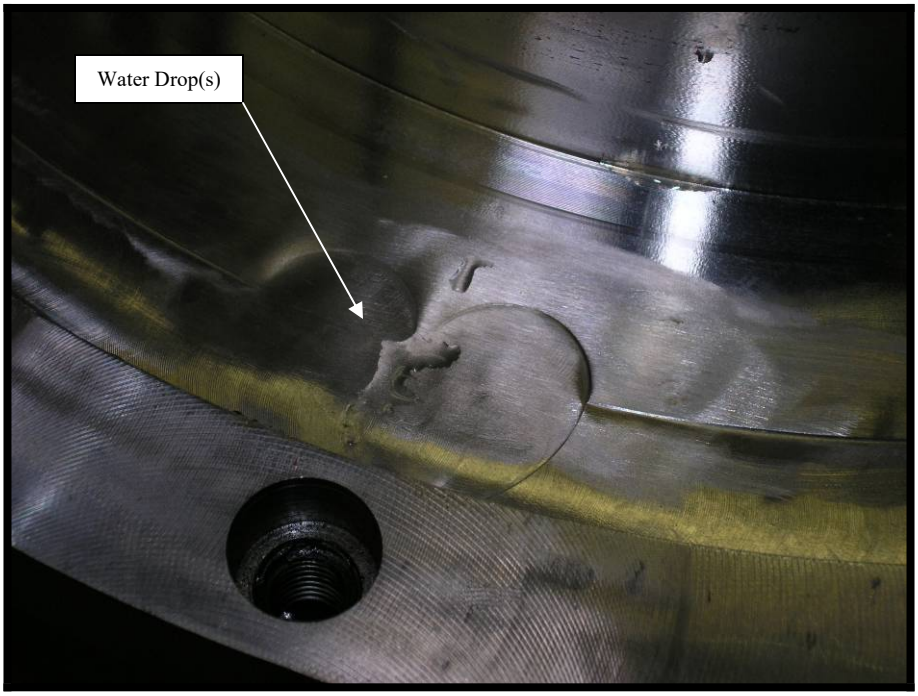


Photograph 50 – **Test 1C Post-Drop Inspection** (View 3)

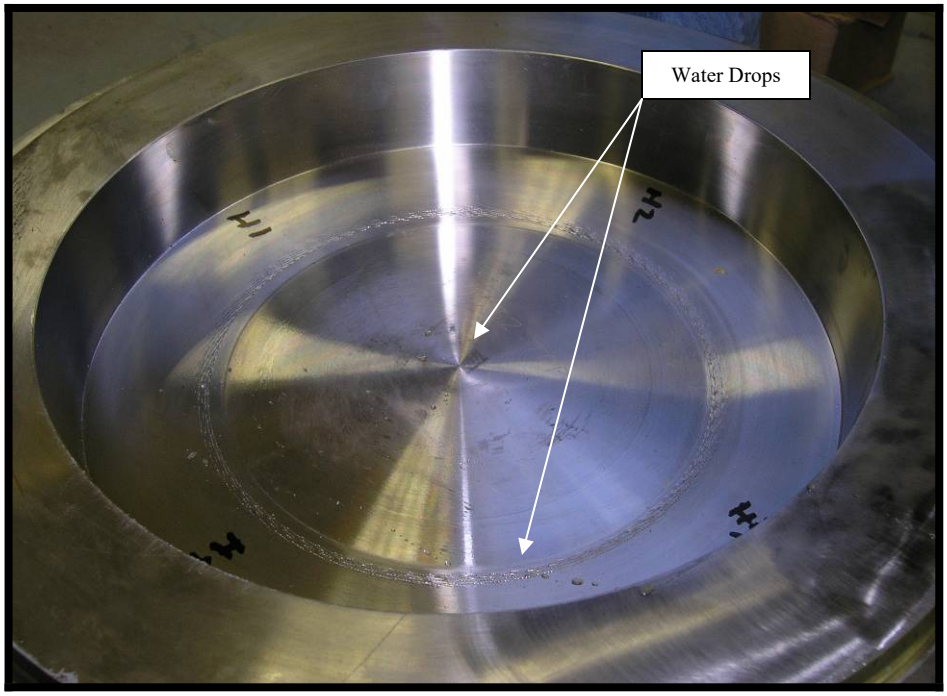


Photograph 51 – **Test 1C Post-Drop Inspection** (View 4)`

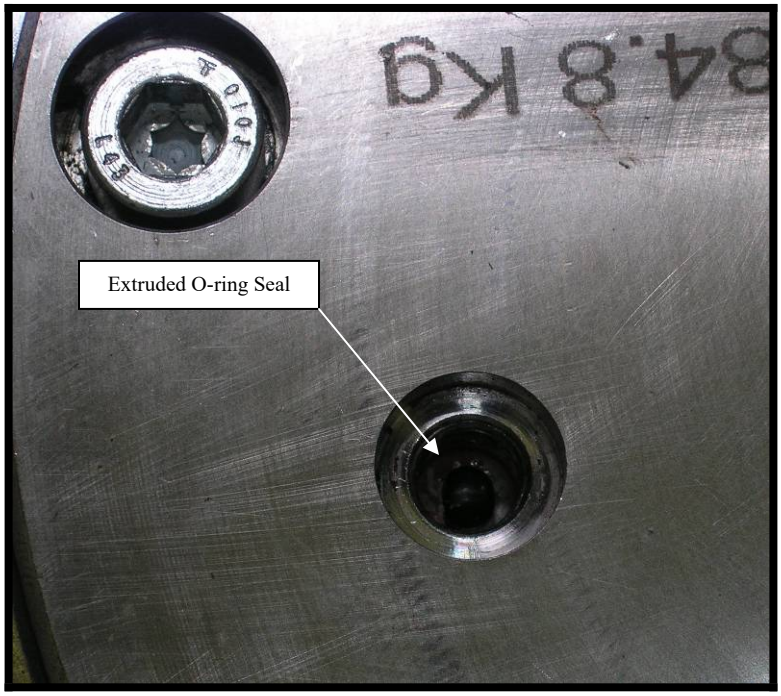


Photograph 52 – **Test 1C Post-Drop Inspection** (View 5)

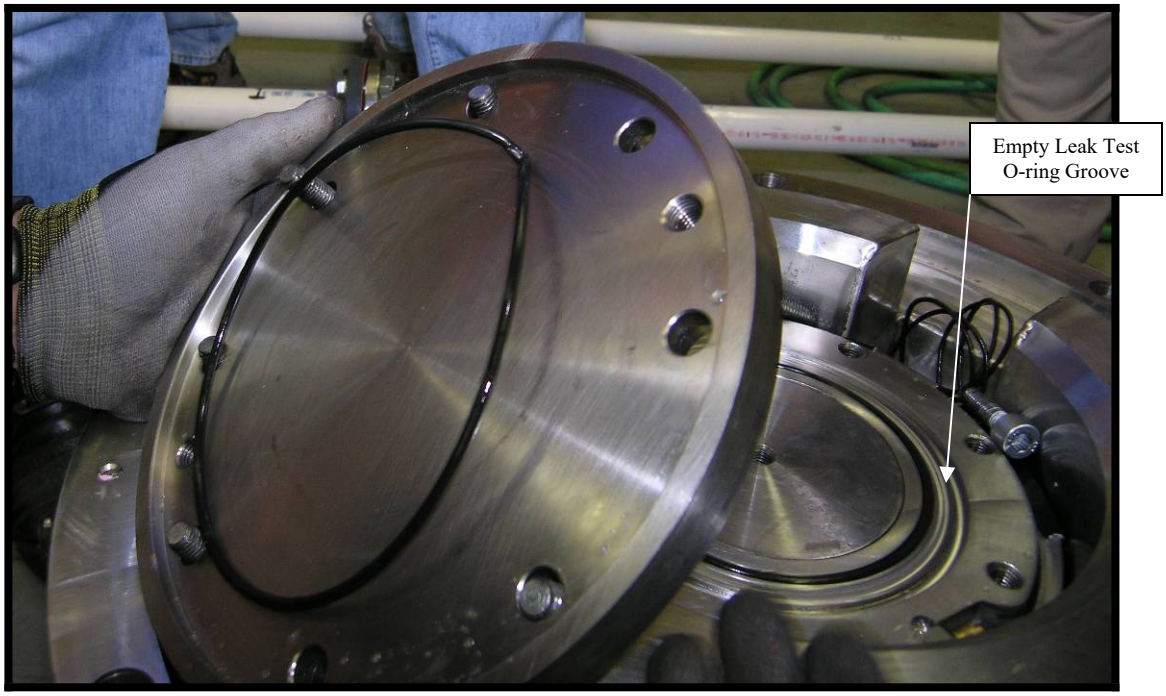


Photograph 53 – **Test 1C Post-Drop Inspection** (View 6)

Photograph 54 – **Supplemental Drop Test Implementation** (View 1)

Photograph 55 – **Supplemental Drop Test Implementation** (View 2)

Photograph 56 – **Supplemental Post-Drop Test Inspection** (View 1)

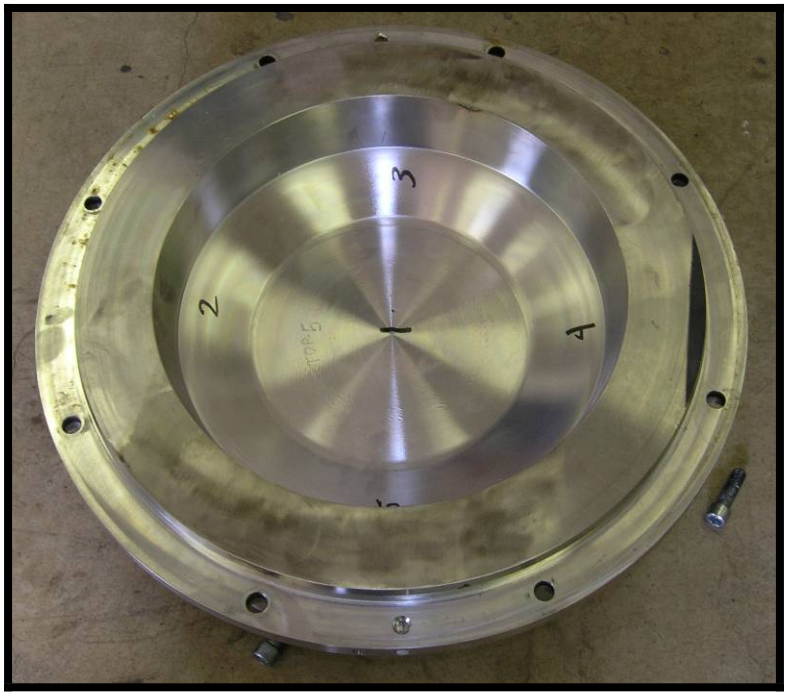


Photograph 57 – **Supplemental Post-Drop Test Inspection** (View 2)

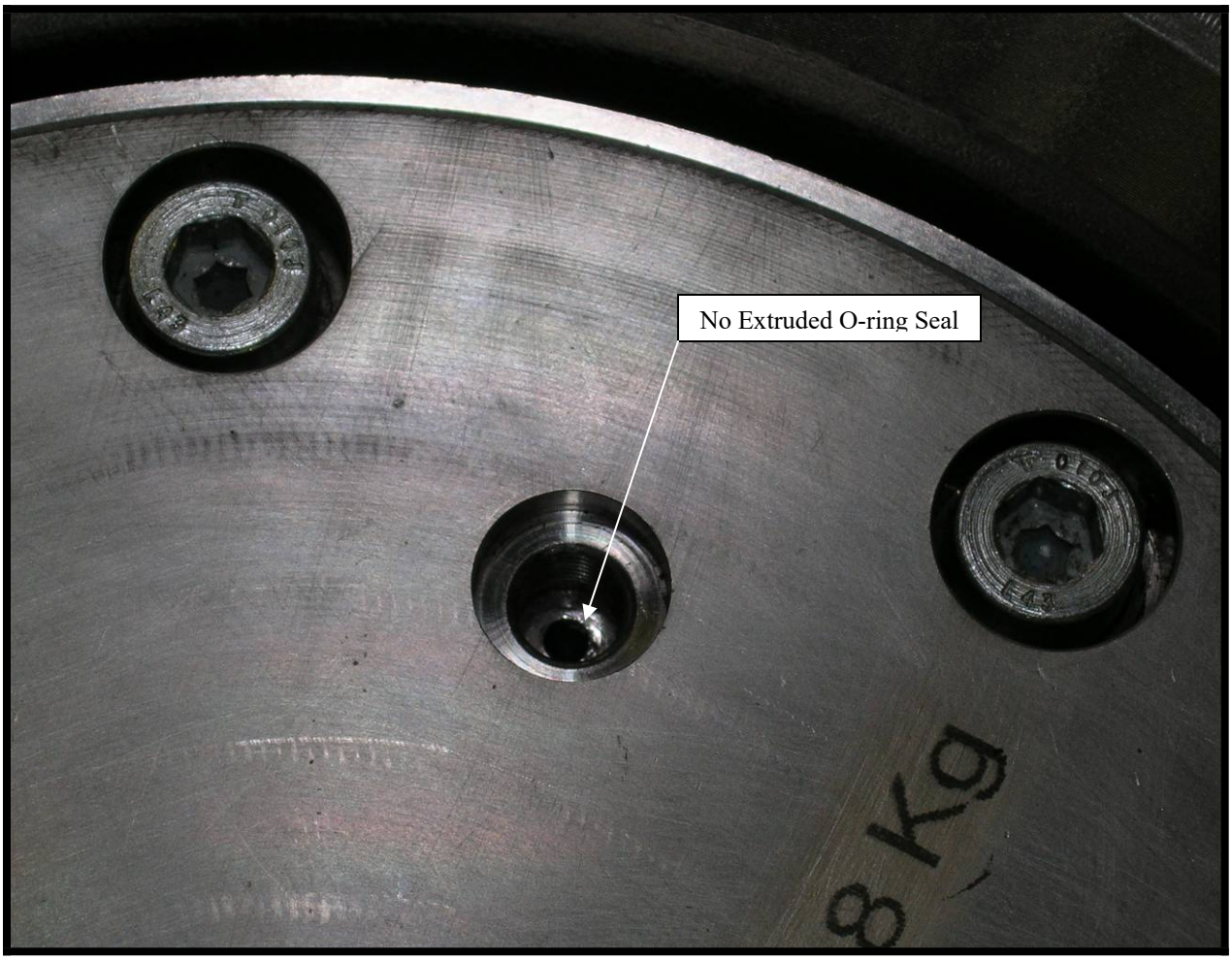


Photograph 58 – **Supplemental Post-Drop Test Inspection** (View 3)

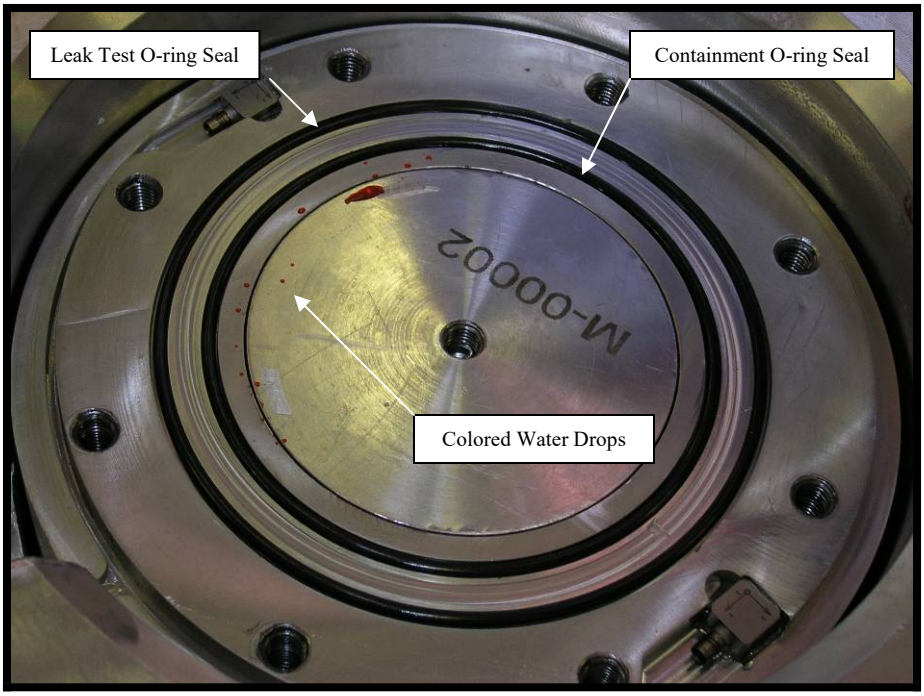


Photograph 59 – **Supplemental Post-Drop Test Inspection** (View 4)

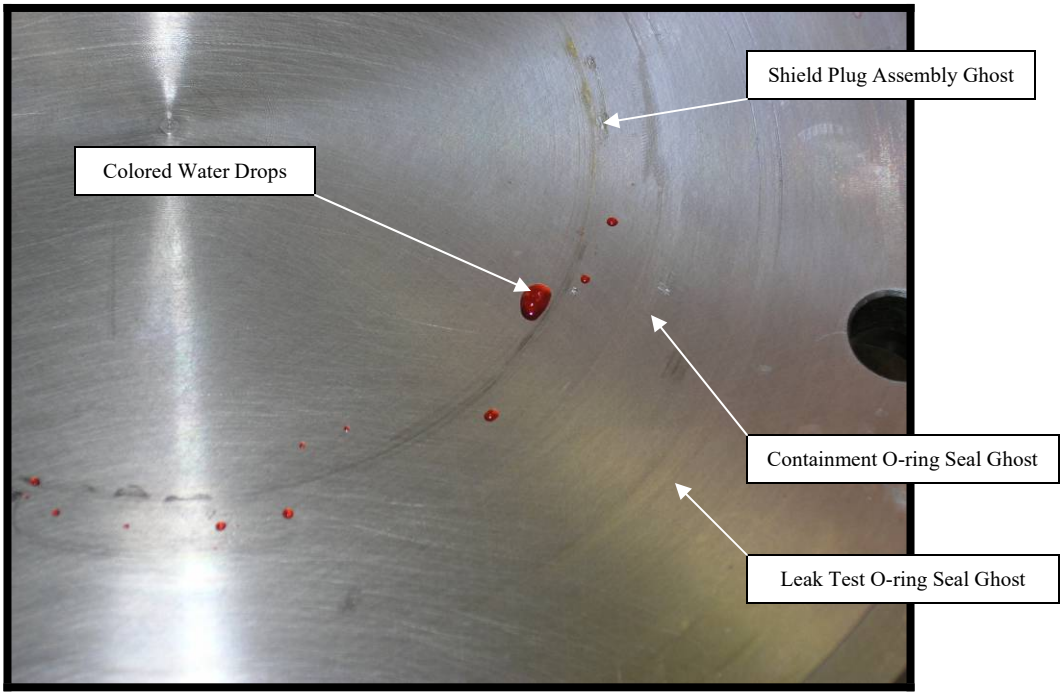


Photograph 60 – **Supplemental Post-Drop Test Inspection** (View 5)

Photograph 61 – **Supplemental Post-Drop Test Inspection** (View 6)

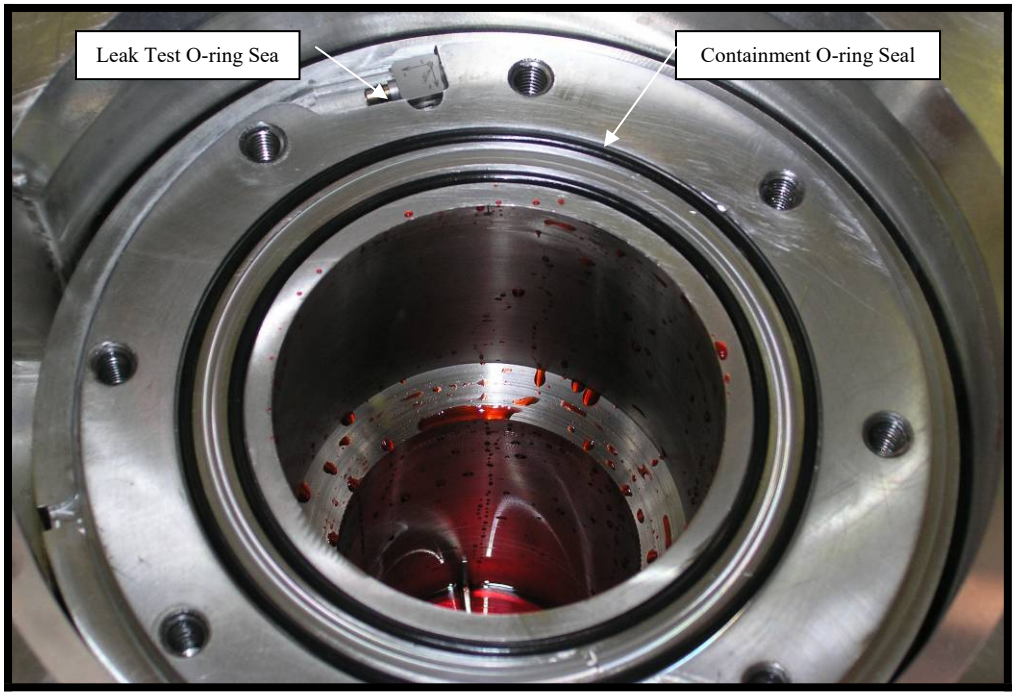


Photograph 62 – **Supplemental Post-Drop Test Inspection** (View 7)

#### 2.12.4.2 Confirmatory Test Reconciliation Analysis

(Attachment: Calc No. TYC01.1114, Revision 0, *MIDUS Confirmatory Drop Test Reconciliation Analysis*)

| BNG Fuel Solutions | **CALCULATION PACKAGE** | Calc. Pkg No. TYC01.1114<br>File No.: TYC01.1114<br>Revision: 0 |
|---|---|---|

**PROJECT/CUSTOMER:**

TYC01 / Mallinckrodt Medical, B.V.

**TITLE:**

MIDUS Confirmatory Drop Test Reconciliation Analysis

**SCOPE:**

Product: ☐ FuelSolutions™ ☐ VSC-24 ☒ Other _MIDUS_____

Service: ☐ Storage ☐ Transportation ☒ Other __Test_____

Conditions: ☒ Normal ☐ Off-Normal ☒ Accident ☐ Other _____

Component(s):

MIDUS Confirmatory Test Article

Prepared by:

Digitally signed by Steven E. Sisley
Reason: I have prepared this document.
Date: 2006.10.20 16:41:13 -07'00'

Verified by:

Digitally signed by Soo Bee Kok
Reason: I have verified this document
Date: 2006.10.20 16:42:26 -07'00'

Approved by Engineering Manager:

Digitally signed by Ram Srinivasan
Reason: I am approving this document
Date: 2006.10.20 17:03:05 -07'00'


© 2006 BNG Fuel Solutions Corporation
All Rights Reserved

## RECORD OF REVISIONS

| REV. | AFFECTED PAGES | AFFECTED MEDIA | DESCRIPTION | NAMES (Print or Type) | |
|---|---|---|---|---|---|
| | | | | PREPARER | CHECKER |
| 0 | 1 - 28. | 1 CD-ROM | Initial Issue | S. Sisley | Soo Bee Kok |
| | | | | | |
| | | | | | |
| | | | | | |

## *RECORD OF VERIFICATION*

| | YES | NO | N/A |
|---|---|---|---|
| (a) The objective is clear and consistent with the analysis. | ☒ | ☐ | |
| (b) The inputs are correctly selected and incorporated into the design. | ☒ | ☐ | ☐ |
| (c) References are complete, accurate, and retrievable. | ☒ | ☐ | ☐ |
| (d) Basis for engineering judgments is adequately documented. | ☒ | ☐ | ☐ |
| (e) The assumptions necessary to perform the design activity are adequately described and reasonable. | ☒ | ☐ | ☐ |
| (f) Assumptions and references, which are preliminary, are noted as being preliminary. | ☐ | ☐ | ☒ |
| (g) Methods and units are clearly identified. | ☒ | ☐ | ☐ |
| (h) Any limits of applicability are identified. | ☒ | ☐ | ☐ |
| (i) Computer calculations are properly identified. | ☒ | ☐ | ☐ |
| (j) Computer codes used are under configuration control. | ☒ | ☐ | ☐ |
| (k) Computer codes used are applicable to the calculation. | ☒ | ☐ | ☐ |
| (l) Input parameters and boundary conditions are appropriate and correct. | ☒ | ☐ | |
| (m) An appropriate design method is used. | ☒ | ☐ | |
| (n) The output is reasonable compared to the inputs. | ☒ | ☐ | |
| (o) Conclusions are clear and consistent with analysis results. | ☒ | ☐ | |

COMMENTS:

None.

Verifier: Digitally signed by Soo Bee Kok
Reason: I have verified this document
Date: 2006.10.20 16:42:59 -07'00'

## TABLE OF CONTENTS


1. INTRODUCTION ..... 7

1.1 Objective ..... 7

1.2 Purpose ..... 7

1.3 Scope ..... 7

2. REQUIREMENTS ..... 8

2.1 Design Inputs ..... 8

2.2 Regulatory Commitments ..... 8

3. REFERENCES ..... 9

3.1 BFS Calculation Packages ..... 9

3.2 General References ..... 9

4. ASSUMPTIONS ..... 10

4.1 Design Configuration ..... 10

4.2 Design Criteria ..... 10

4.3 Calculation Assumptions ..... 10

5. CALCULATION METHODOLOGY ..... 11

6. CALCULATIONS ..... 12

6.1 NCT Bottom End Drop (Test 1A) ..... 12

6.2 HAC Top End Drop (Test 1B) ..... 14

6.3 HAC Top Corner Drop (Test 1C) ..... 16

6.4 HAC Bottom Puncture Drop (Test 1D) ..... 19

6.5 HAC Side Drop (Test 2A) ..... 21

6.6 HAC Side Puncture Drop (Test 2B) ..... 24

7. CONCLUSIONS ..... 26

7.1 Results ..... 26

7.2 Compliance With Requirements ..... 27
7.3 Range of Validity ..... 27
7.4 Summary of Conservatism ..... 27
7.5 Limitations or Special Instructions ..... 27
8. ELECTRONIC FILES ..... 28
8.1 Computer Runs ..... 28
8.2 Other Electronic Files ..... 28

## LIST OF FIGURES

Figure 6-1 - Test 1A Acceleration Time-History Comparison, Measured vs. Post-Test Analysis .....13

Figure 6-2 - Test 1B Acceleration Time-History Comparison, Measured vs. Post-Test Analysis .....15

Figure 6-3 - Test 1C Acceleration Time-History Comparison, Measured vs. Post-Test Analysis .....17

Figure 6-4 - Test 1C Overpack Damage Comparison .....18

Figure 6-5 - Test 1D Overpack Permanent Deformation .....20

Figure 6-6 - Test 2A Acceleration Time-History Comparison, Measured vs. Post-Test Analysis .....22

Figure 6-7 - Test 2A Overpack Damage Deformation .....23

Figure 6-8 - Overpack Assembly Permanent Displacement Contour Plot, HAC 1m Side Oblique Puncture Drop (Test 2B).....25

# 1. INTRODUCTION

Confirmatory drop tests were performed to check the adequacy of the analytical methodology used to predict the responses of the MIDUS package when subjected to the free drop tests specified in 10CFR71 [Design Input 2.1.1]. Prior to performing the confirmatory drop tests, calculations were performed using the same analytical methodology that is used for the safety analyses to predict the package responses for the planned test conditions. The results of these confirmatory drop tests and the comparisons to the pre-test predictions are documented in a test report (Reference 3.2.1). In general, the test report concludes that the analytical methodology used to predict the package response to NCT free drop, HAC free drop, and HAC puncture drop tests is adequate. However, a few notable differences between the pre-test predictions and measured package responses require further analysis to determine if changes to the safety analyses are required. These differences are thought to result from actual impact angles that varied significantly from the planned impact angles and an error in the definition of the moment of inertia (MOI) specified for the rigid-body that represents the cask/shield lid assembly in the analytical model.

## 1.1 Objective

The objective of this analysis is to perform post-test analyses of the confirmatory tests, using the impact angles that occurred during the confirmatory tests and the corrected MOI for the cask/shield lid rigid-body.

## 1.2 Purpose

The purposes of this calculation package are: (1) To confirm that the corrections made to the confirmatory test analysis provide reasonable agreement with the measured results from the confirmatory test, and (2) To identify any necessary changes that must be considered in the package safety analysis.

## 1.3 Scope

The scope of this calculation package includes the structural responses of the MIDUS overpack assembly and cask assembly to the confirmatory drop test conditions (i.e., Tests 1A through 1D, Test 2A, and Test 2B) described in the test report (Ref. 3.2.1).

## 2. REQUIREMENTS

### 2.1 Design Inputs

2.1.1. Title 10, Code of Federal Regulations, Part 71 (10CFR71), *Packaging and Transportation of Radioactive Material*, January 1, 2005.

### 2.2 Regulatory Commitments

None.

## 3. REFERENCES

### 3.1 BFS Calculation Packages

3.1.1. TYC01.1113, Revision 0, "*MIDUS Confirmatory Drop Test Predictions*."

3.1.2. TYC01.1101, Revision 1, "*MIDUS Transportation Package Drop Loads Analysis*."

3.1.3. TYC01.1100, Revision 0, "*MIDUS Transportation Package Mass Properties.*"

### 3.2 General References

3.2.1. TYC01.1071, Revision 0, "MIDUS Transportation Package Confirmatory Test Report."

## 4. ASSUMPTIONS

### 4.1 Design Configuration

The configuration of the package used for the confirmatory drop tests is described in Reference 3.1.1.

### 4.2 Design Criteria

Not applicable to confirmatory drop test predictions.

### 4.3 Calculation Assumptions

All assumptions used in this calculation package are the same as those described in Reference 3.1.1, except for the following:

(a) The MOI of the cask/shield assembly rigid-body is defined about the local center of gravity of the rigid-body. The nominal mass properties of the production unit cask/shield lid assembly are assumed for this analysis. The local MOI of the cask assembly with the shield lid assembly attached is 2.53E+06 kg-mm$^2$ per Reference 3.1.3.

(b) During Test 1A (1.2m Bottom End Drop) the test package impacted to the drop test pad at a small angle rather than flat (i.e., 0° impact angle) as intended. Test 1A records show that the package was oriented at an angle 0.2° when suspended 1.2m above the drop test pad. The actual angle of impact for Test 1A is estimated to be 1° from the high-speed video recording of the test (Ref. 3.2.1, Section 7.3).

(c) During Test 1C (9m Top Corner Drop) the test package impacted to the drop test pad at an angle of approximately 160° (i.e. 20° from a top end drop) (Ref. 3.2.1, Section 7.3) rather than the planned impact angle of 145° (i.e., 35° from a top end drop). The angle of impact for Test 1C was estimated from the high-speed video recording of the test.

(d) During Test 2A (9m Side Drop) the test package impacted to the drop test pad at an angle of approximately 107° (i.e. 17° top end oblique drop) (Ref. 3.2.1, Section 7.3) rather than the planned impact angle of 90° (i.e., a horizontal side drop). The angle of impact for Test 2A was estimated from the high-speed video recording of the test.

## 5. CALCULATION METHODOLOGY

The methodology employed in this calculation package is the same as the methodology used for the MIDUS confirmatory drop test predictions in Reference 3.1.1. The only differences are those discussed in Section 4.3.

## 6. CALCULATIONS

### 6.1 NCT Bottom End Drop (Test 1A)

Test 1A was a free drop from a height of 1.2m onto the bottom end of the test package. The test results show that the package impacted the drop test pad at an angle of approximately 1° versus the 0° impact angle used in the pre-test prediction analysis. Thus, the post-test analysis for Test 1B is performed for a 1° impact angle. In addition, the MOI used for the cask rigid-body is corrected in the post-test analysis, as discussed in Section 4.3.

The results of this post-test analysis are included in computer run I.D. *TEST1A_R1.out*. A comparison of the post-test analysis acceleration time-history results with the measured acceleration time-history results is shown in Figure 6-1. The comparison shows good agreement through the initial peak on "side 1", with the post-test analysis peak acceleration of 240*g* slightly higher than the measured peak acceleration of 234*g*. The differences beyond this initial peak are attributed to variation between cask/overpack interface assumed in the analysis and existing during the test. The results of the post-test analysis for Test 1A also show that the calculated overpack damage is essentially the same as that from the pre-test prediction. Thus, it is concluded that analytical methodology used to prediction the package response to the 1.2m bottom end drop is adequate.

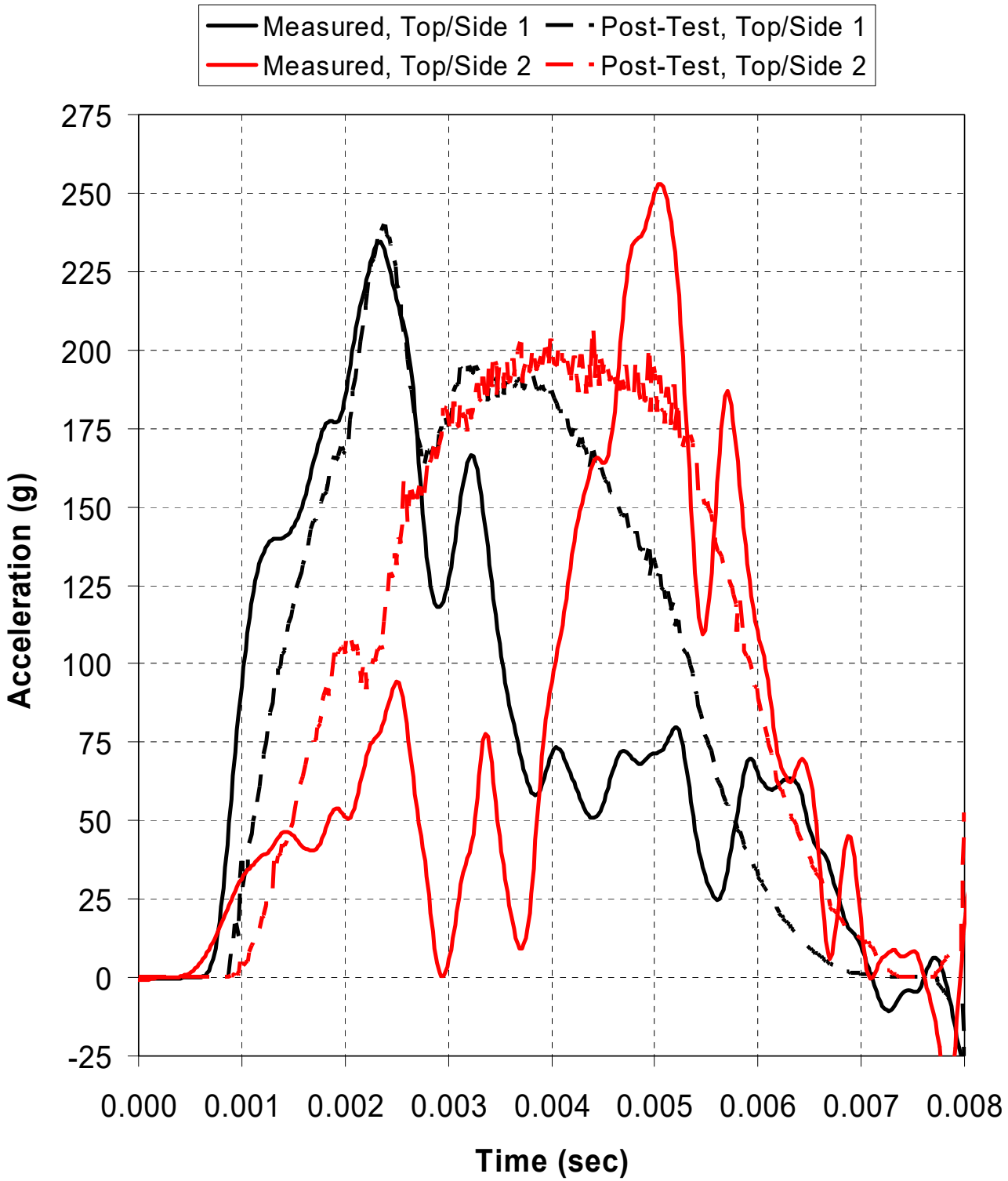


**Figure 6-1 - Test 1A Acceleration Time-History Comparison, Measured vs. Post-Test Analysis**

## 6.2 HAC Top End Drop (Test 1B)

Test 1B was a free drop from a height of 9m onto the top end of the test package. The test results show that the package impacted the drop test pad in the planned orientation. Thus, no corrections are made to the Test 1B impact angle in this analysis. The only change from the pre-test prediction analysis is to the MOI used for the cask rigid-body, as discussed in Section 4.3.

The results of this post-test analysis, which are included in computer run I.D. *TEST1B_R1.out*, show that the change to the MOI has no significant effect on the analysis results. The calculated acceleration time-history response of the cask rigid-body is essentially the same as that from the pre-test prediction. As shown in Figure 6-2, the calculated acceleration time-history response of the cask rigid-body agrees reasonably well with the measured acceleration time-history response of the test cask. The results of the post-test analysis for Test 1B also show that the calculated overpack damage is essentially the same as that from the pre-test prediction.

Therefore, it is concluded that the change to the value of the cask rigid-body MOI has no effect on Test 1B. This is expected for end drops because they should not cause any rotation of the cask rigid-body. The results of the Test 1B post-test analysis confirm that it is not necessary to revise any of the NCT or HAC top or bottom end drop analysis that were previously performed using the incorrect cask MOI since the results are not expected to change.

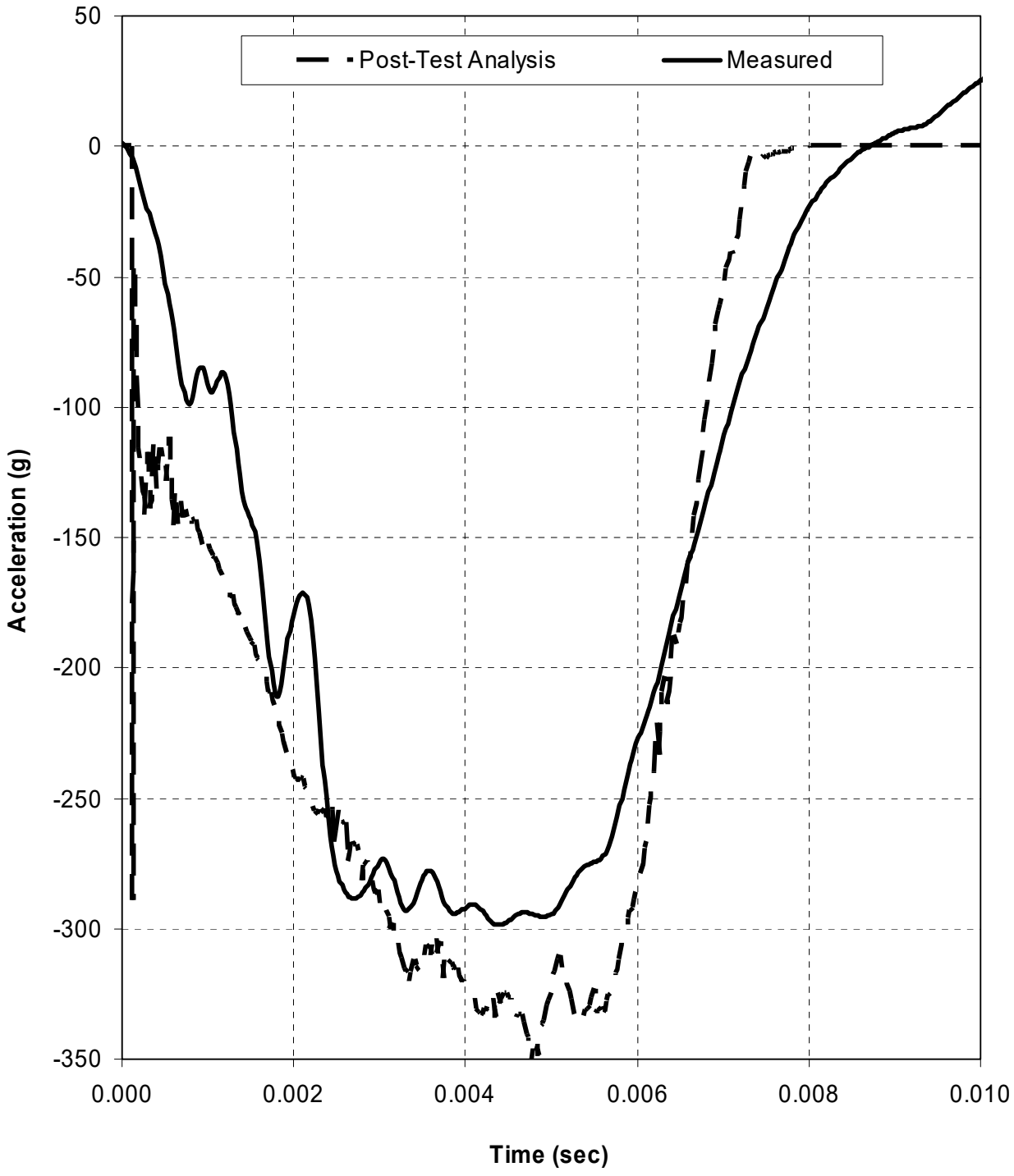


**Figure 6-2 - Test 1B Acceleration Time-History Comparison, Measured vs. Post-Test Analysis**

### 6.3 HAC Top Corner Drop (Test 1C)

Test 1C was a free drop from a height of 9m onto the top corner of the test package. The test results show that the package impacted the drop test pad at an angle of approximately 160° (i.e. 20° from a top end drop) rather than the planned impact angle of 145° (i.e., 35° from a top end drop). Thus, the post-test analysis for Test 1C is performed for a 160° impact angle. In addition, the MOI used for the cask rigid-body is corrected in the post-test analysis, as discussed in Section 4.3.

The results of this post-test analysis are included in computer run I.D. *TEST1C_R1.out*. A comparison of the measured and post-test analysis acceleration time-history results is shown in Figure 6-3. This comparison shows good agreement between the analysis results and the measured results. However, these results do not differ significantly from the pre-test predictions. Most of the difference is attributed to the change in the impact angle. The MOI of the cask rigid-body does not have a significant effect on the solution for impact angles that are close to a "stable" orientation, such as the c.g. over top corner drop. Figure 6-4 shows a comparison of the damage to the exterior of the package from the pre-test prediction, the test results, and the post-test analysis. These results show that the predicted damage from the post-test analysis agrees reasonably well with the damage resulting from the test. The results also show that the changes made in the post-test analysis result in a significant reduction of the closure bolt shear stresses. Again, this is attributed primarily to the impact angle and not the cask MOI.

Therefore, it is concluded that the change to the value of the cask rigid-body MOI has no effect on Test 1C. This is expected for end drops because they should not cause any rotation of the cask rigid-body. The results of the Test 1C post-test analysis confirm that it is not necessary to revise any of the NCT or HAC top or bottom corner drop analyses that were previously performed using the incorrect cask MOI since the results are not expected to change.

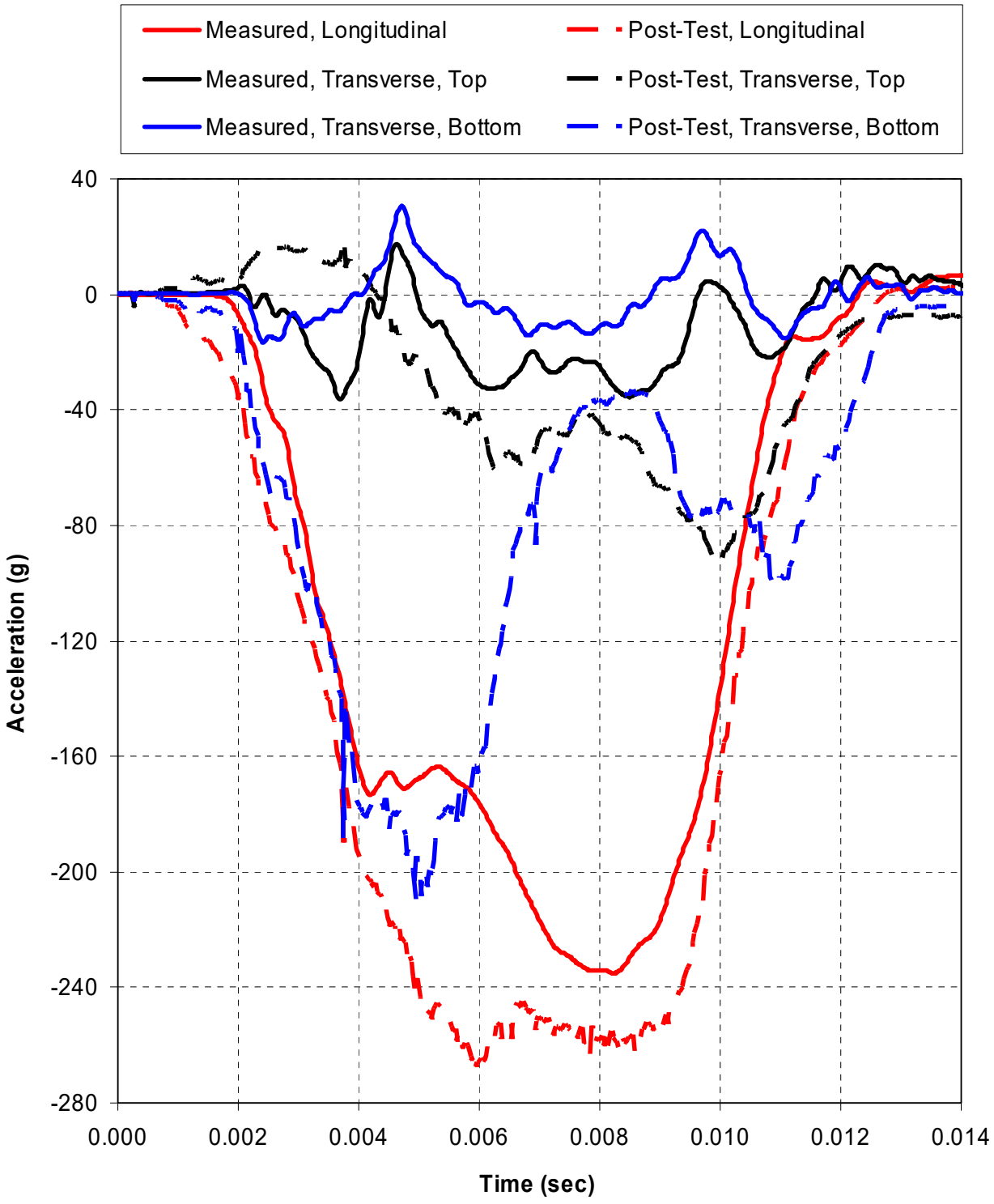


**Figure 6-3 - Test 1C Acceleration Time-History Comparison, Measured vs. Post-Test Analysis**

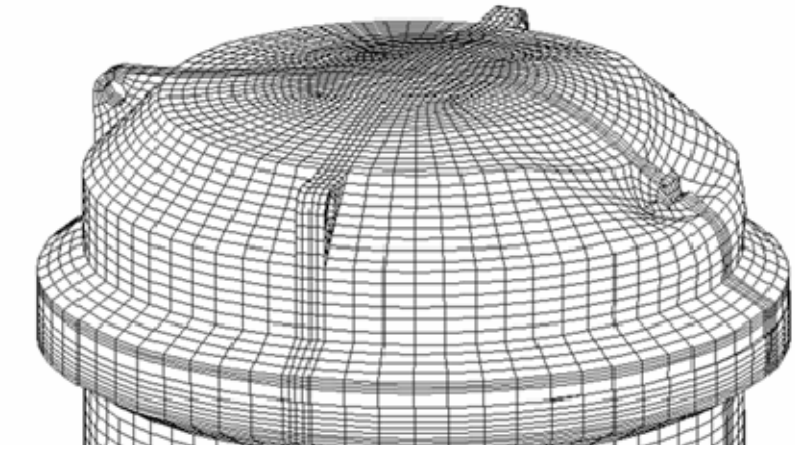

Pre-Test Analysis

Test 1C Result

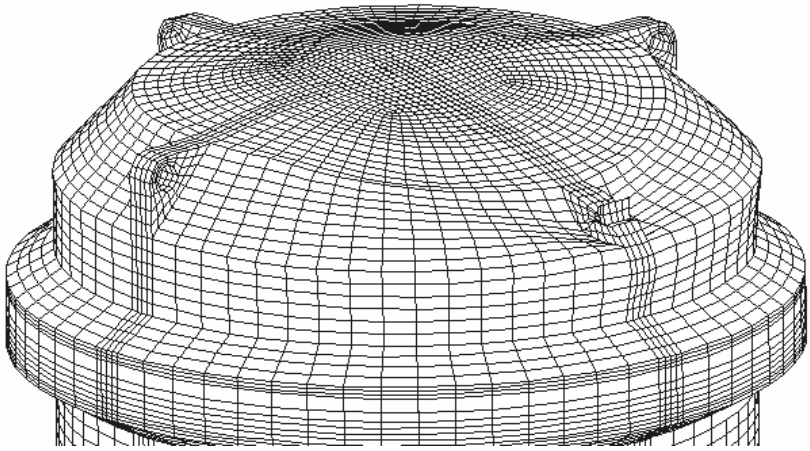

Post-Test Analysis

**Figure 6-4 - Test 1C Overpack Damage Comparison**

### 6.4 HAC Bottom Puncture Drop (Test 1D)

Test 1D was a free drop of the package from a height of 1m onto the top end of a mild steel puncture bar that was mounted on the drop test pad. The test package was oriented at an angle of 25° from vertical, with its center of gravity directly over the top corner of the puncture bar. The test results show that the package impacted the puncture bar in the planned orientation. Thus, no corrections are made to the Test 1D impact angle in this analysis. The only change from the pre-test prediction analysis is to the MOI used for the cask rigid-body, as discussed in Section 4.3.

The Test 1D post-test analysis results show that the maximum strain intensity (EPTOINT) in the overpack base outer bottom plate is 14% (node 5006 at t = 0.0084749 seconds), which is the same as the maximum strain intensity from the pre-test prediction analysis. A comparison of the overpack permanent deformation from the Test 1D pre-test prediction analysis and the post-test analysis is shown in Figure 6-5. The comparison shows that the permanent deformation from the post-test analysis is essentially the same as that from the pre-test prediction analysis. The only difference appears to be slightly more rigid-body rotation of the package in the post-test analysis results, which is expected for the corrected cask MOI.

Therefore, it is concluded that the change to the value of the cask rigid-body MOI has no significant effect on Test 1D. This is expected because Test 1D is a "stable" drop orientation (i.e., package c.g. located directly over the struck corner of the puncture bar) that should not cause any significant rotation of the package. The results of the Test 1D post-test analysis confirm that it is not necessary to revise any of the HAC puncture drop analyses that were previously performed using the incorrect cask MOI since the results are not expected to change significantly.

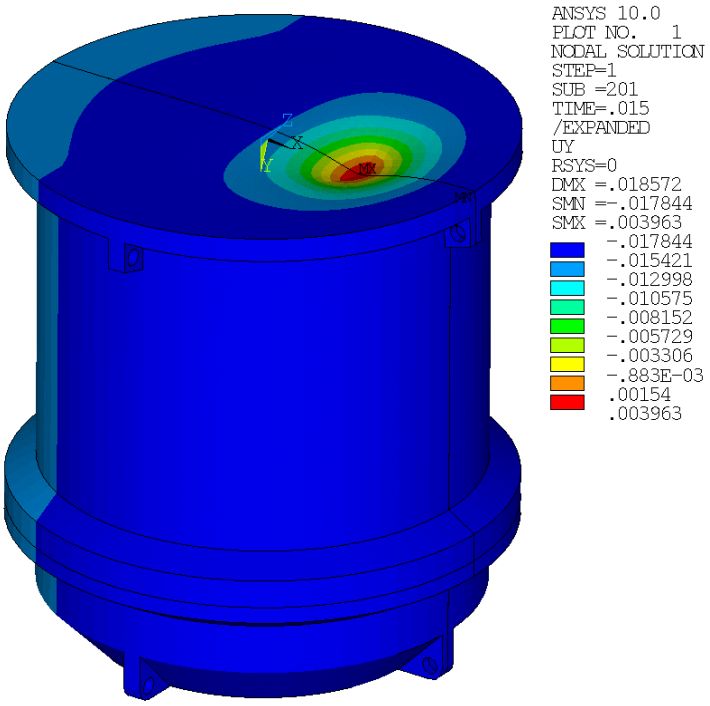


Pre-Test Prediction

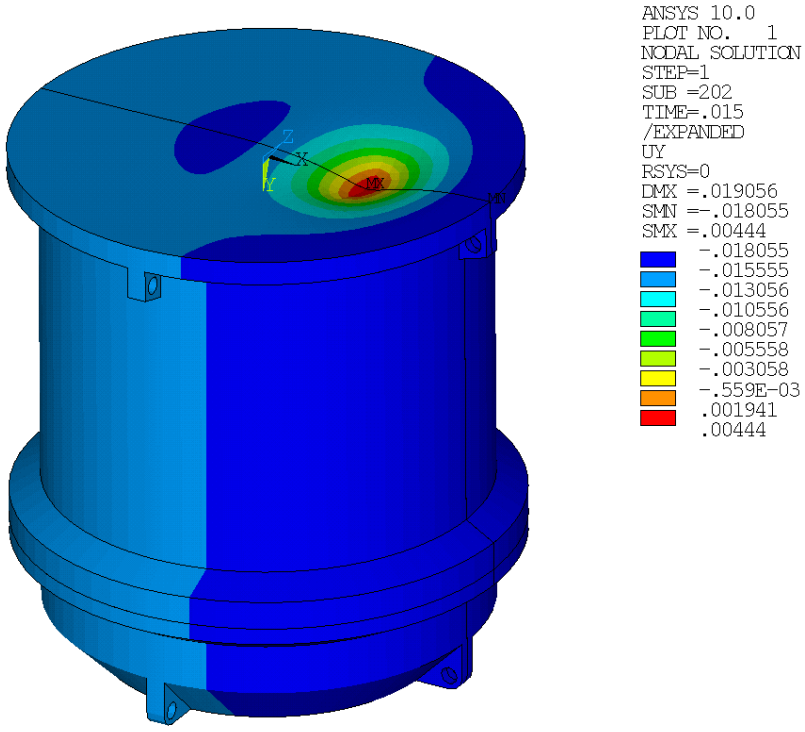


Post-Test Analysis

**Figure 6-5 - Test 1D Overpack Permanent Deformation**

## 6.5 HAC Side Drop (Test 2A)

Test 2A was a free drop from a height of 9m onto the side of the test package. The test results show that the package impacted the drop test pad at an angle of approximately 107° (i.e. 17° from horizontal, impacting on the top end of the package) rather than the planned impact angle of 90° (i.e., a horizontal side drop). Thus, the post-test analysis for Test 2A is performed for a 107° impact angle. In addition, the MOI used for the cask rigid-body is corrected in the post-test analysis, as discussed in Section 4.3.

The results of this post-test analysis are included in computer run I.D. *TEST2A_R1.out*. A comparison of the post-test analysis acceleration time-history results with the measured acceleration time-history results is shown in Figure 6-6. The comparison shows good agreement between the measured and post-test analysis acceleration time-histories, much better than that of the pre-test prediction. This is reasonable agreement considering that the analysis predicts the nominal response of the package as opposed to an upper-bound prediction. Furthermore, the post-test analysis predicts rigid-body response, whereas the test measurements includes dynamic amplification which is accounted for separately in the package safety analyses.

The results of the post-test analysis also show that the none of the overpack closure bolts will fail, which is consistent with the results of Test 2A. The post-test analysis results show that the overpack damage resulting from Test 2A is consistent with the damage predicted in the post-test analysis. The amount of deformation predicted by the post-test analysis is greater than that resulting from the test. This is acceptable since the damage predictions from the analysis are used as inputs to the HAC thermal analysis, and the higher deformation from the drop loads analysis is conservative for the HAC thermal analysis.

These results confirm that the cask MOI was not modeled correctly in the pre-test prediction calculation. Thus, it is concluded that all side drop analyses and oblique drop analyses that were previously performed using the incorrect cask MOI should be revised.

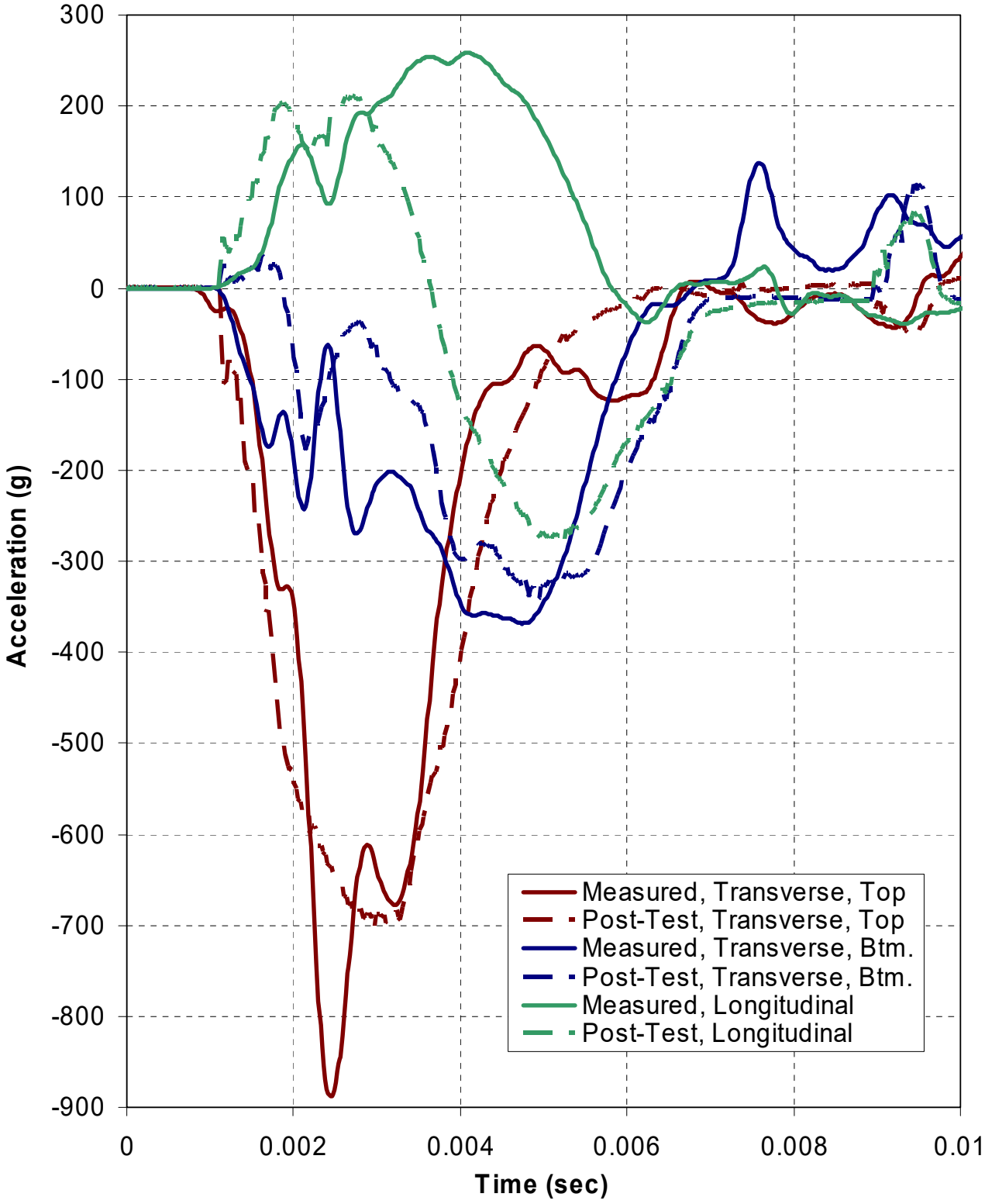


**Figure 6-6 - Test 2A Acceleration Time-History Comparison, Measured vs. Post-Test Analysis**

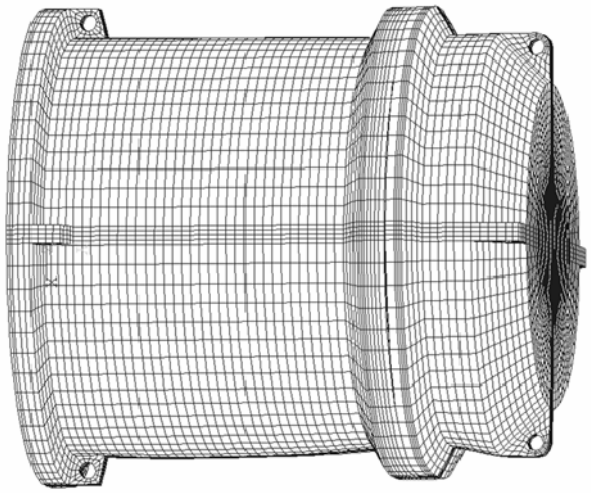

Pre-Test Prediction

Test 2A Results

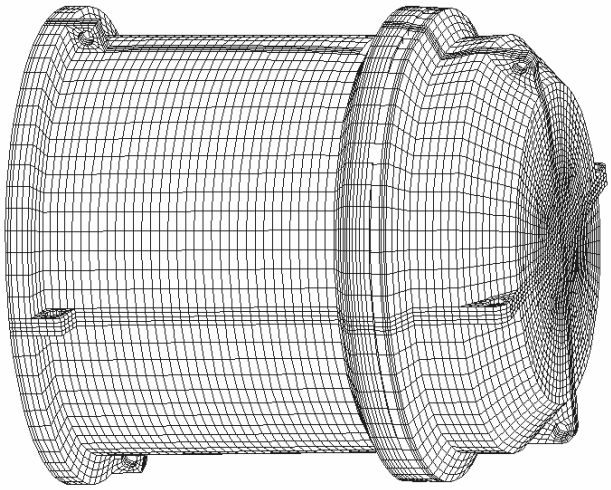

Post-Test Analysis

**Figure 6-7 - Test 2A Overpack Damage Deformation**

### 6.6 HAC Side Puncture Drop (Test 2B)

Test 2B was a free drop of the package from a height of 1m onto the top end of a mild steel puncture bar that was mounted on the drop test pad. The test package was oriented at an angle of 10° from horizontal (i.e, 100° from vertical upright), with its center of gravity directly over the struck corner of the puncture bar. The test results show that the package impacted the puncture bar in the planned orientation. Thus, no corrections are made to the Test 2B impact angle in this analysis. The only change from the pre-test prediction analysis is to the MOI used for the cask rigid-body, as discussed in Section 4.3.

The Test 2B post-test analysis results show that the maximum strain intensity (EPTOINT) in the overpack base outer shell is 15% (node 1528 at t = 0.0082399 seconds), which is the same as the maximum strain intensity from the Test 2B pre-test prediction analysis. A comparison of the overpack permanent deformation from the Test 2B pre-test prediction analysis and the post-test analysis is shown in Figure 6-8. The comparison shows that the permanent deformation from the post-test analysis is essentially the same as that from the pre-test prediction analysis. The only difference appears to be slightly more rigid-body rotation of the package in the post-test analysis results, which is expected for the corrected cask MOI.

Therefore, it is concluded that the change to the value of the cask rigid-body MOI has no significant effect on Test 2B. This is expected because Test 2B is a “stable” drop orientation (i.e., package c.g. located directly over the struck corner of the puncture bar) that should not cause any significant rotation of the package. The results of the Test 2B post-test analysis confirm that it is not necessary to revise any of the HAC puncture drop analyses that were previously performed using the incorrect cask MOI since the results are not expected to change significantly.

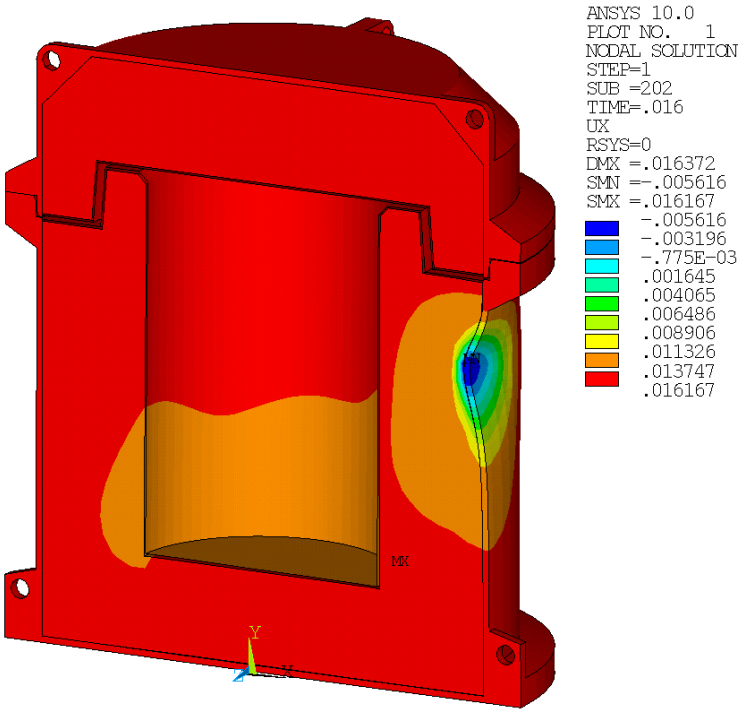


Pre-Test Prediction

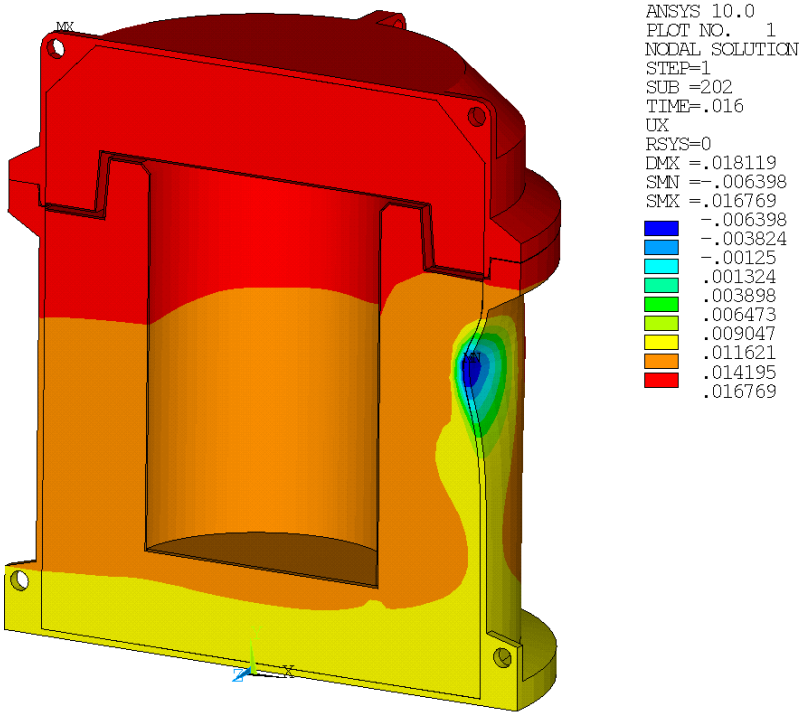


Post-Test Analysis

**Figure 6-8 - Overpack Assembly Permanent Displacement Contour Plot, HAC 1m Side Oblique Puncture Drop (Test 2B)**

# 7. CONCLUSIONS

## 7.1 Results

The results of this calculation package confirm that the analytical methodology used to determine the response of the package to NCT free drops, HAC free drops, and HAC puncture drops is adequate. However, the results show that all side drop and oblique drop analyses must be revised to use the correct value of the MOI for the cask/shield lid assembly (i.e., defined about the local center of gravity of the cask/shield lid assembly rather than about the global origin of the model).

## 7.2 Compliance With Requirements

Not applicable.

## 7.3 Range of Validity

This calculation package is valid for the test conditions and test configurations described in References 3.1.1 and 3.2.1, with the assumptions described in Section 4.3. The conclusions regarding the cask rigid-body MOI are valid for all NCT and HAC side drop and oblique drop conditions.

## 7.4 Summary of Conservatism

Not applicable.

## 7.5 Limitations or Special Instructions

None

## 8. ELECTRONIC FILES

### 8.1 Computer Runs

| Filename[1] | File Date | Computer Code | Cat | Version | Platform | Machine |
|---|---|---|---|---|---|---|
| TEST1A_R1.out | 10/1/06 | ANSYS LS-DYNA PC | 2 | 10.0 | Windows XP | BFS0304 |
| TEST1B_R1.out | 9/29/06 | ANSYS LS-DYNA PC | 2 | 10.0 | Windows XP | BFS0304 |
| TEST1C_R1.out | 9/30/06 | ANSYS LS-DYNA PC | 2 | 10.0 | Windows XP | BFS0304 |
| TEST1D_R1.out | 9/29/06 | ANSYS LS-DYNA PC | 2 | 10.0 | Windows XP | BFS0304 |
| TEST2A_R1.out | 10/1/06 | ANSYS LS-DYNA PC | 2 | 10.0 | Windows XP | BFS0304 |
| TEST2B_R1.out | 9/29/06 | ANSYS LS-DYNA PC | 2 | 10.0 | Windows XP | BFS0304 |

Notes:

(1) Run descriptions are as follows:

| | |
|---|---|
| TEST1A_R1.out: | NCT 1.2m bottom end drop post-test analysis |
| TEST1B_R1.out: | HAC 9m top end drop post-test analysis |
| TEST1C_R1.out: | HAC 9m top corner drop post-test analysis |
| TEST1D_R1.out: | HAC 1.0m bottom oblique puncture drop post-test analysis |
| TEST2A_R1.out: | HAC 9m side drop post-test analysis |
| TEST2B_R1.out: | HAC 1.0m side oblique puncture drop post-test analysis |

### 8.2 Other Electronic Files

None.

# 3 THERMAL EVALUATION

This chapter identifies and describes the principal thermal design features of the MIDUS packaging that are important to safety. In addition, the thermal evaluations of the package under NCT (§71.71) and HAC (§71.73) that demonstrate compliance with the applicable performance requirements of 10 CFR 71 are discussed. The thermal evaluation presented in the body of this chapter is for the liquid payload (i.e., Content #01) described in Section 1.2.2.1. For clarity, the body of this chapter is not revised extensively for additional contents. Instead, the thermal evaluation of each additional payload is presented in SAR addenda, starting in Chapter 9.

The thermal evaluations demonstrate that the maximum temperatures of all components of the package remain below their respective temperature limits under both NCT and HAC. Further, the package is designed, constructed, and prepared for transport such that, in still air at 38°C and in the shade, no accessible surface of the package has a temperature exceeding 50°C. These results assure that the thermal performance of the package will not cause any loss or dispersal of radioactive contents, no significant increase in external surface radiation levels, and no substantial reduction in the effectiveness of the packaging, in accordance with the requirements of §71.43(f) and §71.51(a)(1).

The thermal evaluation of the package is performed by analysis using the Thermal Desktop® and SINDA/FLUINT computer programs. These computer programs are used together to create the thermal models, calculate the solution, and post-process the analysis results. Thermal Desktop® is an application module of AutoCAD™ that provides graphical input and output display functions and computes thermal mass, conduction, and radiation exchange conductors based on the model geometry and thermal/optical properties. SINDA/FLUINT is a general-purpose computer program that is used to solve steady-state and transient finite difference and/or finite element problems. The Thermal Desktop® and SINDA/FLUINT computer programs are tested, installed, operated, and maintained in accordance with the requirements of the Energy*Solutions* QA program. These computer programs have been validated in accordance with the requirements of the Energy*Solutions* QA program and shown to correctly solve the general class of problems that they are used to solve.

The analytical methodology used for the HAC thermal evaluation has been determined to be acceptable based upon the results of the confirmatory tests discussed in Section 2.12.4. A full-scale test package was subjected to sequential HAC free drop, HAC puncture, and HAC thermal tests in accordance with the requirements of §71.73. Prior to performing the confirmatory tests, the package thermal response to the thermal test conditions was predicted using the same analytical methodology used for the HAC thermal analysis. The thermal model was adjusted to reflect the package deformation expected to result from the HAC free drop and HAC puncture drop tests, as well as the differences between the anticipated environment of the furnace test and the regulatory HAC thermal test. The results of the confirmatory test demonstrate that the analytical methodology used for the thermal evaluation provides an accurate representation of the peak package temperatures reached during the 30-minute fire and the

transient temperature response of the package. A detailed discussion of the confirmatory test results is provided in Section 2.12.4.

## 3.1 Description of Thermal Design

The MIDUS package is designed as a totally passive thermal system for transporting up to 4,400 Ci of $^{99}$Mo plus daughters. Full details of the package design are described in Section 1.2. The following sections summarize the design features affecting the thermal performance of the package, including the package geometry, materials of construction, and the decay heat loading.

### 3.1.1 Design Features

Figure 3-1 illustrates the package's key thermal design features. The package is constructed primarily from stainless steel, depleted uranium, and polyurethane foam.

The polyurethane foam provides significant impact and thermal protection during the HAC free drop and thermal tests. However, the same thermal protection afforded by the foam significantly restricts the transfer of heat from the payload to the overpack exterior surfaces under NCT. To counter this effect, the overpack base assembly design has a thermal spider, which is a 3 mm thick ring of copper with eight arched legs that bridge the space between the overpack base inner and outer shells. The thermal spider is brazed to the bottom surface of the overpack base inner shell and to the outer shell, providing good mechanical connections for effective heat transfer. The spider is sized to enhance the transfer of the payload's decay heat load from the interior of the package during NCT conditions, while limiting the transfer of heat into the package under HAC conditions.

The incorporation of an offset in the design of interface between the overpack's base and lid flanges, plus the robust design of the flanges, ensures that the drop events that are assumed to precede the HAC fire event will not significantly deform or "spring" the flanges. Therefore, neither radiative nor convective heat transfer from the HAC fire is able to penetrate to the interior of the package. This design feature, the additional offsets designed into the overpack's base and lid interior closure surfaces, and the relatively thin overpack inner shell effectively isolate the cask from conductive heat transfer from the exterior of the package during the fire event.

The polyurethane foam provides significant impact and thermal protection during the HAC fire event through a combination of low thermal conductivity and thermal decomposition. Since the thermal decomposition of the foam is accompanied by gas generation, the overpack lid and base assemblies have four nylon threaded screws that function as pressure-relief devices during the HAC fire event. During normal operations they remain in place, protecting the foam by means of elastomeric weather seal O-rings  During the fire, they quickly melt, allowing the hot gases produced by the thermal decomposition of the foam to escape the overpack shells. This prevents catastrophic failure (splitting) of the overpack shells due to internal pressure. In addition, the vents aid in heat dissipation by allowing mass transfer of hot gases out of the overpack shells.

The package design does not rely on mechanical cooling systems to meet containment requirements.

### 3.1.2 Content's Decay Heat

The maximum activity of the payload is limited to 4,400 Ci of $^{99}$Mo plus daughters at full transient equilibrium. However, the initial thermal power of the payload is conservatively calculated for a bounding activity of 4,500 Ci of $^{99}$Mo plus daughters at full transient equilibrium using ORIGEN [3.1]. The package payload produces an initial thermal power of 17.8W. This is the same basis as used to derive the radiation source terms, further described in Section 5.2.

$^{99}$Mo is the predominate thermal source, contributing 81% of the thermal power. $^{99m}$Tc contributes the remainder. The payload's initial thermal power decays rapidly due to the short half-lives of these two contributors. The half-lives of $^{99}$Mo and $^{99m}$Tc are approximately 66 hours and 6 hours, respectively. To account for this rapid decay, the thermal source power is modeled as a transient with the following magnitude:

$$Q(t) = Q_o e^{-0.0105t}$$

where $Q_o$ is the initial decay heat (W) and t is time (hours). The time-dependent heat load by this equation was compared to the ORIGEN decay calculations and matched well with ORIGEN's predicted power at several decay times ranging from 0–192 hours.

About 81% of the decay heat energy is deposited in the product, product bottle, and secondary container. The remaining 19% is deposited into the cask cavity shell and depleted uranium (DU) gamma shielding.

### 3.1.3 Summary Tables of Temperatures

Table 3-1 summarizes the maximum package temperatures resulting from NCT heat that affect structural integrity, containment, and shielding. Because a transient thermal analysis is used for the evaluation of NCT heat, the table also reports the time that the peak temperatures are reached. The package has considerable thermal margin for NCT heat. The smallest thermal margins for NCT heat are 82°C for the cask containment O-ring seal and 60°C for the overpack lid foam. The minimum package temperatures are limited only by the minimum ambient temperature due to the rapid decay of the thermal power. Therefore, the minimum temperature for all package components is -40°C.

The peak temperatures of the package resulting from the HAC fire, along with the pre-fire damage condition from which they result and times at which they occur after fire initiation, are summarized in Table 3-2. As seen from the table, significant thermal margin exists for all package components, with the smallest margin of 67°C for the cask containment O-ring seal. The package temperatures under post-fire steady-state conditions will be significantly lower than the peak temperatures for NCT heat. This is due to the rapid decay of the thermal power of the cask payload and the lower thermal resistance of the package following the fire.

### 3.1.4 Summary Tables of Maximum Pressures

Table 3-3 summarizes the maximum normal operating pressure (MNOP) and maximum pressure under HAC.

**Table 3-1 – Summary of Package Temperatures for NCT**

| Package Component/ Location | NCT Heat[1] | | Temperature Limit (°C) |
|---|---|---|---|
| | Max. Temp. (°C) | Time After Loading (Hr) | |
| Cask Cavity Fill Gas (Bulk Avg.) | 78 | 34.25 | N/A |
| Cask Containment O-ring Seal | 68 | 34.25 | 150 |
| Cask Closure Bolt | 67 | 34.25 | 427 |
| Cask Closure Lid | 67 | 34.25 | 427 |
| Cask Inner Shell, Maximum | 71 | 34.25 | 427 |
| Cask Inner Shell, Average[2] | 70 | [2] | 427 |
| Cask Outer Shell | 67 | 34.25 | 427 |
| Cask DU Shield | 67 | 34.25 | 1,130 |
| Shield Plug DU | 72 | 34.50 | 1,130 |
| Overpack Base Outer Shell | 71 | 53.00 | 427 |
| Overpack Base Inner Shell | 66 | 33.00 | 427 |
| Overpack Base Foam, Maximum | 71 | 53.00 | 149 |
| Overpack Base Foam, Bulk Avg. | 65 | 55.25 | 149 |
| Overpack Closure Flanges | 69 | 53.50 | 427 |
| Overpack Lid Outer Shell | 89 | 52.75 | 427 |
| Overpack Lid Flange/Inner Shell | 68 | 53.75 | 427 |
| Overpack Lid Foam, Maximum | 89 | 52.75 | 149 |
| Overpack Lid Foam, Bulk Avg. | 70 | 54.25 | 149 |

Notes:
1. Initial conditions for NCT heat thermal evaluation are maximum decay heat, 38°C ambient air temperature, and insolation. Package is assumed to be at room temperature at time of loading.
2. Average nodal temperature when the cask inner shell maximum temperature is reached.

**Table 3-2 – Summary of Package Temperatures for HAC Thermal Test**

| Package Component/ Location | Controlling Damage Condition | Max. Temp. (°C) | Time After Fire Initiation (hr) | Temp. Limit (°C) |
|---|---|---|---|---|
| Cask Cavity Fill Gas (Bulk Avg.) | Side | 146 | 3.13 | --- |
| Cask Containment O-Ring Seal | Side | 145 | 2.00 | 204(1) |
| Cask Closure Bolt | Side | 147 | 1.88 | 427 |
| Cask Closure Lid | Top | 150 | 1.13 | 427 |
| Cask Inner Shell, Maximum | Side | 142 | 2.63 | 427 |
| Cask Inner Shell, Average(2) | Side | 141 | (2) | 427 |
| Cask Outer Shell | Bottom | 221 | 0.55 | 427 |
| Cask DU Shield | Bottom | 162 | 0.67 | 1,130 |
| Shield Plug DU | Side | 143 | 3.13 | 1,130 |
| Overpack Base Outer Shell | Top | 780 | 0.50 | 1,427 |
| Overpack Base Inner Shell | Top | 465 | 0.53 | 1,427 |
| Overpack Closure Flanges | Bottom | 766 | 0.50 | 1,427 |
| Overpack Lid Outer Shell | Bottom/Side | 782 | 0.50 | 1,427 |

Notes:
1. Temperature limit for exposure for up to 2 hours.
2. Estimated by averaging all component nodal temperatures when the maximum temperature is achieved.

**Table 3-3 – Summary Table of Maximum Pressures in the Containment System**

| Case | Max. Pressure (bar) |
|---|---|
| MNOP | 6.9 |
| HAC | 12.6 |

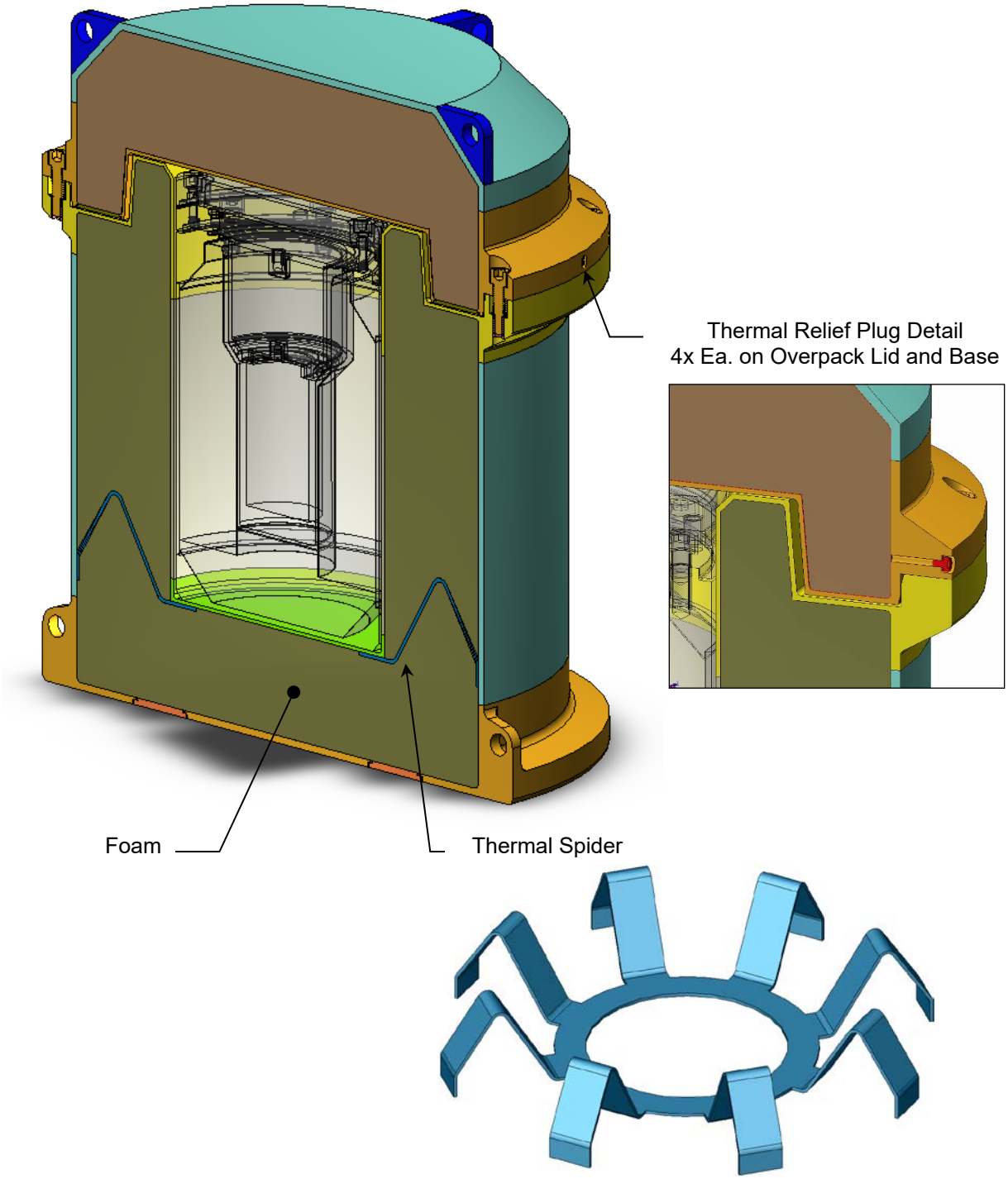


**Figure 3-1 – Package Thermal Design Features**

## 3.2 Material Properties and Component Specifications

### 3.2.1 Material Properties

The package is fabricated primarily from Type 304 and/or Type 316 stainless steel, SA-320/A320, Grade L43 alloy bolting steel, DU alloy, copper, and polyurethane foam materials. The temperature-dependent thermal conductivity and specific heat properties of these materials used for the thermal evaluation are summarized in Table 3-4.

The thermal properties of stainless steel given in Table 3-4 are those for Type 304 stainless steel. As shown in the ASME Code, Section II, Part D [3.2], Table TCD, the temperature-dependent values of thermal conductivity and thermal diffusivity for Type 316 stainless steel (Material Group K) are approximately 5% to 8% lower than those for Type 304 stainless steel (Material Group J) in the temperature range of interest. The use of the Type 304 stainless steel properties for the thermal evaluation does not significantly affect the package temperatures under NCT conditions, but its use conservatively bounds the potential for heat transfer into the package under HAC.

The thermal properties of the air used for the thermal evaluation are summarized in Table 3-5. The mass density of air is calculated based on the ideal gas law using a molecular weight of 28.966 g/mole. The heat transfer correlations for air used in the thermal evaluation are described in Section 3.5.3.

The package surface emissivities and absorptivities used in the thermal evaluation are summarized in Table 3-6. The emissivity of stainless steel varies with surface finish and ranges from 0.25 to 0.28 for as-received finish, 0.40 for commercial sand blast finish, and 0.54 for white metal blast finish [3.3]. The emissivity for weathered stainless steel is in the range of 0.48 to 0.50 ([3.4], Appendix A-1). The surface condition of the overpack exterior is assumed to be weathered and oxidized, since it is exposed directly to the environment and the effects of normal handling. The assumed condition of the different package surfaces, which reflect the anticipated conditions of use and maintenance of the package, and the corresponding emissivities used in the thermal analysis are summarized in Table 3-6.

### 3.2.2 Component Specifications

The technical specifications of the components that are important to the thermal performance of the package include the allowable service temperatures and pressures for NCT and HAC. The allowable service temperatures for all components encompass the maximum and minimum temperatures anticipated during NCT and HAC. The minimum service temperature for all package components is less than or equal to -40°C. The maximum service temperatures of the package components are based on the component's functional requirements for the service conditions. The maximum service temperature for structural components is limited to the maximum temperature limit given in Section II, Part D [3.2] of the ASME Code for the components' material specification(s). The maximum service temperature for components that

are not relied upon for structural support are typically established to prevent gross thermal failure (e.g., melting).

The temperature limit for all steel components of the package that are relied upon for structural support is equal to the maximum temperature limit of 427°C specified in Section II, Part D [3.2] of the ASME Code. The only exception is the temperature limit of the overpack shells for the HAC thermal test. During the HAC thermal test, the overpack shells do not provide structural support, but are relied upon to shield the overpack foam from direct exposure to the fire. Therefore, the temperature limit for the overpack shells under HAC thermal loading is limited to the melting point of stainless steel, which is approximately 1,427°C.

Since neither the copper nor the DU materials of the package are used for any structural components, the maximum operating temperature of these materials is limited by their melting points. Copper has a melting point of approximately 1,080ºC, while the DU has a melting point of 1,130ºC. There is no limit on the minimum allowable operating temperature for either material.

The polyurethane foam material that fills the overpack base and lid shell assemblies has a continuous service temperature range of -40ºC to 149ºC. The material properties of foam do not undergo any irreversible changes within this temperature range. The peak temperature of the polyurethane foam is limited to 149ºC for all NCT and HAC, except for the HAC thermal test. The foam properties used for the structural evaluation of the package for NCT and HAC free drop conditions are based on a maximum bulk average foam temperature of 82ºC. Therefore, the bulk average temperature of the overpack base and lid foam cores should not exceed 82ºC. No temperature limits are imposed on the polyurethane foam for the HAC thermal test since the thermal decomposition of the foam material plays a significant role in the level of thermal protection provided by the package.

The cask containment, leak-test, and cleanliness O-rings are fabricated from an ethylene propylene compound material. This material has a continuous service temperature range of -40ºC to 150ºC [3.5] when exposed to non-aggressive media. The continuous service range is used for the O-ring temperature limits for NCT. During the HAC thermal test, the O-rings are subjected to elevated temperatures for a short period of time. The cask O-ring temperatures typically remain at or near the peak values for only a short period of time: typically one to two hours. The ethylene propylene O-ring compound is capable of withstanding a temperature of 204ºC for up to 2 hours [3.5]. Therefore, the maximum temperature of the O-rings is limited to 204ºC for the HAC thermal test.

**Table 3-4 – Thermal Properties of Packaging Materials (2 Pages)**

| Material | Temperature (°C) | Thermal Conductivity (W/m-ºC)[1] | Specific Heat[2] (J/g-ºC) |
|---|---|---|---|
| Stainless Steel[3] | -40 | *14.25* | *0.4688* |
| | 21.1 | 14.88 | 0.4775 |
| | 37.8 | 15.06 | 0.4799 |
| | 93.3 | 16.10 | 0.4998 |
| | 148.9 | 16.96 | 0.5135 |
| | 204.4 | 18.00 | 0.5284 |
| | 260.0 | 18.87 | 0.5375 |
| | 315.6 | 19.56 | 0.5445 |
| | 371.1 | 20.42 | 0.5527 |
| | 426.7 | 21.11 | 0.5559 |
| | 537.8 | 22.85 | 0.5704 |
| | 648.9 | 24.23 | 0.5782 |
| | 760.0 | 25.79 | 0.5892 |
| | 815.6 | 26.48 | 0.5939 |
| SA-320/A320, Grade L43 Alloy Bolting Steel[4] | -40 | *30.86* | *0.3918* |
| | 21.1 | 33.40 | 0.4383 |
| | 37.8 | 34.10 | 0.4510 |
| | 93.3 | 35.65 | 0.4899 |
| | 148.9 | 36.69 | 0.5231 |
| | 204.4 | 37.04 | 0.5502 |
| | 260.0 | 37.04 | 0.5743 |
| | 315.6 | 36.69 | 0.5971 |
| | 371.1 | 36.17 | 0.6213 |
| | 426.7 | 35.48 | 0.6500 |
| | 537.8 | 33.58 | 0.7159 |
| | 648.9 | 31.15 | 0.8375 |
| | 760.0 | 25.96 | 0.7215 |
| | 815.6 | 25.96 | 0.6326 |
| Polyurethane Foam[5] | --- | 0.038 | 1.478 |

**Table 3-4 – Thermal Properties of Packaging Materials (2 Pages)**

| Material | Temperature (°C) | Thermal Conductivity (W/m-ºC)(1) | Specific Heat(2) (J/g-ºC) |
|---|---|---|---|
| Copper(6) | -73 | 413.0 | 0.356 |
| | 127 | 393.0 | 0.397 |
| | 327 | 379.0 | 0.417 |
| | 527 | 366.0 | 0.433 |
| | 727 | 352.0 | 0.451 |
| | 927 | 339.0 | 0.480 |
| Depleted Uranium(7) | 20 | 25.3 | 0.116 |
| | 60 | 26.0 | 0.117 |
| | 225 | 30.3 | 0.129 |
| | 440 | 33.4 | 0.160 |

Notes:
1. Thermal conductivity values given in units of Btu/hr-ft-°F are multiplied by 1.7295 to convert to SI units.
2. Specific heat is calculated as TC/(TD x density).
3. Based on thermal conductivity (TC) and thermal diffusivity (TD) from ASME Code, Section II, Part D [3.2], Table TCD, Material Group J (18Cr-8Ni). The density of this material is 8.0 g/cm$^3$.
4. Thermal properties for SA-320, Grade L43 steel from ASME Code, Section II, Part D, 1999 Edition, Table TCD, Material 2Ni-3/4Cr-1/3Mo. The density of this material is 7.84 g/cm$^3$.
5. Data from foam manufacturer's on-line product literature [www.generalplastics.com]. Density of material is 0.216 g/cm$^3$.
6. Thermal properties of pure copper [3.6]. Density of copper is 8.933 g/cm$^3$.
7. Thermal properties of depleted uranium [3.7]. Density of DU is 19.06 g/cm$^3$.
8. Values shown in *italics* are calculated by linear interpolation or linear extrapolation.

**Table 3-5 – Thermal Properties of Air**

| Temperature (°C) | Thermal Conductivity (W/m-K) | Specific Heat (J/g-K) | Dynamic Viscosity (N-s/m$^2$ x 10$^6$) |
|---|---|---|---|
| -40.0 | 0.0209 | 1.0042 | 15.184 |
| -17.8 | 0.0227 | 1.0045 | 16.341 |
| 10.0 | 0.0248 | 1.0055 | 17.724 |
| 37.8 | 0.0269 | 1.0071 | 19.044 |
| 93.3 | 0.0308 | 1.0121 | 21.525 |
| 148.9 | 0.0345 | 1.0191 | 23.827 |
| 204.4 | 0.0381 | 1.0278 | 25.985 |
| 260.0 | 0.0415 | 1.0378 | 28.019 |
| 315.6 | 0.0449 | 1.0488 | 29.934 |
| 371.1 | 0.0482 | 1.0606 | 31.744 |
| 426.7 | 0.0514 | 1.0730 | 33.473 |
| 482.2 | 0.0545 | 1.0857 | 35.135 |
| 537.8 | 0.0576 | 1.0986 | 36.735 |
| 648.9 | 0.0634 | 1.1242 | 39.766 |
| 760.0 | 0.0688 | 1.1487 | 42.601 |
| 815.6 | 0.0713 | 1.1603 | 43.953 |

Notes:
1. Properties based on curve fits in [3.8].

**Table 3-6 – Package Surface Emissivity and Absorptivity Properties**

| Package Surface | Surface Material | Surface Condition | Emissivity, ε | Solar Absorptivity, α |
|---|---|---|---|---|
| Overpack Exterior | Type 304/316 stainless steel | Weathered, oxidized | 0.45 | 0.52(1) |
| Overpack Interior | Type 304/316 stainless steel | Slightly oxidized(2) | 0.40 | N/A |
| Cask Surfaces | Type 304/316 stainless steel | Un-oxidized, as-received(3) | 0.28 | N/A |
| Gamma Shields | DU | Oxidized(4) | 0.60 | N/A |
| Product Container/Hardware | Stainless steel | Satin finish(5) | 0.30 | N/A |
| Ambient Environment | --- | --- | 1.00 | N/A |

Notes:
1. Per Reference [3.9].
2. Properties assumed between those for weathered and as-received properties.
3. Assumes some dulling of surface finish from machining.
4. Based on lower-bound value for oxidized finish.
5. Similar to as-received stainless steel.

## 3.3 Thermal Evaluation under Normal Conditions of Transport

This section describes the thermal evaluation of the package under normal conditions of transport (NCT). The evaluation is conducted using analytical methods in accordance with 10 CFR 71 and Regulatory Guide 7.8 for the applicable NCT thermal loads. The results are compared with the allowable limits of temperature and pressure for the package components.

*Analytical Approach*

The thermal analysis of the package is conducted using the SINDA/FLUINT and Thermal Desktop® computer programs. SINDA/FLUINT is a general-purpose code used for both finite difference (i.e., lumped parameter) and finite element solutions under steady-state and transient conditions. Thermal Desktop® is a computer program that provides graphical input and output display functions, as well as computing the thermal mass, conduction, and radiation exchange conductors for the defined geometry and thermal/optical properties. These programs are well benchmarked and widely used for thermal analysis.

For this application, the SINDA/FLUINT and Thermal Desktop® computer programs are used to develop a solids model representation of the package. The geometric and material information contained in this solids model is used to develop and execute thermal models that simulate the steady-state and transient temperatures arising from the evaluated NCT and HAC. The thermal models incorporate temperature-dependent material properties and heat transfer via conduction, convection, and radiation. Algorithms are also programmed into the solution process for the purposes of computing the convective heat transfer coefficients as a function of the local geometry and the gas thermal properties which, in turn, are based on the local species content of the gas and the local temperature and pressure.

*Thermal Model Description*

The three-dimensional half-symmetry finite element model of the package shown in Figure 3-2 is used for NCT thermal evaluation. The package thermal model is constructed from sub-models that represent the overpack base and lid, cask, shield lid, and payload. The thermal model accurately captures the geometry of the package design features, including the lifting/tie down lugs, the base and closure flanges, the circular, sloped, and flat surfaces of the overpack lid, and the multi-facets of the base and lid flanges. A total of approximately 16,200 thermal nodes, 7,950 planar elements, and 9,800 solids are used to provide geometric and thermal resolution within the model.

The thermal sub-models of the overpack base and lid consist of approximately 10,700 nodes, 7,100 solids, and 5,300 planar elements that capture the multi-faceted surfaces of the base and lid flanges. The volume between the inner and outer surfaces of the overpack are filled rigid polyurethane foam that is installed in-situ, providing intimate contact between the foam and the surrounding overpack shells. As such, the heat transfer between the foam and the overpack shells is modeled using a low-contact resistance (i.e., 0.0016 ºC-$m^2$/W).

The shield lid is simulated using approximately 310 nodes to represent the 17 mm thick by 214 mm diameter DU shield and its 3 mm thick stainless steel casing.

The cask is simulated using approximately 5,100 nodes, 2,750 solids, and 2,400 planar elements. The modeling includes elements to simulate the closure bolts, the closure seals, and the shield plug. A separate model is used for the cask lid, the inner and outer shells of the cask, the shield plug casing, and the radial, bottom, and shield plug segments of the DU.

The package payload is modeled as a stepped, right cylinder using 159 thermal nodes. The thermal mass of the payload is determined as the average of 150 ml (150 g) of water and 850 g of stainless steel to represent the combination of the product, the product bottle, the secondary container, the snap ring, and the optional stainless steel cavity dunnage. This level of modeling is adequate since the peak temperature within the payload is not required for the purposes of this calculation. The decay heat load is simulated as a uniform surface heat flux on the exterior of the payload model. As discussed in Section 3.1.2, approximately 81% of the total decay heat is deposited on the surface of the payload container, while the remaining 19% is deposited as a surface heat flux on the inner surface of the cask's inner shell. Heat transfer from the payload to the cask is computed as conduction and radiation across the air space between the payload and the cask's inner shell and as conduction and radiation into the cask's shield plug.

Heat transfer within each component is modeled using temperature-dependent thermal properties for the associated materials from Section 3.2.1. Heat transfer between the separate components of the thermal models is simulated as a combination of radiation and conduction links. The radiation links are computed based on calculated view factors between the various model surfaces and the assigned optical properties for the associated surfaces. The conduction links are computed as conduction across nominal air gaps existing between the components or as a contact resistance for surfaces in direct contact with one another. The size of the gaps is set by the nominal clearance dimensions between the various components as obtained from the design drawings. The thermal conductivity of the air in the gaps is computed as a function of the local temperature.

Heat transfer from the exterior of the overpack to the ambient is computed as a combination of convection and radiation. The convection coefficient for each surface is computed as a function of the temperature difference between the surface and the ambient and the thermo-physical properties of air. The semi-empirical relationships used to predict the applicable convection coefficients are described in Section 3.5.3.

For the purposes of the NCT evaluations, the bottom surfaces of the package are assumed to be an adiabatic boundary. This modeling approach provides a conservative estimate of the package temperatures.

### 3.3.1 Heat and Cold

The thermal evaluations of the package under NCT load conditions are conducted using a transient analysis methodology to capture the temperature response within the package during a typical transportation cycle. This methodology is appropriate given the relatively rapid reduction in the decay heat source, as defined in Section 3.1.2. The transportation cycle is assumed to begin with a sequence of events that include the source being loaded within an empty cask, the cask being sealed and placed within its overpack, and finally the overpack lid being installed and secured. For the purposes of this safety evaluation, all of these operations are assumed to occur instantaneously at time = 0. In practice, some time will be required to accomplish these functions and during this time the payload's thermal source will continue to decay below the initial load limit of 17.8 W.

For the NCT heat evaluation, the package is assumed to be moved outdoors at time = 0 and subjected to a constant ambient temperature of 38ºC and a diurnal insolation cycle. To capture the peak of the insolation cycle during the initial portion of the transportation cycle, the transient analysis assumes a start time of 8 AM. As shown by the results of the structural analysis presented in Section 2.6, no thermally significant damage will occur as result of the NCT drop events. As such, the thermal model described above is used without modification for the evaluations of the thermal performance under NCT.

Figure 3-3 illustrates the predicted transient thermal response of the package for NCT heat. The effect of the diurnal insolation cycle can be seen in the temperature response of the overpack base and lid shells. The initial portion of the temperature response for the cask seals and the gas in the cask cavity is dominated by the initial heat-up of the cask, while the later portion of the response reflects the influence of the diurnal insolation cycling. The transient demonstrates that slightly more than 34 hours is required before the peak cask temperature is achieved. After that time point, the decreasing source decay heat load (also illustrated in the figure) results in ever lower package temperatures. As seen from the figure, the decay heat load is reduced by 50% after approximately 66 hours.

The transient response of the package to NCT heat is also illustrated by the color contour temperature plots presented in Figure 3-5 and Figure 3-6. The temperature distribution at 28.5 hours after loading, when the overpack lid outer shell is near its peak temperature under the diurnal insolation cycle, is shown in Figure 3-5. However, the maximum payload and gas cavity temperature within the cask is not achieved until approximately 34.25 hours after the start of the transient. Figure 3-6 depicts the temperature within the package at the time when the peak payload and gas cavity temperatures are achieved.

The peak package temperatures occurring during the NCT heat transient are summarized in Table 3-1. As seen from the table, a significant thermal margin exists for all components, with the smallest being 82°C for the cask containment O-ring seal and 60°C for the overpack lid foam. The peak bulk average temperature within the gas cavity is predicted to be approximately 78°C which, as seen from Figure 3-3, occurs only for a short time period before reducing under the diurnal heating cycle of the insolation. The subsequent peak in the gas cavity temperature is approximately 3°C cooler due to the continued decrease in the source decay heat level.

A thermal evaluation of the package is also performed for NCT heat with zero insolation to establish the pre-fire package temperatures used in the HAC thermal evaluation and to demonstrate compliance with the requirements of §71.43(g). Without insolation heating, the temperature of the overpack outer shell rises initially due to convective heat transfer with the 38°C ambient air and then continues to rise slowly as the decay heat from the payload makes its way through the cask components. At 36 hours into the transient, the temperature of the overpack outer shell reaches a maximum of 44°C and then slowly decreases as the thermal power of the payload continues to decay. This evaluation confirms that the maximum temperature of the accessible surfaces of the package will be less than 50°C, in accordance with §71.43(g).

For the NCT cold evaluation, the package is assumed to be moved outdoors at time = 0 and subjected to a constant ambient temperature of -29ºC and zero insolation. A transient thermal analysis is performed for NCT cold to account for the rapid decay of the payload thermal power. Figure 3-4 illustrates the predicted transient thermal response of the package for NCT cold. The figure shows that the peak temperatures within the package occur at or shortly after the time of loading. As seen, the overpack shell temperatures decrease rapidly, but do not reach steady-state conditions by the end of the transient. Given the continuous decrease in the decay heat source term, the package temperatures will eventually reach equilibrium with the ambient environment. Therefore, the minimum package temperature of -29°C that may be achieved under this condition is within the allowable limit for all components.

### 3.3.2 Maximum Normal Operating Pressure

The maximum normal operating pressure (MNOP) of the package is calculated for NCT heat, considering the highest bulk average temperature of the gases within the containment system, the minimum free volume of the cask cavity, and all possible sources of gases generated over a period of one-year. These sources include gases present in the containment system at the time of loading and radiolytic decomposition of the product and packaging materials.

The highest bulk average temperature of the gases within the cask cavity is 78°C for NCT heat. As shown in Figure 3-3, the maximum gas temperature is reached at approximately 34 hours after loading and decreases quickly beyond this time due to the rapid decay of the payload's thermal power. However, the maximum bulk average temperature of the gases in the cask cavity is conservatively assumed to exist at any time over a one-year period.

The minimum free volume of the cask cavity is 661 ml. This corresponds to the total cavity volume minus the volumes of the shield plug, payload internals, and product. The maximum volume of the product bottle, secondary container, secondary container O-ring, snap ring, and dunnage (user-supplied payload internals) is 125 ml [Section 1.2.2]. This is the volume of the materials of construction, not counting enclosed spaces. The product volume may vary from 0 to 150 ml.

The payload generates hydrogen due to radiolysis. As a result, the cask cavity will become pressurized during the shipment period. The producer of the $^{99}$Mo has performed extensive

experimental testing to quantify the pressure rise on the identical product. This experimental data is used as the basis for calculating the cask internal pressure. Because the radiolytic properties of the product are highly dependent on its chemical formulation, these results are only valid for the same $^{99}$Mo solution.

Section 3.5.5 shows the experimental test results. The data represent specific gas formation, Q, in gauge bar·cm$^3$/ml versus the specific activity in Ci/ml. All data used to prepare the numerical fit have been extrapolated to t=∞; therefore, the results conservatively include 100% decay of the $^{99}$Mo and daughter product (66 hour and 6 hour half-lives). In addition, a 2σ uncertainty has been added to the experimental data for further conservatism.

There are three independent seals that must fail before the containment seal becomes significantly pressurized (the product bottle, secondary container, and cask cleanliness seals). The volume used for the pressure calculations is, therefore, the total free volume of the containment cavity, and not the volume of the product bottle. The product bottle is designed for internal pressures well beyond the range expected to develop during NCT or HAC service. But the product bottle and other payload internals are user-supplied items and not a part of the certified packaging. A failure of the product bottle would result in the full calculated MNOP against the containment seal.

Using an initial temperature of 20°C, a peak temperature of 80°C, and the maximum specific gas formation, Q, from Section 3.5.5, the calculated MNOP as a function of activity and dispensed product volume are shown in Table 3-7. Inspection of Table 3-7 confirms the intuitive conclusion that greater activities result in greater MNOP. Greater dispensed volumes, however, tend to reduce MNOP because the specific gas generation is a linear function of the specific activity of the product. Higher dispensed volumes dilute the specific activity, thus decreasing the specific gas formation. This effect outweighs the effect of the additional fluid displacing free volume in the cask cavity.

The package is designed for Type B(U) service, so the maximum MNOP is 7 bar. Table 3-7 shows that at a bounding payload activity of 4,500 Ci, the calculated pressure is 7.0 bar for most of the range of dispensed volume. However, at 4,400 Ci, the pressure is 6.8 bar along most of the dispensed volume range. For conservatism, therefore, the maximum payload activity is specified as 4,400 Ci. The activity specification for this package design is governed by radiolytic gas pressure generation.

The producer of the $^{99}$Mo has performed mass spectrometer measurements of the gas samples obtained during the pressure tests. Two samples were tested. The test results show that the composition of the pure evolved gas is determined to be 1.8% and 0.8% hydrogen by volume. The average is 1.3%, with a 2σ uncertainty of 1.4%. So the concentration of hydrogen in the pure evolved radiolysis product is conservatively estimated to be 1.3% + 1.4% = 2.7% by volume. Concentrations in the package will be lower due to dilution from the initial air in the package cavity.

The maximum hydrogen concentration is well below 5% by volume, and, therefore, does not constitute a risk for flammability or ignition.

**Table 3-7 – Calculated MNOP as a Function of Activity and Dispensed Volume**

| Activity Ci | Pressure (bar) vs. Dispensed Product Volume (ml) | | | | | | | | | |
|---|---|---|---|---|---|---|---|---|---|---|
| | 60 | 70 | 80 | 90 | 100 | 110 | 120 | 130 | 140 | 150 |
| 3000 | 4.4 | 4.4 | 4.3 | 4.3 | 4.2 | 4.2 | 4.1 | 4.0 | 4.0 | 3.9 |
| 3100 | 4.6 | 4.6 | 4.5 | 4.5 | 4.4 | 4.3 | 4.3 | 4.2 | 4.2 | 4.1 |
| 3200 | 4.8 | 4.7 | 4.7 | 4.6 | 4.6 | 4.5 | 4.5 | 4.4 | 4.4 | 4.3 |
| 3300 | 5.0 | 4.9 | 4.9 | 4.8 | 4.8 | 4.7 | 4.7 | 4.6 | 4.6 | 4.5 |
| 3400 | 5.1 | 5.1 | 5.1 | 5.0 | 5.0 | 4.9 | 4.9 | 4.8 | 4.8 | 4.7 |
| 3500 | 5.3 | 5.3 | 5.2 | 5.2 | 5.1 | 5.1 | 5.1 | 5.0 | 5.0 | 4.9 |
| 3600 | 5.5 | 5.5 | 5.4 | 5.4 | 5.3 | 5.3 | 5.2 | 5.2 | 5.2 | 5.1 |
| 3700 | | 5.6 | 5.6 | 5.6 | 5.5 | 5.5 | 5.4 | 5.4 | 5.4 | 5.3 |
| 3800 | | 5.8 | 5.8 | 5.7 | 5.7 | 5.7 | 5.6 | 5.6 | 5.6 | 5.5 |
| 3900 | | 6.0 | 6.0 | 5.9 | 5.9 | 5.9 | 5.8 | 5.8 | 5.8 | 5.7 |
| 4000 | | 6.2 | 6.1 | 6.1 | 6.1 | 6.0 | 6.0 | 6.0 | 6.0 | 5.9 |
| 4100 | | 6.3 | 6.3 | 6.3 | 6.3 | 6.2 | 6.2 | 6.2 | 6.2 | 6.1 |
| 4200 | | 6.5 | 6.5 | 6.5 | 6.4 | 6.4 | 6.4 | 6.4 | 6.4 | 6.3 |
| 4300 | | | 6.7 | 6.7 | 6.6 | 6.6 | 6.6 | 6.6 | 6.6 | 6.5 |
| 4400 | | | 6.9 | 6.8 | 6.8 | 6.8 | 6.8 | 6.8 | 6.8 | 6.7 |
| 4500 | | | 7.0 | 7.0 | 7.0 | 7.0 | 7.0 | 7.0 | 7.0 | 6.9 |

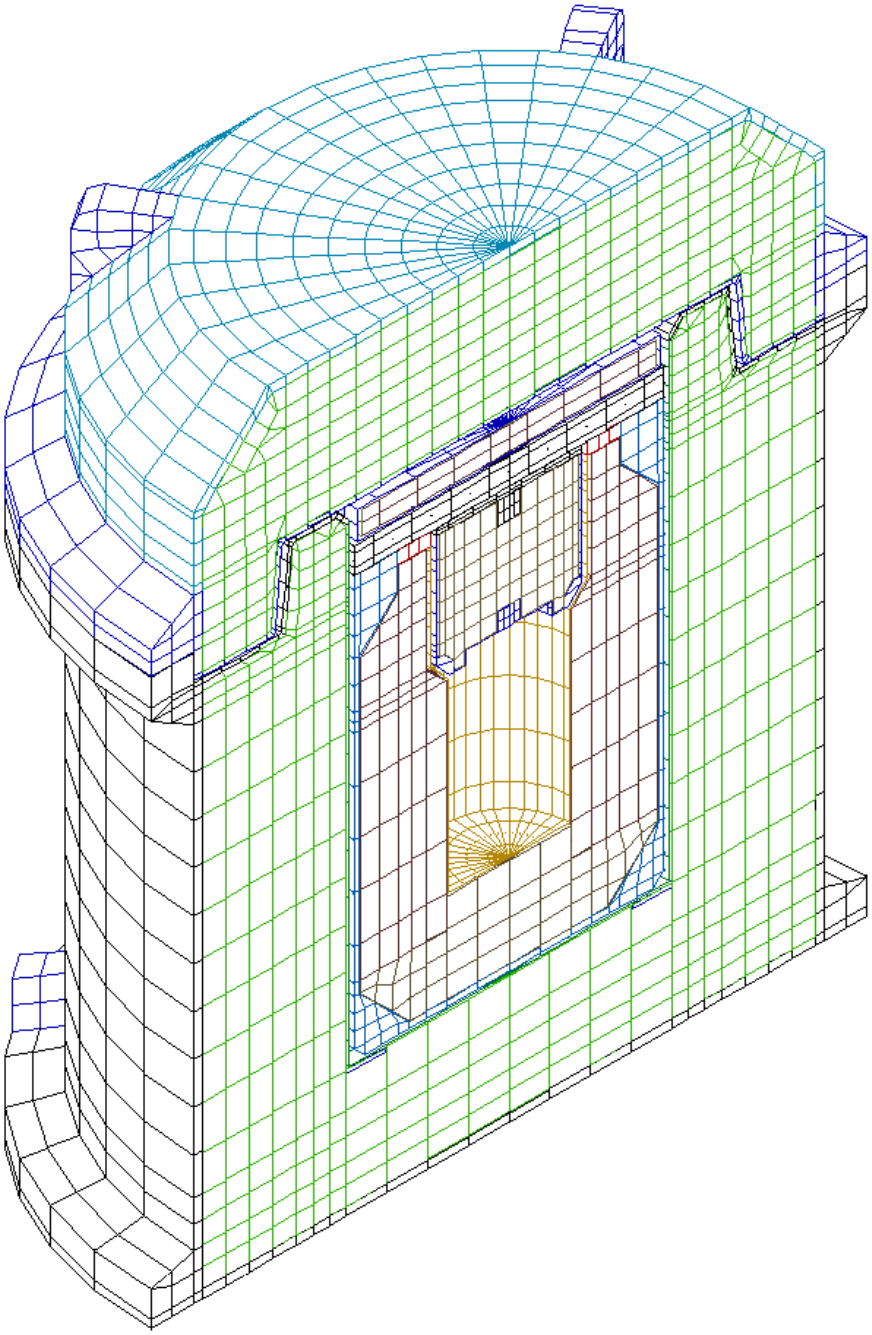

(Note: Payload sub-model not shown)

**Figure 3-2 – MIDUS Package Thermal Model for NCT**

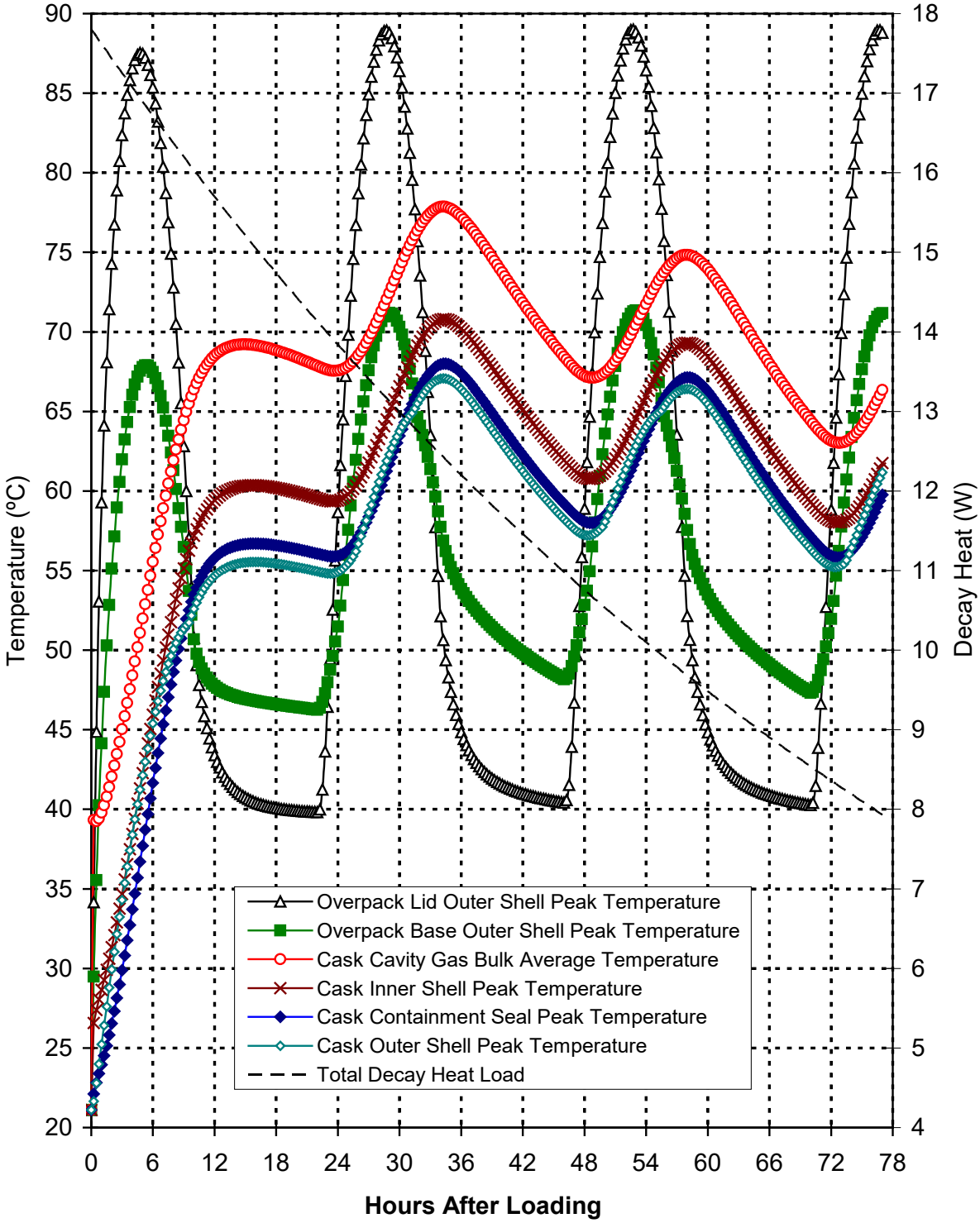


**Figure 3-3 – NCT Heat Temperature Transient Results**

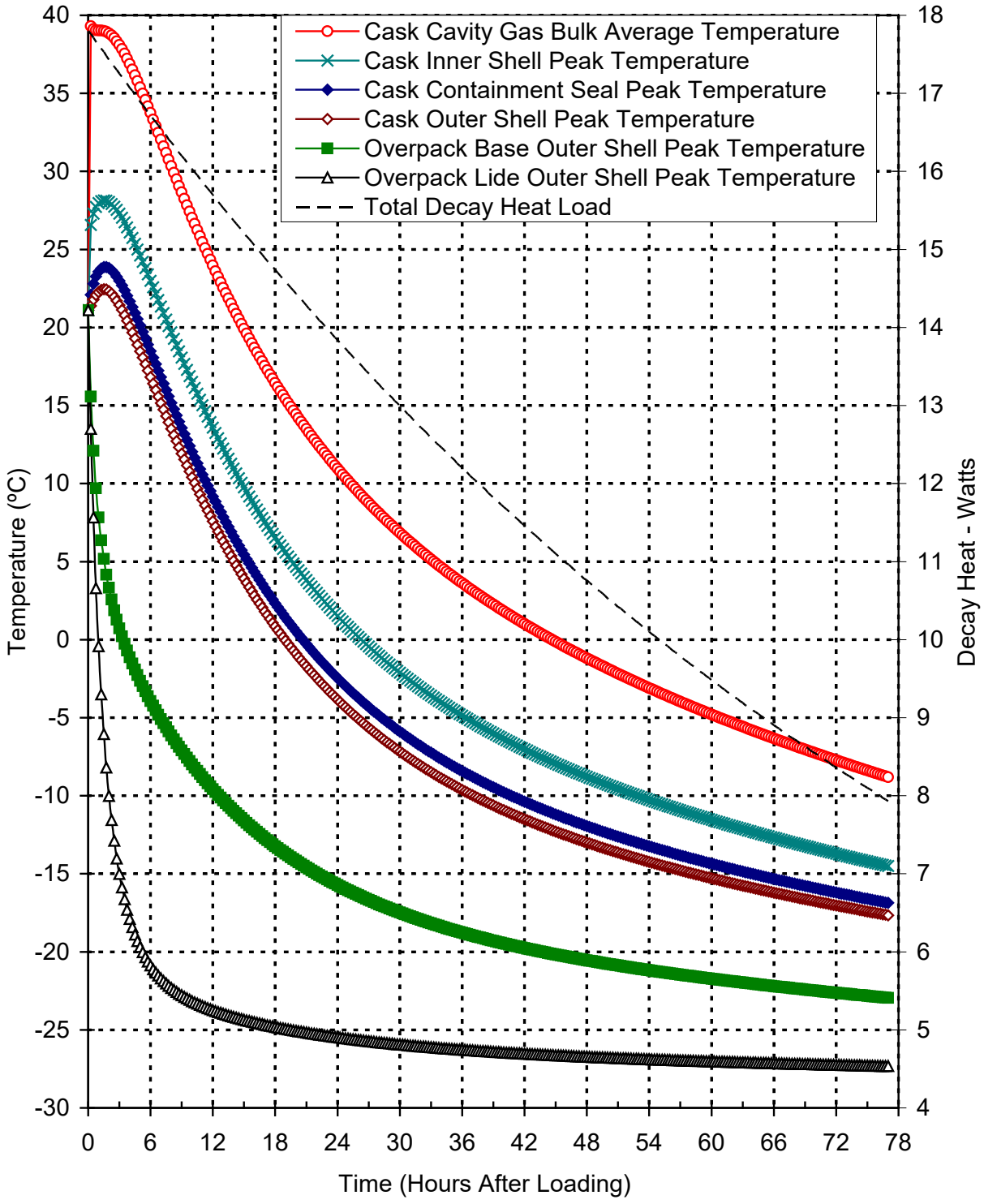


**Figure 3-4 – NCT Cold Temperature Transient Results**

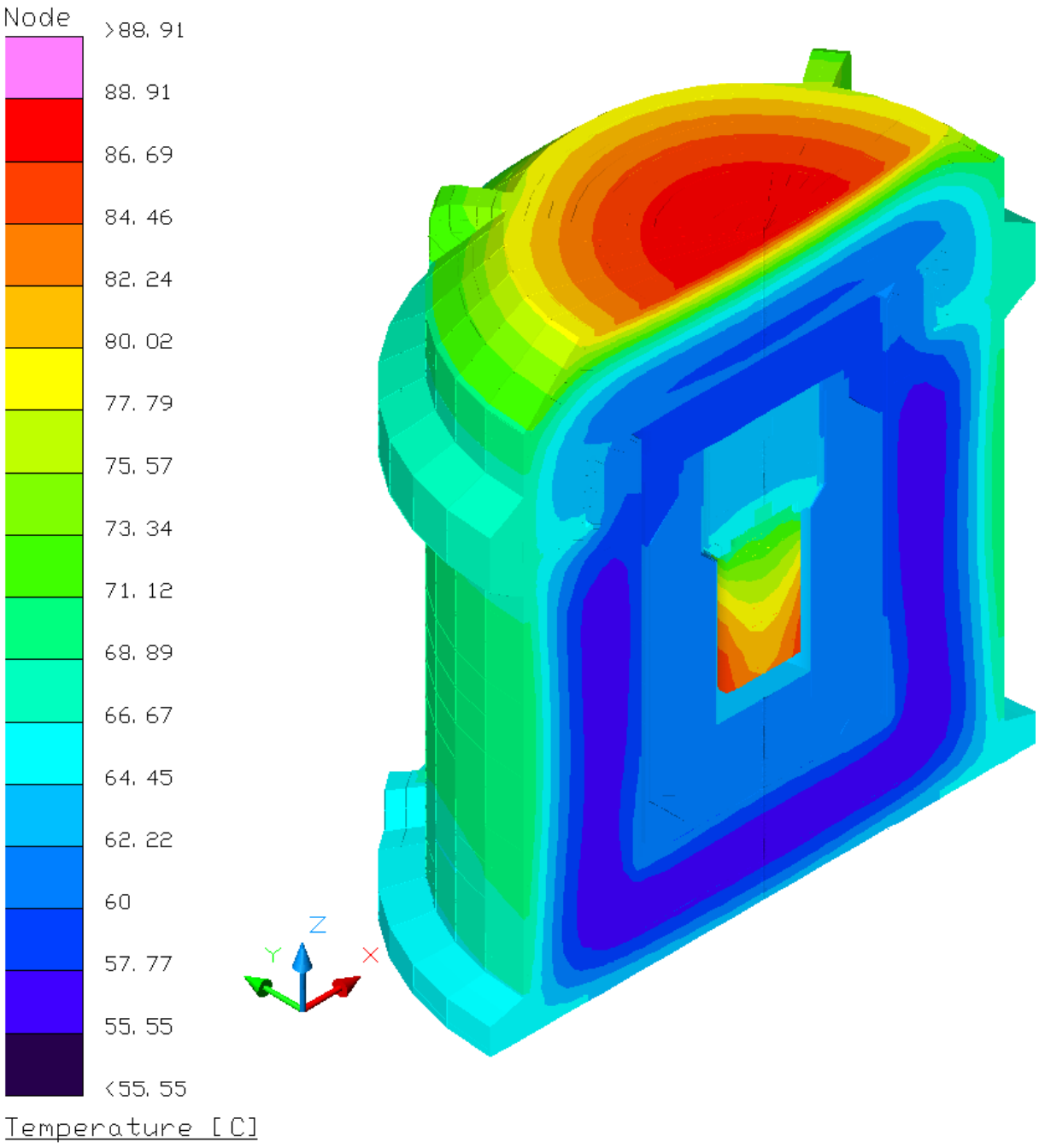


**Figure 3-5 – Package NCT Heat Temperature Distribution at Time of Peak Overpack Shell Temperature (28.5 Hours After Loading)**

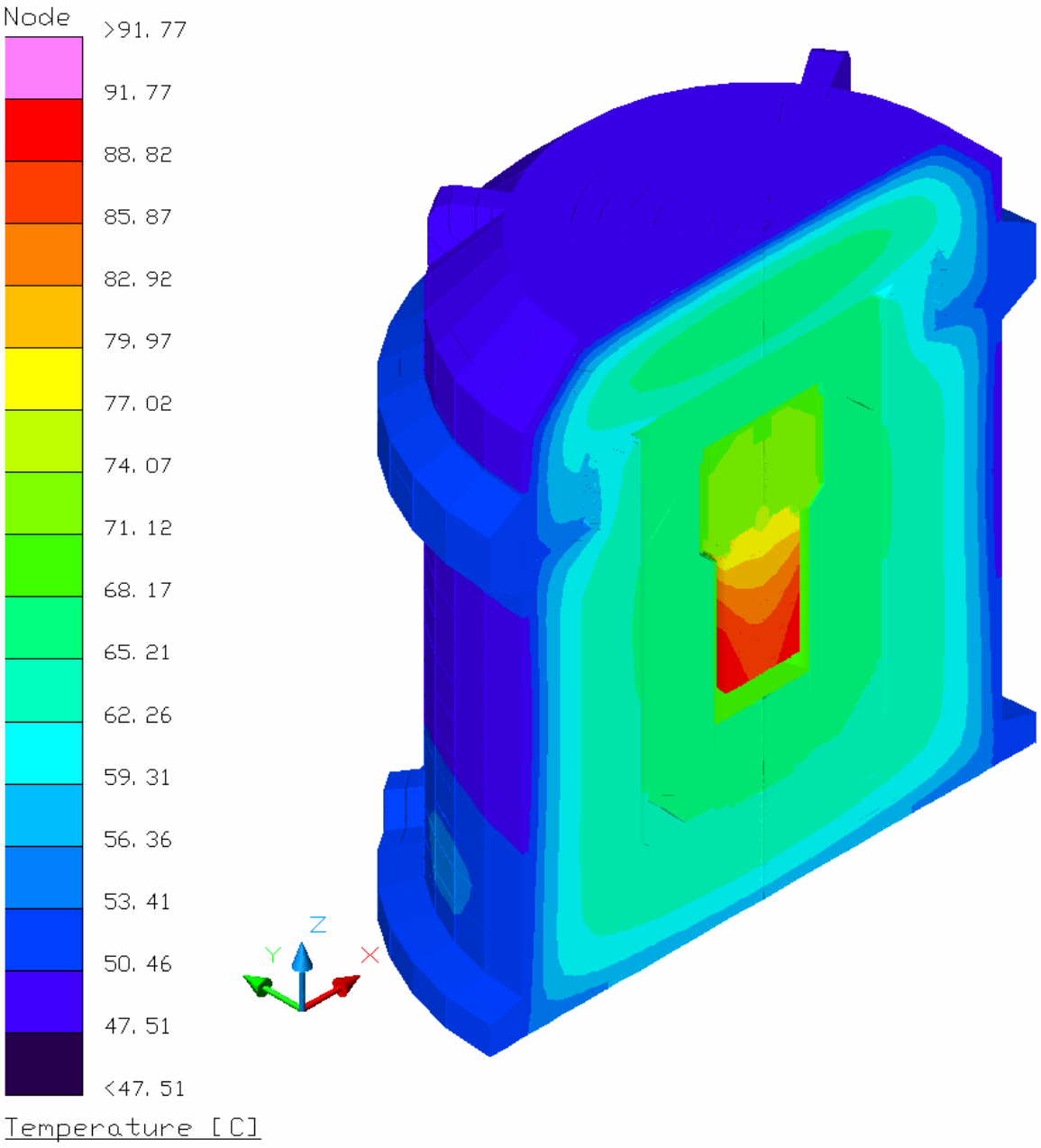


**Figure 3-6 – Package NCT Heat Temperature Distribution at Time of Peak Payload/Cavity Gas Temperature (34.25 Hours After Loading)**

## 3.4 Thermal Evaluation under Hypothetical Accident Conditions

This section presents the predicted system temperatures and pressures for the package under the hypothetical accident condition (HAC) thermal test specified in §71.73(c)(4). Because the solar loading is applied as a diurnal cycle, the starting point for the fire is assumed to be 11:30 a.m. to maximize the solar loading on the package after the fire.

The HAC transient analysis is continued for a sufficient time after the end of the fire to ensure that all package components have reached their peak temperatures. A post-fire, steady-state analysis is not conducted because it would not provide meaningful results. This conclusion is based on a combination of the following facts: 1) the thermal resistance of the damaged package is lower than the undamaged package due to the loss of foam, increased surface emissivity, etc., and 2) the short-term source decay heat load will continue to decrease until it reaches essentially zero. For these reasons, a transient evaluation of the package temperatures after the fire will continue to show a decrease in temperature levels until the source heat load has reached zero. Therefore, the maximum post-fire, steady-state temperatures that can occur will be bounded by those presented for NCT.

### 3.4.1 Initial Conditions

The initial temperature distribution for the HAC evaluation is taken from the NCT heat condition without insolation (see Section 3.3.1). Since that analysis is transient, the time point selected for the extraction of the initial temperatures is when the cask seals and the payload temperature reach their predicted maximums, which occurs at the 34.25 hour point into the transient. For additional conservatism, the temperature of each individual component is set equal to the maximum temperature occurring anywhere within that component.

### 3.4.2 Fire Test Conditions

The thermal evaluation of the package for the HAC thermal test is performed by analysis. The analytical model used for the HAC thermal evaluation is similar to the NCT thermal model described in Section 3.3. The differences between the HAC thermal model and NCT thermal model are described in the following paragraphs.

The emissivities of the package surfaces are increased for the HAC thermal evaluation to reflect the expected surface conditions during the fire. The emissivity of the interior and exterior surfaces of the overpack outer shell is increased from 0.45 to 0.9 for the HAC thermal evaluation to account for a combination of oxidization and/or accumulation of foam char on these surfaces. The emissivity of the overpack bolting flange surfaces is increased from 0.40 to 0.75 near the outer circumference and to 0.60 near the inner circumference to capture the effects of the expected heating and oxidization of these surfaces during the fire. Since the temperatures of the overpack inner shell and the cask surfaces are not expected to increase significantly during the fire, their emissivities are the same as those used for the NCT thermal evaluation.

For the HAC thermal evaluation, all exterior surfaces of the package, including the bottom end of the overpack base, are exposed to simulate a fully engulfing fire. Further, the convective

coefficients used during the 30-minute fire are computed assuming forced convection, assuming a conservatively high gas velocity of 15 m/s, as discussed in Section 3.5.3. The convective heat transfer coefficients following the 30-minute fire are based on natural convection in still air.

The thermal decomposition of the overpack foam is accounted for in the HAC thermal models. When exposed to fire, the overpack foam produces an intumescent char that seals any large voids caused by impact damage and provides a secondary thermal barrier that insulates and protects the underlying materials. The thermal decomposition of the foam produces gases, which are vented through the thermal relief ports in the overpack base and lid. The relatively low thermal conductivity of the remaining undamaged foam also provides significant thermal protection of the cask.

As explained in Section 3.5.4, the depth of foam char during the 30-minute HAC fire event is a strong function of foam density. Since the char depth is higher for lower density foam, the char depth considered in the HAC thermal evaluation is based on a lower-bound foam density. The average density of the foam used in the overpack is required to be within ±10% of 0.216 g/cm$^3$ (13.5 pcf). A lower-bound foam density of 0.187 g/cm$^3$ (11.7 pcf), which is 15% lower than the nominal foam density, is conservatively assumed for the HAC thermal evaluation. As discussed in Section 3.5.4, the predicted char depth of 0.187 g/cm$^3$ foam for a 30-minute fire event is 60 mm. To conservatively bound the thermal effects of foam recession, the outer 60 mm of foam is removed from all exterior regions of the overpack that are not damaged from the HAC free drop. Heat transfer between the exterior shell of the package and the outer surface of the foam is computed assuming radiation and convection across the void space previously occupied by the removed foam segments. A surface emissivity of 0.9 is assumed for both the foam and shell surfaces, while the convection is based on an air-filled space. Since this modeling approach assumes that the foam is immediately decomposed at the start of the fire instead of gradually over a 30-minute time period, and it ignores the thermal protection afforded by the generated foam char, the predicted heat transfer into the package during the fire is conservatively high. The char depth of the foam in the regions of the overpack damaged from the HAC free drop impact is handled in a similar manner, accounting for the increased density of the crushed foam, as discussed below.

The HAC thermal models account for the cumulative damage to the package that is expected to result from the HAC free drop and HAC puncture tests prior to the HAC thermal test. Section 2.7.8 summarizes the cumulative damage sustained by the package from the HAC free drop and HAC puncture tests. The twenty-six HAC free drops and seven HAC puncture tests considered in the structural evaluation are examined for their potential impact on the thermal performance of the package. A qualitative evaluation of the predicted package damage associated with each scenario concludes that the cask does not sustain any significant damage from any of the HAC free drop or HAC puncture tests. The maximum overpack damage results from the drop evaluations performed for the hot thermal condition with the upper-bound cask mass properties and the lower-bound material strength properties. Furthermore, the overpack damage resulting from the HAC top end drop, HAC bottom end drop, and HAC side drop orientations is considered to be the most significant for the thermal evaluation. Although the HAC top and bottom corner drops result in slightly larger foam crush values, the associated foam crush is highly localized and not considered to be thermally significant. Finally, the overpack damage sustained during the HAC puncture tests is localized

and too moderate to warrant separate evaluation. Instead, the overpack damage resulting from the HAC puncture tests is bounded by the conservatisms applied to the evaluated scenarios.

The nature of the overpack damage resulting from the HAC bottom end drop, HAC top end drop, and HAC side drop orientations is sufficiently different in each orientation to warrant three separate evaluations. The three HAC thermal evaluations are summarized as follows:

*Bottom End Drop Damage*

The results of the structural evaluation show that the HAC bottom end drop permanently crushes the foam on the bottom end of the overpack base by approximately 45 mm, reducing the overall foam thickness from 86 mm to 41 mm. A bounding foam crush depth of 60 mm is conservatively assumed for the bottom end drop damage, leaving 26 mm of foam with a compressed density of 0.623 g/cm$^3$. While the reduced foam thickness and higher density yields a lower thermal protection from a thermal conductivity point of view, the higher foam density also yields a significantly higher resistance to thermal decomposition. Based on the same approach used to predict the char depth of the undamaged foam, 12 mm of char depth is predicted in the region of the crushed foam. Thus, the modeled thickness of the foam underneath the bottom end of the overpack cavity, accounting for both the foam crush resulting from the HAC bottom end drop and the foam recession during the 30-minute fire, is 14 mm.

The model used to perform the HAC thermal analysis for the bottom end drop damage is shown in Figure 3-7. The positions of the overpack inner shell and cask are moved downward by 49 mm to bound the permanent damage predicted in the structural evaluation. As shown in Figure 3-7, the entire downward shift is assumed to be accommodated by permanent deformation of the overpack base flange region. The crushed foam directly underneath the bottom end of the overpack cavity, which has an increased density of 0.623 g/cm$^3$, is modeled with the corresponding thermal conductivity of 0.087 W/m-K. The outer regions of the foam that will be charred during the 30-minute fire are removed from the model at the beginning of the HAC thermal transient.

The cask is modeled in the same manner as that described for the NCT thermal evaluation. The package is assumed to remain upright during the HAC thermal test, with the cask resting on the bottom of the overpack cavity. The heat transfer between the shield lid and the inside surface of overpack lid is simulated as conduction across a 54 mm thick air-filled space. The radiation exchange between the exterior of the cask and the interior of the overpack is calculated to account for the shift in the cask and overpack geometry.

*Top End Drop Damage*

The results of the structural evaluation show that the HAC top end drop permanently crushes the foam directly over the overpack cavity by approximately 56 mm, reducing the overall thickness of the foam from 95 mm to 39 mm. A bounding foam crush depth of 62 mm is conservatively assumed for the top end drop damage, leaving 33 mm of foam with a compressed density of 0.534 g/cm$^3$. Based on the same approach used to predict the char depth of the undamaged foam, 17 mm of char depth is predicted in the region of the crushed foam. Thus, the modeled thickness

of the foam above the top end of the overpack cavity, accounting for both the foam crush resulting from the HAC top end drop and the foam recession during the 30-minute fire, is 16 mm.

The model used to perform the HAC thermal analysis for the top end drop damage is shown in Figure 3-8. The positions of the overpack lid inner shell and cask are moved upward by 48 mm to bound the permanent damage predicted in the structural evaluation. The crushed foam directly above the top end of the overpack cavity, which has an increased density of 0.534 g/cm$^3$, is modeled with the corresponding thermal conductivity of 0.074 W/m-K. The outer regions of the foam that will be charred during the 30-minute fire are removed from the model at the beginning of the HAC thermal transient.

The cask is modeled in the same manner as that described for the NCT thermal evaluation. The package is assumed to remain upside down during the HAC thermal test, with the cask resting on the top end of the overpack cavity. The heat transfer from the shield lid to the underside of the overpack lid is simulated as a contact resistance, while the heat transfer between the shield lid and the bottom surface of the overpack cavity is simulated as conduction across a 48 mm thick air-filled space. The radiation exchange between the exterior of the cask and the interior of the overpack is calculated to account for the shift in the cask and overpack geometry.

*Side Drop Damage*

The results of the structural evaluation show that the side drop will cause non-uniform crushing of the foam along the impacted side of the package. At the side of impact, the foam crush depth ranges from 58 mm at the bottom end of the overpack cavity to 35 mm at the top of the overpack cavity. Rather than modeling this variation in form crush depth, a uniform foam crush depth of 49 mm is modeled over the entire length of the overpack cavity. The modeled crush depth bounds the predicted foam crush over the top 60% of the overpack cavity. Since the heat transfer into the bottom end of the overpack cavity is dominated by conductance through the thermal spider, the fact that the predicted crush over the bottom region of the cavity is not bounded by the modeled crush depth is not thermally significant. Also, the separation of the inner shell from the foam along the segment of the package opposite of the drop damage is not modeled since the presence of this layer of air tends to increase the thermal resistance between the inner and outer shell.

As a result of the 49 mm crush depth, the density of the crushed foam is increased by a factor of approximately 1.89. Based on the same approach used to predict the char depth of the undamaged foam, 30 mm of char depth is predicted in the region of the crushed foam. Thus, the modeled thickness of the foam on the impacted side of the overpack cavity, accounting for both the foam crush resulting from the HAC top end drop and the foam recession during the 30-minute fire, is 25 mm.

The model used to perform the HAC thermal analysis for the side drop damage is shown in Figure 3-9. The model incorporates the general modifications for HAC conditions, including conservatively removing those foam segments that are not expected to survive the 30-minute exposure to the HAC fire environment, and compressing the foam along a 60º subtended angle of

the impacted side of the overpack cavity to a density of 0.353 g/cm$^3$ with the associated increase in the local foam conductivity from 0.038 W/m-K to 0.054 W/m-K. Radiation conductors are added to simulate the potential increase in the local heat transfer due to the collapse of the offset segments in the base flange.

The thermal modeling of the cask and payload remains the same as that used for the NCT model. The package is assumed to remain on its side during the HAC thermal test. As such, the cask is modeled as having line contact with the impacted side of the overpack cavity. For conservatism, the heat transfer between the cask bottom end and the overpack cavity is simulated using the same level of contact resistance used in the NCT model for an upright package. The radiation exchange between the exterior of the cask and the interior of the overpack is calculated to account for the shift in the overpack geometry.

For all three HAC thermal analysis, the ambient temperature is raised to 800°C at time = 0 to simulate the presence of a fully engulfing fire and maintained for 30 minutes. After 30 minutes, the ambient temperature is lowered to 38°C. The transient analysis is continued for an additional 9.5 hours to capture the peak temperatures within each of the package components. Solar heating is applied to the exterior of the package in the form of a diurnal cycle, with the peak insolation occurring at the end of the 30-minute fire. The results of the HAC thermal evaluation are discussed in Section 3.4.3.

### 3.4.3 Maximum Temperatures and Pressure

The maximum temperatures of the package components for the HAC thermal test are summarized in Table 3-2. The results show that the maximum temperatures of the package components are all considerably lower than the maximum allowable temperatures. The smallest temperature margin for the HAC thermal test occurs in the cask containment O-ring seal, which reaches a maximum temperature of 145°C versus an HAC temperature limit of 204°C.

The temperature transients of the key components of the package for the three different HAC free drop damage scenarios considered in the HAC thermal evaluation are shown in Figure 3-10 through Figure 3-12. These figures show that the package thermal response is similar for all three HAC free drop damage scenarios. In all cases, the overpack outer shell temperature rises quickly to approximately 780°C, as expected given its relatively low thermal mass. The thermal response of the overpack closure flange lags a bit due to its higher thermal mass, but approaches the flame temperature by the end of the 30-minute fire. In contrast, the overpack inner shell is largely isolated from the high fire temperatures by the shielding effect of the outer shell, the undamaged foam that surrounds it, and the relatively thin metal of the base flange that connects the inner and outer shells. The principal means of heat transfer to the overpack inner shell is conduction through the thermal spider at the base of the overpack cavity. The peak temperatures of the cask components are reached between 1 and 4 hours after the start of the HAC fire test. After the peak temperatures are reached, they continued to fall until equilibrium is eventually reached with the ambient temperature. This is due to the rapid decay of the payload thermal power. The HAC thermal evaluation for the side drop damage results in the highest temperatures for most cask components.

The maximum pressure within the cask cavity under the evaluated damage scenarios is estimated by conservatively assuming that the regulatory NCT pressure limit of 7 bar exists within the cask cavity at the start of the fire event. Assuming that pressurization of the cask cavity under HAC conditions is due to a combination of real gas expansion of the constituents in the cavity at the start of the HAC event and steam vapor generation, the maximum pressure that will be achieved within the cavity during the HAC thermal test ($P_{HAC}$) can be computed from:

$$P_{HAC} = P_{NCT} \times \left( \frac{T_{HAC}}{T_{NCT}} \right) + P_{Saturation}$$

Where $P_{NCT}$ is the maximum pressure at NCT conditions (7 bar), $T_{HAC}$ is the absolute temperature of cask cavity gas at HAC conditions, $T_{NCT}$ is the absolute temperature of cask cavity gas at NCT conditions, and $P_{Saturation}$ is the saturation pressure of steam at HAC temperature.

From Table 3-1 and Table 3-2, the highest bulk average temperatures of gases in the cask cavity for NCT and HAC are 78°C and 146°C, respectively. The saturation pressure of steam at 146°C is approximately 4.2 bar. Therefore, the peak pressure reached within the cask containment system under HAC thermal loading is conservatively estimated to be 12.6 bar. This estimate conservatively assumes that the pressurization under NCT conditions does not involve any steam vapor since any vapor existing in the cavity prior to the HAC event will serve to reduce any further amount of vapor that can accumulate within the cavity.

### 3.4.4 Maximum Thermal Stresses

As discussed in Section 2.7.4.3, the only significant thermal stresses in the cask assembly due to the HAC thermal test occur in the cask closure bolts. The closure bolt stresses arise from differential thermal expansion between the dissimilar materials of the closure lid and closure bolts and from increased internal pressure due to the elevated temperature of the gases in the cask cavity. The results of the structural evaluation show that the maximum stresses in the cask closure bolts due to the HAC thermal test satisfy the applicable allowable stress design criteria. Furthermore, since the closure bolt stresses do not exceed the material yield strength, no inelastic deformation of the cask closure bolts will result from the HAC thermal test.

### 3.4.5 Accident Conditions for Fissile Material Packages for Air Transport

Not applicable.

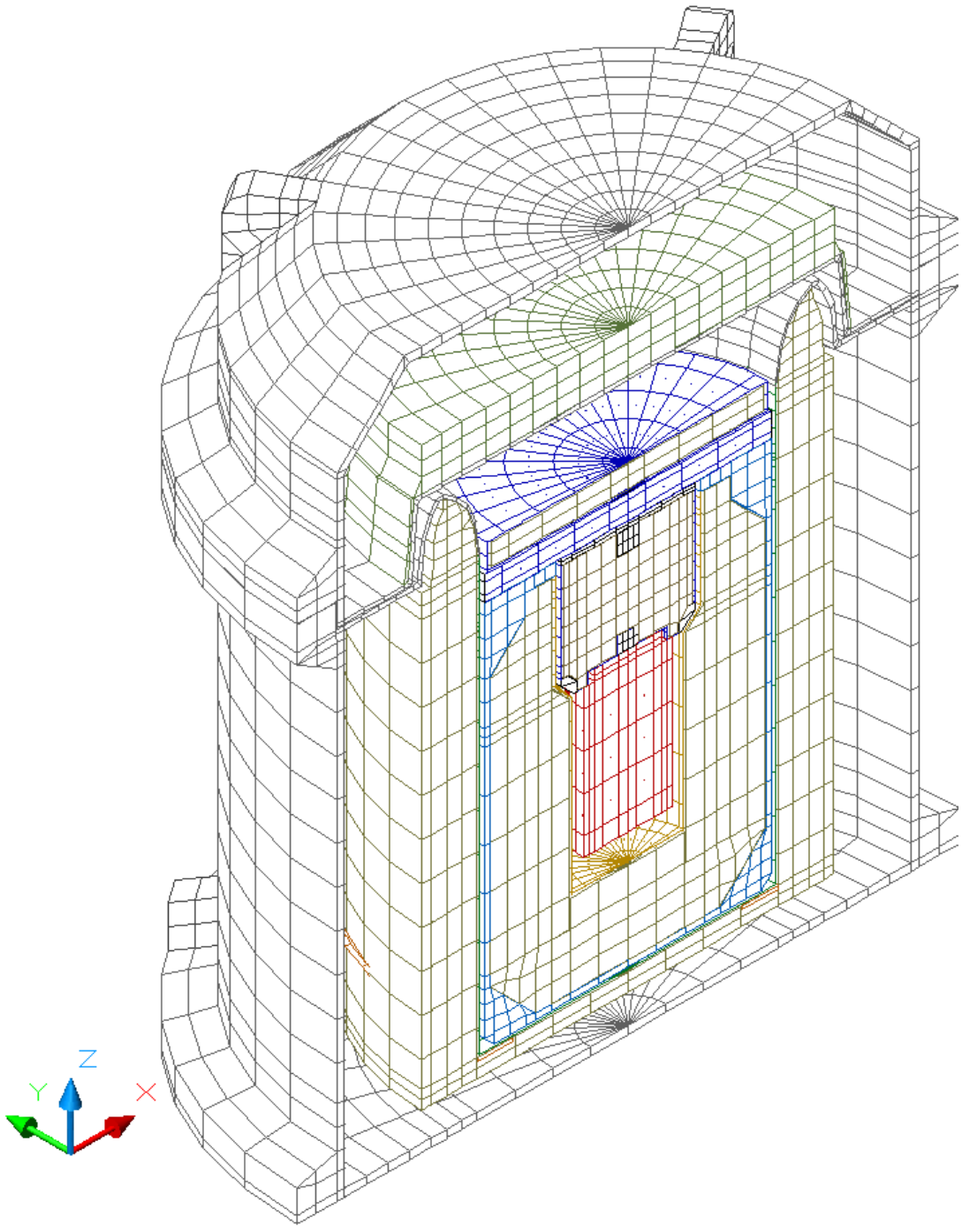


**Figure 3-7 – MIDUS Package HAC Thermal Model, Bottom End Drop Damage Configuration**

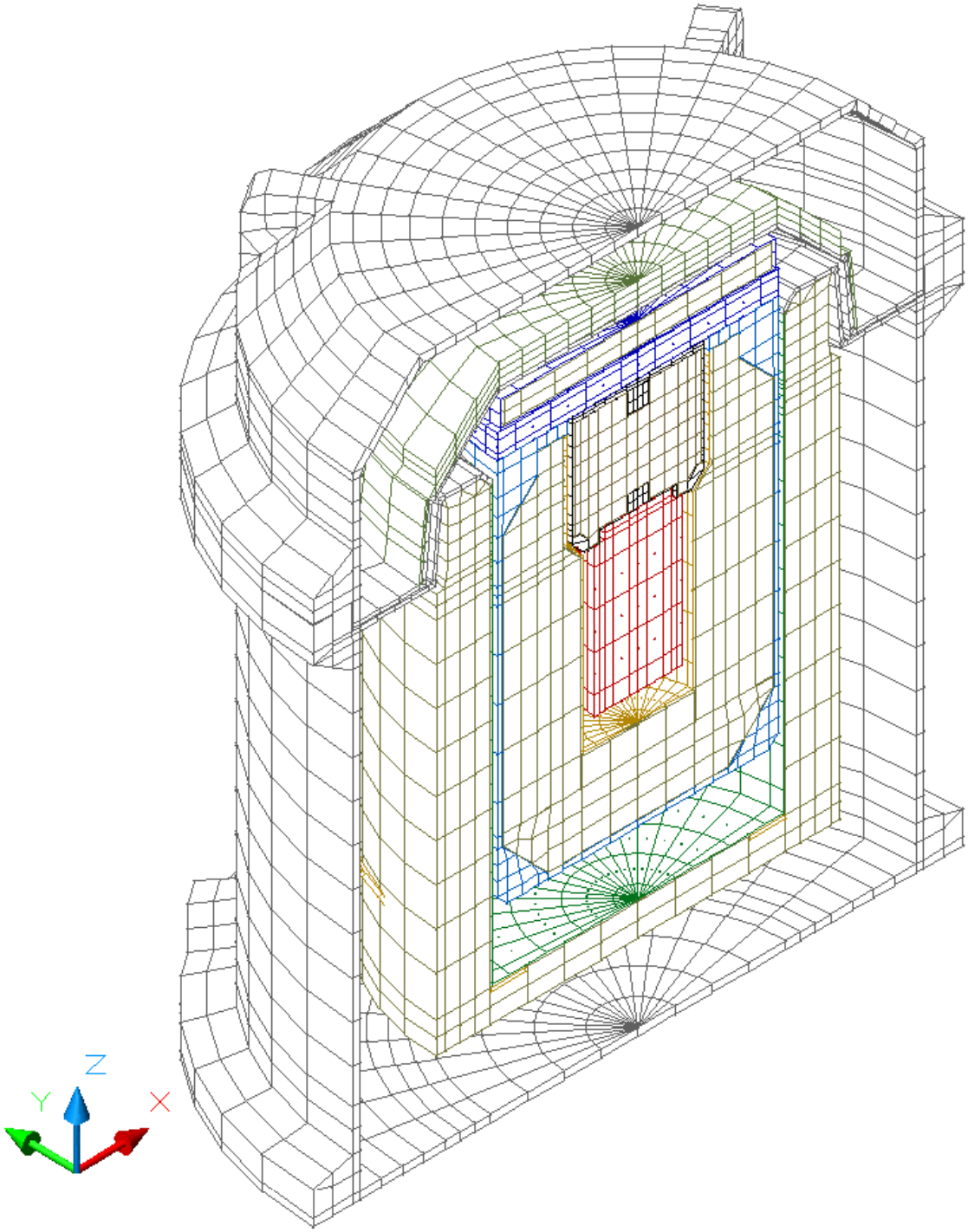


**Figure 3-8 – MIDUS Package HAC Thermal Model, Top End Drop Damage Configuration**

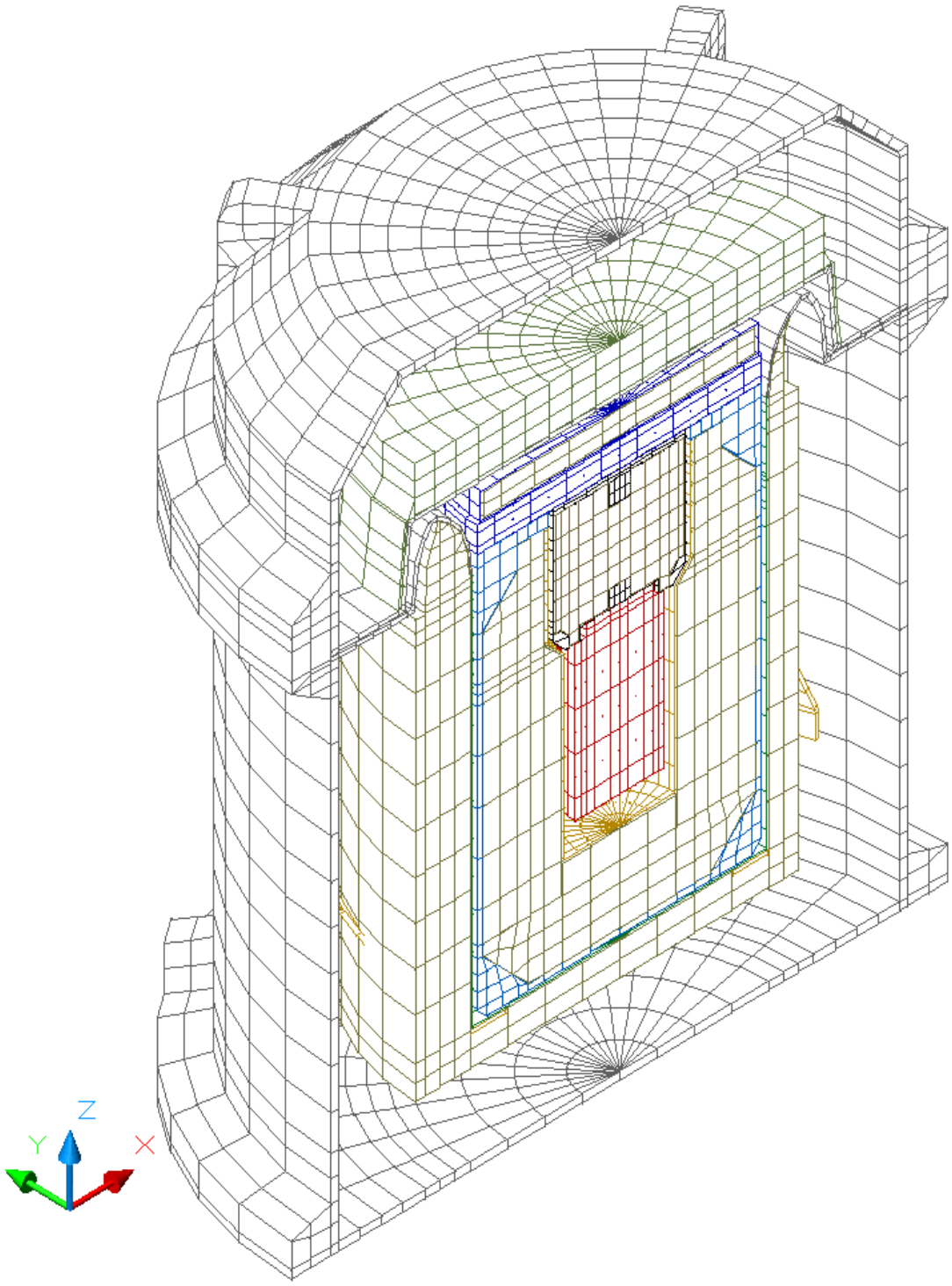


**Figure 3-9 – MIDUS Package HAC Thermal Model, Side Drop Damage Configuration**

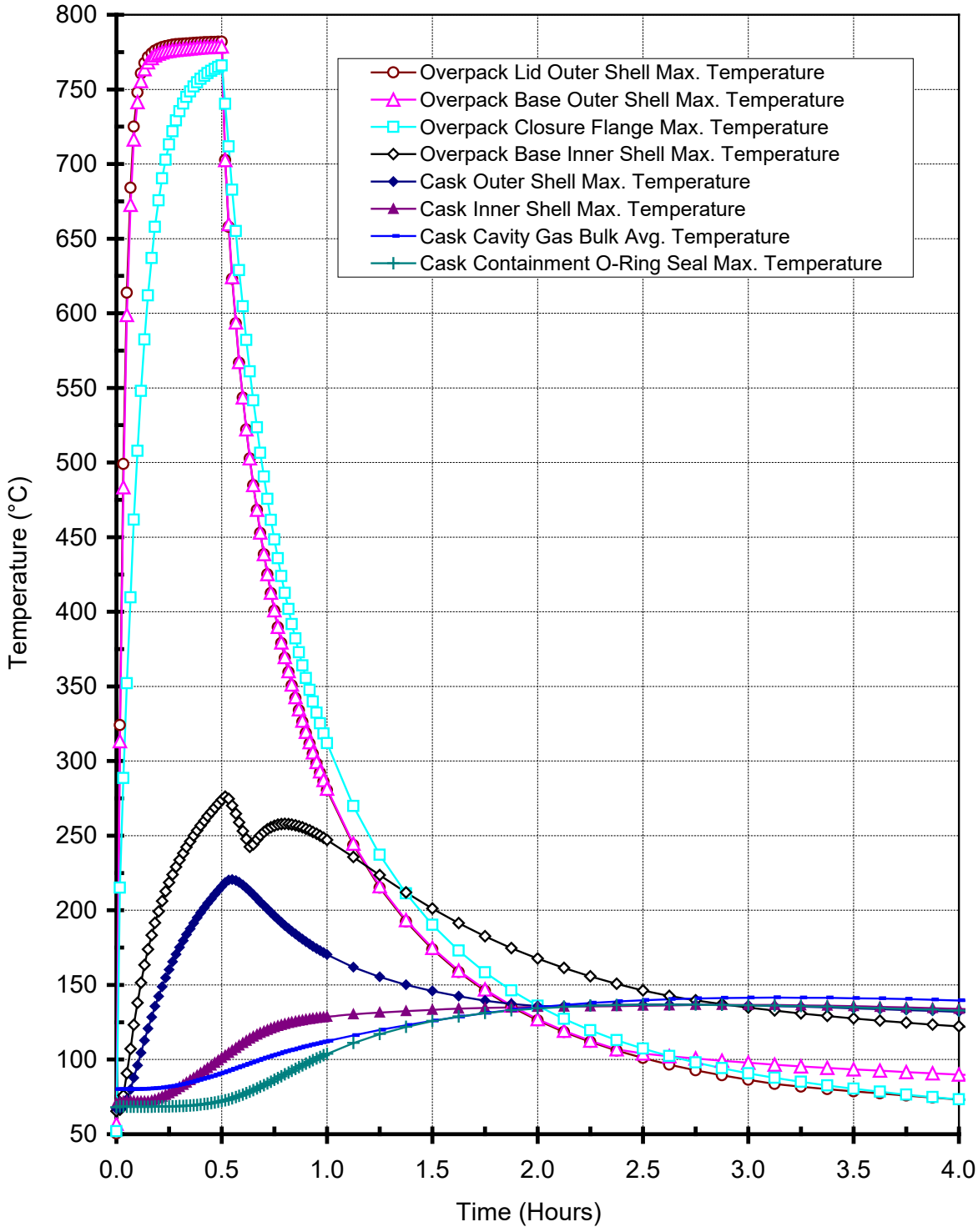


**Figure 3-10 – Package Temperatures for HAC Thermal Test with Bottom End Damage**

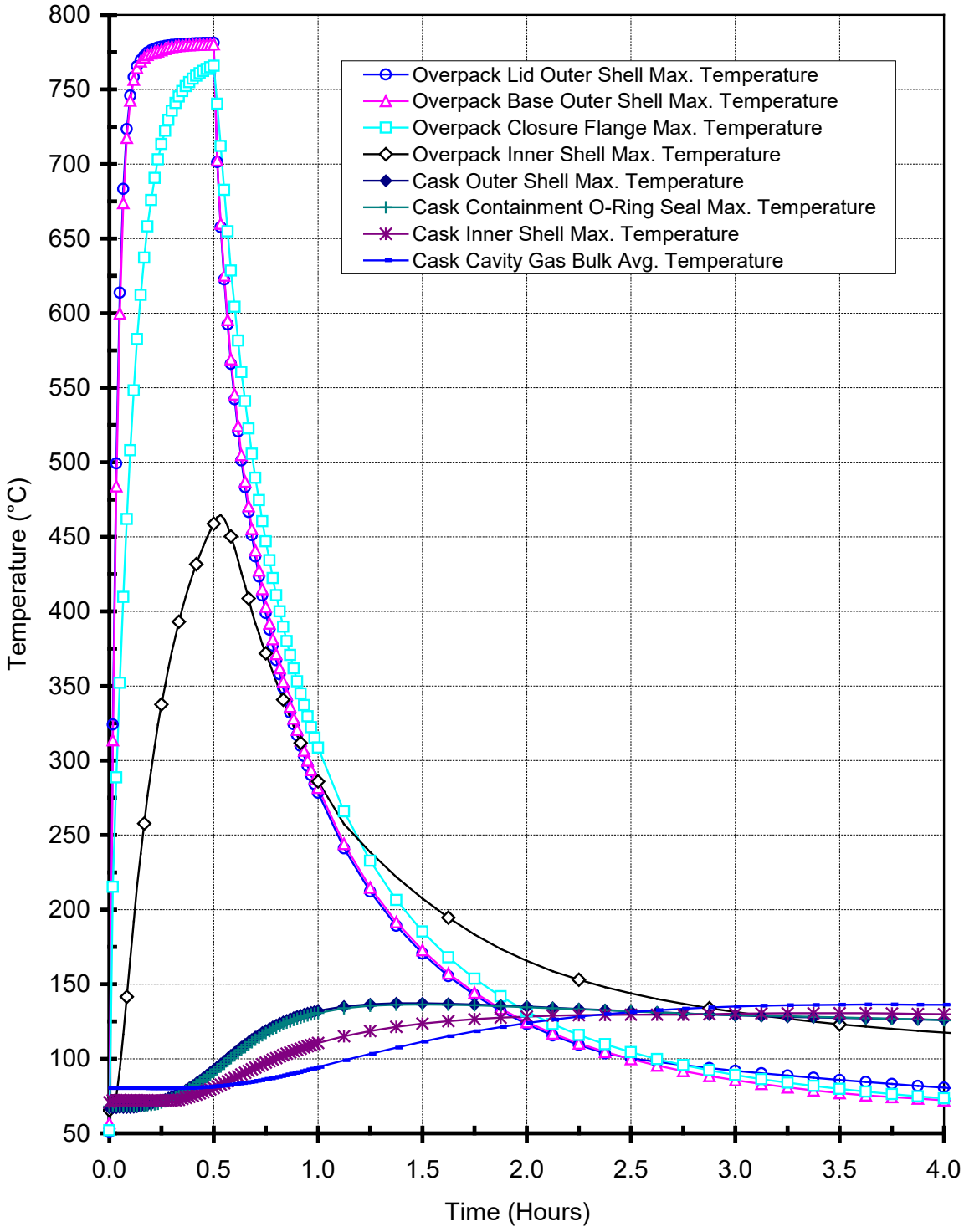


**Figure 3-11 – Package Temperatures for HAC Thermal Test with Top End Damage**

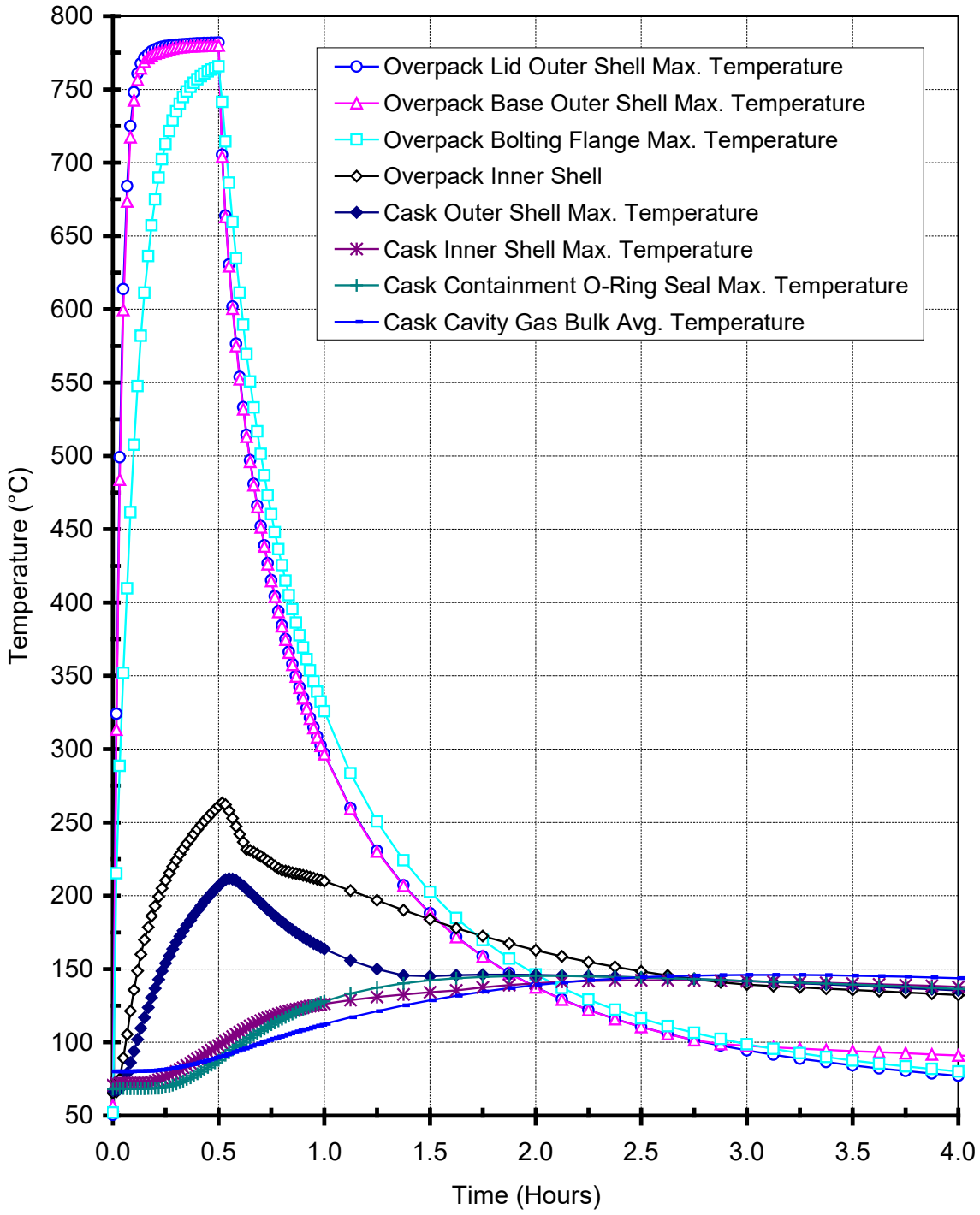


**Figure 3-12 – Package Temperatures for HAC Thermal Test with Side Damage**

## 3.5 Appendix

### 3.5.1 References

[3.1] "ORIGEN 2.1 - Isotope Generation and Depletion Code, Matrix Exponential Method," RSICC Computer Code Collection CCC-371, Oak Ridge National Laboratory, February 1996.

[3.2] American Society of Mechanical Engineers (ASME) Boiler and Pressure Vessel Code, Section II, Part D*, Materials*, 2001 Edition with Addenda through July 1, 2003.

[3.3] Frank, R. C., and W. L. Plagemann, *Emissivity Testing of Metal Specimens.* Boeing Analytical Engineering coordination sheet No. 2-3623-2-RF-C86-349, August 21, 1986. Testing accomplished in support of the TRUPACT-II design program.

[3.4] Surface Optics Corporation, *Surface Optical Property Measurements on Sierra Nuclear Corp. Supplied Sample Materials*, Report #SOC-R6001-030-002-0698, June 1998.

[3.5] Parker Hannifin Corporation, *Parker O-Ring Handbook*, ORD 5700/USA, 2001.

[3.6] Incropera and DeWitt, *Fundamentals of Heat and Mass Transfer*, 5th Edition, John Wiley & Sons Publishers, 2002.

[3.7] General Electric, *Properties of Solids, Thermal Conductivity, Metallic Materials, Heat Transfer Division*, July 1974.

[3.8] Rohsenow, Hartnett, and Choi, *Handbook of Heat Transfer*, 3rd Edition, McGraw-Hill Publishers, 1998.

[3.9] G. G. Gubareff, J. E. Janssen, and R. H. Torborg, *Thermal Radiation Properties Survey*, 2nd Edition, Honeywell Research Center, 1960.

[3.10] Guyer, E.C., *Handbook of Applied Thermal Design*, McGraw-Hill, Inc., 1989.

[3.11] Rohsenow, Hartnett, and Ganic, *Handbook of Heat Transfer Fundamentals*, 2nd Edition, McGraw-Hill Publishers, 1985.

[3.12] Kreith, Frank, *Principles of Heat Transfer*, 3rd Edition, Harper & Row, 1973.

[3.13] C.L. Williamson, Z.L. Iams, "Thermal Assault and Polyurethane Foam Evaluating Protective Mechanisms for Transport Containers." General Plastics Manufacturing Company, Tacoma, WA, presented at Waste Management '05 Symposium, Tucson, AZ, 2005.

[3.14] C.L. Williamson, Z.L. Iams, "Thermal Assault and Polyurethane Foam - Evaluating Protective Mechanisms." General Plastics Manufacturing Company, Tacoma, WA, presented at PATRAM International Symposium, Berlin, Germany, 2004.

### 3.5.2 Computer Analysis Results

Due to the extent of the computer output associated with each design load case, a sample input and output file are not provided.

### 3.5.3 Heat Transfer Correlations

The evaluation of the thermal performance of the package over the wide range of potential operating conditions encountered during NCT and HAC conditions is based on semi-empirical relationships for convection heat transfer. The convective heat transfer coefficient, $h_c$, has a form of:

$$h_c = Nu \frac{k}{L}$$

where k is the thermal conductivity of the gas at the mean film temperature and L is the characteristic length of the vertical or horizontal surface. These semi-empirical relationships are chosen to account for the variation in convection heat transfer rates between laminar and turbulent operating conditions, the orientation of the package, and the shape and orientation of the specific surface experiencing convective heat transfer.

The natural convective heat transfer coefficient, h, for the sidewall surfaces of a vertically oriented package is calculated from the correlation for a vertical cylinder [3.10]. This correlation relates the heat transfer coefficient, h, to the Nusselt number, a non-dimensional parameter. The Nusselt number, in turn, is computed as follows:

$$Nu = \left[ \left( Nu_{l,cyl} \right)^6 + \left( Nut \right)^6 \right]^{1/6}, \quad 1 < Ra < 10^{12},$$

$$Nu_{l,cyl} = Cf \, Nu_l,$$

$$Nu_l = \frac{2.8}{\ln\left[ 1 + \frac{2.8}{\left( Cl \, Ra^{1/4} \right)} \right]},$$

$$Cl = \frac{0.671}{\left[1+\left(\frac{0.492}{Pr}\right)^{\frac{9}{16}}\right]^{\frac{4}{9}}},$$

$$Cf = \frac{1.8\phi}{\ln\left[1+1.8\phi\right]},$$

$$\phi = \frac{\frac{Lc}{D}}{Cl\,Ra^{1/4}},$$

$$Nu_t = C_v Ra^{\frac{1}{3}},$$

$$Cv = \frac{0.13\left(Pr^{0.22}\right)}{\left(1+0.61\,Pr^{0.81}\right)^{0.42}},$$

$$Ra = \frac{\beta\, g\, \Delta T\, Lc^3}{\nu\,\alpha},$$

$$Pr = \frac{\mu\, Cp}{k},$$

where,

h = heat transfer coefficient
k = thermal conductivity of air
α = thermal diffusivity
Cp = specific heat at constant pressure
ν = kinematic viscosity
β = coefficient of thermal expansion
g = acceleration due to gravity,
Lc = length of cylinder
D = diameter of cylinder,
ΔT = temperature difference between surface and surroundings

Once the Nusselt number, Nu, is determined, the convection coefficient used in the thermal model is computed via:

$$h_c = Nu\frac{k}{L}$$

In a similar manner, the natural convection from vertical surfaces, such as the ends of a horizontal package, is computed using Equations 6-39 to 6-42 of [3.11], where the characteristic length is the height of the surface. These equations, which are applicable over the range of Rayleigh number (Ra) between 1 and $10^{12}$, are as follows:

$$Nu^T = \overline{C}_L Ra^{1/4}$$

$$\overline{C}_1 = \frac{4}{3}\left[\frac{0.503}{\left(1+\left(0.492/Pr\right)^{9/16}\right)^{4/9}}\right]$$

$$Nu_L = \frac{2.8}{\ln\left(1+2.8/Nu^T\right)}$$

$$Nu_t = C_t^V Ra^{1/3}$$

$$C_t^V = \frac{0.13\,Pr^{0.22}}{\left(1+0.61\,Pr^{0.81}\right)^{0.42}}$$

$$Nu = \frac{h_c L}{k} = \left[(Nu_L)^6 + (Nu_t)^6\right]^{1/6}$$

where

$$Ra_L = \frac{\rho^2 g_c \beta L^3 \Delta T}{\mu^2} \times Pr$$

$h_c$ = convection coefficient
Nu = Nusselt number
$g_c$ = gravitational acceleration
$\beta$ = coefficient of thermal expansion
$\Delta T$ = temperature difference
$\rho$ = density of air at the film temperature
$\mu$ = dynamic viscosity
Pr = Prandtl number
L = characteristic length
$k$ = thermal conductivity of air at the mean film temperature
Ra = Rayleigh number
$h_c$ = convection coefficient

Note that k, $c_p$, and $\mu$ are each computed as a function of air temperature, as taken from Table 3-5. Values for $\rho$ are computed using the ideal gas law, $\beta$ for an ideal gas is simply the inverse of the absolute temperature of the gas, and Pr is computed using the values for k, $c_p$, and $\mu$. Unit conversion factors are used as required to reconcile the units for the various properties used.

Calculation of the convection coefficient between the overpack shell and the ambient environment when the package is horizontal is computed using a correlation for horizontal cylinders [Equation 3-43, Chapter 1, [3.9]]. The characteristic length, D, is the outer diameter of the cylinder. This equation, applicable for $10^{-5} < Ra < 10^{12}$, is as follows:

$$Nu = \frac{h_c D}{k} = \left\{ 0.60 + \frac{0.387 Ra_D^{1/6}}{\left[1 + (0.559/Pr)^{9/16}\right]^{8/27}} \right\}^2$$

Natural convection from horizontal surfaces is computed from Equations 4.39 and 4.40 of [3.8] where the characteristic dimension (L) is equal to the plate surface area divided by the plate perimeter. For a heated surface facing upwards or a cooled surface facing downwards and $Ra > 1$:

$$Nu = \frac{h_c L}{k} = \left[ (Nu_L)^{10} + (Nu_t)^{10} \right]^{1/10}$$

$$Nu_L = \frac{1.4}{\ln\left(1 + 1.677 / \left(\overline{C_L} Ra^{1/4}\right)\right)}$$

$$\overline{C_L} = \frac{0.671}{\left[1 + (0.492/Pr)^{9/16}\right]^{4/9}}$$

$$Nu_t = 0.14 Ra^{1/3}$$

For a heated surface facing downwards or a cooled surface facing upwards and $10^3 < Ra < 10^{10}$, the correlation is as follows:

$$Nu = Nu_L = \frac{2.5}{\ln\left(1 + 2.5/Nu^T\right)}$$

$$Nu^T = \frac{0.527}{\left(1 + (1.9/Pr)^{9/10}\right)^{2/9}} Ra^{1/5}$$

For forced convection encountered during the HAC fire event, the convective heat transfer coefficient, $h_c$, is computed from correlations for flat surfaces [Table 6-5, [3.12]] where the characteristic dimension (L) is equal to the length along the surface. For conservatism, a gas velocity of 15 m/s and a characteristic length of 38 mm are used when computing the forced convection coefficient for all surfaces.

For Reynolds number (Re) < $5 \times 10^5$ and Prandtl number (Pr) > 0.1, the forced convection coefficient is computed via:

$$Nu = 0.664 Re_L^{0.5} Pr^{0.33}$$

For Reynolds number (Re) > $5x10^5$ and Prandtl number (Pr) > 0.5, the forced convection coefficient is computed via:

$$Nu = 0.036\,Pr^{0.33}[Re_L^{\ 0.8} - 23{,}200]$$

*Radiation Heat Transfer*

Radiation heat transfer is computed using the standard gray-body relationship as expressed by equation 1-8 of [3.12]:

$$q = \sigma A_1 \mathbf{F_{1-2}} \left(T_1^4 - T_2^4\right)$$

where $\sigma$ is the Stefan-Boltzmann constant, and values of ($A_1$ $\mathbf{F_{1-2}}$) are calculated within the Thermal Desktop computer program using a Monte Carlo ray tracing algorithm. The SINDA/FLUINT program automatically computes the $T^4$ values using the absolute temperature and adds the Stefan-Boltzmann constant $\sigma$.

### 3.5.4 Foam Response to Fire

The General Plastics LAST-A-FOAM® FR-3700 rigid polyurethane foam [www.generalplastics.com] has been used in numerous radioactive materials (RAM) packages. The FR-3700 formulation is specially designed to allow predictable impact-absorption performance under dynamic loading, while also providing an intumescent char layer that insulates and protects the underlying materials, even when exposed to pool-fire conditions. Upon exposure to fire temperatures, this proprietary foam decomposes into an intumescent char that swells and tends to fill voids or gaps created by free drop or puncture bar damage. The thermal decomposition absorbs a significant amount of the heat transferred into the foam, which is then expelled from the package as a high-temperature gas. At the same time, the resultant char layer shields the underlying undamaged foam from further direct exposure to the external high temperatures. This behavior has been observed in numerous fire tests of other RAM packages.

Since the decomposition of the foam under elevated temperatures is an endothermic process, the foam is self-extinguishing and will not support a flame once the external fire is removed. However, the gases generated by the decomposition process are combustible and will burn under piloted conditions. Further, a portion of these generated gases could remain trapped within the charred layer of the foam for a period of time after the cessation of the HAC fire event and could support further combustion, although at a much reduced level, until a sufficient time has passed for their depletion from the cell structure.

The mechanisms behind the observed variations in the thermal properties and behavior of the FR-3700 foam at elevated temperatures are varied and complex and only limited research has been conducted in this area. No definitive analytical model of the foam properties under HAC conditions currently exists. Instead, a combination of empirical data and modeling conservatism is used to simulate the thermal performance of the LAST-A-FOAM® FR-3700 polyurethane foam for this application.

The [3.13] and [3.14] references describe the setup and results of a series of fire tests conducted on 5-gallon cans filled with FR-3700 foam at densities from 0.107 to 0.412 g/cm$^3$ (6.7 to 25.8 pounds per cubic foot (pcf)). Under the fire tests, one end of the test articles (i.e., the hot face surface) was subjected to an open diesel fueled burner flame at temperatures of 980 to 1,200ºC (1,800 to 2,200ºF) for 30+ minutes. A thermal shield prevented direct exposure to the burner flame on any surface of the test article other than the hot face. Each test article was instrumented with thermocouples located at various depths in the foam. In addition, samples of the foam were subjected to thermogravimetric analysis (TGA) to determine the thermal decomposition vs. temperature. The exposure temperatures for the tests varied from 21 to 820°C (70 to 1,500ºF) and were conducted in both air and nitrogen atmospheres. Since the results for the nitrogen environment (see Figure 3-13) are more representative of the low oxygen environment existing for the encased foam, it is used for the basis of this evaluation. These test results indicate that the following steps occur in the thermal breakdown of the foam under the level of elevated temperatures reached during the HAC fire event:

- Below 120°C (250ºF), the variations in foam thermal properties with temperature are slight and reversible. Thus, fixed values for specific heat and thermal conductivity are appropriate.
- Between 120 and 260°C (250 and 500ºF), small variations in foam thermal properties occur as water vapor and non-condensable gases are driven out of the foam. Thus, fixed values for specific heat and thermal conductivity are appropriate.
- Irreversible thermal decomposition of the foam begins as the temperature rises above 260°C (500ºF) and increases non-linearly with temperature. Based on the TGA testing (see Figure 3-13), approximately two-thirds of this decomposition occurs over a narrow temperature range centered about 354°C (670°F).
- The decomposition is accompanied by vigorous outgassing from the foam and an indeterminate amount of internal heat generation. The internal heat generation arises from the gases generated by the decomposition process that are combustible under piloted conditions. However, since the decomposition process is exothermic, the foam will not support combustion indefinitely and further, the outgassing process removes a significant amount of heat itself via mass transport.
- The weight loss due to outgassing not only has a direct effect on the heat flux into the remaining virgin foam, but changes the composition of the resulting foam char, since the foam constituents are lost at different rates. This change in composition affects both the specific heat and the thermal conductivity of the foam char layer.
- As temperature continues to rise, the developing char layer begins to take on the characteristics of a gas-filled cellular structure where radiative interchange from one cell surface to another becomes a significant portion of the overall heat transfer mechanism. This change in the dominant heat transfer mechanism causes the apparent heat conductivity to take on a highly non-linear relationship with temperature.
- Finally, at temperatures above 675°C (1,250) ºF, the thermal breakdown of the foam is essentially completed and only about 5 to 10% of the original mass is left. In the absence

of direct exposure to a flame or erosion by the channeling of the outgas products through the foam, the char layer will be the same or slightly thicker than the original foam depth. This char layer will continue to provide radiative shielding to the underlying foam material.

The sharp transition in the state of the foam noted in Figure 3-13 at or about 354°C (670°F) can be used to correlate the depth of the foam char and the occurrence of this temperature level within the foam. Figure 3-14 illustrates the relationship between foam recession (i.e., char depth) and foam density following exposure to a 30-minute fire as compiled from a series of tests. The correlation between the foam recession depth and the foam density is expressed by the relation:

$$y = -0.94681 - 11.64 \times \log_{10}(x)$$

where, y = the recession depth, cm
x = foam density ($g/cm^3$)

Based on this correlation, the recession depth expected for nominal 0.216 $g/cm^3$ (13.5 pcf) density foam is estimated to be 6.8 cm (2.7 inches). The fabrication tolerance for the foam density is $\pm$15%. Therefore, the actual foam density that may exist within the packaging ranges from 0.187 to 0.248 g/cm3 (11.7 to 15.5 pcf). The recession depth associated with the lower bound on the foam density is 7.5 cm (3 inches).

An additional correction to the expected recession is required to account for the fact that the thermal testing upon which the correlation is based used a flame temperature 980 to 1,200ºC (1,800 to 2,200ºF), whereas the regulatory fire flame temperature is specified as 800ºC (1,475ºF). Instrumented fire test results for 0.128, 0.256, and 0.384 g/cm3 (8, 16, and 24 pcf) density foam are used to estimate the correction to the predicted foam recession depth. Figure 3-15 illustrates the predicted foam temperature vs. depth and foam density at the end of a 30-minute fire event with a flame temperature of 800ºC (1,475ºF). Interpolating the figure data for a foam density of 0.187 g/cm3 (11.7 pcf) and foam temperature of 354°C (670°F) indicates that this temperature would be reached at a depth of approximately 4.5 cm (1.8 inches) after 30 minutes. This compares with the predicted recession depth of 7.5 cm (3 inches) at the higher flame temperature. For conservatism, the average of these two values is assumed for the predicted recession depth, or 6 cm (2.4 inches). The portions of the foam at depths greater than this from the exterior surfaces of the package are predicted to remain essentially unaffected by the HAC fire event.

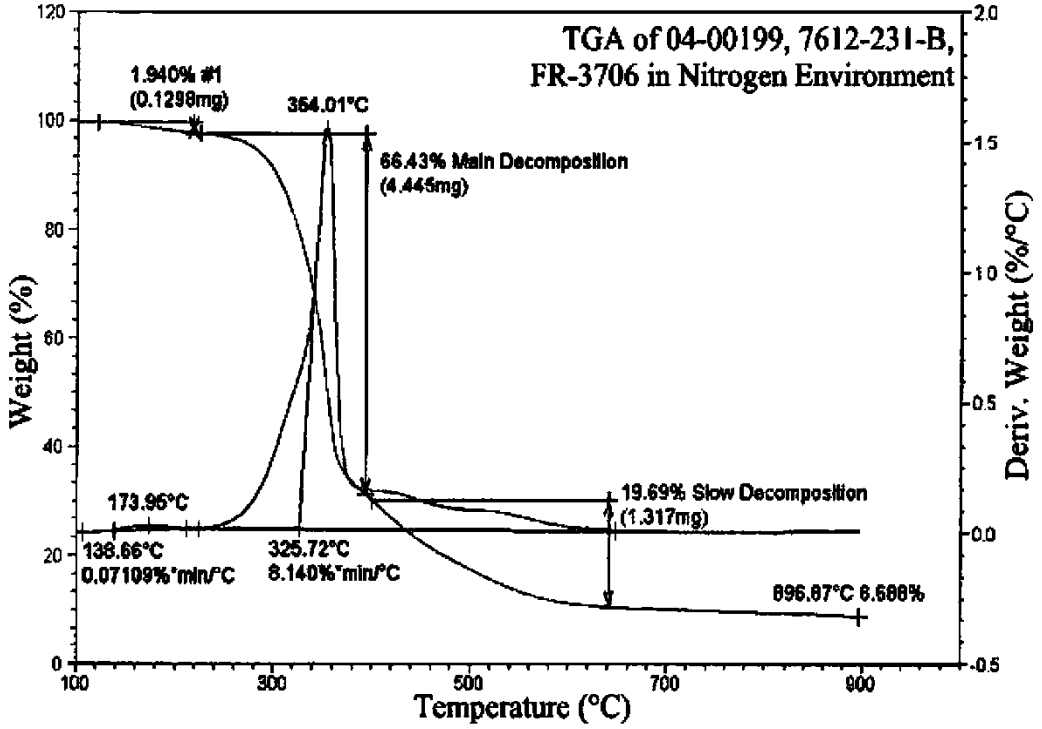


**Figure 3-13 – TGA Analysis of Foam Decomposition in Nitrogen**

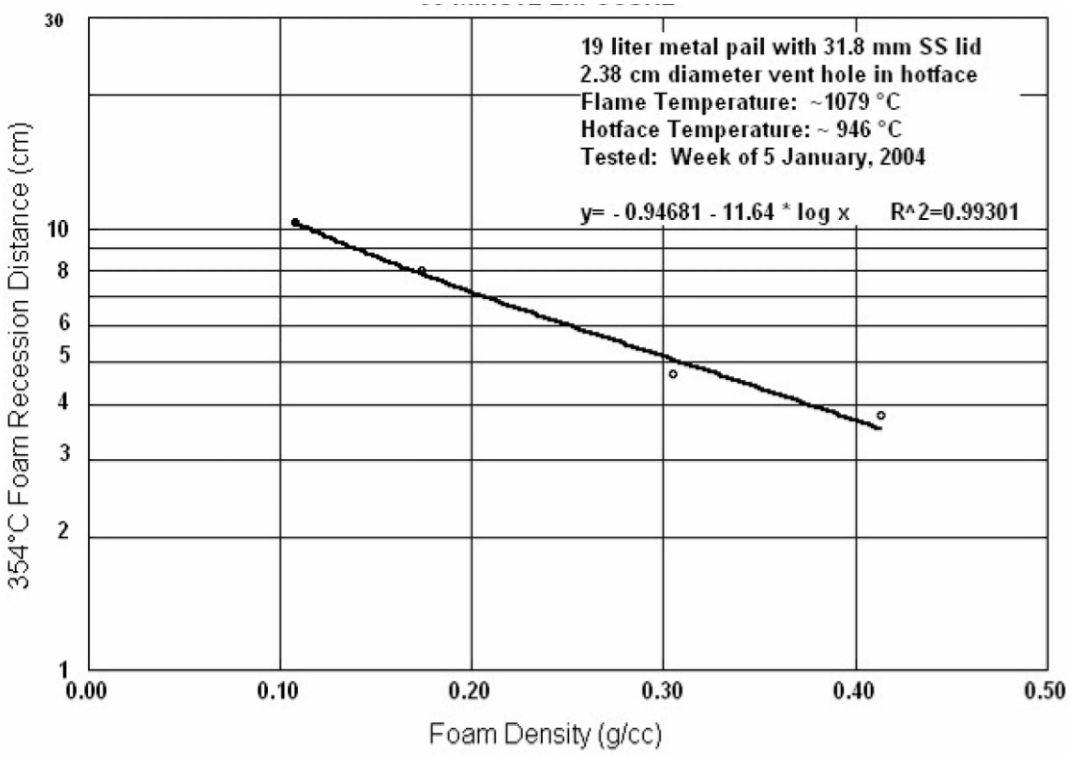


**Figure 3-14 – Foam Recession vs. Density for 30-Minute Fire**

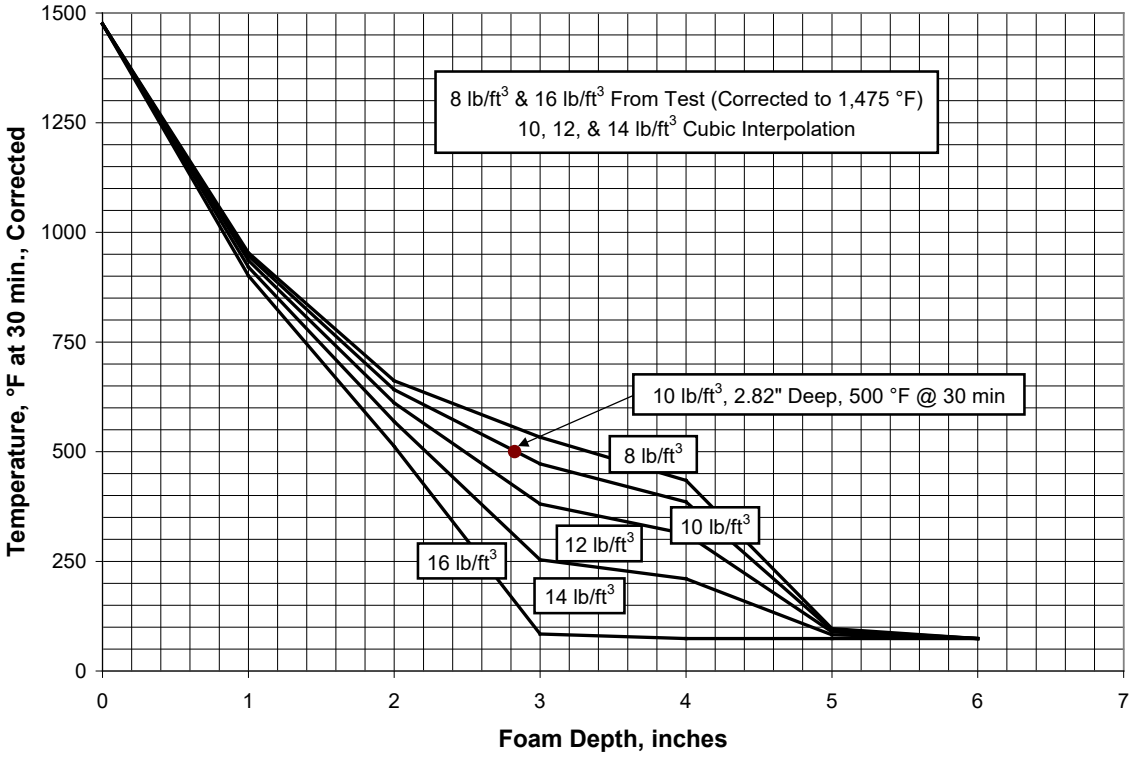


**Figure 3-15 – Foam HAC Performance, Corrected for 1,475°F Flame Temperature**

### 3.5.5 Radiolytic Gas Generation in Mallinckrodt Produced $^{99}$Mo Solutions

(Proprietary Attachment)

Proprietary Attachment Withheld

### 3.5.6 Hydrogen Generation in Mallinckrodt Produced $^{99}$Mo Solutions

(Proprietary Attachment)

Proprietary Attachment Withheld

This page intentionally blank.

# 4 CONTAINMENT

The MIDUS package containment boundary is designed, constructed, operated, and maintained to assure no loss or dispersal of radioactive contents under the tests specified in 10 CFR 71, §71.71 and §71.73. This chapter describes the package's containment system design and how it meets the containment requirements under NCT and HAC tests, and defines the criteria for leak-rate testing during package fabrication, use, maintenance, and repair.

## 4.1 Description of the Containment System

The package has a simple, robust containment system design. There are no welds within the containment boundary. Other than the main closure, there are no penetrations to the containment system, and no valves or pressure relief devices of any kind. The package does not rely on any filter or mechanical cooling system to meet containment requirements.

The containment system materials of construction are evaluated in Section 2.2.2 and selected to avoid chemical, galvanic, or other reactions. The materials of construction are compatible with each other and the chemical form of the payload.

The containment system is designed, fabricated, examined, tested, and inspected in accordance with the ASME B&PV Code, Section III, Division 3, Subsections WA and WB with certain exceptions. Section 2.1.4 and Table 2-9 and Table 2-10 of this SAR discuss the exceptions and their bases.

Figure 4-1 shows an overview of the package containment design. The package is securely closed using eight steel closure bolts (figure item 1). The containment system consists of a stainless-steel closure lid (item 2), an elastomeric containment O-ring (item 3), and a monolithic stainless-steel inner containment shell (item 4), which is integral with the cask flange. Figure 4-2 illustrates the package containment boundary.

There are two other seals indicated in Figure 4-1: a test O-ring (item 6) located outside the containment seal, and a cleanliness O-ring (item 8) located on the shield plug (item 7). The test port (item 5) is a tapped hole that communicates with the small space between the containment and test O-rings. It provides a means for performing a pre-shipment leak test. The cleanliness O-ring performs a housekeeping function, and it indirectly provides a post-accident shielding function as discussed in Sections 5.1.1.1 and 5.3.1.2. A third seal, not shown in the figure, is the metal-to-metal seal on the product bottle cap. Although none of these seals are relied upon for containment, each is capable of providing containment-quality sealing and thus provides a substantial safety margin to the package design.

The complete specifications for the containment system, including the materials of construction, testing requirements, required material thicknesses, O-ring seal specifications, and bolt torques, are listed in Drawings TYC01-1604 and -1605, in Section 1.3.2.

The cask closure bolts are physically protected from damage by the closure lid's recessed bolt-hole design. The closure lid also has a shear lip feature that protects the bolts from shear failure due to transverse impact loads. The closure bolts are positive fasteners that securely close the package. They cannot be opened unintentionally, or by any pressure that may arise within the package (Section 2.4.3). In addition, a tamper-indicating seal applied to the package prior to shipment further assures that the package cannot be opened unintentionally.

Ethylene-propylene is the specified containment O-ring material. It offers good resistance to sodium hydroxide and sodium nitrate [4.1], the two components of the payload solution. The manufacturer's recommended temperature range for continuous service of ethylene-propylene O-rings is -40ºC to 150ºC. For short exposures, the material can withstand a temperature 204ºC for 2 hours or less [4.1]. Sections 3.3.1 and 3.4.3 show that the containment O-ring temperatures are below these recommended values for the NCT and HAC conditions, respectively. A Sandia National Laboratories test program compared several elastomeric O-ring compounds for performance under transportation package conditions [4.2]. It found that ethylene-propylene O-rings perform well at both cold and high temperatures, independently confirming the manufacturer's ratings.

Radiation can affect the properties of O-ring materials, reducing their resistance to compression set. Ethylene propylene elastomers have good radiation-resistance properties and, like many O-ring compounds, provide adequate performance into the $10^6$–$10^7$ rads exposure range [4.1]. For conservatism, the radiation-resistance for the containment O-ring is specified as $10^6$ rads.

Radiation exposure to the containment seal during shipping is very low. The package is designed for contact maintenance at the cask flange area. At those exposure rates, the service life for an elastomeric seal would be many hundreds of thousands of use-cycles. Thus, exposure of the containment O-ring during package shipment is not a controlling factor for O-ring replacement.

During package loading, the payload is lowered into the cask cavity. It travels past the containment seal for a few seconds per loading cycle, shielded only by the product and the steel in the payload internals. Calculations show that the maximum instantaneous energy deposition in the containment seal is on the order of $2x10^5$ rads/hr. At this peak exposure rate, it would take five continuous hours, or about 900 load/unload cycles at 10 seconds' effective exposure per insertion or removal, to reach $10^6$ rads. Since no significant increase in compression setting would occur until 1 to 1000 times this exposure, replacement of the containment seal is controlled by general wear and damage considerations, and not radiation exposure.

Flammable gas is generated by the payload due to radiolysis during shipment. Experiments using the identical product show that these gases do not accumulate beyond 5% (by volume) of the free gas volume in any confined region of the package. No credit is taken for getters, catalysts, or other recombination devices. Therefore the package-cavity gas does not constitute a flammability hazard. The flammable gas generation is discussed further in Section 3.3.2.

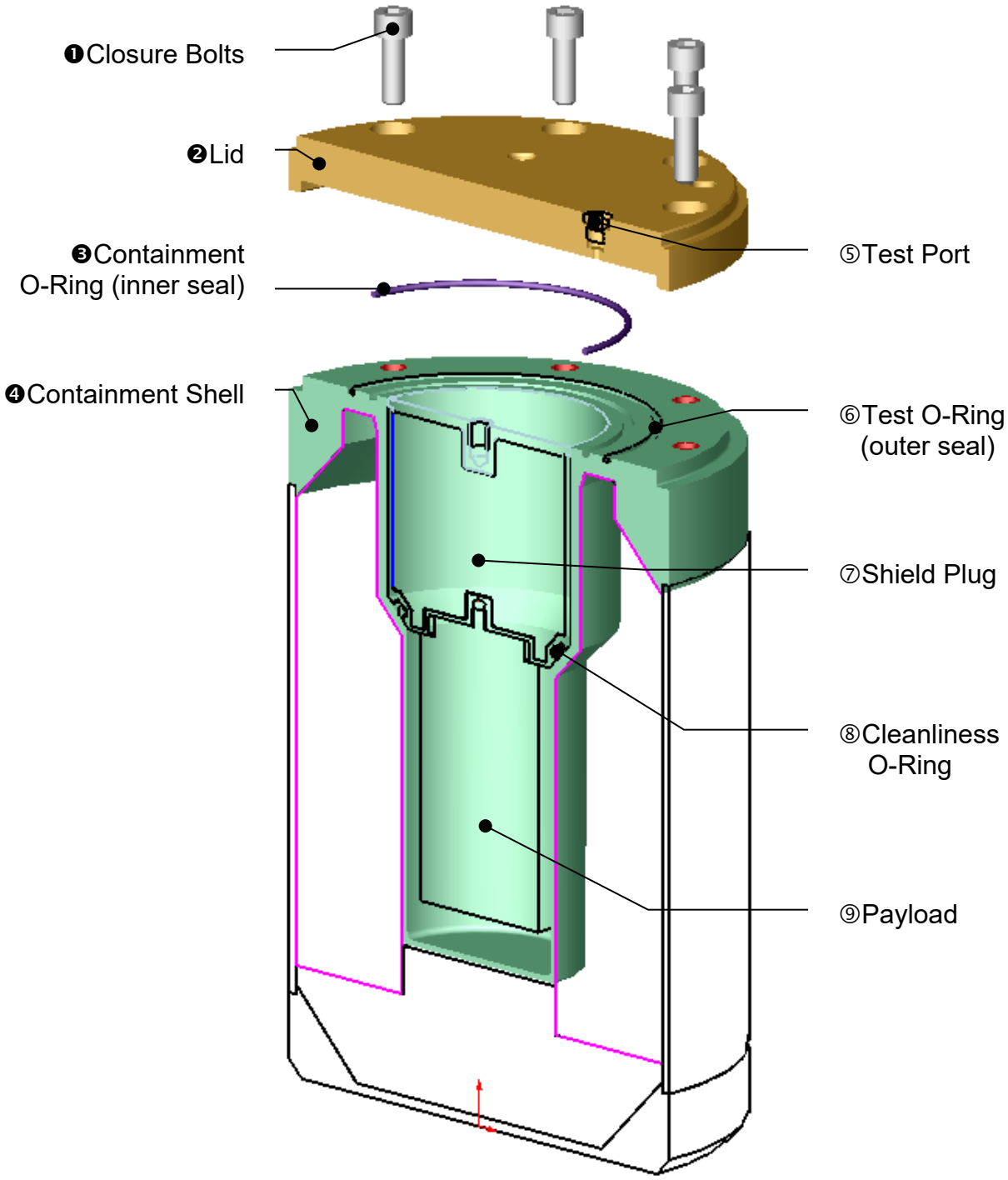


**Figure 4-1 – Containment System Overview**

(Filled numbers represent containment features)

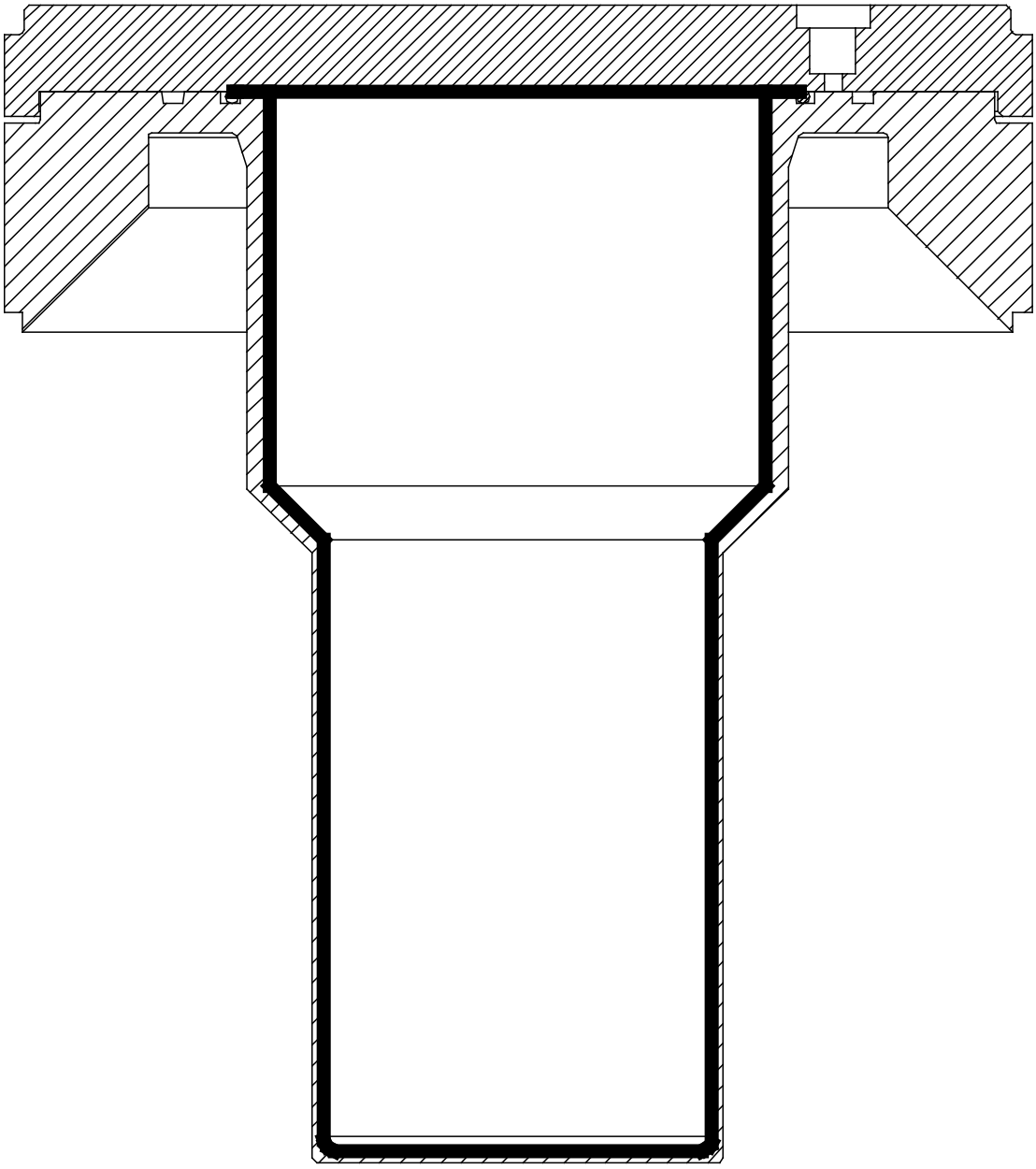

**Figure 4-2 – Package Containment Boundary**

## 4.2 Containment under Normal Conditions of Transport

### 4.2.1 NCT Pressurization of the Containment Vessel

The package maximum normal operating pressure (MNOP) is 7 bar, based on the definition of a Type B(U) packaging. Section 3.3.2 further discusses the NCT pressurization.

### 4.2.2 NCT Containment Criterion

The package is designed to a "leaktight" containment criterion per ANSI N14.5 [4.3], therefore the containment criterion is $1 \times 10^{-7}$ ref-cm$^3$/s (air).

### 4.2.3 Compliance with NCT Containment Criterion

Compliance with the NCT containment criterion is demonstrated by analysis. The structural evaluation in Section 2.6 shows that there would be no loss or dispersal of radioactive contents, and that the containment boundary, seal region, and closure bolts do not undergo any inelastic deformation when subjected to the conditions of §71.71. The thermal evaluation in Section 3.3.1 shows that the seals, bolts and containment system materials of construction do not exceed their temperature limits when subjected to the conditions of §71.71.

## 4.3 Containment under Hypothetical Accident Conditions

### 4.3.1 HAC Pressurization of the Containment Vessel

The containment evaluation for HAC is performed assuming that the maximum package pressure is 13.0 bar.

### 4.3.2 HAC Containment Criterion

The package is designed to a "leaktight" containment criterion per ANSI N14.5 [4.3], therefore the containment criterion is $1 \times 10^{-7}$ ref-cm$^3$/s (air).

### 4.3.3 Compliance with HAC Containment Criterion

Compliance with the HAC containment criterion is demonstrated by analysis. The structural evaluation in Section 2.7 shows that there would be no loss or dispersal of radioactive contents, and that the containment boundary, seal region, and closure bolts do not undergo any inelastic deformation when subjected to the conditions of §71.73. The thermal evaluation in Section 3.4.3 shows that the seals, bolts and containment system materials of construction do not exceed their temperature limits when subjected to the conditions of §71.73.

Although the confirmatory test program is not the basis for package acceptance, the test sequence did include a post-drop, post-fire pressure test. The damaged package passed a $10^{-3}$ ref-cm$^3$/s pressure-rise test. Calibrated temperature-indicating strips showed that the seal

temperatures remain below the seal material limits. The complete test report is included in Section 2.12.4.

## 4.4 Leak Rate Tests for Type B Packages

### 4.4.1 Fabrication Leak Rate Test

The packaging is leak rate tested during fabrication to the leaktight criteria equivalent to $1 \times 10^{-7}$ ref-$cm^3$/s (air) to demonstrate that each packaging, as fabricated, provides the required level of containment. The fabrication leak rate test is further described in Section 8.1.4.

### 4.4.2 Maintenance Leak Rate Test

The packaging is leak rate tested after maintenance to the leaktight criteria equivalent to $1 \times 10^{-7}$ ref-$cm^3$/s (air) to confirm that maintenance, repair, or replacement of components has not degraded the containment system performance. The maintenance leak rate testing and the replacement or repair activities that require a maintenance leak rate test are further described in Section 8.2.2.

### 4.4.3 Periodic Leak Rate Test

The containment O-ring closure shall be leak rate tested within 12 months prior to shipment as described in ANSI N14.5 [4.3] to the leaktight criteria equivalent to $1 \times 10^{-7}$ ref-$cm^3$/s (air) to confirm that the containment capabilities have not deteriorated over an extended period of use. The periodic leak rate test is further described in Section 8.2.2.

### 4.4.4 Pre-shipment Leak Rate Test

Each package is leak rate tested prior to shipment to confirm that the containment system is properly assembled for shipment, as required in ANSI N14.5 [4.3]. The acceptance criterion for the pre-shipment leak test is no detected leakage when tested to a sensitivity of $1 \times 10^{-3}$ ref-$cm^3$/s (air) or more sensitive. The pre-shipment leak rate test is further described in Section 7.4.1

## 4.5 Appendix

[4.1] Parker Hannifin Corporation, *Parker O Ring Handbook*, ORD 5700/USA, 2001.

[4.2] Bronowski, D. R., *Performance Testing of Elastomeric Seal Materials Under Low- and High-Temperature Conditions: Final Report*, SAND94-2207, Sandia National Laboratories, June 2000.

[4.3] ANSI N14.5, *American National Standard for Radioactive Materials - Leakage Test on Packages for Shipment*, American National Standards Institute, Inc., 2014.

This page intentionally blank.

# 5 SHIELDING EVALUATION

## 5.1 Description of Shielding Design

The MIDUS package is designed to meet the regulatory requirements of 10 CFR 71 for a non-fissile, non-exclusive-use packaging. This chapter provides the description of the package shielding design and the shielding evaluation (§71.31(a)(1), §71.31(a)(2), and §71.35(a)). Chapter 1 provides the general package description (§71.3). The shielding evaluation presented in the body of this chapter is for the liquid payload (i.e., Content #01) described in Section 1.2.2.1. For clarity, the body of this chapter is not revised for additional contents. Instead, the shielding evaluation of each additional payload is presented in SAR addenda, starting in Chapter 9.

The package is designed, fabricated, assembled, tested, maintained, and used in accordance with the codes and standards described in Chapters 1, 7, and 8 to assure radiological safety (§71.31(c)).

The package is designed, constructed, and prepared for shipment so that, under the NCT tests specified in §71.71, there will be no loss or dispersal of radioactive contents as demonstrated to a sensitivity of $10^{-6}$ $A_2$ per hour, no significant increase in external surface radiation levels, and no substantial reduction in the effectiveness of the packaging (§71.43(f)).

Sections 5.1.2 and 5.4.4 show that, under the NCT tests specified in §71.71, the external radiation levels meet the requirements of §71.47(a) for non-exclusive-use (§71.43(f)), and that, under the HAC tests specified in §71.73, the external radiation level does not exceed 1000 mrem/hr at one meter from the surface of the package (§71.51(a)(2)).

### 5.1.1 Design Features

Figure 5-1 shows the shielding features of the cask assembly. The major subassemblies are the payload, cask body assembly, cask closure lid assembly, and shield lid assembly. The cask is constructed of steel and depleted uranium (DU), with thick radial and axial DU shields in the cask body, a DU shield plug, and an additional DU shield lid atop the cask closure lid. This special shield lid is designed to mitigate the potential effects of post-accident dose rate increases that could occur if the liquid payload were to seep into the capillary spaces surrounding the shield plug.

#### 5.1.1.1 Payload Shielding Design Features

The product is loaded into the package using remote operations in a hot cell. The product is first transferred into a steel product bottle. This bottle has a metal-to-metal seal that is designed to isolate the payload and withstand the pressure buildup during shipping. Although this seal is vital for operational reasons, specifically contamination control, it is not credited as a containment seal in the safety analysis.

While still in the hot cell, the product bottle is placed into a secondary steel container, and a lid with an elastomeric O-ring seal is inserted using remote equipment. The lid is called the "snap ring" because it snaps onto the product bottle, facilitating handling in the hot cell. The secondary seal in the snap ring provides another contamination barrier for operations, but it is not credited for package containment. The top of the snap ring has a threaded stud that screws into the bottom of the shield plug as a handling aid in the hot cell.

The product bottle, secondary container, and snap ring are provided by the user and are not a part of the package design. It is anticipated that the user may occasionally require design changes to these components for production purposes; therefore, neither of the components are credited for their radiation attenuation or containment capacities. The product bottle and secondary container are always present, though, and they will provide additional photon attenuation beyond the results predicted by the safety analysis.

Although no credit is taken for attenuation by the payload materials of construction, the shielding analyses include cases to evaluate the *geometric* effects of the payload internals. The final shielding results show the worst-case situation considering the possible source fluid geometry with and without the presence of the payload internals.

The package has a third seal in the payload area. The "cleanliness seal" is an elastomeric O-ring seal between the shield plug and cask inner shell. This seal provides a housekeeping function for operations, and it provides the necessary compliance to press the shield plug against the closure lid, thereby minimizing the potential volume for flooding in the post-HAC condition.

These three seals are not credited as package containment seals, but credit is taken for their presence and effectiveness to confine the product within the boundary of the cask cavity under NCT. Since there are three independent seals, it is reasonable to assume that the payload will not enter the spaces around and above the shield plug under NCT tests.

For conservatism, it is assumed that all three of these seals fail during HAC tests, allowing the product to fill the capillary spaces around and above the shield plug. In this event, dose rates on the package top end are mitigated by an additional top DU shield lid, as discussed in Section 5.1.1.3 below.

### 5.1.1.2 Cask Shielding Features

The cask includes the cask body, shield plug, and closure lid assemblies. The body is constructed from two depleted uranium parts: a radial shield and a bottom axial shield. These DU components are sheathed in stainless steel by steel inner and outer shells. The shield plug is a cylinder of DU that is also sheathed by stainless steel. The closure lid is stainless steel.

Tolerances in the cask are controlled to minimize radiation streaming, allow ease of fabrication and use, and enhance the package's structural response to drop events. Section 5.3.1 summarizes the key gap sizes assumed for the shielding models.

Table 5-1 shows the key shielding parameters for the cask.

#### 5.1.1.3 Shield Lid Assembly Shielding Features

In order to mitigate the radiological consequences of the HAC free drop, the package has a shield lid that bolts to the closure lid. The shield lid provides additional attenuation for the scenario in which the product is postulated to escape the seals on the two inner payload containers, breach the cleanliness seal, and collect in the annular space around the shield plug and in the gap between the shield plug and closure lid. In this unlikely accident scenario, some of the product seeps past much of the DU shielding in the shield plug and cask body, potentially resulting in high top axial dose rates. Without additional shielding outside the cask closure lid, HAC exposure rates in the top axial direction could exceed regulatory limits; therefore, additional shielding is necessary. The shield lid addresses the industry lesson learned from a routine $^{192}$Ir shipment event in January, 2002 [5.1].

The shield lid is designed to bolt onto the closure lid, rather than being fixed to the overpack lid assembly, to avoid the separation that could potentially occur following an end drop.

Table 5-2 shows the key shielding parameters for the shield lid.

### 5.1.2 Summary of Maximum Radiation Levels

Table 5-3 shows the package maximum NCT dose rates for non-exclusive use. On the package surface, the dose rates comply with the regulatory limits in 10 CFR 71.47 with a large margin (factors of 2.5 to 37). At 1 meter, the dose rates comply, and the margins are even larger (factors of 4 to 28).

Table 5-4 shows the package maximum HAC dose rates. At 1 meter, the dose rates comply, and the margins range from 16% to a factor of 29.

The NCT results consistently show the largest margin on the package top end, followed by the package bottom and side surfaces. The HAC results differ because the some of the source is assumed to flow around the shield plug, changing the configuration of the source and shield. The HAC bottom end results show the largest margin, followed by the top and side locations.

**Table 5-1 – Key Cask Body Shielding Parameters[1,2]**

| Parameter | Part | Value |
|---|---|---|
| DU Density | Radial shield, Axial Shield, Shield plug core | ≥ 18.0 g/cm$^3$ |
| DU radial thickness | Radial shield | ≥ 6.21 cm |
| DU axial thickness (downward) | Bottom shield | ≥ 6.44 cm |
| DU axial thickness (upward) | Shield plug DU (total height) | ≥ 9.07 cm |

Notes:

1. The dimensional values presented above are the lower-bound values (modeled in the shielding analyses) for the overall DU thickness on the cask side, bottom and top. Detailed DU shielding component dimensions, including nominal dimensions, tolerances, and the values modeled in the shielding analyses, are presented in Table 5-6 and in Drawing TYC01-1606 (in Section 1.3.2). Other, non-DU cask system components, for which nominal dimensions were modeled, are also described in Table 5-6 and in the Section 1.3.2 drawings.
2. The densities and compositions of the materials modeled in the shielding analyses are given in Table 5-9. The DU density presented above (which was modeled in the shielding analyses) is a conservative, lower-bound value

**Table 5-2 – Key Shield Lid Shielding Parameters**

| Parameter | Part | Value |
|---|---|---|
| DU Density | Shield lid core | ≥ 18.0 g/cm$^3$ |
| DU axial thickness | Shield lid core | ≥ 1.67 cm |

Notes:

1. The shield lid component dimensions and materials are described in more detailed in Table 5-6, Table 5-9 and Drawing TYC01-1602.

**Table 5-3 – Summary Table of External NCT Radiation Levels**

| Normal Conditions of Transport | Package Surface mSv/h (mrem/h) | | | 1 Meter from Package Surface mSv/h (mrem/h) | | |
|---|---|---|---|---|---|---|
| Location | Top | Side | Bottom | Top | Side | Bottom |
| Radiation | 0.053 (5.3) | 0.81 (81) | 0.80 (80) | 0.0035 (0.35) | 0.023 (2.3) | 0.017 (1.7) |
| 10 CFR 71.47(a) Limit | 2 (200) | 2 (200) | 2 (200) | 0.1 (10) | 0.1 (10) | 0.1 (10) |

**Table 5-4 – Summary Table of External HAC Radiation Levels**

| Hypothetical Accident Conditions | 1 Meter from Package Surface mSv/h (mrem/h) | | |
|---|---|---|---|
| Location | Top | Side | Bottom |
| Radiation | 6.3 (626) | 8.4 (841) | 0.34 (34) |
| 10 CFR 71.51(a)(2) Limit | 10 (1000) | 10 (1000) | 10 (1000) |

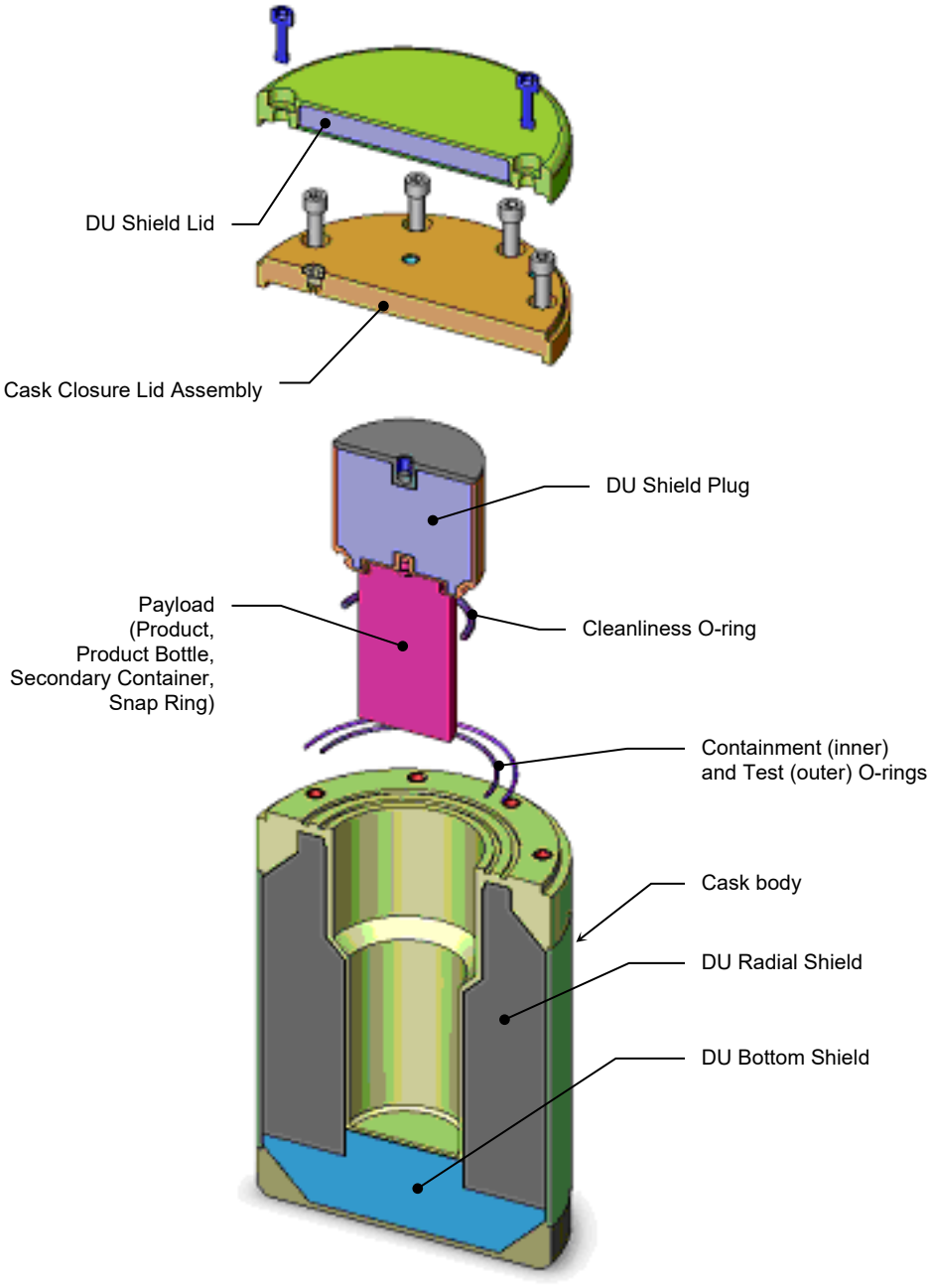


**Figure 5-1 – MIDUS Cask Shielding Features**

## 5.2 Source Specification

The shielding safety evaluations are performed assuming a bounding product activity of 4,500 Ci of $^{99}$Mo in liquid form. For lower activity specifications (refer to Section 1.2.2), the shielding results would be reduced by a corresponding factor. The payload is a medical-grade solution that does not vary in composition, other than the concentration.

### 5.2.1 Gamma Source

The nuclide $^{99}$Mo emits beta particles, electrons, and photons with a half life of 66.02 hours [5.2]. It decays to $^{99}$Tc (13%) and $^{99m}$Tc (87%), where $^{99m}$Tc is a metastable state of $^{99}$Tc. With a 6.007 hour half life, $^{99m}$Tc decays 100% to $^{99}$Tc. Because of its short half life, $^{99m}$Tc is included in the source term calculations as a contributor. Since $^{99}$Tc has an extremely long half life (214,000 years), it can be neglected as a significant source term contributor and no further decay daughters are considered.

The betas and electrons can be neglected as shielding source terms because they are 100% absorbed in the packaging materials and thus will not contribute to the exterior package dose rates.

The photon source term used for the shielding analyses is conservatively based on a bounding activity of 4,500 Ci of $^{99}$Mo plus the maximum amount of the $^{99m}$Tc daughter (Section 1.2.2.1 specifies a maximum payload of 4,400 Ci). Since the $^{99}$Mo manufacturing timeline determines the amount of daughter products in a shipment, the exact amount of initial daughter products that will accompany the $^{99}$Mo in each shipment may vary. For conservatism, the source term is developed assuming that the $^{99}$Mo processing time is infinite, and, thus, that the $^{99m}$Tc is in full transient equilibrium with the $^{99}$Mo. The amount of $^{99m}$Tc assumed for developing the source term is therefore 4,500 Ci · 0.87 = 3,915 Ci.

The photon sources in Table 5-5 were calculated for discrete energy lines using Table of Isotope data [5.3] for $^{99}$Mo and $^{99m}$Tc, and the total activities for $^{99}$Mo and $^{99m}$Tc.

### 5.2.2 Neutron Source

Not applicable.

**Table 5-5 – Photon Source**

| Sorted by Energy | | |
|---|---|---|
| MeV | photons/s | MeV/s |
| 1.056197 | 1.80E+09 | 1.90E+09 |
| 1.017000 | 1.02E+09 | 1.03E+09 |
| 1.001340 | 9.16E+09 | 9.17E+09 |
| 0.986440 | 2.50E+09 | 2.46E+09 |
| 0.960750 | 1.58E+11 | 1.51E+11 |
| 0.861200 | 1.17E+10 | 1.00E+10 |
| 0.822970 | 2.22E+11 | 1.83E+11 |
| 0.777921 | 7.09E+12 | 5.52E+12 |
| 0.761774 | 6.66E+08 | 5.07E+08 |
| 0.739500 | 2.02E+13 | 1.49E+13 |
| 0.689600 | 6.99E+08 | 4.82E+08 |
| 0.621771 | 4.30E+10 | 2.67E+10 |
| 0.620030 | 3.83E+09 | 2.37E+09 |
| 0.599600 | 3.50E+09 | 2.10E+09 |
| 0.581300 | 1.67E+09 | 9.68E+08 |
| 0.580505 | 5.33E+09 | 3.09E+09 |
| 0.537790 | 5.49E+09 | 2.95E+09 |
| 0.528700 | 9.49E+10 | 5.02E+10 |
| 0.490530 | 1.83E+09 | 8.98E+08 |
| 0.469630 | 4.50E+09 | 2.11E+09 |
| 0.457600 | 1.35E+10 | 6.17E+09 |
| 0.455840 | 2.16E+09 | 9.87E+08 |
| 0.411491 | 2.43E+10 | 1.00E+10 |
| 0.410274 | 3.16E+09 | 1.30E+09 |
| 0.391700 | 5.33E+09 | 2.09E+09 |
| 0.380130 | 1.73E+10 | 6.58E+09 |
| 0.366421 | 1.98E+12 | 7.27E+11 |
| 0.322410 | 1.41E+08 | 4.53E+07 |
| 0.249030 | 6.49E+09 | 1.62E+09 |
| 0.242290 | 4.16E+09 | 1.01E+09 |
| 0.232720 | 1.23E+07 | 2.87E+06 |
| 0.181063 | 9.97E+12 | 1.81E+12 |
| 0.162370 | 1.98E+10 | 3.22E+09 |
| 0.158782 | 3.15E+10 | 5.00E+09 |
| 0.142628 | 2.71E+10 | 3.86E+09 |
| 0.140511 | 2.78E+14 | 3.90E+13 |
| 0.089400 | 5.00E+09 | 4.47E+08 |
| 0.040585 | 1.75E+12 | 7.10E+10 |

| Sorted by Power | | |
|---|---|---|
| MeV | photons/s | MeV/s |
| 0.140511 | 2.78E+14 | 3.90E+13 |
| 0.739500 | 2.02E+13 | 1.49E+13 |
| 0.777921 | 7.09E+12 | 5.52E+12 |
| 0.181063 | 9.97E+12 | 1.81E+12 |
| 0.366421 | 1.98E+12 | 7.27E+11 |
| 0.822970 | 2.22E+11 | 1.83E+11 |
| 0.960750 | 1.58E+11 | 1.51E+11 |
| 0.040585 | 1.75E+12 | 7.10E+10 |
| 0.528700 | 9.49E+10 | 5.02E+10 |
| 0.621771 | 4.30E+10 | 2.67E+10 |
| 0.861200 | 1.17E+10 | 1.00E+10 |
| 0.411491 | 2.43E+10 | 1.00E+10 |
| 1.001340 | 9.16E+09 | 9.17E+09 |
| 0.380130 | 1.73E+10 | 6.58E+09 |
| 0.457600 | 1.35E+10 | 6.17E+09 |
| 0.158782 | 3.15E+10 | 5.00E+09 |
| 0.142628 | 2.71E+10 | 3.86E+09 |
| 0.162370 | 1.98E+10 | 3.22E+09 |
| 0.580505 | 5.33E+09 | 3.09E+09 |
| 0.537790 | 5.49E+09 | 2.95E+09 |
| 0.986440 | 2.50E+09 | 2.46E+09 |
| 0.620030 | 3.83E+09 | 2.37E+09 |
| 0.469630 | 4.50E+09 | 2.11E+09 |
| 0.599600 | 3.50E+09 | 2.10E+09 |
| 0.391700 | 5.33E+09 | 2.09E+09 |
| 1.056197 | 1.80E+09 | 1.90E+09 |
| 0.249030 | 6.49E+09 | 1.62E+09 |
| 0.410274 | 3.16E+09 | 1.30E+09 |
| 1.017000 | 1.02E+09 | 1.03E+09 |
| 0.242290 | 4.16E+09 | 1.01E+09 |
| 0.455840 | 2.16E+09 | 9.87E+08 |
| 0.581300 | 1.67E+09 | 9.68E+08 |
| 0.490530 | 1.83E+09 | 8.98E+08 |
| 0.761774 | 6.66E+08 | 5.07E+08 |
| 0.689600 | 6.99E+08 | 4.82E+08 |
| 0.089400 | 5.00E+09 | 4.47E+08 |
| 0.322410 | 1.41E+08 | 4.53E+07 |
| 0.232720 | 1.23E+07 | 2.87E+06 |

## 5.3 Shielding Model

### 5.3.1 Configuration of Source and Shielding

#### 5.3.1.1 NCT Shielding Models

Figure 5-2 shows an overview of the baseline NCT shielding model, including the significant shielding features discussed above. NCT tests do not significantly affect the nominal package configuration from the shielding standpoint. Table 5-6 shows the key package component dimensions, and the corresponding dimensions used in the baseline NCT shielding model. Because of modeling simplifications, the model dimensions in Table 5-6 differ from the actual package dimensions.

The modeling approach is to represent the significant shielding components, specifically the DU, at the least material condition (LMC), accounting for manufacturing tolerances. Other package components are modeled at nominal thicknesses. The package is precision-machined; therefore, the tolerances are relatively small, and manufacturing tolerances on the steel components do not significantly impact the package shielding performance. Many overpack features are neglected, such as the joining flanges, resulting in extra conservatism in the models.

Gaps that are perpendicular to the radiation paths are neglected to simplify the MCNP models. In these cases, the gaps are neglected and overall model dimensions are compressed by a corresponding amount. Gaps that are collinear with the radiation paths, e.g., around the shield plug area, are modeled at the largest credible gap size. Figure 5-3, Figure 5-4, and Figure 5-5 show the key gap sizes assumed in the shielding models.

Several MCNP models are required because the product can be positioned at varying locations depending on the package orientation. The models cover upright, inverted, and horizontal package orientations. They also cover the range of possible product locations with and without confinement by the payload internals, because the confinement of fluid to the product bottle influences the geometric relation between source and shields. However, no credit is taken for mass attenuation by the payload internals.

Figure 5-2 is a scale illustration of the normal, upright orientation model. The figure identifies the different materials of construction as different shades, and the MCNP particle splitting surfaces as lines that subdivide the DU regions. The source fluid is modeled as a disk with an 85 mm diameter and a volume of 75 ml (4,500 Ci divided by the maximum specific activity of 60 Ci/ml). This model does not includes confinement by the product bottle or the secondary container. This case is conservative since it artificially places more source closer to the bottom end of the package and closer to the corners, thus challenging the streaming path between the radial and bottom DU pieces in the cask body. Additional cases are performed, as described below, to investigate the geometric effects of the presence of the payload internals.

Two inverted cases are run as shown in Figure 5-6. The cases represent different assumptions about the fluid displacement by the snap ring assembly of the internal product bottle shown in Figure 1-1. The dimensions of the payload internals are subject to change within the restrictions

of Section 1.2.2.1, therefore the fraction of the upper section of the cask interior cavity (illustrated in Figure 5-6) that is occupied by snap ring steel may vary. To account for this uncertainty, two extreme cases are evaluated. One case (shown on the left in Figure 5-6) assumes that the snap ring completely fills the upper cavity section, preventing any source fluid from entering the region in the event of an inverted cask. It should be noted that, although source fluid is excluded from the upper cavity zone for this first case, no steel is modeled within that zone (i.e., no credit is taken for the snap ring steel), with the exception of the small threaded hole in the bottom of the shield lid, which is modeled as being filled with the steel of the product bottle pintle. The second case (shown on the right in Figure 5-6) assumes a negligible snap ring steel volume, and models the upper cavity section as being completely filled with source fluid (while maintaining the total fluid volume of 75 ml). A third case, similar to the second case shown on the right in Figure 5-6, that models source fluid (as opposed to steel) in the small threaded hole in the bottom of the shield lid is also analyzed. As shown in Figure 5-6, the second assumption allows some of the source fluid to move into the upper section of the cask cavity, closer to the top end of the cask, but reduces the amount of fluid in the upper corner of the main cask cavity, near the streaming path between the shield plug and the cask flange.

Additional cases are performed, as described below, to investigate the geometric effects of the presence of the payload internals.

Figure 5-7 shows the horizontal case model geometry. 75 ml of fluid is modeled in a puddle along the length of the cask payload cavity. Due to the azimuthally asymmetric shape of the source region, MCNP point detectors are specified along the plane of symmetry.

Cases were run with a spherical source located near the top or bottom of the cavity. The purpose of these cases is to evaluate the geometric impact of the payload internals, which will confine the payload fluid under typical operations. The sphere is modeled with a volume of 75 ml, and its location for the top end case is chosen to closely represent the location the fluid would occupy in the neck of the product bottle in the inverted orientation. The bottom end sphere case elevates the centroid of the source region and reduces its diameter as would the presence of the payload internals.

#### 5.3.1.2 HAC Shielding Models

The post-HAC test package configuration changes in four ways that affect the shielding models. First, the product is postulated to escape the product bottle and secondary container, and flow via capillary action around the shield plug and into the gap under the cask lid. Second, the configuration of the source and shield in the damaged package is slightly different due to the foam crush. The outside of the package does not deform significantly from a shielding standpoint, but the inside-out crush behavior means that the source will be located closer to the 1-meter package distance than in the nominal geometry models. Third, it is assumed that the shield plug is radially offset to the maximum extent possible, increasing the potential gap. Fourth, the mass of the foam is reduced due to charring and off-gassing that occur as a result of the HAC fire event. This effect is conservatively treated by assuming 100% foam loss for the purpose of the shielding models.

If the product were to leak into the thin spaces around the shield plug, four distinct regions could become flooded with a significant amount of radioactive fluid: the annular region surrounding the shield plug, the disk-shaped region above the shield plug, the threaded hole on top of the shield plug, and the small free volume of the containment O-ring groove that is not occupied by the O-ring. Each of these regions has a maximum potential source term that is proportional to its volume. The volumes and related source term fractions are summarized in Table 5-7.

The function of the cleanliness O-ring is to assure that the shield plug is in contact with the closure lid, thus minimizing the potential volume in which liquid could collect during the HAC. The disk volume presented in Table 5-7, is based on the specified surface flatness of the top of shield plug top surface and the closure lid bottom surface, and the cleanliness O-ring provides the compliance necessary to ensure that no additional gap is present. No credit is taken for the cleanliness O-ring as a seal, only that it be present and provide the compliance necessary to ensure contact. Functional testing during manufacturing (Section 8.1.5.2), maintenance (Section 8.2.5.3), and operation (Section 7.1.2, step 0) assure that the cleanliness O-ring is correctly installed and that it will perform this function. Furthermore, the cleanliness O-ring is replaced every shipment, therefore it is not susceptible to compression set.

During the HAC drop, the cask body deforms the overpack inner shell upward, downward, or to the side, depending on the drop orientation. The package's gross outer dimensions are essentially unchanged, location of the cask body (within the overpack) shifts so that it is closer to the package side, top or bottom surface (as a result of a side, top, or end drop, respectively). The top, bottom, and side drops produce the largest gross deformation. Oblique and corner drops produce local deformations, but do not appreciably change the relative cask-overpack geometry. The package stays intact (no foam or steel is dislodged). The only significant change to the cask configuration, between NCT and HAC conditions, occurs within the foam. Crushing of the foam results in a reduction in foam thickness, on the package side, top or bottom (as a result of a cask side, top end, or bottom end drop, respectively). The foam mass is also reduced as a result of the fire. No significant deformations or alterations occur in any other system components, other than the shifting of the cask body location (within the overpack) that occurs as a result of the foam crush.

To account for the package deformations (i.e., the reductions in foam thickness, and the resulting reduction in distance between the source region and the package outer surfaces), the defined 1-meter dose tally surfaces are moved inward, towards the shielding model source zone. The inward shift of each tally surface is equal to the amount of foam crush that occurs within the corresponding overpack zone (i.e., side, top or bottom). The HAC shielding models also replace all foam material with void, to conservatively bound the effects of any degree of foam mass reduction (from the fire). The above approach yields accurate calculated dose rates, as both the thickness of the steel and DU shielding components, and the distance between the source zone and the dose tally surface, are accurately modeled.

Table 5-8 shows the reduction in foam thickness for the top end, side and bottom end overpack regions, for the HAC configuration versus the NCT configuration. Table 5-8 lists the foam thickness reductions modeled in the HAC shielding analyses, and compares them to the final

foam crush depths calculated by the structural evaluation presented in Section 2.7. The hot condition drop governs for all three cases. The HAC foam thickness reductions assumed in the shielding analyses, which were estimated based on preliminary structural analysis results, are roughly equal to or greater than the final reported structural results listed in the right column of Table 5-8. Modeling a larger amount of foam crush is conservative, and the 2 mm difference between the top end crush depths is not significant. The effect of moving the 1-meter top detector 2 mm closer to the source zone would be negligible, especially considering the large HAC dose rate margin calculated for the cask top end.

### 5.3.2 Material Properties

The shielding evaluations were performed using the material densities shown in Table 5-9. These properties are valid for the purpose of shielding evaluations under the NCT and HAC package conditions. The DU was modeled with the specified 2% Mo alloy, at the 18.0 g/cc minimum density specified in Drawing TYC01-1606. All steel components are modeled at the standard, nominal stainless steel density of 8.027 $g/cm^3$. The O-rings were modeled as water for convenience. The foam was modeled at a 12 $lb/ft^3$ density (0.193 $g/cm^3$), conservatively lighter than the specified density.

The radioactive $^{99}Mo$ will not precipitate under the MIDUS service conditions. Under very cold conditions, the product will freeze before it precipitates because the solubility is approximately 1600 times higher than the maximum allowable payload concentration. If precipitation were to occur, it would be a concern because it could produce a higher specific activity than is assumed for the calculations. Such an increase could potentially invalidate the conclusions of this calculation package for the HAC shielding cases if precipitation were possible.

**Table 5-6 – Summary of Key Component Dimensions**

| Feature | Nominal Design (cm) | Corresponding NCT Shielding Model Dimensions (cm) | Notes |
|---|---|---|---|
| Cask Cavity | ø8.5 x 13.4 | ø8.50 x 13.4 | Identical. |
| Shield Plug | ø10.8 x 9.8 | ø10.8 x 9.77 | Modeled shorter because of neglected gaps (perpendicular to primary radiation path). |
| Shield Plug DU | ø10.15 x 9.1 | 10.12 x 9.07 | DU modeled at least material condition (LMC). |
| Cask Assembly | ø22.5 x 32.4 | ø22.5 x 32.37 | Modeled shorter because of neglected gaps (perpendicular to primary radiation path). |
| Cask Body Radial DU Shield | ø21.63 outside<br>ø11.98 inside<br>ø9.13 inside | ø21.61, ø12.05, ø9.20 | DU modeled at least material condition (LMC). |
| Cask Body Bottom DU Shield | ø21.63 x 6.5 | ø21.61, 6.44 | DU modeled at least material condition (LMC). |
| Cask Lid | ø22.5 x 1.9 | ø22.5, 1.9 | 1.9 cm is the thickness of lid not counting the shear ring on the edge. |
| Shield Lid | ø22.5 x 2.3 | ø22.5, 2.27 | 2.3 cm is the thickness of lid not counting the shear ring on the edge. |
| Shield Lid DU | ø21.4, 1.7 | ø21.2, 1.67 | DU modeled at least material condition (LMC). |
| Overpack Cavity | ø23 x 35.2 | ø23 x 34.94 | Modeled shorter because of neglected gaps (perpendicular to primary radiation path). |
| Overpack | ø45.7 x 55.1 | ø45.7 x 54.64 | Modeled shorter because of neglected gaps (perpendicular to primary radiation path). |
| 1m Surface | ø245.7 x 255.1 | ø245.7, 254.64 | Modeled shorter because of neglected gaps (perpendicular to primary radiation path). |

**Table 5-7 – Summary of Post-HAC Source Region Volumes**

| Region | Effective Source Volume [ml] | Percentage of 75 ml Source Volume |
|---|---|---|
| Annulus | 15.38 | 20.5% |
| Disk | 3.97 | 5.3% |
| Thimble | 1.56 | 2.1% |
| Ring | 0.553 | 0.7% |

**Table 5-8 – Post-HAC Reductions in Foam Thickness**

| Drop Orientation[1] | Shielding Model[2] | Structural Evaluation[3] |
|---|---|---|
| Top End Drop | 5.4 cm | 5.6 cm |
| Side Drop | 5.85 cm | 5.8 cm |
| Bottom End Drop | 5.4 cm | 4.5 cm |

Note:

1. The values presented for the top end, side and bottom end drops refer to the resulting reduction in thickness of the top, side and bottom foam regions, respectively. The reductions in foam region thickness listed above are the only significant difference between the NCT and HAC cask system shielding configurations.
2. These are the foam thickness reduction values assumed in the shielding analyses. The treatment of this foam crush by the shielding analyses is discussed in Section 5.3.1.2.
3. These are the foam thickness reductions calculated by the final structural evaluations presented in Section 2 of this SAR.

**Table 5-9 – Shielding Material Properties**

| Element | Water 1.00 g/cm$^3$ | Steel[1] 8.027 g/cm$^3$ | Depleted U[2] 18.0 g/cm$^3$ | Foam[3] 0.193 g/cm$^3$ | Air 0.0013 g/cm$^3$ |
|---|---|---|---|---|---|
| O | 11.20% | -- | -- | 21.82% | 23.45% |
| H | 88.80% | -- | -- | 6.36% | -- |
| Cr | -- | 19.00% | -- | -- | -- |
| Mn | -- | 2.00% | -- | -- | -- |
| Fe | -- | 69.75% | -- | -- | -- |
| Ni | -- | 9.25% | -- | -- | -- |
| U | -- | -- | 98.00% | -- | -- |
| Mo | -- | -- | 2.00% | -- | -- |
| C | -- | -- | -- | 63.64% | -- |
| N | -- | -- | -- | 7.27% | 76.55% |
| K | -- | -- | -- | 0.91% | -- |
| | 100.00% | 100.00% | 100.00% | 100.00% | 100.00% |

Notes:

1. This is the standard, nominal density for stainless steel.
2. This is the minimum density specified in the TYC01-1606 drawing.
3. This is a lower-bound value, based on the foam density range of 12.3- to 14.9 specified in Drawing TYC01-1608.

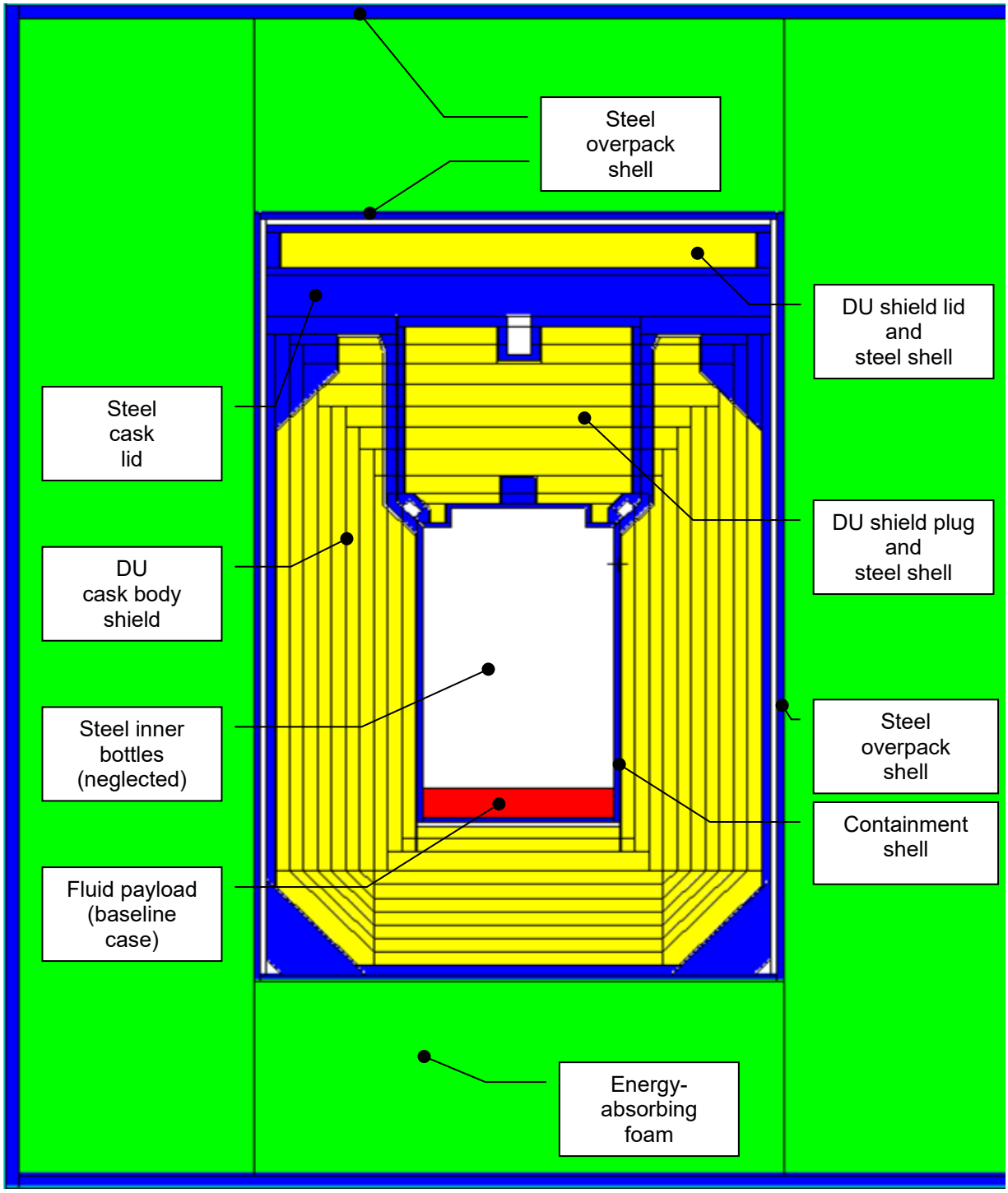


**Figure 5-2 – MIDUS Package Shielding Model Overview (NCT Baseline Case)**

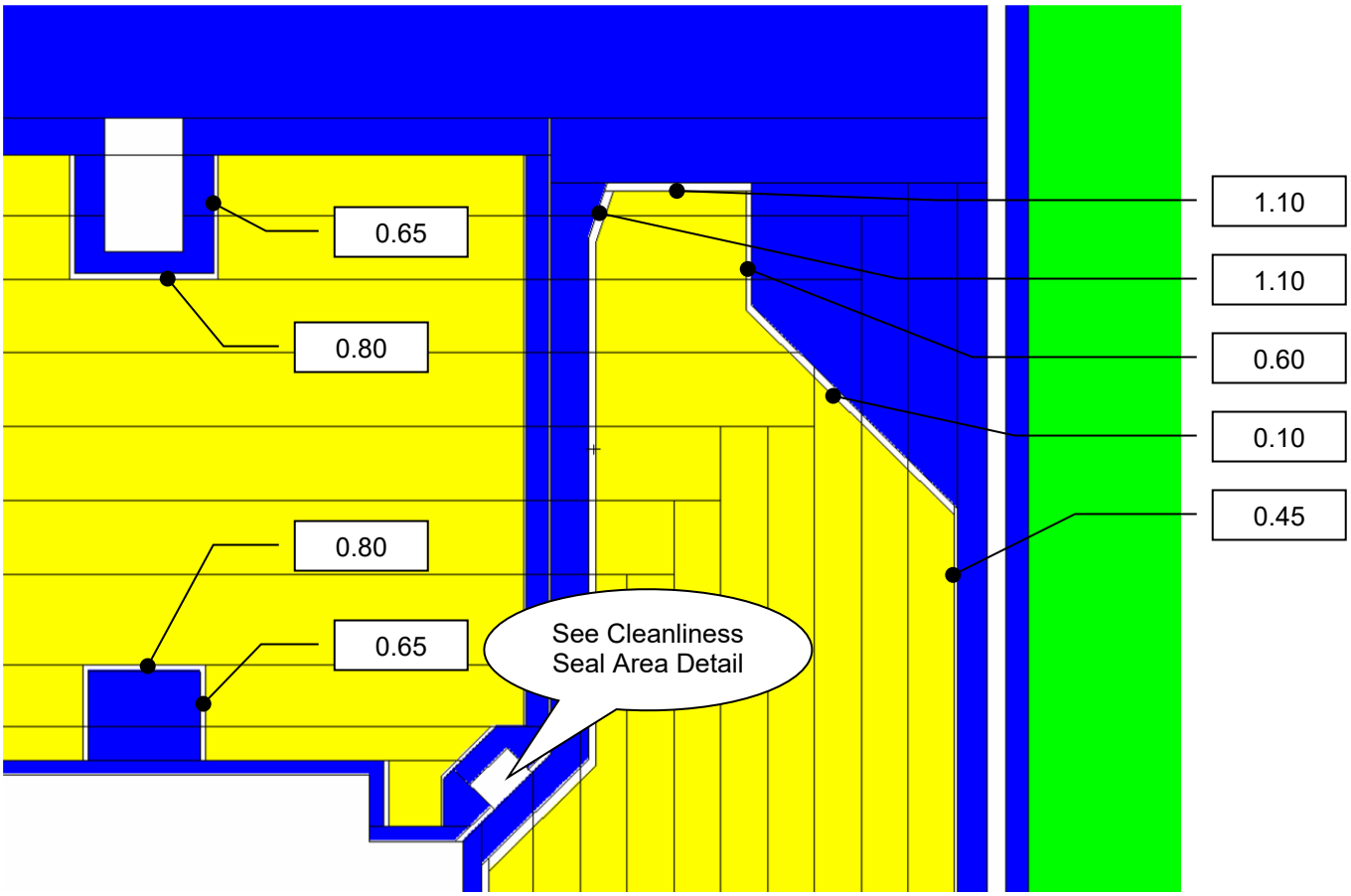


**Figure 5-3 – Cask Body Top End Gaps (mm)**
**All Models - NCT & HAC**

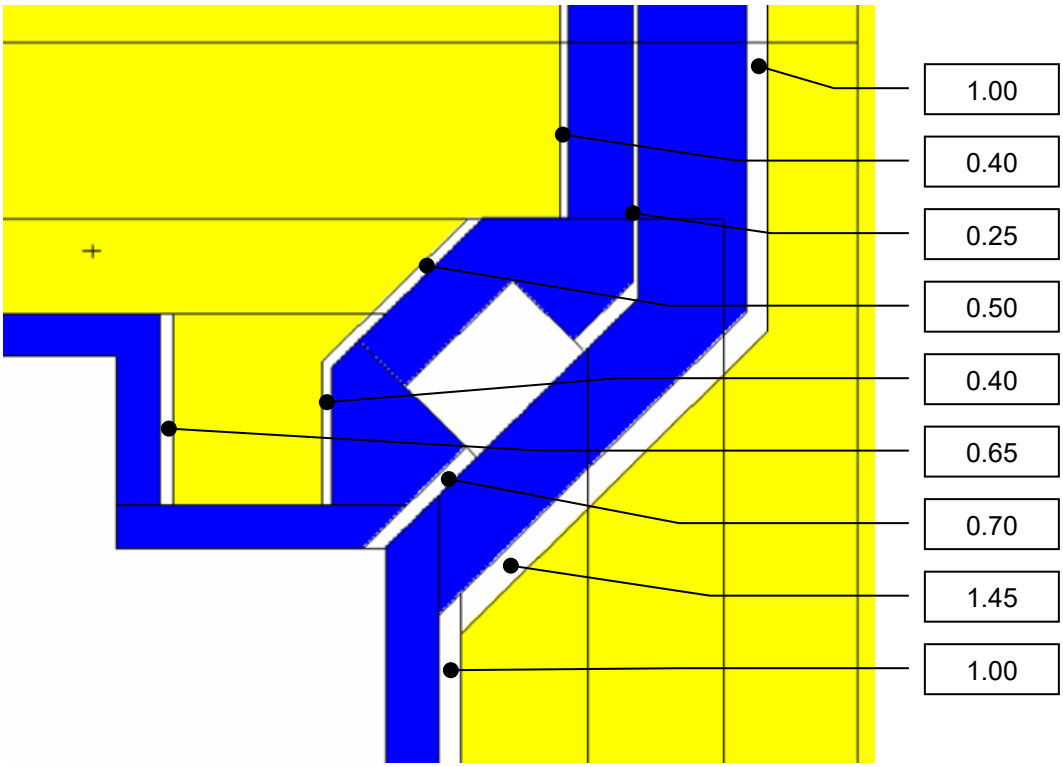


**Figure 5-4 – Cleanliness Seal Area Gaps (mm) - NCT & HAC**

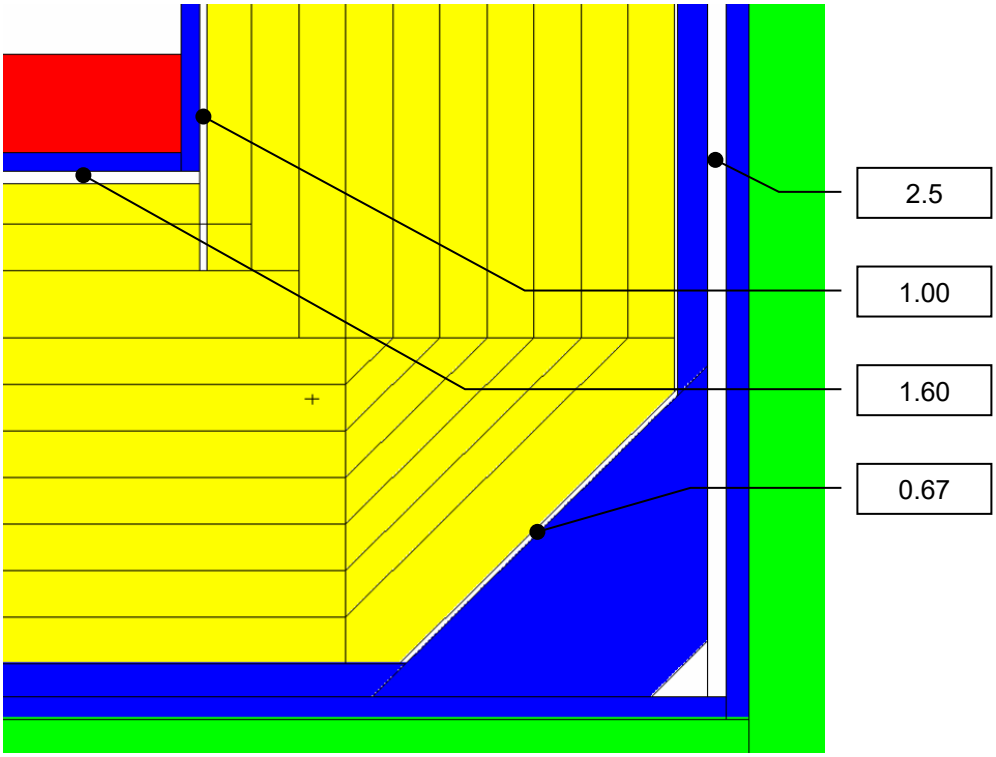


**Figure 5-5 – Cask Body Bottom End Gaps (mm)
NCT & HAC**

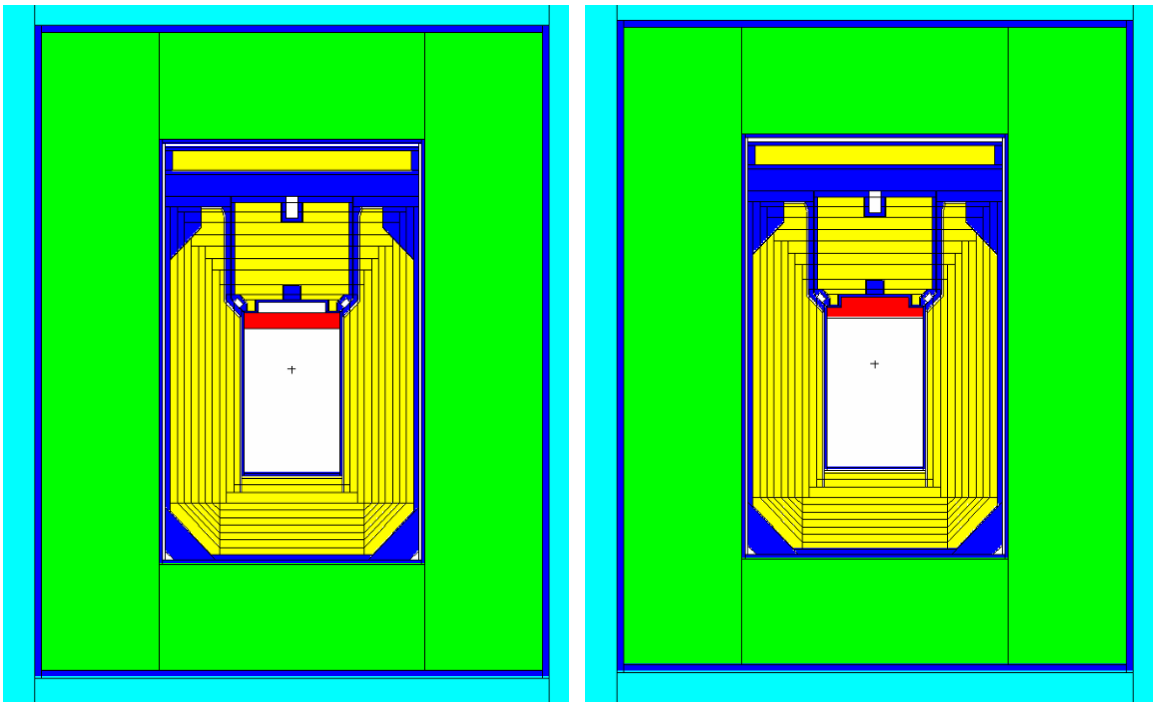

**Figure 5-6 – Inverted NCT Model Geometries (Different Snap Ring Assumptions)**

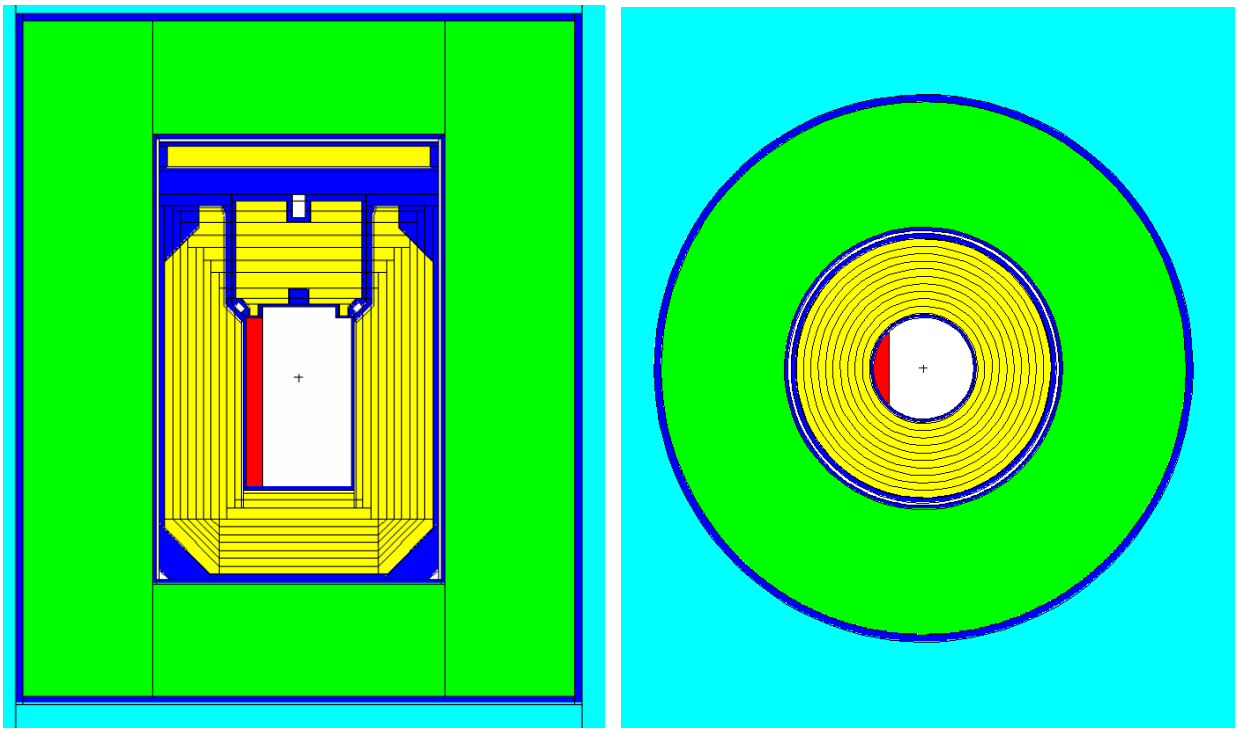

**Figure 5-7 – Horizontal NCT Model Geometry**

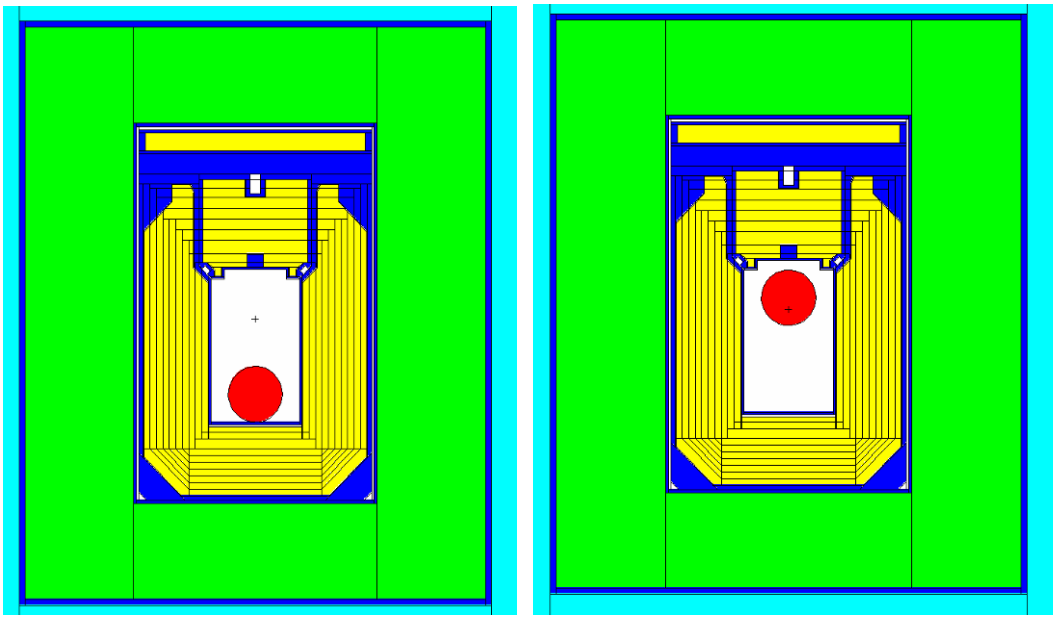

**Figure 5-8 – Spherical Source Cases NCT Model Geometry**

## 5.4 Shielding Evaluation

### 5.4.1 Methods

MCNP5 is a general-purpose Monte Carlo N-Particle code that can be used for neutron, photon, electron, or coupled neutron/photon/electron transport [5.4]. Specific areas of application include, but are not limited to, radiation protection and dosimetry, radiation shielding, radiography, medical physics, nuclear criticality safety, detector design and analysis, nuclear oil-well logging, accelerator target design, fission and fusion reactor design, decontamination, and decommissioning. The code treats an arbitrary three-dimensional configuration of materials in geometric cells bounded by first- and second-degree surfaces and fourth-degree elliptical tori.

Pointwise cross-section data are used, although group-wise data also are available. MCNP's neutron capabilities are not used for this application because the payload does not produce neutrons. For photons, the code accounts for incoherent and coherent scattering, the possibility of fluorescent emission after photoelectric absorption, absorption in pair production with local emission of annihilation radiation, and bremsstrahlung. A continuous-slowing-down model is used for electron transport that includes positrons, k x-rays, and bremsstrahlung, but does not include external or self-induced fields.

Calculations are performed using the MCPLIB04 cross-section data library for photon transport. This library is derived from the ENDF/B-VI.8 data. Cross-section data are given for incident photon energies from 1 keV to 100 GeV. Since the payload does not produce neutrons, a coupled cross-section library is not needed.

MCNP5 includes a powerful general source, criticality source, and surface source; both geometry and output tally plotters; a rich collection of variance reduction techniques; a flexible tally structure; and an extensive collection of cross-section data. Distributed volumetric sources are used for the MIDUS package models.

MCNP5 contains numerous flexible tallies: surface current & flux, volume flux (track length), point or ring detectors, particle heating, fission heating, pulse height tally for energy or charge deposition, mesh tallies, and radiography tallies. Surface crossing tallies and point detectors are used in the package models.

### 5.4.2 Input and Output Data

The shielding models are constructed in R-Z symmetric geometry. The photon sources are modeled as volumetric homogeneous regions with source particles started uniformly throughout. Source biasing and geometry splitting are used to improve the convergence rate of the problem. The number of histories executed in a typical run is on the order of 70 million. The variance reduction techniques applied in the models are conservative and the computer runs are well-converged, as shown by the MCNP figure of merit stability. Tally relative errors are generally less than 1%. Due to the size of the MCNP input and output files, they have not been reproduced in this report.

### 5.4.3 Flux-to-Dose-Rate Conversion

MCNP results are converted from particles/cm$^2$-sec to dose rate units using the ANSI/ANS 6.1.1-1977 flux-to-dose conversion factors shown in Table 5-10 [5.5].

### 5.4.4 External Radiation Levels

#### 5.4.4.1 NCT Radiation Levels

Figure 5-9 summarizes the NCT radiation levels 1 meter from the package surface. The maximum dose rate is 2.3 mrem/hr, occurring at the package side. For clarity, the top, side, and bottom results are combined into a single plot. The effectiveness of the top end DU shield lid can be seen in the asymmetry of the plot. The left hand side of the "W" shape is suppressed due to the extra shielding provided by the shield lid. The middle and right portions of the "W" correspond to the expected peak at the package midplane and bottom centerline. Since these data are for the 1-meter package surface, the effect is less pronounced than the surface results. Sections 5.4.4.1.1 through 5.4.4.1.3 discuss the calculated profiles 1 meter from the individual sides of the package in more detail.

Figure 5-13 summarizes the NCT radiation levels along the package surface. The maximum dose rate is 80.6 mrem/hr, occurring at the package side. Again, the top, side, and bottom results are combined into a single plot. Because the bottom and radial shields are similar, the contact dose rate is almost the same at the package bottom on centerline. The effectiveness of the top end DU shield lid can again be seen in the asymmetry of the plot. The modest streaming through the shield plug steel area is also apparent in Figure 5-13, where the middle peak is skewed upwards on it's left side. Sections 5.4.4.1.4 through 5.4.4.1.6 discuss the calculated profiles along the individual sides of the package in more detail.

##### 5.4.4.1.1 Package Top 1-Meter NCT Profile

Figure 5-10 shows the worst-case MCNP results for the 1-meter surface above the top end of the package. Due to the top DU shield lid, all dose rates at the top end of the package are very low, on the order of a factor of 28 below the regulatory limit of 10 mrem/hr. The results show that the highest dose rates at the top end occur when the package is in the inverted position. This places the product closest to the top end, and most directly challenges the streaming paths around the cask shield plug. The highest peak dose rates were produced by the top spherical source case shown on the right in Figure 5-8, which is the source of the dose rate profile shown in Figure 5-10. The peak dose rates are relatively flat out to the package radius, then rise monotonically out to the 1-meter distance in the radial direction, indicating that the shield plug has a "shadowing" effect and that the streaming paths around the shield plug are not the dominating factor.

The dose rate plot in Figure 5-10 shows a rise with increasing radial distance from the package. Since the DU shield lid suppresses the top-end photon flux in the upward direction, the dose rates above the package are suppressed, resulting in the shape of Figure 5-10. Due to spatial attenuation, the dose rates eventually drop off in the radial direction. Since the dose rates along

the side at 1 meter plane are all within the allowable limits as shown in Figure 5-11, it can be concluded that the dose rates along the top 1-meter plane are also below the limits. Note that the dose rates at the rightmost point in Figure 5-10 match the corresponding rightmost point in Figure 5-11.

The maximum dose rate on the package top 1-meter surface is 0.347 mrem/hr (T.I. = 0.35).

#### 5.4.4.1.2 Package Side 1-Meter NCT Profile

Figure 5-11 shows the worst-case MCNP results for the 1-meter surface on the side of the package. All dose rates are low, on the order of a factor of 4 below the regulatory limit of 10 mrem/hr. The highest peak dose rate on the side occurs when the package is in the inverted position (specifically, for the top spherical source model illustrated on the right in Figure 5-8). The top spherical source configuration is the basis for the axial dose rate profile shown in Figure 5-11. The dose rate profile is slightly peaked toward the top of the package due to the contribution from the top-end streaming.

The maximum dose rate on the package side 1-meter surface is 2.30 mrem/hr (T.I. = 2.3).

#### 5.4.4.1.3 Package Bottom 1-Meter NCT Profile

Figure 5-12 shows the worst-case MCNP results for the 1-meter surface below the bottom end of the package. All dose rates are low, on the order of a factor of 5 below the regulatory limit of 10 mrem/hr. The results show that the highest dose rates at the bottom end occur when the package is in the upright, vertical position. Specifically, the peak dose rates occur for the “lower sphere” source distribution shown on the left in Figure 5-8.

The maximum dose rate on the package bottom 1-meter surface is 1.73 mrem/hr (T.I. = 1.7).

#### 5.4.4.1.4 Package Top Surface NCT Profile

Figure 5-14 shows the worst-case MCNP results for the package top surface. Due to the top DU shield lid, all dose rates at the top end of the package are very low, on the order of a factor of 37 below the regulatory limit of 200 mrem/hr. The very large margin is due to the presence of the shield lid, which is designed to mitigate the higher top-end dose rates in the post-HAC condition.

The results show that several competing effects occur depending on the assumed source configuration. The highest peak dose rate at the top end occurs when the package is in the inverted position (specifically, for the top sphere source case illustrated on the right in Figure 5-8, which is the basis for the entire inverted-case dose rate profile shown in Figure 5-14). This places the product closest to the top end, and most directly challenges the streaming paths around the cask shield plug. The highest dose was noted for the inverted package, i.e., the top sphere source case, in which the peak dose rate occurs out at the radial edge of the package top surface. The peak occurs near the edge because the DU in the shield plug shadows much of the cask top surface. The most significant streaming for this case is through the chamfer in the radial DU shield and the streaming gaps near the shield plug chamfer.

A slightly smaller peak occurs at about a 6 cm radius when the cask is in the upright orientation (for the bottom sphere source case illustrated on the left in Figure 5-8, which is the basis for the entire upright-case dose rate profile shown in Figure 5-14). This peak is lower by a factor of 1.3 than the inverted case. It occurs because of streaming through the shield plug steel when the source is more collimated due to its location in the bottom of the cavity in the upright orientation.

The maximum dose rate on the package top surface is 5.33 mrem/hr.

#### 5.4.4.1.5 Package Side Surface NCT Profile

Figure 5-15 shows the worst-case MCNP results for the package side surface. The peak dose rate at the package side surface is low, on the order of a factor of 40% of the regulatory limit of 200 mrem/hr. The highest peak dose rate on the side surface occurs when the package is in the inverted position (specifically, for the top sphere source case illustrated on the right in Figure 5-8, which is the basis for the entire axial dose rate profile shown in Figure 5-15). This places the product at the top of the cavity where the streaming paths around the shield plug are challenged most significantly.

The maximum dose rate on the package side surface is 80.6 mrem/hr.

#### 5.4.4.1.6 Package Bottom Surface NCT Profile

Figure 5-16 shows the worst-case MCNP results for the package bottom surface. The peak dose rate at the bottom end of the package is low, on the order of 40% of the regulatory limit of 200 mrem/hr. The dose rates fall off monotonically with increasing radius. The highest peak dose rate was produced by the baseline upright cask orientation case illustrated in Figure 5-2. The peak dose rates occur at the centerline of the package. The nominal source geometry in Figure 5-2 showed a slightly higher dose rate than the upright spherical case shown in the left in Figure 5-8, because the disk-shaped source challenged the DU gap to a greater extent than the smaller radius of the spherical source.

The maximum dose rate on the package bottom surface is 80.1 mrem/hr.

#### 5.4.4.1.7 NCT Conclusions

The package dose rate margins range from a factor of 2.5 to 37 on the surface. At 1 meter, the margins range from factors of 4 to 28.

The package orientation affects the package dose rates. Different orientations produce maximum dose rates on the different respective package locations (top, side, and bottom). No credit is taken for attenuation in the materials of construction of the payload internals, but the studies show that the geometrical restriction of the internals increases the dose rates slightly over the baseline models for most locations of interest.

### 5.4.4.2 Post-HAC Radiation Levels

The results from each of the four post-HAC case runs are shown in Figure 5-17 for the 1-meter side, 1-meter top, and 1-meter bottom surfaces, respectively. The results are superimposed graphically to obtain a better understanding of the relative contributions from each of the HAC source regions.

#### 5.4.4.2.1 1-Meter Side HAC Profile

The results show a peak side dose of 841 mrem/hr. The annulus source is the largest contributor, accounting for over one-half of the peak. The annulus source's spatial distribution favors the upper end of the package (to the right in the plot) due to the orientation of the DU in relation to the annulus. The next largest source contribution comes from the disk source, at about one-third of the total. The O-ring, thimble, and payload cavity sources are minimal contributors at the package side.

The dose rate contribution from the shield plug annulus model was conservatively doubled for the side results to account for any potential eccentric positioning of the shield plug. This assumes the shield plug could be displaced such that it was in contact with the containment cavity wall, increasing the thickness of the fluid layer to as much as double the nominal value. The cleanliness O-ring should keep the plug centered; therefore this approach introduces a considerable conservatism. If the shield plug is in its nominal position following the HAC, the peak side dose rate would be about 268 mrem/hr lower than reported.

The contribution from the product remaining in the cask cavity (approximately 2/3) was conservatively accounted for by taking 100% of the contribution from a spherical source of 75 ml centered in the payload cavity.

#### 5.4.4.2.2 1-Meter Top HAC Profile

The results show a peak top dose of 626 mrem/hr. The annulus and disk sources are the largest contributors, each accounting for about 40% of the peak. The thimble source is a more significant contributor at the top, providing in most of the remaining peak dose.

The contribution from the shield plug annulus was taken at 100% of the MCNP output values since eccentric positioning of the plug would not appreciably affect top-end dose rates.

The contribution from the product remaining in the cask cavity (approximately 2/3) was conservatively accounted for by taking 100% of the contribution from a spherical source of 75 ml centered in the payload cavity.

#### 5.4.4.2.3 1-Meter Bottom HAC Results

The results show a peak bottom dose of only 33.9 mrem/hr. The annulus and disk sources source are the largest contributors, together accounting for about 97% of the peak.

The contribution from the shield plug annulus was taken at 100% of the MCNP output values since eccentric positioning of the plug would not appreciably affect bottom-end dose rates.

The contribution from the product remaining in the cask cavity (approximately 2/3) was conservatively accounted for by taking 100% of the contribution from a spherical source of 75 ml centered in the payload cavity.

#### 5.4.4.2.4 HAC Conclusions

The package margins range from 16% under the regulatory allowable to a factor of 29.

The annulus and disk contributions dominate the top and bottom cases. Due to the offset assumption, the annulus source dominates the side dose.

**Table 5-10 – Photon Dose Rate Response Functions**

| E, MeV | Factor (mrem/hr) / γ/cm$^2$-sec |
|---|---|
| 0.015 | 1.95E-03 |
| 0.025 | 8.01E-04 |
| 0.045 | 3.17E-04 |
| 0.08 | 2.61E-04 |
| 0.15 | 3.79E-04 |
| 0.3 | 7.59E-04 |
| 0.5 | 1.15E-03 |
| 0.65 | 1.44E-03 |
| 0.75 | 1.60E-03 |
| 0.9 | 1.83E-03 |
| 1.25 | 2.32E-03 |
| 1.75 | 2.93E-03 |
| 2.5 | 3.72E-03 |
| 3.5 | 4.63E-03 |
| 4.5 | 5.42E-03 |
| 5.5 | 6.19E-03 |
| 6.5 | 6.93E-03 |
| 7.5 | 7.66E-03 |
| 9 | 8.77E-03 |
| 12 | 1.10E-02 |

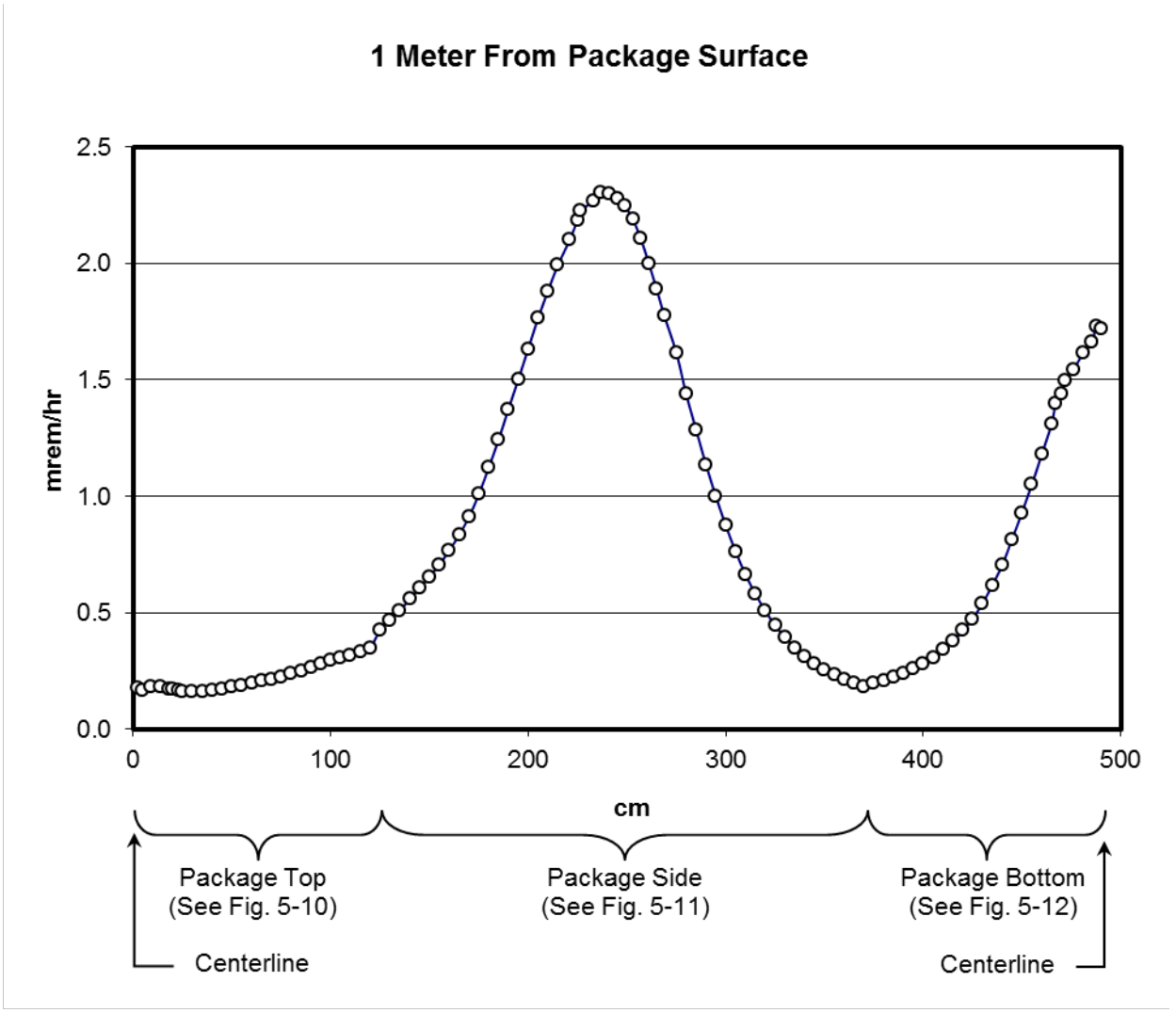


**Figure 5-9 – Summary Profile for 1-Meter NCT Dose Rates**

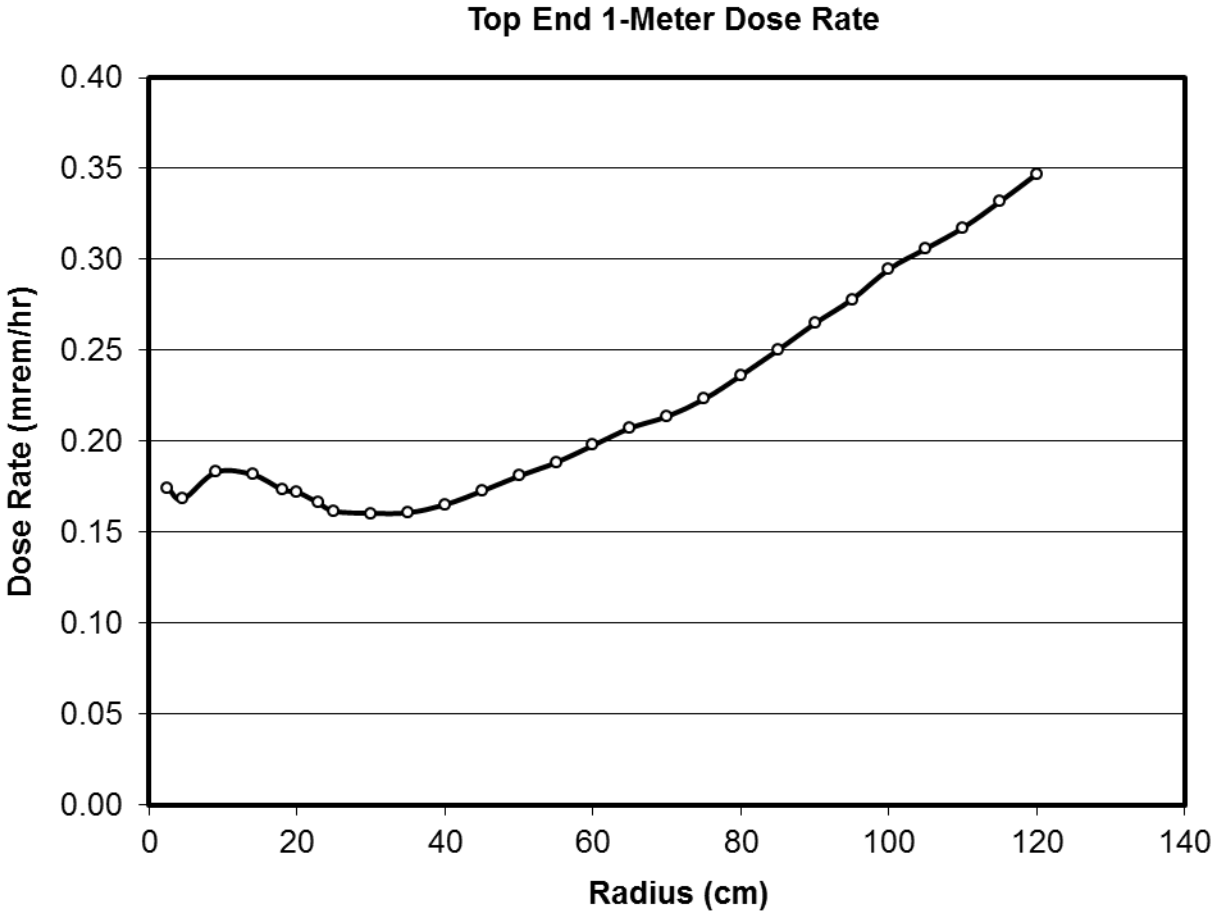


**Figure 5-10 – Top-End 1-Meter Dose Rate Profile**

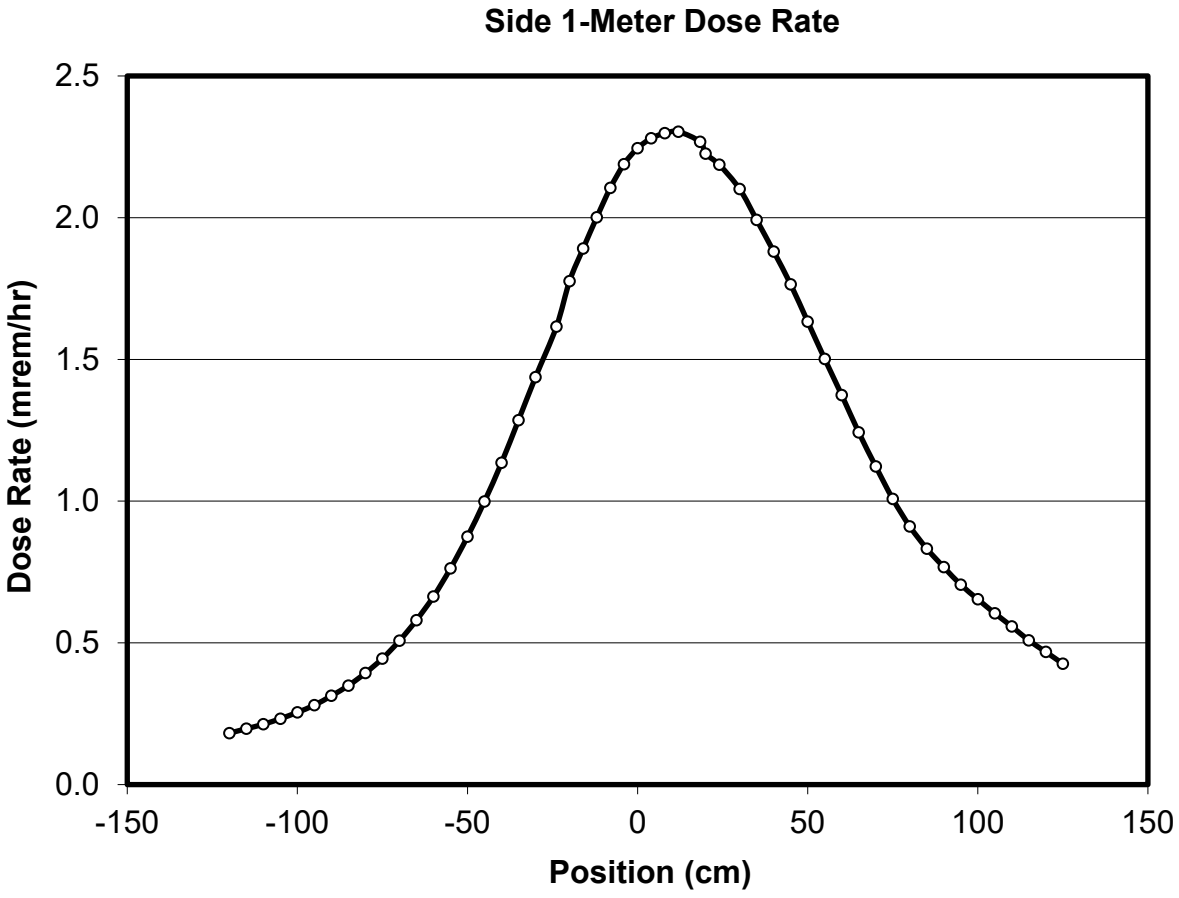


**Figure 5-11 – Side 1-Meter Dose Rate Profile**

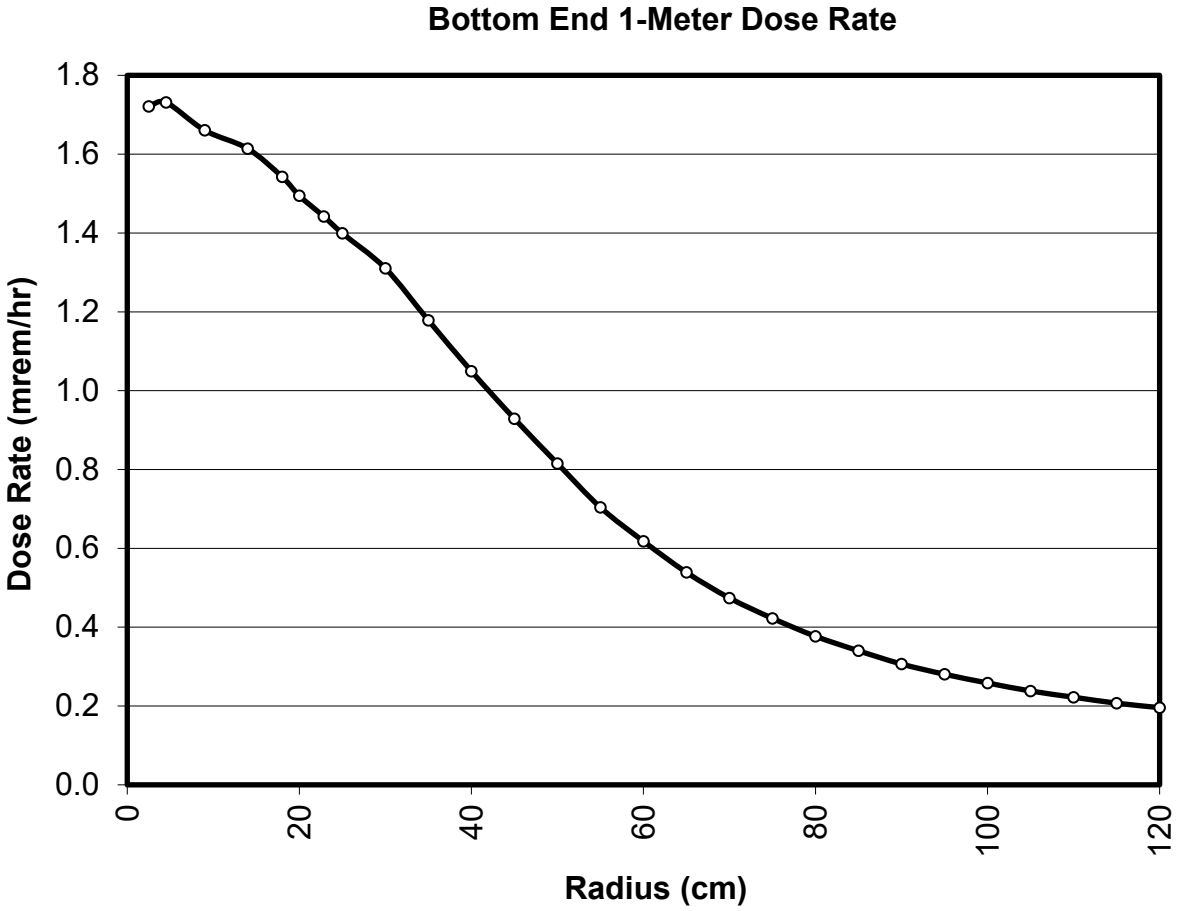


**Figure 5-12 – Bottom-End 1-Meter Dose Rate Profile**

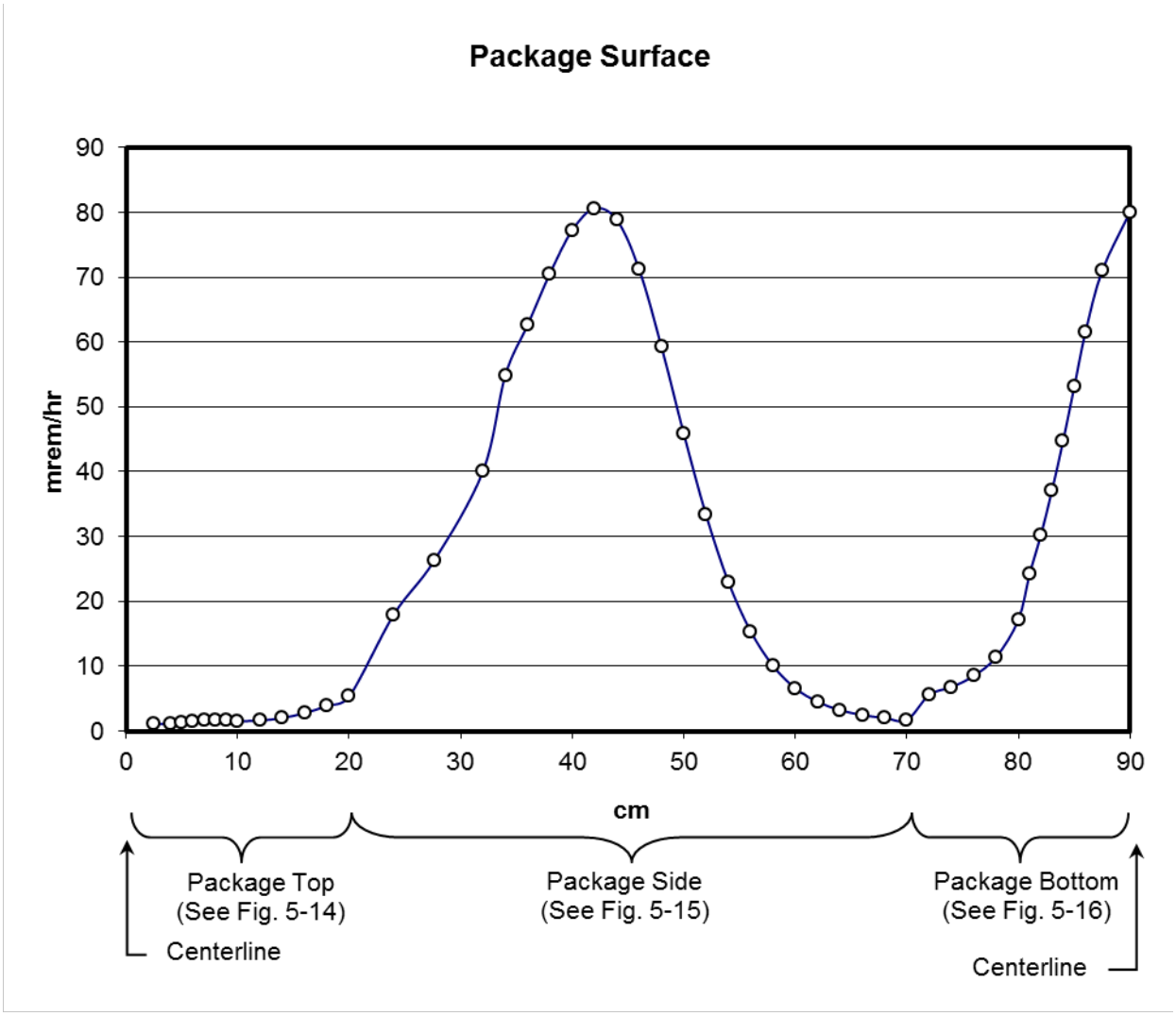


**Figure 5-13 – Summary Profile for Package Surface NCT Dose Rates**

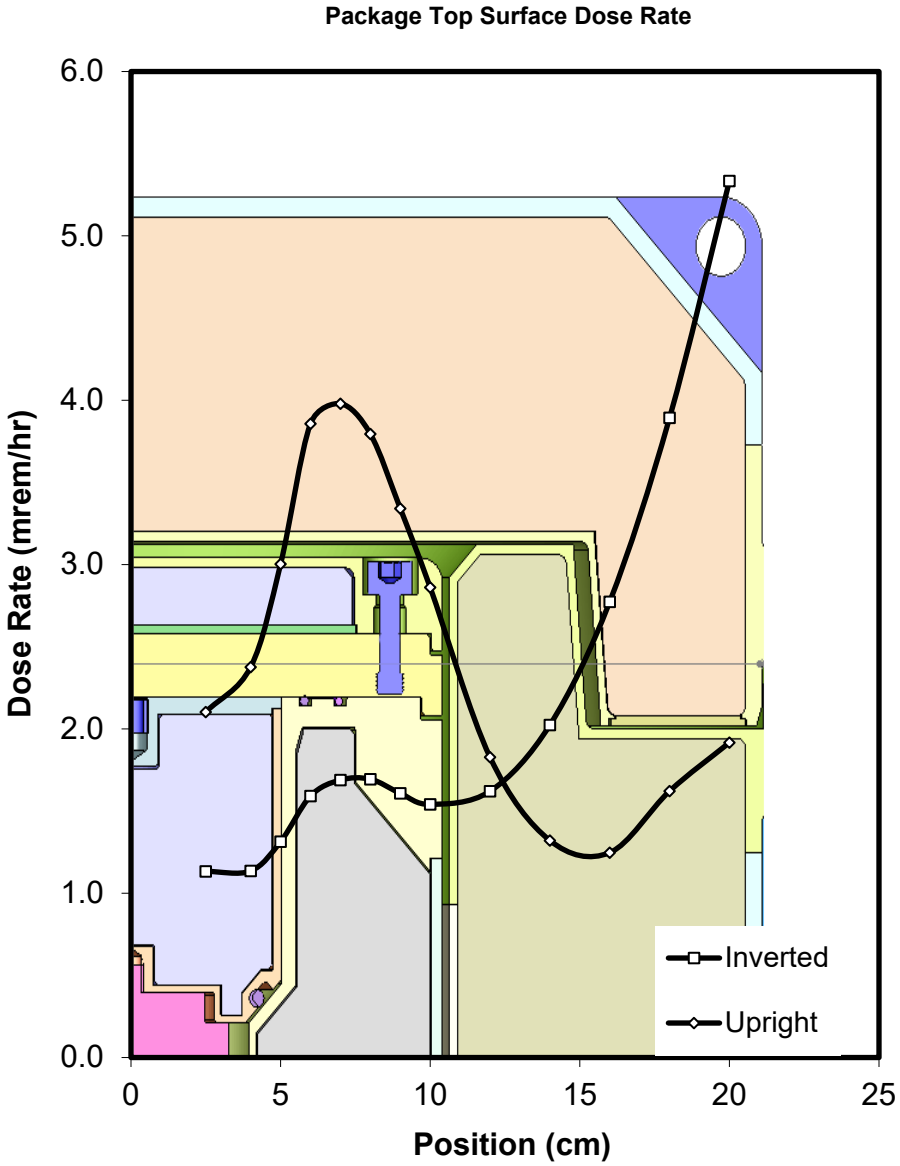


**Figure 5-14 – Top-End-Surface Dose Rate Profile**

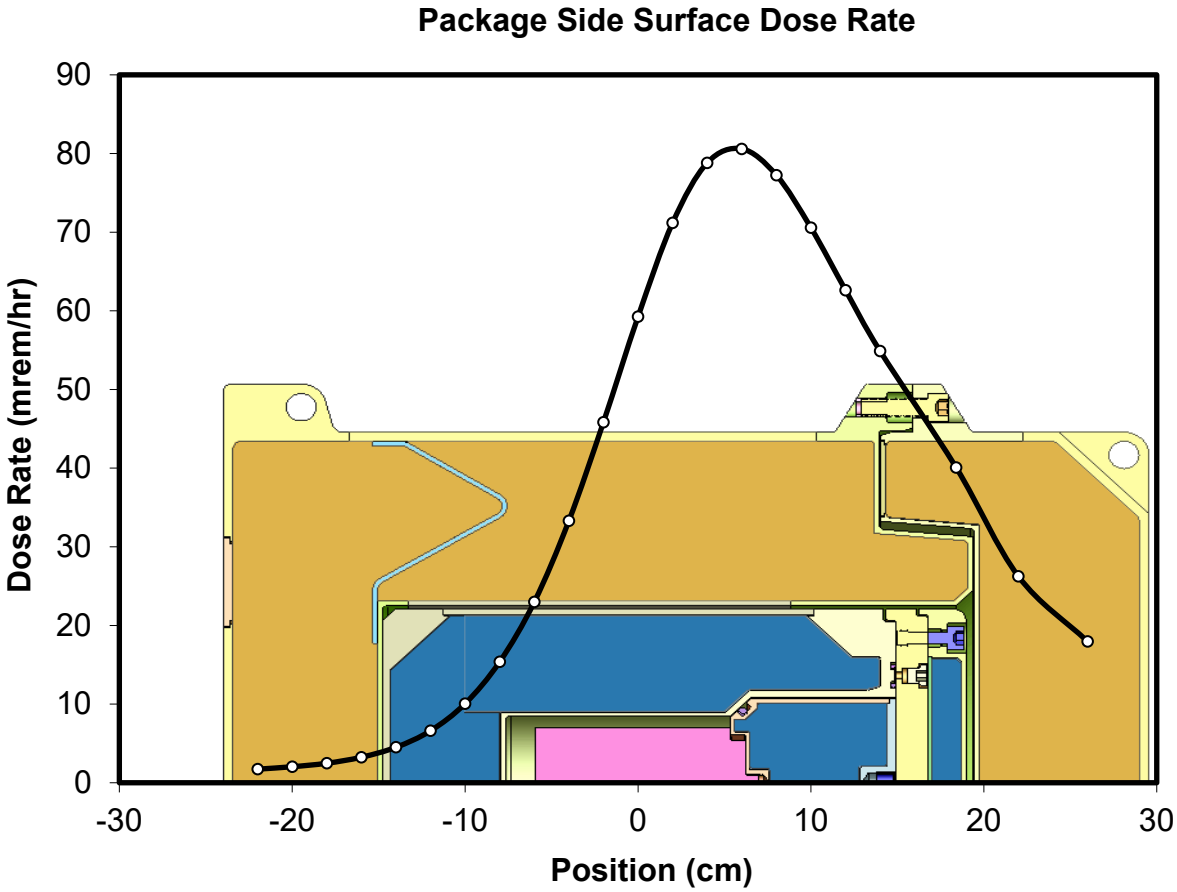


**Figure 5-15 – Side-Surface Dose Rate Profile**

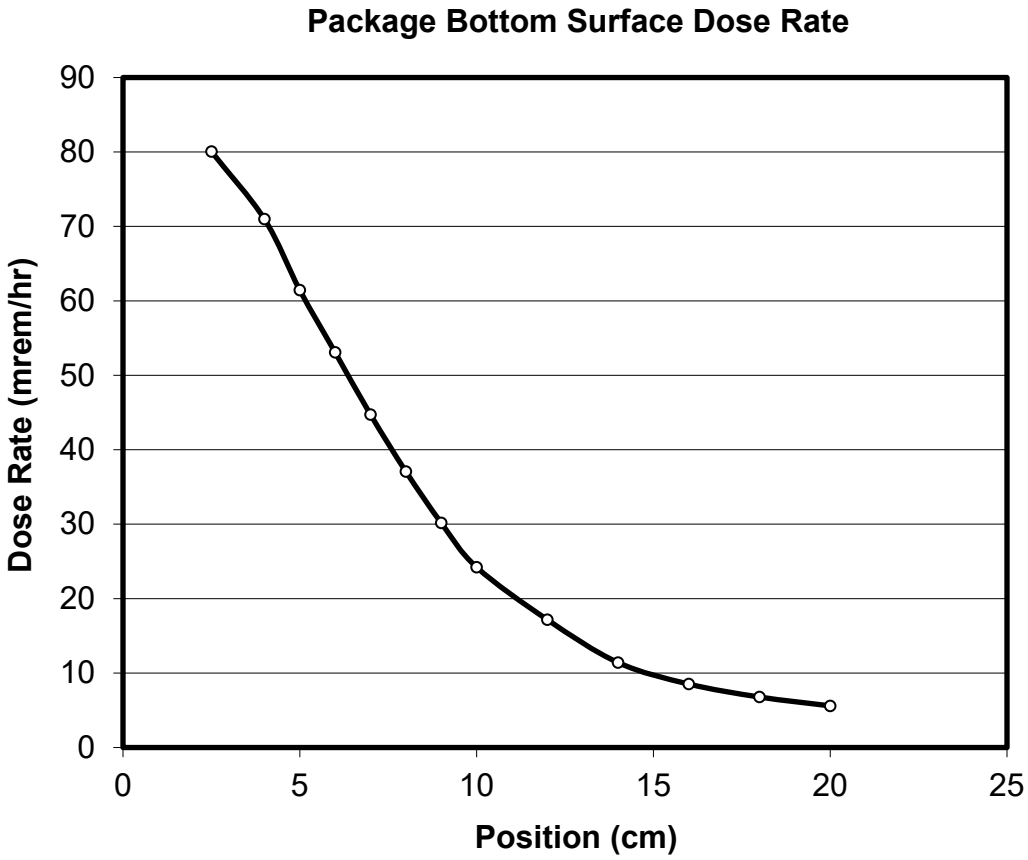


**Figure 5-16 – Bottom-Surface Dose Rate Profile**

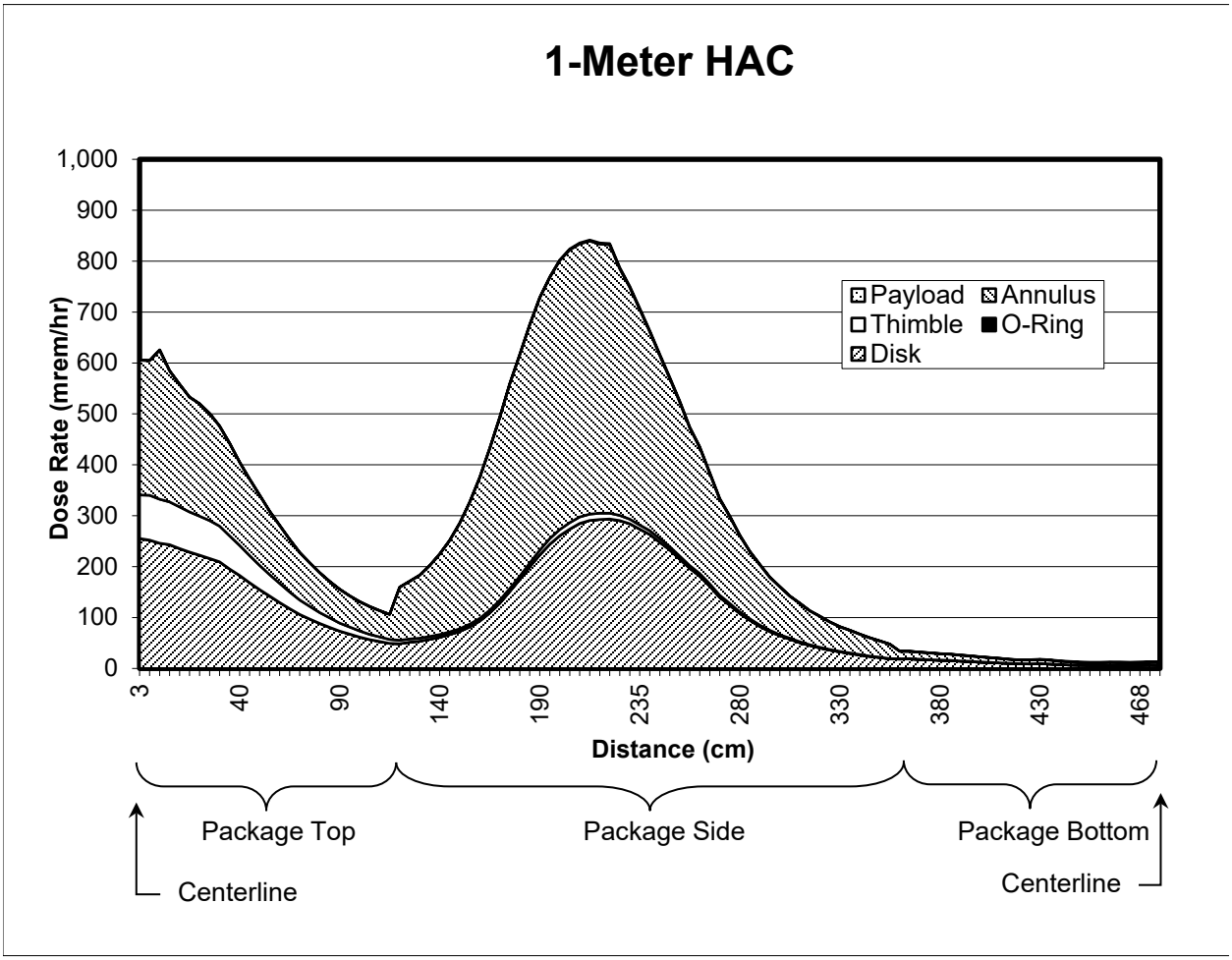


**Figure 5-17 – 1-Meter HAC Results**

## 5.5 Appendix

### 5.5.1 References

[5.1] *Federal Register*/Vol. 68, No. 75/Friday, April 18, 2003/Notices.

[5.2] Lederer, C., Shirley, V. Ed., *Table of Isotopes*, 7th Edition, John Wiley & Sons, New York, 1978.

[5.3] Ernest O. Lawrence Berkeley National Laboratory, *WWW Table of Radioactive Isotopes*, The Berkeley Laboratory Isotopes Project, http://ie.lbl.gov/education/isotopes.htm (accessed January 18, 2006).

[5.4] *MCNP — A General Monte Carlo N-Particle Transport Code, Version 5*, LA-UR-03-1987, Los Alamos National Laboratory, Los Alamos, New Mexico, April 2003.

[5.5] American National Standard ANSI/ANS-6.1.1-1977, *Neutron and Gamma-Ray Flux-to-Dose-Rate Factors*.

# 6 CRITICALITY EVALUATION

Not applicable.

This page intentionally blank.

# 7 PACKAGE OPERATIONS

This chapter describes the operations used to load the MIDUS package and prepare it for transport (Section 7.1), unload the package (Section 7.2), and prepare the empty package for transport (Section 7.3). It presents the fundamental operating steps in the order in which they are performed. The operating steps are intended to ensure that the package is properly prepared for transport, consistent with the package evaluation in Chapters 2 through 6, and to ensure that occupational exposure rates are as low as reasonably achievable (ALARA).

The package shall be operated in accordance with detailed written procedures that are based on, and consistent with, the operations described in this section. To provide a comprehensive description of the package operations, this chapter describes a particular sequence for steps and makes reference to specific facility areas. The specific sequence and locations in the detailed written operating procedures may be tailored to meet facility requirements.

## 7.1 Package Loading

This section describes loading-related preparations, tests, and inspections for the package. These include the inspections made before loading the package to determine that it is not damaged and that radiation and surface contamination levels are within the regulatory limits.

### 7.1.1 Preparation for Loading

*Special Equipment Required:* *Radioactive contamination detector, radiation survey meter*

*Special Controls or Precautions:* *The contents are highly radioactive. To avoid injury in the unlikely event that a loaded cask is received for preparation, DO NOT REMOVE THE SHIELD PLUG UNTIL A RADIATION SURVEY IS PERFORMED.*

1. Visually inspect the package for cleanliness and swipe for radioactive contamination in accordance with facility procedures. Clean or decontaminate the package as necessary. If decontamination is necessary, determine the cause and take precautionary measures before opening the package for preparation.

2. Remove any tie-downs and transfer the package to the assembly area.

3. Remove the overpack closure bolts and lift the overpack lid.

4. Perform a radiation survey to confirm that the package is empty. If radiation levels indicate that the package may have an active payload, discontinue operations, determine the cause, and take corrective actions.

5. Visually inspect the accessible interior surfaces of the package to assure cleanliness. Swipe the accessible interior surfaces of the package for surface contamination in accordance with

facility procedures. Clean or decontaminate the interior surfaces if necessary. If decontamination is necessary, determine the cause and take precautionary measures before proceeding further.

6. Remove the shield lid.

7. Using the two closure lid lifting points, remove the cask from the overpack.

8. Remove the cask closure bolts and the closure lid.

9. Remove the test port from the closure lid.

10. Using the shield plug lifting point, remove the shield plug and any other items from the payload cavity.

11. Visually inspect the cavity and shield plug for cleanliness and damage. If necessary, clean with a soft, clean cloth and demineralized water. Repair damaged items per Section 8.2.3.

12. Visually inspect the following for damage that may have occurred during shipping and handling:

    - Overpack lid and base
    - Closure lid and cask body
    - Overpack and cask closure bolts
    - Closure lid test port plug
    - Overpack base, cask body, and closure lid threaded inserts
    - Closure lid test port plug drilled and tapped holes

    Repair or replace damaged items per Section 8.2.3.

13. Remove the leak test, containment, and cleanliness seals.

14. Gently wipe away any debris from the O-ring grooves and sealing surfaces with a soft, clean cloth and demineralized water. Visually inspect the following surfaces for scratches, blemishes, adhered particles, debris, etc.:

    - The sealing surfaces on the bottom of the closure lid
    - The O-ring grooves on the cask flange
    - The O-ring groove on the shield plug
    - The cleanliness O-ring sealing surface on the beveled surface of the containment shell
    - The closure lid test port plug seal surface

    Repair any damage to the sealing surfaces per Section 8.2.3.

15. Discard the cleanliness seal and obtain a new one.

16. Gently wipe away the lubricant and any debris from the O-rings with a soft, clean cloth and demineralized water. Visually inspect the O-rings for pliability, nicks, scratches, cuts, and debris. Replace any damaged O-rings as necessary. Apply a thin film of approved lubricant and install all three of the O-rings. Assure that the following conditions are met:

    - If the containment O-ring has not been replaced and/or helium leak tested within 12 months prior to the shipment, then replace containment O-ring and perform a helium leak test as described in Section 8.2.2, and return to this step. Performance of the helium leak test does not relieve the need to perform the pre-shipment leak rate test in Section 7.1.3, step 1.

### 7.1.2 Loading of Contents

*Special Equipment Required:* *Calibrated torque wrench*

*Special Controls or Precautions:* *Because the contents are highly radioactive, some loading operations are performed in a hot cell in accordance with facility procedures. DO NOT REMOVE THE SHIELD PLUG OUTSIDE THE HOT CELL AFTER THE CASK IS LOADED.*

1. Confirm that the intended payload, including the product, product container(s), and optional dunnage, meets the contents specification in the Certificate of Compliance.

2. Optional step: Before performing step 6, place any optional dunnage into the cask cavity, as required by facility procedures.

3. Move the cask to the hot cell.

4. Put the product into the product container(s).

5. Place the product container(s) and any other associated payload internals into the cask, or attach them to the shield plug, in accordance with facility procedures.

6. Carefully lower the shield plug (and payload, if applicable) into the cask body.

7. Remove the cask from the hot cell.

8. Visually or mechanically inspect the top of the shield plug to confirm that it is slightly higher than the cask flange, Figure 7-1. If the top of the shield plug is lower than the cask flange, return the cask to the hot cell, remove the shield plug, assure that the new cleanliness O-ring has been installed, and re-perform this step.

9. Place the closure lid onto the cask body with alignment marks aligned.

10. Visually inspect the leak test port to assure that it is not blocked by an O-ring. If any O-ring material is visible, remove the cask lid, inspect the O-ring(s) for damage, reinstall the O-ring(s) and cask lid, and re-perform this step.

**Figure 7-1 - Shield Plug Fit-Up**

- If the containment O-ring must be replaced, then perform a helium leak test using the package and replacement O-ring as described in Section 8.2.2, and return to this step. Performance of the helium leak test does not relieve the need to perform the pre-shipment leak rate test in Section 7.1.3, step 1.

11. Coat the cask closure bolts with anti-seize coating as needed and reinstall to a torque of 10 ± 0.5 N-m.

12. Transfer the cask to the leak test area.

### 7.1.3 Preparation for Transport

*Special Equipment Required:* *Pre-Shipment leak test equipment, radioactive contamination detector, radiation survey meter, thermometer or other temperature measurement device*

*Special Controls or Precautions:* *In Step 2 below, if the contents must be removed for any purpose, DO NOT REMOVE THE SHIELD PLUG OUTSIDE THE HOT CELL.*

1. Perform a pre-shipment leak rate test per Section 7.4.1.
2. If the leak rate is unacceptable:
   - Recheck all the connections and seals of the test equipment.
   - If the test equipment is functioning properly, disconnect it from the cask.
   - Remove the cask closure bolts and remove the closure lid.

- Inspect, clean, and replace the containment or test O-ring(s) as necessary using the appropriate steps from Section 7.1.1 and 7.1.2, or return the cask to the hot cell and transfer the payload to another cask unit.
- Repeat Step 1 of this section.

3. Disconnect the leak test equipment and reinstall the test port.
4. Transfer the cask to the assembly area and lower it into the overpack base.
5. Place the shield lid on top of the closure lid and tighten the shield lid attachment bolts.
6. Place the overpack lid onto the base, assuring that the alignment marks are aligned.
7. Apply anti-seize coating as needed to the overpack closure bolts and install the bolts.
8. Perform a contamination survey of the external surfaces of the package to determine if the contamination levels are as low as reasonably achievable. If the non-fixed surface contamination exceeds local requirements, then decontaminate the external surfaces using distilled water or a mild decontamination agent.[2]
9. Perform a radiation survey of the package. If the external radiation levels exceed 200 mrem/h, return the cask to the hot cell, investigate the cause of the high radiation levels, and begin again at Section 7.1.3, Step 1 or earlier. Because of the radiolytic gas generation, it is not acceptable to allow the payload to decay until the external radiation reaches acceptable levels.
10. Check the temperature on the outside surface of the package. If the temperature exceeds 50°C, investigate the cause of the high temperature, and take corrective action. If necessary, return the cask to the hot cell and begin again at Section 7.1.2.
11. Install the tamper-indicating seal.
12. Optional step: Attach the package to the shipping pallet using the package's lower lugs.

    *Note: The lower lugs may be used for attachment to a shipping pallet, or they may be used directly for securing the package in combination with the four upper lugs. It is not necessary to render the lower lugs inoperable for use as lifting or tie-down devices.*
13. Transfer the package and its shipping pallet, to the transport conveyance and connect the tie-downs in accordance with the specifications in Section 1.3.2, Drawing No. TYC01-1609.
14. Review the package loading/closure documentation for completeness.
15. Visually inspect the package nameplate to assure that it is not obstructed from view or degraded and that the information is clear and legible. If it is not, clear the obstruction as necessary to make the information legible.
16. Before releasing the package for shipment, assure that the procedures for opening and unloading the package (per Section 7.2) have been forwarded to the Consignee receiving the package. If they have not, then forward them before releasing the package for shipment.

[2] Requirements for swiping and acceptance criteria are based on 49 CFR 173.443, or other applicable regulation.

17. Release the package to the Carrier for shipment to the Consignee.

## 7.2 Package Unloading

This section describes the package unloading operations, including the inspections, tests, and preparations of the package for unloading.

### 7.2.1 Receipt of Package from Carrier

*Special Equipment Required:* *Radioactive contamination detector, radiation survey meter*

*Special Controls or Precautions:* *None*

1. Before handling the package, the Consignee must have and understand the procedures for opening and unloading the package.

2. Perform a radiation survey of the package. If the external radiation levels exceed 200 mrem/h, then take the following steps:
   a) Notify the Consignor immediately.
   b) Investigate the cause of the high radiation levels before proceeding.
   c) Take extra precautions as necessary when proceeding with the remaining unloading steps.

3. Perform a contamination survey of the external surfaces of the package to determine if contamination has occurred during transit. If contamination levels exceed shipping release levels[3], then take the following steps.
   a) Notify the Consignor.
   b) Investigate the cause of the contamination.
   c) Decontaminate using distilled water or a mild decontamination agent.
   d) Take extra precautions as necessary before opening the package for unloading.

4. Assure that the tamper-indicating seal is intact. If it is NOT intact, investigate the cause and take actions per facility procedures.

5. Remove the tie-downs.

6. Transfer the package to the assembly area.

[3] Requirements for swiping and acceptance criteria are based on 49 CFR 173.443, or other applicable regulation.

### 7.2.2 Removal of Contents

*Special Equipment Required:* *Radioactive contamination detector, radiation survey meter*

*Special Controls or Precautions:* *Because the contents are highly radioactive, some loading operations are performed in a hot cell in accordance with facility procedures. DO NOT REMOVE THE SHIELD PLUG OF A LOADED CASK OUTSIDE THE HOT CELL. To avoid injury, CHECK THE EMPTY CASK FOR RADIATION AND CONTAMINATION PRIOR TO REMOVING THE SHIELD PLUG FOR INSPECTION AND PREPARATION FOR RETURN SHIPMENT (Step* 8*).*

1. Remove the overpack closure bolts and the overpack lid.
2. Remove the shield lid.
3. Lift the cask from the overpack base and transfer it to the hot cell using the two closure lid lifting points.
4. Remove the cask closure bolts and the closure lid.
5. Lift the shield plug (and payload, if applicable) from the cask body. If the payload internals are not mechanically attached to the bottom of the shield plug or if they do not lift out with the shield plug, then remove them from the cask cavity.
6. Process the payload in the hot cell in accordance with the Consignee's facility procedures.
7. Return the cask body, dunnage (if present), shield plug, closure lid, closure bolts, and shield lid to the assembly area. Process the payload internals in accordance with facility procedures.
8. Perform radiation and contamination surveys in accordance with facility procedures before proceeding to Section 7.3. Decontaminate as necessary in order to continue work.

## 7.3 Preparation of Empty Package for Transport

*Special Equipment Required:* *Radioactive contamination detector, radiation survey meter*

*Special Controls or Precautions:* *None*

1. Visually inspect the following components for damage that may have occurred during shipping and handling:
   - Overpack lid and base
   - Shield lid, closure lid, cask body, and shield plug
   - Overpack and cask closure bolts
   - Closure lid test port plug
   - Overpack base, cask body, closure lid, and shield plug threaded inserts

- Closure lid test port plug and shield plug payload container drilled and tapped holes

Notify the Consignor of any damage. Prepare damaged items for return shipment as instructed by the Consignor.

2. Visually inspect the containment, leak test, and cleanliness O-rings for scratches, blemishes, adhered particles, debris, etc. As needed, remove the O-ring(s) and gently wipe away any debris with a soft, clean cloth and clean, demineralized water. Notify the Consignor if any damaged or missing O-rings must be replaced. Prepare any damaged items for return shipment as instructed by the Consignor.

3. Perform a contamination survey of the internal surfaces of the package (cask cavity, cask flange, and underside of the closure lid) and any empty payload internals to be shipped. If the non-fixed surface contamination exceeds local requirements for empty package shipment, then decontaminate using distilled water or a mild decontamination agent.[4]

4. Carefully lower the shield plug into the cask body. Optionally, the empty product container(s) may be loaded if desired.

5. Install the closure lid onto the cask body with the alignment marks aligned.

6. Apply anti-seize coating as needed to the cask closure bolts and reinstall them.

7. Place the cask into the overpack base.

8. Install the shield lid onto the cask closure lid.

9. Install the overpack lid onto the overpack base with the alignment marks aligned.

10. Apply anti-seize coating as needed to the overpack closure bolts and install them.

11. Optional step: Attach the package to the shipping pallet using the package's lower lugs.

    *Note: The lower lugs may be used for attachment to a shipping pallet, or they may be used directly for securing the empty package. It is not necessary to render the lower lugs inoperable for use as lifting or tie-down devices.*

12. Assure that the package and shipping pallet are assembled correctly and are in unimpaired physical condition.

13. Transfer the package and its shipping pallet to the transport container/conveyance and connect its associated tie-downs.

[4] Internal contamination cannot exceed 100 times the limits in 49 CFR 173.443(a), or other applicable regulation.

14. Perform a contamination survey of the external surfaces of the package to determine if the surface contamination levels are as low as reasonably achievable. If the non-fixed surface contamination exceeds local requirements, then decontaminate using distilled water or a mild decontamination agent.[5]

15. Perform a radiation survey to confirm that the package is empty and meets the requirements for shipment of empty packagings.[6]

16. Release the package to the Carrier for the return shipment.

## 7.4 Other Operations

The package containment seal is a reusable, elastomeric O-ring, which is tested before each loaded shipment. This section provides the requirements for package pre-shipment leak rate testing. More sensitive leak testing procedures are necessary for certain maintenance activities as described in Section 8.2.

### 7.4.1 Pre-Shipment Leak Rate Test

Pre-shipment leak rate test is required before each Type B shipment of a loaded package to verify that the containment system is properly assembled for shipment. The following requirements of ANSI N14.5 [7.1] for pre-shipment leak rate testing procedure shall be met:

a) Testing method – Pressure Change Testing, by either Gas Pressure Drop, or Gas Pressure Rise method comparable to that described in ANSI N14.5 [7.1], Appendix A, Sections A.5.1 or A.5.2.

b) Acceptance Criteria – There shall be no detected leakage when tested to the required sensitivity below.

c) Sensitivity – The sensitivity shall be equal to or more sensitive than $1 \times 10^{-3}$ ref-$cm^3$ /s (air).

d) Leak Rate Test Procedures – Leak rate testing shall be performed in accordance with written procedures. Leak rate test procedures shall be qualified and approved by personnel whose qualifications and certification on the nondestructive method of leakage testing includes certification by a nationally recognized society at a level appropriate to the writing and/or review of leak rate test procedures.

e) Leak Rate Test Personnel- Leak rate testing shall be performed by personnel that are qualified and certified in accordance with the American Society of Non-Destructive Testing, Recommended Practice No. SNT-TC-1A [7.2] or alternative qualification/certification program by a nationally recognized society at a level appropriate for performing leak rate testing.

If containment closure does not satisfy the pre-shipment leakage rate test acceptance criteria, it shall be inspected, cleaned (if needed), reassembled, and retested prior to shipment.

[5] Requirements for swiping and acceptance criteria are based on 49 CFR 173.443, or other applicable regulation.

[6] Requirements for external radiation acceptance criteria are 0.5 mrem/hr based on 49 CFR 71.421(a)(2), as referenced in 49 CFR 71.428, or other applicable regulation.

## 7.5 Appendix

### 7.5.1 References

[7.1] ANSI N14.5, American National Standard for Radioactive Materials – *Leakage Tests on Packages for Shipment*, American National Standards Institute, 2014.

[7.2] Recommended Practice No. SNT-TC-1A, Personnel Qualification and Certification in Nondestructive Testing, American Society of Non-Destructive Testing, 2006 edition or later.

# 8 ACCEPTANCE TESTS AND MAINTENANCE PROGRAM

This chapter presents the acceptance tests and maintenance program for the MIDUS Package. These activities assure that the packaging meets the requirements of 10 CFR 71, Subpart G.

## 8.1 Acceptance Tests

This section describes the tests to be performed before the first use of each packaging. The acceptance tests confirm that each packaging is fabricated in accordance with the general arrangement drawings in the Certificate of Compliance.

### 8.1.1 Visual Inspections and Measurements

Packaging components shall receive visual and mechanical inspections to verify that the package has been fabricated and assembled in accordance with the general arrangement drawings in Section 1.3.2. The dimensions, tolerances, and surface finishes shown on the drawings shall be verified by measurement on each package. Nonconforming components shall be reworked or replaced.

### 8.1.2 Weld Examinations

All package welds shall be examined to the requirements in drawings TYC01-1602 and TYC01-1603 (included in Section 1.3.2). Nonconforming components shall be reworked or rejected.

All brazed joints shall be visually examined on all accessible surfaces to determine whether there has been adequate flow of brazing metal between the thermal spider and overpack shells. Nonconforming components shall be reworked or rejected.

### 8.1.3 Structural and Pressure Tests

A pressure test shall be performed on each package to verify the capability of the containment system to maintain its structural integrity at the test pressure. The test will be performed per ASME BPVC, Subsection WB [8.1], to a pressure of 1050 kPa (150% of the package MNOP). The acceptance criteria is no unacceptable leakage, in accordance with WB-6224. Nonconforming packages shall be reworked or rejected.

### 8.1.4 Leakage Tests

For packaging fabricated prior to January 1, 2022, the packaging containment boundary, defined in Section 4.1, shall be leak rate tested in accordance with Section 8 of ANSI N14.5 [8.2] to an acceptance criterion of $1 \times 10^{-7}$ ref-cm$^3$/s (air). Leak rate testing shall be performed using the Evacuated Envelope-Gas Detector method of ANSI N14.5, Section A.5.4, using a test procedure sensitivity of $5 \times 10^{-8}$ ref-cm$^3$/s (air) or more sensitive.

For packaging fabricated after January 1, 2022, the packaging containment boundary, defined in Section 4.1, shall be leak rate tested in accordance with Section 8 of ANSI N14.5 [8.3] to an acceptance criterion of $1 \times 10^{-7}$ ref-cm$^3$/s (air) with required test procedure sensitivity of $5 \times 10^{-8}$ ref-cm$^3$/s (air) or more sensitive. Leak rate testing shall be performed using Gas Filled Envelope (gas detector) and/or Evacuated Envelope (gas detector) methods comparable to that described in ANSI N14.5, Appendix A, Sections A.5.3 and/or A.5.4.

Leak rate testing shall be performed in accordance with written procedures. Leak rate test procedures shall be qualified and approved by personnel whose qualifications and certification on the nondestructive method of leakage testing includes certification by a nationally recognized society at a level appropriate to the writing and/or review of leak rate test procedures.

Leak rate testing shall be performed by personnel that are qualified and certified in accordance with the American Society of Non-Destructive Testing, Recommended Practice No. SNT-TC-1A [8.4] or alternative qualification/certification program by a nationally recognized society at a level appropriate for performing leak rate testing.

Packages not meeting the acceptance criteria shall be reworked or rejected.

### 8.1.5 Component and Material Tests

#### 8.1.5.1 Package Weight

The packaging shall be weighed to determine that it does not exceed 329 kg, such that the total weight of the package including the payload does not exceed the maximum specified weight of 330 kg. Nonconforming packages shall be reworked or rejected.

#### 8.1.5.2 Shield Plug Fit Up

The shield plug shall be visually or mechanically inspected to assure proper fit up. Without the cleanliness O-ring in place, the inspection shall determine that the top of the shield plug is below the plane of the cask flange. With the cleanliness O-ring in place, the inspection shall determine that the top of the shield plug is above the plane of the cask flange. Assemblies not meeting the acceptance criteria shall be reworked or rejected.

#### 8.1.5.3 Overpack Foam

Each batch of overpack foam shall be tested for the following attributes:

- Average density
- Static crush strength
- Flame retardancy
- Intumescence

Foam not meeting the acceptance criteria in drawings TYC01-1607 and TYC-1608 (included in Section 1.3.2) shall be rejected.

#### 8.1.5.4 Depleted Uranium

The density of depleted uranium (DU) components shall be determined by measuring their weight and volume. The chemical composition of each DU heat will be analyzed to assure that the alloy meets the specifications. Finished DU components shall be visually examined to verify that their surfaces are free of voids, cracks, or porosity. DU components not meeting the acceptance criteria in drawing TYC01-1606 (included in Section 1.3.2) shall be rejected.

### 8.1.6 Shielding Tests

Section 8.1.5 discusses the material tests for the DU parts.

### 8.1.7 Thermal Tests

Section 8.1.5 discusses the material tests for the overpack foam. The material tests provide assurance that the material will perform under NCT and HAC conditions. Section 8.1.2 describes the examination of the overpack thermal spider brazing. The function of the thermal shunt is to balance the heat rejection (i.e., provide a similar heat transfer path as provided by the overpack flange). Because of the package's low heat load (less than 18 watts peak) and the large design margins on allowable material temperatures (Table 3-1, Table 3-2), no additional thermal test are necessary.

### 8.1.8 Miscellaneous Tests

Not applicable.

## 8.2 Maintenance Program

Table 8-1 summarizes the MIDUS maintenance program. The program includes periodic inspections, tests, and maintenance activities designed to ensure continued performance of the packaging. This section describes the periodic testing, inspection, and replacement schedules, as well as the criteria for replacement and repair of components and subsystems on an as-needed basis.

### 8.2.1 Structural and Pressure Tests

There are no routine structural or pressure tests required for the package. This includes the replacement of cask closure bolts or cask bolting flange threaded inserts as exempted by ASME BPVC, Section III, Division 3, Subsection WB, Paragraph WB-6111. Replacement requirements for threaded components or inserts are presented in Section 8.2.3.

### 8.2.2 Periodic and Maintenance Leak Test

Each Type B radioactive material shipment shall be made with a containment seal that has been replaced and has had periodic leak rate testing performed within the 12 months prior to shipment as described in ANSI N14.5 [8.3]. In addition, leak test is required when the following maintenance activities occur:

- Replacement of the containment seal
- Repair of the containment seal sealing surface, including the O-ring gland surface, or the cask closure lid sealing surface
- Repair or replacement of the shield plug or closure lid

The following requirements of ANSI N14.5 [8.3] for periodic/maintenance leak testing procedure shall be met:

a) Testing method – Gas Filled Envelope (gas detector) or Evacuated Envelope (gas detector) methods comparable to that described in ANSI N14.5 [8.3], Appendix A, Sections A.5.3 and/or A.5.4.

b) Acceptance Criteria – The acceptance criteria shall be equivalent to $1 \times 10^{-7}$ ref-cm$^3$ /s (air).

c) Sensitivity –The test shall be sensitive to the equivalent of $5 \times 10^{-8}$ ref-cm$^3$ /s (air) or more sensitive.

d) Leak Rate Test Procedures – Leak rate testing shall be performed in accordance with written procedures. Leak rate test procedures shall be qualified and approved by personnel whose qualifications and certification on the nondestructive method of leakage testing includes certification by a nationally recognized society at a level appropriate to the writing and/or review of leakage rate test procedures.

e) Leak Rate Test Personnel- Leak rate testing shall be performed by personnel that are qualified and certified in accordance with the American Society of Non-Destructive Testing,

Recommended Practice No. SNT-TC-1A [8.4] or alternative qualification/certification program by a nationally recognized society at a level appropriate for performing leak rate testing.

If the containment closure does not satisfy the periodic/maintenance leak rate test acceptance criteria, it shall be inspected, cleaned (if needed), reassembled, and retested.

### 8.2.3 Component and Material Tests

The following sections describe the periodic maintenance program for package operation. Additional maintenance may be required on an as-needed basis when wear or damage is noted during routine operations. When as-needed maintenance is performed, the associated repair, replacement, and records-keeping activities shall follow the maintenance program requirements for the corresponding periodic maintenance activity.

#### 8.2.3.1 O-ring Seals

The following O-ring seals shall be replaced annually, or as needed, with seals as specified in the general arrangement drawings in Section 1.3.2. The replacements shall be recorded in the packaging maintenance log.

- Containment O-ring
- Leak Test O-ring
- Leak Test port plug O-ring

Cleanliness O-rings are replaced with every shipment and therefore do not require annual replacement.

#### 8.2.3.2 Sealing Surfaces

The following O-ring sealing surfaces shall be inspected annually for damage and wear. If sealing surfaces show damage or wear in excess of the surface finish requirements specified in the general arrangement drawings in Section 1.3.2, then the damage may be repaired using emery cloth or a similar polishing agent to return the surface to the specifications in the drawings. The inspection results, and any necessary repairs, shall be recorded in the packaging maintenance log. The annual sealing surface inspection shall include, as a minimum, the following surfaces:

- Containment seal groove sealing surfaces (bottom and outside diameter of groove)
- Containment seal contact surface on the cask closure lid

#### 8.2.3.3 Fasteners

All package fasteners shall be visually inspected annually for excessive wear or damage. Fasteners which show visible signs of excessive wear or damage shall be replaced in accordance with the specifications in the general arrangement drawings in Section 1.3.2. The inspection

results, and any necessary replacements, shall be recorded in the packaging maintenance log. The fasteners to be inspected include:

- Cask closure bolts
- Shield lid attachment bolts
- Test port plug
- Overpack closure bolts

Fastener holes with threaded inserts shall be visually inspected annually for excessive wear or damage. Threaded inserts which show visible signs of excessive wear or damage shall be replaced in accordance with the specifications in the general arrangement drawings in Section 1.3.2. The threaded inserts at the following locations shall be inspected:

- Cask closure bolts
- Shield lid attachment bolts
- Cask lifting attachment points
- Shield plug lift point
- Overpack closure bolts

The inspection results, and any necessary replacements, shall be recorded in the packaging maintenance log.

When inspections reveal mild damage or wear to threaded fasteners or tapped holes, repairs may be performed as follows. Barbs may be removed, taking care not to further damage the threads. Threads may be refurbished using taps and dies specifically intended for thread chasing or repair.

When inspections reveal more significant damage to threaded fasteners, or threaded inserts, they shall be replaced according to the specifications in the general arrangement drawings in Section 1.3.2 and the manufacturer's instructions. Replacements shall be noted in the package's maintenance log. The associated assemblies shall be functionally tested to confirm proper fit and function.

Tapped holes for threaded inserts may be refurbished using the manufacturer's thread repair tools. Tapped holes without threaded inserts may be refurbished using taps specifically intended for thread chasing or repair.

The overpack thermal relief plugs shall be visually inspected for damage, wear, or weathering of the nylon material, threads, and elastomeric weather seals. Damaged or missing thermal relief plugs or O-rings shall be replaced according to the specifications in the general arrangement drawings in Section 1.3.2. The inspection results, and any necessary replacements, shall be recorded in the packaging maintenance log.

The overpack locating pins shall be visually inspected annually for damage. Damaged or missing locating pins shall be repaired or replaced. The inspection results, and any necessary replacements or repairs, shall be recorded in the packaging maintenance log.

#### 8.2.3.4 Package Visual Inspections

Chapter 7 describes the requirements for visual inspections of the packaging during each phase of operation. As permitted by §71.87(b), their physical condition may contain superficial defects such as marks and dents that do not impair the operation of the components.

Superficial polishing of package components may be performed using emery cloth or a similar fine abrasive to remove corrosion, scratches, blemishes, adhered material/particles, etc.

The following replacement and repair tasks shall be evaluated and approved by the Certificate Holder/Designer prior to implementation:

- Any change to the configuration of the package as shown in the general arrangement drawings in Section 1.3.2
- Any metal removal that reduces the thickness of a containment, structural, shielding, or thermal component below its licensed dimension including all tolerances as shown in the general arrangement drawings in Certificate of Compliance
- Any welding repair
- Any re-tapping of a hole to accommodate a larger threaded component
- Mechanical straightening the overpack lugs or opening a damaged lug eye

Each package shall be visually inspected annually, and the results shall be noted in the package's maintenance log confirming:

- General condition of packaging (significant scratches, marks, or dents)
- Identification numbers of cask body, shield plug, closure lid, shield lid, overpack base, and overpack lid for configuration control
- Legibility of the nameplate information

### 8.2.4 Thermal Tests

Not applicable.

### 8.2.5 Miscellaneous Tests

The following subsections discuss the requirements following replacement of package components. These requirements apply to newly manufactured components (spares), or substituted components from other MIDUS packages. For the purpose of configuration management, the overpack base unit is the host component because it bears the package nameplate. Other components may be substituted following these procedures.

#### 8.2.5.1 Replacement of a Shield lid

In the event that a shield lid must be replaced, the replacement shall be noted in the package's maintenance log.

#### 8.2.5.2 Replacement of a Closure Lid

In the event that a closure lid must be replaced, a maintenance leak rate test shall be performed in accordance with Section 8.1.4 above. The replacement shall be noted in the package's maintenance log along with the test results.

#### 8.2.5.3 Replacement of a Shield Plug

In the event that a shield plug must be replaced, the functional fit-up tests described in 8.1.5.2 shall be performed to assure proper operation. The replacement shall be noted in the package's maintenance log along with the inspection results.

#### 8.2.5.4 Replacement of a Cask Body

In the event that a cask body must be replaced, the steps in Sections 8.2.5.2 and 8.2.5.3 shall be performed to assure proper fit-up of the closure lid and shield plug. A maintenance leak rate test shall be performed in accordance with Section 8.1.4 above. The replacement shall be noted in the package's maintenance log along with the test and inspection results.

#### 8.2.5.5 Replacement of an Overpack Lid

In the event that an overpack lid must be replaced, the replacement shall be noted in the package's maintenance log.

#### 8.2.5.6 Replacement of a Cask Assembly

In the event that an entire cask assembly (cask body, shield plug, closure lid, and shield lid) must be substituted, the replacement shall be noted in the package's maintenance log. The substitute cask assembly must either be a unit currently in service, or another unit manufactured or refurbished to the requirements shown in the general arrangement drawings in Section 1.3.2.

**Table 8-1 – Package Maintenance Program Summary**

| Item | SAR Section[2] | Inspection/Test/Maintenance[1] | | |
|---|---|---|---|---|
| | | Each Use | Replace / Repair[3] | Annual |
| Containment O-ring | 8.2.3.1 | V, LT1 | LT2 | R, LT2 |
| Containment O-ring sealing surfaces | 8.2.3.2 | V | LT2 | V |
| Leak Test O-ring | 8.2.3.1 | V | | R |
| Leak Test O-ring sealing surfaces | 8.2.3.2 | V | | V |
| Cleanliness O-ring | 8.2.3.1 | R | | |
| Cleanliness O-ring sealing surfaces | -- | V | | V |
| Thermal relief plugs and hole threads | 8.2.3.3 | | | V |
| Thermal relief plug O-rings | 8.2.3.3 | | | V |
| Cask closure bolts | 8.2.3.3 | V | | V |
| Threaded inserts-cask closure bolts | 8.2.3.3 | | LT2 | V |
| Shield lid attachment bolts | 8.2.3.3 | V | | V |
| Threaded inserts-shield lid bolts | 8.2.3.3 | | | V |
| Tapped holes[4] | 8.2.3.3 | | | |
| Test port plug | 8.2.3.3 | V | | V |
| Test port plug O-ring | 8.2.3.1 | V | | V |
| Threaded insert-shield plug lift point | 8.2.3.3 | | | V |
| Threaded inserts-cask lid lift points | 8.2.3.3 | | | V |
| Overpack closure bolts | 8.2.3.3 | V | | V |
| Threaded inserts-overpack bolts | 8.2.3.3 | | | V |
| Overpack locating pins | 8.2.3.3 | | | V |
| Nameplate | 8.2.3.4 | | | V |

Notes:
1. R = Replace, V = Visual Inspection,
   LT1 = Pre-shipment leak test (Section 7.4.1),
   LT2 = maintenance/periodic leak test (Section 8.2.2).
2. Reference SAR section.
3. Tests or inspections necessary when replacement or repair as needed.
4. Tapped holes without threaded inserts: shield plug bottom, and test port

## 8.3 Appendix

### 8.3.1 References

[8.1] American Society of Mechanical Engineers (ASME) Boiler and Pressure Vessel Code (BPVC), Section III, Division 3, Subsection WB, Class TP (Type B) Containment, 2001 Edition with Addenda through July 1, 2003.

[8.2] ANSI N14.5, American National Standard for Radioactive Materials – *Leakage Tests on Packages for Shipment*, American National Standards Institute, 1997.

[8.3] ANSI N14.5, American National Standard for Radioactive Materials – *Leakage Tests on Packages for Shipment*, American National Standards Institute, 2014.

[8.4] Recommended Practice No. SNT-TC-1A, Personnel Qualification and Certification in Nondestructive Testing, American Society of Non-Destructive Testing, 2006 edition or later.

# 9 EVALUATION OF CONTENT #02

This SAR addendum describes the evaluation of the MIDUS package for Content #02.

## 9.1 Content #02 – General Information

Content #02 is a solid payload, or product, consisting of $^{99}$Mo with its daughter products as solid metallic molybdenum. This payload is non-fissile and does not generate neutrons. The specification for Content #02 is provided on Drawing No. TYC01-1601 in Section 1.3.2 and discussed below.

The maximum product activity is 4,400 Ci of $^{99}$Mo at the time of shipment. The maximum product *specific* activity is limited to 60 Ci/ml $^{99}$Mo at the time of shipment. The specific activity affects the concentration of the potential radiological source terms for HAC, in the event that molybdenum powder or fines were to migrate within the containment boundary. Both the activity and specific activity specifications are the same as for Content #01.

The product is solid and does not generate gas by radiolytic decomposition.

The maximum mass of the product and payload internals shall not exceed 1.0 kg.

The contents volume is not restricted because there are no sources of radiolytic decomposition that would result in gas generation. Sections 9.2 and 9.3 further discuss package pressures.

The package materials of construction have been evaluated and are compatible with the chemical form of the product and payload internals. Section 9.2 discusses the materials evaluation in further detail.

The payload internals are provided by the user and include sealed aluminum target cans (which contain the irradiated molybdenum disks), and aluminum carriers. Figure 9-1 shows a typical configuration.

The $^{98}$Mo target material is prepared in the form of high-purity metallic disks, placed in dry, thin-walled, close-fitting aluminum target cans, which are seal-welded and then leak tested prior to irradiation. After irradiation, $^{99}$Mo and its daughter product $^{99m}$Tc are the only significant activation sources. There are several configurations of target cans (containing various quantities of disks) and carriers to suit the requirements for particular shipments. No containment or other safety credit is taken for the target cans.

The carrier is constructed from aluminum and serves as a hot-cell handling aid during the cask loading and unloading processes, and as dunnage during shipment. There is no safety credit taken for the presence of the aluminum carriers.

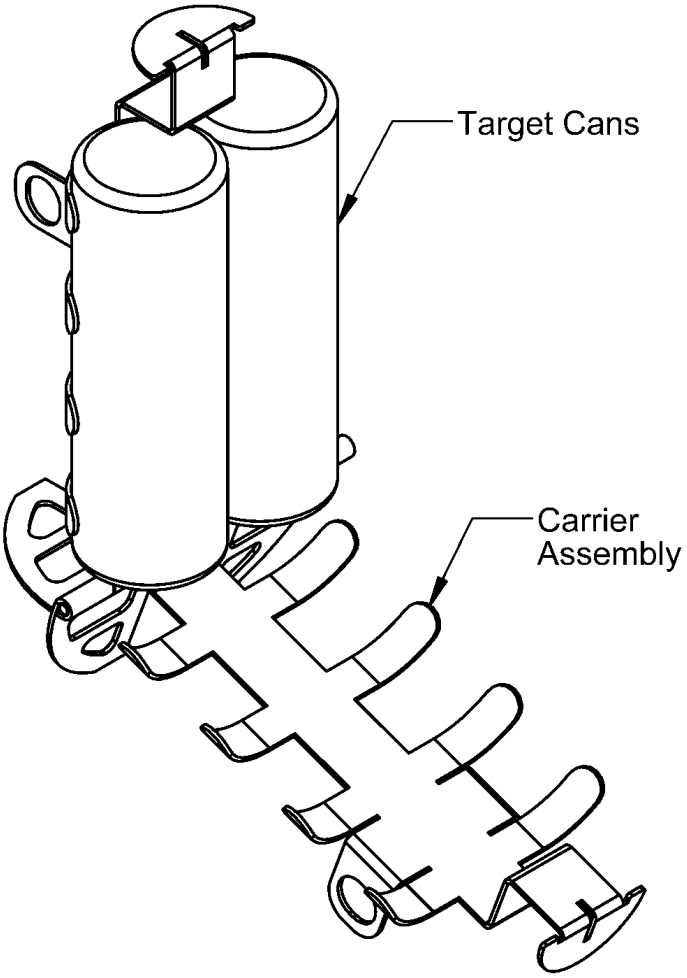


**Figure 9-1 – Content #02 Payload Internals**

## 9.2 Content #02 – Structural Evaluation

The structural evaluation in Chapter 2 bounds Content #02 based on the comparison of the structural analysis inputs for the Content #02 (i.e., mass, internal pressure, and temperature) to those used in the baseline structural analysis.

The total mass of the product and product containers for Content #02 is limited to 1.0 kg, which is less than the 1.1 kg payload mass assumed in the base structural analysis. Furthermore, the base structural analysis takes no credit for structural support provided by the product containers, and instead conservatively applies the inertia loading from the payload as pressure on the supporting cavity surfaces. Therefore, the applied loads used in the base structural analysis to account for the payload are bounding for Content #02.

As discussed in Section 9.3, the package temperatures and internal pressures for Content #02 are bounded by the baseline design. Therefore, the temperature and internal pressure loads used in the base structural analysis are bounding for content #02.

Since the inputs used in the baseline structural analysis for the contents (i.e., mass, internal pressure, and temperature) all bound those for Content #02, the stress results of the baseline structural analysis are also bounding for Content #02.

Content #02 includes metallic molybdenum and aluminum, which were not evaluated previously in Chapter 2 for compatibility with the package materials of construction. Neither the aluminum target cans nor the metallic molybdenum disks will result in significant chemical, galvanic, or other reactions with gas production or corrosion potential because of the favorable galvanic potentials and lack of aqueous environment in the containment cavity.

## 9.3 Content #02 – Thermal Evaluation

The thermal analysis in Chapter 3 was based on an initial thermal power resulting from 4,500 Ci of $^{99}$Mo. The maximum activity of Content #02 is 4,400 Ci of $^{99}$Mo. Because content #02 has a lower allowable number of Curies than was used for the analyses in Chapter 3, the package temperatures for Content #02 will be bounded by those from the baseline thermal analysis.

The package internal pressure loads for NCT and HAC are calculated in Chapter 3 for the highest bulk average temperature of the gases within the containment system for Content #01 considering gas generation due to radiolysis of the liquid payload. But radiolytic gas generation does not occur in Content #02 because the form is solid, metallic molybdenum. The package pressures for Content #02 will therefore be significantly lower than predicted in Chapter 3.

Because content #02 has a lower initial thermal power than that used in the base thermal analysis and it does not generate gas due to radiolysis, it is concluded that the package temperatures and internal pressures for Content #02 will be bounded by the baseline thermal analyses in Chapter 3.

## 9.4 Content #02 –Containment Evaluation

Chapter 4 describes that the package is designed to a "leak-tight" containment criterion per ANSI N14.5 [4.3], therefore the containment criterion is $10^{-7}$ ref-cm$^3$/s and is not dependent on the source specification. Content #02 is therefore bounded by the baseline design discussed in Chapter 4.

## 9.5 Content #02 – Shielding Evaluation

### 9.5.1 Source Specification

Section 5.2.1 discusses the photon source term calculations, including all significant equilibrium daughter products. Because Content #02 has the same source specification as the baseline liquid payload, the source terms are identical.

#### 9.5.1.1 Evaluation of Metallic Form

The baseline shielding analysis described in Chapter 5 was performed for 4,500 Ci of Mo-99 (plus $^{99m}$Tc in full equilibrium) in an aqueous solution that was modeled as water for shielding purposes. An MCNP model was run to determine whether Content #02 is bounded by the baseline shielding analysis. The liquid $^{99}$Mo source in a representative NCT MIDUS shielding model was substituted with the solid molybdenum source in Content #02. Like the baseline Content #01, the Content #02 payload is limited to 60 Ci/ml maximum specific activity, therefore the smallest possible amount of self-shielding is present when the volume of molybdenum metal is 4,500 Ci / 60 Ci/ml = 75 ml. This corresponds to a sphere of molybdenum with a radius of 2.62 cm (Figure 9-2), the same as radius of the liquid source. No changes were made to the other model parameters, including source terms and importance biasing.

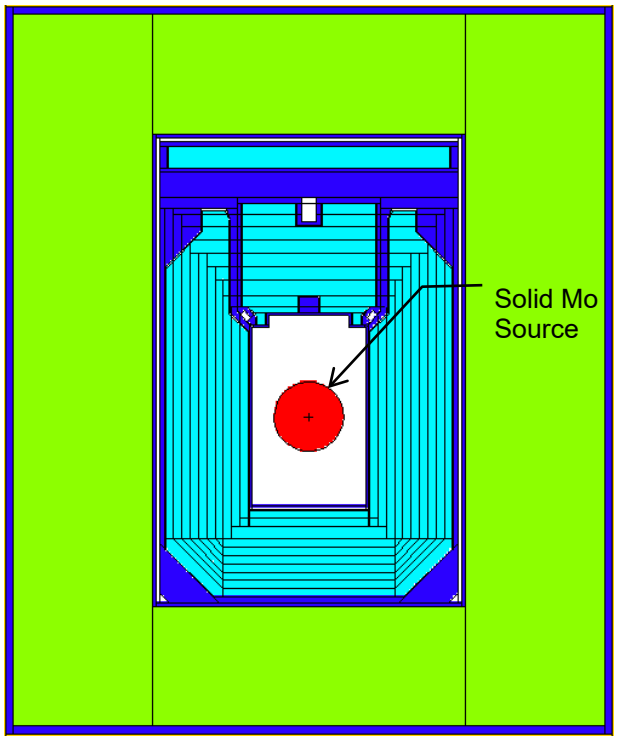


**Figure 9-2 – Solid Source MCNP Model**

The calculation was performed using MCNP5, v.1.51 and the MCPLIB84 cross section data library for photon transport[7]. At the two highest package exposure rate locations (the radial and bottom surfaces), the resulting photon exposure rates were less than one-half of those for the baseline liquid payload analyzed in Chapter 5.

[7] LA-UR- 00-3581, "Electron Upgrade for MCNP4B," Los Alamos National Laboratory.

Due to the increased attenuation in the metallic source region, the package dose rates for Content #02 are well bounded by the baseline evaluation in Chapter 5. There is an additional margin of conservatism since the $^{99}$Mo activity specification for Content #02 is 4,400 Ci, versus the 4,500 Ci analyzed in Chapter 5.

### 9.5.1.2 Evaluation of Bremsstrahlung Radiation

Bremsstrahlung radiation is x-ray or gamma radiation caused by betas or electrons during the stopping process. The production of bremsstrahlung radiation is known to increase with the atomic number of the attenuating medium. Since the atomic number of molybdenum (Z=42) is greater than the constituents of the Content #01 $^{99}$Mo solution (Z= 1, 7, 8, 11), there is a possibility that bremsstrahlung radiation could be a significant contributor to package dose rates for Content #2.

An MCNP model was prepared to investigate whether bremsstrahlung radiation might be a significant contributor for Content #02. The model described in Section 9.5.1.1 was modified for electron transport using the 'mode' card in MCNP. Beta and electron emission data for 4,500 Ci of $^{99}$Mo plus equilibrium daughters were input as source terms. $^{99}$Mo and $^{99m}$Tc produce relatively low-energy beta-rays and electrons, with most of the power resulting from the $^{99}$Mo beta with $E_{avg}$ = 442.9 keV. Betas from the $^{99m}$Tc and $^{99}$Tc decays were neglected because of their low energies, small branching ratio (0.0037 for $^{99m}$Tc) and very long half life (200,000 years for $^{99}$Tc).The bremsstrahlung photon production was biased using the MCNP 'bbrem' card, and the beta/electron sources were biased by their energy levels.

The calculated bremsstrahlung exposure rate at the package radial surface was 0.05 mrem/hr, or 0.07% of the corresponding primary gamma exposure rate from the model described in Section 9.5.1.1. By comparison, 4,400 Ci is 2.2% less than 4,500 Ci, and the Content #02 package exposure rates are expected to be less 50% of the baseline liquid payload analyzed in Chapter 5. Bremsstrahlung production is therefore not a significant contributor in Content #02.

## 9.6 Content #02 – Criticality Evaluation

Not applicable.

## 9.7 Content #02 – Operating Procedures

The operating procedures for the package with content #02 are the same as described in Chapter 7.

## 9.8 Content #02 – Acceptance Tests and Maintenance Program

The acceptance tests and maintenance program for the package with Content #02 are the same as described in Chapter 8.